The University of Nottingham

School of the Built Environment

A Theoretical and Experimental Investigation of Jet-Pump Refrigeration system

By

Ali E. Ablwaifa
BSc., MSc.

Thesis submitted to the University of Nottingham for the degree of Doctor of Philosophy

May 2006

Abstract

This thesis describes a theoretical and experimental investigation of the jet-pump refrigerator, and the application of Computational Fluid Dynamics (CFD) to improve the performance of the jet-pump, which lies at its heart.

Within this thesis a number of new studies aimed at improving the COP of jet-pump refrigerators are carried out. These include an investigation of a novel jet-pump design methodology, (the Constant Rate of Momentum Change method), the application of CFD in the design of jet-pumps, the experimental testing of two new refrigerant fluids and finally, a comparative experimental investigation of performance benefits resulting from two cycle improvements that had not been tested before - these are the introduction of (i) a pre-heater (or recuperator) between the jet-pump and condenser, to preheat the liquid flow to the vapour generator, and (ii) a pre-cooler (or economiser) in the suction line between the evaporator and jet-pump, in order to sub-cool the liquid refrigerant in the line between the condenser and evaporator.

Literature studies of jet-pump refrigerator technology and jet-pump design methodology are reviewed and discussed. A CFD model has been developed, assessed and validated against given experimental data. Simulations of a jet-pump that is part of a jet-pump refrigerator cycle was carried out to investigate the refrigerant flow structure and to assess the dominant influence of operating conditions and geometry. The validated CFD code was then used to optimize the design of the jet-pump for two new refrigerants (R236fa and R245fa). The resulting optimized jet-pumps were manufactured and tested experimentally over a wide range of operating conditions, using an adaptable test rig that was purpose-developed as part of this research work.

Detailed experimental studies were carried out. All the experimentally determined results were compared to the CFD predicted values, and these showed good agreement for all the jet-pumps tested. These results showed that CFD has the potential to be an effective and powerful tool for simulating and optimising jet-pumps. The results also show that the jet-pump refrigerator should be considered if sources of low-grade heat are available.

Acknowledgements

During my study at Nottingham University in the School of the Built Environment, I received a lot of support and help from many people, who I would like to thank. The first is my supervisor Professor Ian Eames, who introduced the jet-pump refrigerator to me and guided me in the right way from the very first. His effort, encouragement, and guidance were generous throughout. He created an excellent research environment from which I benefited. The second person I wish to thank is Professor Volodymye Petrenko, who gave me his generous expert advice on jet-pump technology and for his help in the experimental part. I would also like to thank Dr Mohamed Gadi for his help and support.

I wish to thank Mr. David Oliver for his technical skill and patient support, which he has given me. I would also like to thank the other technical staff, particularly Mr Dave Taylor, Mr Jonathan Moss and Mr Bob Clarke for their technical assistance over whole period of experimental work.

I also wish to thank Dr Fathi Aboud from The Mechanical Engineering Department, for his help in quantifying and measuring of some of experimental components.

I also would like to express my sincere gratitude to the CANMET (Energy Technology Centre - Canada) for their financial support. In particular I would like to thank Mr. Brandon, who visited the research project and offered guidance for several interesting parts of the experimental study. Also, sincere appreciation to my Government, which provided me a scholarship for part of my time at Nottingham.

Finally, I wish to express my sincere thanks to all my family, particularly my wife for her great encouragement and support to achieve my goal.

Ali Ablwaifa, ...2006

Table of Contents

Abstract i
Acknowledgment ii
Table of Contents iii
List of Figures vii
List of Tables xii
Nomenclature xiv

Chapter 1. Introduction 1

1.1 Preamble 1
1.2 Description of the Jet-pump Refrigeration System 2
1.3 Historical Context 3
1.4 Jet-pump Performance 4
1.5 Thesis Content 5
1.6 Thesis Structure 6
1.7 Conclusion 8

Chapter 2. Past Research on Jet-pump Refrigeration System and Jet-pump Theory ..9

2.1 Introduction 9
2.2 Jet-Pumps 9
2.3 Jet-pump Design (The Theory) 10
2.4 Previous Work on Steam Jet-pump Refrigeration Systems 13
2.5 Previous Work on Jet-pump Refrigeration System with Low Boiling Refrigerants 17
2.6 Solar Jet-pump Refrigeration System 21
2.7 Hybrid-Novel Jet-pump-absorption Refrigeration System 23
2.8 Enhancement of the Jet-pump Refrigeration System 24
2.9 Jet-pump Irreversibility and CRMC Jet-pump 26
2.10 Working Fluids 27
2.11 CFD Studies on Jet-pump Performance 30
2.12 Conclusion 33

Chapter 3. Constant Rate of Momentum Change Method " CRMC" and Computational Fluid Dynamics (CFD) Simulation 34

3.1 Introduction 34
3.2 Jet-pump Design Analysis “One-Dimensional analysis” 34
3.2.1 Assumptions Made in the One-dimensional Analysis 35
3.2.2 Primary Nozzle Design 36
3.2.2.1 Flow Conditions at Nozzle Throat 36
3.2.2.2 Flow Conditions at the Nozzle Exit 37
3.2.3 Diffuser Section Design 38

3.2.3.1 Mixing Section 38
3.2.3.2 Thermodynamic Shock Process 40
3.2.3.3 Sub-sonic Diffuser Section 41
3.2.4 Data Acquisition 42
3.2.5 Method of Solution and Design 43
3.3 The Theory of CRMC Design method 43
3.3.1 The CRMC Assumption 44
3.3.2 Entrainment Region Boundary 45
3.3.3 Diffuser Section 45
3.3.4 Determining the Diffuser Length LD 45
3.3.5 Entrainment Region Coordinates 47
3.4 CFD Modelling 49
3.4.1 CFD Uncertainly 51
3.4.1.1 Uncertainty and Errors in Computational Fluid Dynamics 51
3.4.2 Jet-pump Geometry 53
3.4.3 Computational Mesh 54
3.4.3.1 Mesh Adaption 58
3.4.4 Turbulence Modelling 59
3.4.5 Physical Properties 63
3.4.6 Optimised Numeric for CFD Code 64
3.5 CFD validation 66
3.5.1 Comparison Between CFD and Experimental Results 66
3.5.1.1 Mass Flow Through the Primary Nozzle 66
3.5.1.2 Comparison of Critical Condenser Pressure 67
3.5.1.3 Comparison of Maximum Entrainment Ratio 68
3.5.2 Parametric Study 69
3.5.2.1 Effect of the Nozzle Position on the Jet-pump Performance 69
3.5.2.2 Effect of Operating Conditions 71
3.6 Conclusion 81

Chapter 4. Conventional and CRMC Jet-pump Desing with CFD Optimization.....83

4.1 Introduction 83
4.2 Using R236fa as the working fluid 83
4.2.1 R236fa Conventional Jet-pump 84
4.2.1.1 R236fa Conventional Jet-pump CFD Simulation "design and off-design operating conditions 85
4.2.2 CFD Optimised R236fa Conventional Jet-pump 86
4.2.2.1 CFD Optimised R236fa Conventional Jet-pump "off-design operating conditions" 88
4.2.3 R236fa CRMC Jet-pump 89
4.2.3.1 R236fa CRMC Diffuser CFD Simulation (design operating conditions) 90
4.2.4 CFD Optimized R236fa CRMC Diffuser 90
4.2.4.1 CFD Optimized R236fa CRMC Jet-pump "off-design operation conditions" 93
4.3 Using R245fa as the working Fluid 93
4.3.1 R245fa Conventional Jet-pump 93
4.3.1.1 R245fa Conventional Jet-pump CFD Simulation (design operating conditions) 95
4.3.2 CFD Optimised R245fa Conventional Jet-pump 96

4.3.2.1 CFD Optimised R245fa Conventional Jet-pump "off-design operating condition" 98
4.3.2.2 Optimised R245fa Conventional Jet-pump "New design conditions" 98
4.3.2.3 Optimised R245fa Conventional Diffuser With Two New Nozzles 99
4.3.3 R245fa CRMC Jet-pump 100
4.3.3.1 R245fa CRMC Jet-pump CFD Simulation "design operating conditions" ... 101
4.3.3.2 CFD Optimized R245fa CRMC Jet-pump Diffuser C "off-design operating condition" 103
4.4 Discussion on CFD Optimisation 104
4.5 Conclusion 110

Chapter 5. Design and Manufacture of the Experimental Jet-pump refrigerator...111

5.1 Introduction 111
5.2 Experimental Apparatus: Design and Construction 111
5.2.1 The Steam Boiler 114
5.2.2 The Evaporator 114
5.2.3 The Condenser 116
5.2.4 The Generator 116
5.2.5 The Separator 117
5.2.6 The Generator Feed Pump 117
5.2.7 The Jet-pump 119
5.2.7.1 Cutting Tools for R236fa Conventional Jet-pump 120
5.2.7.2 Cutting Tools for Optimized R236fa CRMC Jet-pump 121
5.2.7.3 Cutting Tools for Optimized R245fa Conventional Jet-pump (Diffuser and primary nozzle) 123
5.2.7.4 Cutting Tools for The Optimized CRMC R245fa Jet-pump 124
5.3 Other Components 126
5.3.1 The Pre-Cooler and the Recuperator 126
5.3.2 Thermal Insulation 126
5.3.3 Instrumentation and control 126
5.4 Pressure Test and Leak Detection 133
5.5 Commissioning of the Experimental Rig 133
5.6 Heat Balance Test 134
5.7 Experimental Rig Troubleshooting 135
5.8 Conclusion 137

Chapter 6. Experimental Studies of R236fa and R245fa Jet-pumps 139

6.1 Introduction 139
6.2 Experimental Method 139
6.3 Experimental Results 142
6.3.1 Calibration of Primary Nozzles 142
6.3.2 Optimal Nozzle Exit Position "NXP" 143
6.3.3 R236fa and R245fa Jet-pumps (with Design and Off-design Operating Conditions) 145
6.3.4 The Effect of Using Regeneration Unit (RG) (pre-cooler and recuperator) 152
6.3.5 Evaluation the R236fa Jet-pumps Performance Using Thermodynamic Data 155
6.4 Comparison of CFD and Experimental Results 157
6.5 Effect of Primary Nozzle Geometry 162

6.6 Experimental Data with Real-gas Modelling.....164
6.7 Conventional and CRMC Jet-pumps Performance.....166
6.8 R236fa and R245fa Performance.....168
6.9 Conclusion.....170

Chapter 7. Discussion, Conclusions and Recommendations.....172

7.1 Discussion.....172
7.2 Conclusions.....176
7.3 Recommendations.....180

References.....182

Appendices.....191

Appendix A: Working Fluid Thermodynamics Properties.....191
Appendix B: Realized CFD code setup.....195
Appendix C: Computational Mesh.....210
Appendix D: Experimental Jet-pump Assembly.....218
Appendix E: CFD and Experimental Results.....226

List of Figures

Figures of Chapter 1

Figure 1.1 A schematic representation of jet-pump refrigeration system 2
Figure 1.2 A schematic representation of the jet-pump 3
Figure 1.3 Thesis Structure 7

Figures of Chapter 2

Figure 2. 1 Constant area Mixing Jet-pump 11
Figure 2. 2 Constant-Pressures Mixing 11
Figure 2. 3 Schematic view of jet-pump & and pressure-velocity variation along jet-pump, ... 12
Figure 2. 4 Schematic diagram of solar jet refrigeration system with separated loops 21
Figure 2. 5 Combined jet-pump absorption cycle 23
Figure 2. 6 Jet-pump refrigerators with a pre-cooler and a Pre-Heater 24
Figure 2. 7 Jet-pump refrigerator systems with Booster 25
Figure 2. 8 Geometry of a CRMC Jet-pump 27
Figure 2. 9 Expansion region of refrigerant within the primary nozzle 29

Figure of Chapter 3

Figure 3. 1 Schematic of a supersonic jet-pump showing the nomenclature used in this analysis 35
Figure 3. 2 Convergent-divergent (de-Laval) nozzle 37
Figure 3. 3 Mixing section 38
Figure 3. 4 Shock wave position 40
Figure 3. 5 Geometry of a CRMC jet-pump 44
Figure 3. 6 Steam jet-pump dimensions (m) 53
Figure 3. 7 R141b jet-pump dimension (mm) 53
Figure 3. 8a 1.5cell in each 1mm X direction (steam jet-pump) 55
Figure 3. 8b 2.5 cells in each 1mm X direction (R141b jet-pump) 56
Figure 3. 9 Y* Refinement 58
Figure 3. 10 Pressure Gradient Refinements 59
Figure 3. 11 Predicted supersonic regions within steam jet-pump with different turbulence models 61
Figure 3. 12 Predicted turbulent intensity distributions along the steam jet-pump centreline 61
Figure 3. 13 Predicted turbulence intensity along the steam jet-pump centreline (Te=5°C, CFD results) 62
Figure 3. 14 Predicted Supersonic regions within R141b Jet-pump 62
Figure 3. 15 Predicted turbulence intensity distributions along the R141b jet-pump centreline (CFD results) 63
Figure 3. 16 Predicted strain rate contours within mixing section 65
Figure 3. 17 Predicted total temperature contours within mixing section 65
Figure 3. 18 Primary mass flows through primary nozzle- R141b jet-pump 67
Figure 3. 19 Comparison results (Critical condenser pressure –R141b jet-pump) 67
Figure 3. 20 Comparison of critical Rm at different Tg(R141b Jet-pump, Te=8°C) 68
Figure 3. 21 Predicted optimum NXP (R141b jet-pump- CFD results) 69

Figure 3. 22 Predicted static pressure profiles along R141b jet-pump Centreline (CFD results) 70
Figure 3. 23 Predicted Supersonic region of R141b jet-pump at different NXP..... 71
Figure 3. 24 Predicted Variation of Rm with Tc and Tg (Te=8°C R141b jet-pump)..... 72
Figure 3. 25 Predicted Static pressure profile along jet-pump centreline(Te=8°C & Tg=90°C)(CFD results)..... 73
Figure 3. 26 Predicted Mach No contours at different Tc (Te=8°C & Tg=90°C)..... 74
Figure 3. 27 Predicted effect of Tg on jet-pump performance (CFD results) 75
Figure 3. 28 Predicted static pressures profiles along jet-pump centreline (R141b jet-pump-CFD results)..... 76
Figure 3. 29 Predicted Supersonic region at different Tg(Te=8°C & Te=28°C)..... 76
Figure 3. 30 Predicted Strain rate at different Tg (Te=10°C and Tc= 26°C) 77
Figure 3. 31 Predicted effect of Te on jet-pump performance (Tg 90°C &CFD results) ... 78
Figure 3. 32 Predicted Static pressures profiles along jet-pump centreline at different Te 79
Figure 3. 33 Predicted supersonic region flow region at different Te (Tg=90°C & Tc=29°C) 80
Figure 3. 34 Predicted AR effect on jet-pump performance (CFD results)..... 81

Figure of Chapter 4

Figure 4. 1 Theoretical R236fa conventional jet-pump performance 84
Figure 4. 2 R236fa primary nozzle dimensions..... 84
Figure 4. 3 R236fa Conventional Diffuser dimension..... 85
Figure 4. 4 R236fa conventional jet-pump performance (CFD results)..... 85
Figure 4. 5 R236fa conventional jet-pump operating design map (CFD results)..... 86
Figure 4. 6 R236fa conventional diffuser with area ratio (β) = 1.2..... 86
Figure 4. 7 R236fa conventional diffuser with area ratio (β) = 1.36..... 87
Figure 4. 8 Optimised R236fa conventional diffusers (CFD results)..... 87
Figure 4. 9 Static pressure profile for R236fa optimized Conventional diffuser (CFD results) 88
Figure 4. 10 Optimized R236fa conventional jet-pump operating design map (CFD results) 88
Figure 4. 11 R236fa CRMC diffuser profile with modification at entry plane of mixing section..... 89
Figure 4. 12 Optimal NXP CRMC-R236fa Jet-pump (CFD results) 90
Figure 4. 13 Optimised R236fa CRMC diffusers (CFD results)..... 91
Figure 4. 14 R236fa CRMC Diffuser C NXP=18mm 91
Figure 4. 15 Static pressure profile along centreline, optimized R236fa-CRMC jet-pump (CFD results)..... 92
Figure 4. 16 Optimized R236fa CRCM diffuser C design operating map (CFD results)... 93
Figure 4. 17a Conventional R245fa jet-pump performance at different T_g..... 94
Figure 4. 17b Conventional R245fa jet-pump performance, Tg=120°C..... 94
Figure 4. 18 R245fa Primary nozzle dimensions..... 95
Figure 4. 19 R245fa conventional diffuser dimensions 95
Figure 4. 20 R245fa conventional jet-pump performance (β=1) CFD results..... 95
Figure 4. 21a R245fa conventional jet-pump of β =1.34 specification..... 96
Figure 4. 21b R245fa conventional jet-pump of β =1.46 specification..... 96
Figure 4. 21c R245fa conventional jet-pump of β =1.55 specification..... 96
Figure 4. 22 Optimum NXP for Optimized R245fa conventional diffuser (β=1.34) (CFD results) 97

Figure 4. 23 Static pressure profiles along centreline of optimized R245fa 97
Figure 4. 24 Optimized R245fa conventional jet-pump of (β) =1.34 design map (CFD results) 98
Figure 4. 25 Comparison of nozzle A and B performance at design operation conditions 99
Figure 4. 26 Optimized conventional R245fa of A_r =1.34 with nozzle A design map (CFD results) 100
Figure 4. 27 CRMC diffuser C specifications 102
Figure 4. 28 Optimum NXP of optimised R245fa CRMC diffuser (C) (CFD results).....102
Figure 4. 29 The specification of modified R245fa CRMC diffuser (C) 102
Figure 4. 30 Static pressure profile along the centreline of optimized R245fa-CRMC diffuser (C).....103
Figure 4. 31 Optimized R245fa CRMC-jet-pump "diffuser C" design map.....103
Figure 4. 32 Supersonic region of optimized R245fa conventional jet-pump (β=1.34) 105
Figure 4. 33 Turbulence intensity within Conventional R245fa jet-pump.....106
Figure 4. 34 Strain rate contours within Conventional R245fa jet-pump (NXP=0mm)....107
Figure 4. 35 Velocity vectors at the diffuser section of R236fa CRMC jet-pump.....108
Figure 4. 36 Sonic line (iso Mach M=1) for different NXP for R245fa CRMC diffuser C 109

Figures of Chapter 5

Figure 5. 1 Schematic Diagram of Experimental Rig.....112
Figure 5. 2 Photograph of experimental rig without insulation 113
Figure 5. 3 The Steam Boiler 114
Figure 5. 4 The Evaporator 115
Figure 5. 5 Schematic layout of the evaporator with the jet-device.....116
Figure 5. 6 The condenser.....116
Figure 5. 7 The generator feed pump 118
Figure 5. 8 Schematic diagram of jet-pump Assembly.....119
Figure 5. 9 Photograph of Jet-pump Assembly 119
Figure 5. 10 R236fa conventional jet-pump cutting tools.....120
Figure 5. 11 CRMC drilling tools (I for the mixing chamber & II for the diffuser).....122
Figure 5. 12 R245fa Conventional Experimental nozzle and diffuser cutting instruments 123
Figure 5. 13 R245fa CRMC diffuser cutting tools 125
Figure 5. 14 RTD thermocouples 127
Figure 5. 15 Primary stream flow meters 128
Figure 5. 16 Secondary stream flow meters 128
Figure 5. 17a Photograph of Experimental calibration rig.....128
Figure 5. 17b Schematic diagram of the Calibration loop 129
Figure 5. 18 Primary flow meter calibrations with R236fa.....130
Figure 5. 19 Secondary flow meter calibration with R236fa 130
Figure 5. 20 Primary flow meter calibration with R245fa.....130
Figure 5. 21 Secondary flow meter calibration with R245fa 131
Figure 5. 22 Condenser flow meter calibration 131
Figure 5. 23 Evaporator flow meter calibrations 132
Figure 5. 24 Sub-cooling flow meter calibration.....132
Figure 5. 25 Microscopic replica features of the pump gears surface.....136
Figure 5. 26 Dust collected from the experimental rig cleanup filter.....136

Figure 4. 23 Static pressure profiles along centreline of optimized R245fa 97
Figure 4. 24 Optimized R245fa conventional jet-pump of (β) =1.34 design map (CFD results) 98
Figure 4. 25 Comparison of nozzle A and B performance at design operation conditions 99
Figure 4. 26 Optimized conventional R245fa of A_r =1.34 with nozzle A design map (CFD results) 100
Figure 4. 27 CRMC diffuser C specifications 102
Figure 4. 28 Optimum NXP of optimised R245fa CRMC diffuser (C) (CFD results).....102
Figure 4. 29 The specification of modified R245fa CRMC diffuser (C) 102
Figure 4. 30 Static pressure profile along the centreline of optimized R245fa-CRMC diffuser (C).....103
Figure 4. 31 Optimized R245fa CRMC-jet-pump "diffuser C" design map.....103
Figure 4. 32 Supersonic region of optimized R245fa conventional jet-pump (β=1.34) 105
Figure 4. 33 Turbulence intensity within Conventional R245fa jet-pump.....106
Figure 4. 34 Strain rate contours within Conventional R245fa jet-pump (NXP=0mm)....107
Figure 4. 35 Velocity vectors at the diffuser section of R236fa CRMC jet-pump.....108
Figure 4. 36 Sonic line (iso Mach M=1) for different NXP for R245fa CRMC diffuser C 109

Figures of Chapter 5

Figure 5. 1 Schematic Diagram of Experimental Rig.....112
Figure 5. 2 Photograph of experimental rig without insulation 113
Figure 5. 3 The Steam Boiler 114
Figure 5. 4 The Evaporator 115
Figure 5. 5 Schematic layout of the evaporator with the jet-device.....116
Figure 5. 6 The condenser.....116
Figure 5. 7 The generator feed pump 118
Figure 5. 8 Schematic diagram of jet-pump Assembly.....119
Figure 5. 9 Photograph of Jet-pump Assembly 119
Figure 5. 10 R236fa conventional jet-pump cutting tools.....120
Figure 5. 11 CRMC drilling tools (I for the mixing chamber & II for the diffuser).....122
Figure 5. 12 R245fa Conventional Experimental nozzle and diffuser cutting instruments 123
Figure 5. 13 R245fa CRMC diffuser cutting tools 125
Figure 5. 14 RTD thermocouples 127
Figure 5. 15 Primary stream flow meters 128
Figure 5. 16 Secondary stream flow meters 128
Figure 5. 17a Photograph of Experimental calibration rig.....128
Figure 5. 17b Schematic diagram of the Calibration loop 129
Figure 5. 18 Primary flow meter calibrations with R236fa.....130
Figure 5. 19 Secondary flow meter calibration with R236fa 130
Figure 5. 20 Primary flow meter calibration with R245fa.....130
Figure 5. 21 Secondary flow meter calibration with R245fa 131
Figure 5. 22 Condenser flow meter calibration 131
Figure 5. 23 Evaporator flow meter calibrations 132
Figure 5. 24 Sub-cooling flow meter calibration.....132
Figure 5. 25 Microscopic replica features of the pump gears surface.....136
Figure 5. 26 Dust collected from the experimental rig cleanup filter.....136

Figures of Chapter 6

Figure 6. 1 Calibration of R236fa primary nozzle 142
Figure 6. 2 Calibration of R245fa primary nozzle 142
Figure 6. 3 Measured variations in the entrainment ratio (Rm) with NXP, R236fa jet-pumps 143
Figure 6. 4 Measured variations in the entrainment ratio "Rm" with NXP, R245fa jet-pumps 143
Figure 6. 5 Effect of T_c on the R_m, conventional R236fa jet-pump (experimental) 145
Figure 6. 6 Effect of Tc on the COP, conventional R236fa jet-pump (experimental) 146
Figure 6. 7 Effect of Tc on the Q_r, conventional R236fa jet-pump (experimental) 146
Figure 6. 8 Conventional R236fa jet-pump T_g=85°C (experimental) 147
Figure 6. 9 Optimized conventional R236fa jet-pump performances Tg=85°C (experimental) 147
Figure 6. 10 Optimized CRMC-R236fa jet-pump performances Tg=85°C (experimental) 147
Figure 6. 11 Optimized conventional R245fa jet-pump performances Tg=120°C (experimental) 147
Figure 6. 12 Optimized CRMC R245fa jet-pump performances Tg=120°C (experimental) 147
Figure 6. 13 Optimized conventional R245fa jet-pump performance Tg=100°C(experimental) 148
Figure 6. 14 Optimized conventional R245fa jet-pump performance Tg=110°C (experimental) 148
Figure 6. 15 Optimized CRMC R245fa jet-pump performance Tg=100°C(experimental) 149
Figure 6. 16 Optimized CRMC R245fa jet-pump performance Tg=110°C(experimental) 149
Figure 6. 17 Conventional R236fa jet-pump Critical COP at different operating conditions(experimental 150
Figure 6. 18 Conventional R236fa jet-pump Critical cooling capacity at different operating conditions(experimenta 150
Figure 6. 19 Optimized conventional R245fa jet-pump , COP (experimental) 151
Figure 6. 20 Optimized conventional R245fa jet-pump, cooling capacity(experimental). 151
Figure 6. 21 Optimized conventional R245fa jet-pump 'secondary mass flow rates' (experimental) 152
Figure 6. 22 The effect of using RG unit (conventional R236fa jet-pump)(experimental) 154
Figure 6. 23 The effect of using RG (conventional R245fa jet-pump) (experimental) 154
Figure 6. 24 The effect of using RG (CRMC R245fa jet-pump) (experimental) 154
Figure 6. 25 Schematic showing the flows across the jet-pump 155
Figure 6. 26 Comparison of Tc* at different T_e (T_g=85°C) Optimized conventional R236fa jet-pump 158
Figure 6. 27 Comparison of Tc* at different Te (Tg=85°C) Optimized CRMC R236fa jet-pump 158
Figure 6. 28 Comparison of Tc* at different Tg (Te=15°C) Optimized conventional R245fa jet-pump 159
Figure 6. 29 Comparison of Tc* at different Tg (Te=15°C) Optimized CRMC R245fa jet-pump 159

Figure 6. 30 Comparison of R_m at different Te (Tg=85°C) Optimized conventional R236fa jet-pump.....160
Figure 6. 31 Comparison of R_m at different Te (Tg=85°C) Optimized CRMC R236fa jet-pump.....160
Figure 6. 32 Comparison of R_m at different Tg (Te=15°C) Optimized conventional R245fa jet-pump.....160
Figure 6. 33 Comparison of R_m at different Tg (Te=15°C) Optimized CRMC R245fa jet-pump.....160
Figure 6. 34 Alignment check tool.....161
Figure 6. 35 Optimized CRMC R245fa jet-pump characteristics with 2.2mm nozzle (experimental).....163
Figure 6. 36 Optimized CRMC R245fa jet-pump COP with 2.2mm nozzle (experimental) 163
Figure 6. 37 Optimized CRMC R245fa jet-pump Q_e with 2.2mm nozzle (experimental) 163
Figure 6. 38 Conventional R236fa jet-pump performances with real gas modelling.....164
Figure 6. 39 Comparisons of all R236fa jet-pumps performance (design conditions) (experimental).....167
Figure 6. 40 Comparisons of all R245fa jet-pumps performance (design conditions) (experimental).....168
Figure 6. 41 Optimized conventional R245fa Jet-pump with R236fa, T_g=120°C (CFD results) 169
Figure 6. 42 Optimized conventional R245fa Jet-pump with R236fa, T_g=110°C (CFD results) 169

List of Tables

Table of Chapter 2

Table 2. 1 The properties of fluids used in this study 30

Tables of Chapter 3

Table 3. 1 The specification of Nozzle A "R141b" 54
Table 3. 2 The specification of diffuser D "R141b" 54
Table 3. 3a Mesh size test with (redial-1mm=1.5 cell) (Steam jet-pump) 56
Table 3. 3b Mesh size test with (redial -1mm=2 cell)(Steam Jet-pump) 56
Table 3. 4a Mesh size test with (redial-1mm=1.5 cell) (R141b jet-pump)..... 56
Table 3. 4b Mesh size test with (redial-1mm=2 cell)(R141b Jet-pump)..... 57
Table 3. 5a Turbulent models results-steam jet-pump T_g=120°C, T_e=5°C 59
Table 3. 5b Turbulent models results -steam jet-pump T_g=120°C, T_e=10°C 59
Table 3. 6 Turbulent models results - R141b jet-pump T_g=90°C, T_e=8° 60
Table 3. 7 Steam and R141b physical properties..... 64
Table 3. 8 Specification of R141b diffusers B and C 80

Tables of Chapter 4

Table 4. 1 R236fa Jet-pump design operating conditions..... 83
Table 4. 2 The specification of two optimized R236fa conventional diffusers..... 86
Table 4. 3 R236fa CRMC diffuser coordinates 89
Table 4. 4 The new coordinator of optimised R236fa CRMC (diffuser C)..... 92
Table 4. 5 R245fa jet-pump design operating condition..... 93
Table 4. 6 Coefficient and efficiency used in jet-pump design..... 94
Table 4. 7 CFD prediction of optimised R245fa Conventional jet-pumps..... 96
Table 4. 8 New design conditions with (β =1.34) optimized conventional jet-pump..... 98
Table 4. 9 New nozzle specifications 99
Table 4. 10 Different R245fa CRMC diffusers (A, B and C) coordinate as obtained from the computer programm 101
Table 4. 11 CFD results for A, B, C R245fa CRMC jet-pumps at NXP=0mm 101

Tables of Chapter 5

Table 5. 1 The standard data of each of condenser, evaporator and generator.....117
Table 5. 2 R236fa CRMC drilling tools coordinates 121
Table 5. 3 Optimized R245fa CRMC jet-pump coordinates.....124
Table 5. 4 Condenser flow meter calibration results 131
Table 5. 5 Evaporator flow meter calibration results.....132
Table 5. 6 Sub-cooling flow meter calibration 132
Table 5. 7a Heat input and output (condenser and evaporator).....134
Table 5. 7b Heat input and output (sub cooling and generator) 135
Table 5. 7c Total heat input and output (refrigeration side).....135

Tables of Chapter 6

Table 6. 1 The effect of using pre-cooler and recuperator in the R236fa jet-pump system 153
Table 6. 2a Energy balance calculated R_m (conventional R236fa jet-pump) 156
Table 6. 2b Energy balance calculated R_m (optimized conventional R236fa jet-pump) ...156
Table 6. 2c Energy balance calculated R_m (optimized CRMC R236fa jet-pump).....157
Table 6. 3 Comparison of NXP results.....157
Table 6. 4 Comparison of optimized CRMC R245fa jet-pump performance with two nozzles 164
Table 6. 5a R236fa primary mass flow rate.....165
Table 6. 5b R245fa primary mass flow rate 165

Tables of Chapter 7

Table 7. 1 Summary of CFD and experimental results for all jet-pump tested 175

Nomenclature

Symbol	Quantity	SI Unit
A	Area	(m^2)
a	Speed of sound	(m/s)
C	Velocity Component	(m/s)
C^*	Velocity at Sonic Velocity within Nozzle Throat	(m/s)
C_D^*	Critical Flow Velocity at CRMC Diffuser Throat	(m/s)
C'	Isentropic velocity	(m/s)
C_p	Specific Heat at Constant Pressure	(kJ/kg.K)
COP	Coefficient Of Performance	(Dimensionless)
d	Change on the Component	(Dimensionless)
D	Flow Area Diameter	(mm)
d	Throat Diameter	(mm)
D_D^*	Critical CRMC Diffuser Diameter	(mm)
h	Enthalpy	(kJ/kg.K)
$h_{g,Tg}$	Specific Enthalpy of Primary Vapour at T_g	(kJ/kg.K)
$h_{f,Tc}$	Specific Enthalpy of Saturated Liquid at T_c	(kJ/kg.K)
K	Thermal Conductivity	(kW/mk)
L	Length	(mm)
$\dot{m}$	Mass Flow Rate	(kg/s)
m_g	Primary Mass Flow Rate	(kg/s)
m_s	Secondary Mass Flow Rate	(kg/s)
m^*	Critical primary mass flow rate	(kg/s)
M	Momentum	(kg.m/s)
M	Mach Number	(Dimensionless)
NXP	Nozzle Exit Position	(mm)
P	Pressure	(Pa)
P_D^*	Pressure of Flow at the CRMC Diffuser Throat	(Pa)
Q	Heat Flow Rate	(kW)
R	Individual gas Constant	$kJ.(kg.K)^{-1}$
R_m	Entrainment Ratio	(Dimensionless)
T	Temperature	(K) or (°C)

T_c^*	Critical condenser temperature	(K) or (°C)
T	Temperature	(K) or (°C)
T^*	Temperature at Sonic Velocity Within Nozzle Throat	(K) or (°C)
T_D^*	Temperature of flow at CRMC Diffuser Throat	(K) or (°C)
ν	Velocity Component	(m/s)
x	Distance Along Diffuser	(mm)
Y^*	Non Dimensional Distance (Wall unity)	(Dimensionless)

Greek

ρ	Density	(kg/m^3)
ρ*	Critical density of primary flow at nozzle throat	(kg/m^3)
γ	Specific Heat Ratio	(Dimensionless)
η_N	Isentropic Efficiency of Primary Nozzle	(Dimensionless)
η_e	Suction line Efficiency	(Dimensionless)
η_m	Momentum Loss Coefficient	(Dimensionless)
η_d	Diffuser Efficiency	(Dimensionless)
π		(Dimensionless)
α	Constant	(Dimensionless)
β	Diffuser Area Ratio	(Dimensionless)
μ	Viscosity	(kg/ms)
θ	Angle	(Degree)
ΣF	Sum of the Force	(N)

Subscript

c	Condenser
D	Diffuser
DE	Diffuser Exit
D_p	Design point
D_x	Distance x within the Diffuser
e	Evaporator
f	Fluid
g	Generator
g	Gas
j	Primary Jet
m	Momentum
mix	Mixture

N	Nozzle
N-exit	Nozzle exit
p	Jet-pump Primary Flow
s	Jet-pump Secondary Flow
t	Total
t_g	Total at Generator Conditions
t_e	Total at Evaporator Conditions
1,2,3,.	Numbers for the Cross Sectional and The States

Chapter 1

Introduction

1. Introduction

1.1 Preamble

This thesis is to describe and present the results of a theoretical and experimental study into jet-pump refrigerators and performance improvements brought about by innovative cycle modifications, the application of new working fluids and importantly, the combination of a novel design theory and the application of computational fluid dynamics to the design of jet-pumps.

Recently there has been the need to conserve energy and reduce the environmental impact of refrigerator systems that derive their primary motive power from high cost of fossil fuels. The global warming and ozone depletion caused by some greenhouse gases have intensified concern to protect our environment and so there is also a need to find alternative refrigerants that are used as working fluids in these systems. International agreements have produced a gradual phase out of environmentally harmful refrigerants aimed at reducing greenhouse emissions to their 1990 levels [Trott et al (2000)]. It is also important to use energy more efficiently and the utilization of low-grade heat, such as waste and solar thermal energy, is considered an effective way to achieve this.

Heat powered refrigeration systems are able to make use of waste heat as their driver and by employing environmentally acceptable working fluids, offer a way of reducing the consumption of fossil fuels and reducing the impact of refrigeration on the environment. Systems include the absorption cycle, adsorption cycle and the jet-pump cycle.

The jet-pump refrigeration system enjoys several advantages when compared with other types of heat powered (thermally activated) system. Its main advantages are; simplicity of design, reliability, ruggedness, long lifetime and potentially, low initial and running costs. The main disadvantage is their low coefficient of performance, (COP). However, because of its ability to utilize low grade waste heat, the jet-pump cycle has attracted renewed interest in recent years. Although jet-pump refrigeration systems offer a potential solution in some cases, electrically powered vapour compression refrigerator

systems still dominate all market sectors. In order to promote the use of jet-pump refrigerators further research is required to increase thermal efficiency and to reduce unit cost. This is the reason of the work described in this thesis. However, the main objectives of this thesis are as follow:

- Evaluation CRMC design theory that proposed to minimise effect of shock process.
- Using CFD code to enhance jet-pump design, manufacturing resulting design and testing designs in purposed test rig.
- Theoretical and experimental testing of R236fa and R245fa as working fluids for jet-pump refrigeration.
- Experimentally testing of inclusion of pre-cooler and pre-heater into the jet-pump refrigeration.

1.2 Description of the Jet-pump Refrigeration System

The jet refrigeration cycle is similar to conventional refrigeration cycle; all the basic system components are the same except that the compressor is replaced by a sub-system made up from a liquid feed-pump, a vapour generator, and the jet-pump. The jet-pump is used to compress refrigerant vapour from the evaporator pressure to the condenser pressure. The generator is used to produce high pressure vapour to drive the jet-pump and the feed-pump is used to return liquid refrigerant coming from the condenser to the vapour generator.

Figures 1.1 and 1.2 provide schematic representations of a jet-pump refrigeration system and of the jet-pump, respectively.

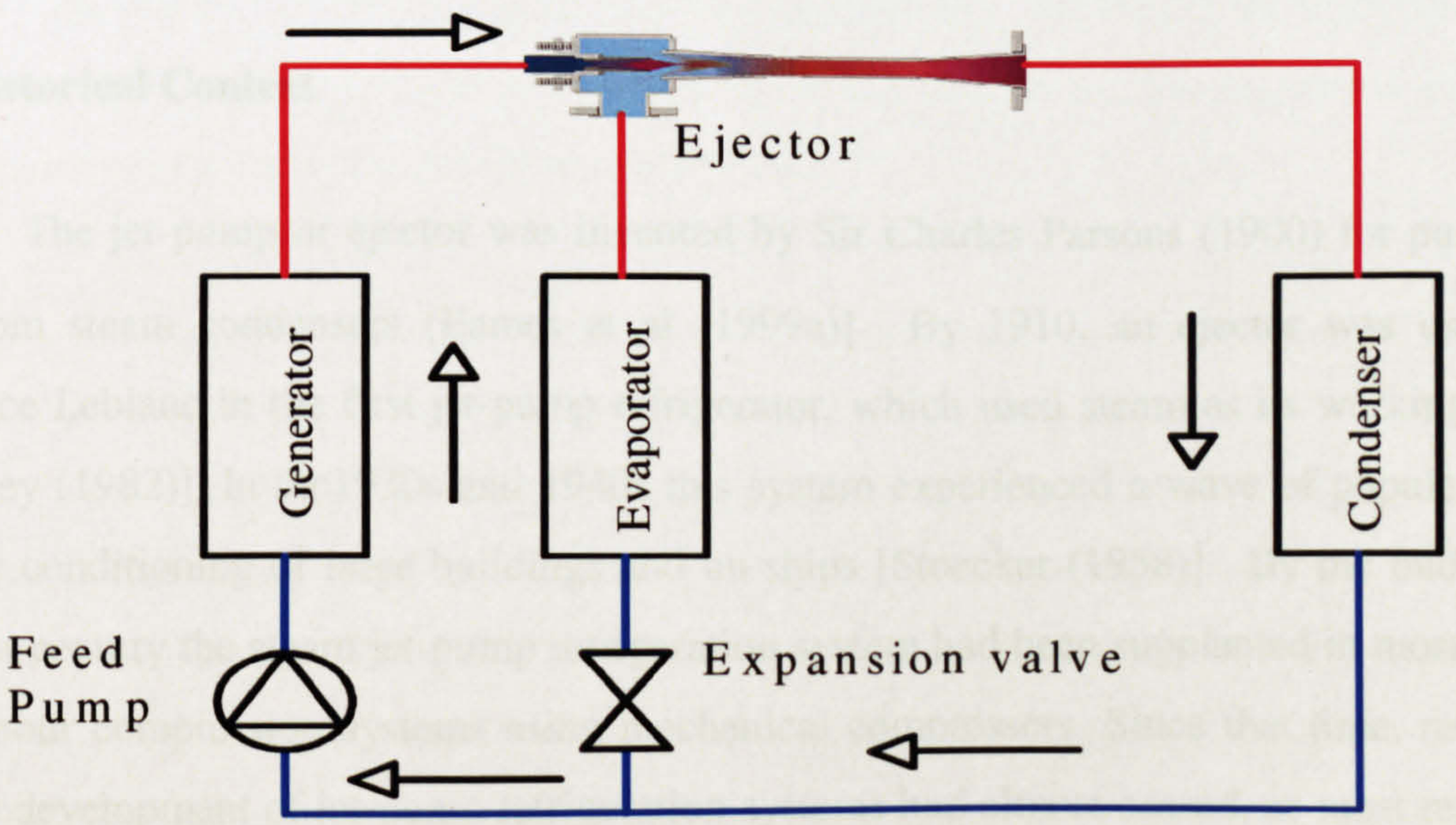

Figure 1.1 A schematic representation of jet-pump refrigeration system

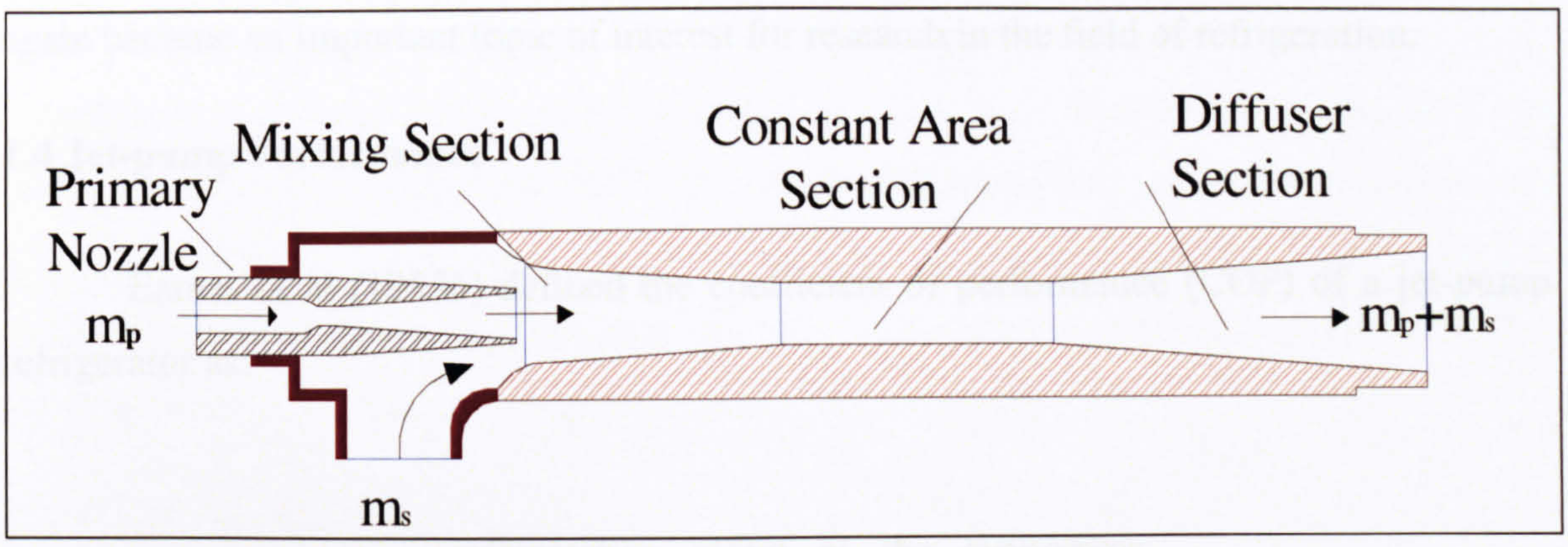

Figure 1.2 A schematic representation of the jet-pump

Referring to Figure 1.1, the jet-pump refrigerator operates as follows: heat is absorbed by the generator and this causes liquid refrigerant to be vaporised at a high pressure. This vapour (m_p) is fed to the primary nozzle of the jet-pump, (shown in Figure 1.2), through which it is accelerated to supersonic velocity. At the nozzle exit, a jet is formed, which entrains the suction or secondary stream (m_s) coming from the evaporator. The primary and secondary streams combine within the mixing section. The kinetic energy of this combined stream is transformed into pressure energy in the diffuser section of the jet-pump from where the combined vapour stream is fed to the condenser [Eames et al (1995b)]. The heat of condensation is rejected to the environment via the condenser and part of the resulting condensate is fed back to the generator via feed-pump whilst the remainder is expanded, via a throttling valve, to the evaporator where it absorbs heat at low temperature, causing it to vaporise and produce the desired refrigeration effect.

1.3 Historical Context

The jet-pump or ejector was invented by Sir Charles Parsons (1900) for pumping air from steam condensers [Eames et al (1999a)]. By 1910, an ejector was used by Maurice Leblanc in the first jet-pump refrigerator, which used steam as its working fluid [Gosney (1982)]. In the1930s and 1940s this system experienced a wave of popularity in the air conditioning of large buildings and on ships [Stoecker (1958)]. By the middle of the last century the steam jet-pump refrigeration system had been supplanted in most cases by vapour compression systems using mechanical compressors. Since that time, research on the development of jet-pump refrigeration systems had almost ceased, as most research effort concentrated on improving vapour compression refrigeration systems. In recent

years, however, due to the concerns about the environment, the jet-pump refrigeration has again become an important topic of interest for research in the field of refrigeration.

1.4 Jet-pump Performance

Eames et al (1995b) defined the coefficient of performance (COP) of a jet-pump refrigerator as:

$$COP = \frac{\text{refrigeration effect at the evaporator}}{\text{heat rate at the generator} + \text{power consumption by the pump}} \quad [1\text{-}1]$$

The power absorbed by the circulation pump is typically less than 1% of the heat supplied to the generator and thus it is usually ignored to simplify thermodynamics calculation. Therefore, for the calculation of overall system performance, COP, equation [1-2] is used:

$$COP = R_m \frac{\Delta h_{evap}}{\Delta h_{generator}} \quad [1\text{-}2]$$

Where R_m is the entrainment ratio of the jet-pump defined as:

$$R_m = \frac{\text{secondary mass flow}}{\text{primary mass flow}} = \frac{\dot{m}_s}{\dot{m}_p} \quad [1\text{-}3]$$

Entrainment ratio is a function of jet-pump geometry and operating condition, thus the corresponding COP of the system will vary dependently. However, for fixed jet-pump geometry, designed for specific refrigerator operating conditions, the maximum COP of the system is obtained at the maximum value of R_m.

In practice the secondary flow is usually determined by the amount of cooling required. Therefore, the challenge for the designer is to minimise the primary flow for a given secondary flow. To do this it is necessary to minimise the irreversible flow processes that occur within the jet-pump. These were classified under three headings by Arbel (2003) and Chunnanond et al (2004a) as follows: mixing process losses, kinetic energy losses and shock wave losses. For the nozzle and diffuser some researchers have taken these irreversibilities into account by introducing isentropic efficiencies to account for pressure loss due to frictional effects. An important source of irreversibility is that which

occurs due to compression shock processes that occur as the combined flow stream is compressed during its deceleration in the diffuser from supersonic to subsonic velocity in conventional jet-pumps, of the type illustrated in Figure 1.2. Shock waves normally form just downstream of the constant area section, within the first part of the divergent section. Thermodynamic shock is an irreversible process and its effect in this case is to reduce the maximum back pressure that the jet-pump can overcome. Minimising the effect of this shock process is, therefore, an important aim of this research.

1.5 Thesis Content

In order to minimise the performance losses incurred by thermodynamic shock, Eames (2002) proposed the constant rate of momentum change (CRMC) method of diffuser design. It is primarily a detailed investigation of this CRMC theory, which formed the principle aim of this research and the subject of this thesis. This new design theory is described and discussed in Chapter 3 and in Chapter 4 its performance is theoretically compared with more traditional designs.

An understanding of the flow processes within the jet-pump can help to improve the system performance. In the present study this was achieved by using computational fluid dynamics (CFD), in order to try to explain some of the mysteries surrounding the mixing/entrainment process. CFD analysis of the flow field within the jet-pump had previously been carried out using older versions of CFD packages that did not take account for real behaviour of working fluids and boundary layer effects. In the present study a more recent version which is able to model a fluid as real gas, has been used to compute the flow field. The CFD model has also been validated against published experimental work based on trials with a number of fluids: steam [Eames et al (1999b)] and R141b [Huang et al (2001)]. This validation of the CFD code for the design of jet-pumps offers an original contribution to jet-pump design. These results are presented in Chapter 3.

It is believed that the use of CFD in the design of jet-pumps for jet-pump refrigerators is a more convenient and economical way of producing optimised solutions, particularly when several types of fluid are being assessed. Therefore, one of the main aims of this study was to use a CFD package to improve jet-pump design for a range of fluids and to manufacture the resulting designs and test these in a purpose-built rig.

Efforts for identifying environmentally safe working fluids and their adaptability to jet-pump refrigeration systems have been previously carried out by Cizungu et al (2000) and Selvaraju et al (2003). This published research was entirely theoretical. This PhD study, however, is the first time a combined theoretical and experimental investigation to identify the applicability of two new refrigerants (R236fa and R245fa) for jet-pump applications has been carried out, which is a further original contribution to the study of jet-pump refrigeration.

Enhancement of jet-pump refrigeration cycle performance has been suggested by Sokolov et al (1990a) through the introduction of a pre-cooler (economizer) and the pre-heater (recuperator) into the simple jet-pump cycle to reduce the heat absorbed by the generator and increase the heat absorbed at the evaporator. As far as this researcher is aware these techniques have never been tested experimentally and therefore, an aim of this study was to carry this out using a purpose built refrigerator which is described later. This part of the present study also provides an original contribution to the filed of jet-pump refrigeration.

1.6 Thesis Structure

Figure 1.3 shows the thesis structure. The literature on current and past research regarding the theoretical and experimental studies of jet-pumps was evaluated including a review of the previous CFD applications in jet-pump analysis. Some details about the merits and thermodynamic properties of the working fluids which can be used in jet-pump system are described in Chapter 2. The mathematical models used in the design of the jet-pump, based on 1-D conventional and CRMC jet-pump design theories, are described in Chapter 3.

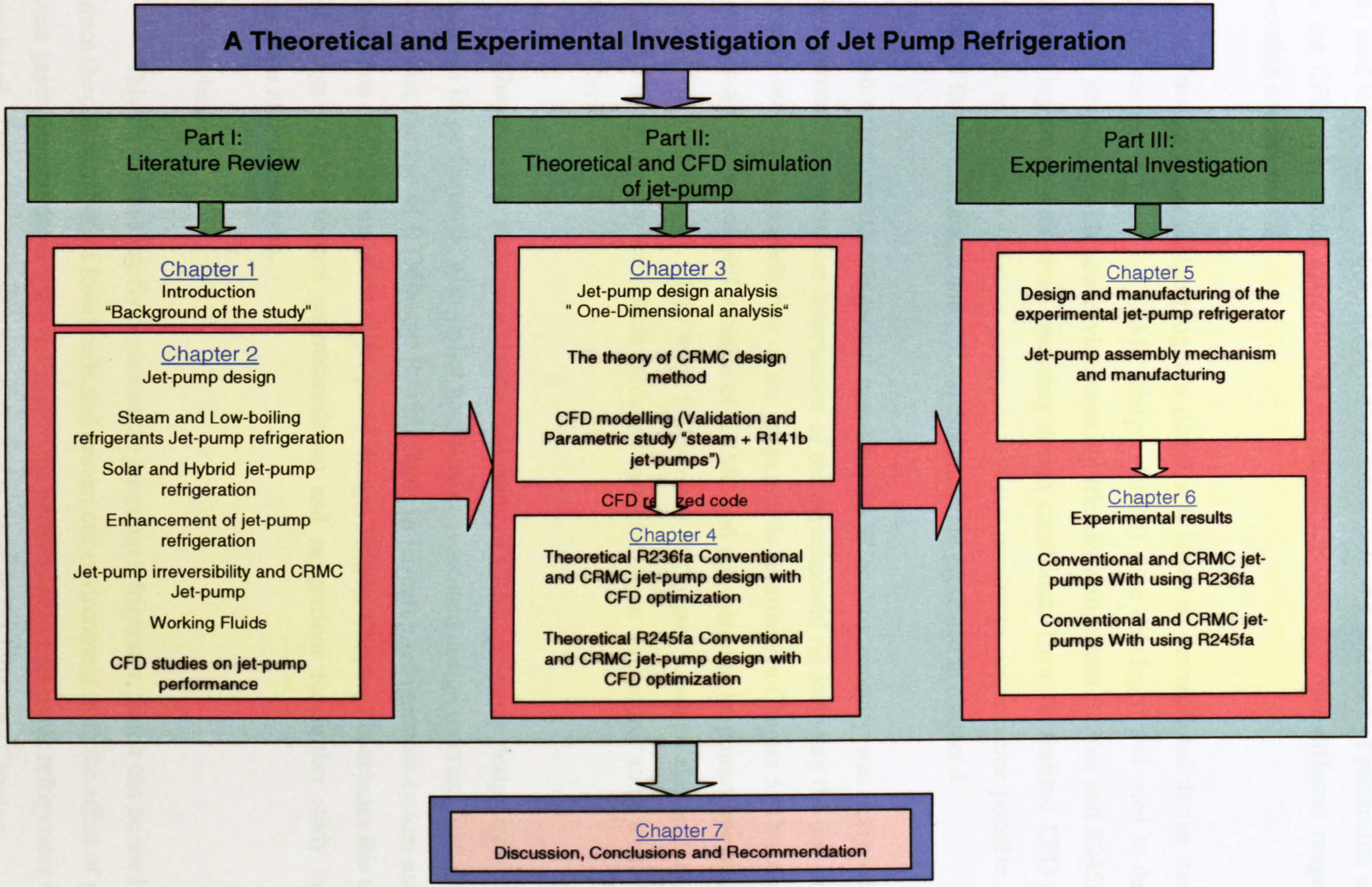

Figure 1.3 Thesis structure

Chapter 3 also, details the development of the CFD code for jet-pump design that was used in this study. This includes the validation data and outcomes of parametric study for the CFD code based upon two experimental data sets and over different ranges of operating conditions.

Two computer design programs (the first is based on conventional design method and the second is based on CRMC design method) were developed and used to design different jet-pumps with new environmentally friendly refrigerants R236fa and R245fa as the working fluids with given operating design conditions. Then the realized CFD code was used to optimize these jet-pumps to achieve maximum performance possible. The results of theoretical design and CFD optimization are presented in chapter 4.

An experimental refrigerator based on 3 kW cooling capacity was designed and manufactured. The technical information of the experimental rig including the designs for the tools used in the manufacture of the jet-pumps is described in Chapter 5. This rig was used to study the actual performance of CRMC and conventional jet-pumps operating on both R236fa and R245fa. This work is described in Chapter 6, which also includes the results of the study into the effects produced by including an economizer and a recuperator into the cycle.

Chapter 6 also includes a critical evaluation of CRMC jet-pump design method and compares its performance with earlier and more conventional design theories. Additionally it evaluates the use of R236fa and R245fa fluids in jet-pump refrigerators system and the application of CFD simulation on jet-pump design. Finally, Chapter 7 concludes this thesis and brings together several recommendation and suggestions for further study in this important area of research.

1.7 Conclusions

This chapter has briefly described the jet-pump refrigerator, which can be used to reduce the consumption of fossil fuels and protect our environment from the effect of green house gases. Several novel ways to improve the performance of jet-pump refrigerator were introduced. These are discussed and evaluated in detail in the following Chapters.

Chapter 2

Past Research on Jet-pump Refrigeration System and Jet-pump Theory

2. Past Research on Jet-pump Refrigeration System and Jet-pump Theory

2.1 Introduction

The aim of the investigation described in this thesis was to find ways to improve the performance of jet-pump refrigeration systems. This mainly concentrated on the design of the jet-pump or ejector itself by evaluating different design methods; Using computational CFD to understand the flow physics and from which the jet-pump design can be optimised and enhanced; testing new 'environmentally friendly' working fluids that have the ability to be used in jet-pump refrigeration systems; and to modify and develop the whole system by incorporating pre-cooler and pre-heater into the cycle.

This chapter provides and describes: jet-pump theory and applications, reviews past research, considering methods of system enhancement, working fluids and the computational research that has been conducted into understanding the internal flow process within jet-pumps.

2.2 Jet-Pumps

Jet-pumps are simple pieces of equipment, they often are used to pump gases and vapour from a system to create a vacuum. They have a number of industrial applications and they take different names according to their function. Jet-pumps are also known as ejectors, evacuators, vacuum augmenters, thrust augmenters, thermo compressors and injectors. The theory of operation is the same in each case. Jet-pump or evacuators are normally used to pump an incompressible fluid, whereas the others are used for compressing and pumping compressible vapours and gases. In the field of vacuum processing, steam jet-pumps have been most widely used to provide the vacuum, including distillation, freeze drying, vacuum drying and removal of air from turbine condensers. Thermo-compressors are used to entrain and boost a low pressure fluid to an intermediate reusable pressure. They are used in some industrial process such as food processing, paper production and petrochemical industries to reclaim waste steam and reduce steam water consumption. In thrust augmentation, jet engines generate thrust by expanding a fluid with higher pressure than ambient through an exhaust nozzle. Normally shroud jet-pumps are placed around a jet exhaust and are used for noise suppression, capture and reduce IR

radiation, and thrust augmentation. Thrust is generated by expanding energy in the exhaust flow and viscous mixing between primary and secondary fluid. However, the jet-pumps used for thrust augmentation are characteristically short to save both space and weight as well to reduce losses due to friction while promoting sufficient mixing between primary and secondary streams.

In refrigeration systems, supersonic jet-pumps are used to compress and pump the working fluid from the evaporator to the condenser through the use of a primary fluid which is normally the same fluid used in the whole system. The steam jet-pump refrigeration system was used first to air condition large commercial buildings, and it was designed with large capacities up to 1000 tons of refrigeration [Al-khalidy et al (1995)]. The operation and maintenance costs of these systems were low in comparison with vapour-compression systems at the time. But they have disadvantages, which made them uncompetitive when vapour compression systems were later developed. The main disadvantages were their relatively low efficiency and for steam systems, they cannot supply cooling at temperatures below 0°C [ASHRAE (1979)]. Applications of low-boiling temperature refrigerants in jet-pump refrigeration systems were introduced to overcome the previous disadvantage of steam-jet systems [Al-khalidy (1997)]. Over the last two decades, due to the demand for efficient systems for air conditioning and refrigeration applications, both steam and low boiling refrigerants jet-pump refrigeration have gained more interest. Recently, research has been extensively performed to improve their performance.

2.3 Jet-pump Design (The Theory)

The principle of operation of all supersonic jet-pumps is the same, regardless of which design method is used and in what ever field they are applied. There were two concepts for jet-pump design based on one-dimensional theory. The first was introduced by Keenan and Newman (1942 & 1950) as the constant-area-mixing method. The mathematical analysis was based on an ideal gas dynamics. The Constant-area method is simple to use as the mixing chamber is of a constant cross-sectional area as shown Figure 2.1.

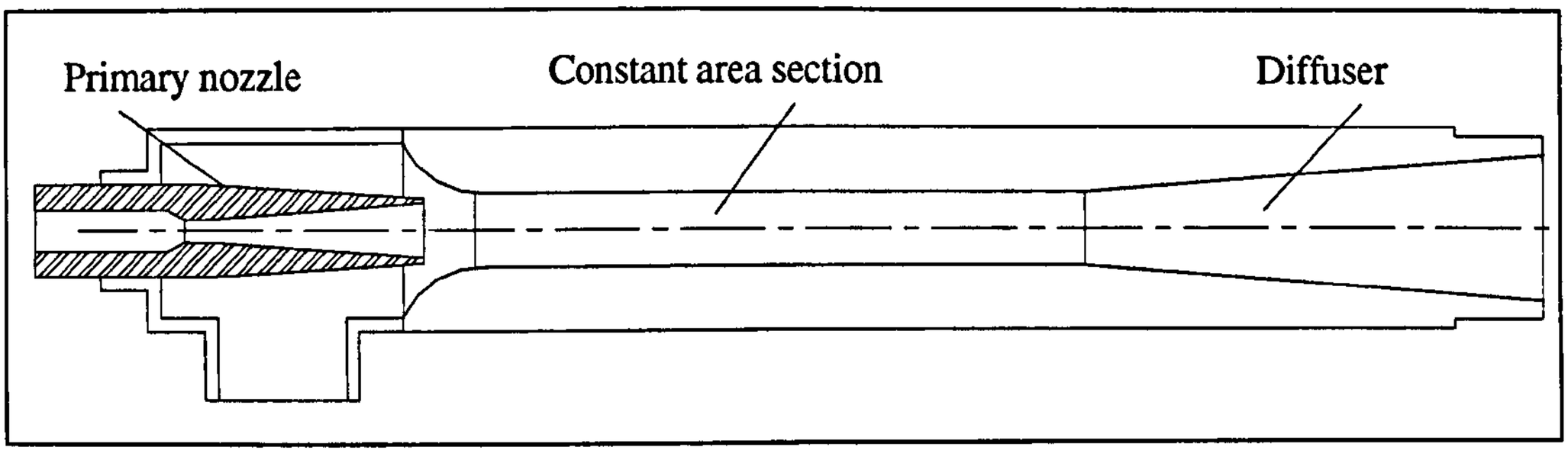

Figure 2. 1 Constant area Mixing Jet-pump

The second concept is constant pressure design method, which was also introduced by Keenan et al (1950). Jet-pumps designed on this principle are the most commonly encountered design due to their better performance and ease of manufacture. The jet-pump geometry of constant pressure design takes the shape as in Figure 2.2, where the nozzle exit is located within the suction chamber in front of the constant area section.

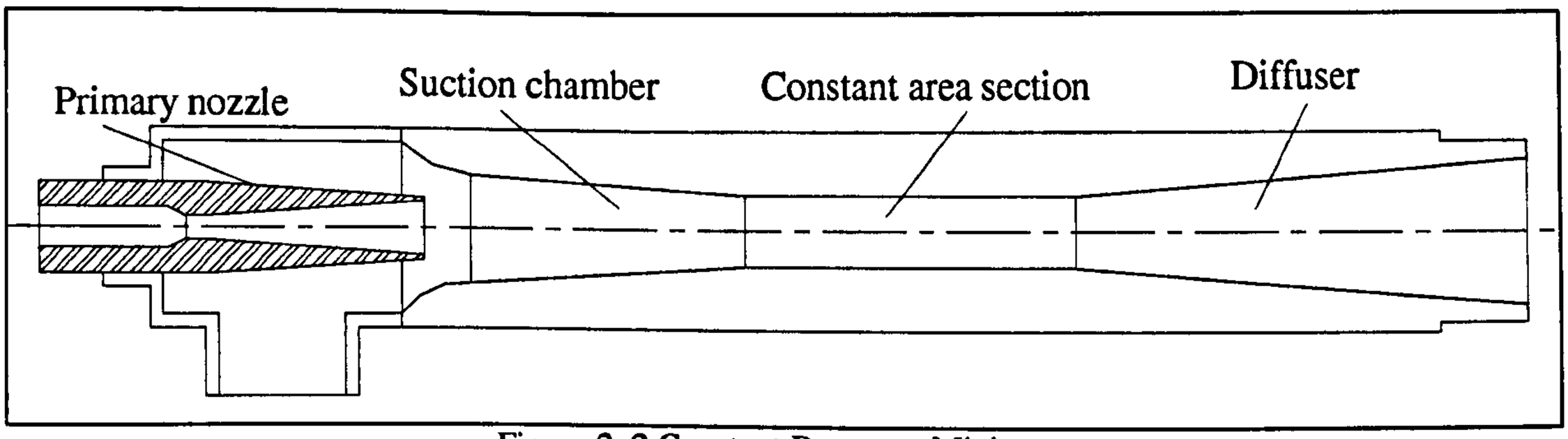

Figure 2. 2 Constant-Pressures Mixing

In the beginning, it was thought that a constant–area mixing jet-pump performs better by entraining a larger amount of secondary flow than the constant pressure design, [Keenan et al (1942)]. Both types of jet-pump have been extensively studied in different ranges of applications. Extensive experimental work was carried out over intervening years, and it was found that the constant pressure jet-pump has better performance than the constant area one and it compares favourably against experimental data. As a result most of recent studies have focused on the constant pressure design. In this study, the jet-pumps used for CFD validation and some in the experimental work, were designed mainly on constant pressure design with taking into account the primary nozzle and diffuser efficiencies and the pressure losses within the suction line.

In the kind of jet-pump designed by the constant pressure concept, the mixing of the primary and the entrained streams are assumed to occur in the suction chamber with a uniform pressure. i.e. the primary and the secondary "entrained flows" have identical

pressures, and the mixing of two streams begins at the nozzle exit with constant pressure until the inlet of constant area section.

In 1977 Munday and Bagster proposed a semi-empirical approach which was to some extent different from previous concepts. This approach uses the constant capacity characteristic of jet-pump, in which the primary flow fans out without mixing with the entrained flow and with the internal wall, creates a converging channel that acts as a nozzle for the secondary flow, causing it to be accelerated to sonic velocity in a hypothetical throat located at some distance downstream of the primary nozzle exit position. After that, mixing of the two streams is assumed to occur. Accordingly, this approach was adopted by most researchers in their subsequent studies, which lead to assumptions regarding the behaviour of the flow in terms of static pressure and velocity as illustrated Figure 2.3.

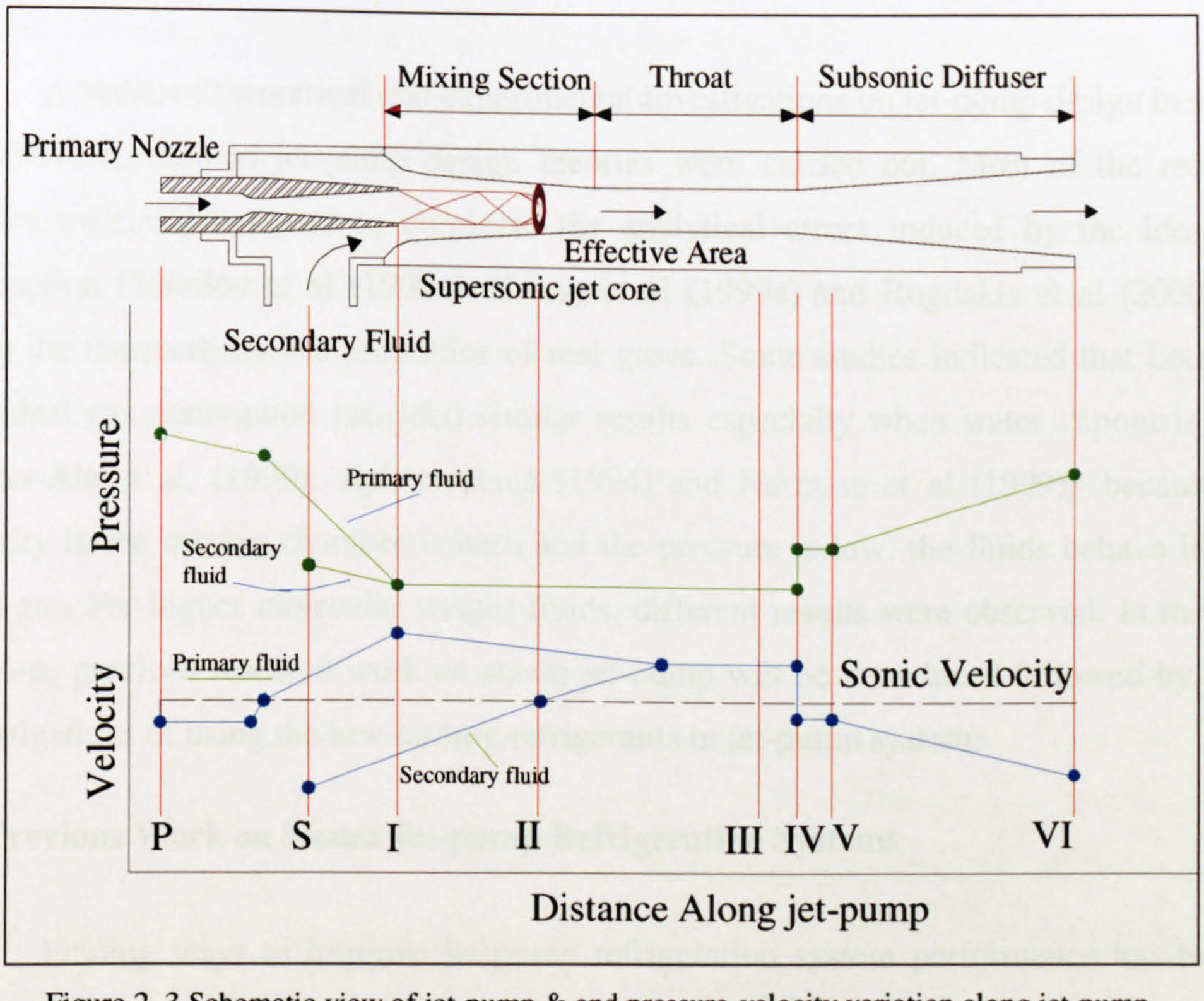

Figure 2. 3 Schematic view of jet-pump & and pressure-velocity variation along jet-pump, according to Munday and Bagster theory (1977)

Referring to the Figure 2.3, the primary fluid enters the primary nozzle with pressure P after which it expands and accelerates to supersonic speed at the nozzle exit, (I), where it fans-out, creating a low pressure region in the mixing section. The pressure of the

secondary fluid at point (S) is in this case a little higher, and due to pressure difference it is entrained into the mixing chamber. The supersonic primary fluid at the nozzle exit forms a convergent duct with the jet-pump body without mixing with secondary fluid. The secondary flow accelerates within this convergent duct and reaches sonic velocity at a cross section (II) and where it chokes. This cross-section was defined by Munday and Bagster (1977) as the 'effective area'. Mixing then takes place after this effective area is passed, whilst the static pressure was assumed to remain constant at all sections to the end of the mixing (point III). Because of high pressure region downstream of the mixing section, a normal shock is induced (IV). This shock causes a sudden increase of pressure creating compression effect, which simultaneously decreases the flow Mach number from supersonic to subsonic. In the diffuser section further compression is achieved as the flow is brought to a stagnation state to point (VI). In this 1-D method, the shock wave occurs at the end of the constant area section with essentially zero thickness.

A series of theoretical and experimental investigations on jet-pump design based on the above mentioned jet-pump design theories were carried out. Most of the research studies were implemented to eliminate the analytical errors induced by the ideal gas assumption [Sokolov et al (1990a), Huang et al (1999a) and Rogdakis et al (2000)] by using the thermodynamics properties of real gases. Some studies indicated that both real and ideal gas assumption provided similar results especially when water vapour is used [Abdel-Ala et al, (1990), Aphornratana (1994) and Narmine et al (1999)]; because the velocity in the mixing chamber is high and the pressure is low, the fluids behave like an ideal gas. For higher molecular weight fluids, different results were observed. In the next sections, previous research work on steam jet-pump will be introduced followed by other investigations of using the low-boiling refrigerants in jet-pump system.

2.4 Previous Work on Steam Jet-pump Refrigeration Systems

Finding ways to improve jet-pump refrigeration system performance has been a challenge for the researchers in recent years. Work has mainly focused on optimising jet-pump design, and reducing irreversibilities, Firstly, due to consideration of many assumptions related to isentropic efficiency, including the effects of friction heating and pressure loss on theoretical designs. Secondly, research has aimed at providing jet-pump

passage profiles and finding optimal working fluids. In the following section, the most recent work on the steam jet pump refrigeration system is reviewed.

Eames et al (1995b) undertook a theoretical and experimental study of a small-scale steam jet-pump refrigerator. In their theoretical model they included the irreversibilities associated with the primary nozzle, mixing chamber, and diffuser. Their design was based on fixed jet-pump geometry. They found that the actual performance was about 83% of the ideal, and their studies showed that COP and cooling capacity are both dependent on operating temperatures and jet-pump geometry. Encouraged by these results Sun (1996) conducted analytical modelling based on jet-pump theory proposed by Keenan et al (1950), taking into account appropriate jet-pump efficiencies and real gas properties to evaluate a 5-kW steam-jet refrigerator using variable geometry jet-pump. It was found that variable geometry jet-pump can perform better than a fixed geometry to deal with different operation conditions. Following up Chen et al (1997) built and tested an experimental small scale steam-jet refrigerator, to investigate the controlling parameters of a steam jet-pump, including operational conditions and the exit Mach number of the primary nozzle. Moreover based on the experimental results, they constructed a jet-pump operation map that is useful for practical design as well as deriving empirical equations that were helpful for jet-pump evaluation. They proposed a two-stage jet-pump configuration to enhance the entrainment ratio in the second stage jet-pump and, which in turn, showed it is possible to utilize low grade heat to reduce the operational cost of jet-pump refrigeration systems. They tried to observe the flow field by using a transparent jet-pump, because understanding the flow structure especially in the mixing section can help to improve the jet-pump performance. They observed some water droplets appearing in the mixing section; these water droplets can affect the jet-pump performance. Eliminating them is difficult, because to achieve the design-point critical condenser temperature, the flow at the nozzle exit is supersonic, with a higher Mach number and low temperature. Moreover, to include the effects of these droplets in the theoretical design, through the use of some assumption, increases the complexity of numerical methods available.

Aphornratana et al (1997) conducted experimental studies to examine the effect of the nozzle position on steam jet-pump performance. It was thought that jet-pump performance can be optimized by adjusting the nozzle exit position. Theoretically designed jet-pumps provide a fixed nozzle position, and the optimum position can be

experimentally determined. Even so, design guides, like that provided by ESDU (1985) suggest that the nozzle should be placed at a distance of 0.5 to 1.0 times the mixing chamber throat diameter upstream of the mixing chamber inlet. However, the optimum nozzle position was found to vary dependently on the jet-pump geometry and on the operating conditions. COP and cooling capacity were found to be varied by as much as 100% by changing the nozzle position. A similar investigation that described the effect of the nozzle position on jet-pump performance was carried out by Eames et al (1999b). According to their results, a particular optimum nozzle position cannot be defined to meet all operating conditions.

Eames et al (1999a) and Eames et al (1999b) reported theoretical and experimental investigation on steam jet-pumps for application in jet-pump refrigerators powered by low-grade heat. They designed a steam jet-pump that could be utilized for the production of cooling for building air conditioning and process refrigeration systems and they examined some features of jet-pump geometry and their effects on performance. They present a one dimensional mathematical analysis of supersonic vapour-vapour jet-pump, with full details including the jet-pump irreversibility at primary nozzle, mixing section and diffuser. Also, the thermodynamic shock process and thermodynamic property relationships were used as they were provided from previously established analytical models of the shock system [Hodge and Koening (1995)]. The process of calculating the thermodynamic properties of steam, used to solve the mathematical equation was presented. However, the theoretical model presented in their study was used in this investigation to conduct analytical study of jet-pump system; also one of their jet-pumps, which was tested experimentally, was used to validate the CFD simulation as shown later in Section 3.4. The effect of each of the operating condition, nozzle outlet area, nozzle exit position (NXP) and diffuser throat area were examined experimentally and it was found that the jet-pump entrainment ratio and critical condenser pressure were functions of the aforementioned parameters. The experimental results were found to agree within 12 to 17% with theoretical results and thus, the 1-D analysis was shown capable of being used for steam jet-pump design for any application.

Narmine et al (1999) conducted computer simulation models with two approaches to investigate the effect of operating conditions on steam jet-pumps. Their first approach

was with ideal gas assumption and the second was with perfect gas assumption. Their results showed that there is a good agreement between the two assumptions.

Enhancement of a steam jet-pump refrigerator performance was thought to be achieved if the petal nozzle is used instead of conventional conical nozzle. This was studied by Chang et al (2000), who conducted an experimental study to investigate the performance of steam jet-pumps using a petal nozzle. The effects of operational conditions and jet-pump area ratio were examined, and for comparison, a conventional conical nozzle with the same Mach number as that of petal nozzle was tested. In their experimental study, it was postulated that using a petal nozzle will achieve efficient mixing in jet-pump and thus more energy will be available to overcome higher critical back pressure. Their experimental results showed that petal nozzles can achieve higher back pressure when used with jet-pump area ratio greater than 180, whereas with lower area ratios the performance of jet-pump with conventional nozzle was found to be much better.

El-dessouky et al (2002) developed a semi-empirical model for the design and rating of steam jet-pumps. Their model includes correlations for the entrainment ratio in choked and non choked flow. They used a large set of design data and experimental measurements to solve their empirical model to obtain entrainment ratios over a range of operating conditions.

Alexis et al (2003) have used a mathematical model to conduct a verification study of steam refrigeration systems. They developed the theory of Munday and Bagster described earlier, by taking into account the shock phenomena and the isentropic efficiency in the jet-pump. The parameter they used to compare the mathematical and experimental results, was based on the evaporation per unit of motive steam. Their results were in good agreement with the experimental work of Eames et al (1995b).

More recently Khattab et al (2002) conducted an analytical study to determine the performance of steam jet refrigeration systems utilizing low temperature solar energy as driving medium. They pointed out that the expansion of steam occurs as wet vapour. Because of this thermodynamic data were taken directly from steam tables. The overall performance of the system was found to be affected by the performance of the solar collector and thus they presented the predicted overall system performance in two parts: one for prediction of steam jet-pump performance and another for solar collector

performance. However, their results showed that the low temperature solar steam jet cooling system can be optimised to meet the cooling requirements for air conditioning over a range of evaporator temperatures between 10°C to 15°C.

Chunnanond et al (2004a) conducted an experimental investigation of small scale steam jet-pump refrigerator systems. They analysed experimentally the static pressure profile along the jet-pump in order to understand the flow and the mixing process. The flow phenomenon affected operating conditions and jet-pump geometry was well explained. The COP of the system was found to be in good agreement with the study of Eames et al (1995b) and Aphornratana et al (1997).

2.5 Previous Work on Jet-pump Refrigeration System with Low Boiling Refrigerants

The coefficient of performance of jet-pump refrigeration systems, when water is used as the refrigerant, is low. Also, the use of water limits the cooling temperature to above 0°C. In addition the large specific volume of water, at typical evaporator conditions, results in the pressure losses that are significant without the use of larger diameter tubing. Most previous experimental work showed that the system requires relatively low condenser pressures to be effective, thus an air cooled condenser cannot normally be used with steam-jet refrigeration for any practical range of applications. Moreover, the required vapour generator temperature is quite high, usually between 120°C to 200°C. However, in order to increase the efficiency of the jet-pump system and widen the utilization of low-grade energy to run these systems, many attempts have been made to use high molecular weight refrigerant fluids, which are often more suitable than water.

Experimental studies of jet-pumps operating with various working fluids were carried out by Work et al (1939) and Holton (1951). They studied the performance characteristics of jet-pumps using vapours with different ranges of molecular weight. They showed that for a fixed geometry jet-pump the performance is very similar at different operating conditions. Most earlier theoretical and experimental work using various halocarbon-based refrigerants was based on the 1-D constant pressure theory developed by Keenan and Neumann (1950). Defrate and Hoerl (1959) developed a computer programme to calculate the performance of jet-pumps working with ideal gases including the effects of operating temperatures and molecular weights.

Huang et al (1985) used Munday and Bagster's method to design a jet-pump working with Freon-113. They applied the conservation of mass, momentum and energy in their mathematical equation, ignoring the friction and heat loss. Also, they conducted an experiment to study jet-pump performance characteristics at different operating conditions. They showed that the effective area of the secondary vapour at choke conditions is not constant for a jet-pump as Munday and Bagater presumed, but it varies with operating conditions.

Sun (1999) developed a computer programme to simulate the jet refrigerator system with various refrigerants including, R11, R12, R13, R21, R123, R142b, R134a, R152a, RC318, R500 and water. The thermodynamic properties of some mentioned refrigerants were taken from published literature whereas properties for others were calculated based on the ASHRAE (1984) published equations. Jet-pump isentropic and momentum loss efficiencies were taken as constants in the program and all equal to 0.85. The study showed that R12 has the better performance in terms of entrainment ratio and COP and also indicated that refrigerants with larger latent heat values can make the jet refrigeration system more competitive.

Al-khalidy (1998) also conducted a theoretical study of various refrigerants: R717, R11, R12, R113 and R114. R113, which has greater molecular weight, was found more suitable for use in the jet-pump cycle and thus it was selected for experimental investigation. The results showed that the system can operate efficiently at condenser temperatures up of 45°C, over a range of vapour generator temperatures between 70°C and 100 °C.

Huang et al (1999a) conducted a 1-D analysis of jet-pump performance, by assuming that the constant pressure mixing process occurs inside the constant area section. R141b was used as the working fluid which for design purpose was assumed to be an ideal gas with constant properties. Also, they took into account frictional and mixing losses by using coefficients, which was later determined experimentally. They designed and tested 11 jet-pumps to verify their analytical results and to determine the actual empirical coefficients, which were used in their 1-D analysis. The base of their theoretical study was the assumption that the primary flow fans out as it leaves the nozzle without mixing and the secondary flow is chocked at a hypothetical throat where the two streams mix at

constant pressure. The entrainment ratio "R_m" obtained experimentally for a range of jet-pumps was found to coincide fairly well with their theoretical calculation. For this reason, in this study, one of their jet-pumps, with R141b as working fluid, was used in CFD simulation for validation purposes and for evaluation of the flow structure within the jet-pump at different operating conditions. This work is presented in Chapter 3. Their experimental study showed that the coefficient related to frictional loss is more sensitive than other coefficients and care should be taken in jet-pump design to account for this with different jet-pump area ratios. It depends mainly on jet-pump design, manufacturing technique, good centre line alignment and interior surface polishing, to reduce pressure loss. Moreover, their findings showed that, for a fixed jet-pump critical back pressure, the required jet-pump area ratio should be increased with increasing primary flow inlet pressure, and for a fixed vapour generator temperature, the jet-pump area ratio increases with decreasing critical condensing temperature. Encouraged by these results Huang et al (1999b) derived two empirical correlations from testing another 15 jet-pumps with R141b as their working fluid. The empirical correlation was used to develop a method of jet-pump design and performance prediction. The prediction of entrainment ratio R_m using this correlation was found by them to be within ±10% of that obtained experimentally, and R141b was shown to be a good working fluid for jet-pump refrigeration.

Cizungu et al (2001) developed a computer code and analyzed the performance of jet-pump refrigeration systems operating with pure environmentally friendly refrigerants. R123, R134a, R152a and R717 (ammonia) were tested. For design purpose they were assumed to be ideal gases and the losses were represented by a friction factor and isentropic efficiencies. Comparative results showed that all the tested working fluids give more or less the same performance characteristics depending on jet-pump geometry and the operating conditions.

The same conclusion was obtained by Selvaraju (2004) who developed a computer code on the basis of the one-dimensional jet-pump theory to analyze the jet-pump performance at critical mode. He also included the effect of losses and internal irreversibility along with the ideal gas assumption. The code validated against the R141b experimental results provided by Hunag et al (1999a) over a range of generator and condensing temperatures and with keeping evaporator temperature at 8°C. The results were in good agreement with experimental data with a 10 to 15% deviation. However, based on

this work, they conducted comparative performance studies with environmentally friendly refrigerants: R134a, R152a, R290, R600a and R717. Their results showed that among all the refrigerants tested, R134a exhibits a better entrainment at all operating conditions, and also showed that all refrigerants can be used on jet-pump refrigeration systems powered by a heat source of temperatures between 65°C to 90°C.

Alexis et al (2004) conducted an analytical study to investigate the behaviour of methanol in a jet-pump refrigeration system with a medium temperature thermal source between 110°C to 130°C. Their computer programme was based on the theory of Munday and Bagster (1977) and included the equations of state proposed by Alexis and Rogdakis (2002a). They investigated the performance of the system over a range of generator, condenser, and evaporator temperatures. The system COP was found to be a linear function of generator pressure and temperature, as the generator pressure increased the system COP decreased. The maximum COP achieved was 0.467.

Ouzzane et al (2003) developed a mathematical model with two versions of a computer programme for jet-pump refrigeration cycles. One version was used for optimal jet-pump design while another for full simulation of jet-pump at different operating conditions. For design purposes the refrigerant and the operating conditions were fixed to determine the jet-pump geometry, whereas for simulation the designed geometry was fixed and the operating conditions were varied. They used a 1-D analysis proposed by Munday and Bagster (1977) to take into account the change in refrigerant properties within the flow with axial position, which was thought to represent the operation of a jet-pump more accurately. The computation process was based on Mach number increments for both primary and secondary flow to produce their critical conditions. The results obtained from the programme were validated also against R141b data provided by Huang et al (1999a) for the same geometry and operational characteristics. The results were in good agreement under all operating conditions. For design-point conditions the entrainment ratio and critical condensing temperature were predicted to within 6% and 8% respectively. Based on the good validation of their programme, they used it to conduct jet-pump analysis with R142b as the working fluid over a range of operating conditions and jet-pump geometries, taking account of changes of flow variables along the jet-pump.

Based on the analytical and experimental results provided in this section jet-pump refrigeration systems, which use low-boiling refrigerants seem to be more convenient to provide low cooling temperature than systems using water as refrigerants. Also they can provide a practical cooling duty even in high environmental temperatures. Therefore, it is possible to use a solar collector and air-cooled condenser to run these systems over an acceptable range of ambient temperatures. In the next section a review of a solar jet refrigeration system is presented.

2.6 Solar Jet-pump Refrigeration System

Low temperature thermal energy, such as solar energy and waste heat energy, can be utilized to run jet refrigeration systems, especially for air conditioning. In hot regions the solar-jet air conditioning system can provide space comfort cooling. A solar collector can be used to collect or absorb the solar thermal energy, which is then used to drive the jet-pump system. Normally the heat from the solar collector is carried by a separate medium and transferred to the working fluid by the vapour generator heat exchanger. The heat transferring mediums should have good heat transfer properties with a boiling point greater than the possible temperature in the system. Figure 2.4 shows the solar-jet refrigeration system with separated solar and refrigeration system loops.

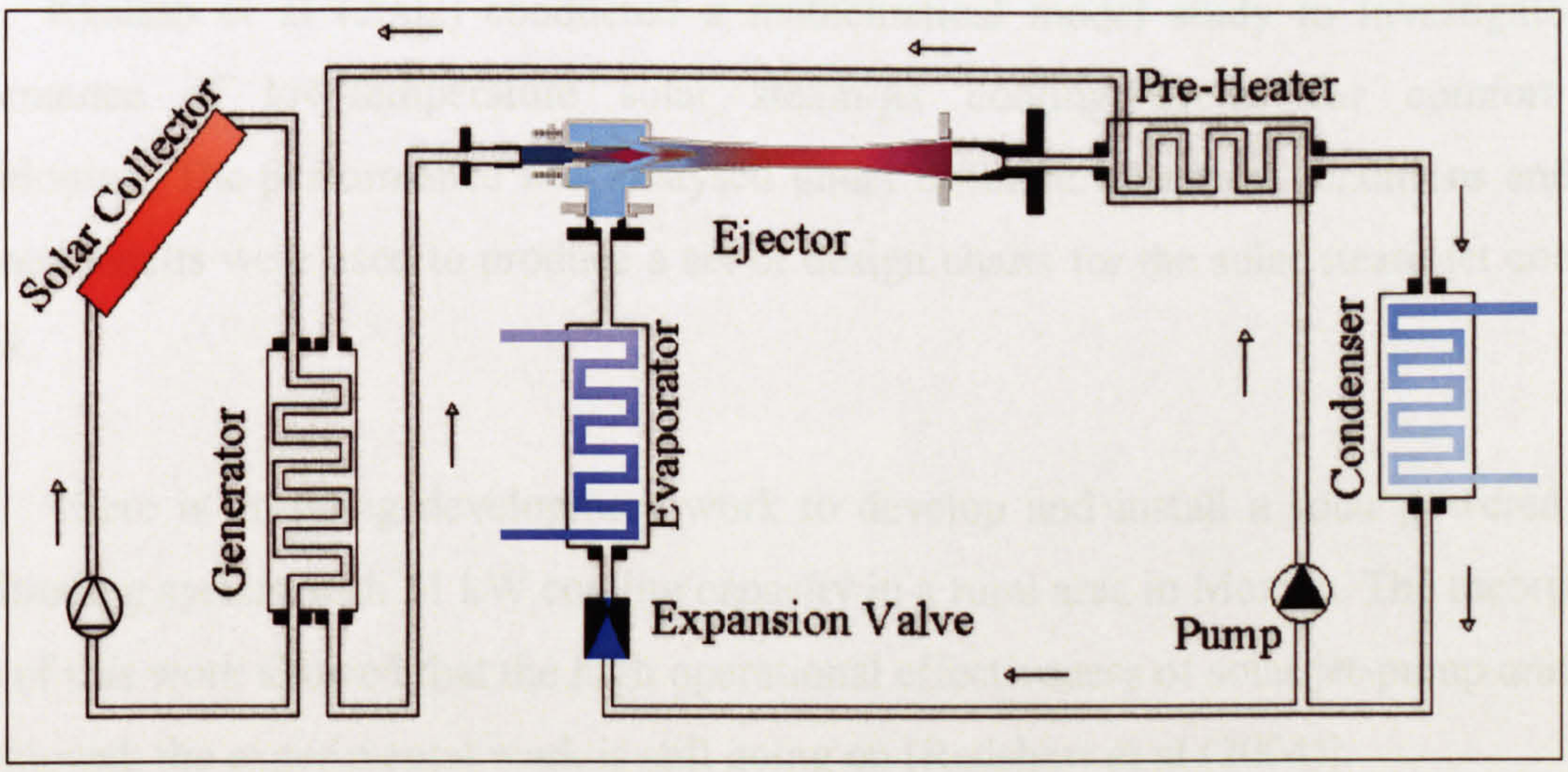

Figure 2. 4 Schematic diagram of solar jet refrigeration system with separated loops

The overall performance of the solar-jet refrigerator is affected by the thermal efficiency of the solar collector which depends on the collector type, intensity of solar radiation and the system operating conditions. For moderate generator temperatures,

between 70°C to 100°C, single glazed or double glazed flat type collectors with a selective surface are recommended; [Khattab et al (2002) and Huang et al (1998)]. Many researchers have carried out analytical and experimental studies to investigate the implementation of solar energy to run the jet refrigeration system. Sokolov (1993) studied the performance of a solar-jet system with using R114 as the working fluid, and later Arbel and Sokolov (2004) updated this work using R142b as the working fluid. Huang (1998) carried out an analytical study to implement solar energy in a jet-pump refrigeration system with R141b as the working fluid. A commercially available, double glazed, selective-surface flat plate solar collector was used in their analytical study because of the availability of performance characteristics. They showed that the system can have an optimum overall efficiency around 0.22 at a vapour generator temperature 95°C and an evaporator temperature at 8°C, and for solar radiation at 700 W m^{-2}.

Nguyen et al (2001) developed and experimentally tested a solar-powered passive jet-pump cooling system with 7 kW cooling capacity. Thermomax evacuated tube heat-pipe solar collectors were used to provide boiler heater water temperature up to 110°C. The system was installed in an office building in Loughborough-UK, to provide 50% of the total building's cooling load; a COP of 0.3 was obtained.

Khattab et al (2002) conducted a mathematical model study to investigate the performance of low-temperature solar steam-jet cooling cycles for comfort air conditioning. The performance was analysed under different operation conditions and the obtained results were used to produce a set of design charts for the solar steam-jet cooling cycles.

There is on-going development work to develop and install a solar powered air-conditioning system with 11 kW cooling capacity in a rural area in Mexico. The theoretical stage of this work showed that the high operational effectiveness of solar jet-pump unit can be achieved; the experimental work is still going on [Redshaw et al (2004)].

Eames et al (2005) demonstrated the feasibility of a 1.5 kW solar powered package jet-pump refrigerator for an air conditioning application. R245fa was used as the working fluid; a COP of 0.4 was achieved.

2.7 Hybrid-Novel Jet-pump-absorption Refrigeration System

Applying the jet-pump to an absorption system was found to have a significant improvement on the system COP. The jet-pump function in the absorption cycle is to enhance evaporation, absorption and concentration processes. Many researchers have attempted to use the jet-pump in order to improve the cycle performance. Chung et al (1984) and Chen (1998) conducted experimental studies to use a jet-pump in the cycle to increase the absorber pressure over the evaporator pressure which will lead to improve the COP of the system when appropriate refrigerant is used.

Eames et al (1995a) developed a computer simulation programme for the combined cycle and used it to determine the performance of the system using LiBr-H_2O at different operation conditions; this cycle is shown in Figure 2.5. The jet-pump is placed between a generator and condenser. The steam jet-pump was driven by high pressure water-vapour from the generator of the absorption cycle. However, the vaporisation process in this novel cycle is enhanced as some parts are entrained to the jet-pump and another is absorbed by the solution, thus a higher COP was expected.

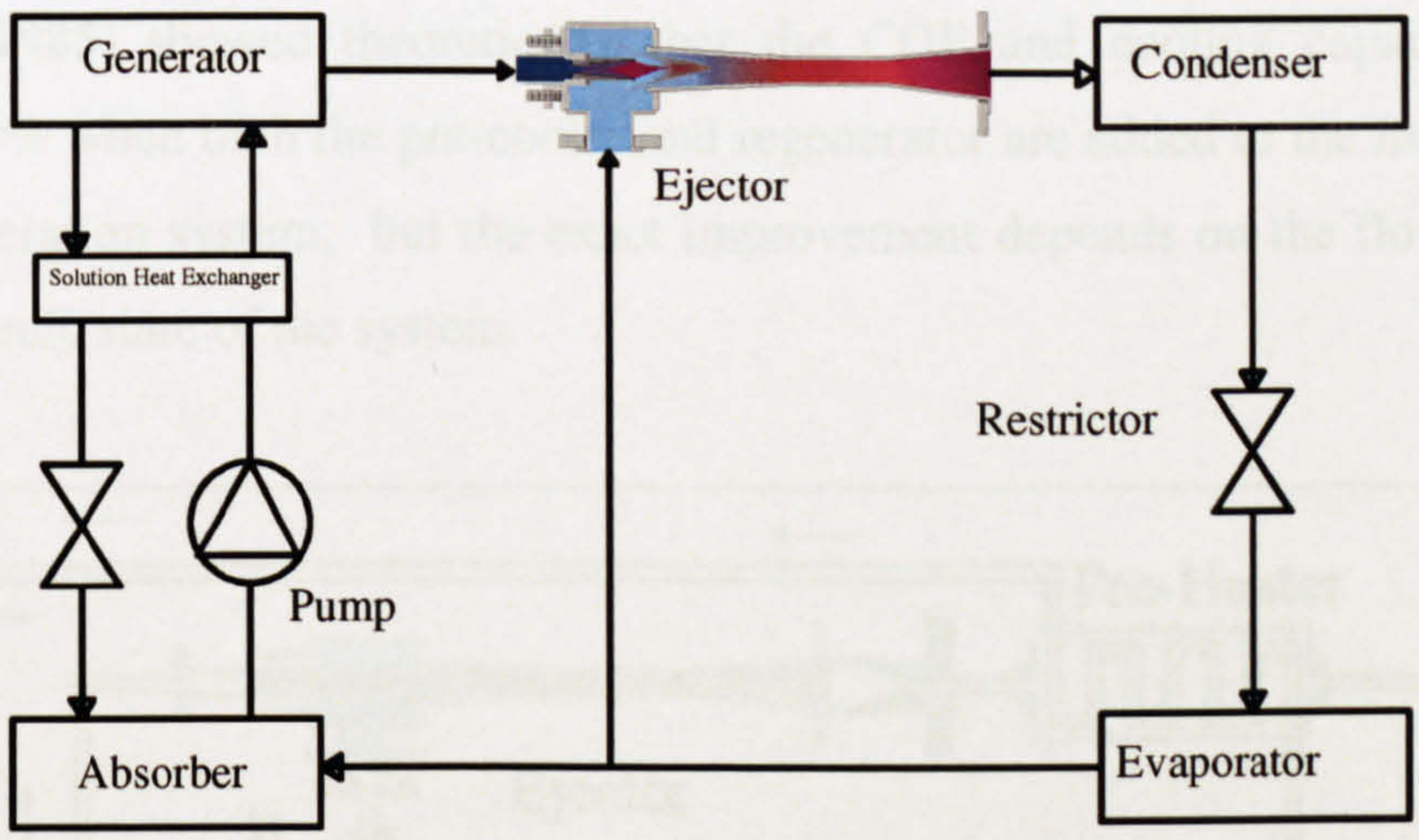

Figure 2. 5 Combined jet-pump absorption cycle

An experimental investigation on this cycle showed that a COP of 0.8 to 1.04 for 5°C cooling temperature could be achieved, but with a very high generator temperature of at least 200°C which is considered the major drawback of this system as it can lead to an increase on corrosion rates which may be problematic. The mathematical simulation of this novel cycle was reported and given by Sun et al (1996). A series of studies of different

proposed approaches of using jet-pumps with the absorption cycle were conducted and well documented, [Wu et al (1998), Eames et al (2001), Alexis et al (2002a), Jiang (2002), Sozen (2003), Eames et al (2000) and Alexis et al (2002b)].

2.8 Enhancement of the Jet-pump Refrigeration System

In order to improve jet-pump refrigeration system efficiency, by reducing the amount of heat transported and hence reducing the equipment's size, theoretical studies of adoption of the pre-cooler (economizer) and the pre-heater (recuperator) "RG unit" into the simple jet-pump cycle were carried out, [Sun et al (1996), Huang et al (1985), Sokolov et al (1990b,c), Chen et al (1987), Sokolov et al (1990a) and Sun (1999)] as illustrated in Figure 2.6. Positioning the pre-heater as shown will reduce the heating requirement at the generator as the temperature of refrigerant returning back into the boiler is increased within the pre-heater. Also it will ease the load for the condenser which will need less circulation of cooling medium. On the other hand, the heat absorbed at the evaporator can be increased when the temperature of refrigerant entering the evaporator is reduced within the pre-cooler. Entrainment ratios may remain the same as without RG unit, but the water mass flow rate into the evaporator will be increased thus the cooling capacity will be improved. Huang et al (1985) showed theoretically that the COP and cooling capacity can be increased by 20% when both the pre-cooler and regenerator are added to the main cycle of jet-pump refrigeration system, but the exact improvement depends on the flow rates and the thermodynamic state of the system.

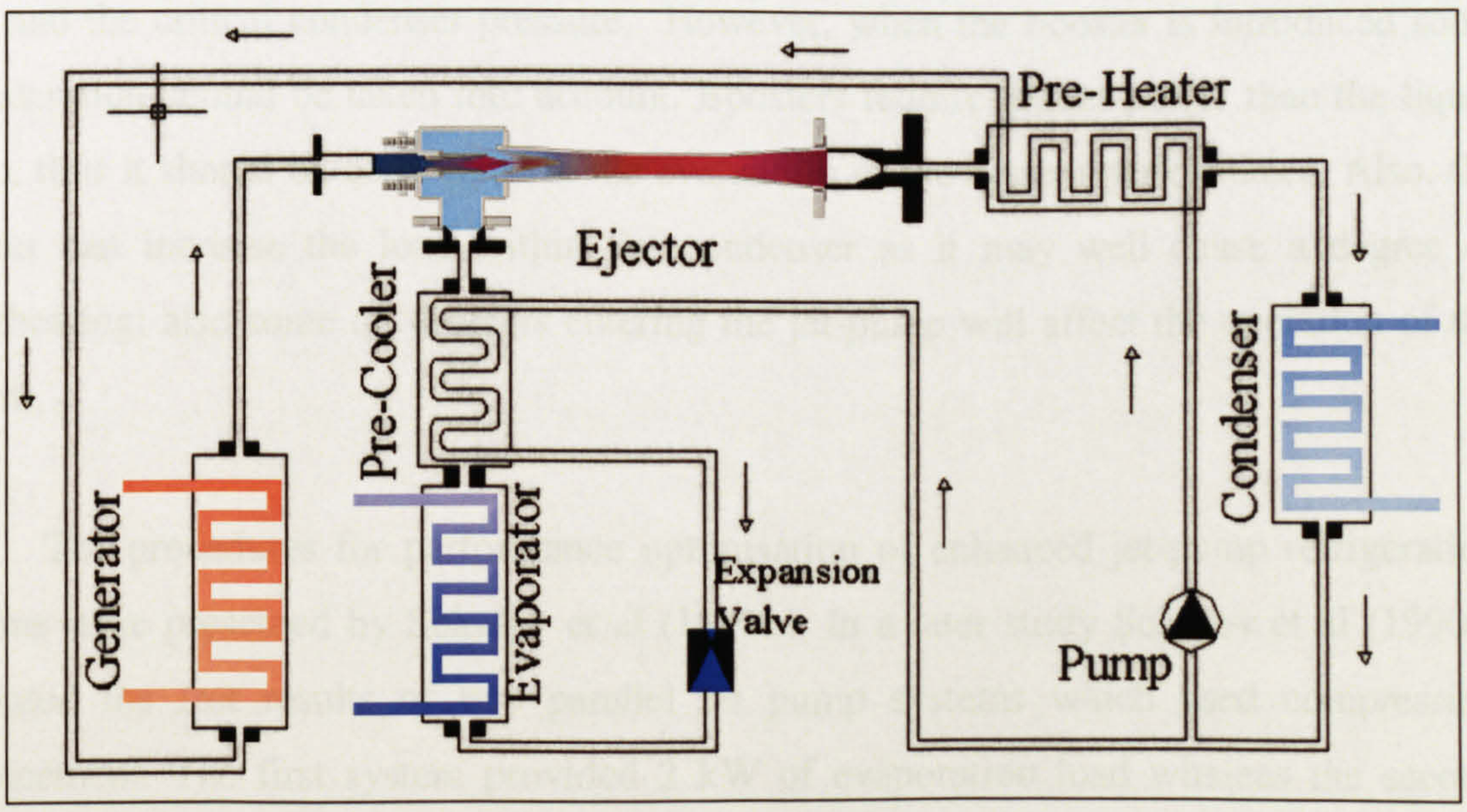

Figure 2. 6 Jet-pump refrigerators with a pre-cooler and a Pre-Heater

On the other hand Sokolov et al (1990a) and Dorantes et al (1996), introduced the booster assisted jet-pump refrigeration system as illustrated in Figure 2.7, where the mechanical pressure booster is used to improve the system performance "COP" and smooth the fluctuations in working conditions.

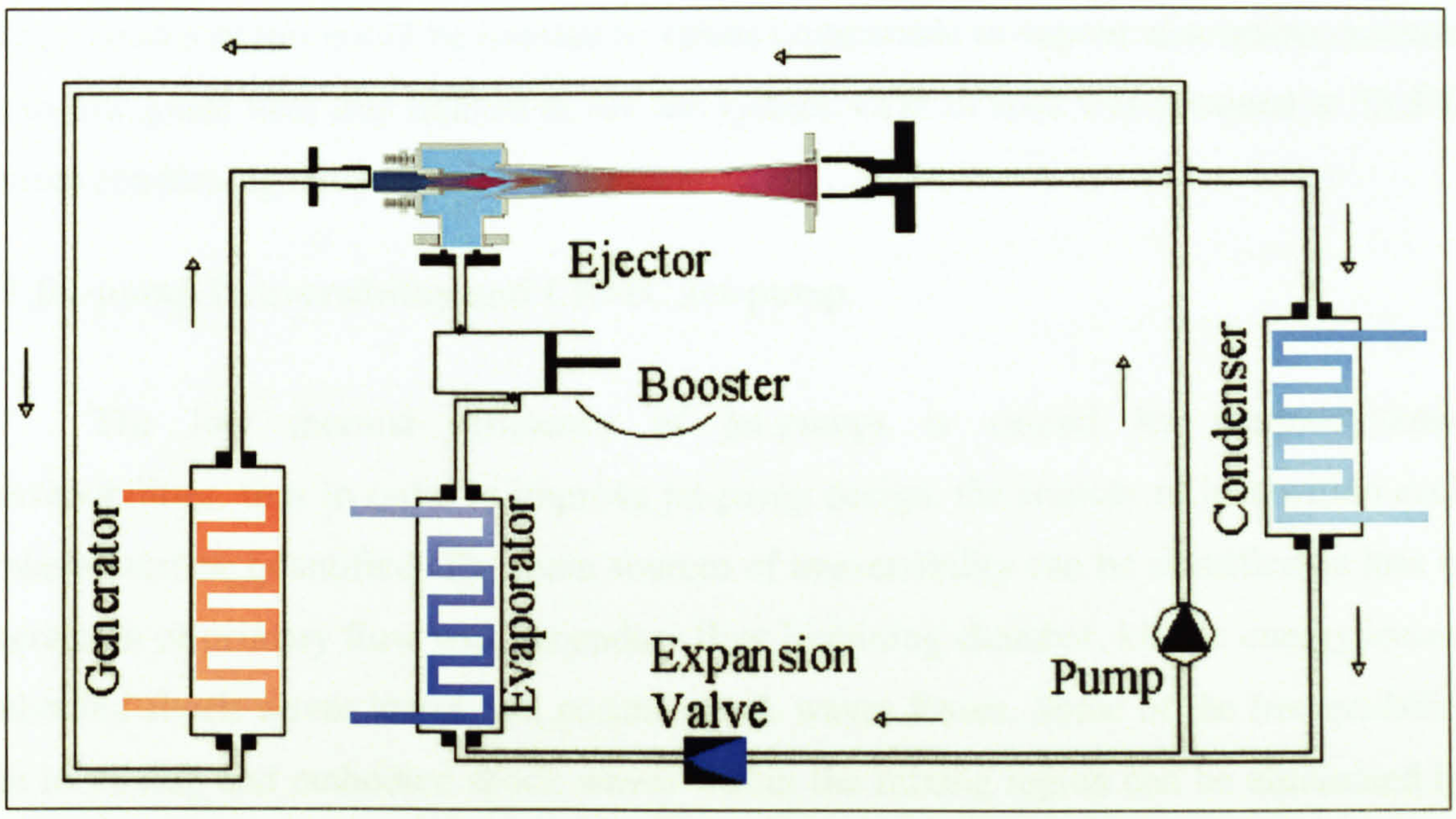

Figure 2. 7 Jet-pump refrigerator systems with Booster

The booster is placed between the evaporator and the jet-pump suction line. In this way, the vapour from the evaporator will undergo two stages of compression. First compression is made by the booster and the second compression is made by the jet-pump. The pressure of secondary flow within the jet-pump suction line will increase without disturbing the refrigeration temperature and this result in increases in both the entrainment ratio and the critical condenser pressure. However, when the booster is introduced some consideration should be taken into account. Boosters require higher power than the liquid pump, thus it should be considered in the evaluation of the system performance. Also, the booster can increase the load within the condenser as it may well cause a degree of superheating; also some oil droplets entering the jet-pump will affect the operation of the system.

The procedures for performance optimisation of enhanced jet-pump refrigeration systems were presented by Sokolov et al (1990b). In a later study Sokolov et al (1990c) evaluated the test results of two parallel jet pump systems which used compression enhancement. The first system provided 2 kW of evaporation load whereas the second

provided 3 kW. It was shown that the work input into the booster and feed-pump was close to 0.2 kW in the case of 2 kW of refrigeration and was less than 0.5 kW in the case of 3 kW of refrigeration. The system was shown to operate smoothly with jet-pump changeover depending on environment conditions. Their works demonstrate that the COP of jet-pump refrigeration systems could be boosted to values comparable to vapour absorption systems, when low grade heat was utilised to run the system. COP of 0.42 was obtained at 53.5°C critical condensing temperature.

2.9 Jet-pump Irreversibility and CRMC Jet-pump

The low thermal efficiency of jet-pumps is caused by thermodynamic irreversibilities, thus in order to improve jet-pump design, the sources of loss within each process must be quantified. The main sources of irreversibility can be classified as loss of interaction of primary flow with secondary flow in mixing chamber, kinetic energy losses, embodied shock waves losses and normal shock waves losses. Some of the irreversibility due to mixing and embodied shock waves within the mixing region can be eliminated by appropriate choice of working fluid, and with adjustable nozzle position [Sun et al (1996)].

Kinetic energy losses are those which occur within the convergent part of the nozzle and within the diffuser. These result from frictional effects caused by flow separation. Flow separation occurs mostly on the divergent passages when flow area increases rapidly. This leads to strong turbulence near the wall. However, these losses can be reduced with a good surface finish and close axial alignment between the nozzle and the diffuser. In practice, these can be achieved easily with large jet-pump nozzles as they are less difficult to manufacture. Nozzle efficiency should be selected accordingly.

Arbel et al (2002), presented an analysis of jet-pump irreversibilities using the entropy production method. They showed that entropy production is equivalent to the losses within the jet-pump, and hence it can be used for optimization and improvement of designs.

Losses associated with normal shock system, as mentioned is Chapter 1, is that it causes loss in total pressure of the mixed stream, and thus has a direct effect on reducing the maximum back pressure that a jet-pump can overcome. However, to improve the

system efficiency the effect of the normal shock must be minimized in order to maintain the highest critical pressure.

The CRMC jet-pump proposed by Eames (2002) produces a diffuser geometry that can provide the optimum flow passage area. This is expected to reduce the thermodynamic shock at design operating conditions and hence, increase the performance of a jet-pump. Figure 2.8 shows a diffuser geometry designed using the CRMC method. The geometry allows the static pressure to rise gradually from entry to exit within the jet-pump; thus at the design-point operating conditions the thermodynamic shock process will disappear and their losses will be minimised.

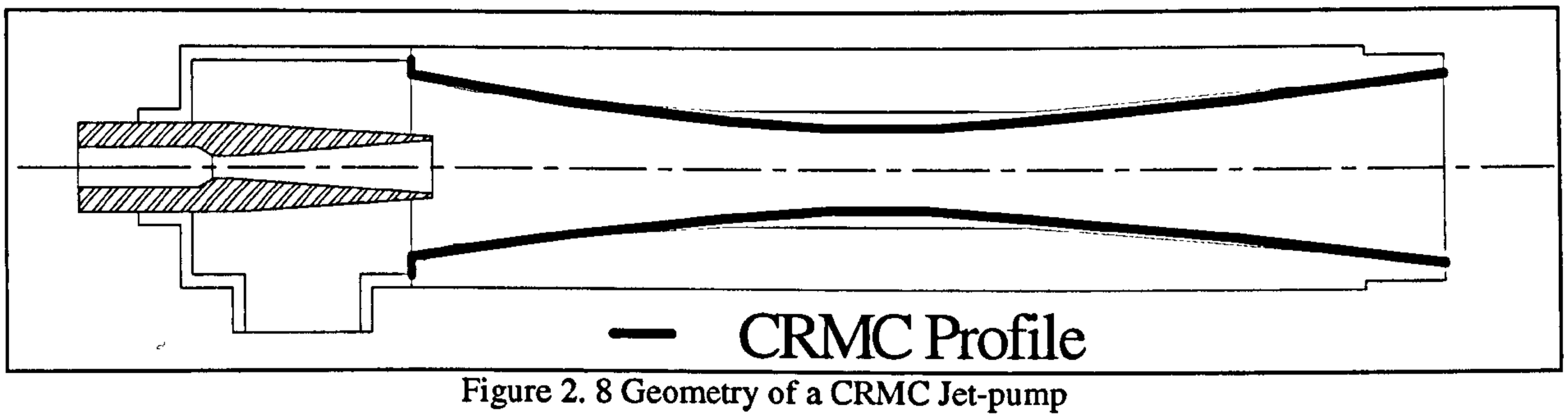

Figure 2. 8 Geometry of a CRMC Jet-pump

An investigation of the CRMC method forms an important part of this research and is discussed in detail in the following Chapters.

2.10 Working Fluids

The thermodynamic properties of the working fluid have a direct effect on the performance of jet-pump refrigeration systems. There are some important criteria that the working fluid should have. These are as following:

- The fluid should have a large latent heat of vaporization and small specific volume. This minimizes the circulation rate for designed cooling capacity and avoids large diameter pipe work.

- Reasonable working pressure, "not too high" at the boiler side in order to minimize the power required by the pump and also to avoid any risk from the construction of the boiler. Also the working fluid should vaporize and condense at suitable

temperatures and pressures, thus in the evaporator side the pressure is preferable to be always above the atmospheric pressure.

- High critical temperature.

- Non-corrosive, non-toxic and non flammable.

- Favourable transport properties should be inherent in the fluid to be selected in order to promote heat transfer.

- Fluids with high molecular weight are more favourable [Holton (1951)] because they tend to give high entrainment ratios.

- The specific heat of vapour should be high and for liquid should be small to reduce the superheating region and increase the degree of sub-cooling respectively [Al-khalidy (1998)].

- Environmentally friendly. This is an important issue for selecting refrigerants in new systems. There has been a radical change over the last decade due to action of international agreements such as the Montreal and Kyoto protocols. These protocols address global environmental issues and provide guidelines needed to ensure that all refrigerants are environmentally safe. Therefore, various alternative refrigerants have been introduced as 'environmentally friendly' and a large number of development projects to design new systems based on these have been carried out.

- There are two categories of working fluids based on the slope of saturated vapour line on T-S diagram [Chen et al (1998)]. Wet vapour fluids which have a negative slope saturated line; and dry vapour fluids which have a positive slope line. Figure 2.9 shows the difference between them. As shown in the Figure 2.9 for the dry vapour type expansion processes take place entirely within the dry region. Whereas, for wet vapours, expansion processes take place mostly in the wet region, causing small droplets to form at the nozzle exit. These have a direct effect on the

expansion of the jet and form a barrier with the wall for the secondary flow, which can damage and affect the jet-pump performance; [Chen et al (1998) and ASHRAE (1983)]. When working fluids of negative slope are used, superheating the fluid before entering the nozzle is required to avoid the droplet problem and this result in a decrease in jet-pump efficiency [Sokolov et al (1990a)]. Dry vapour is the more efficient fluid to use in jet-pump refrigeration systems.

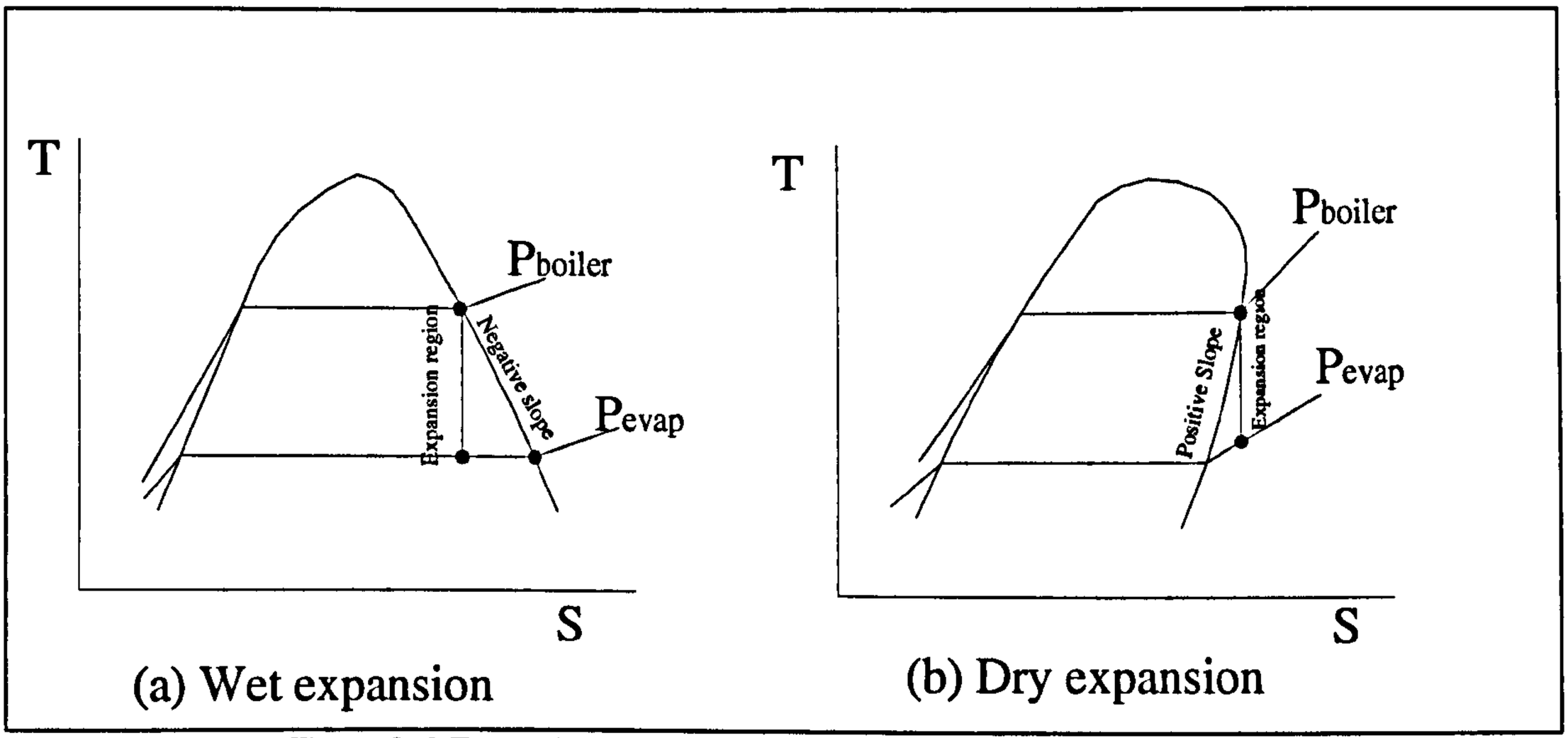

Figure 2. 9 Expansion region of refrigerant within the primary nozzle

However, no single fluid has all aforementioned merits and therefore, research and development is still going on to find optimal fluids. It has been mentioned that using water as the working fluid for a jet refrigerator has many advantages in terms of environmental impact and power required for the pump but its small COP makes the other refrigerants of low-boiling temperature more advantageous. Most of the well known halocarbons-based refrigerants (CFCs, HCFCs and HFCs) have already been investigated for use in jet-pump refrigeration system, as discussed in Section 2.5.

In this investigation two relatively new refrigerants are studied. These are 1,1,1,3,3,3 hexafluoropropane "R236fa" and 1,1,1,3,3,-pentafluoropropane "R245fa". R245fa has been developed as replacement fluid for R141b zero Ozone depletion potential and low Global warming potential, whereas R236fa has been developed as replacement fluid for R-114 for use in centrifugal chillers [Dupont (2004)]. Both R236fa and R245fa fulfil most of the afore mentioned conditions. They both generally have a low boiling point and a high heat capacity. This enables a small amount of the refrigerant to transfer a large

amount of heat efficiently and a high temperature is not needed to obtain the motive vapour in the boiler.

The most important properties of these two refrigerants, compared with steam and R141b used in the CFD simulation, are listed in Table 2.1. In addition, the physical properties of each of steam, R141b, R236fa and R245fa, over a range of temperatures between 0°C to 130°C, are provided in Appendix A.

Table 2. 1 The properties of fluids used in this study

Property	R236fa	R245fa	R141b	Water/Steam
Chemical Formula	$CF_3CH_2CF_3$	$CHF_2CH_2CF_3$	CH_3CCL_2F	H_2O
Molecular Weight	152.04	134.05	116.95	18.02
Critical Temperature	124.9C	150	204.15	373.99
Critical Pressure (MPa)	3.200	3.39	4.25	22.064
Specific Heat, Liquid@ 25°C (kJ/kg.K)	1.1085	1.36	1.16	4.183
Specific Heat, Vapour @25°C (kJ/kg.K)	0.8444	0.93	0.775	1.887
Ozone-depletion potential	0.0	0.0	0.15	0
Boiling point at 1 atm (° C)	-1.44	15.3	32.2	100
Heat of vaporization @ boiling point (kJ/kg)	160		223	2260
Saturated line slope	positive	positive	positive	negative

2.11 CFD Studies on Jet-pump Performance

The application of CFD to study jet-pump performance began over thirty years ago. In 1974, Hedges and Hill developed a 2-D model to calculate the mixing of a compressible jet in plane and axisymmetric variable ducts by considering turbulent phenomena. This model was incapable in dealing with recirculation and strong shock waves. Different forms of jet-pump were simulated by adopting a finite difference program utilising the K-Є turbulent model and applied only to the incompressible flow in a jet pump [Croft et al (1976)]. Nilavalagen et al (1988) also presented a similar technique for simulation of a

compressible flow jet-pump, however, previous problem faced by Hedges et al (1974) were not overcome.

Recently, commercial CFD programmes such as Fluent were used to simulate jet-pumps with some success. However, understanding the numerical approach in which CFD is based is important for obtaining reasonable results that can be believed and accepted. The varieties of options associated with CFD commercial programmes can lead to problems in obtaining qualitative results and therefore, caution must be exercised in the results obtained.

Recent studies of jet-pump performance using CFD were based on jet-pumps used in refrigeration and air conditioning systems, which use one type of refrigerant in their cycle. Riffat et al (1996) applied CFD to simulate jet-pumps with different types of refrigerants. They claimed that in order to predict detailed flow fields accurately, the jet-pump must be modelled three-dimensionally. Different shapes of primary nozzle with different nozzle positions were investigated. However, due to their computer constraints, an independent mesh test for 3-D model was difficult to conduct and also at that time, the governing equations related to the compressible flow were too complicated; due to complicated geometry and computational difficulties, converged solutions for compressible flow simulation were difficult to achieve. Also later study of Chin et al (1997) showed that modelling jet-pump three-dimensionally is an unnecessary complexity.

Riffat and Smith (1997) also used Fluent to simulate a supersonic steam jet-pump, but neglected compressibility flow effects. They studied the influence of nozzle position and generator temperature on jet-pump performance. Also, due to the computational constraints that limited the mesh resolution used, and with the assumption of incompressible flow, it was difficult for them to achieve reasonable results.

Chin et al (1997) compared two commercially available finite volume codes; segregated and coupled solvers, in the application of supersonic jet-pump simulation. They applied a two-dimensional axisymmetric geometry and applied a boundary condition for motive stream based on the flow conditions at the nozzle exit calculated from 1-D compressible flow theory. However, these calculated conditions at the nozzle exit may have lead to significant errors with respect to experimental results. From their findings, the

coupled solver was shown to perform better than the segregated solver in predicting mixing process and shock system. Also, it was shown that applying the related numerical approach and with sufficient refined mesh, the jet-pump can be simulated accurately.

Hart (2002) conducted CFD investigations for different jet-pumps that were used for different applications. He modelled the steam jet-pump as a simplified two-dimensional axisymmetric geometry. The simulations were used to assess the influence of geometry and operating conditions on the jet-pump performance. Comparison between segregated and coupled solvers with independent mesh tests was conducted. The coupled numeric solvers were found more suited to the simulation of compressible process that occurred within the jet-pump. Near wall modelling and turbulent models were investigated with a coupled solver only. K-Є turbulent model was found to perform the best over all other models. The shock system and mixing processes within jet-pump were identified clearly and the findings from geometrical studies showed that current design guidelines [ESDU (1985)] of jet-pump to be well set. The application of CFD to alternative jet-pump design such as in thrust augmentation and in generating a vacuum have been investigated Hart (2002). However, CFD was shown that it has the potential to be an effective tool for simulation of different ranges of jet-pump, when careful attention is paid to the selection of numerical parameters.

Chunnanond et al (2004a), conducted a CFD study to simulate the steam jet-pump refrigerator. Assumptions of perfect and compressible gas were applied to a 2-D jet-pump. Different models of K-Є models were also applied. A coupled-implicit solver, with standard wall function was adopted. Experimental static pressure profiles close to the jet-pump wall were used to verify the CFD results. The simulated results were validated with experiment data and good agreement was obtained. The effects of operating conditions on jet-pump performance were discussed. Good explanation of flow field and the mixing process within the wetted area of jet-pump was given.

2.12 Conclusions

This chapter described the main theory and development of research strategies for jet-pump refrigeration systems. The principle of work of the critical component, the jet-pump, was discussed and evaluated.

The review shows that, the use of steam and low-boiling refrigerants with jet-pump refrigeration system have been investigated both theoretically and experimentally by several researchers and it was concluded that most of the low-boiling refrigerants were suitable for the practical application of jet-pump refrigeration systems. Compared with steam systems, the higher performance can be achieved with low-boiling refrigerants, as they can be used efficiently even with low vapour generator temperatures ranging above 60 °C. Fluid selection criteria for the jet-pump refrigeration systems were evaluated. Dry expansion vapour fluids were highlighted as more efficient.

This review showed that low temperature thermal energy can be used to drive jet-pump refrigerators, especially for air conditioning applications, particularly when low-boiling refrigerants are used. Also it was shown that the performance of jet-pump refrigeration systems could be enhanced by incorporate the regenerating unit within the cycle. In order to improve the performance of jet-pump, recent studies proposed a new measure in designing jet-pumps by identifying the irreversible losses and minimize them. Thus the methods of minimizing the performance losses were evaluated. The main source of inefficiency was found to be that produced by shock waves. Losses from mixing and frictional effect were also identified. Ways to eliminate losses by designing jet-pump with adjustable throat profile and selecting the appropriate working fluids and adjust the nozzle position were also highlighted.

A review of recent applications of CFD simulation of jet-pumps showed that, the method allows for the representation of flow phenomena within jet-pumps which cannot be or may be difficult to obtain experimentally and thus it can be used widely to optimize and improve jet-pump performance.

Chapter 3

Constant Rate of Momentum Change method "CRMC" and Computational Fluid Dynamics (CFD) Simulation

3. Constant Rate of Momentum Change method "CRMC" and Computational Fluid Dynamics (CFD) Simulation

3.1 Introduction

One purpose of this research is to demonstrate that the performance of jet-pump systems can be improved in order to make them competitive with other types of refrigeration systems. To achieve optimum performance of a jet-pump two methods are used in this study. First, by reducing the shock wave characteristic of conventional jet-pump system by introducing the new concept of CRMC design method and second by implementation of Computational Fluid Dynamics (CFD) to understand clearly the nature of flow structure and the mixing process within the jet-pump, with assessment of the influence of operating conditions and geometry. In this chapter, the Conventional and CRMC design methods are presented and evaluated. The details of optimized numerical CFD model are also presented. The CFD commercial code used was Fluent versions "5.5, and 6.1". To be assured that the model is correctly representing the flow behaviour and thus the jet-pump performance, the numerical code was verified and validated using available experimental data from two jet-pump geometries using two different working fluids. The first jet-pump used water as its working fluid and the second jet-pump used R141b. Independent tests for both mesh and turbulence models have been carried out and these are presented in this Chapter. The optimal calculation domain for the realized code, including other significant association criteria of the model is provided. In addition, a full study of the effect of operating conditions and nozzle exit position for both selected jet-pumps are explored and discussed using CFD visualization. From this the main phenomenon of jet-pump performance characteristics are described.

3.2 Jet-pump Design Analysis "One-Dimensional analysis"

In this section the one-dimensional analysis used to determine the dimensions of critical flow passages, which are the primary nozzle throat and exit diameters and the diffuser throat and exit diameters. The one-dimensional analysis described by Eames et al (1995b) with developments by this author were used throughout this design analysis. The analysis is based on steady state and steady flow equations of energy, momentum and

continuity which, are applied through all critical points of flow passages. The nomenclature used in this analysis is shown in Figure 3.1.

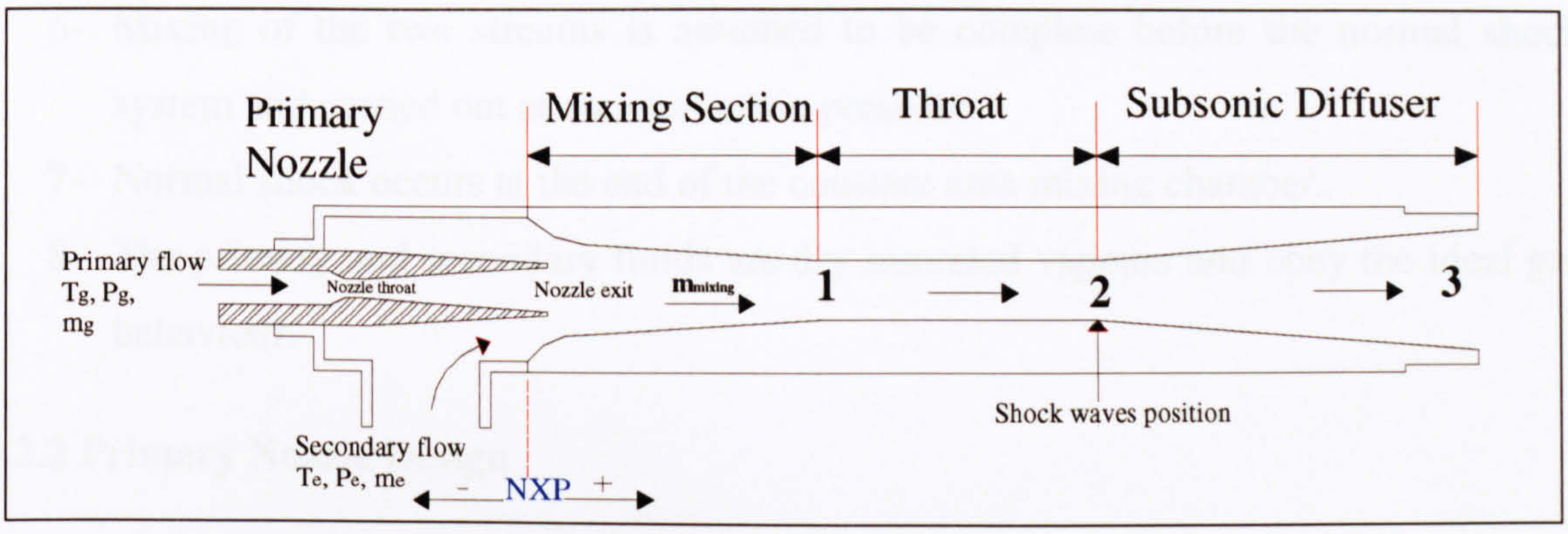

Figure 3. 1 Schematic of a supersonic jet-pump showing the nomenclature used in this analysis

Energy equation for an adiabatic process between states 1 and 2 in one dimensional analysis is:

$$\Sigma m_1\left(h_1+{V_1^2}/{2}\right)=\Sigma m_2\left(h_2+{V_2^2}/{2}\right) \qquad [3\text{-}1]$$

Momentum equation:

$$p_1 A_1+\Sigma m_1 V_1=p_2 A_2+\Sigma m_2 V_2 \qquad [3\text{-}2]$$

Continuity equation:

$$\Sigma \rho_1 V_1 A_1=\Sigma \rho_2 V_2 A_2 \qquad [3\text{-}3]$$

Where m is mass flow, h is specific enthalpy, V is velocity, P is pressure, ρ is density and A is area.

3.2.1 Assumptions Made in the One-dimensional Analysis

Based on Eames et al (1995b) the following simplifying assumptions are made with the mentioned governing equation:

1- The flow inside the jet-pump is steady and one dimensional.
2- Velocities at the inlets of primary and secondary fluids and at the exit of the diffuser are negligible.
3- Frictional and mixing losses are defined in terms of isentropic efficiencies in the nozzle, and diffuser.

4- The walls of the nozzle and diffuser are adiabatic.
5- The primary and secondary fluids are identical; they have the same molecular weight and the same ratio of specific heat values.
6- Mixing of the two streams is assumed to be complete before the normal shock system and carried out at constant static pressure.
7- Normal shock occurs at the end of the constant area mixing chamber.
8- The primary and secondary fluids are dry saturated vapours and obey the ideal gas behaviour.

3.2.2 Primary Nozzle Design

Knowing the design cooling load, and entrainment ratio, it is possible to calculate the required primary mass flow from which the primary nozzle throat area can be determined. The cooling load is found from equation [3-4].

$$\dot{Q}_e = \dot{m}_s(h_{g,e} - h_{f,c}) \qquad [3\text{-}4]$$

Where, $\dot{m}_s$ is the evaporation rate = secondary mass flow rate at steady state conditions

$h_{g,e}$ is the specific enthalpy of vapour at the evaporator temperature, and $h_{f,c}$ is the specific enthalpy of liquid at the condenser saturation temperature.

$\dot{m}_s$ can be calculated directly from equation [3-4], when each of evaporator and condenser saturated temperatures are known.

Entrainment ratio is defined by:

$$R_m = \frac{\dot{m}_s}{\dot{m}_p} \qquad [3\text{-}5]$$

For a given R_m, then the primary mass flow "$\dot{m}_p$"can be calculated.

3.2.2.1 Flow Conditions at Nozzle Throat

To determine the primary nozzle throat area, the Conservation of Mass equation is applied at the nozzle throat:

$$m^* = \rho^* C^* A \qquad [3\text{-}6]$$

The flow properties at the throat of the nozzle are given:

$$\rho^* = \frac{p^*}{R\ T^*} \qquad [3\text{-}7]$$

$$P^* = P_g\left(\frac{2}{\gamma+1}\right)^{\frac{\gamma}{\gamma-1}} \qquad [3\text{-}8]$$

$$T^* = T_g\left(\frac{2}{\gamma+1}\right) \qquad [3\text{-}9]$$

$$C^* = \sqrt{\gamma R T^*} \quad = a = \text{speed of sound} \qquad [3\text{-}10]$$

Where $M_n = 1$

From equation [3-6], nozzle throat area can be determined.

3.2.2.2 Flow Conditions at the Nozzle Exit

Referring to Figure 3.2, the velocity of primary flow at the nozzle exit can be determined [Eames et al (1995)] by applying energy equation between point P and nozzle exit.

$$C'_{N-exit} = \sqrt{2C_p\left(T_g - T_{N-exit}\right)} \qquad [3\text{-}11]$$

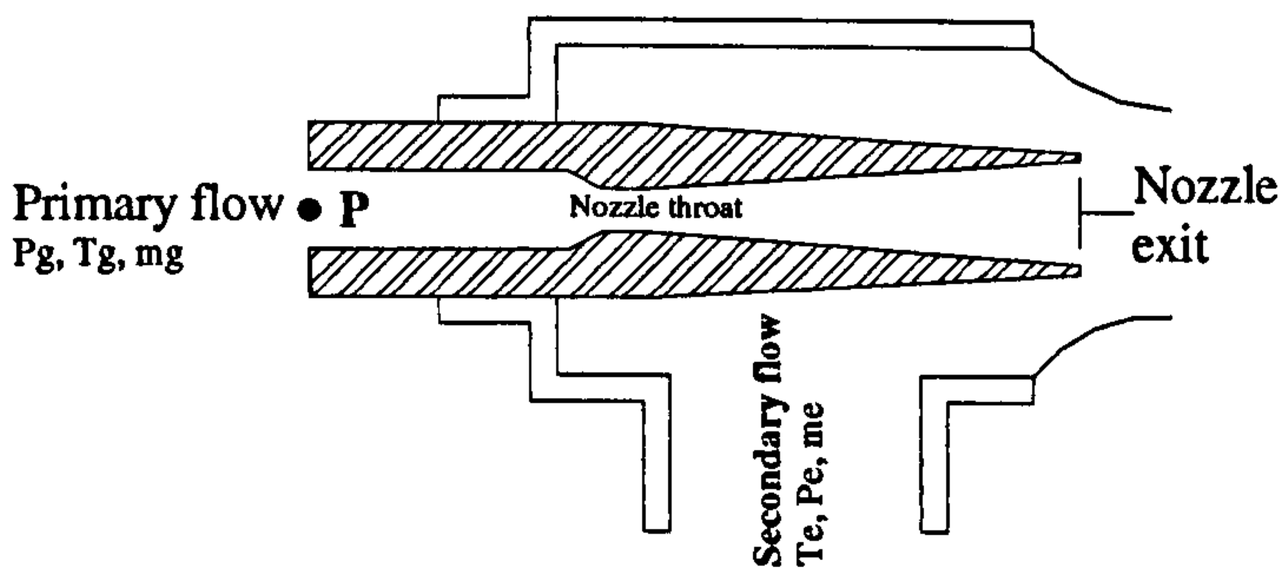

Figure 3. 2 Convergent-divergent (de-Laval) nozzle

In reality the flow velocity is less than that given by equation [3-12] because of the effect of friction between the fluid and the sides of the nozzle, as well as dissipation of energy due to eddies formed in the fluid itself. Therefore to account for this, an isentropic efficiency of the primary nozzle is introduced "η_N".

Thus the actual flow velocity of primary flow at the nozzle exit =

$$C_{N-exit} = \sqrt{2 C_P \eta_N \left(T_g - T_{N-exit}\right)} \qquad [3\text{-}12]$$

Typical values of η_N lie between 0.97 and 0.99, ESDU (1985).

From the isentropic relationship between pressure and temperature ratios, temperature at nozzle exit can be obtained.

$$\frac{T_g}{T_{N-exit}} = \left(\frac{P_g}{P_{N-exit}}\right)^{\frac{\gamma-1}{\gamma}} \qquad [3\text{-}13]$$

P_{N-exit} "Pressure at the nozzle exit" is given by Equation [3-14] after accounting for the losses through secondary inlet.

$$P_{N-exit} = \eta_e P_e \qquad [3\text{-}14]$$

Where, P_e is the secondary flow pressure and η_e is the suction line loss coefficient. Then by applying the conservation of mass equation at the nozzle exit, the nozzle exit Mach number and the nozzle exit area can be obtained.

$$A_{N-exit} = \frac{m_g}{\frac{p_{N-exit}}{R\ T_{n-exit}} C_{N-exit}} \qquad [3\text{-}15]$$

$$M_{N-exit} = \frac{C_{N-exit}}{\sqrt{\gamma R\, T_{N-exit}}} \qquad [3\text{-}16]$$

3.2.3 Diffuser Section Design

3.2.3.1 Mixing Section

Referring to Figure 3.3 the mixing of the primary and secondary fluids is assumed to occur at a constant static pressure inside the mixing section which is bounded between nozzle exit plane and point 1.

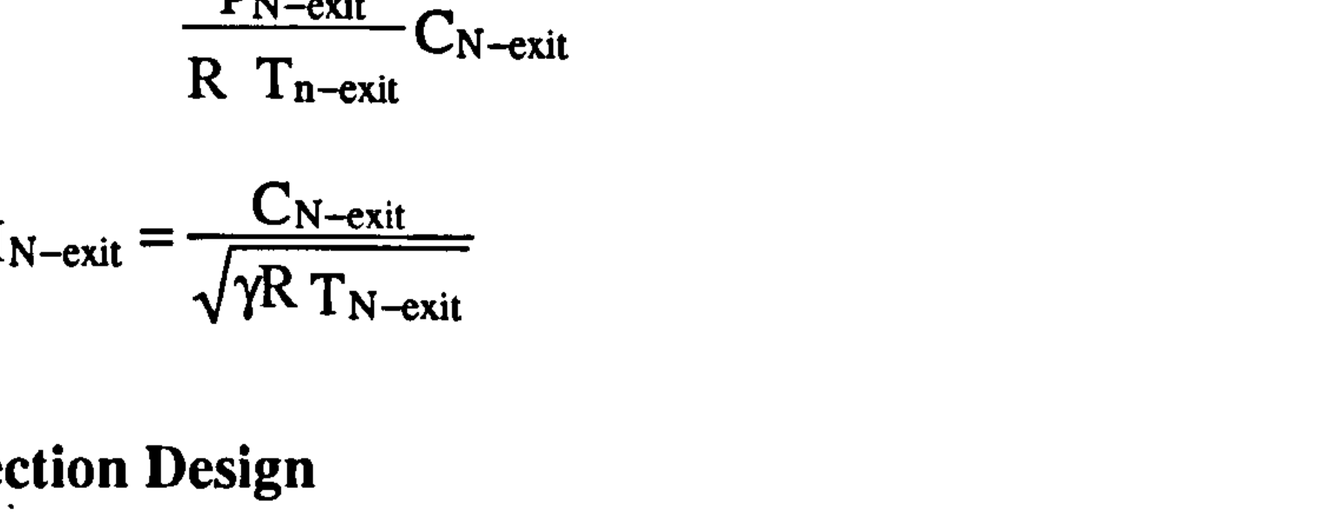

Figure 3. 3 Mixing section

By applying Newton's 2nd law of motion to the control volume between nozzle exit plane and (point1), with assuming that the walls of the mixing section offer no frictional resistance yields:

$$\sum F = \int A \, .dp = \dot{m}_{mix} C_1 - \dot{m}_g C_{N-exit} - \dot{m}_e C_e \qquad [3\text{-}17]$$

As the assumption that mixing process takes place at constant static pressure from nozzle exit to the end of constant area section, thus $dp = 0$; equation [3-17] can be rearranged as:

$$\dot{m}_{mix} C_1 = \dot{m}_g c_{N-exit} + \dot{m}_e c_e \qquad [3\text{-}18]$$

From mass flow continuity:

$$\dot{m}_{mix} = \dot{m}_g + \dot{m}_e \qquad [3\text{-}19]$$

Substituting [3-5] and [3-19] into [3-18] yields on rearrangement:

$$C_1 = \frac{C_{N-exit} + R_m C_e}{1 + R_m} \qquad [3\text{-}20]$$

The velocity of secondary fluid is negligible thus equation [3-20] can be rewritten as:

$$C_1 = \frac{C_{N-exit}}{1 + R_m} \qquad [3\text{-}21]$$

By taking into account the momentum loss coefficient (η_m) in the mixing chamber to account for the effect of wall friction, then the actual mixed flow velocity in the constant area section is given by:

$$C_{1act} = \eta_m C_1 \qquad [3\text{-}22]$$

Typical values of η_m lie between 0.85 and 0.9, ESDU (1985).

To determine other state properties of the mixed stream at Section 1, the steady flow energy equation can be applied across the control volume between section nozzle exit plane and point 1, with assuming that the mixing process is adiabatic.

Total enthalpy and total temperature at (point1) can be obtained from equations [3- 23] and [3-24]:

$$h_{t1} = \frac{h_{tg} + R_m h_{te}}{1 + R_m} \qquad [3\text{-}23]$$

For an ideal gas this reduces to:

$$T_{t1} = \frac{T_{tg} + R_m T_{te}}{1 + R_m} \qquad [3\text{-}24]$$

Static temperature at section 1 can be calculated from:

$$T_1 = T_{t1} - \frac{C_{1act}^2}{2C_p} \qquad [3\text{-}25]$$

Mach number at section 1 can be calculated from:

$$M_1 = \frac{C_{1act}}{\sqrt{\gamma\ R\ T_1}} \qquad [3\text{-}26]$$

Density:

$$\rho_1 = \frac{P_1}{R\ T_1} \qquad [3\text{-}27]$$

$$A_1 = \frac{\dot{m}_{mix}}{\rho_1 C_1} \qquad [3\text{-}28]$$

All flow properties remains constant along the constant area section.

3.2.3.2 Thermodynamic Shock Process

The flow basically changes within the constant area section from supersonic to subsonic. A normal shock process is associated with this change and, it occurs over a very thin region and large gradients in fluid properties occur with rapid change in pressure. It is assumed that this process is adiabatic; viscosity effects are neglect and flow area, where it occurs, remains constant. Thus by knowing the initial conditions before the shock then the conditions downstream of shock can be calculated [Hodge and Koenig (1995)].

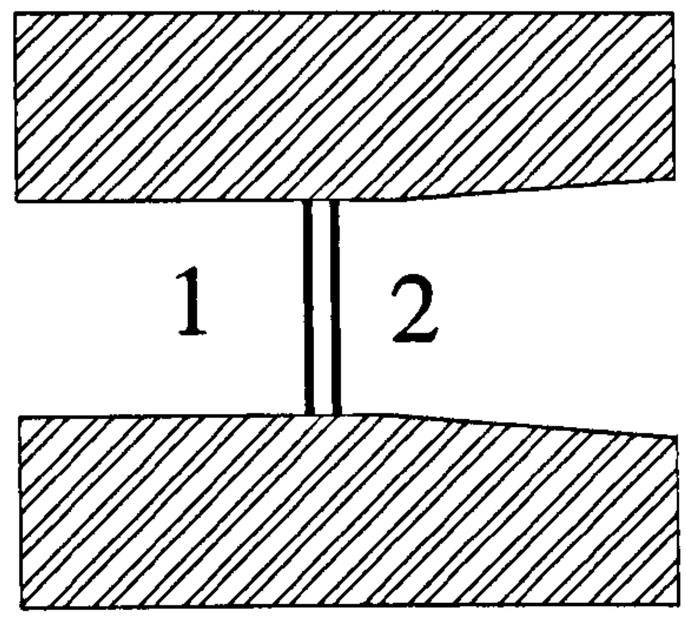

Figure 3. 4 Shock wave position

Referring to Figure 3.4 a normal shock process is assumed to occur at the end of the constant area section between state points 1 and 2.

Static pressure ratio:

$$\frac{p_2}{p_1} = \frac{2\gamma M_2^2}{\gamma+1} - \frac{\gamma-1}{\gamma+1} \qquad [3\text{-}29]$$

Static temperature ratio:

$$\frac{T_2}{T_1}=\frac{\left(1+\frac{\gamma-1}{2}M_1^2\right)\left(\frac{2\gamma}{\gamma-1}M_1^2-1\right)}{M_1^2\left(\frac{2\gamma}{\gamma-1}+\frac{\gamma-1}{2}\right)} \qquad [3\text{-}30]$$

Density ratio:

$$\frac{\rho_2}{\rho_1}=\frac{c_1}{c_2}=\frac{(\gamma+1)M_1^2}{(\gamma-1)M_1^2+2} \qquad [3\text{-}31]$$

Mach number:

$$M_2^2=\frac{M_1^2(\gamma-1)+2}{2\gamma M_1^2-(\gamma-1)} \qquad [3\text{-}32]$$

Total temperature:

$$T_{t2}=T_{t1} \qquad [3\text{-}33]$$

Total pressure:

$$\frac{p_{t2}}{p_{t1}}=\left(\frac{\frac{1}{2}(\gamma+1)M_1^2}{1+\frac{1}{2}(\gamma-1)M_1^2}\right)^{\gamma/\gamma-1}\left(\frac{1}{\frac{2\gamma}{\gamma+1}M_1^2-\frac{\gamma-1}{\gamma+1}}\right)^{1/\gamma-1} \qquad [3\text{-}34]$$

3.2.3.3 Sub-sonic Diffuser Section

There is a loss in total pressure through the diffuser which can be expressed by:

$$\eta_d=\frac{p_{t3}}{p_{t2}} \qquad [3\text{-}35]$$

Where $0.9\le\eta_d\le0.96$, ESDU (1985) then:

$$p_{t3}=\eta_d\, p_{t2} \qquad [3\text{-}36]$$

By applying the steady flow energy equation in the diffuser section the static enthalpy, static temperature, static pressure, density and Mach number at the diffuser outlet can be calculated from the following equations:

Static enthalpy:
$$h_3=h_2+\frac{c_2^2-c_3^2}{2}=h_{t1}-\frac{c_3^2}{2} \qquad [3\text{-}37]$$

Static temperature:
$$T_3=T_{t2}-\frac{c_3^2}{2c_p} \qquad [3\text{-}38]$$

Static pressure:
$$\frac{T_{t2}}{T_3} = \frac{1}{1 - \frac{c_3^2}{2 c_p T_{t2}}} = \left[\frac{p_{t3}}{p_3}\right]^{\gamma-1/\gamma} \quad [3\text{-}39]$$

Mach number:
$$M_3^2 = \frac{2}{\gamma - 1}\left[\left(\frac{T_{t3}}{T_3}\right) - 1\right] \quad [3\text{-}40]$$

Density:
$$\rho_3 = \frac{P_3}{R\ T_3} \quad [3\text{-}41]$$

C_3 is usually small, therefore from Bernoulli's equation the maximum back-pressure that a jet-pump can overcome will be:

$$P_3 = \eta_d p_{t2} - \frac{\rho_3 C_3^2}{2} \quad [3\text{-}42]$$

$$A_3 = \frac{\dot{m}_{mix}}{\rho_3 C_3} \quad [3\text{-}43]$$

3.2.4 Data Acquisition

The data required to solve all previous equations is dependent on the assumptions of the gas thermodynamic behaviour. In the case of ideal gas assumption, the data can be taken directly with constant C_P and γ ; whereas in the case of perfect gas assumption, the previous ideal gas equation still applies but taking the C_P and γ as functions of temperature.

However, in order to eliminate analytical errors induced by the assumption of an ideal gas for high pressure operation conditions, particularly close to the critical-point condition of the working fluid, the real-gas data can be used to provide the thermodynamic properties of the refrigerants, either as tabulated data or in the form of equation. Temperature, pressure, enthalpy and specific volume in saturated liquid and saturated vapour states can be calculated using equations of state, for example some are given by ASHRAE (1984). Also it is possible to use proprietary software as REFPROP Package that provides properties for many pure refrigerants including R236fa and R245fa.

3.2.5 Method of Solution and Design

It should be noted that the solution of the simulation programme will only give the predicted design-point performance "The optimum jet-pump and cycle performance" of a particular jet-pump under given operating conditions. Thus when the operating conditions are altered, the geometry of the jet-pump will also be changed.

In practical use, the saturated conditions of primary and secondary flow rates are specified, with the designed entrainment ratio and cooling load, then the optimum jet-pump performance can be evaluated and the working conditions on the condenser side can be determined. However by knowing R_m and the cooling load, the required heat source Q_g can be established. This procedure requires iterative calculation. In this procedure the system pressures "primary and secondary at stagnation conditions" and the entrainment ratio are defined, the back pressure is then calculated. Iterations are then made over a range of entrainment ratios so that a map of design-point can be constructed.

3.3 The Theory of CRMC Design method

This section provides the theoretical basis for the CRMC method of designing jet-pumps of the type used in jet-pump cycle refrigerators. The CRMC method, [Eames (2002)] produces diffuser with internal flow passage geometries that seeks to remove or eliminate the thermodynamic shock process within the diffuser at the design-point operating conditions. In this method the momentum of the flow is allowed to change at constant rate as it passes through the diffuser passage. This assumption can be applied to the whole region within the jet-pump. But, due to the complicated mixing flow within the entrainment region as the primary flow fans out without mixing totally up to certain distance and also the secondary flow accelerates to sonic velocity without mixing totally for the same distance downstream, the CRMC assumption will be applied directly for the region where the mixing process is completed up to the diffuser exit (L_2+L_3) Fig 3.5.

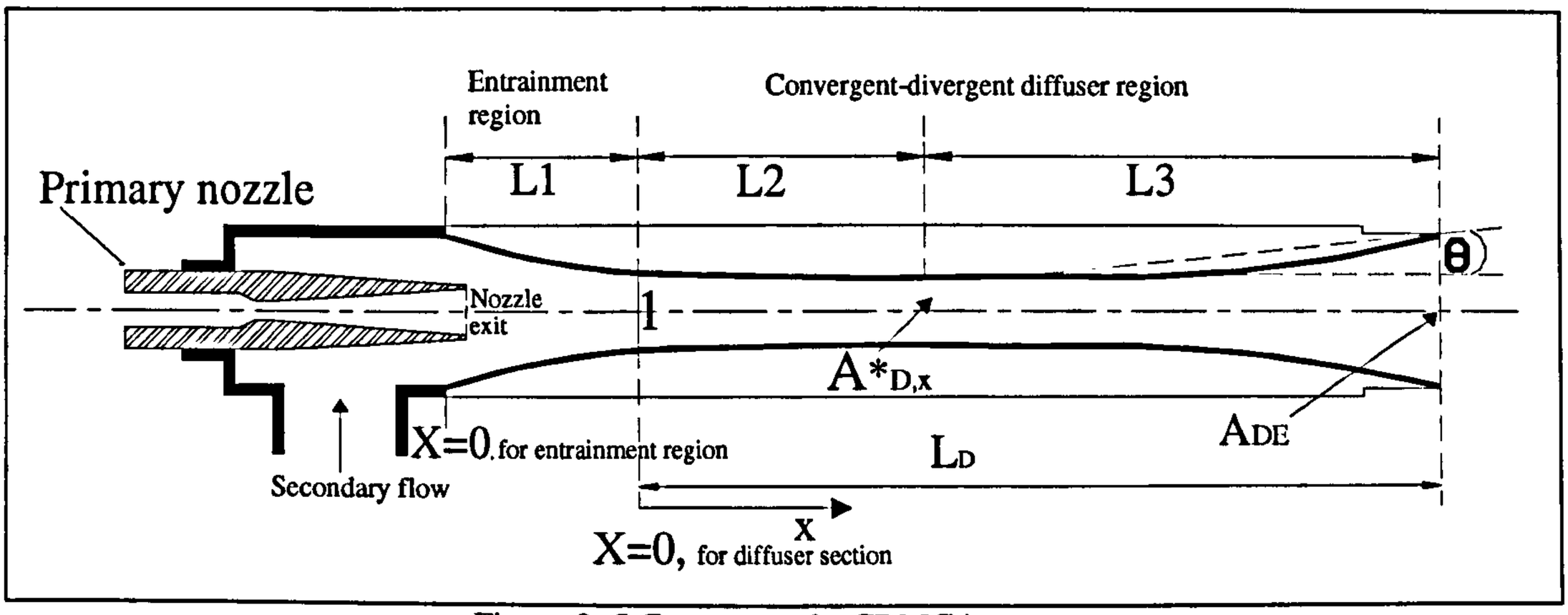

Figure 3. 5 Geometry of a CRMC jet-pump

3.3.1 The CRMC Assumption

The flow is 1-D steady and smooth, so viscosity and the interaction with the inner surface of the diffuser can be ignored and the momentum change is accounted in x direction only. Then the CRMC assumption can be expressed by equation [3-44].

$$\frac{d\dot{M}_o}{dx} = \dot{m}_{mix}\frac{dc}{dx} = \dot{m}_g(1+R_m)\frac{dc}{dx} = \alpha \qquad [3\text{-}44]$$

Where α =constant

Referring to the Figure 3.5, the boundary conditions for the above equation are:

$c_{D,x} = c_1$ at $x = 0$ and $c_{D,x} = c_{DE}$ at $x = L_D$

Where c_{DE} is the velocity at the diffuser exit plane. This can be assumed to be a small value at the design point in order to avoid pressure loss at the diffuser exit.

Solving the equation [3-44] using above boundary conditions gives:

$$c_{D,x} = c_1 - \frac{(c_1 - c_{DE})x}{L_D} \qquad \text{For } 0 \le x \le L_D \qquad [3\text{-}45]$$

L_D is the length of the diffuser section and it can be determined from the semi-empirical method described below.

3.3.2 Entrainment Region Boundary

The flow conditions at the entrainment region entrance "at nozzle exit and suction inlet" where the mixing process starts can be determined from the same equation presented in Section 3.2.2.2. Referring to the Figure 3.5 the flow conditions at point 1 can be obtained from previous equations from [3-18] to [3-24]. The static pressure is assumed to remain constant within the entrainment region bounded by nozzle exit and point 1 in the above Figure 3.5 and is equal to the pressure at the nozzle exit. The total pressure at the section (1), diffuser entrance, can be found from the following equation:

$$p_{t1} = P_{N-exit}\left(\frac{T_{t1}}{T_1}\right)^{\frac{\gamma}{\gamma-1}} \qquad [3\text{-}46]$$

Where the static pressure at the nozzle exit is given by:

$$P_{N-exit} = P_{ts} - \frac{\rho_s C_s^2}{2} \qquad [3\text{-}47]$$

3.3.3 Diffuser Section

To determine the flow area and thus the diameter of the diffuser, at any distance (X) along the diffuser, the continuity equation is used, thus A_x is given by:

$$A_x = \frac{\dot{m}_g(1 + R_m)}{\rho_x C_{D,x}} \qquad [3\text{-}48]$$

Where

$$\rho_x = \frac{p_x}{R\ T_x} \qquad [3\text{-}49]$$

$$T_x = T_{t1} - \frac{C_{D,x}^2}{2 * C_p} \qquad [3\text{-}50]$$

$$P_x = P_{t1}\left(\frac{T_x}{T_{t1}}\right)^{\frac{\gamma}{\gamma-1}} \qquad [3\text{-}51]$$

3.3.4 Determining the Diffuser Length L_D

To determine L_D to be used in the calculation of $C_{D,x}$ in Equation [3-45], the following semi-empirical method is used. The well known empirical finding is that slope

angle of the walls of subsonic diffuser should be between 8° and 10°. Thus referring to the Figure 3.5, the subsonic part of diffuser where the flow area changes from the sonic throat to the exit exhibits a distance of L3, that would give an equivalent half angle θ ranging between 4° and 5°. Also the distance from the entrance of the diffuser to the sonic throat exhibits the length L2. From the assumption of the CRMC design that the transonic flow through the diffuser must reach critical conditions "M=1" at the throat where $d_A/d_x = 0$

Then from equation [3-45]:

$$C^*_{D,x} = c_1 - \frac{(c_1 - c_{DE})L_2}{L_D} \qquad [3\text{-}52]$$

As the flow velocity is a linear function of distance x:

Then

$$L_2 = L_D\left(\frac{C_1 - C^*_{D,x}}{C_1 - C_{DE}}\right) \qquad [3\text{-}53]$$

But $$L_D = L_2 + L_3 \qquad [3\text{-}54]$$

Then, Referring to Figure 3.1:

$$L_2 = \frac{L_3\left(\frac{C_1 - C^*_{D,x}}{C_1 - D_{DE}}\right)}{1 - \left(\frac{C_1 - C^*_{D,x}}{C_1 - C_{DE}}\right)} \qquad [3\text{-}55]$$

$$L_3 = \frac{D_{DE} - D^*_{D,x}}{\tan\theta} \qquad [3\text{-}56]$$

Cohen et al (1972) provided the well know relationship for area change in compressible flow that can be used to determine the ratio of the exit diameter, D_{DE} to the throat diameter, D^*_{Dx}, where the local Mach number is unity.

Thus:

$$\frac{D_{DE}}{D^*_{D,x}} = \frac{2}{\sqrt{M_{DE}}}\left(\frac{2 + (\gamma - 1)M^2_{DE}}{\gamma + 1}\right)^{(\gamma+1)/4(\gamma-1)} \qquad [3\text{-}57]$$

Where:

$$M_{DE} \cong \frac{C_{DE}}{\sqrt{\gamma R T_{t1}}} \qquad [3\text{-}58]$$

Critical diffuser diameter:

$$D^*_{D,x} = 2\sqrt{\frac{\dot{m}_g(1+R_m)\sqrt{R\,T^*_{D,x}}}{\pi P^*_{D,x}\sqrt{\gamma}}} \qquad [3\text{-}59]$$

Where:

$$P^*_{D,x} = P_{t1}\left(\frac{2}{\gamma+1}\right)^{\gamma/\gamma-1} \qquad [3\text{-}60]$$

$$T^*_{D,x} = T_{t1}\left(\frac{2}{1+\gamma}\right) \qquad [3\text{-}61]$$

The solution of all above equations can be carried out straightaway knowing the operating conditions and the thermodynamic properties of the working fluid which is used in the design.

3.3.5 Entrainment Region Coordinates

To calculate the entrainment region coordinates L_1, referring to Figure (3.5), the following equation can be used:

* Length of mixing section:

$$L_1 = 7 * D^*_{D,x} \qquad [3\text{-}62]$$

Where, 7 is the empirical constant from ESDU (1985).

* Primary jet velocity at distance x, (x=0 at nozzle exit):

$$C_{j,x} = \left[\left(\frac{L_1 * (C_{N-exit} * C_1)}{C_{N-exit} - C_1}\right)\Big/_x\right] \qquad [3\text{-}63]$$

* Entrainment ratio at distance x:

The mixing process between portions of secondary fluid and primary stream was thought to start as a secondary flow is induced and accelerated with the primary stream expanded wave. This mixing is called 'shear mixing' and occurs because of shear stress layer interfacing between primary and secondary streams. Thus the entrainment ratio at any distance x within the mixing section is accounted by:

$$R_{m,x} = \left[\left(\frac{C_{N-exit} - C_S}{C_{j,x} - C_S}\right) - 1\right] \qquad [3\text{-}64]$$

Then,

Primary jet mass flow rate at distance x is given by:

$$m_{j,x} = m_g * (1 + R_{m,x}) \quad [3\text{-}65]$$

Secondary flow rate at distance x, is given by:

$$m_{s,x} = m_g * (R_m - R_{m,x}) \quad [3\text{-}66]$$

Total temperature of primary jet at distance x:

$$T_{o,jx} = \left(\frac{T_g + (R_{m,x} * T_s)}{1 + R_{m,x}} \right) \quad [3\text{-}67]$$

Static temperature of primary jet at distance x:

$$T_{j,x} = T_{o,jx} - \left(\frac{C_{j,x}^2}{2 * C_p} \right) \quad [3\text{-}68]$$

Density of primary jet at distance x:

$$\rho_{j,x} = \left(\frac{P_{N-exit}}{R * T_{j,x}} \right) \quad [3\text{-}69]$$

Density of secondary flow at distance x:

$$\rho_{S,x} = \left(\frac{P_{N-exit}}{R * T_s} \right) \quad [3\text{-}70]$$

Flow area of primary jet at distance x:

$$A_{j,x} = \left(\frac{m_{j,x}}{\rho_{j,x} * C_{j,x}} \right) \quad [3\text{-}71]$$

Flow area of secondary flow at distance x:

$$A_{s,x} = \left(\frac{m_{s,x}}{\rho_{s,x} * C_s} \right) \quad [3\text{-}72]$$

Total flow area of entrainment region at distance x:

$$A_{t,x} = A_{j,x} = A_{s,x} \quad [3\text{-}73]$$

Diameter of flow area at distance x:

$$D_x = 2 * \sqrt{\frac{A_{t,x}}{\pi}} \quad [3\text{-}74]$$

Two computer simulation programs, one based on the conventional one-dimensional analysis and second based on CRMC design method were developed by the author and used to design different nozzles and jet-pumps for CFD and experimental investigations. The dimension of each designed nozzle and diffuser will be mentioned in their related section over the next Chapters.

3.4 CFD Modelling

Computational fluid dynamics "CFD" is a crucial tool for analysis of systems involving fluid flow, heat and mass transfer, and chemical reactions in complex geometries by means of computer based simulation. It can be used for optimisation and design in a variety of applications. The foundation of CFD is the Navier-Stokes equations for a viscous and compressible fluid, and a numerical approach with Finite Volume method is used to solve these equations. The approach is capable of handling turbulence by modifying the governing equations to be time-averaged or ensemble-averaged, which resolves the effects on the mean flow; that is what is normally required rather than the full details of the turbulent fluctuations which are difficult to simulate directly. The time averaged approach is adopted by Fluent which is used in this study. However, with this approach extra terms with respect to the Navier–Stokes equations are produced; these terms account for the time-average effects of turbulence on the flow field and is termed the Reynolds stress. Different turbulent models have been introduced to deal with Reynolds stresses, either a direct solution using Reynolds stress models, or the application of the eddy viscosity concept on which a number of the most common models are based. Reynolds stress is computationally intensive and not considered within this study. The other approaches include: one equation (Spalart-Allmares) and two equation Models (K-ϵ) includes (Standard, RNG and Realisable). These are currently the most widely used models due to their lower computational demand compared with other complex models that are available.

In this study, a coupled solver with explicit scheme was used to solve the discretised equations. With the coupled solver the pressure is linked directly to density, however, accurate results can be obtained for compressible flow problems because the representation of real physical relation is achieved with a coupled solver. The explicit approach can utilize large time steps while maintaining stability, therefore fewer time steps are needed to achieve converged solutions. It is more accurate and less expensive than

implicit scheme for capturing shock waves in jet-pump mixing section [Hart (2002)] and therefore it has been used throughout all modelling cases described in this work.

The discretization method has been used for approximating the differential equations, which are based on the finite volume method. A second order upwind difference scheme is applied for discretization of the equations. When the grid points in the flow domain are infinitely large, the numerical results would be mesh dependent. Versteeg and Malalasekera (1995) showed that for coarse meshes, numerical solutions can vary from exact solutions. Therefore some properties were used to make an assessment of the applicability and performance of the schemes. Among these properties are 'conservativeness' that the numerical scheme used to solve the equation must apply the conservation laws of physics; 'boundedness' that solution value in a computational point must be bounded by the solution values in the surrounding points; and 'transportivness', meaning that a property flux will be transported downstream maintaining the relationship between the magnitude of the Peclet number and the directionality of flow variables. There is ability to accelerate the solution process to save time in the modelling process. Initialisation of the calculation with patching variables, controlling under-relaxation factors and the use of multi-grid techniques can all accelerate the converged solution, and therefore, have been used in this study.

However, to perform a numerical simulation for a jet-pump, the flow geometry has to be represented by a computational mesh consisting of a large number of nodes that solve the flow field according to the conservation equations. The accuracy and quality of the results obtained depend on the quality and the number of cells defined. Cells have to be distributed on particular areas according to the flow gradients, so that cells of small sizes are clustered in regions that suffer severe shock processes and also regions near the wall for turbulent modelling.

A quadrilateral mesh was used for all two-dimensional axisymmetric cases used in these simulations of the jet-pump. However this type of mesh can produce higher quality mesh, because it is easy to maintain the cell aspect ratio and also easy to align the mesh with the dominant flow direction. Meshes were generated using Gambit software which is a powerful mesh generating tool and easy to use. The vertices points and edges are used to form a computational domain, which is divided into more manageable areas that is

controlling the mesh resolution in specific areas enabling Fluent to perform the calculation process in the best way. Detailed description of the methodology and the CFD code that were used to define the optimal mesh size used in this research work are shown in section 3.4.3, page 54 of this Chapter.

3.4.1 CFD Uncertainly

The first step in the application of the CFD model was to ensure that the model correctly represents the flow field inside the jet-pump. However, the CFD code used in this investigation must be validated for a specific range of operating conditions for which there is experimental data. Thus, when the code was validated, it was possible to apply it to predict different ranges of flow and operating conditions beyond the region of validity. The first task was to verify both the code and the calculation, by evaluating errors and determining the accuracy of calculation. This was done by checking the mass conservation within the jet-pump, and checking that the total mass flow at the outlet was equal to the primary and secondary mass flows at the inlet. An independent grid test was conducted to avoid computational errors. This was done by monitoring the iterative convergence of all variables. The code was then calibrated to specific experimental data, in order to improve the agreement of computational and experimental results by, considering uncertainly and errors with the code. Two experimental data sets were used for this purpose.

Before presenting the CFD code results in the validation procedure, the determination and assessment of errors and uncertainty will be discussed first. The assessment will be included for all choices of physical model, turbulent model, discretization scheme and geometry including the mesh type and density.

3.4.1.1 Uncertainty and Errors in Computational Fluid Dynamics

Mehta (1991) believed that uncertainties come in two groups, computational and fluid dynamic. Computational uncertainties come from the choice of governing equations which are solved, models for the fluid and the physical model. In the present case, independent tests of turbulent models have been done for validation; these are presented in the Section 3.4.4.

The discretization scheme that represents the governing flow equations and other physical models has some errors depending on the mesh used. Grid spacing influences the

discretization scheme; as the mesh is refined, the uncertainly is reduced. However, it is important to improve the quality of mesh by avoiding skewing of cells against the flow direction and keeping the cell aspect ratios within the limits range recommended by CFD solvers. Previous work of Issa and Lockwood (1986) for modelling supersonic flows showed that the computational aspect ratio should be maintained as near to 1:1 as possible. The aspect ratio for 2-D model can be defined as the cell length in axial direction / cell length in radial direction. Other considerations for the grid depend on how features of the flow, such as mixing regions, shear layer and shockwaves regions should be applied. The grid should be fine enough to minimize the change in the flow variables from cell to cell, which will reduce the level of discretization errors. Thus, in the present investigation independent tests for the computational mesh, upon which the calculations were performed, have been carried out to properly capture flow details, and enable the determination of the level of discretization error existing in a CFD solution.

The residuals errors (convergence criteria) should be reduced to a certain number to improve the accuracy of the solutions; in all these studies the level of residuals has been set to the 10^{-6} order of magnitude. Steady state was found to be achieved in all cases with this level of residuals. Also monitoring the change in these residuals for all flow variables during the calculation process can help to manage the time and avoid errors. Moreover, with achieving convergence, the accuracy of results obtained should be checked. Some flow values have been monitored from time to time during the iteration process, and at convergence level primary and secondary flow rates that remained unchanged have been checked with respect to the number of iterations.

Fluid dynamic phenomena associated with modelling of a supersonic jet-pump can lead to uncertainties. These include the requirements that the flow must be chocked at the nozzle throat, the flow at nozzle exit must be supersonic and the shockwaves positions. The static pressure profile also has related uncertainties that should be reduced in the modelling process. Related modelling work to these phenomena in jet-pumps is rare and therefore in this study these phenomena are optimised using theoretical results. From initial stage of this study, a degree of uncertainly was avoided, because an appropriate setting of the level of options which are used were related to the previous investigation of supersonic jet-pump [Hart (2002)].

A simplified model has been used within the CFD code for more efficient computation. This includes an axisymmetric assumption because it was thought this assumption leads to problems in detecting some of phenomena mentioned, but from this study it was found that all results are quite acceptable.

As the validation of the CFD code's results was conducted by comparing them with experimental results, it should take into account many uncertainties that are associated with the experiment itself. Consideration of experimental uncertainties, such as measurements, geometric irregularities (e.g. roughness), pressure loss in suction line and co-axial geometry between primary nozzle and the diffuser improved the CFD model.

3.4.2 Jet-pump Geometry

Experimental data was available for two different jet-pump geometries for which different refrigerants were used. These were used to validate the mathematical model. The first set of experimental data was based on the work of Eames et al (1999b) where steam was the working fluid. Second set were taken from the work of Huang et al (2001) for which R141b was the working fluid. Figures 3.6 and 3.7 show the steam and R141b jet-pumps respectively with their dimensions which was used in the CFD validation.

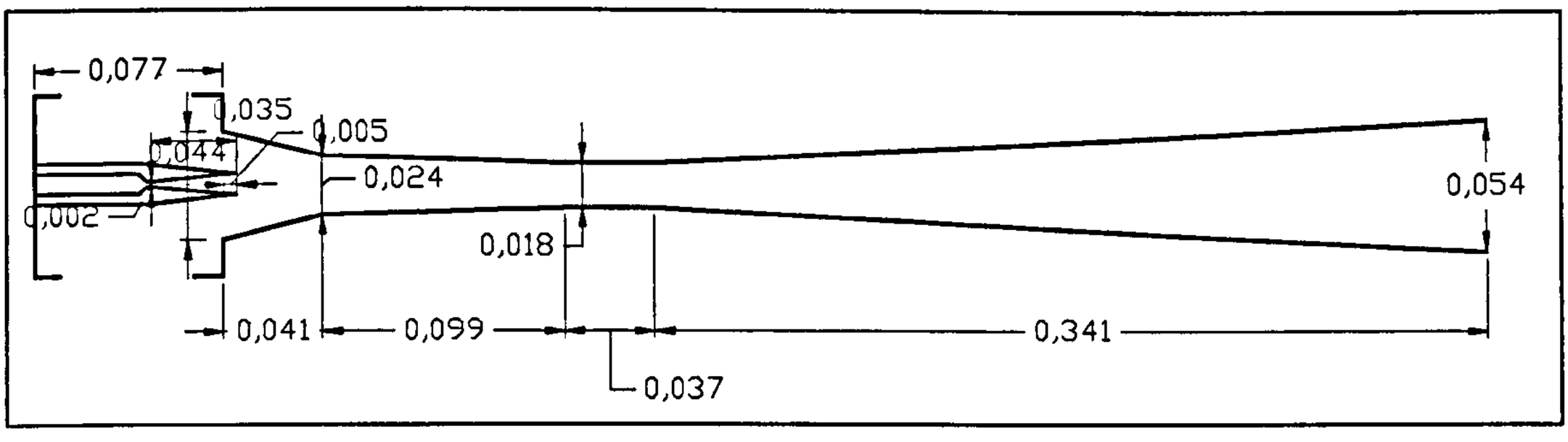

Figure 3. 6 Steam jet-pump dimensions (m)

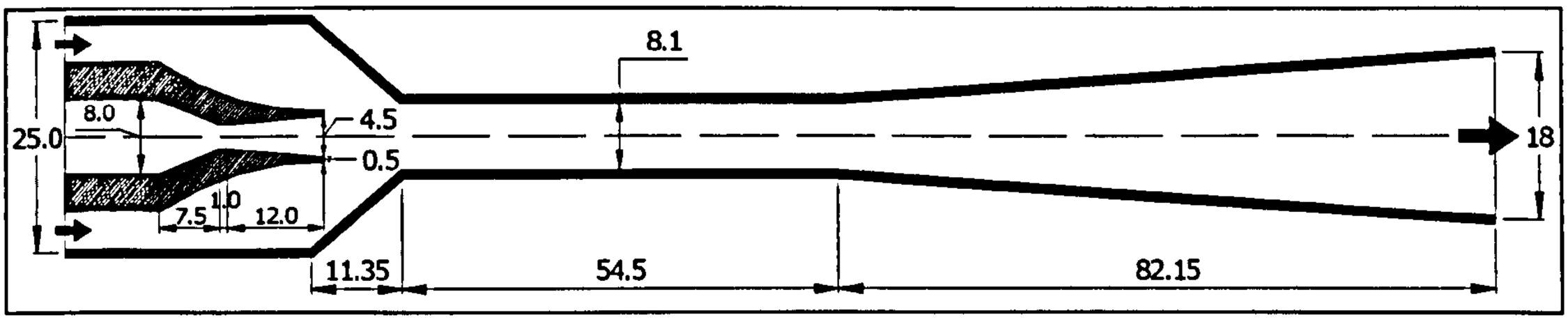

Figure 3. 7 R141b jet-pump dimension (mm)

For the R141b jet-pump there was data for a number of different geometries available with different operating conditions, however, for CFD validation, only one nozzle (Nozzle A) and one diffuser (diffuser D) were used. Referring to Figure 3.3 their specifications are shown in the following Tables:

Table 3. 1 The specification of Nozzle A "R141b"

Nozzle	Throat diameter d_t	Exit diameter d_1	Area ratio A_1/A_t
A	2.64 mm	4.5 mm	2.91

Table 3. 2 The specification of diffuser D "R141b"

Diffuser	Throat diameter D_t	Suction conical part length L1	Constant area length L2
D	8.1 mm	11.35 mm	54.5mm

3.4.3 Computational Mesh

A grid dependency check is required for more accurate CFD modelling results, and also one must find the minimum mesh resolution that is in the asymptotic convergence region. Coarse grids can lead to the conservativeness property not being fulfilled; however, to ensure that the solution is fully converged, successively grid dimensions are reduced to obtain more closely a true derivative approximation with reduction in errors. At certain levels of this process, the computed values will remain unchanged. This increase on accuracy will be no longer obtained and there are no further benefits from increasing refinement of the grid. Any further increase in grid refinement will need more computer resources which are time consuming; therefore the optimal mesh should be selected.

Ideally there should be only very small or negligible grid dependence for steam and R141b jet-pumps. Since the working principle and the flow phenomena inside the jet-pumps are the same, the grid test was conducted in the same manner for both jet-pumps to ensure that.

A mesh resolution study only was performed. Only a quadrilateral mesh, was used in this test as this was recommended to provide a high quality mesh, more acceptable for 2-D modelling and accurate results had previous been obtained with this mesh type [Hart (2002)]. Also this type of mesh has characteristics of simplicity and suitability for multi-grid, and as the flow inside the jet-pump is dominantly in the axial direction, this type of mesh was though to improve alignment between the mesh and flow direction thus accurate results could be obtained.

Eight different mesh size levels were used in the validation process. Depending on the length of the geometry, a coarser mesh with one cell for every 1.5 mm in the axial direction, the other levels are 1 & 1.5 and 2 cells in each 1mm. For radial directions, there were two mesh levels tested 1.5 and 2 cells for every 1mm based on the two inlets high. As these two levels for radial direction can give a good grid ratio for the four levels selected in axial direction, it is likely that changing the grid in the radial direction will produce some variation; but the range of changing is negligible. Some considerations have been also applied for regions of importance such as those close to the wall and those that have high gradients, such as within the mixing of the two streams; shear layer and shock systems. A gradient mesh was used for near wall modelling and dense mesh was used for the mixing layer and shock regions. The grid was designed in these regions to provide as much detail as possible of the flow field. The complete mesh in all eight cases for R141b was identical to that used for steam jet-pump, except for a difference in one mesh in axial direction. As a consequence there were no differences at all in the radial direction.

Tables 3.3 a & b and Tables 3.4a & b show the mesh independent test results for steam and R141b jet-pumps respectively. It should be take into account that, in each case, a realizable turbulent model was adopted because this had been validated for different ranges of flow including jets, mixing layers and boundary layer flows that are specifying the flow phenomena inside the jet-pump [Kim et al (1997) and Shih et al (1995)]. For near-wall models a standard wall function approach was adopted. Independent turbulent model tests were carried out and their results are shown in Section 3.4.4.

Figures 3.8a and 3.8b show the complete mesh system used for both steam and R141b jet-pumps, (for de Laval nozzle and mixing section). The same mesh was used for R141b jet-pump except for the difference in geometry. Graphics of each mesh and for each jet-pump are provided in Appendix C.

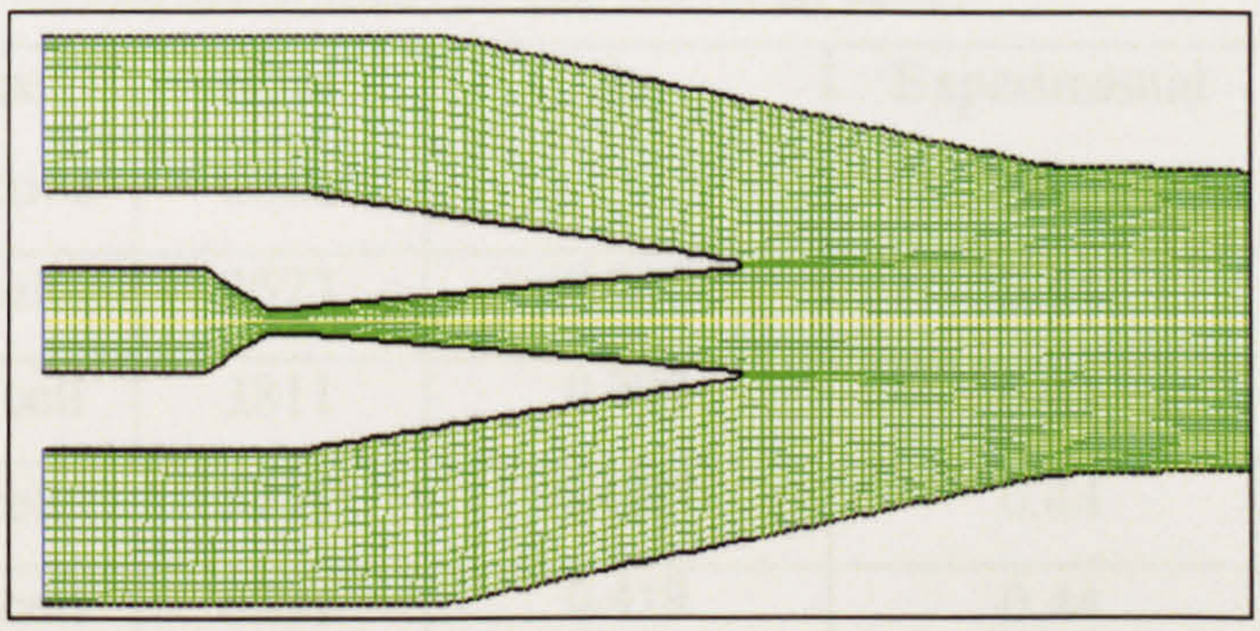

Figure 3. 8a 1.5cell in each 1mm X direction (steam jet-pump)

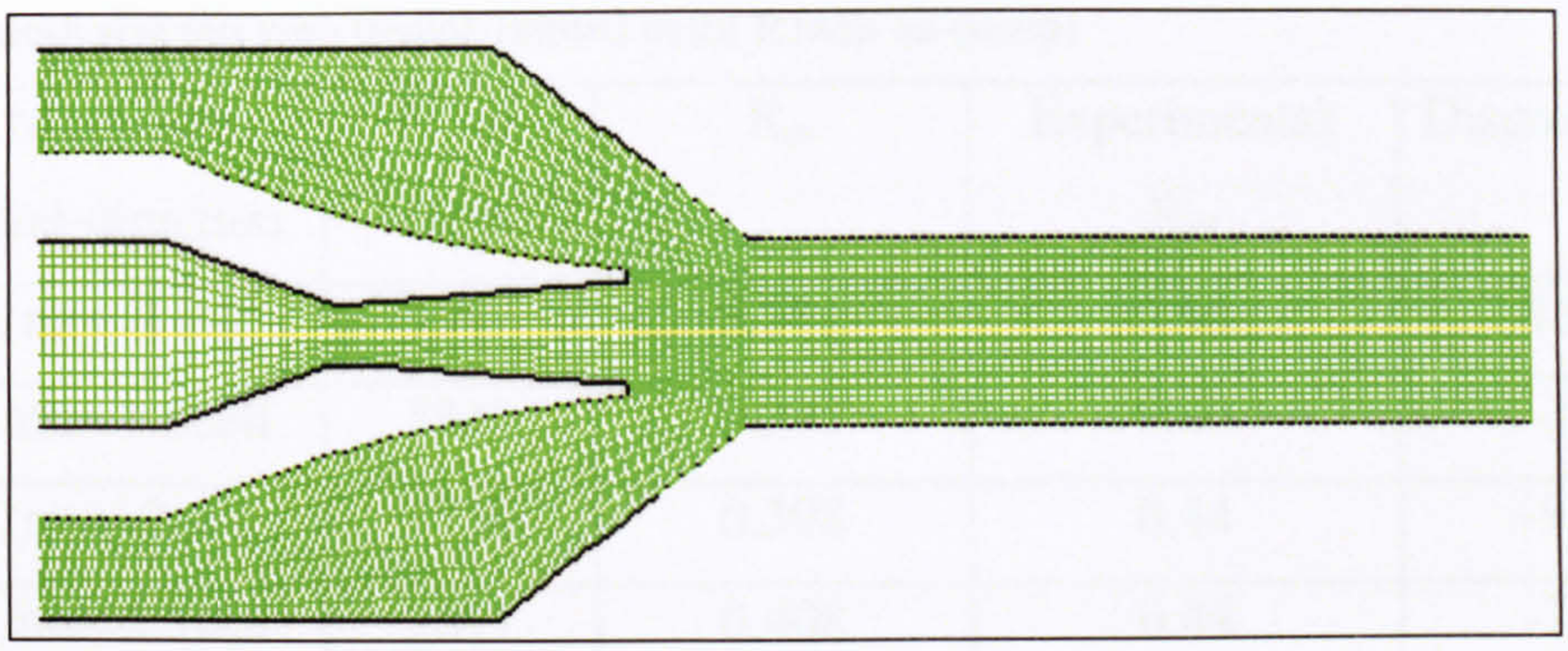

Figure 3. 8b 2.5 cells in each 1mm X direction (R141b jet-pump)

The operating conditions used in the mesh study were those of the steam jet-pump as (T_g=120°C, T_e=10°C, and the T_c was varied from 25 to 31°C), and the R141b jet-pump (T_g=90°C, T_e=8°C and T_c was varied from 26°Cto30°C).

Table 3. 3a Mesh size test with (redial-1mm=1.5 cell) (Steam jet-pump)

Mesh N°	Mesh size axial-direction	N° of Cells	R_m	Experimental R_m	Discrepancy
S-1	1.5mm=1cell	8712	0.639	0.586	+9.1
S-2	1mm=1cell	13243	0.606	0.586	+3.4
S-3	1mm=1.5cell	19795	0.599	0.586	+2.26
S-4	1mm=2cell	26304	0.595	0.586	+1.6

Table 3. 3b Mesh size test with (redial -1mm=2 cell)(Steam Jet-pump)

Mesh N°	Mesh size axial-direction	N° of Cells	R_m	Experimental R_m	Discrepancy
S-5	1.5mm=1cell	12388	0.644	0.586	+9.9073
S-6	1mm=1cell	18617	0.602	0.586	+2.8103
S-7	1mm=1.5cell	27825	0.591	0.586	+0.8996
S-8	1mm=2cell	36976	0.592	0.586	+1

Table 3. 4a Mesh size test with (redial-1mm=1.5 cell) (R141b jet-pump)

Mesh N°	Mesh size axial-direction	N° of Cells	R_m	Experimental R_m	Discrepancy
R-1	1mm=1cell	2577	0.323	0.44	-26.475
R-2	1mm=1.5cell	3811	0.398	0.44	-9.498
R-3	1mm=2cell	5115	0.4087	0.44	-7.111
R-4	1mm=2.5cell	6891	0.419	0.44	-4.814

Table 3. 4b Mesh size test with (redial-1mm=2 cell)(R141b Jet-pump)

Mesh N°	Mesh size axial-direction	N° of Cells	R_m	Experimental R_m	Discrepancy
R-5	1mm=1cell	3597	0.381	0.44	-13.3
R-6	1mm=1.5cell	5313	0.387	0.44	-12
R-7	1mm=2cell	7139	0.398	0.44	-9.5
R-8	1mm=2.5cell	9691	0.408	0.44	-7.1

The results of independent mesh test for both jet-pumps are tabulated in Tables 3.3a, 3.3b, 3.4a, 3.4b. From these tables it is clear that the results of finest mesh demonstrate close agreement across the various mesh density used, and also it can be seen that as the mesh is refined the computed values become less sensitive to the grid size; and at some point in this process of refinement the error becomes smaller or negligible and no longer can significant increases in accuracy be obtained. Therefore this level of mesh density was used. However, for steam jet-pump, due to computational constraints, it is possible to select mesh N° *S-3* or *S-7* which included the level of 1.5 cells in each 1mm for axial direction and also 1.5 cells or 2 cells in each 1mm for radial direction depending on the nozzle throat diameter. For nozzle throat diameters less than 2mm, 1.5 cells in each 1mm in radial direction were used, but for any nozzle throat diameter greater than 2mm, 2 cells for every 1mm were used. For R141b jet-pump, mesh N° *R-4* was selected for the remaining R141b simulations in the validation process and the following parametric study.

It was clear that mesh resolution played an important role in correctly modelling the scale of jet-pumps. Using gradient grid level in the near-wall region has proved to provide a good Y^{*} (1) level that was appropriate with using the standard wall function for wall model. Also, using a refined high computational grid quality, for regions of high gradients, achieved accurate numerical simulations for shock phenomena and the remaining flow field features. Also, by comparing the grid test for both steam and R141b, it can be said that it is unlikely that grid independent solutions can be achieved on a fixed grid for different geometries.

(1), Y^{*} is a wall unity, used to clarify the distance of adjacent cell to wall for standard wall function approach. Details of how calculate Y* are given in Fluent INC.2003

3.4.3.1 Mesh Adaption

In some cases, in order to obtain a better simulation, an alternative strategy, which is 'adaptive mesh refinement', has been used. In this case the grid is refined in regions where it is needed, depending on the source of gradient selected and it has been used to improve the resolution of shock systems. Pressure gradient adaption was used throughout all cases that needed adaption. The number of adapted cells in each refinement ranged from 400 to 2500 cells. In almost all cases the limit of the Y^* value, using the standard wall function was achieved due to the reasonable grid density and cell aspect ratios used. Thus further cell adoption was not required.

The standard wall function was used throughout all simulations for the independent mesh tests and also for parametric studies and for the optimisation of jet-pumps. The standard wall functions work reasonably well for a broad range of wall-bounded flows and more reliable with flow behaviour identical to ideal conditions, and this agreement of results shows that the fluid used with supersonic flow has features that are comparable with ideal gas. With a standard wall function when the $Y^* > 11.225$, the log-law was employed because is more acceptable for turbulent flows. Therefore, the size of the cell adjacent to the wall must retain Y^* value that > 11.255 and is more preferable to be between 30-60, (Fluent help). If cell thicknesses are too small, then the near-wall boundary conditions will be modelled through wall function model as if the flow was laminar, and this may will provide results that depart for accurate turbulent transport processes in jet-pump modelling.

Most mesh adaption was done for the throat region of the de Laval nozzle, as this region is influenced by high pressure gradients. One refinement for near wall mesh was performed for some cases, as shown in Figure 3.9. In other cases, one refinement was done based on the pressure gradient at the nozzle throat as shown in the Figure 3.10.

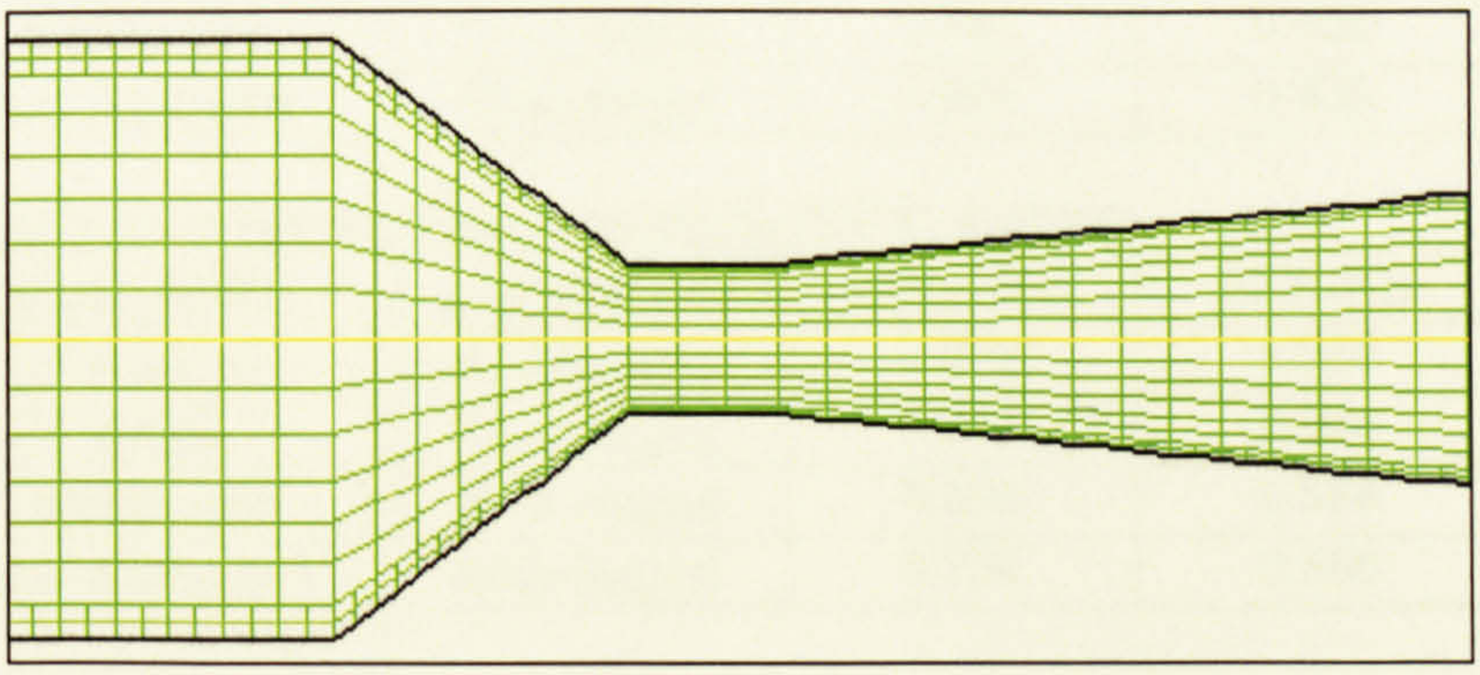

Figure 3. 9 Y^* Refinement

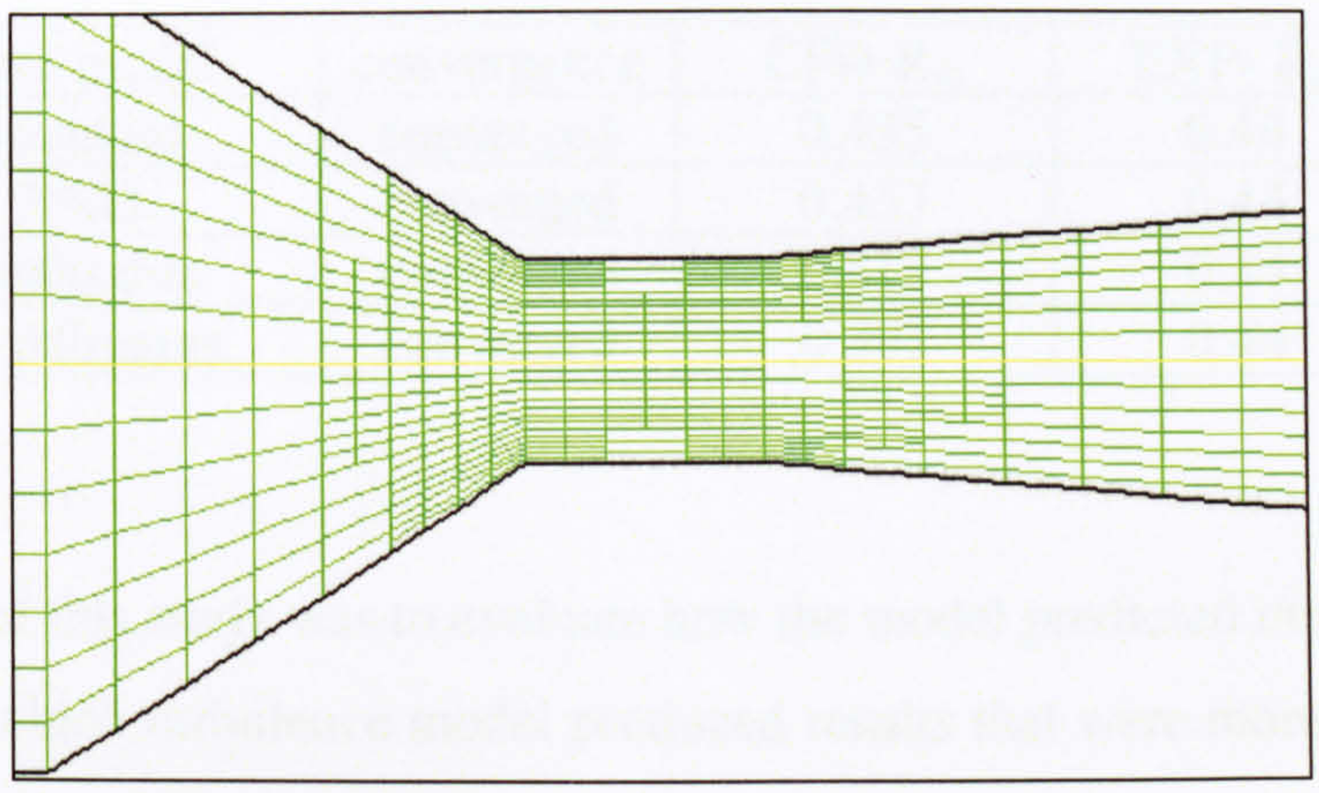

Figure 3.10 Pressure Gradient Refinements

3.4.4 Turbulence Modelling

Mesh N° *S-3* was used for all types of turbulent models investigated for the steam jet-pump, and mesh N° *R-4* was used for R141b jet-pump. A standard wall function was used to resolve the boundary layer and it was found that there was no requirement for any further refinement; the solution was converged in all cases. For the steam simulation, two different evaporator temperatures were used; 5°C and 10°C with 120°C generator temperature and with nozzle exit position "NXP"=26mm, whereas for R141b jet-pump one evaporator temperature of 8°C with 90°C generator temperature and NXP=6mm were used. Condensing temperature was varied during the investigation and its effect was observed.

Results of turbulent models for steam are shown in Tables 3.5a and 3.5b, whereas for R141b jet-pumps the results are shown Table 3.6.

Table 3. 5a Turbulent models results-steam jet-pump T_g=120°C, T_e=5°C

N°	Turbulent model	convergence	CFD-Rm	EXP-Rm	Discrepancy
T-1	K-Є Standard	Converged	0.439	0.405	+8.28
T-2	K-Є RNG	Converged	0.444	0.405	+9.522
T-3	K-Є Realisable	Converged	0.412	0.405	+1.66
T-4	Spalart-Allmaras	Converged	0.504	0.405	+24.37

Table 3. 5b Turbulent models results -steam jet-pump T_g=120°C, T_e=10°C

N°	Turbulent model	convergence	CFD- Rm	EXP-Rm	Discrepancy
T-1	K-Є Standard	Converged	0.612	0.586	+4.4
T-2	K-Є RNG	Converged	0.617	0.586	+5.2
T-3	K-Є Realisable	Converged	0.566	0.586	-3
T-4	Spalart-Allmaras	Converged	0.734	0.586	+25.2

Table 3. 6 Turbulent models results - R141b jet-pump T_g=90°C, T_e=8°

N°	Turbulent model	convergence	CFD-R_m	EXP- R_m	Discrepancy
T-1	K-Є Standard	converged	0.435	0.44	-1.0
T-2	K-Є RNG	converged	0.433	0.44	-1.5
T-3	K-Є Realisable	converged	0.418	0.44	-4.8
T-4	Spalart-Allmaras	converged	0.397	0.44	-9.6

The aim of this study was to evaluate how the model predicted the flow field within a jet-pump, and which turbulence model produced results that were more comparable with the experiment data. From previous Tables, it can be seen that the Realisable model performed best of all the K-Є models. It predicted entrainment values that agreed well with experiment data over range of operation condition tested. Whereas, calculations with standard K-Є model are seen to yield good agreement with R141b experimental values. It is seems that the jet-pump geometry has direct effect on the stream wise development of flow, which is generally dominated by turbulent stresses, i.e. 'steam jet-pump geometry coincides with constant pressure design shown in Figure 3.6. Whereas, R141b jet-pump coincides with constant area design, shown in Figure 3.7. Thus calculations are sensitive to proper turbulence modelling.

In both jet-pumps, the two equation K-Є models better predict the flow field than the one-equation (Spalart-Allmaras) model. However, longer running time was found, but predicted entrainment values agreed fairly well with experimental results. As is mentioned in section 3.4.3.1, the standard wall function was adopted for all cases in this study; the advantage of this approach is that it avoids the need to account for viscous effects in the turbulence model. However, this approach worked well with all turbulence models tested. The influence of these models upon supersonic region and mixing process can be explained through the use of Mach number contours in the supersonic region and the plotting of turbulent intensity along the jet-pump centreline. Figure 3.11 shows the supersonic region with the steam jet-pump at T_g=120°C, T_e=10°C, and T_c=26°C.

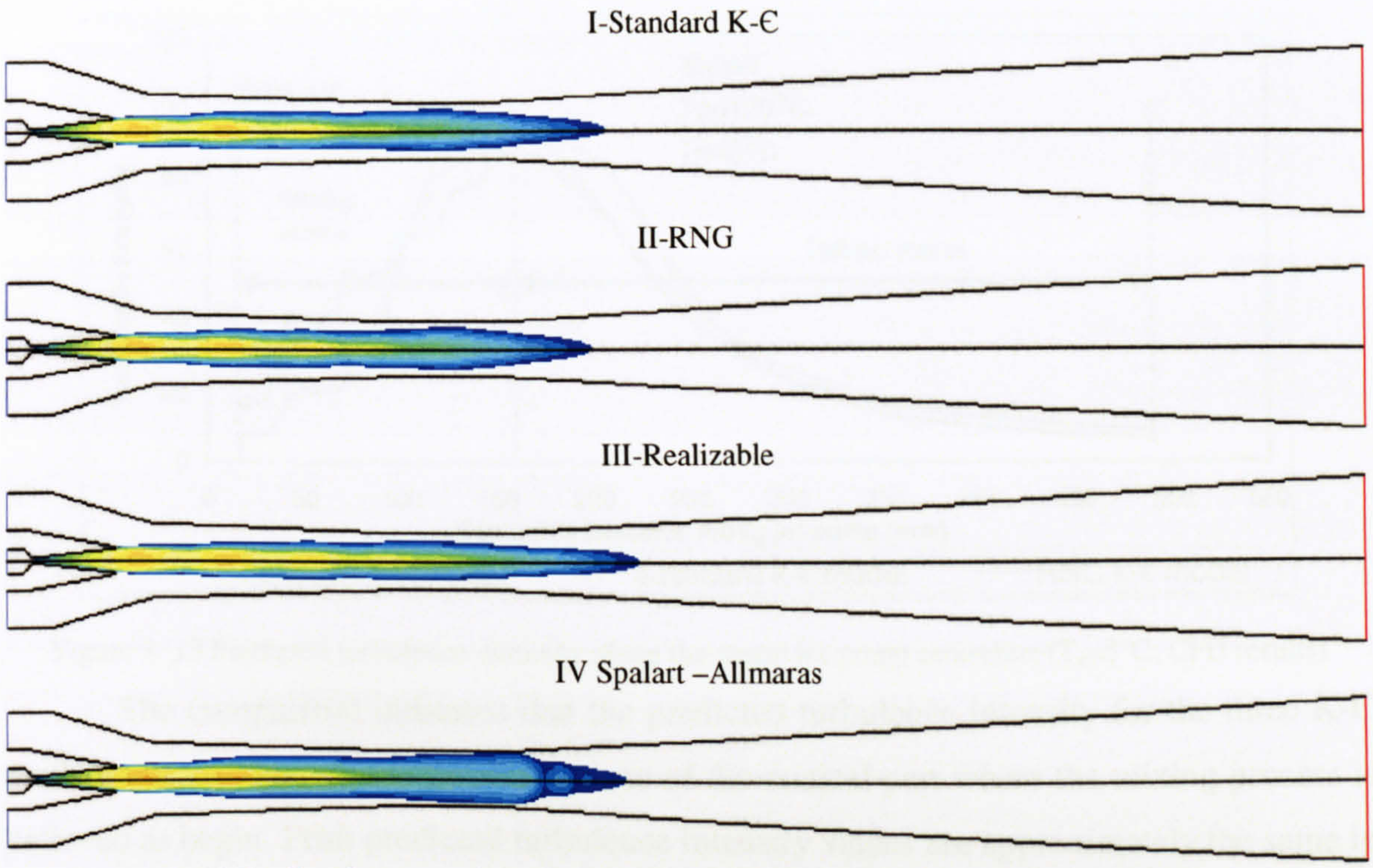

Figure 3. 11 Predicted supersonic regions within steam jet-pump with different turbulence models

(T_g=120°C, T_e=10°C, T_c=28°C steam jet-pump)

From Mach No contours, it can be seen that, the three K-Є models have the same contours and it is clear that the jet-pump throat is choked at the middle section. The supersonic flow however is predicted to spread with the realizable mode, though it seems that all three k-Є Models are able to capture the essential features of flow field with jet-pump at the same range. Figures 3.12, 3.13 show the turbulence intensity distribution along the jet-pump centreline-steam jet-pump at T_e=10°C and T_e=5°C respectively.

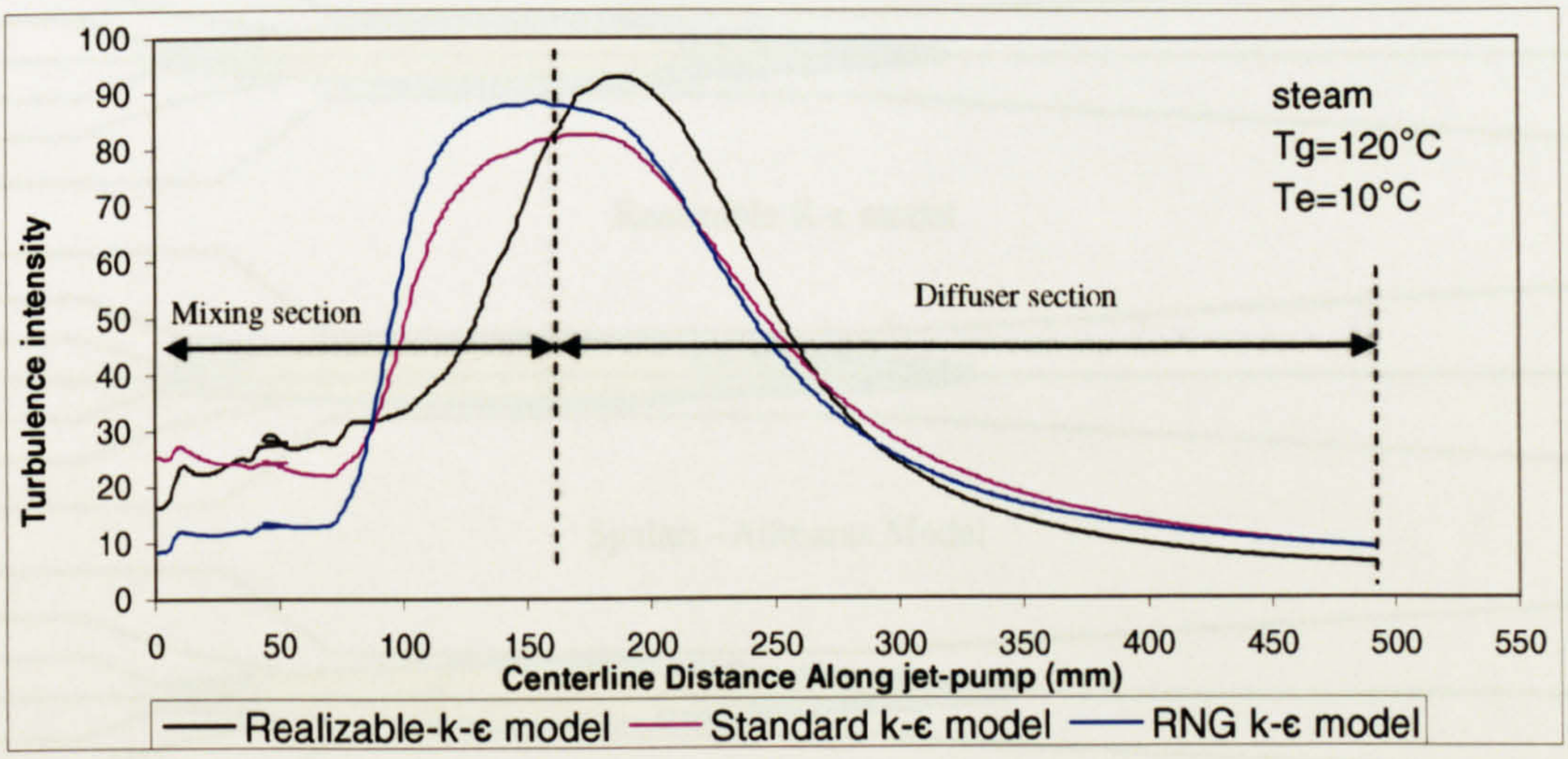

Figure 3. 12 Predicted turbulent intensity distributions along the steam jet-pump centreline

(T_e=10°C, CFD results)

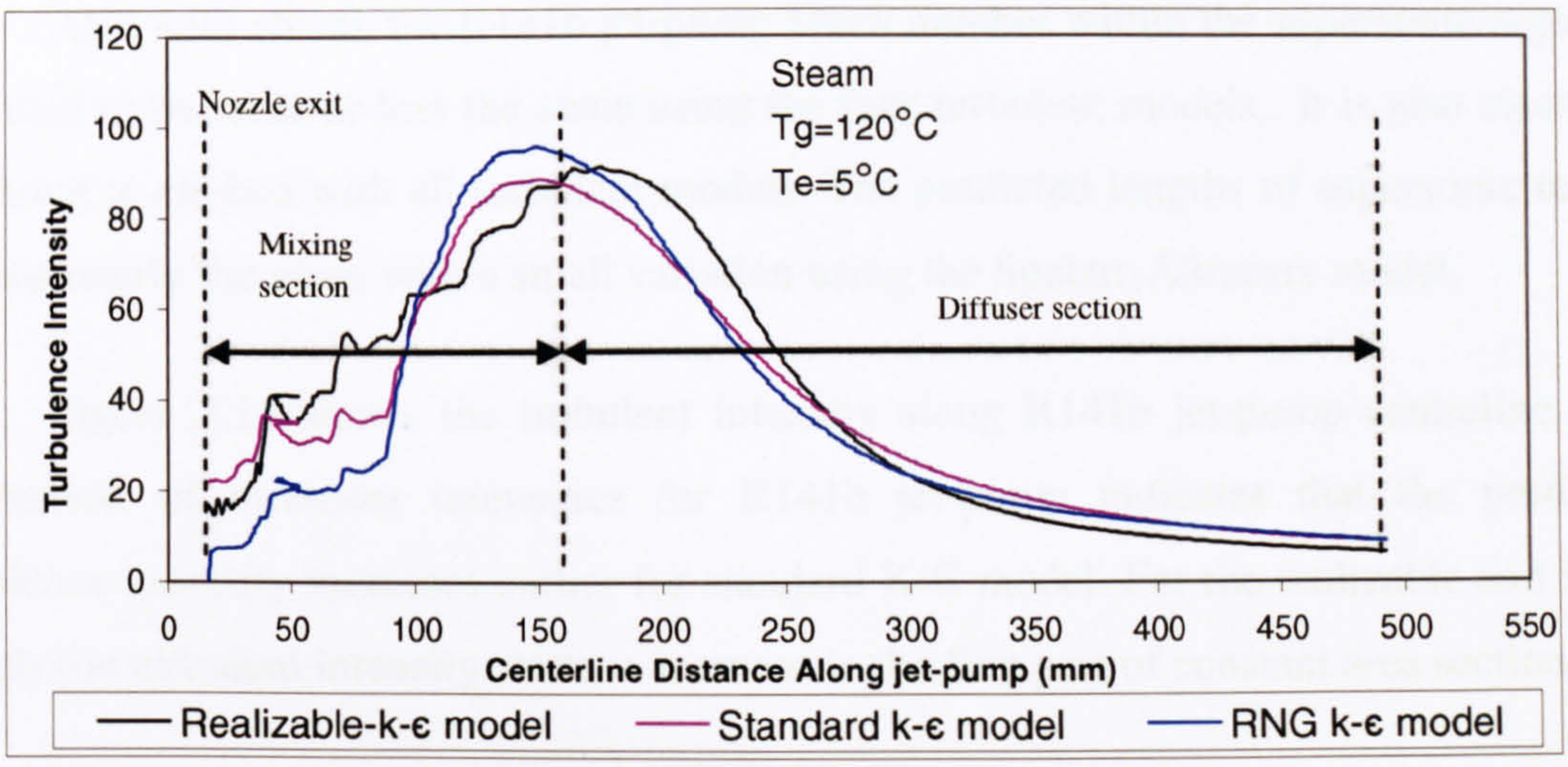

Figure 3. 13 Predicted turbulence intensity along the steam jet-pump centreline (T_e=5°C, CFD results)

The comparison indicates that the predicted turbulence intensity for the three K-Є models starts to increase at the entry plane of the conical part where the mixing process is believed to begin. Peak predicted turbulence intensity values are approximately the same in each case and occur at the end part of the jet-pump throat. Then the turbulent intensity decreases gradually up to end of the diffuser. For comparison with steam, Figure 3.14 shows the supersonic region within R141b jet-pump at T_g=90°C, T_e=8°C and T_c=28°C with different turbulence models.

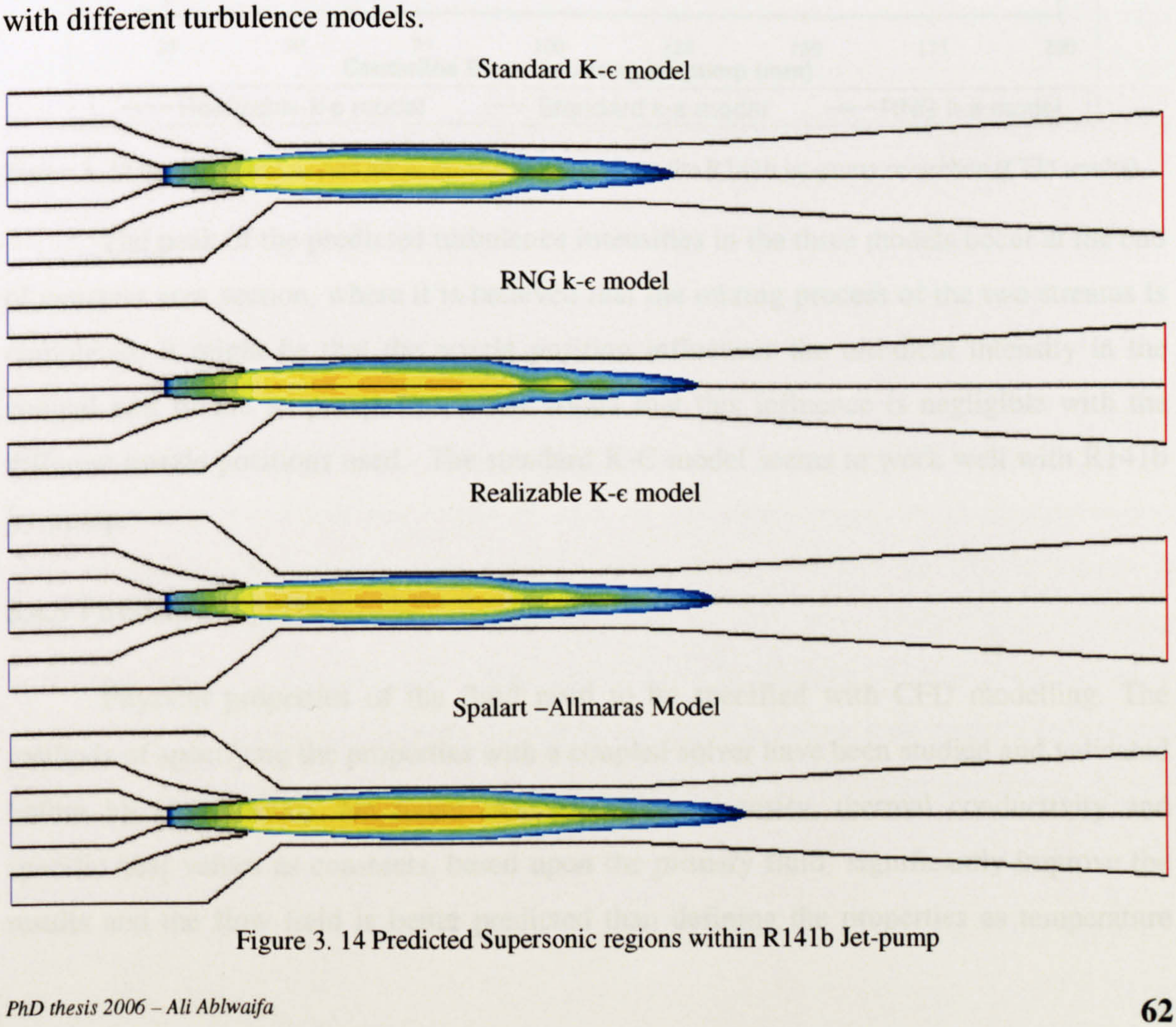

Figure 3. 14 Predicted Supersonic regions within R141b Jet-pump

Also with steam, the R141b jet-pump Mach number within the supersonic region is predicted to be more or less the same using the four turbulent models. It is also clear that the throat is choked with all turbulent models. The predicted lengths of supersonic region are also nearly the same with a small variation using the Spalart-Allmears model.

Figure 3.15 shows the turbulent intensity along R141b jet-pump centreline. The comparison of turbulent intensities for R141b jet-pump indicates that the predicted turbulence intensity increases earlier for standard K-Є model. For the realizable and RNG models the turbulent intensity starts to increase in the first part of constant area section.

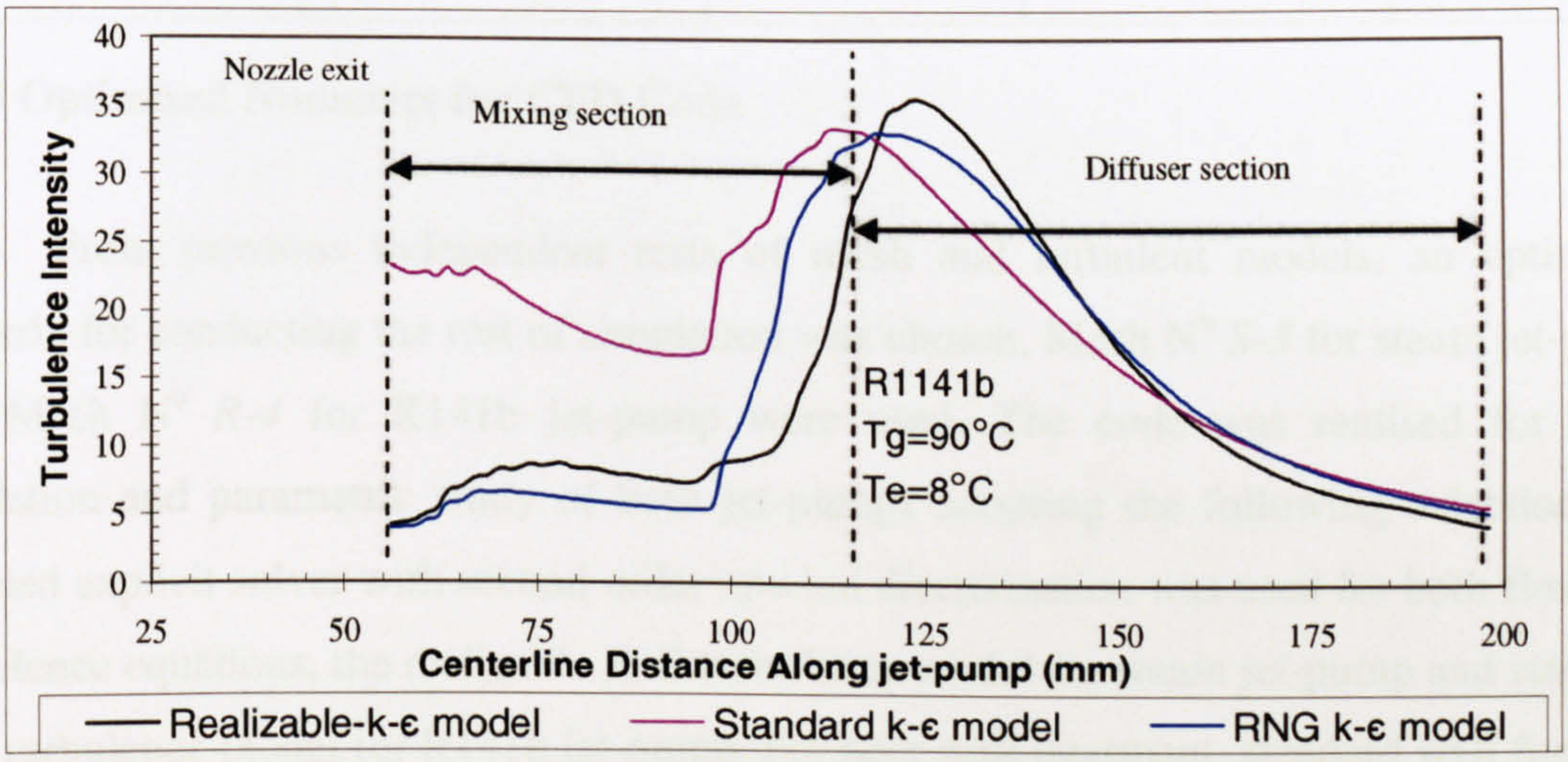

Figure 3. 15 Predicted turbulence intensity distributions along the R141b jet-pump centreline (CFD results)

The peak of the predicted turbulence intensities in the three models occur at the end of constant area section, where it is believed that the mixing process of the two streams is completed. It might be that the nozzle position influences the turbulent intensity in the conical part of the jet-pump, but it was found that this influence is negligible with the different nozzle positions used. The standard K-Є model seems to work well with R141b jet-pump.

3.4.5 Physical Properties

Physical properties of the fluid need to be specified with CFD modelling. The methods of specifying the properties with a coupled solver have been studied and validated before by Hart (2000). He found that specifying viscosity, thermal conductivity and specific heat values as constants, based upon the primary fluid significantly improve the results and the flow field is better predicted than defining the properties as temperature

dependent polynomials and piecewise-linear, or piecewise-polynomial. Therefore, all related physical properties of each fluid have been set as constant and depending on the operating conditions in each case as shown in Table 3.7. For R141b, the physical properties were selected on secondary flow variables. Only density was modelled using the ideal gas law. For real gas modelling described in "Chapter 6", no physical properties were entered as real data were used.

Table 3. 7 Steam and R141b physical properties

Jet pump (Refrigerant)	μ (kg/ms)E-6	K(kW/mk)E-6	Cp(J/kgK)	Mol Wt.
Steam	12.8	26.8	2090	18
R141b	380	9500	763	116.9

3.4.6 Optimised Numerics for CFD Code

From previous independent tests of mesh and turbulent models, an optimised numeric for conducting the rest of simulation was chosen. Mesh N° *S-3* for steam jet-pump and Mesh N° *R-4* for R141b jet-pump were used. The code was realised for more validation and parametric study of both jet-pumps adopting the following selection: the coupled explicit solver with second order upwind discretization was used for both flow and turbulence equations, the realizable K-Є turbulence model for steam jet-pump and standard K-Є turbulence model for R141b jet-pump. For near wall treatment, standard wall function was used in both jet-pump simulations as mentioned previously, this can give reasonably accurate results for very high Reynolds numbers. Because the mesh was designed to capture the boundary layer near the wall and to deal with shock waves, however, only in some cases was the mesh adaptive required to enhance the convergence of the solution.

Figures 3.16 and 3.17 show the CFD prediction of flow structure at the exit of the de Laval nozzle and within the mixing section of both jet-pumps at design conditions and with optimal nozzle position. The predicted flow structure within the two jet-pumps is more or less the same. Differences where they exist are though to be caused by operating conditions and the geometry. The shear mixing layer and boundary layer are observable clearly form strain rate contours shown in Figure 3.16. The mixing process starts between primary and secondary streams is clearly shown from total temperature contours in Figure 3.17.

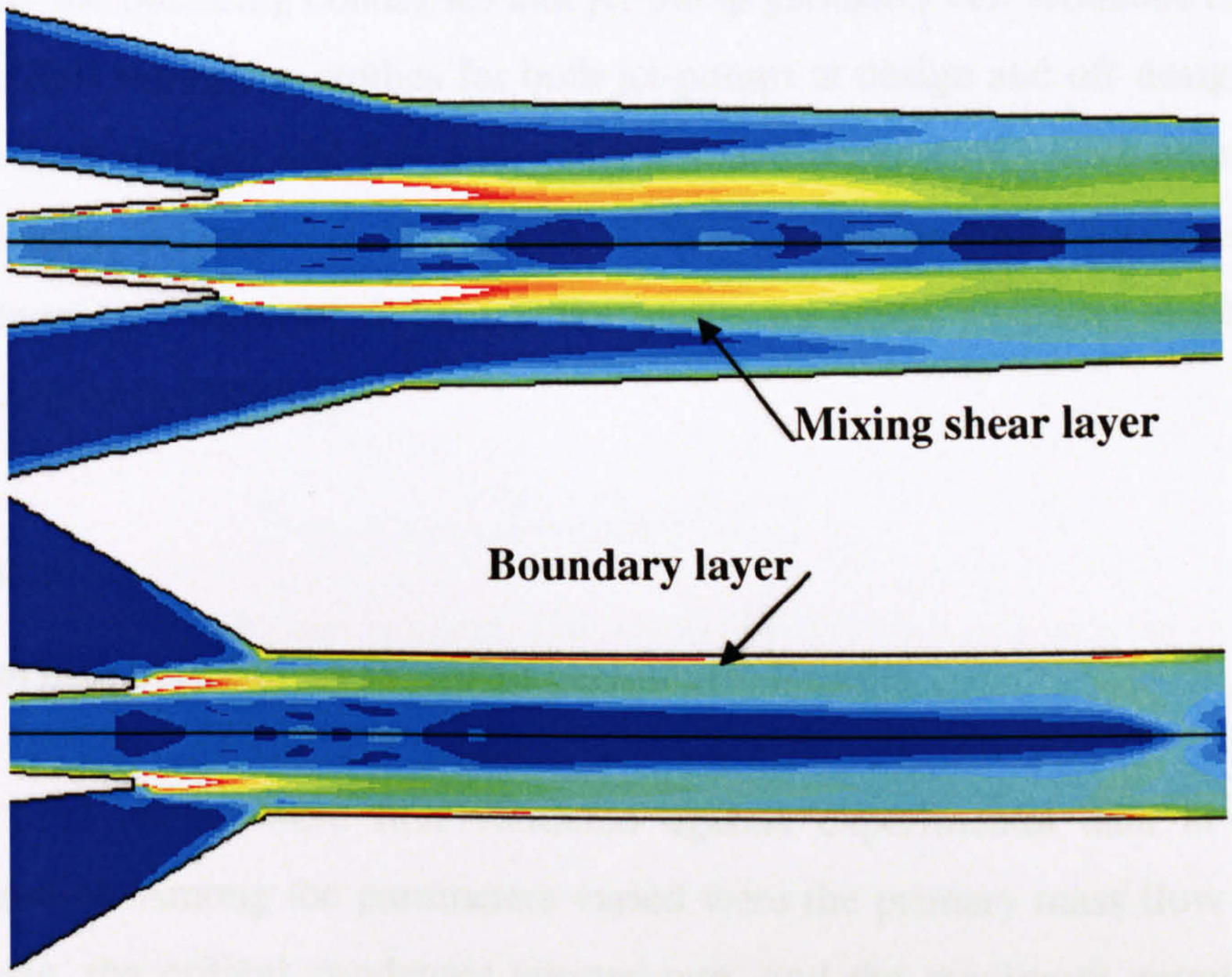

Figure3. 16 Predicted strain rate contours within mixing section

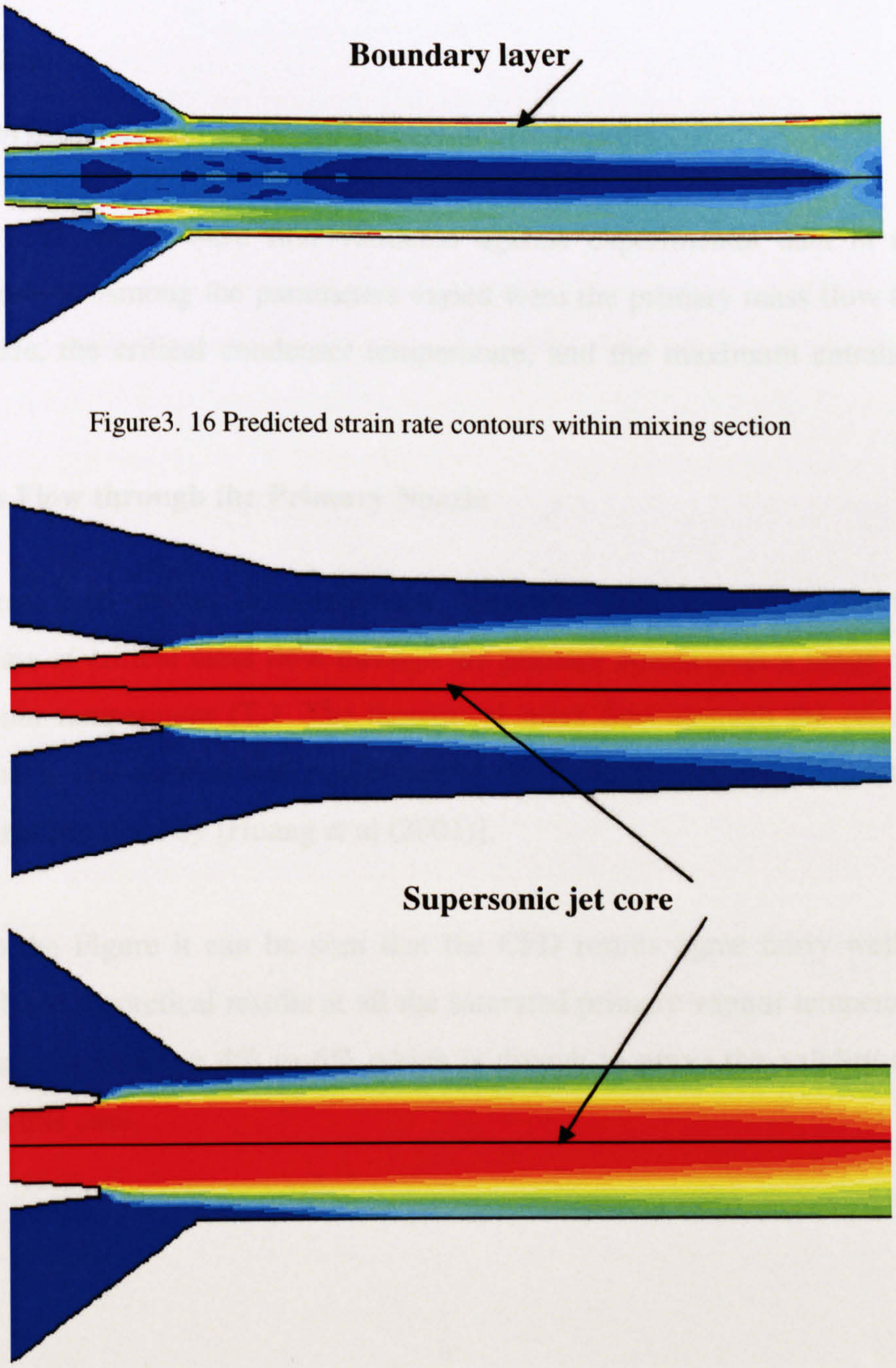

Figure 3. 17 Predicted total temperature contours within mixing section

There was no significant difference between the two modelled jet-pumps in terms of flow structure within the jet-pumps, even though they were designed by different methods. Only the operating conditions and jet-pump geometry can influence the jet-pump performance. Full simulation studies for both jet-pumps at design and off-design operating conditions were performed and the same validation and performance were obtained. In the next two sections, 3.5 and 3.6, the results of CFD validation and parametric study for R141b jet-pump are evaluated. Whereas, the results for steam jet-pump can be found in [Eames and Ablwaifa (2004b)].

3.5 CFD validation

3.5.1 Comparison between CFD and Experimental Results

The CFD results were first validated against experimental data in a series of parametric studies. Among the parameters varied were the primary mass flow through the primary nozzle, the critical condenser temperature, and the maximum entrainment ratio achieved.

3.5.1.1 Mass Flow through the Primary Nozzle

Figures 3.18 shows a comparison between CFD results, experimental and theoretical data of critical mass flow through the primary nozzle over a range of saturated primary vapour temperature (T_g). The theoretical mass flow through the primary nozzle was based on a one-dimensional compressible flow theory. The experimental data for R141b was that provided by [Huang et al (2001)].

From the Figure it can be seen that the CFD results agree fairly well with both experimental and theoretical results at all the saturated primary vapour temperature tested. The error range is between 4% to 6% which is though to prove the validity of the CFD simulation in this case.

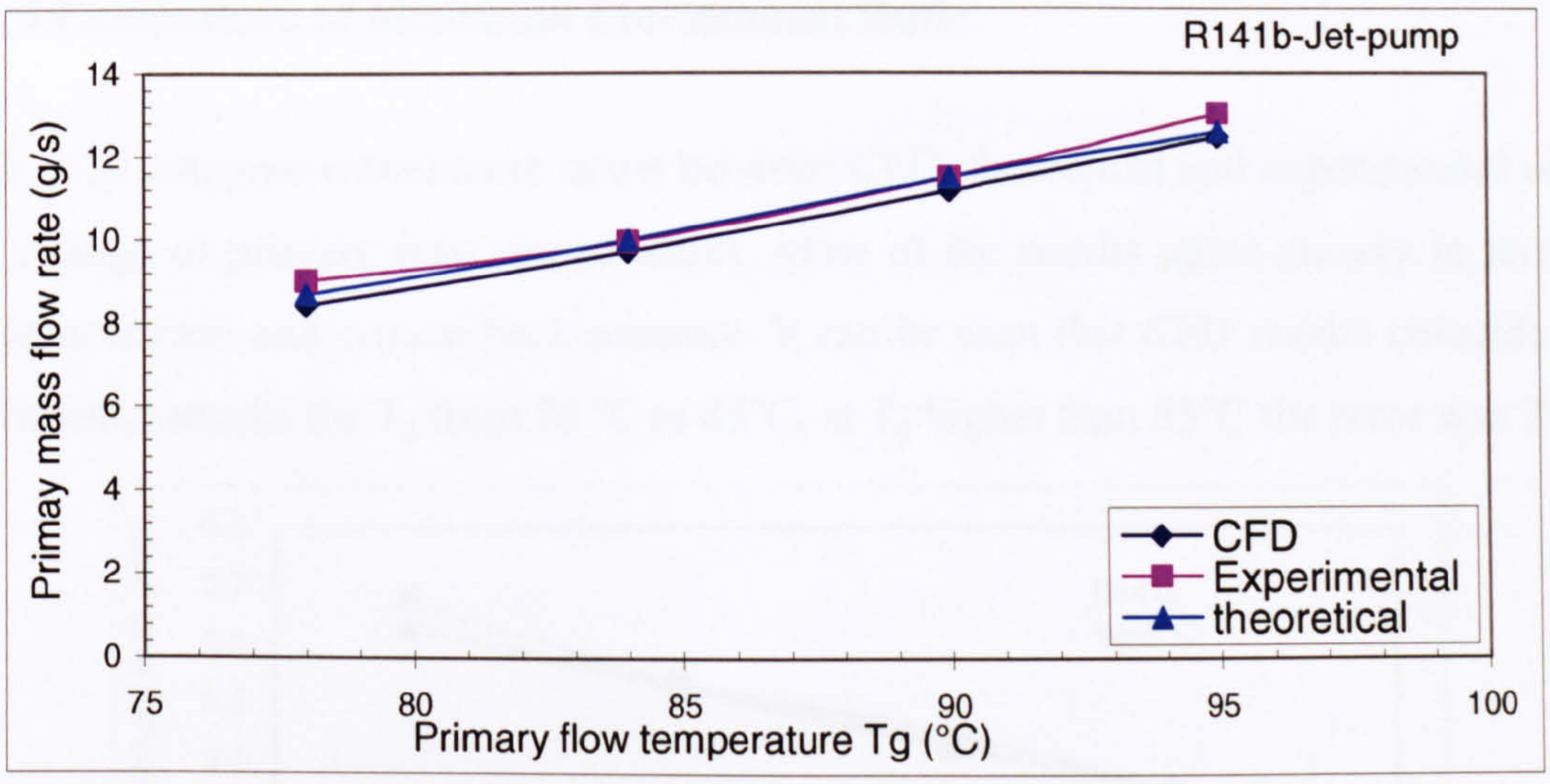

Figure 3. 18 Primary mass flows through primary nozzle- R141b jet-pump

3.5.1.2 Comparison of Critical Condenser Pressure

The condenser pressure at which the entrainment ratio starts to fall off is known as the critical condenser pressure (T^*_C) [Chen et al (1997)]. Figure 3.19 presents a comparison of CFD, experimental and theoretical results over a range of $T_{c\text{-}crit}$ obtained at different T_g. In each case T_e equalled 8°C. From the Figure 3.19 it can be seen that the CFD obtained results agree well with experimental and theoretically provided results. The difference between CFD and other results is approximately constant at all T_g values tested and never exceeds 8% decrease in critical condenser temperature. The reason for this difference may be related to small tolerance on the dimensions between that one tested experimentally and the one created for CFD simulation.

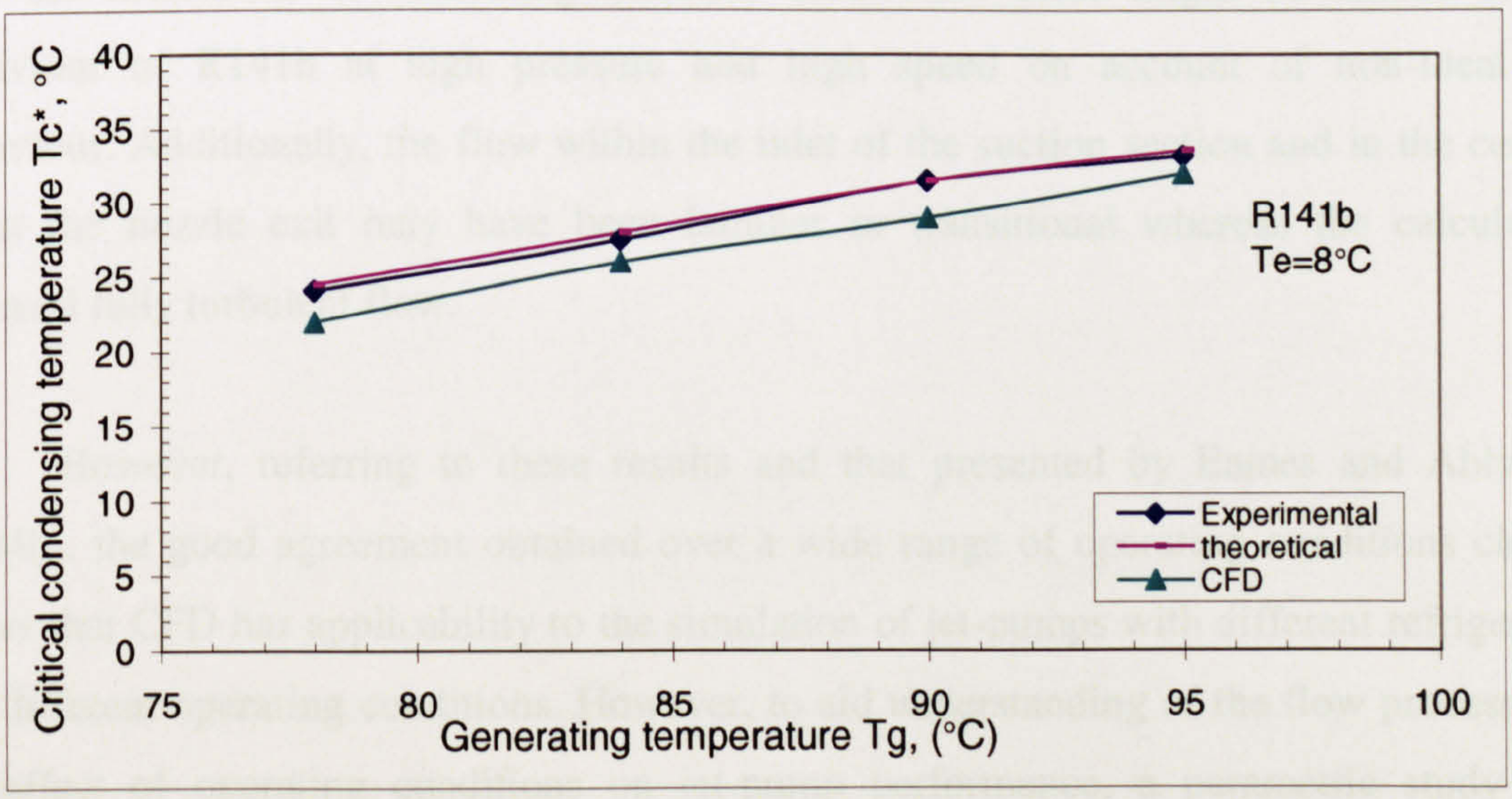

Figure 3. 19 Comparison results (Critical condenser pressure –R141b jet-pump)

3.5.1.3 Comparison of Maximum Entrainment Ratio

Figure 3.20 compare entrainment ratios between CFD, theoretical and experimental results over a range of primary flow temperatures. Most of the results agree closely in terms of entrainment ratio and critical back pressure. It can be seen that CFD results coincide with experimental results for T_g from 78 ℃ to 85°C, at T_g higher than 85°C the error was 2%.

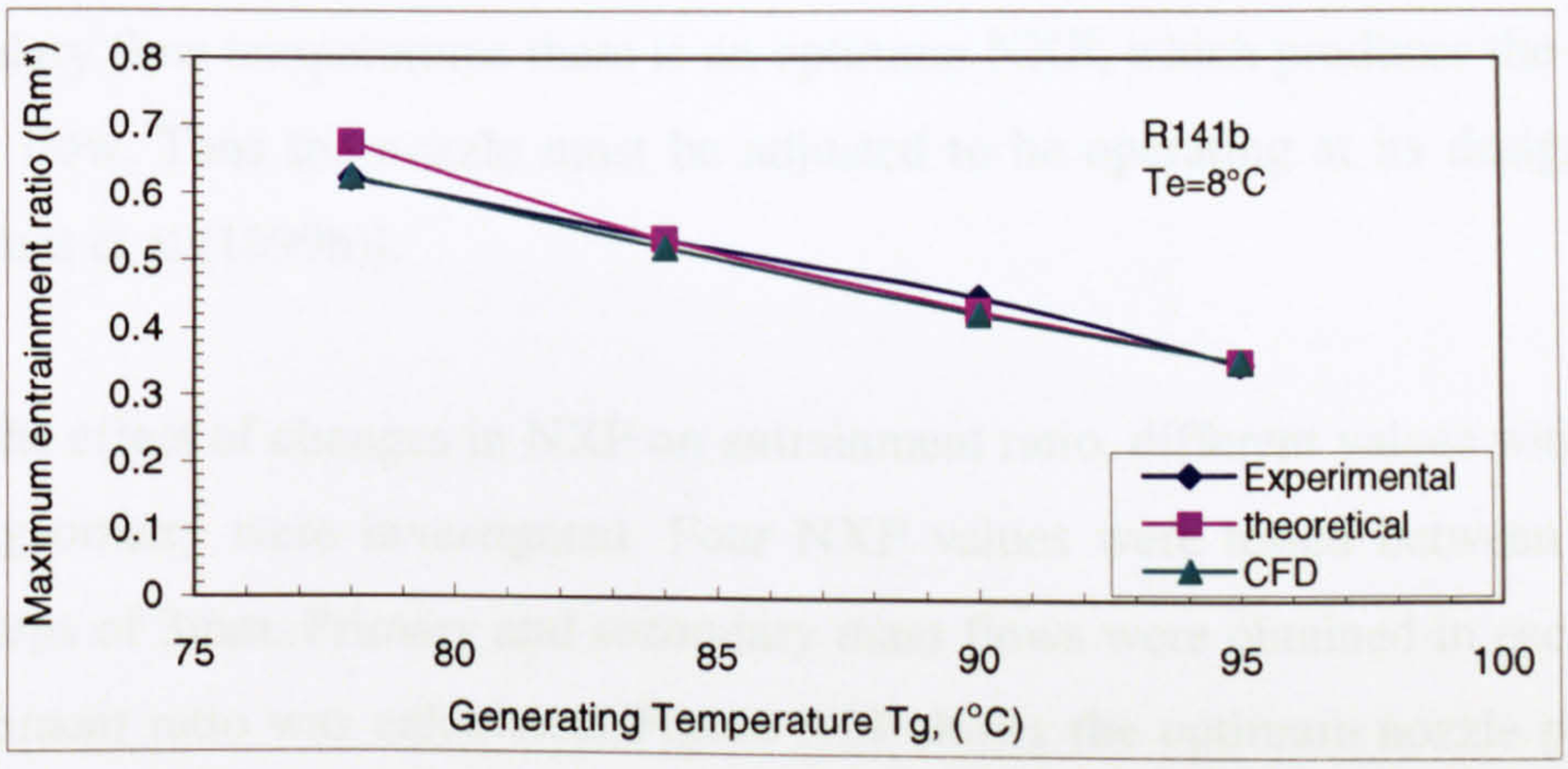

Figure 3. 20 Comparison of critical R_m at different T_g(R141b Jet-pump, T_e=8°C)

The results shown in Figures 3.18 to 3.20 show a good correlation between the experimental, theoretical and CFD values for the primary flow through the primary nozzle, critical condenser temperature and maximum entrainment ratios over a range of operating conditions. The small discrepancies between experimental and the CFD calculation may be related to the uncertainties in jet-pump dimension between the one tested experimentally and the one created for CFD testing or they may be due the experimental errors associated with the limitations of measuring facilities used. Also these might be related to the behaviour of R141b at high pressure and high speed on account of non-ideal gas behaviour. Additionally, the flow within the inlet of the suction section and in the centre-jet at the nozzle exit may have been laminar or transitional whereas the calculation assumed fully turbulent flow.

However, referring to these results and that presented by Eames and Ablwaifa (2004b), the good agreement obtained over a wide range of operating conditions clearly shows that CFD has applicability to the simulation of jet-pumps with different refrigerants and different operating conditions. However, to aid understanding of the flow process and the effect of operating conditions on jet-pump performance, a parametric study was conducted. This is described in the following section.

3.5.2 Parametric Study

3.5.2.1 Effect of the Nozzle Position on the Jet-pump Performance

In this study the distance of the nozzle exit (NXP) is measured from the primary nozzle exit plane to the entry plane of the first conical part of the jet-pump. Moving the nozzle away or into the mixing chamber affects the entrainment ratio. For given primary and secondary flow temperatures there is an optimum NXP, which produces the maximum secondary flow. Thus the nozzle must be adjusted to be operating at its design pressure value [Eames et al (1999b)].

To study the effect of changes in NXP on entrainment ratio, different values with the same jet-pump geometry were investigated. Four NXP values were tested between 0mm and 9mm in steps of 3mm. Primary and secondary mass flows were obtained in each case and the entrainment ratio was calculated. Figure 3.21 shows the optimum nozzle position for R141b jet-pump. In this jet-pump T_g and T_e were held constant and equal to 90°C and 8°C respectively (design operating conditions). Condensing temperature, T_c, was varied over a range between 26°C to 32°C. It is clear from the Figure that NXP =6mm is the optimal nozzle position with an entrainment ratio of 0.425 and a critical temperature 29°C.

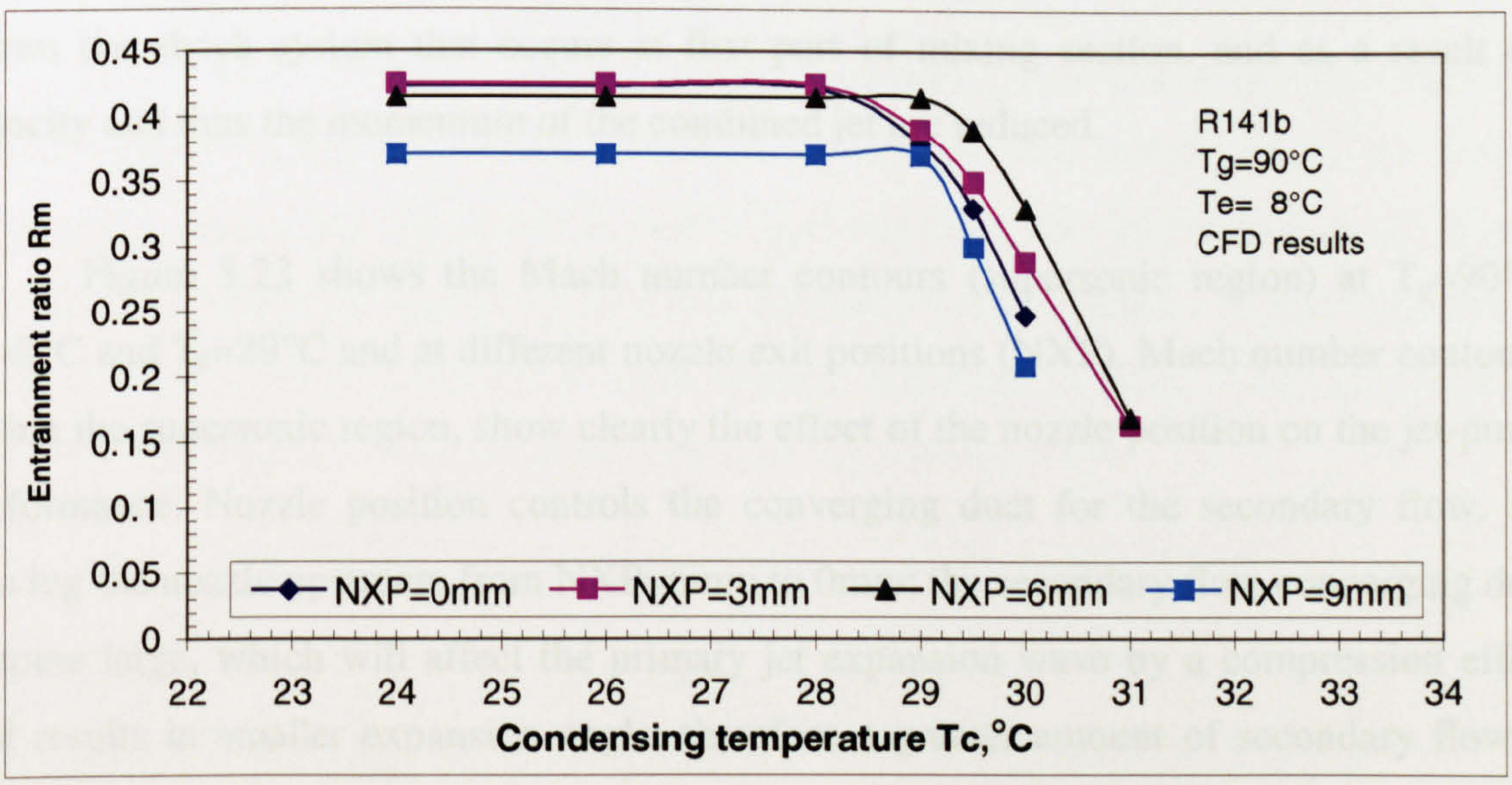

Figure 3. 21 Predicted optimum NXP (R141b jet-pump- CFD results)

In order to explain the effect of moving the nozzle within the mixing section, it is possible to plot contours of the static pressure and Mach number along the jet-pump axis. Figure 3.22 shows the static pressure along the centreline of the R141b jet-pump.

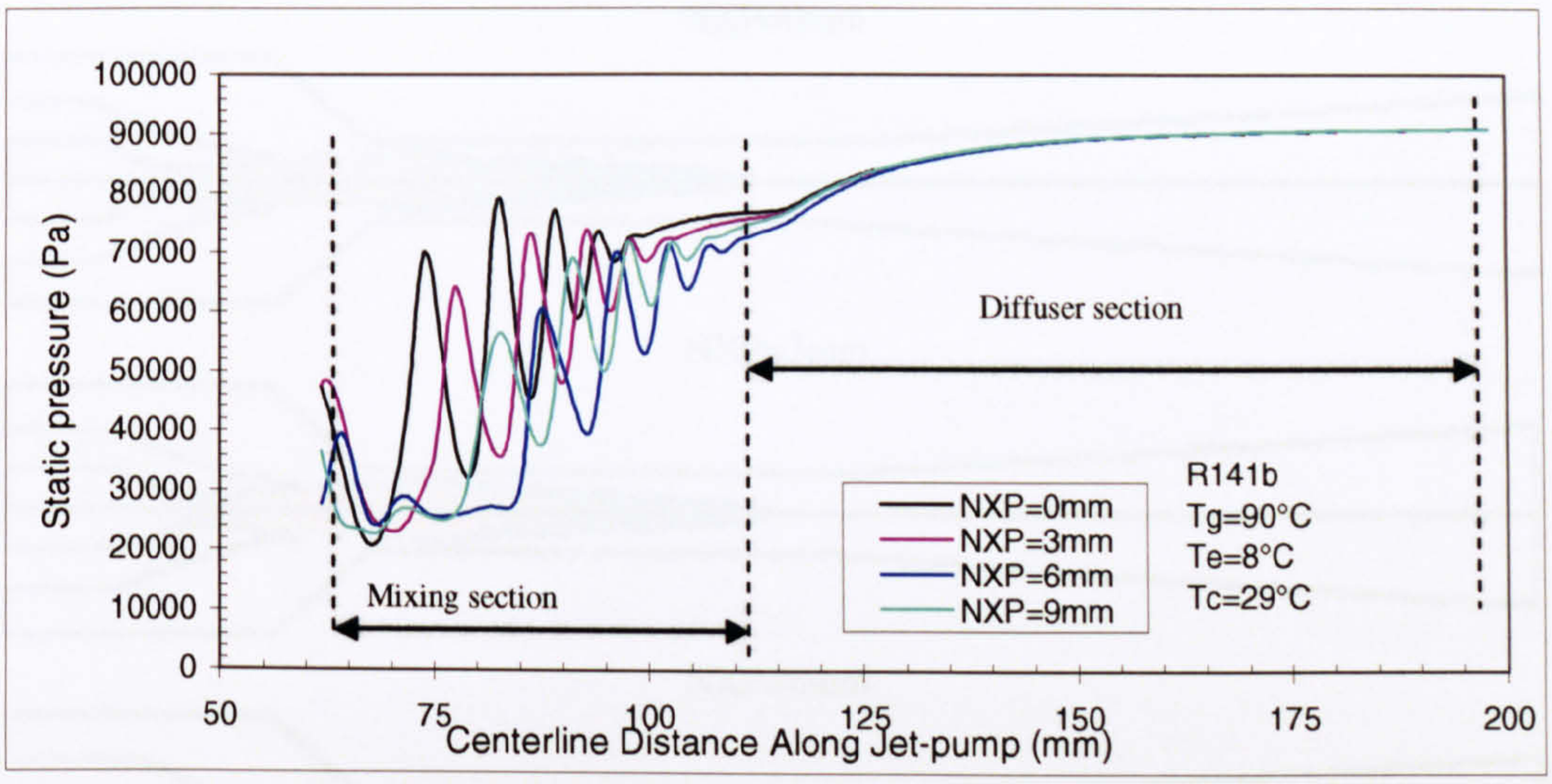

Figure 3. 22 Predicted static pressure profiles along R141b jet-pump Centreline (CFD results)

From the above Figure, the fluctuation of static pressure inside the mixing section shows the influence of NXP on jet-pump performance. With the NXP set at its optimal value of 6mm, the static pressure does not fluctuate through the first part of the mixing section, thus there is rise in the amount of secondary fluid introduced, which increases the momentum and velocity of the mixed stream to achieve higher critical condenser pressure. The early fluctuation of static pressure at other nozzle positions shows the non-equilibrium between the two streams which will affect the jet-pump performance. This fluctuation shows the shock system that occurs at first part of mixing section, and as a result the velocity and thus the momentum of the combined jet are reduced.

Figure 3.23 shows the Mach number contours (supersonic region) at T_g=90°C, T_e=8°C and T_c=29°C and at different nozzle exit positions (NXP). Mach number contours, within the supersonic region, show clearly the effect of the nozzle position on the jet-pump performance. Nozzle position controls the converging duct for the secondary flow. By moving the nozzle upstream from NXP=6mm to 0mm; the secondary flow converging duct become large, which will affect the primary jet expansion wave by a compression effect that results in smaller expansion angle, therefore a greater amount of secondary flow is entrained. However, in this case the momentum of mixed stream decreases and the shock position moves upstream, thus a lower critical condenser pressure is achieved.

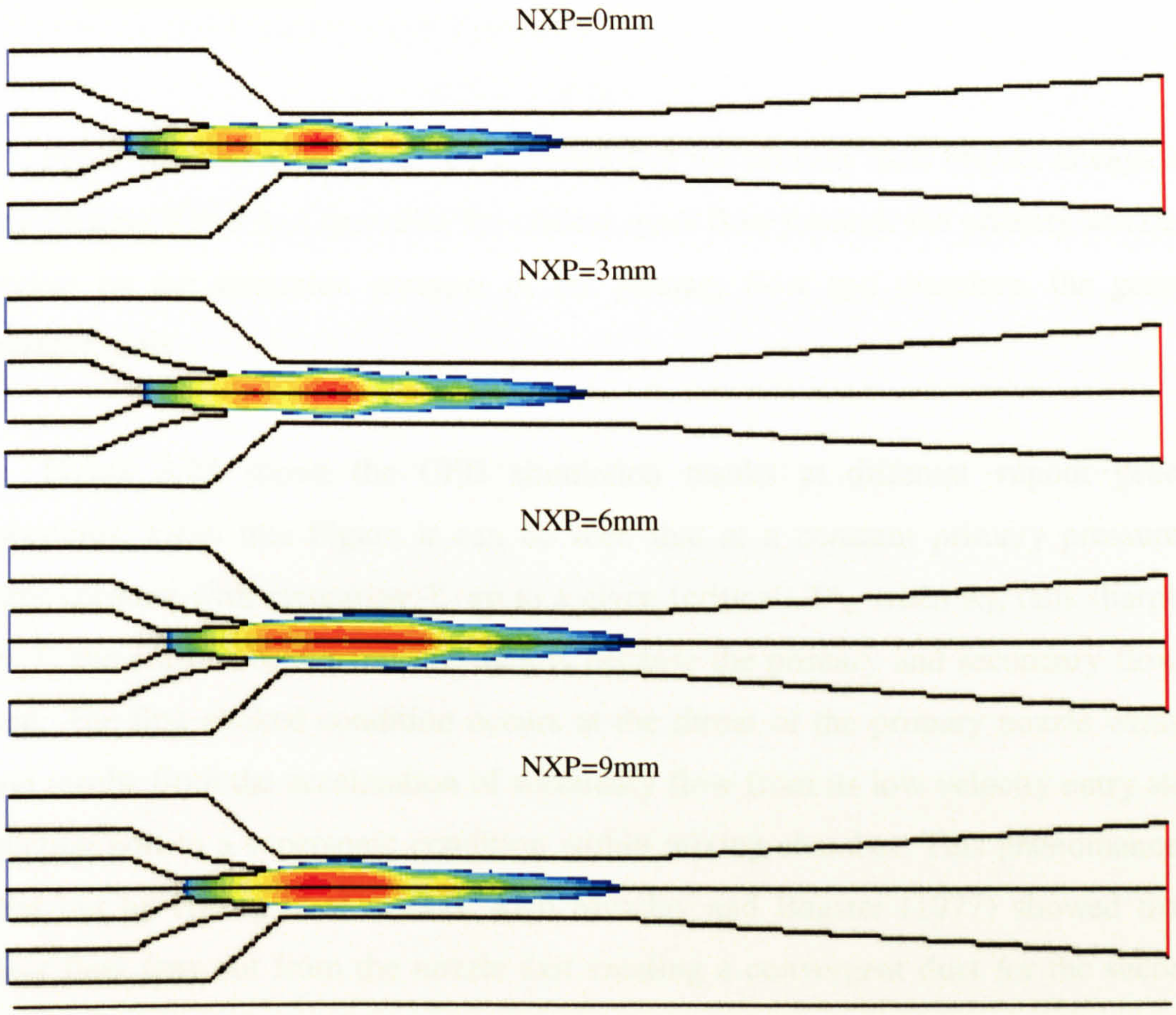

Figure 3. 23 Predicted Supersonic region of R141b jet-pump at different NXP

When NXP =9mm the nozzle is close to secondary flow convergent duct reducing entrainment. Also, the momentum of mixed stream is lower, which affects the critical condenser temperature. The optimal nozzle position with this jet-pump is 6mm, which provide best portion of secondary flow that increases the momentum of mixed stream to obtain highest critical temperature with highest entrainment ratio. Also, the obtained optimum NXP coincides with that recommended by ESDU (1985).

3.5.2.2 Effect of Operating Conditions

In this section, the effects of operating conditions on jet-pump performance for the R141b jet-pumps are evaluated using CFD data. An NXP=6mm was used to study the jet-pump performance.

Effect of Back and Primary Flow Pressures

From the CFD simulation, it was found that the primary flow chokes always at the primary nozzle throat and therefore the critical mass flow through the primary nozzle was dependent on the saturation pressure of the primary flow and therefore, the generator temperature only.

Figure 3.24 shows the CFD simulation results at different vapour generator temperatures. From this Figure it can be seen that at a constant primary pressure, R_m remains constant with increasing T_c up to a given (critical) T^*_c, when R_m falls sharply. At lower T_c the reason R_m remains constant is because the primary and secondary flows are choked. The first choked condition occurs at the throat of the primary nozzle whilst the second results from the acceleration of secondary flow from its low velocity entry state at the suction port to a supersonic condition within mixing chamber. This phenomenon was pointed out by Huang et al (1985). Also Munday and Bagster (1977) showed that the primary flow fans out from the nozzle exit creating a convergent duct for the secondary flow in which is accelerated to sonic velocity during entry and it chokes at effective area, whereby the mixing of two streams starts.

However, jet-pump entrainment ratio depends inversely on the condenser pressure, and the jet-pump can only operate efficiently below its critical back pressure (double choking) which is dependent on both the primary and secondary flow stagnation pressures.

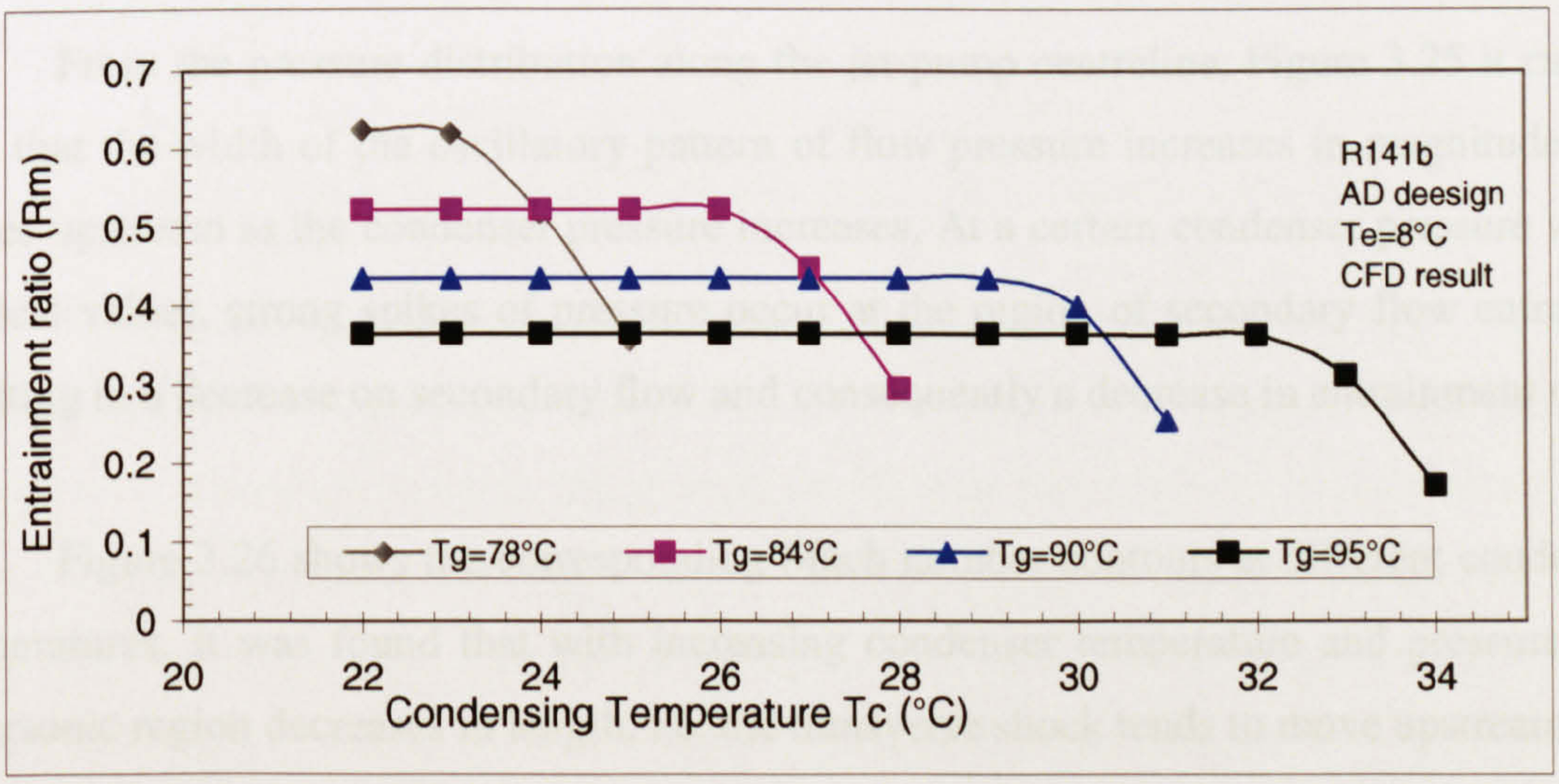

Figure 3. 24 Predicted Variation of R_m with T_c and T_g (T_e=8°C R141b jet-pump)

Moreover it can be clearly seen from the above Figure that an increase in vapour generator temperature at fixed secondary flow conditions leads to a fall in entrainment ratio with corresponding increase in the critical condenser temperature. Thus, in order to obtain better performance, the primary vapour pressure and temperature should be selected according to the operational critical back pressure and condenser temperature; otherwise, some input energy at the generator will be wasted.

The influence of increasing condenser pressure upon jet-pump performance can be explained through the static pressure profile along the jet-pump centreline and also through supersonic region within the jet-pump. Figure 3.25 shows the static pressure plots along the jet-pump centreline, at T_g=90°C, T_e=8°C and with different T_c.

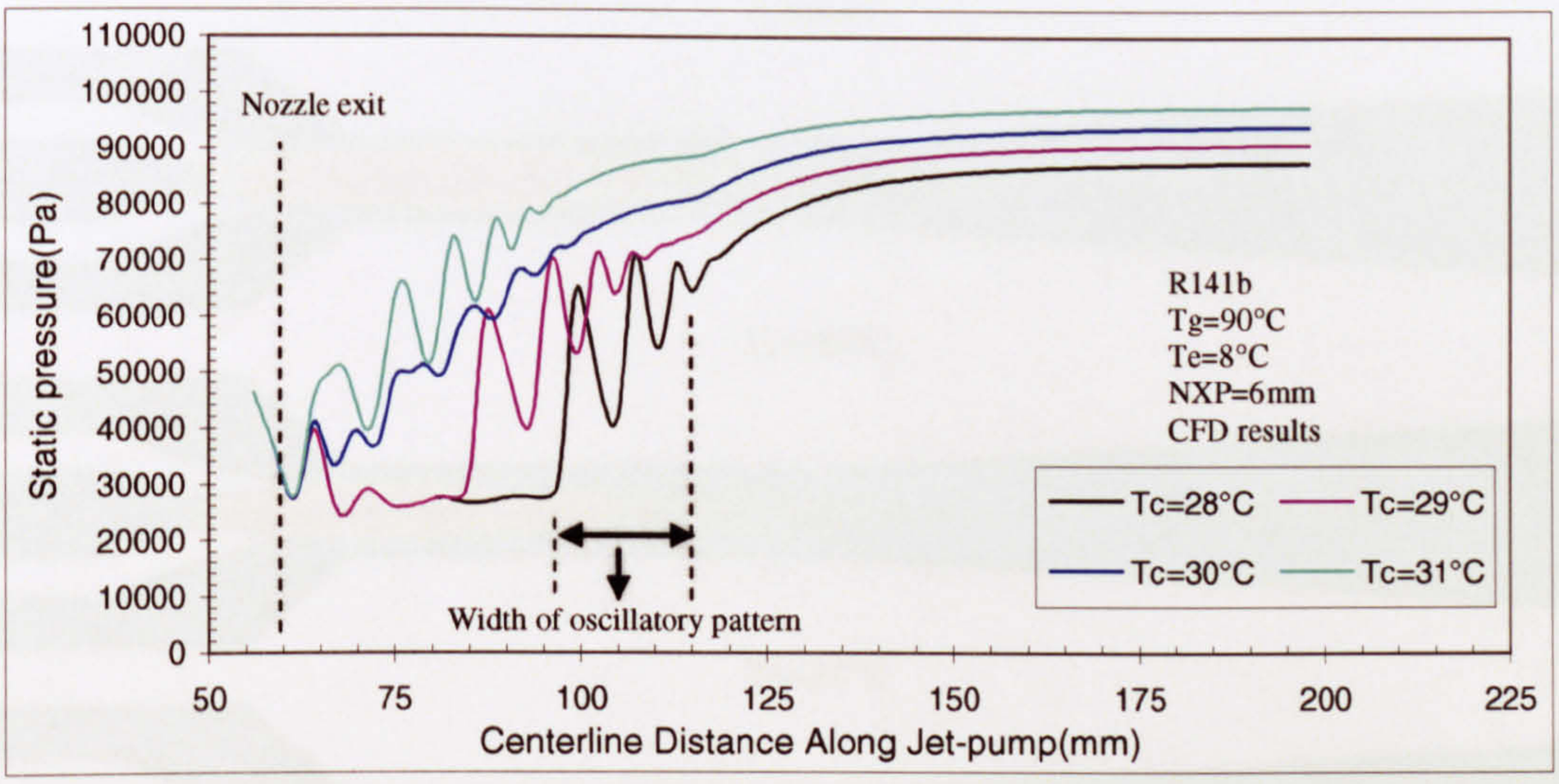

Figure 3. 25 Predicted Static pressure profile along jet-pump centreline(T_e=8°C & T_g=90°C)(CFD results)

From the pressure distribution along the jet-pump centreline, Figure 3.25 it can be seen that the width of the oscillatory pattern of flow pressure increases in magnitude and moves upstream as the condenser pressure increases. At a certain condenser pressure value (critical value), strong spikes of pressure occur at the region of secondary flow entrance, resulting in a decrease on secondary flow and consequently a decrease in entrainment ratio.

Figure 3.26 shows the corresponding Mach number contours at different condenser temperatures. It was found that with increasing condenser temperature and pressure, the supersonic region decreases in length, i.e. the transverse shock tends to move upstream into jet-pump throat. In the first three contours, with condenser pressure less than critical, the shock appears not to affect the mixing process, as it is clear that the properties of the flow

in the entry plane of conical part, where the mixing process begins, remain unchanged. Thus it is independent of downstream conditions, which confirm that the secondary flow is choking. As the condenser pressure is increased above its critical value, the shock moves further into the jet-pump throat and begins to disturb the entrainment process. In this case the secondary fluid becomes unchoked and entrainment decreases. Further increase in condenser pressure causes reverse flow into evaporator.

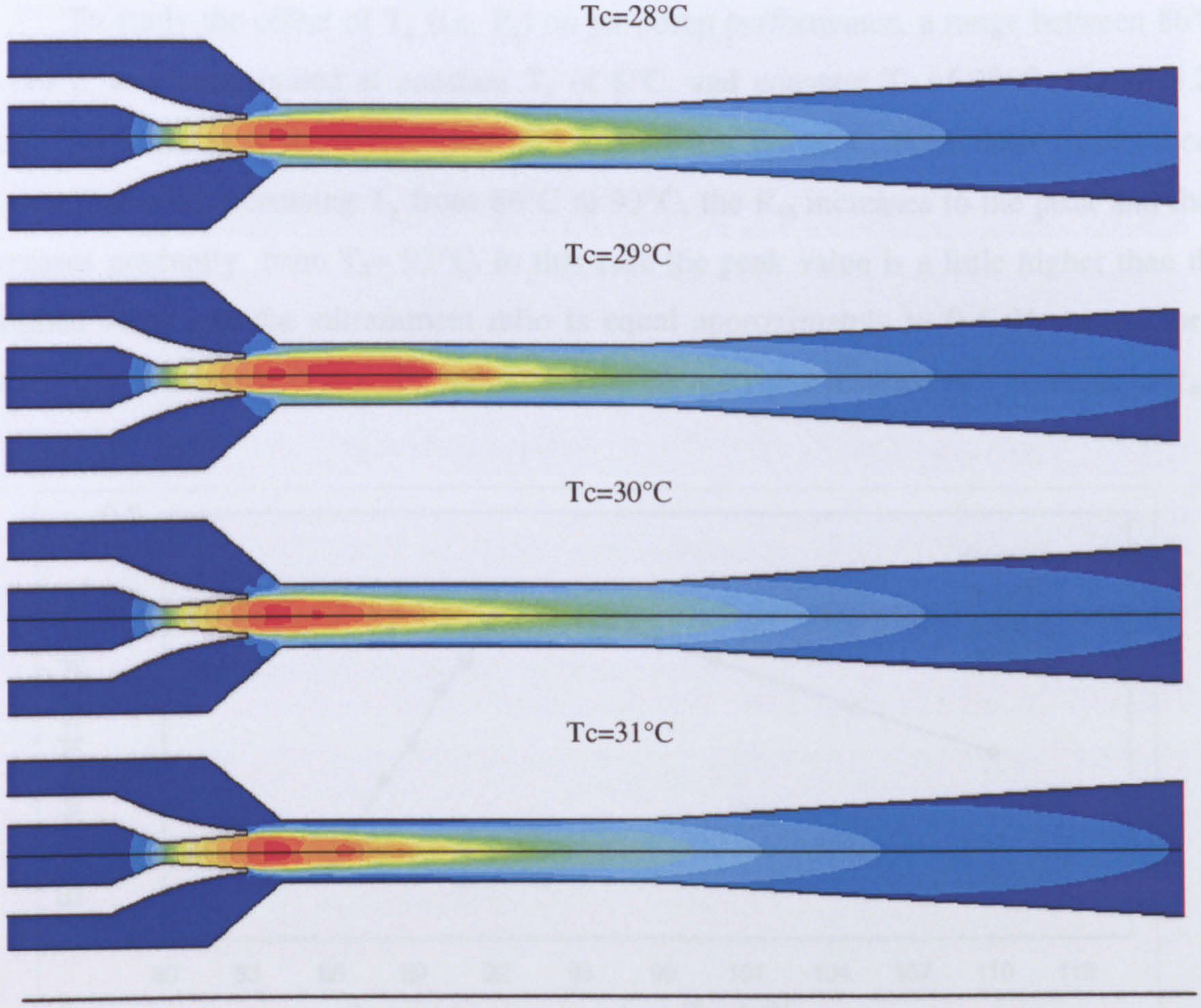

Figure 3.26 Predicted Mach No contours at different T_c (Te=8°C & Tg=90°C)

Also, referring to Figures 3.24 and 3.26, the effect of primary flow pressure with constant evaporator conditions can be explained. Increasing primary flow pressure increases the mass flow through the primary nozzle and thus the velocity and momentum of the flow are increased. The increasing of momentum will accelerate the primary flow with large expansion angle, i.e. enlarging the jet core, which reduces the annulus effective area for secondary flow. It was found that when increasing the primary flow pressure, the secondary mass flow rate increases, but at lower rate than the rate of increase in primary flow rate. This increase in secondary flow can be recognized because when the exit

velocity of motive jet increases, the rate at which secondary flow entered increased and offsets the decrease on annulus effective area. This disproportionate rise in secondary mass flow to the primary mass flow affects the overall jet-pump performance causing the entrainment ratio to fall. Also, with higher momentum of the primary flow the choke position moves downstream, as shown in the Mach No contours Figure 3.26, and the jet-pump can operate at higher discharge pressures.

To study the effect of T_g (i.e. P_g) on jet-pump performance, a range between 86°C to 110°C was investigated at constant T_e of 8°C, and constant T_c of 28°C. Figure 3.27 shows the variation of R_m with respect of T_g at constant T_e and T_c. From these results it can be seen that with increasing T_g from 86°C to 93°C, the R_m increases to the peak and then decreases gradually from T_g= 93°C. In this case the peak value is a little higher than the designed value and the entrainment ratio is equal approximately to 0.4. However, for a given T_e, increasing the T_g i.e. P_g, more than the design value resulted in a decrease in R_m.

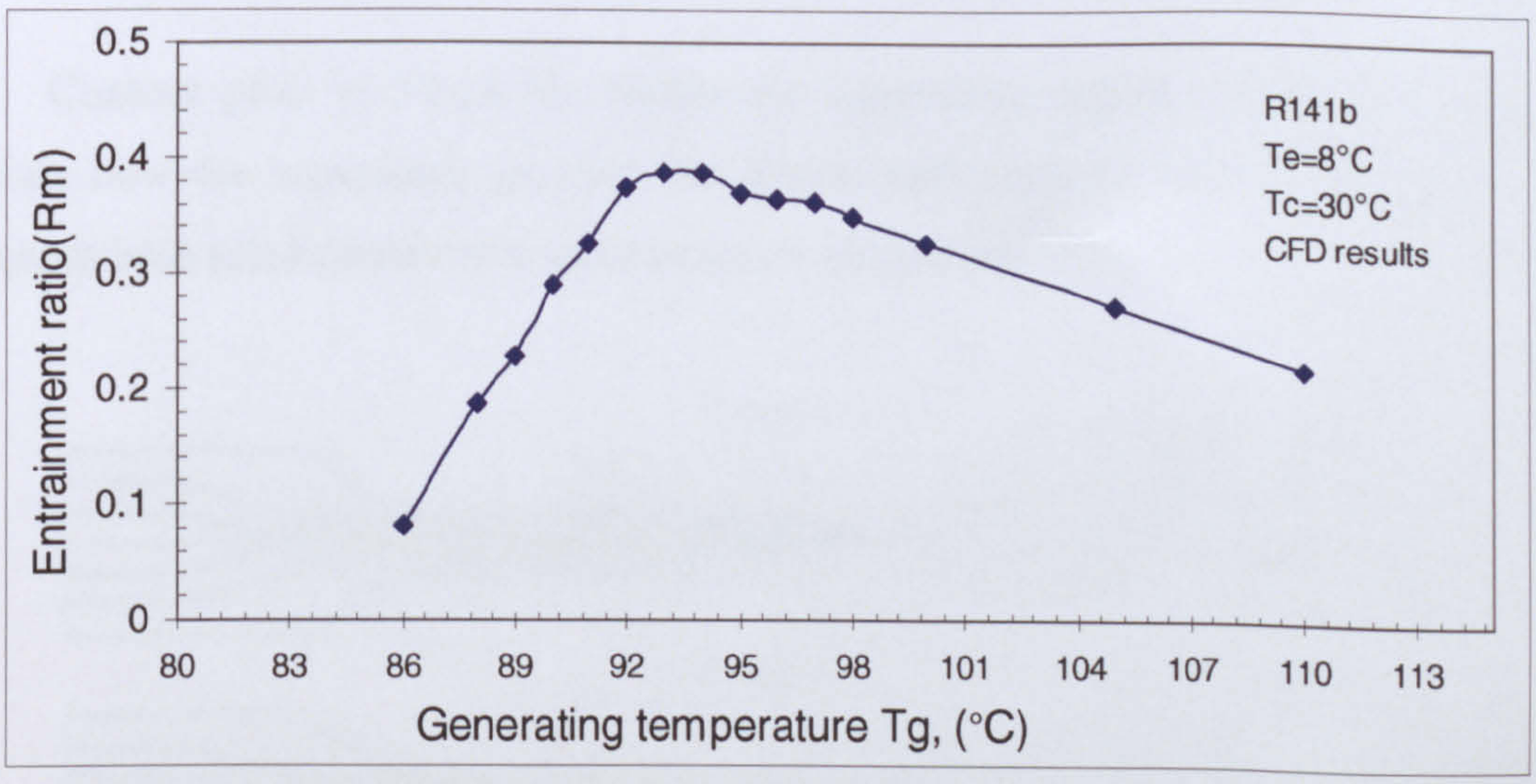

Figure 3. 27 Predicted effect of T_g on jet-pump performance (CFD results)

Figure 3.28 shows the static pressure plots along the centreline of the R141b jet-pump, with all generator temperatures tested. The oscillatory pressure field at the nozzle exit shows the effect of supersonic flow on pressure. These oscillations occur along the entire length of the mixing section with decreasing magnitude downstream as far as the first part of constant area section, and then they disappear within the second part of constant area section. When the supersonic jet gets to the end of the throat, a sudden jump in the pressure is followed by large pressure fluctuations. This indicates a normal shock

system, which moves downstream and increases in magnitude as the vapour generator temperature is increased, because of the increasing of stream velocity, i.e. momentum combined with increase in T_g.

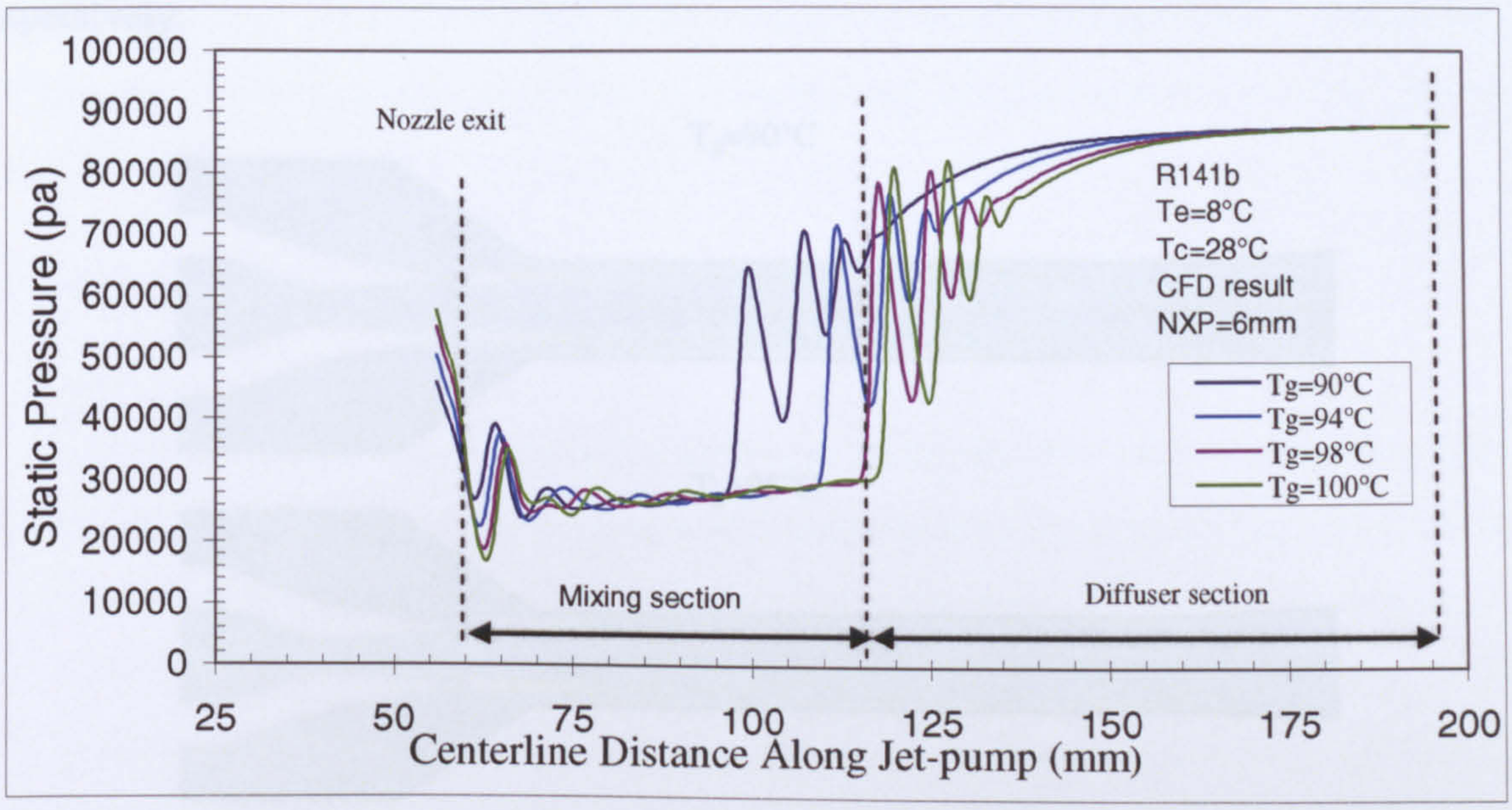

Figure 3. 28 Predicted static pressures profiles along jet-pump centreline (R141b jet-pump-CFD results)

Contour plots of Mach No within the supersonic region, shown in Figure 3.29 illustrate how the supersonic jet exits the nozzle and expands with increasing T_g. This influences both entrainment ratio and condenser critical pressure.

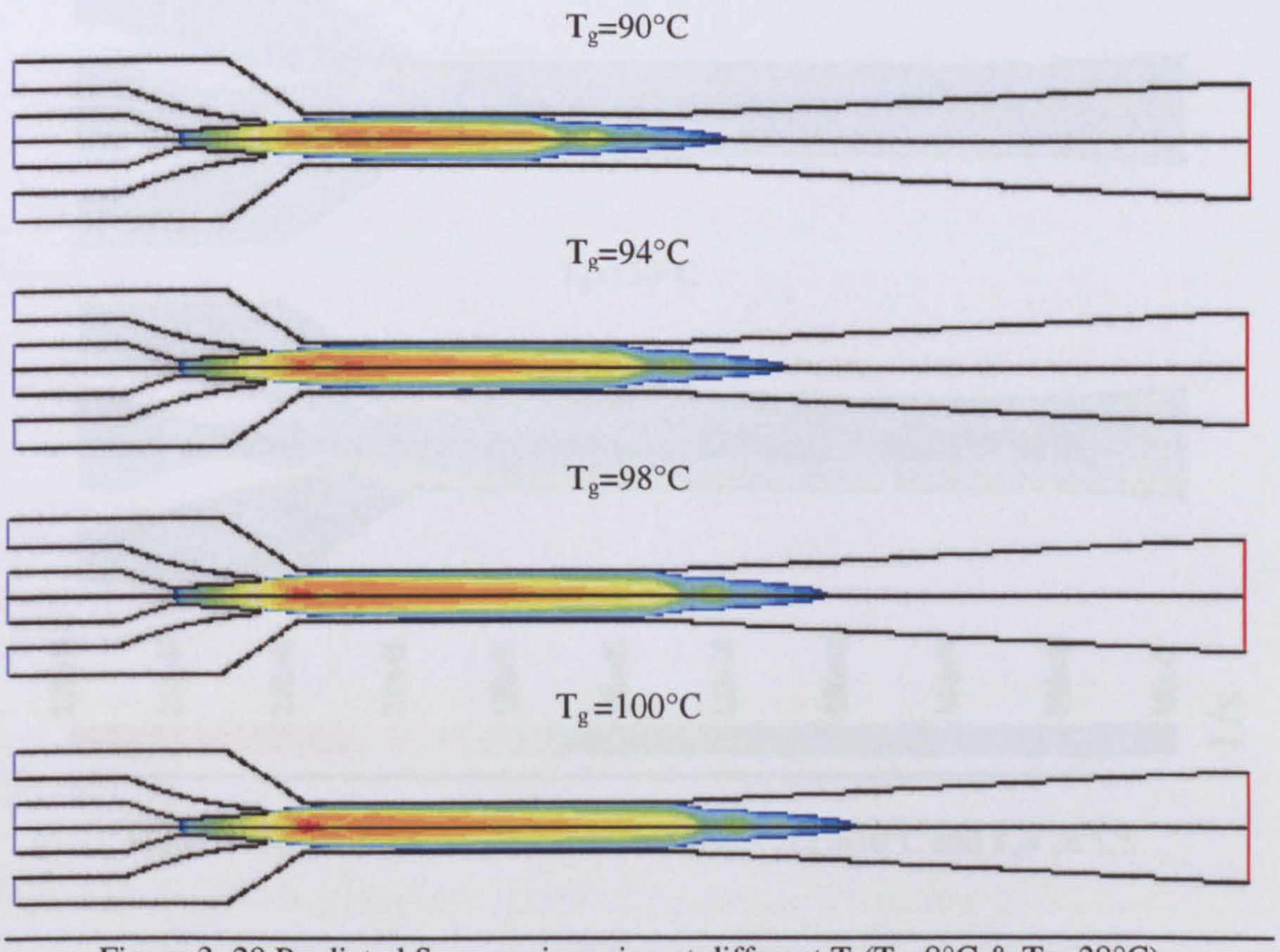

Figure 3. 29 Predicted Supersonic region at different T_g(T_e=8°C & Te=28°C)

Also the flow structure within the mixing section of the supersonic jet-pump can be identified by using strain rate contours, as shown in Figure 3.30. This shows the strain rate contours at different T_g values and with fixed T_e and T_c, which were 10°C and 26°C respectively.

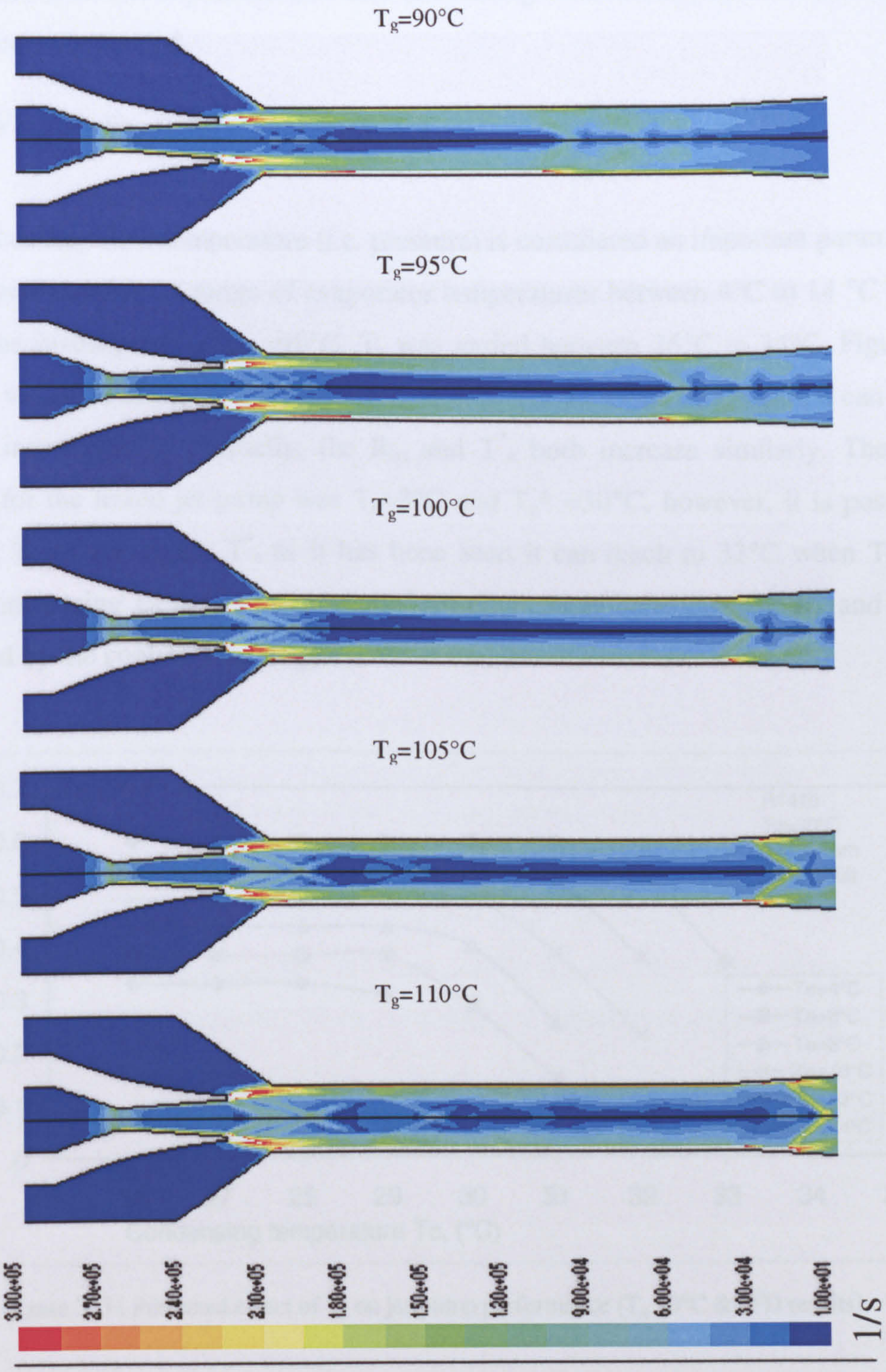

Figure 3. 30 Predicted Strain rate at different T_g (T_e=10°C and T_c= 26°C)

Strain rate contours show the shear layer at the mixing area between the two streams. They also show the boundary layer near the wall and the embedded shock structure within the supersonic jet. It is clear from these contours that as the primary pressure increases the intensity and interaction of the shock structure grows. Downstream of the nozzle exit, the expansion rate into the mixing section increases and the nozzle is becomes under-expanded.

Effect of Varying Secondary Flow Pressure

Secondary flow temperature (i.e. pressure) is considered an important parameter for jet-pump performance. A range of evaporator temperatures between 4°C to 14 °C in steps of 2°C, was investigated at T_g =90°C. T_c was varied between 26°C to 34°C. Figure 3.31 shows the variation of R_m with respect of T_c at different T_e. From this Figure it can be seen that with increasing T_e gradually, the R_m and T^*_c both increase similarly. The design condition for the tested jet-pump was T_e=8°C and T_c* =30°C, however, it is possible by increasing T_e, to get higher T^*_c as it has been seen it can reach to 32°C when T_e=12°C. Although increasing T_e and P_e has merits of simultaneously increasing the R_m and the T^*_C, it is limited by the cooling load target.

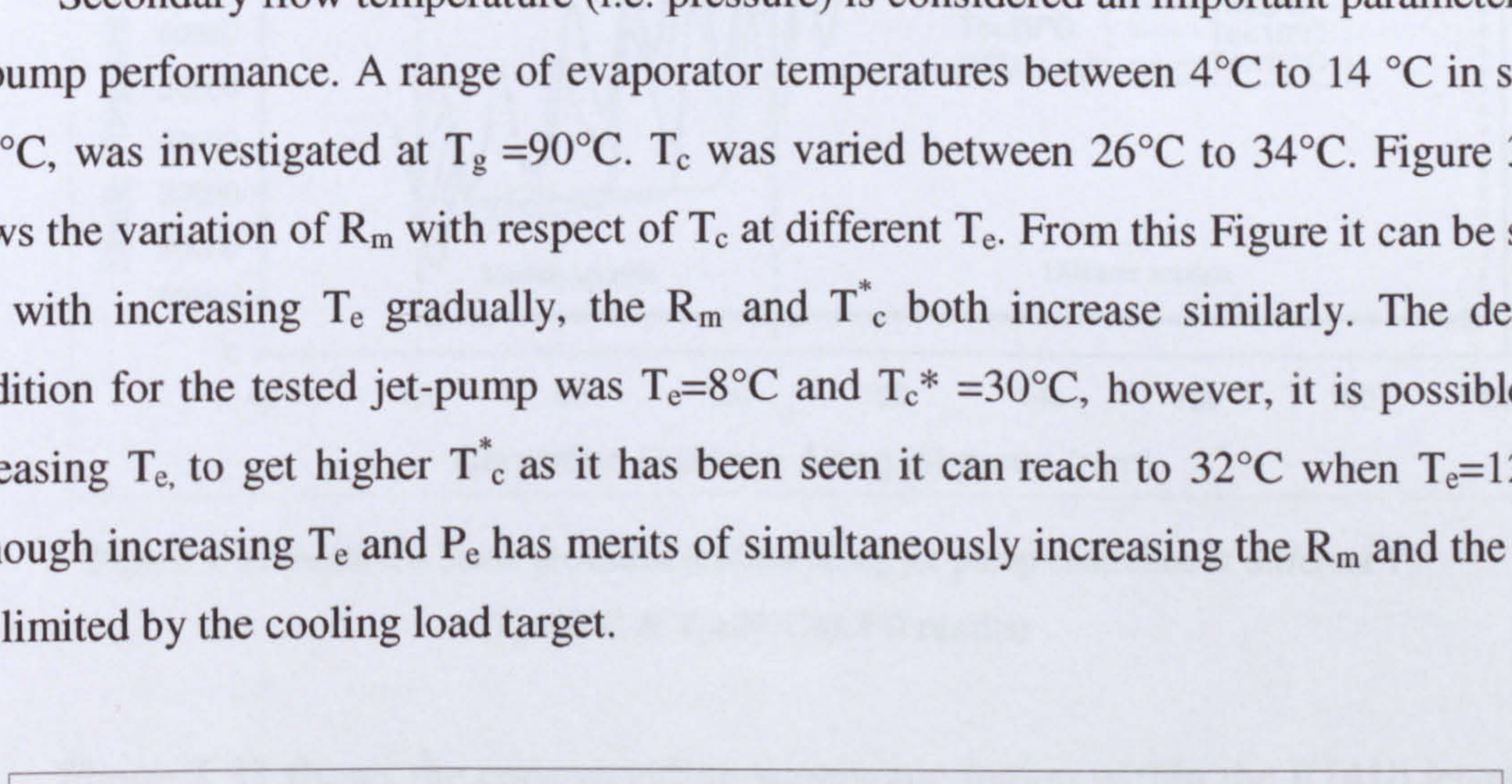

Figure 3. 31 Predicted effect of T_e on jet-pump performance (T_g 90°C &CFD results)

Figure 3.32 shows the predicted variation in centreline static pressure along the centre axis of the R141b jet-pump, T_g and T_c is equal 90°C and 29°C respectively. This Figure shows the characteristics of flow within the mixing section. At higher T_e, a

barrelling effect of the supersonic flow region seems lower in magnitude and disappears within the constant area section. At the entrance of the diffuser, a normal shock system occurs which move downstream as T_e is increased. At lower values of T_e, large fluctuations in pressure occur from the primary nozzle exit to the end of constant area section. This results in lower momentum of the mixed stream and therefore, some energy of the flow is expected to dissipate within this region.

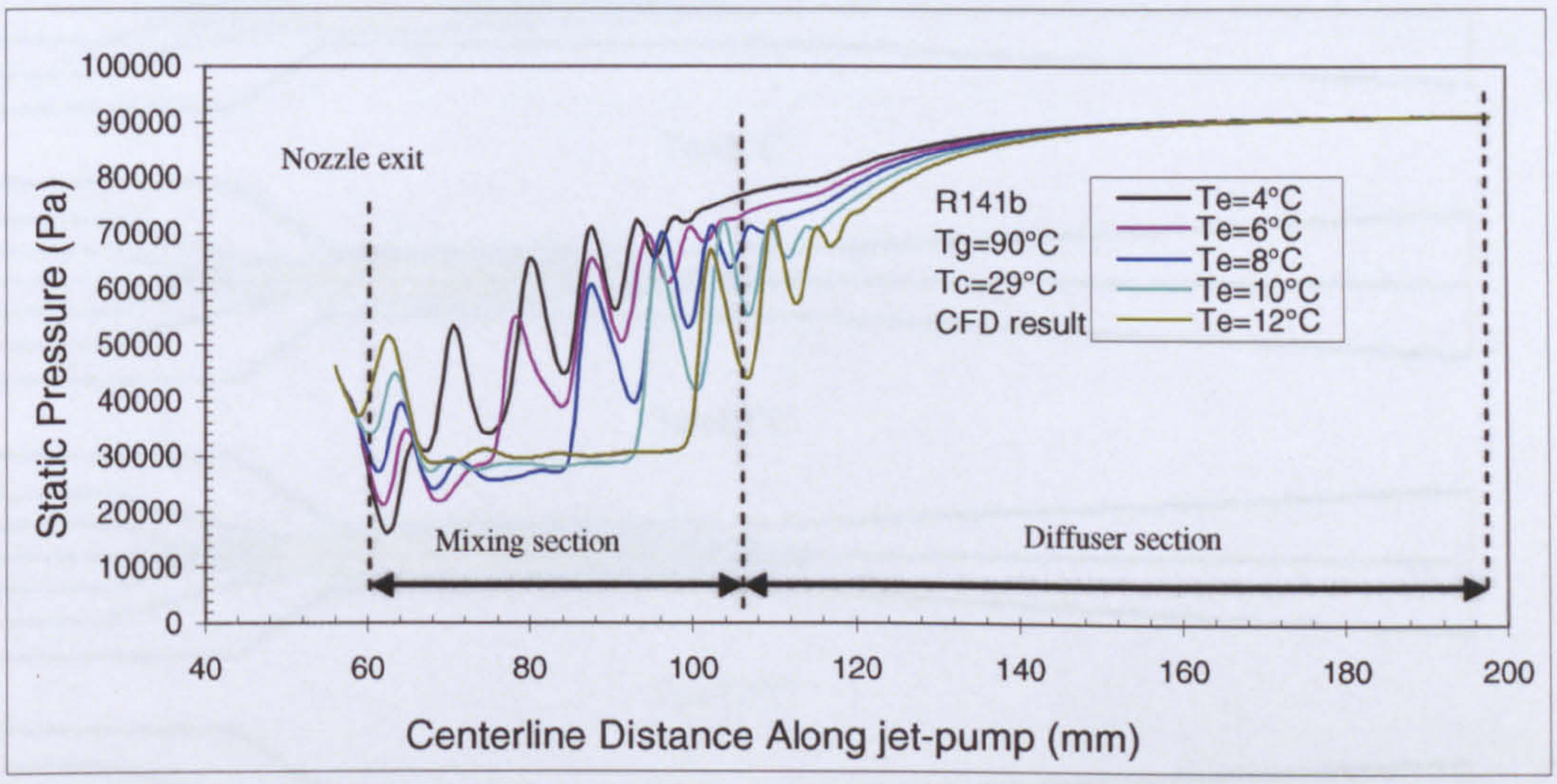

Figure 3. 32 Predicted Static pressures profiles along jet-pump centreline at different T_e (T_g=90°C & T_c=29°C)(CFD results)

Figure 3.33 shows the corresponding supersonic region within the R141b jet-pump at different T_e values. From the Mach number contours the expansion of the combined jet increases and the choke position of secondary flow moves downstream with increasing secondary flow inlet pressure. At lower evaporator temperatures, the expansion wave of the jet existing the nozzle increases in width and closes the flow area for the secondary flow, thus reducing the secondary flow. Whereas, at higher evaporator temperatures, the expansion angle of primary jet reduces, allowing more secondary flow to enter and at the same time allowing the momentum of the two streams to increase, and with it the critical condenser temperature.

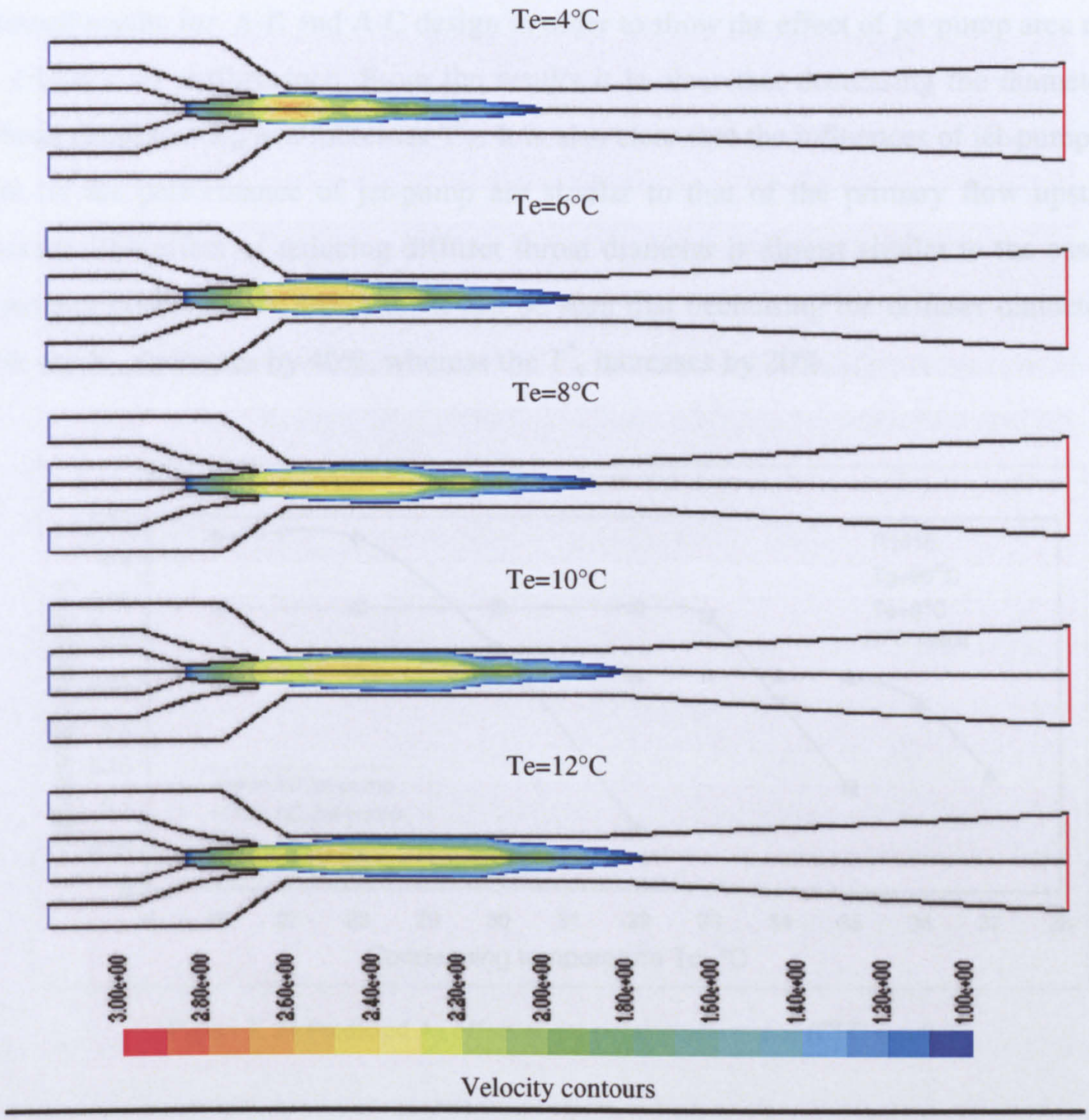

Figure 3. 33 Predicted supersonic region flow region at different T_e(T_g=90°C & Tc=29°C)

Effect of Jet-pump Area Ratio, A_R (A_3/A_t)

A_R is the area ratio of constant area section of diffuser to nozzle throat. In order to evaluate the jet-pump performance with different area ratios, Nozzle type A and Diffusers Types B & C were modelled, instead of jet-pump type D. The specification of Diffusers B and C are shown in Table 3.8 below.

Table 3. 8 Specification of R141b diffusers B and C

Diffuser	Throat diameter D_t	Suction conical part length (L1)	Constant area length(L2)
B	6.98mm	12.4mm	53.1mm
C	7.5 mm	11.9 mm	53.6 mm

The operating conditions were fixed at T_g =90°C and T_e=8°C, whereas the T_c was varied over a range between 26°C to 37°C. NXP =6mm was used for these different

geometries. Figure 3.34 plots the previous CFD results of the A-D design along with those obtained results for A-B and A-C design in order to show the effect of jet-pump area ratios A_R (A_3/A_t), on performance. From the results it is clear that decreasing the diameter of diffuser decreases R_m and increases T^*_c. It is also clear that the influences of jet-pump area ratio on the performance of jet-pump are similar to that of the primary flow upstream pressure. The effect of reducing diffuser throat diameter is almost similar to the cases of increasing primary flow pressure. It can be seen that decreasing the diffuser diameter by 14%, the R_m decreases by 40%, whereas the T^*_c increases by 20%.

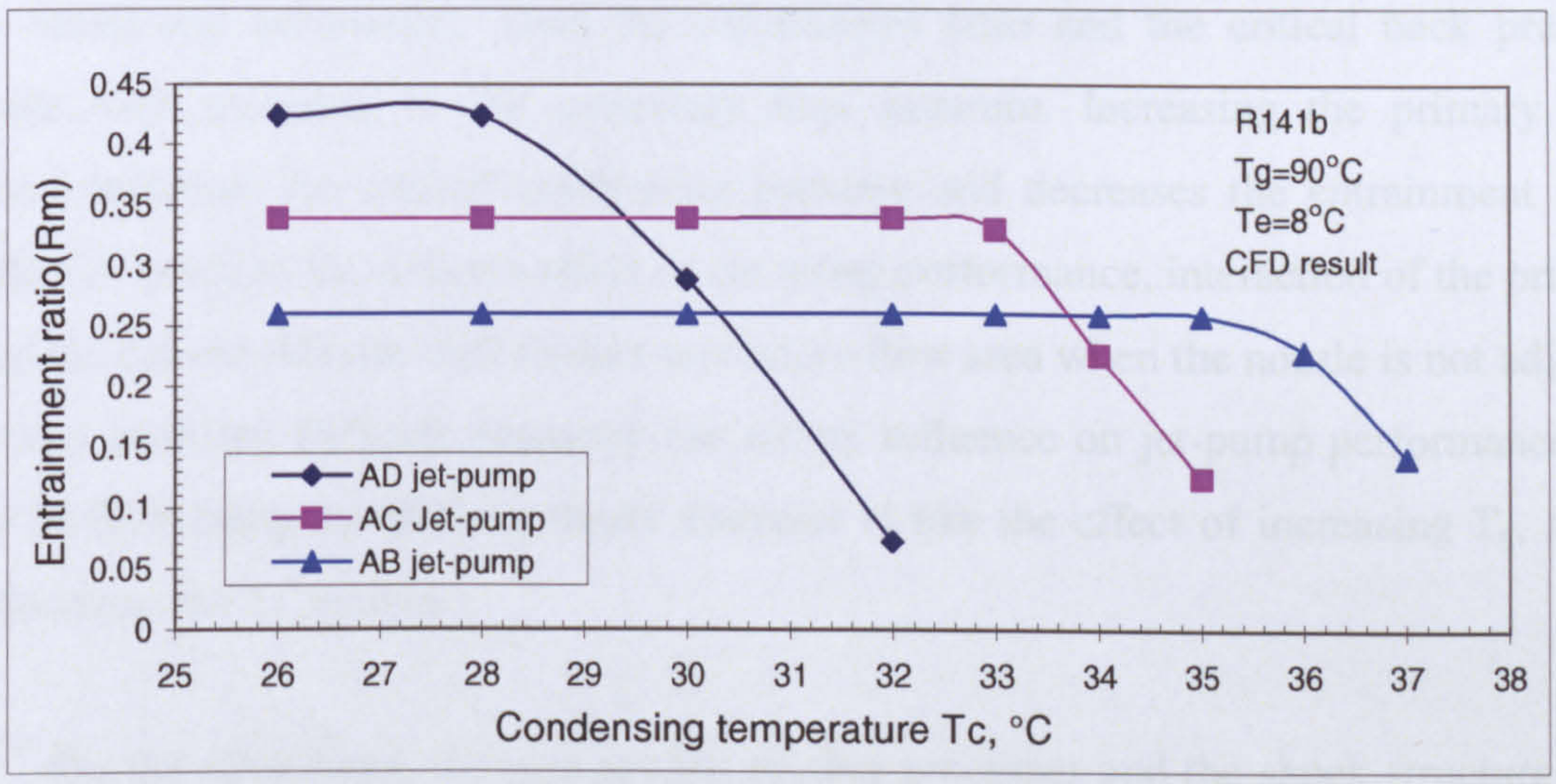

Figure 3. 34 Predicted A_R effect on jet-pump performance (CFD results)

3.6 Conclusions

In this Chapter, the theoretical concept of conventional and CRMC design methods were introduced. Also this chapter provided a full description of Computational study of a flow within supersonic jet-pump.

In order to optimize a CFD code that has ability to correctly simulate jet-pump performance, both independent mesh and turbulent model tests were carried out for two different jet-pump geometries working with two different fluids (Steam and R141b). Independent mesh tests showed that mesh plays an important role in the supersonic jet-pump simulation. It has been shown that the errors can be reduced to a minimum with optimal mesh aspect ratio and with good choice of near wall model. Different types of k-ε turbulent models can provide close results, and it was found that the standard K-Є model

provide results in good agreement with experimental results for R141b jet-pump whereas realizable K-Є model is more appropriate to steam jet-pump simulation. From the modelling results it was found that the flow behaviour in terms of flow velocity, entrainment ratio and critical condenser pressure agree reasonably well with data provided by Eames et al (1999b) and Huang et al (2001), the percentage of error was found between 3% to 8%. Detailed operational studies were performed to understand the influence of most important parameters that affect the jet-pump performance. Parameters such as generator, condenser, and evaporator temperatures were implemented in this modelling beside the nozzle exit position. The jet-pump performance was found to be dependent mainly on all afore mentioned parameters. Both the entrainment ratio and the critical back pressure increase with increases in the secondary flow pressure. Increasing the primary flow pressure increases the critical condensing pressure and decreases the entrainment ratio. Nozzle exit position has a direct effect on jet-pump performance, interaction of the primary jet and the curved diffuser wall restrict secondary flow area when the nozzle is not adjusted in correct position. Diffuser geometry has strong influence on jet-pump performance, the effect of decreasing the diffuser throat diameter is like the effect of increasing T_g, as R_m will decrease but T_c^* increase.

On the other hand, the primary jet, mixing processes and the shock structure have been identified clearly from the clear visualisation of the flow phenomena within the simulated jet-pumps. The shock intensity and its position also were identified with different operation conditions. Strain rate contours showed clearly the shear layer within the mixing section and show also the embedded shock structure within the supersonic jet.

However, the cross comparison presented in this work proves that the CFD commercial code is reliable and delivers the expected performance in terms of accuracy and convergence and it can be used widely for verification and understanding of jet-pump as well as to provide optimum jet-pump design data for the system. Thus in this investigation the realized CFD code was used to optimise different jet-pump "*Conventional and CRMC*" with two different refrigerants which are R236fa and R245fa, to achieve maximum performance. The optimised jet-pump specifications and CFD results are shown in the next Chapter.

Chapter 4

Conventional and CRMC Jet-pump Design with CFD Optimization

4. Conventional and CRMC Jet-pump Design with CFD Optimization

4.1 Introduction

This chapter presents the theoretical design and the CFD simulation that were conducted to improve the jet-pump performance. From previous CFD results with experimental validation of the predicted jet-pump performance as illustrated in the performance curves in Chapter 3, it can fairly be said that the CFD method is an efficient tool for simulating highly-compressible, turbulent flow conditions. Therefore, CFD can play a vital role in the pre-development phase of jet-pump design by determining some optimization of geometrical parameters which will result in the greatest efficiency. Thus, optimization in this Chapter means that is the field of using CFD to find improved or optimum designs for jet-pumps. A prior step that was taken is the initial theoretical design for both conventional and CRMC jet-pumps at given operating conditions, first with using R236fa as the working fluid and second with using R245fa as the working fluid. Then CFD was implemented to find out the prediction of designed jet-pump performance at design operating conditions. From the initial CFD prediction, an attempt to determine the optimal diffuser geometries that enhance the system performance "entrainment ratio" and keeping the critical condenser temperature as designed were carried out and presented. Optimized jet-pumps with higher performance were selected to be manufactured and investigated experimentally and they were simulated over different range of operating conditions to establish their design characteristics map and to produce recommendations for optimum operating mode with respect of environment conditions. The specifications of all selected jet-pumps are provided in this Chapter.

Note, each jet-pump is named based on the fluid and design method that were used.

4.2 Using R236fa as the working fluid

The design operating conditions used for designing R236fa jet-pumps are shown in Table 4.1.

Table 4. 1R236fa Jet-pump design operating conditions

Generator temperature, T_g=85°C	Generating pressure, P_g =14bar
Evaporator temperature, T_e=8°C	Evaporator pressure, P_e =1.48 bar
Critical condenser temperature T^*_c=30°C	Condensing pressure, P_c =3.21 bar
Entrainment ratio R_m =0.4	Cooling capacity, Q_e =1.5kw

4.2.1 R236fa Conventional Jet-pump

A Computer programme was developed based on a 1-D theory presented by Huang et al (1999) and it was used to design the jet-pump with using the above operating conditions. In order to get characteristic figures of variation in the jet-pump performance with critical condensing temperature (T_C^*) at different entrainment ratio, a range of R_m between 0.1 to 0.55 steps of 0.05 and evaporator temperature of 8°C were used in the computer programme. The computer programme results are shown in Figure 4.1.

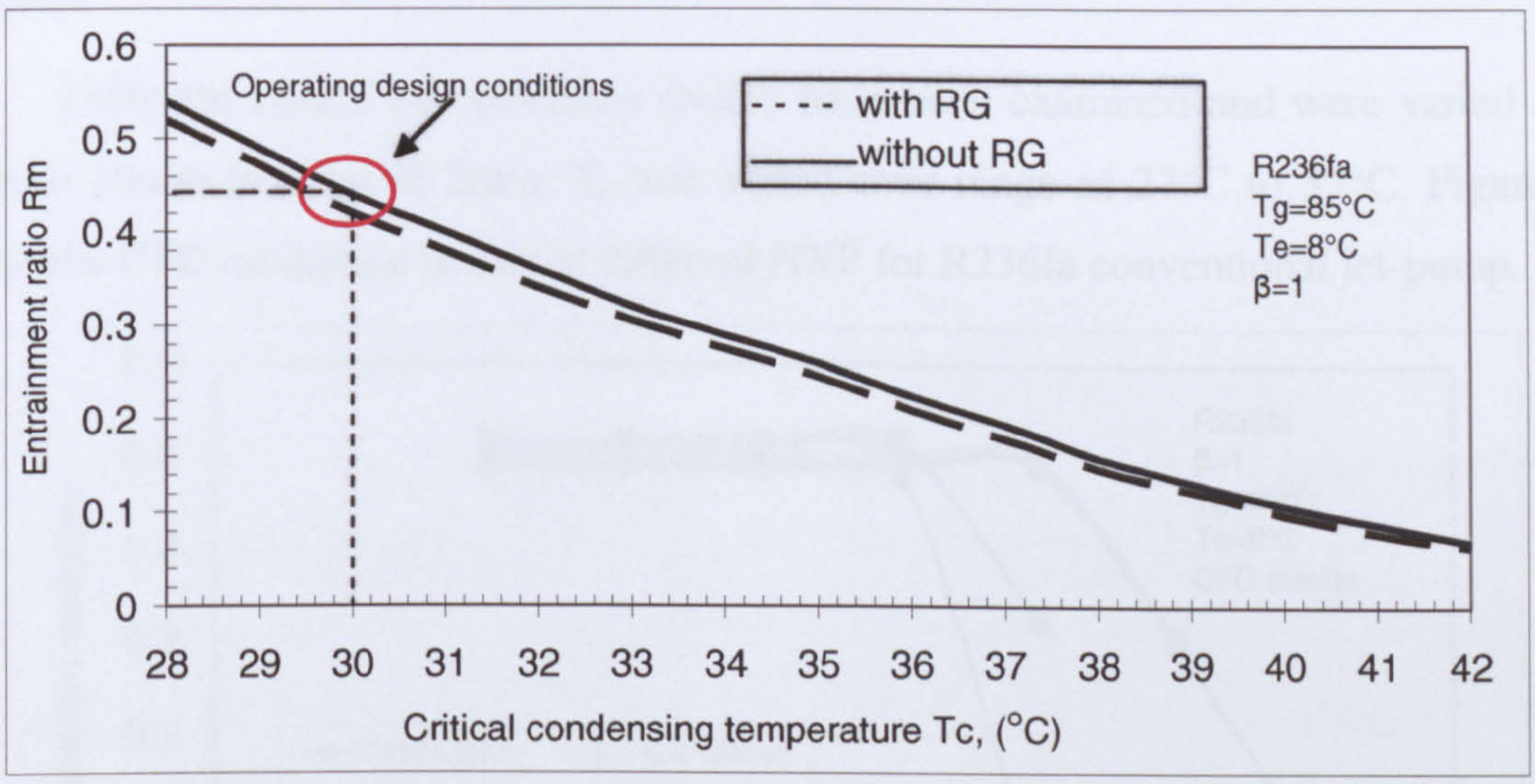

Figure 4. 1 Theoretical R236fa conventional jet-pump performance

The diffuser and nozzle geometries at design operating conditions (T_c*=30°C& R_m =0.43) were selected to be simulated by CFD and constructed for experimental investigation, their dimensions are shown in Figures 4.2 and 4.3 respectively.

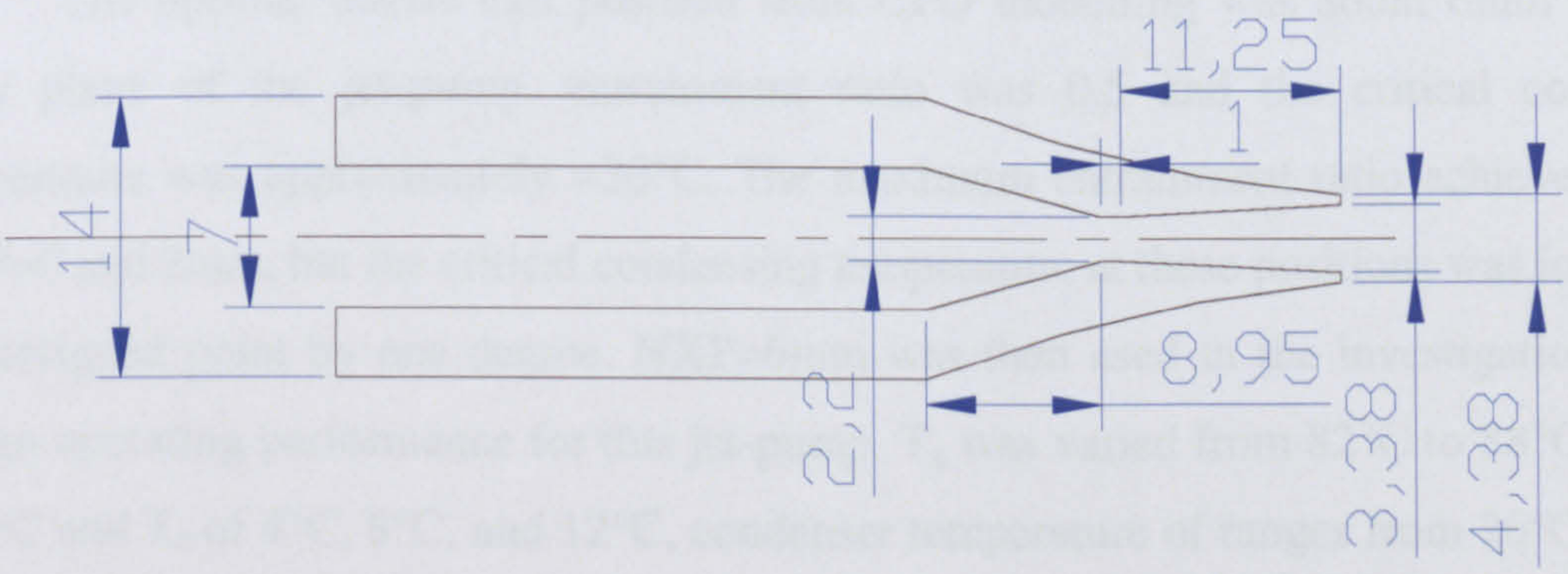

Figure 4. 2 R236fa primary nozzle dimensions (mm)

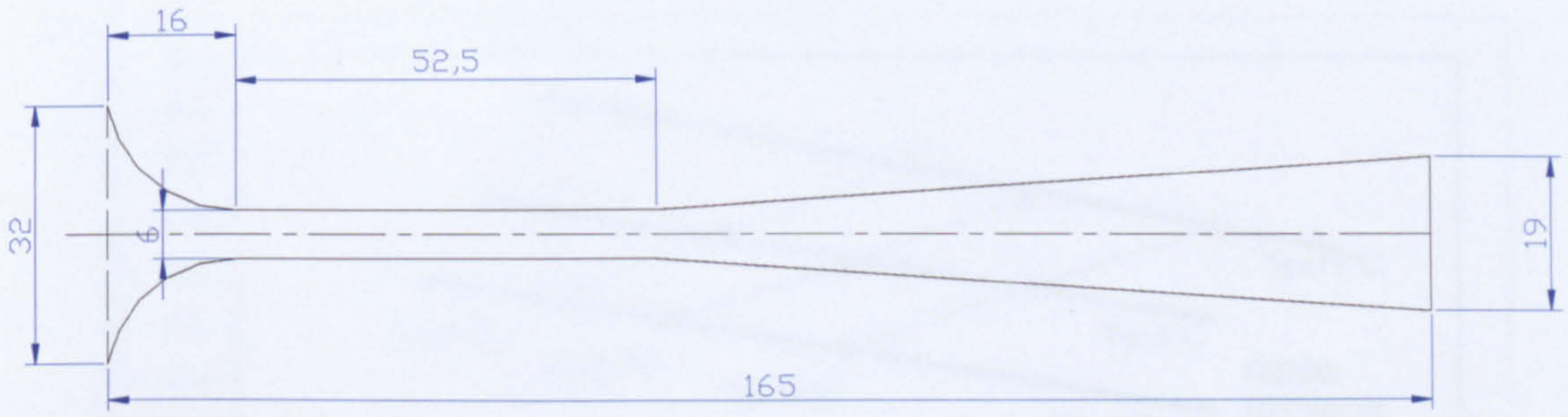

Figure 4. 3 R236fa Conventional Diffuser dimensions (mm)

4.2.1.1 R236fa Conventional Jet-pump CFD Simulation "design and off-design operating conditions"

Different nozzle exit positions (NXP) have been examined and were varied from 0mm to 10mm in steps of 2mm. T_c was varied over range of 27°C to 32°C. Figure 4.4 shows the CFD modelling results at different NXP for R236fa conventional jet-pump.

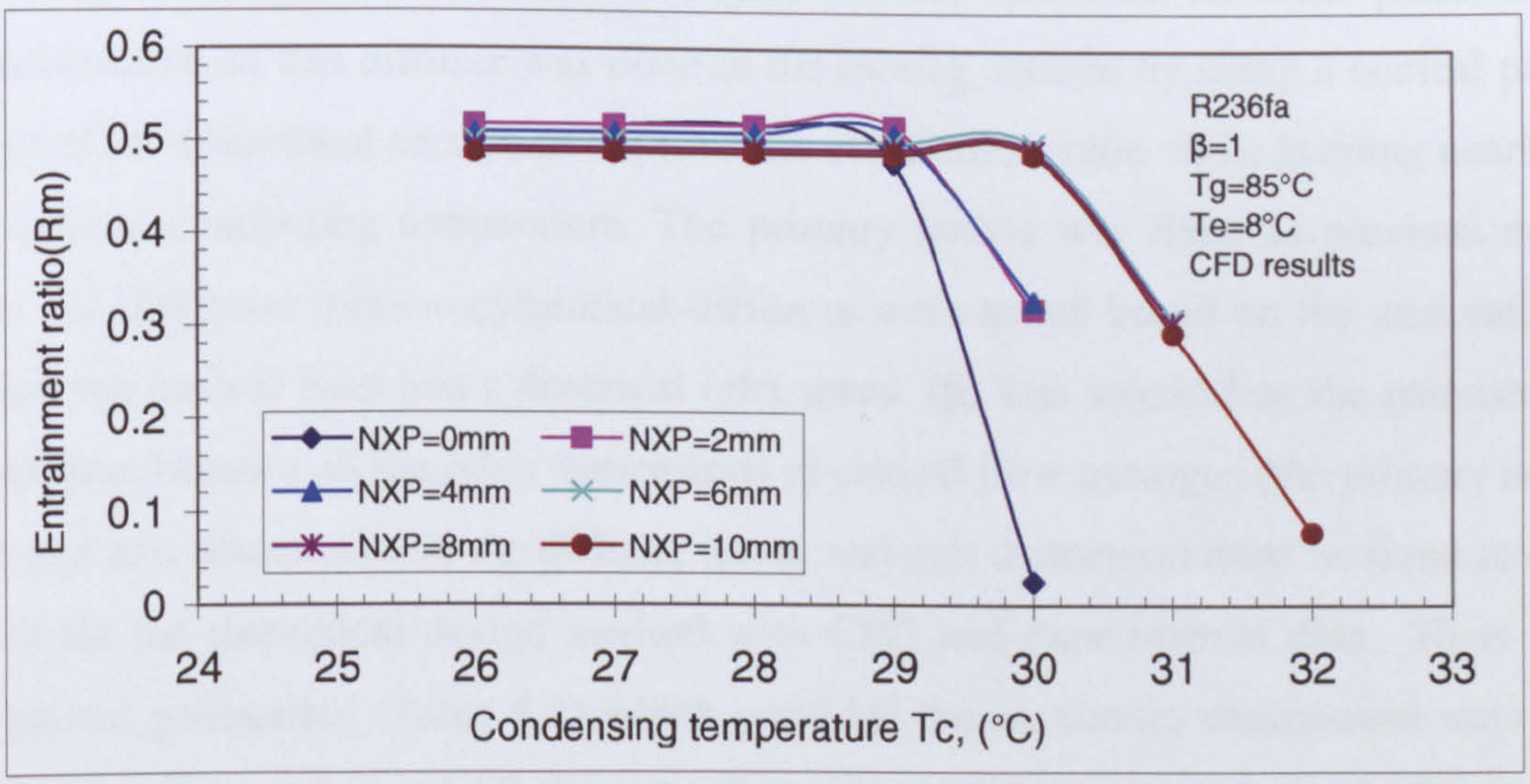

Figure 4. 4 R236fa conventional jet-pump performance (CFD results)

The optimal nozzle exit position from CFD modelling was about 6mm from the entry plane of the jet-pump, entrainment ratio was 0.5 and the critical condensing temperature was approximately =30°C. The maximum entrainment ratio achieved was at NXP=0 and 2mm, but the critical condensing temperature at these positions was lower than the designed point by one degree. NXP=6mm was then used in the investigation of off-design operating performance for this jet-pump. T_g was varied from 82°C to 88°C in steps of 3°C and T_e of 4°C, 8°C, and 12°C, condenser temperature of ranges from 26°C to 32°C in steps of 1°C was used in the modelling. Figure 4.5 shows the constructed operating design map for R236fa conventional jet-pump based on CFD predicted results.

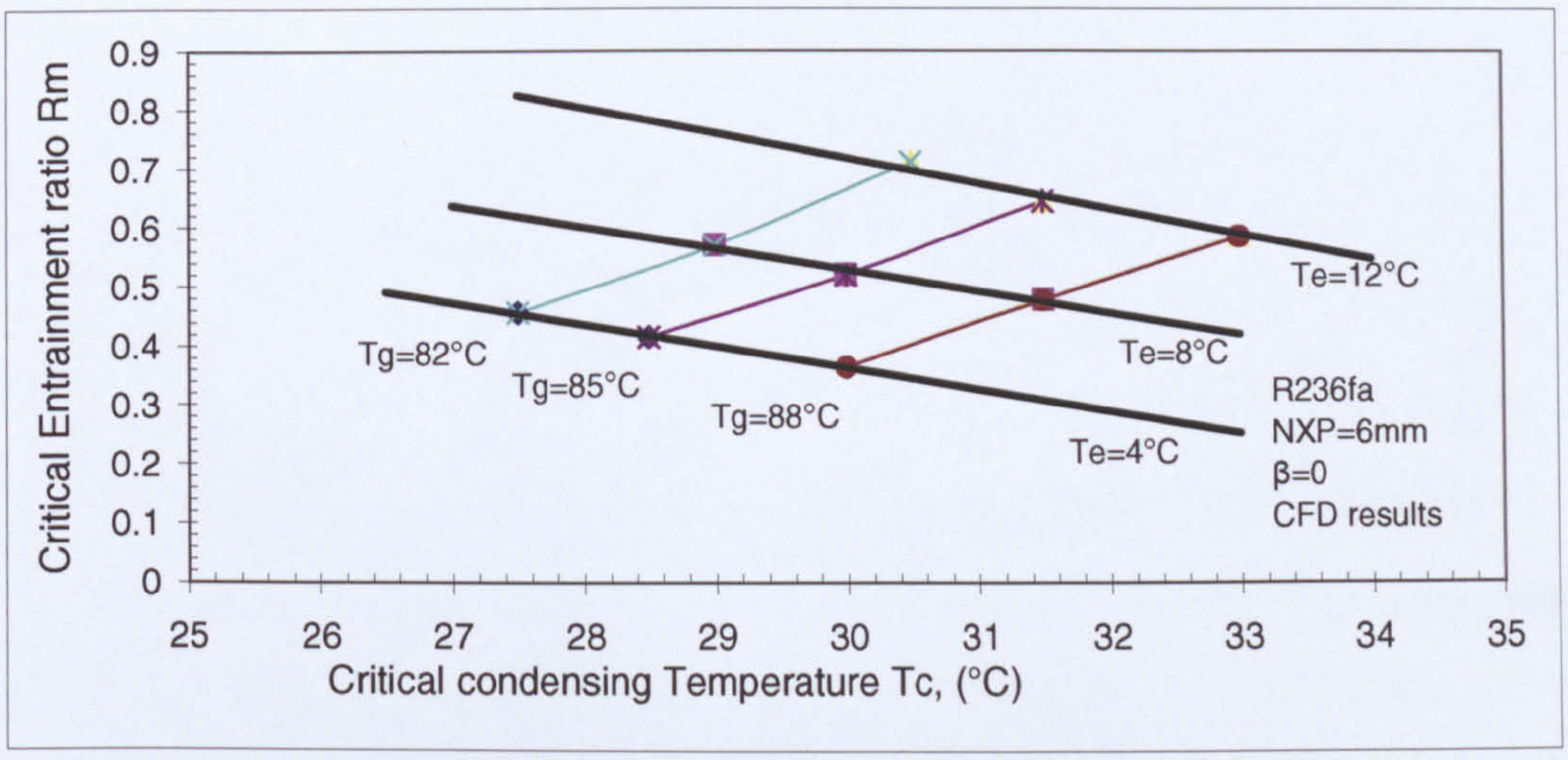

Figure 4. 5 R236fa conventional jet-pump operating design map (CFD results)

4.2.2 CFD Optimised R236fa Conventional Jet-pump

The same previous diffuser as shown in Figure 4.3 was optimised for better performance; the optimisation of this diffuser was done in the mixing section by using a conical profile in front of the cylindrical section to improve the entrainment ratio while keeping nearly the same critical condensing temperature. The primary nozzle was fixed as previous nozzle Figure 4.2. Different conical-cylindrical diffusers were tested based on the area ratio (β) between the conical inlet and cylindrical inlet areas. (β) was selected as the parameter of optimization because all the other dimensions of critical flow passages (the primary nozzle throat and exit diameters and the diffuser throat and exit diameters) must be fixed in order to evaluate the theoretical design method with CFD and experimental data.. There were two optimal geometries (Table 4.2) which provided the maximum entrainment ratio with designed T_c^*. Figures 4.6 and 4.7 show the dimensions of these two optimized diffusers.

Table 4. 2 The specification of two optimized R236fa conventional diffusers

Area Ratio (β)	Conical Radius	Cylindrical Radius	Slope angle	Conical profile length
1.2	3.3mm	3mm	1°	17.2mm
1.36	3.5mm	3mm	1°	28.6mm

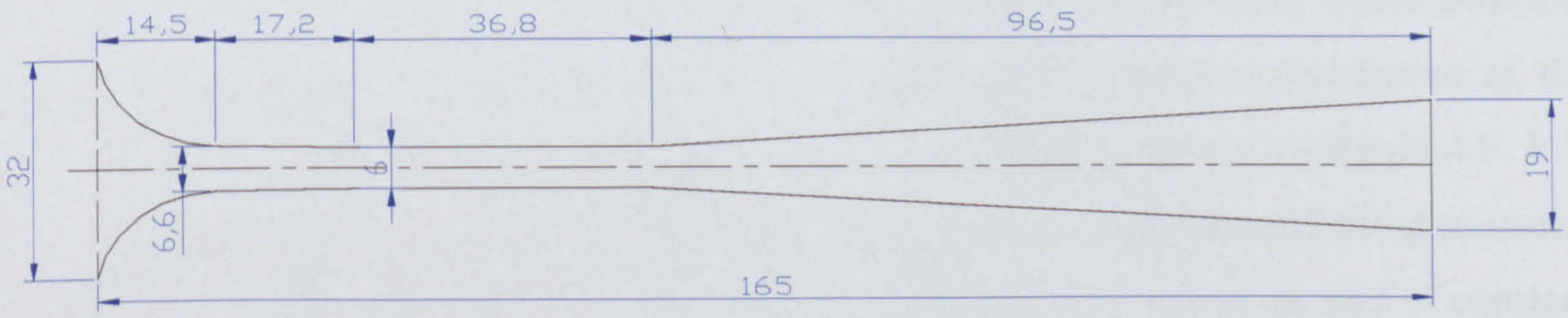

Figure 4. 6 R236fa conventional diffuser with area ratio (β) = 1.2, dimensions (mm)

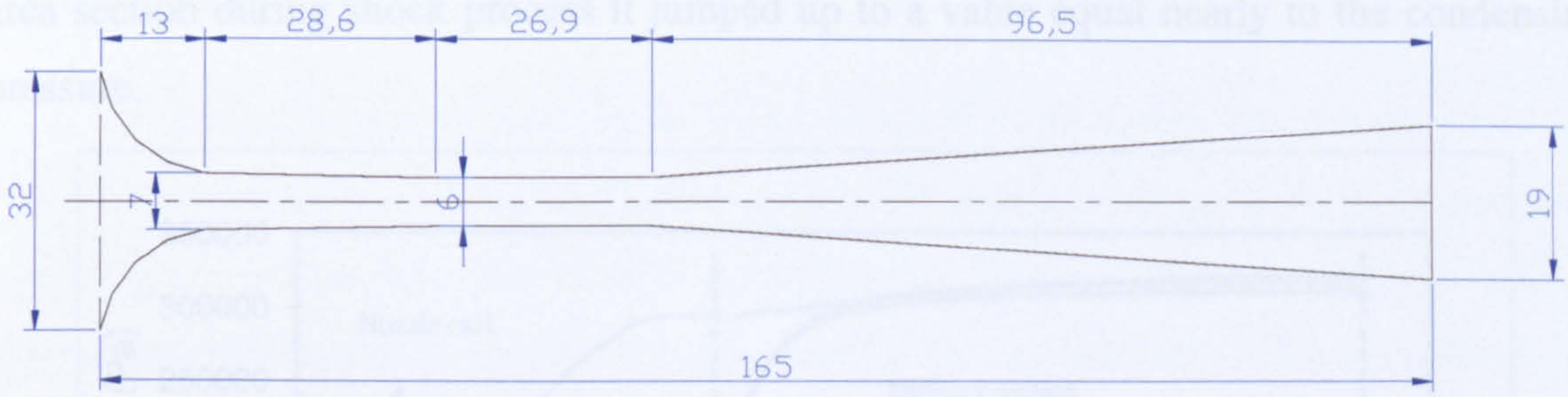

Figure 4. 7 R236fa conventional diffuser with area ratio (β) = 1.36, dimensions (mm)

Different nozzle positions were examined at the same design operating conditions. The obtained CFD results of optimal nozzle positions for the two optimised R236fa conventional diffusers are shown in the Figure 4.8. It was found that as the area ratio increased the nozzle must be moved downstream to maintain the designed critical condensing pressure. The optimal NXP for (β) =1.2 was 9mm, whereas for (β) =1.36 was 10mm.

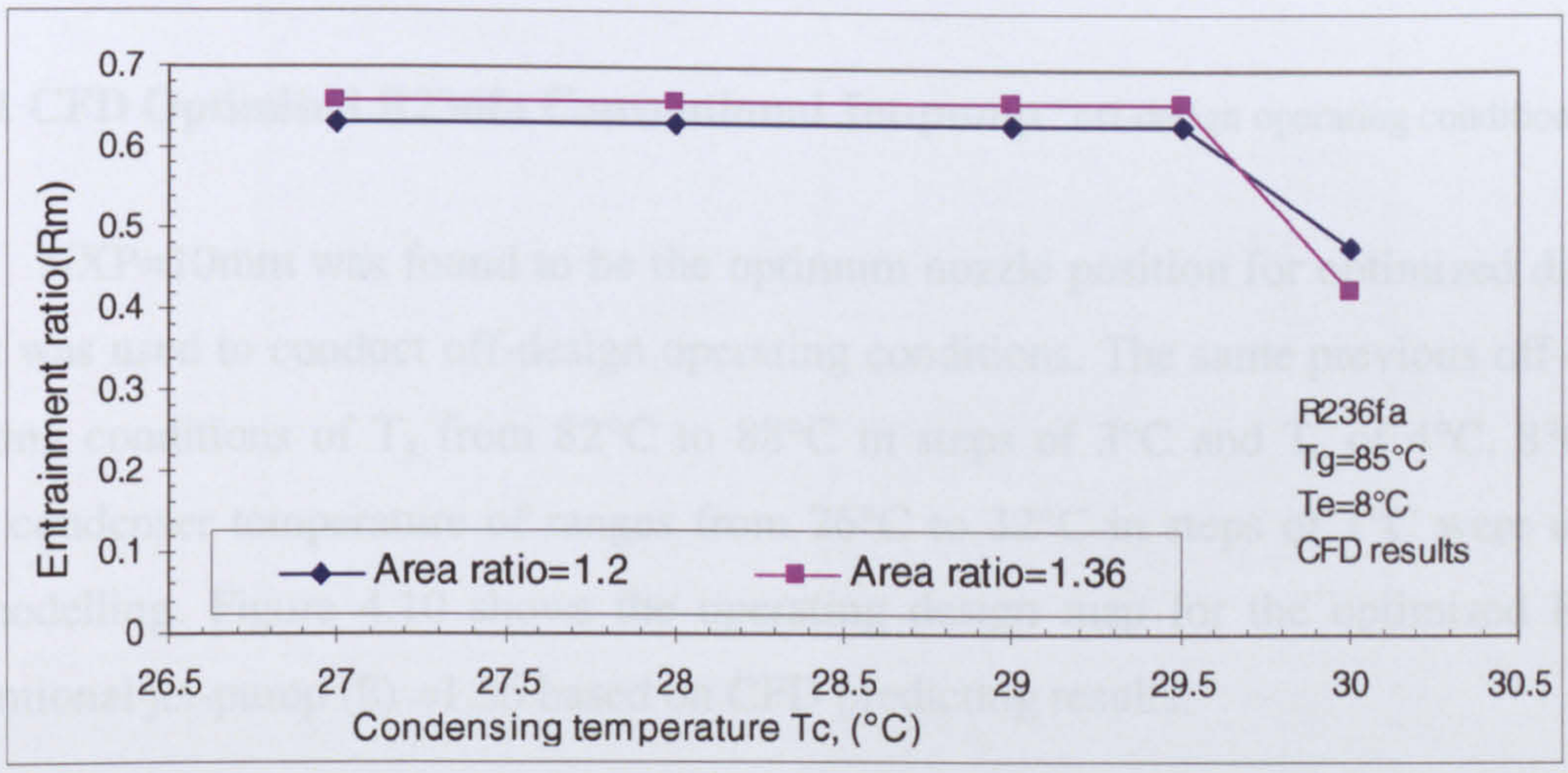

Figure 4. 8 Optimised R236fa conventional diffusers (CFD results)

From the above Figure, it is clear that the conical diffuser (β) =1.36 provided about 0.655 maximum entrainment ratios with 29.5°C critical condensing temperature and therefore it was selected to be manufactured and tested experimentally at design and off-design operating conditions.

In order to evaluate the internal static pressure profile of the conventional diffusers against that of CRMC diffusers, the static pressure profile along the centreline of the selected R236fa optimised conventional diffuser was plotted as shown in Figure 4.9. It is clear from Figure 4.9 that when the diffuser worked below the critical condensing pressure, the pressure inside the mixing section remained nearly constant and at the end of constant

area section during shock process it jumped up to a value equal nearly to the condensing pressure.

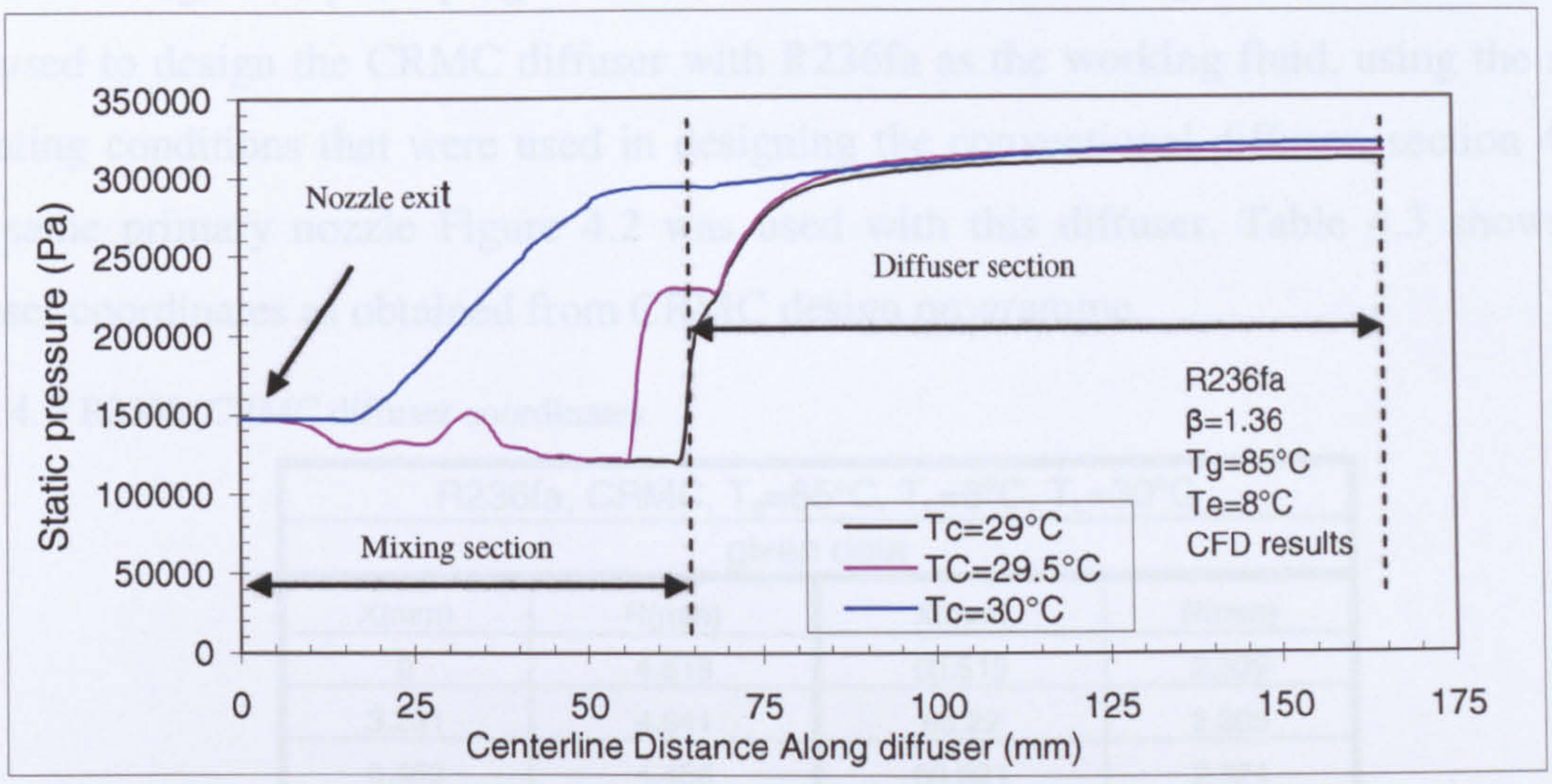

Figure 4. 9 Static pressure profile for R236fa optimized Conventional diffuser (CFD results)

4.2.2.1 CFD Optimised R236fa Conventional Jet-pump "off-design operating conditions"

NXP=10mm was found to be the optimum nozzle position for optimized diffuser, thus it was used to conduct off-design operating conditions. The same previous off-design operating conditions of T_g from 82°C to 88°C in steps of 3°C and T_e of 4°C, 8°C, and 12°C, condenser temperature of ranges from 26°C to 32°C in steps of 1°C were used in this modelling. Figure 4.10 shows the operating design map for the optimized R236fa conventional jet-pump (β) =1.36 based on CFD predicting results.

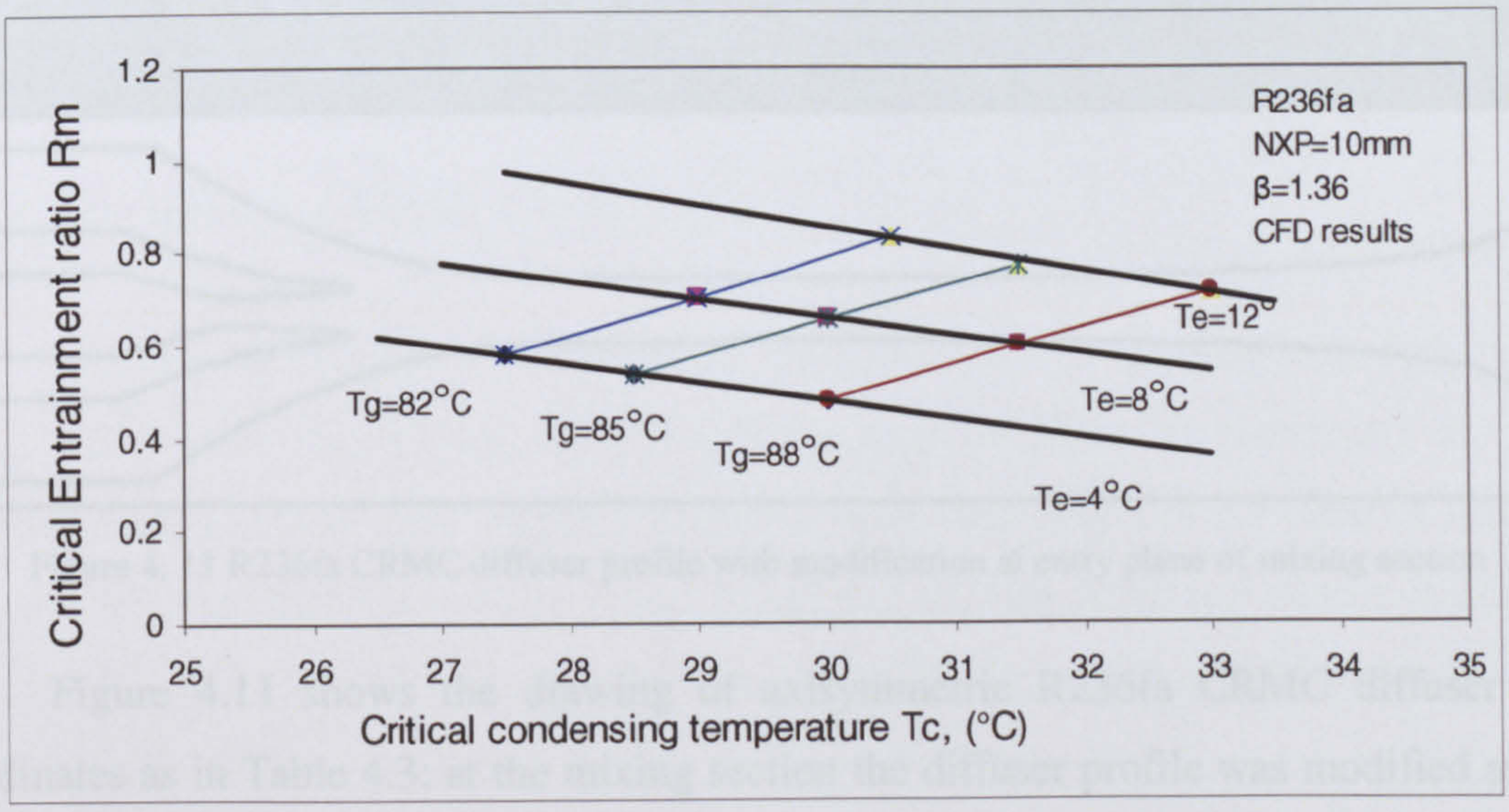

Figure 4. 10 Optimized R236fa conventional jet-pump operating design map (CFD results)

4.2.3 R236fa CRMC Jet-pump

A design computer programme based on the CRMC design method (Section 3.3) was used to design the CRMC diffuser with R236fa as the working fluid, using the same operating conditions that were used in designing the conventional diffuser, section 4.2.1. The same primary nozzle Figure 4.2 was used with this diffuser. Table 4.3 shows the diffuser coordinates as obtained from CRMC design programme.

Table 4. 3 R236fa CRMC diffuser coordinates

R236fa, CRMC, T_g=85°C, T_e=8°C, T_c=30°C			
given data			
X(mm)	R(mm)	X(mm)	R(mm)
0	4.818	60.519	2.309
3.231	4.641	65.22	2.309
6.463	4.456	69.921	2.321
9.694	4.264	74.622	2.345
12.925	4.062	79.323	2.384
16.156	3.85	84.024	2.439
19.388	3.625	88.725	2.514
22.619	3.386	93.425	2.614
25.85	3.128	98.126	2.745
29.081	2.847	102.827	2.919
32.313	2.535	107.528	3.155
37.014	2.47	112.229	3.487
41.715	2.417	116.93	3.987
46.416	2.374	121.631	4.837
51.117	2.342	126.332	6.744
55.818	2.32		

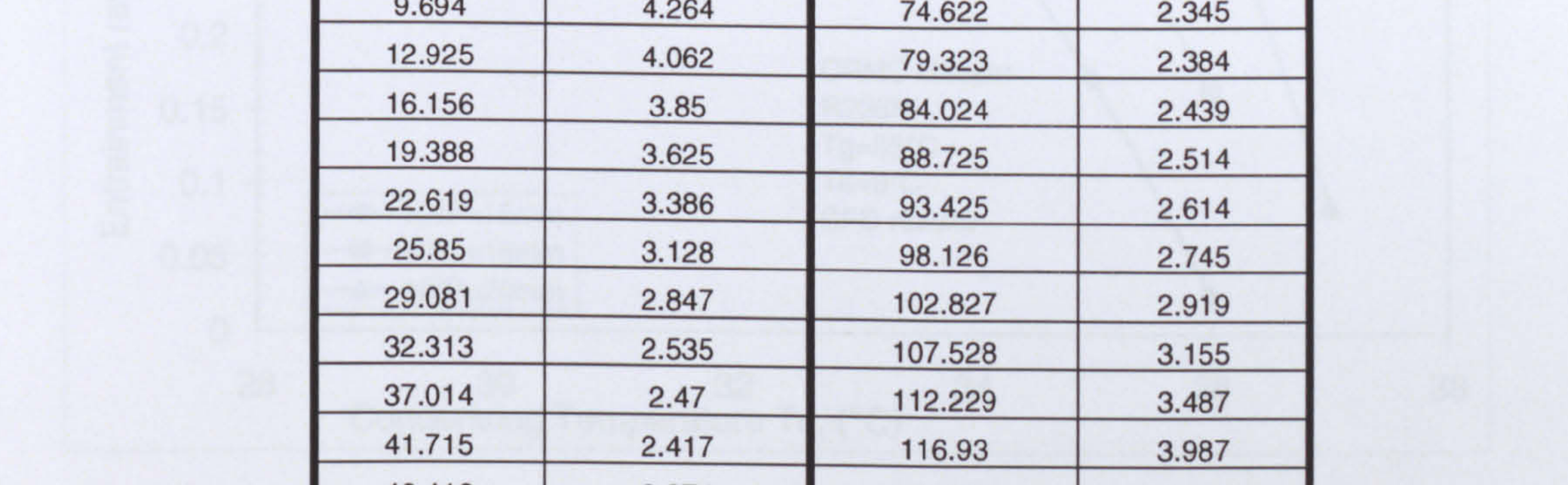

Figure 4. 11 R236fa CRMC diffuser profile with modification at entry plane of mixing section

Figure 4.11 shows the drawing of axisymmetric R236fa CRMC diffuser with coordinates as in Table 4.3; at the mixing section the diffuser profile was modified as it is

clear to take shape of conical profile. This made it easier to position the primary nozzle allowing enough gaps for the secondary flow.

4.2.3.1 R236fa CRMC Diffuser CFD Simulation (design operating conditions)

The CFD simulation was conducted to find out the performance of the theoretically designed R236fa CRMC diffuser and also to find the optimal NXP. The CFD obtained results are shown in Figure 4.12.

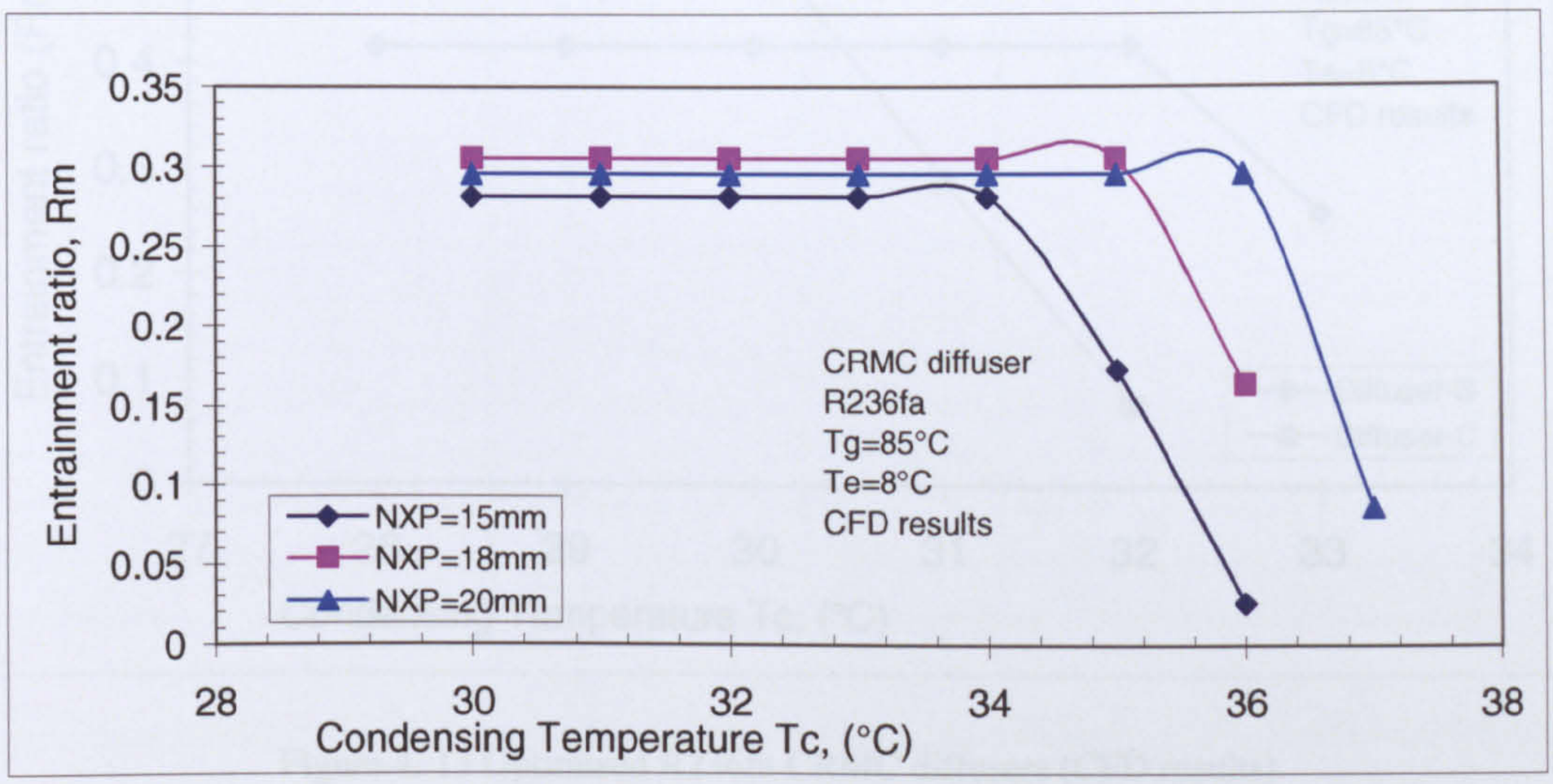

Figure 4. 12 Optimal NXP CRMC-R236fa Jet-pump (CFD results)

From the above Figure, it is clear that the maximum entrainment ratio obtained is 0.30 at NXP=18mm, but the critical condensing temperature was about 35°C to 36°C which was greater than that of designed value. Therefore, this diffuser was modified to achieve better performance with designed critical condensing temperature T_c*=30°C.

4.2.4 CFD Optimized R236fa CRMC Diffuser

In order to increase the R_m for the designed CRMC diffuser with keeping the design Tc* value, the R236fa CRMC diffuser was modified by increasing all cross sectional areas to allow more secondary flow to enter. The length of the diffuser was kept as in the designed diffuser because it was found that the length did not change much with changing R_m. Only the optimal NXP that was obtained from previous CFD simulation with CRMC calculated data was tested with all modified diffusers.

Figure 4.13 shows the CFD results for two optimised R236fa CRMC diffusers (diffusers B and C); from the Figure it is clear that diffuser C (minimum radius *1.2) could provide a maximum entrainment ratio of 0.528 with designed critical condenser temperature of 30°C). Therefore this diffuser was decided to be manufactured and tested experimentally.

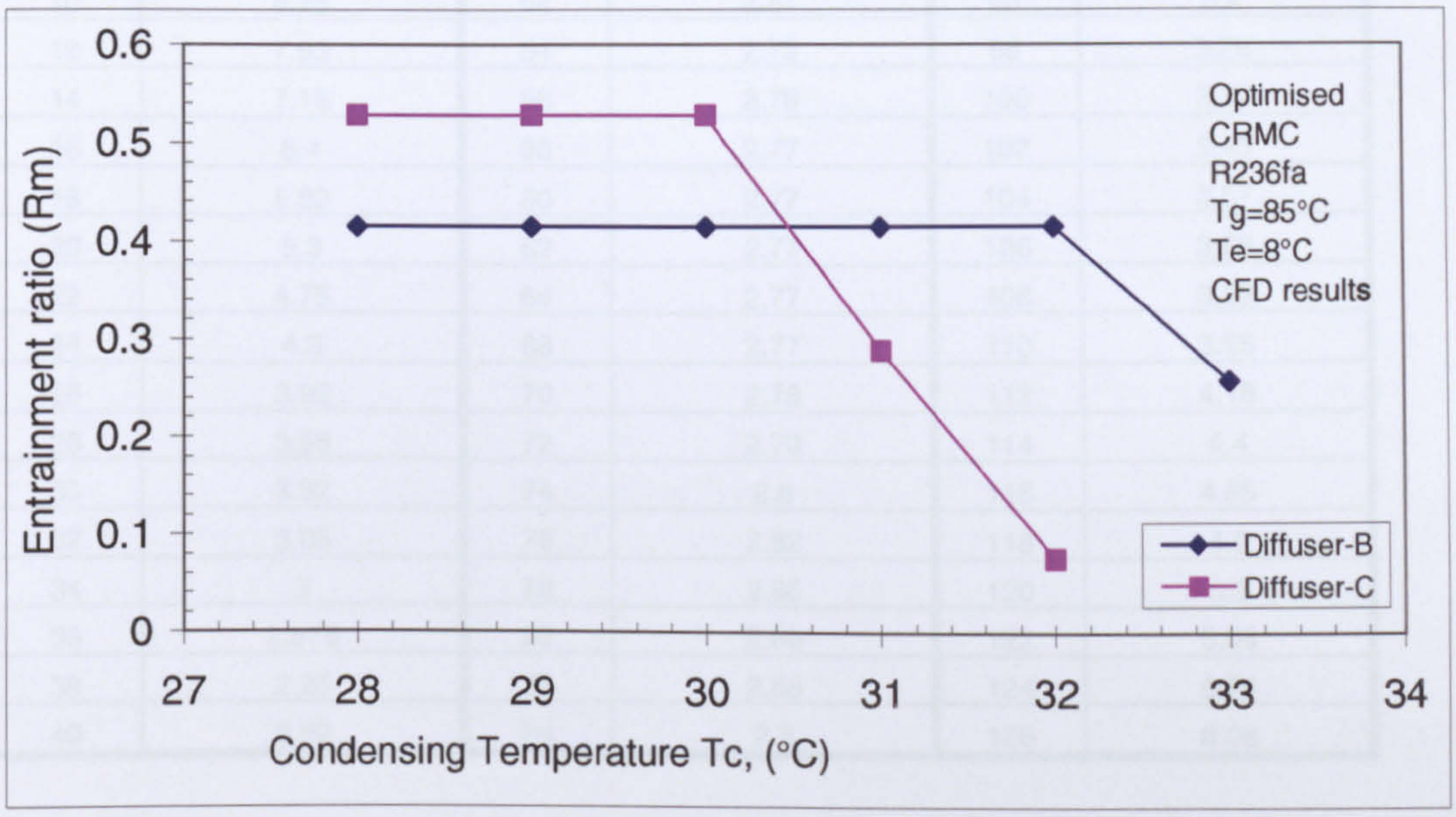

Figure 4. 13 Optimised R236fa CRMC diffusers (CFD results)

The coordinates and the profile of diffuser C are shown in the Table 4.4 and Figure 4.14 respectively.

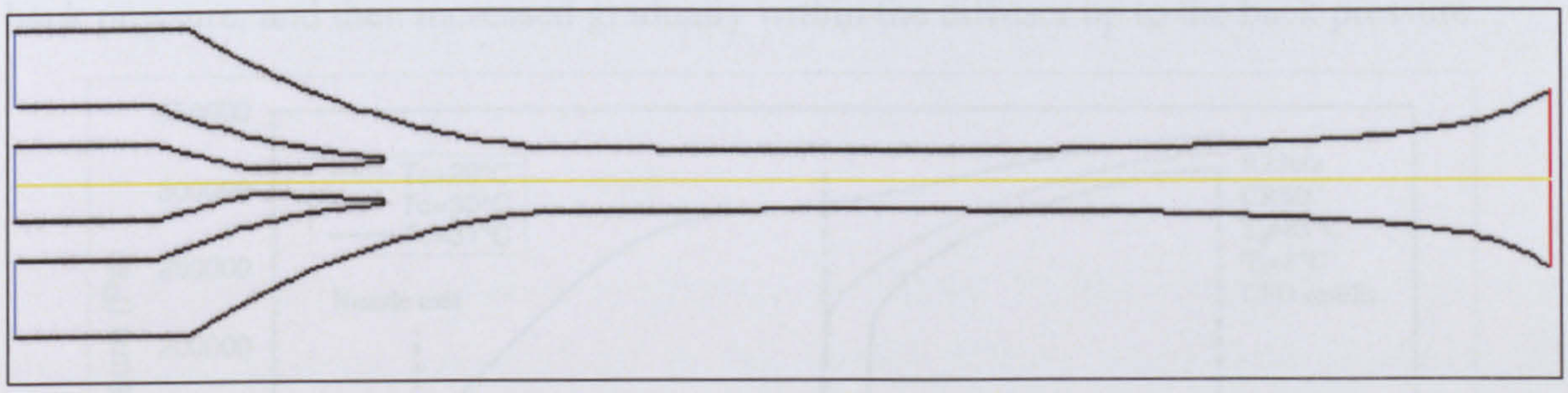

Figure 4. 14 R236fa CRMC Diffuser C NXP=18mm

Table 4. 4 The new coordinator of optimised R236fa CRMC (diffuser C)

Operation conditions (Tg=85°C, Te=8°C, T*c=30°C , Rm=0.48 -0.50)					
X(mm)	New radius (mm)	X(mm)	New radius (mm)	X(mm)	New radius (mm)
0	14	42	2.895	86	2.95
2	12.8	44	2.88	88	2.99
4	11.65	46	2.845	90	3.04
6	10.64	48	2.84	92	3.1
8	9.6	50	2.82	94	3.15
10	8.75	52	2.81	96	3.2
12	7.93	54	2.79	98	3.28
14	7.15	56	2.78	100	3.37
16	6.4	58	2.77	102	3.45
18	5.82	60	2.77	104	3.57
20	5.3	62	2.77	106	3.68
22	4.75	64	2.77	108	3.82
24	4.3	68	2.77	110	3.95
26	3.92	70	2.78	112	4.18
28	3.58	72	2.79	114	4.4
30	3.32	74	2.8	116	4.65
32	3.08	76	2.82	118	4.9
34	3	78	2.85	120	5.3
36	2.975	80	2.86	122	5.95
38	2.95	82	2.88	124	6.75
40	2.92	84	2.9	126	8.08

The static pressure profile along the diffuser centreline, Figure 4.15, shows that the static pressure remained nearly constant in the mixing section when the jet-pump operated below its critical condensing temperature value. The pressure jump (shock system) at the end of constant area section could not be avoided with this design, but it is considered lower than that of conventional design. It jumped to pressure value approximately half of the diffuser back pressure, and then increased gradually within the diffuser up to the back pressure.

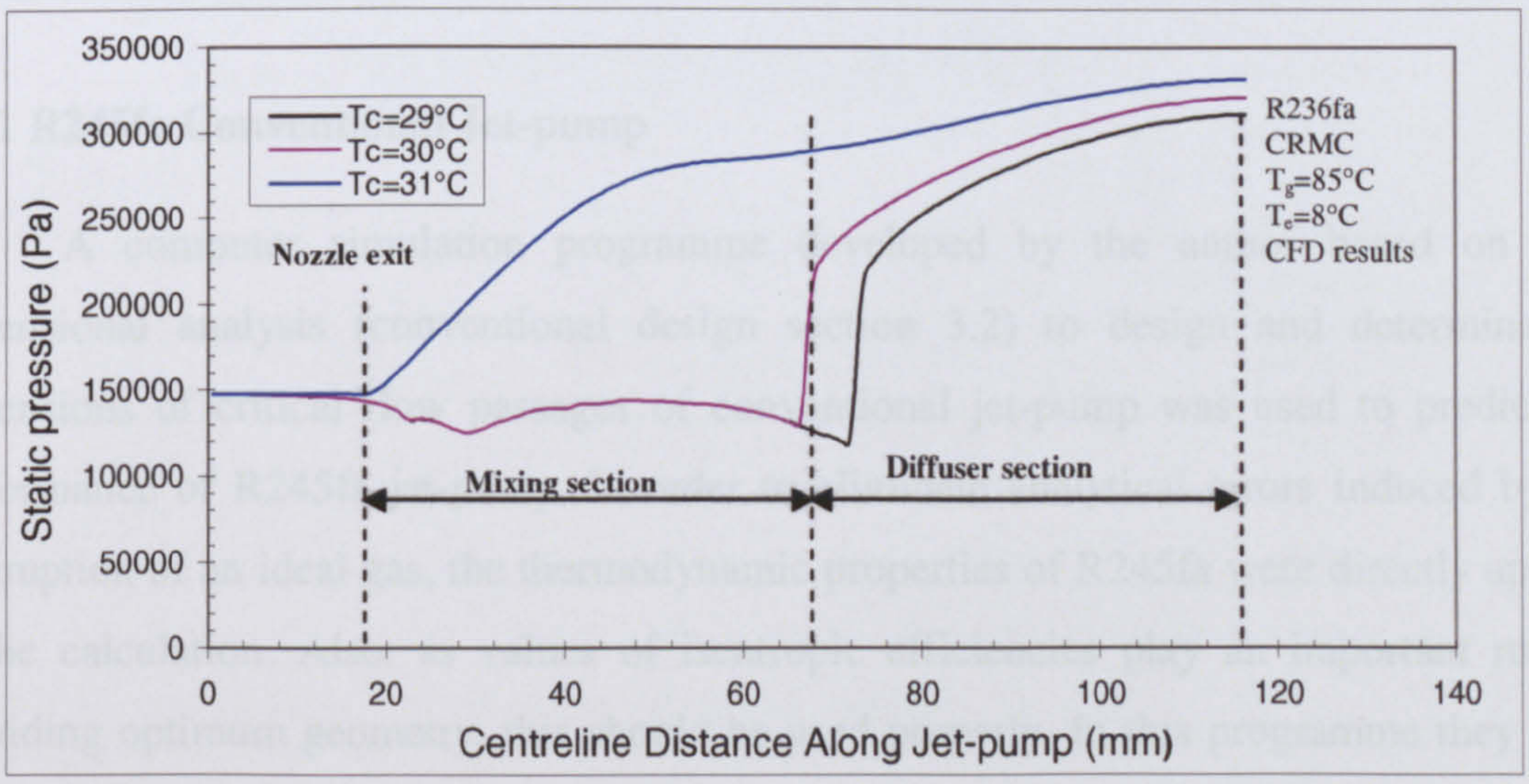

Figure 4. 15 Static pressure profile along centreline, optimized R236fa-CRMC jet-pump (CFD results)

4.2.4.1 CFD Optimized R236fa CRMC Jet-pump "off-design operation"

The same previous off-design conditions were used with this jet-pump. Figure 4.16 shows the operating characteristic of the optimised R236fa CRMC jet-pump.

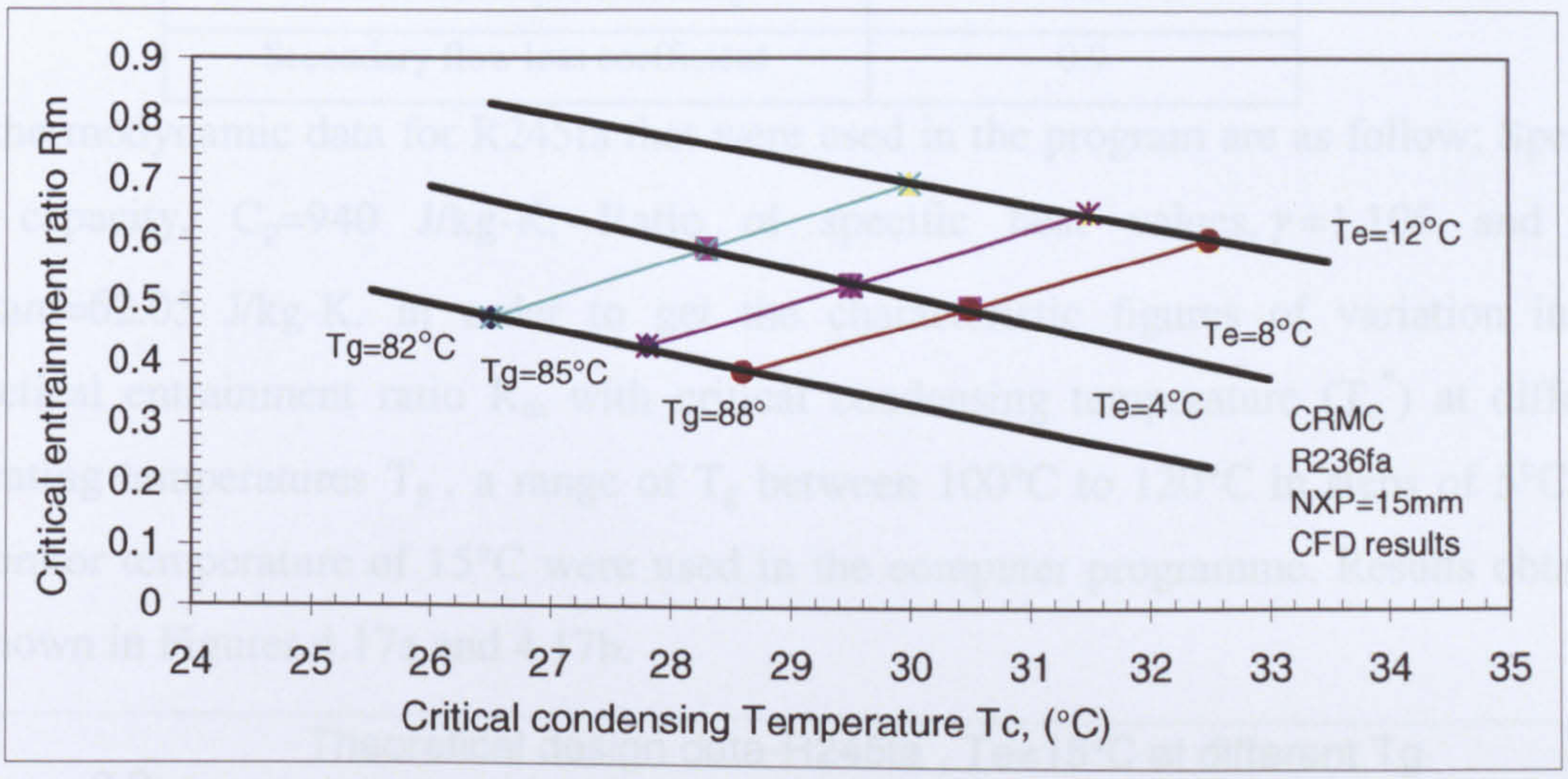

Figure 4. 16 Optimized R236fa CRMC diffuser C design operating map (CFD results)

4.3 Using R245fa as the working fluid

The design operating conditions used for designing R245fa jet-pumps are shown in Table 4.5.

Table 4. 5 R245fa jet-pump design operating condition

Generating temperature, T_g =120°C	Generating pressure, P_g =1921.0 kPa
Evaporating temperature, T_e =15°C	Evaporating pressure, P_e=102.0 kpa
Critical Condensing temperature, T^*_c =46°C	Condensing pressure, P_c =315.05 kPa
Entrainment ratio, R_m=0.3	Cooling capacity, Q_e =2.0 kW

4.3.1 R245fa Conventional Jet-pump

A computer simulation programme developed by the author based on one-dimensional analysis (conventional design section 3.2) to design and determine the dimensions of critical flow passages of conventional jet-pump was used to predict the performance of R245fa jet-pump. In order to eliminate analytical errors induced by the assumption of an ideal gas, the thermodynamic properties of R245fa were directly applied in the calculation. Also, as values of isentropic efficiencies play an important rule in providing optimum geometry, this should be used properly. In this programme they were set a little less than typical values (Table 4.6) that were recommended by ESDU (1985).

Table 4. 6 Coefficient and efficiency used in jet-pump design

Parameter	Value
Nozzle isentropic efficiency	0.85
Momentum loss coefficient	0.9
Diffuser isentropic efficiency	0.8
Secondary flow loss coefficient	0.9

The thermodynamic data for R245fa that were used in the program are as follow; Specific heat capacity, C_p=940 J/kg-K, Ratio of specific heat values, γ=1.106 and Gas constant=62.05 J/kg-K. In order to get the characteristic figures of variation in the theoretical entrainment ratio R_m with critical condensing temperature (T_c^*) at different generating temperatures T_g , a range of T_g between 100°C to 120°C in steps of 5°C and evaporator temperature of 15°C were used in the computer programme. Results obtained are shown in Figures 4.17a and 4.17b.

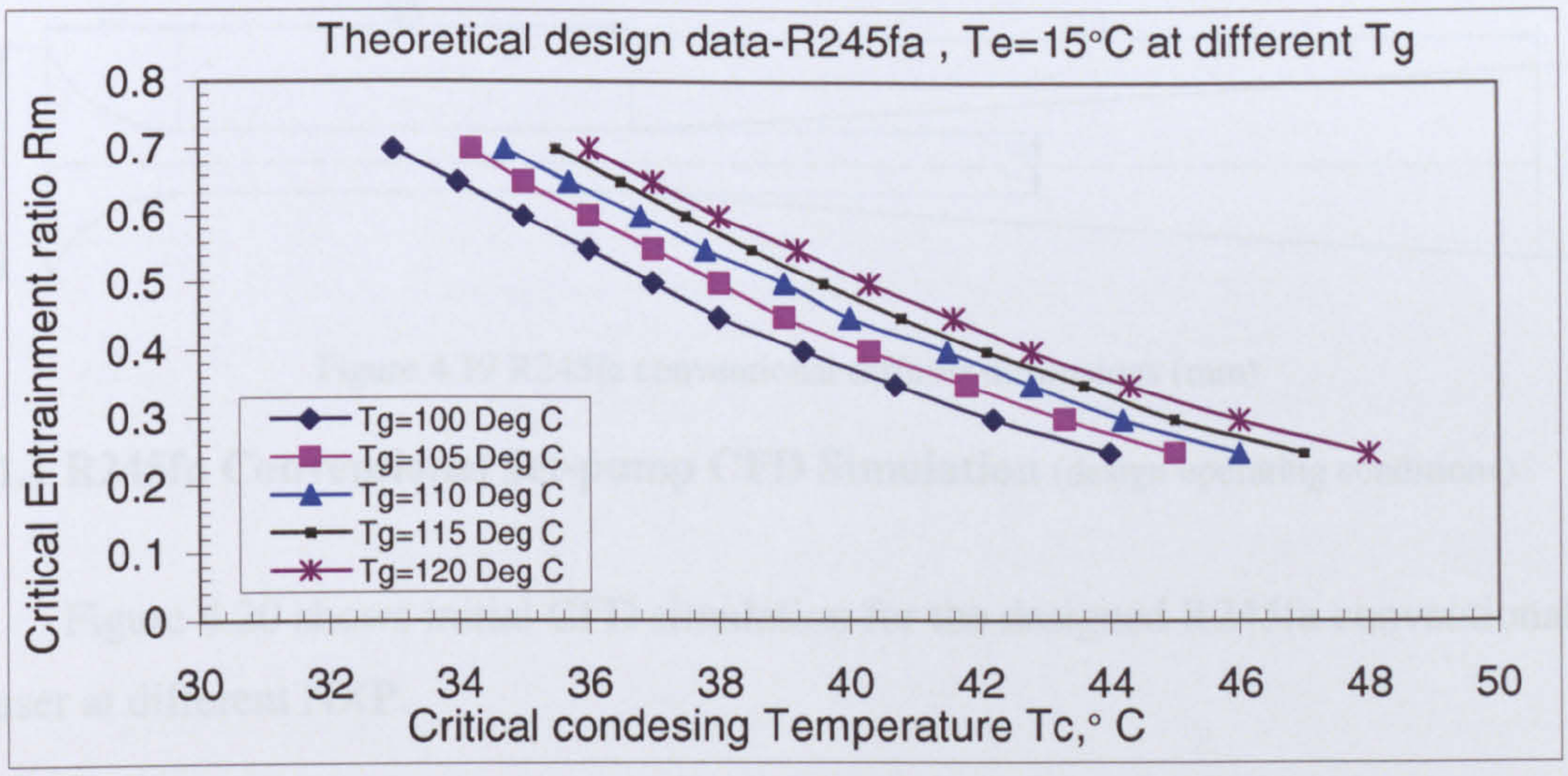

Figure 4. 17a Conventional R245fa jet-pump performance at different T_g

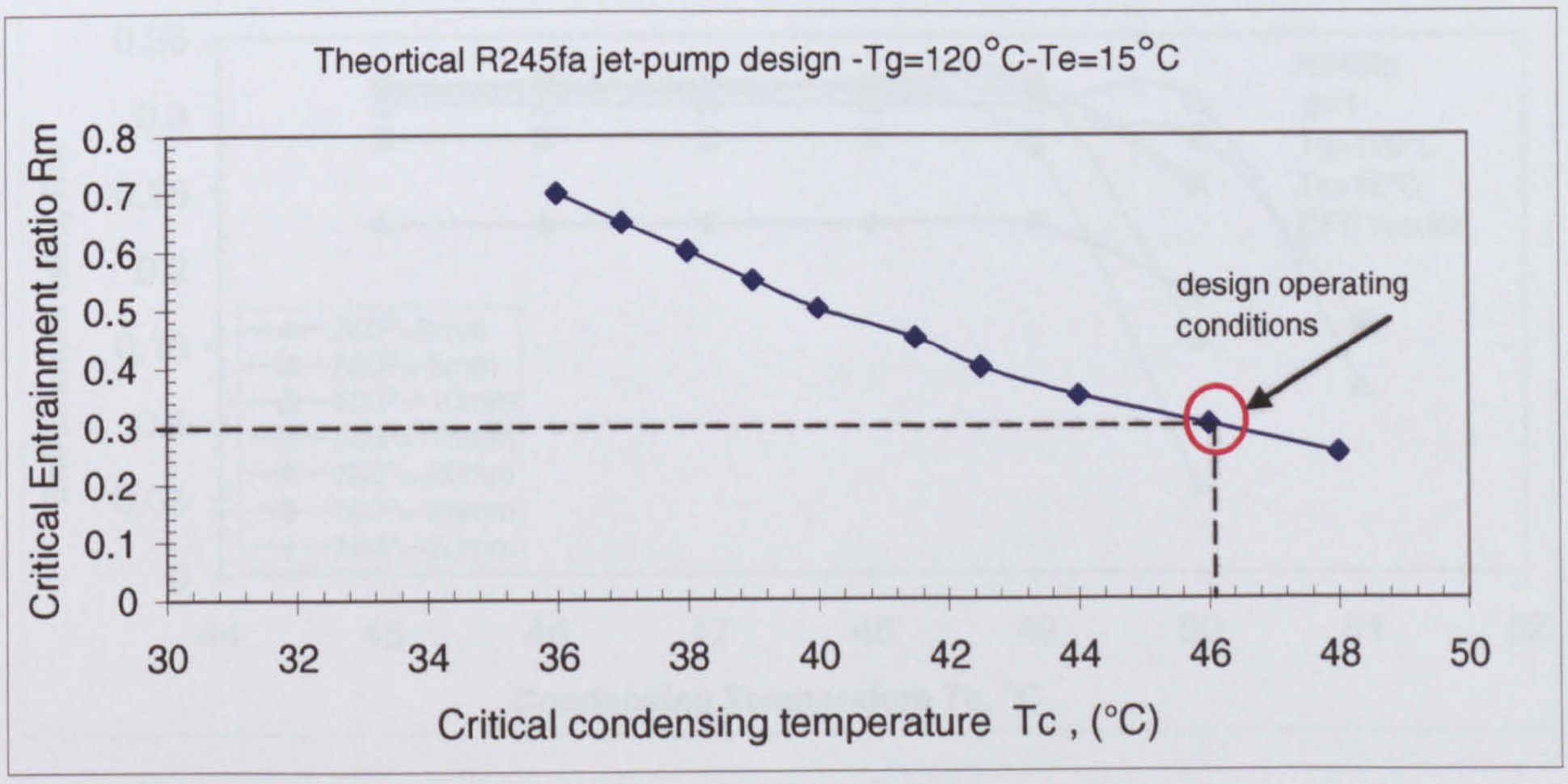

Figure 4. 17b Conventional R245fa jet-pump performance, Tg=120°C

The diffuser and nozzle geometries at design conditions (T_c*=46°C& R_m =0.3) were selected to be simulated by CFD at different operating conditions. The specifications of selected primary nozzle and diffuser are shown in Figures 4.18 and 4.19 respectively.

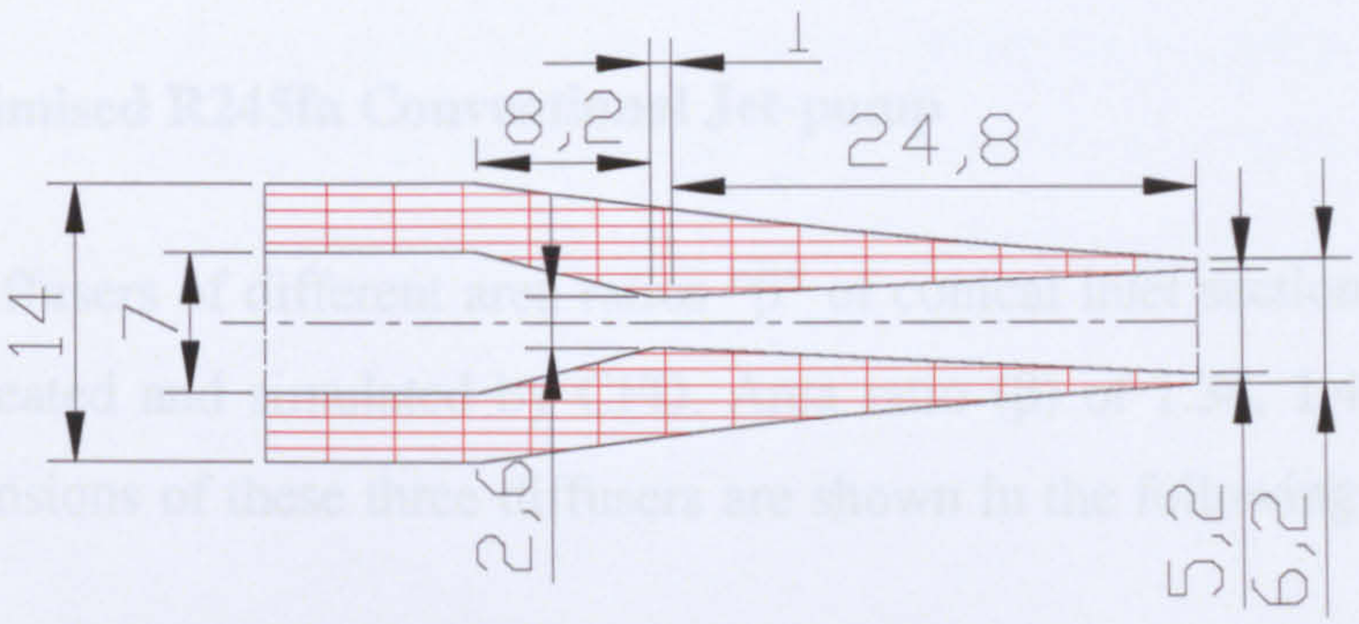

Figure 4. 18 R245fa Primary nozzle dimensions (mm)

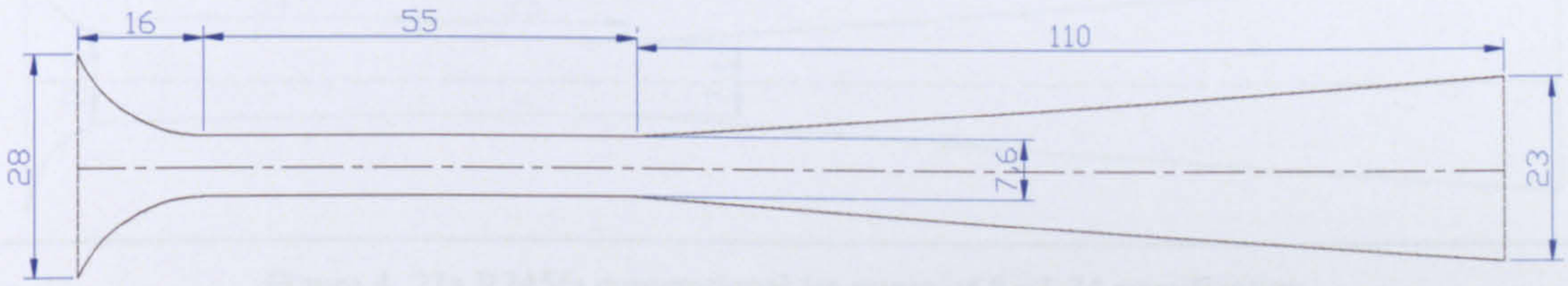

Figure 4.19 R245fa conventional diffuser dimensions (mm)

4.3.1.1 R245fa Conventional Jet-pump CFD Simulation (design operating conditions)

Figure 4.20 shows initial CFD simulation for the designed R245fa conventional diffuser at different NXP.

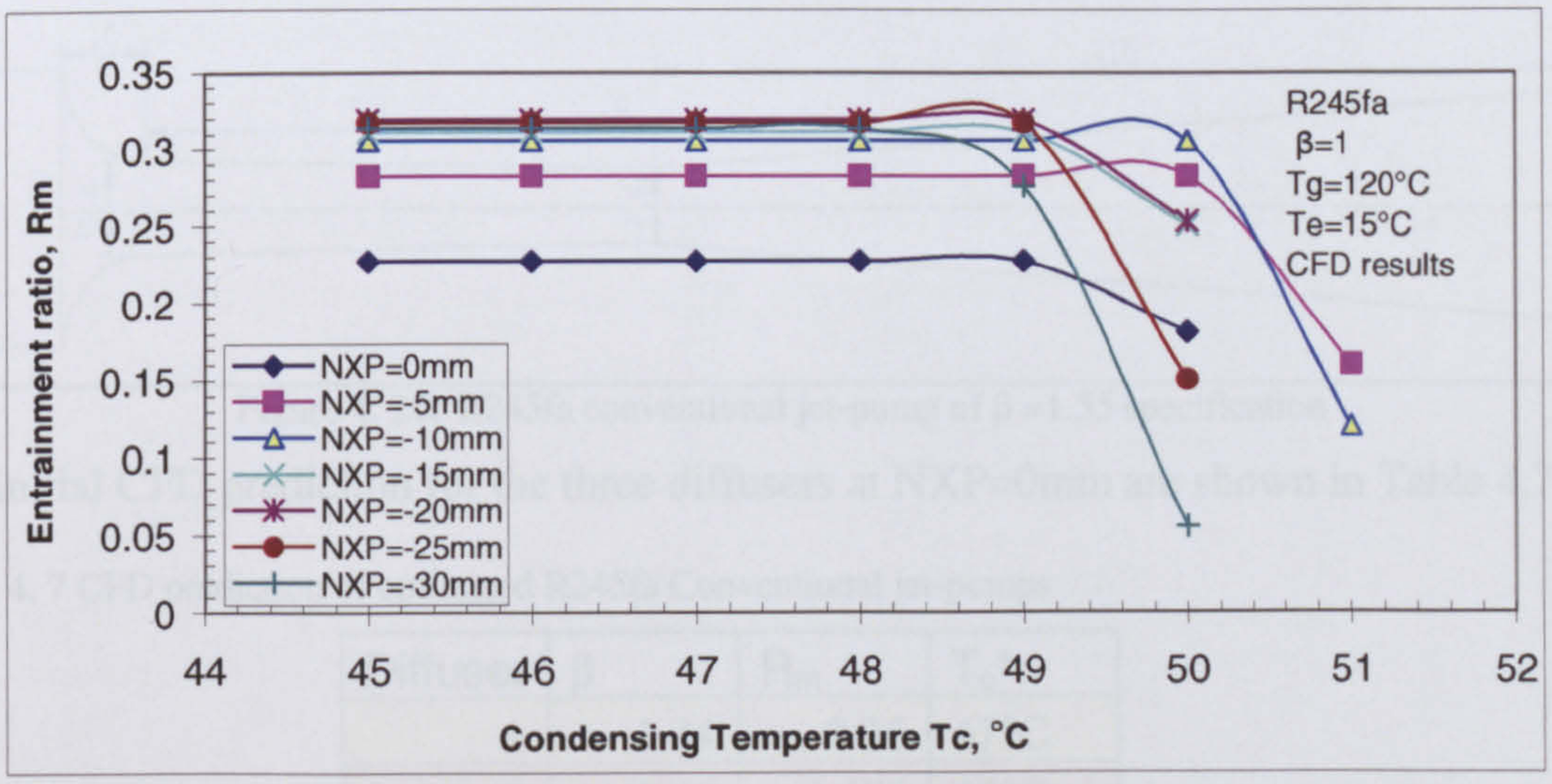

Figure 4. 20 R245fa conventional jet-pump performance (β=1) (CFD results)

From Figure 4.20 it is clear that a conventional jet-pump with β =1 could provide higher T_c^* than theoretically designed conditions, maximum R_m achieved was 0.32. Thus this conventional diffuser was optimised with a different area ratio (β) to obtain better performance at designed value of T_c*.

4.3.2 CFD Optimised R245fa Conventional Jet-pump

Three diffusers of different area ratios "β" of conical inlet section to constant area section were created and simulated by CFD. Area ratio (β) of 1.34, 1.46 and 1.55 were used. The dimensions of these three diffusers are shown in the following Figures 4.21a, b and c.

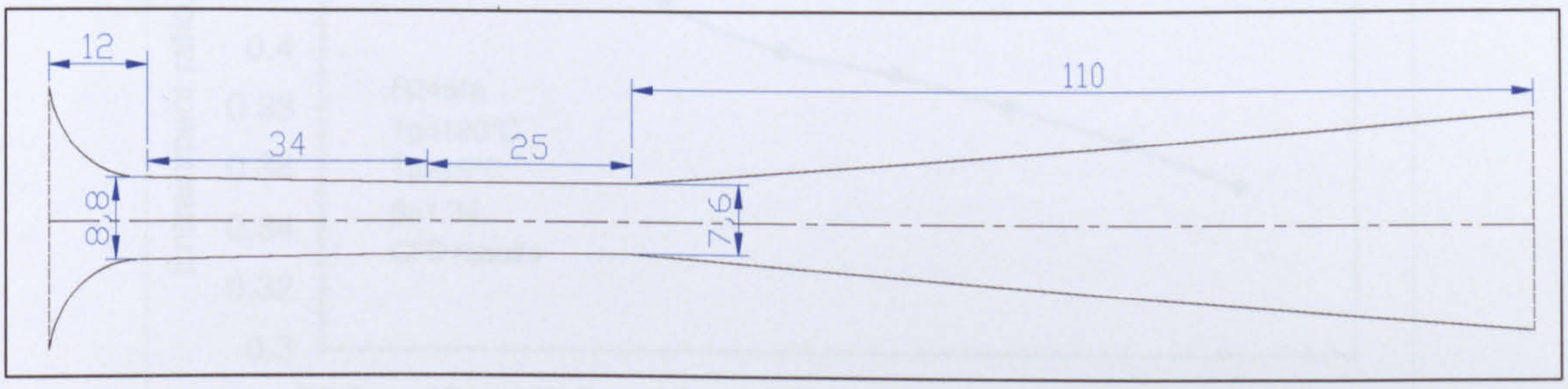

Figure 4. 21a R245fa conventional jet-pump of β =1.34 specification

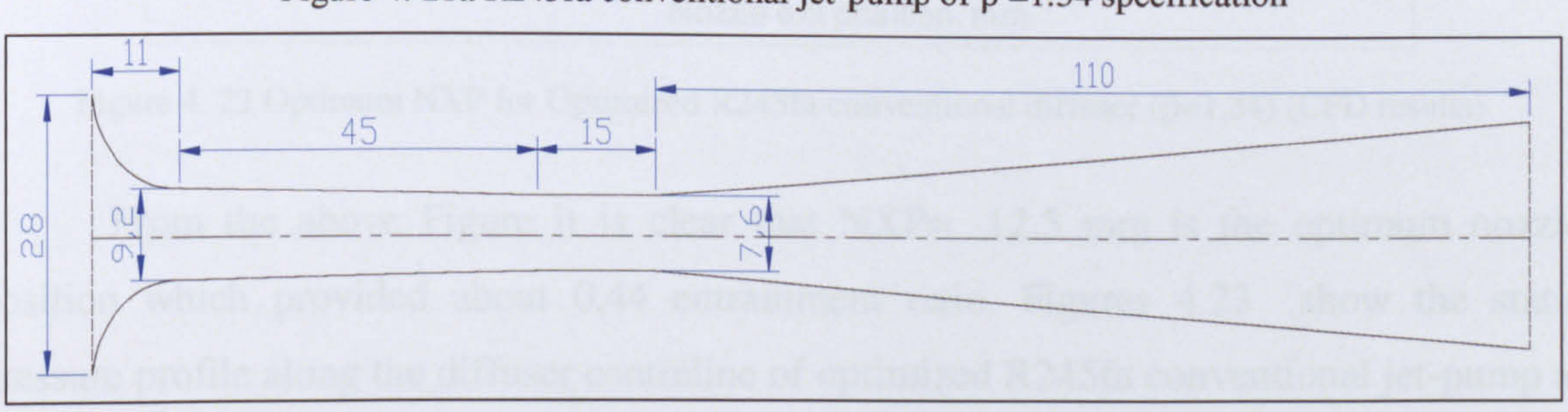

Figure 4. 21b R245fa conventional jet-pump of β =1.46 specification

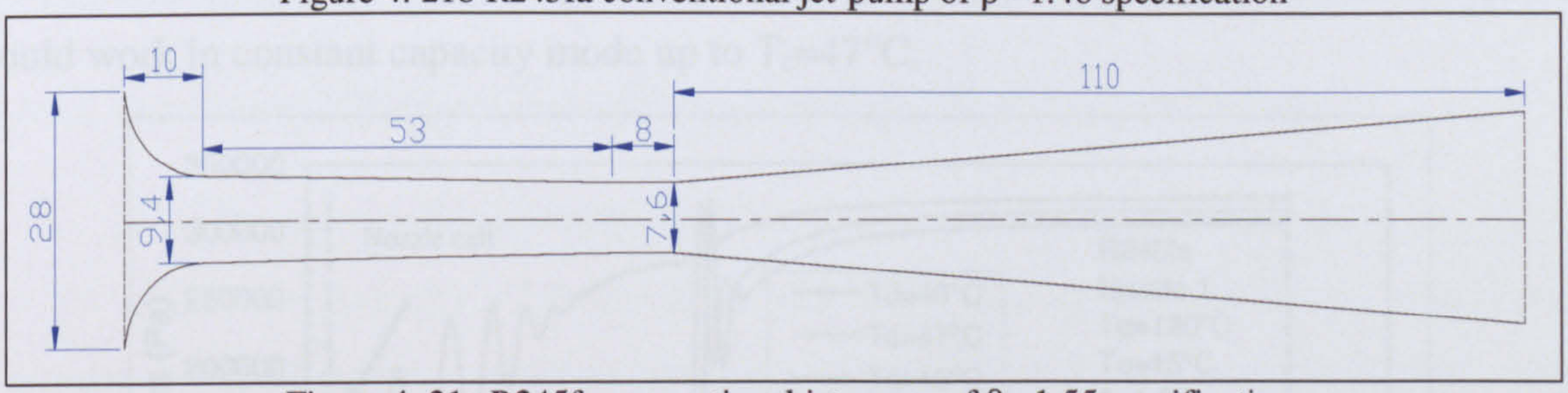

Figure 4. 21c R245fa conventional jet-pump of β =1.55 specification

The initial CFD prediction for the three diffusers at NXP=0mm are shown in Table 4.7.

Table 4. 7 CFD prediction of optimised R245fa Conventional jet-pumps

Diffuser	β	R_m	T_c*
1	1.34	0.36	47°C
2	1.46	0.405	46°C
3	1.55	0.425	45°C

From Table 4.7 it is clear that as (β) increased the R_m increased, whereas T_c^* decreased, because more secondary fluid is entrained. CFD results have showed reasonably good correlation with theoretical results, especially the jet-pump with β =1.34, which could provide R_m=0.36 with critical condenser pressure=47°C; therefore this jet-pump was selected to be further simulated and designed for experimental investigation. To find out the optimum nozzle position of selected jet-pump, a range of NXP between -15 to 2.5 in steps of 2.5mm was tested. The optimal NXP found from the CFD simulated results are shown in Figure 4.22 below.

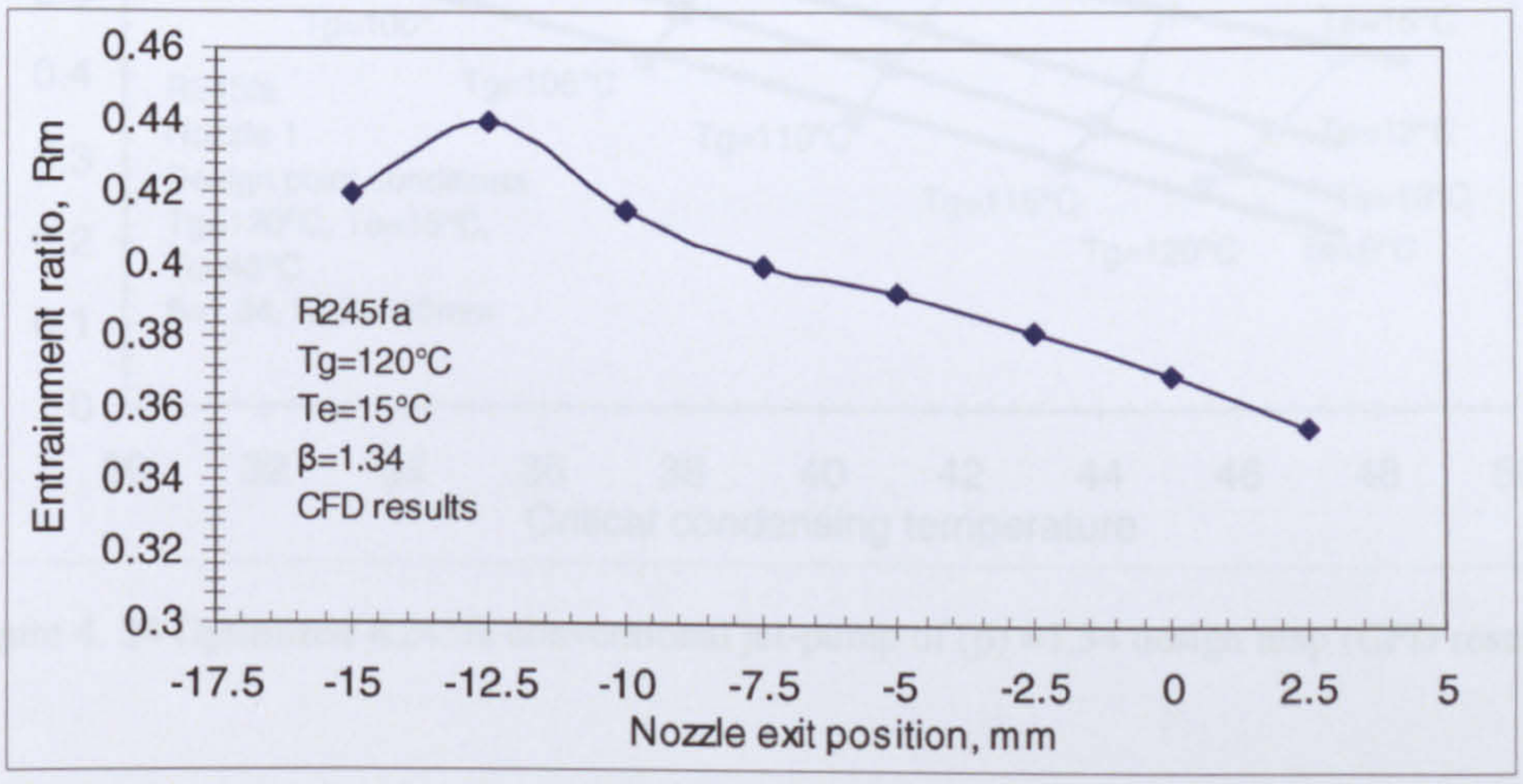

Figure 4. 22 Optimum NXP for Optimized R245fa conventional diffuser (β=1.34) (CFD results)

From the above Figure it is clear that NXP= -12.5 mm is the optimum nozzle position which provided about 0.44 entrainment ratio. Figures 4.23 show the static pressure profile along the diffuser centreline of optimized R245fa conventional jet-pump at different condensing temperatures "T_g=120°C, T_e=15°C", it is clear that the jet-pump could work in constant capacity mode up to T_c=47°C.

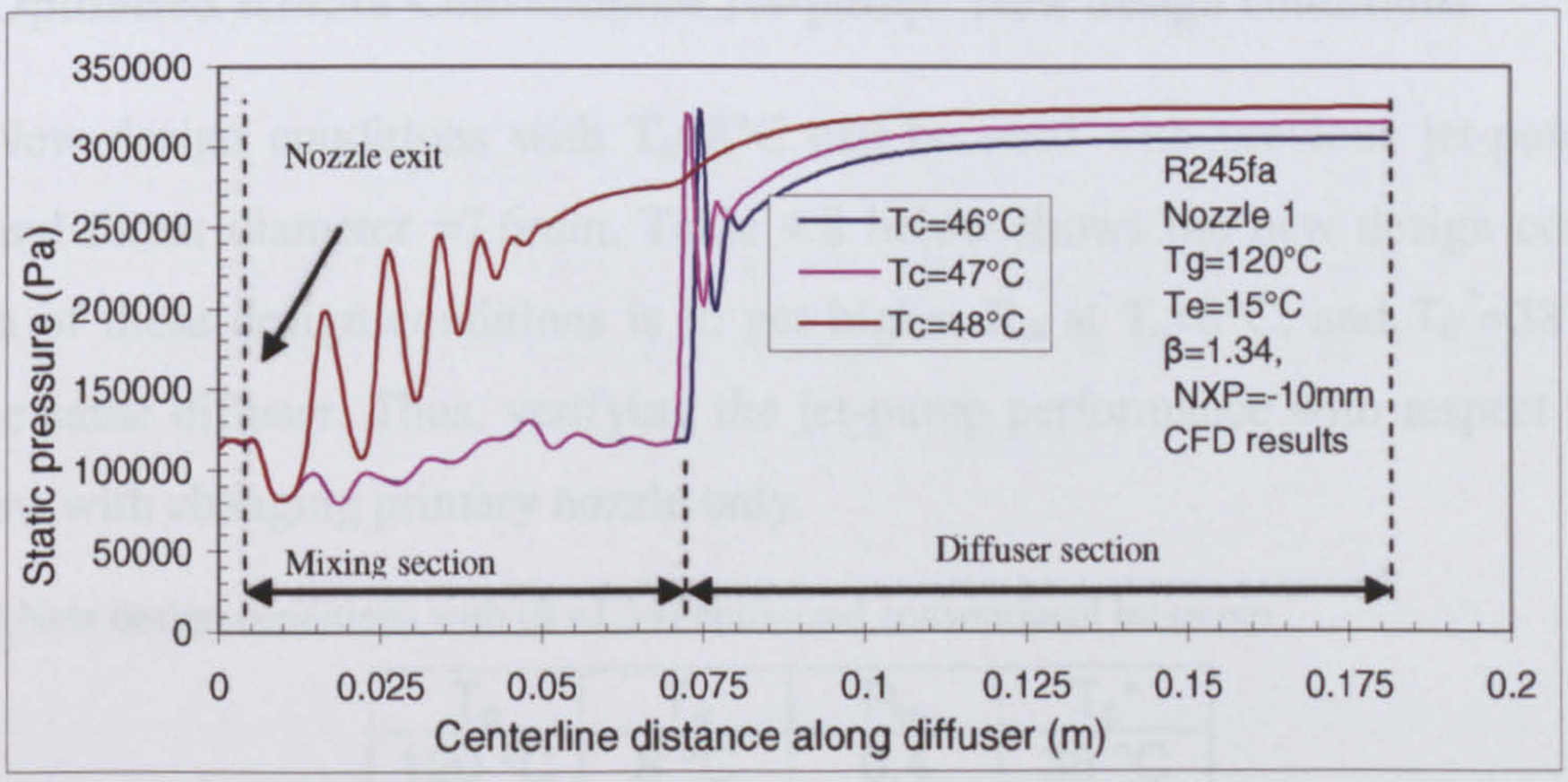

Figure 4. 23 Static pressure profiles along centreline of optimized R245fa Conventional jet-pump (β=1.34)(CFD results)

4.3.2.1 CFD Optimised R245fa Conventional Jet-pump "off-design operating condition"

Design conditions of T_g from 100°C to 120°C in steps of 5° and T_e of 8°C, 10°C, 12°C, and 15°C were simulated with NXP=-10mm. The obtained design map is shown in Figure 4.24 below.

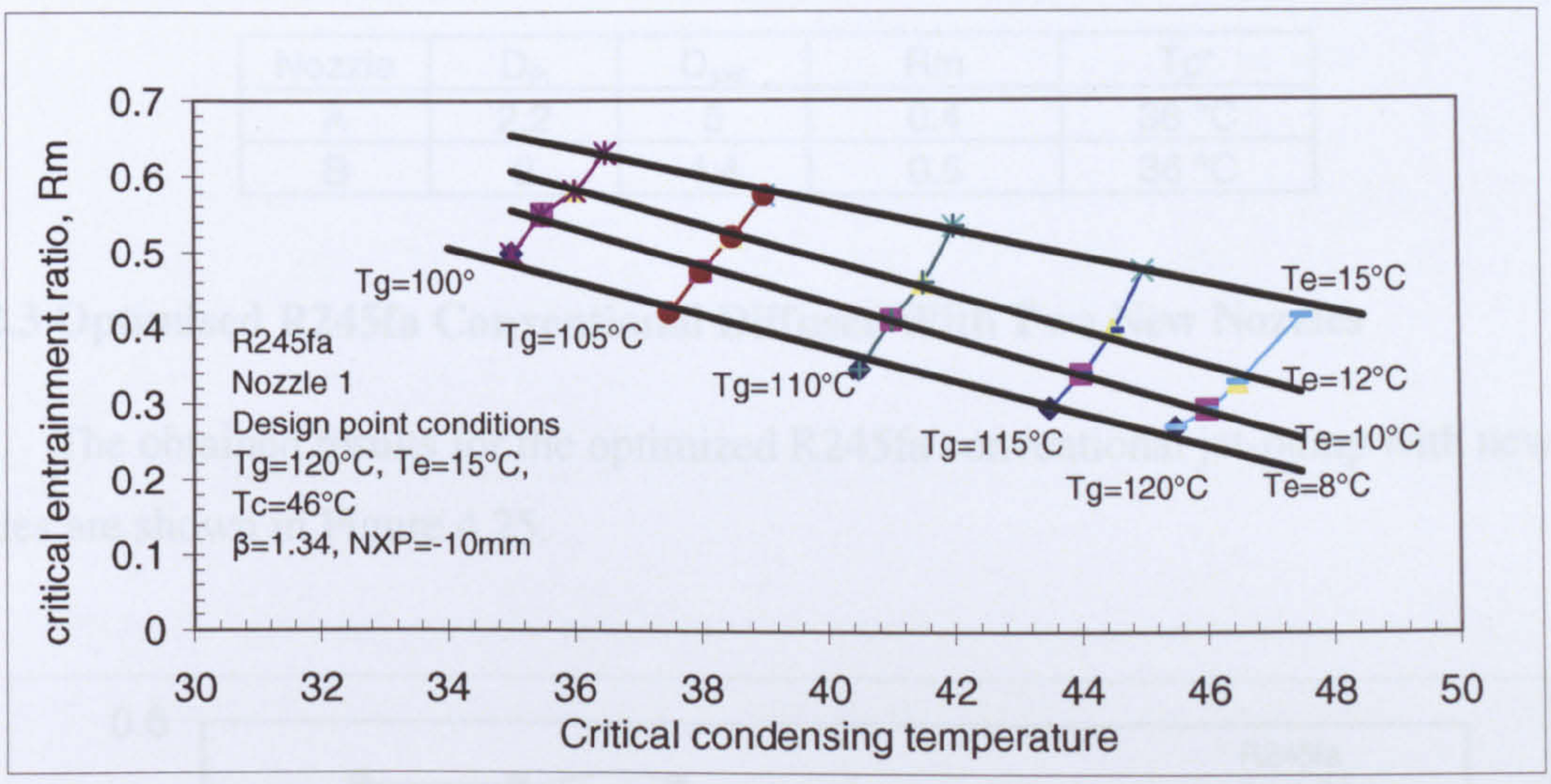

Figure 4. 24 Optimized R245fa conventional jet-pump of (β) =1.34 design map (CFD results)

At part load for this jet-pump, an increase in evaporator saturation temperature from 8°C to 15°C could increase entrainment ratio substantially by 50% to 60%, with a small increase in critical condensing temperature. It is observed that with each 2K increase in evaporator temperature there is 0.5K increase in critical condensing temperature. Whereas at fixed evaporator temperature, 3K increase in T_c^* could be obtained with each 5°K increase in generator temperature.

4.3.2.2 Optimised R245fa Conventional Jet-pump "New design conditions"

New design conditions with T_e=8°C can be used with previous jet-pump of (β =1.34) and throat diameter =7.6mm. Table 4.8 below shows the new design conditions. The idea of these design conditions is to get higher R_m at T_e=8°C, and T_C^*=38°C, with using the same diffuser. Thus, verifying the jet-pump performance with respect to outlet conditions with changing primary nozzle only.

Table 4. 8 New design conditions with (β =1.34) optimized conventional jet-pump

T_g	T_e	R_m	T_c^*
120 °C	8 °C	0.4	38 °C
120 °C	8 °C	0.5	36 °C

The same developed computer program of conventional jet pump design was used to design two new nozzles depending on afore mentioned new design conditions and with keeping the same previous diffuser geometry "D_{th}=7.6mm and A_r=1.34". However, two new nozzles were obtained, their specification are shown in the table 4.9 below.

Table 4. 9 New nozzle specifications

Nozzle	D_{th}	D_{exit}	Rm	Tc*
A	2.2	5	0.4	38 °C
B	2	4.4	0.5	36 °C

4.3.2.3 Optimised R245fa Conventional Diffuser With Two New Nozzles

The obtained results for the optimized R245fa conventional jet-pump with new nozzles are shown in Figure 4.25.

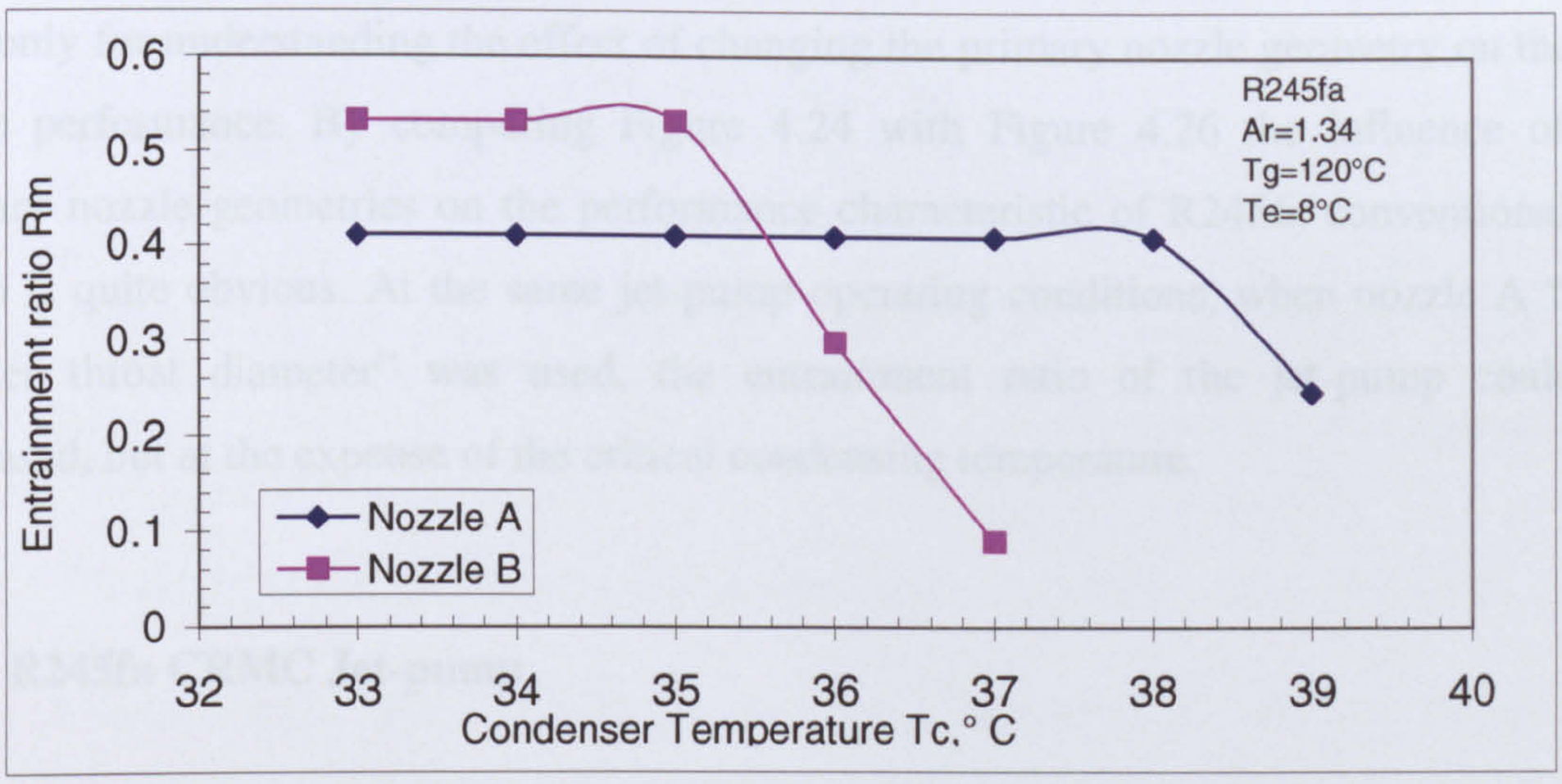

Figure 4. 25 Comparison of nozzle A and B performance at design operation conditions

There is a good agreement between the theoretical and CFD results: it is clear that nozzle A provided a 0.41 entrainment ratio with a 38°C condenser critical temperature. The nozzle position used in this simulation was 0mm which may not be the optimal NXP. If the NXP is altered, higher jet-pump performance could be achieved.

The jet-pump of 1.34 area ratio with nozzle A was selected to be further simulated over a range of generator and evaporator temperatures, to obtain new design map.

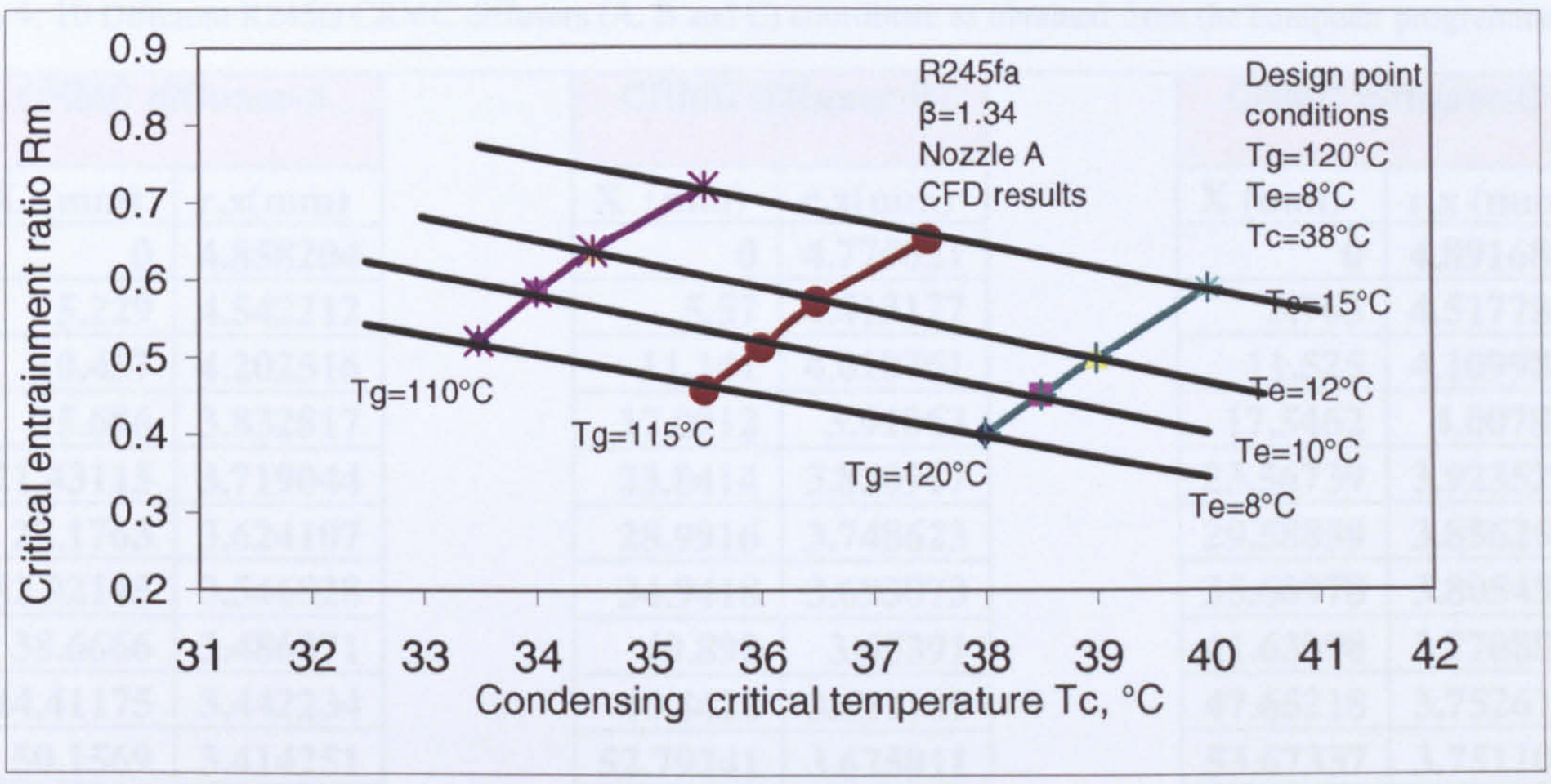

Figure 4. 26 Optimized conventional R245fa of A_r =1.34 with nozzle A design map (CFD results)

This new primary nozzle would not be examined experimentally, but it is shown here only for understanding the effect of changing the primary nozzle geometry on the jet-pump performance. By comparing Figure 4.24 with Figure 4.26 the influence of the primary nozzle geometries on the performance characteristic of R245fa conventional jet-pump is quite obvious. At the same jet-pump operating conditions, when nozzle A "with smaller throat diameter" was used, the entrainment ratio of the jet-pump could be increased, but at the expense of the critical condensing temperature.

4.3.3 R245fa CRMC Jet-pump

The same previous CRMC computer programme was used to design CRMC diffusers with R245fa as working fluid. Some modification on the design of the first part of mixing section was applied. The length of the mixing was reduced to equal 3* D^*_d in equation [3.62] Chapter 3; this was found to be more practical with CRMC diffuser. The same previous operating conditions for R245fa jet-pumps section 4.3 were used in designing R245fa CRMC jet-pump with using the same previous coefficients and thermodynamics data. Three different CRMC diffusers (A, B, C) were designed to work with the same primary nozzle Figure 4.18; the coordinates of these CRMC diffusers are shown in Table 4.10 below.

Table 4. 10 Different R245fa CRMC diffusers (A, B and C) coordinate as obtained from the computer programme

CRMC diffuser-A		CRMC diffuser-B		CRMC diffuser-C	
X (mm)	r,x(mm)	X (mm)	r,x(mm)	X (mm)	r,x (mm)
0	4.858204	0	4.775021	0	4.891689
5.229	4.542212	5.57	4.413127	5.763	4.517784
10.457	4.202516	11.141	4.018761	11.525	4.109985
15.686	3.832817	17.0912	3.91063	17.5462	4.00782
21.43115	3.719044	23.0414	3.820917	23.56739	3.923529
27.1763	3.624107	28.9916	3.748623	29.58859	3.856257
32.92145	3.546828	34.9418	3.693073	35.60978	3.805455
38.6666	3.486371	40.892	3.65391	41.63098	3.770881
44.41175	3.442234	46.8422	3.631109	47.65218	3.752616
50.1569	3.414251	52.79241	3.625011	53.67337	3.751102
55.90205	3.402622	58.74261	3.636374	59.69457	3.7672
61.6472	3.40796	64.69281	3.666469	65.71576	3.802287
67.39235	3.431372	70.64301	3.717219	71.73696	3.858407
73.13749	3.474594	76.59321	3.791419	77.75816	3.938491
78.88264	3.540194	82.54341	3.89309	83.77935	4.046729
84.62779	3.631908	88.49361	4.028053	89.80055	4.18915
90.37294	3.75518	94.44381	4.204901	95.82174	4.374625
96.11809	3.918091	100.394	4.436753	101.8429	4.616655
101.8632	4.133032	106.3442	4.744639	107.8641	4.936811
107.6084	4.419948	112.2944	5.16465	113.8853	5.371975
113.3535	4.813226	118.2446	5.765102	119.9065	5.991627
119.0987	5.37837	124.1948	6.696065	125.9277	6.947274
124.8438	6.260629	130.145	8.382015	131.9489	8.661819
130.589	7.877967				

4.3.3.1 R245fa CRMC Jet-pump CFD Simulation "design operating conditions"

A conical cone of 28mm inlet diameter and 12mm long was added at the entrance of the mixing section of these diffusers. This was used as recommended by ESDU, to smooth the flow through the mixing section and reduce losses in the diffuser. The initial results of CFD modelling of these three diffusers at NXP=0mm and at design operating conditions are shown in Table 4.11 below.

Table 4. 11 CFD results for A, B, C R245fa CRMC jet-pumps at NXP=0mm

diffuser	T_g °C	T_e °C	R_m	T_c^* °C
A	120	15	0.27	52
B	120	15	0.33	50
C	120	15	0.366	49

From this Table it is clear that diffuser "C" has better performance with T_c^* a little higher than the designed value "T_c*=47°C". Thus this diffuser was selected to be further modelled, to find out the optimum nozzle position and then at that position the diffuser was

modelled at off-design operating conditions to establish the design map. The specifications of diffuser (C) are shown in Figure 4.27.

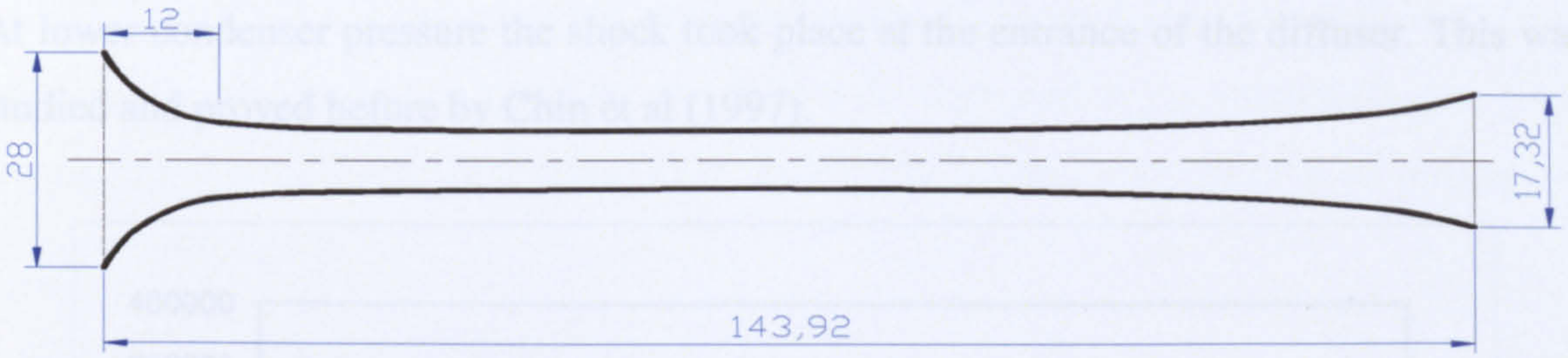

Figure 4. 27 CRMC diffuser C specifications

To find out the optimal NXP for this jet-pump (Diffuser C), different values from -5 to 5 in steps of 2.5 were tested; the obtained results are shown in Figure 4.28.

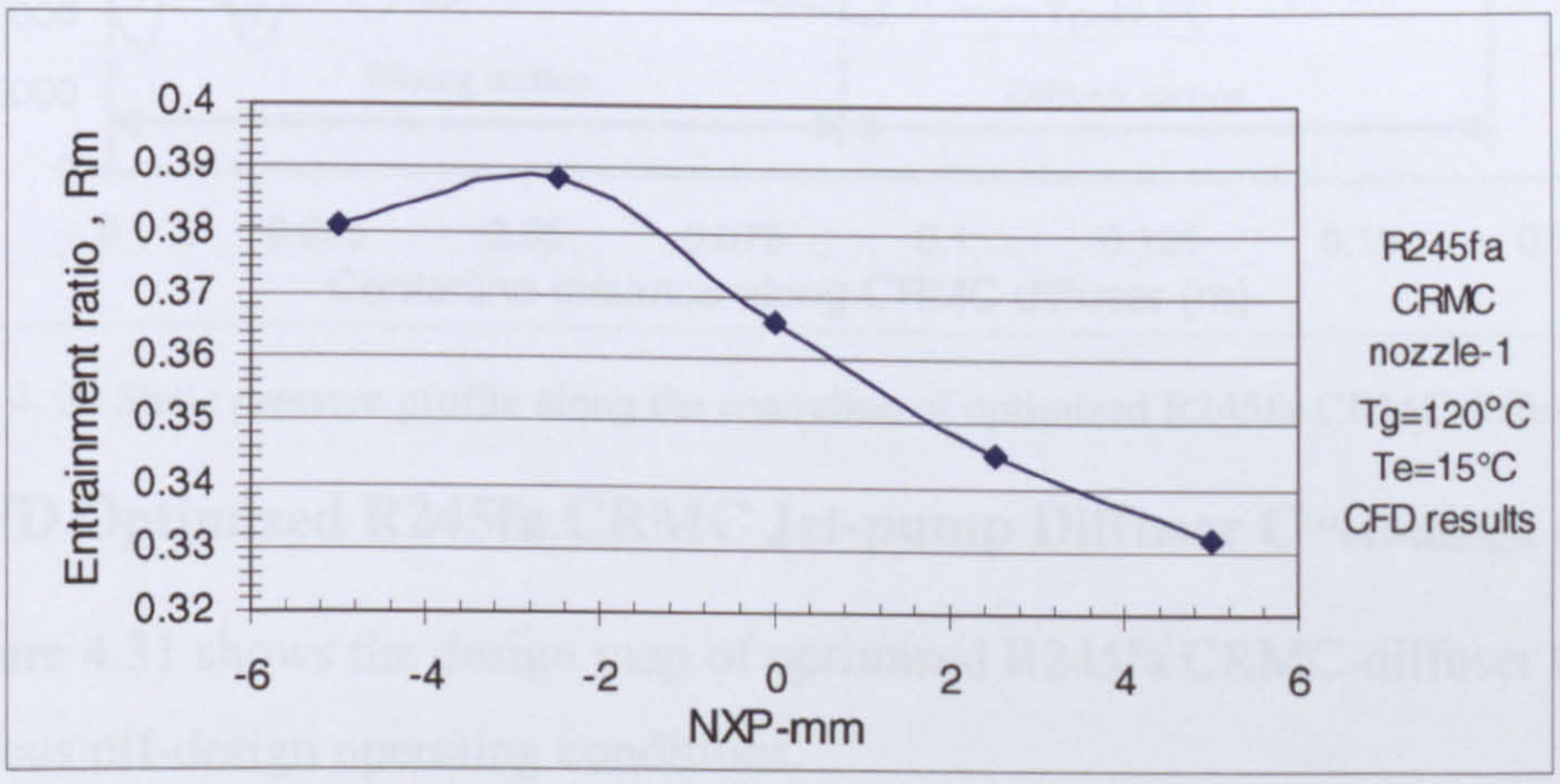

Figure 4. 28 Optimum NXP of optimised R245fa CRMC diffuser (C) (CFD results)

It is clear that the jet-pump has better performance when the nozzle was positioned at 2.5mm in front of the entry plane of mixing section. Thus at this NXP, the jet-pump was simulated at different operational conditions. Diffuser "C" was modified at the outlet of diffuser section as shown in Figure 4.29 to fit exactly on the experimental rig; this modification does not have any effect on jet-pump performance.

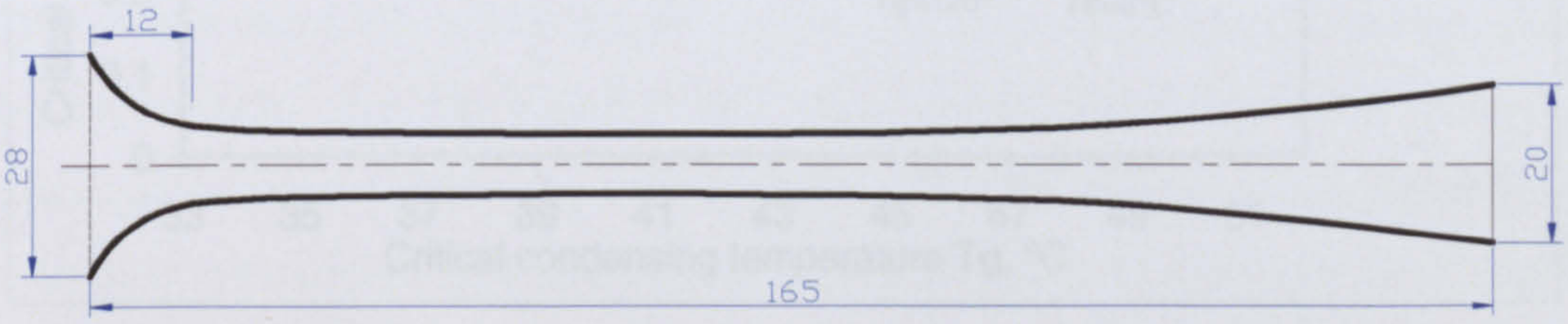

Figure 4. 29 The specification of modified R245fa CRMC diffuser (C)

The operating characteristics for the optimized R245fa CRMC jet-pump(diffuser C), can be identified clearly from the static pressure profiles at different condensing temperatures, as shown in Figure 4.30. It is clear that across the shock, pressure jumped to

value closed to back pressure, where as the velocity reduced to a subsonic value. At the critical condenser pressure, the shock wave occurred at the exit to the constant area throat. At lower condenser pressure the shock took place at the entrance of the diffuser. This was studied and proved before by Chin et al (1997).

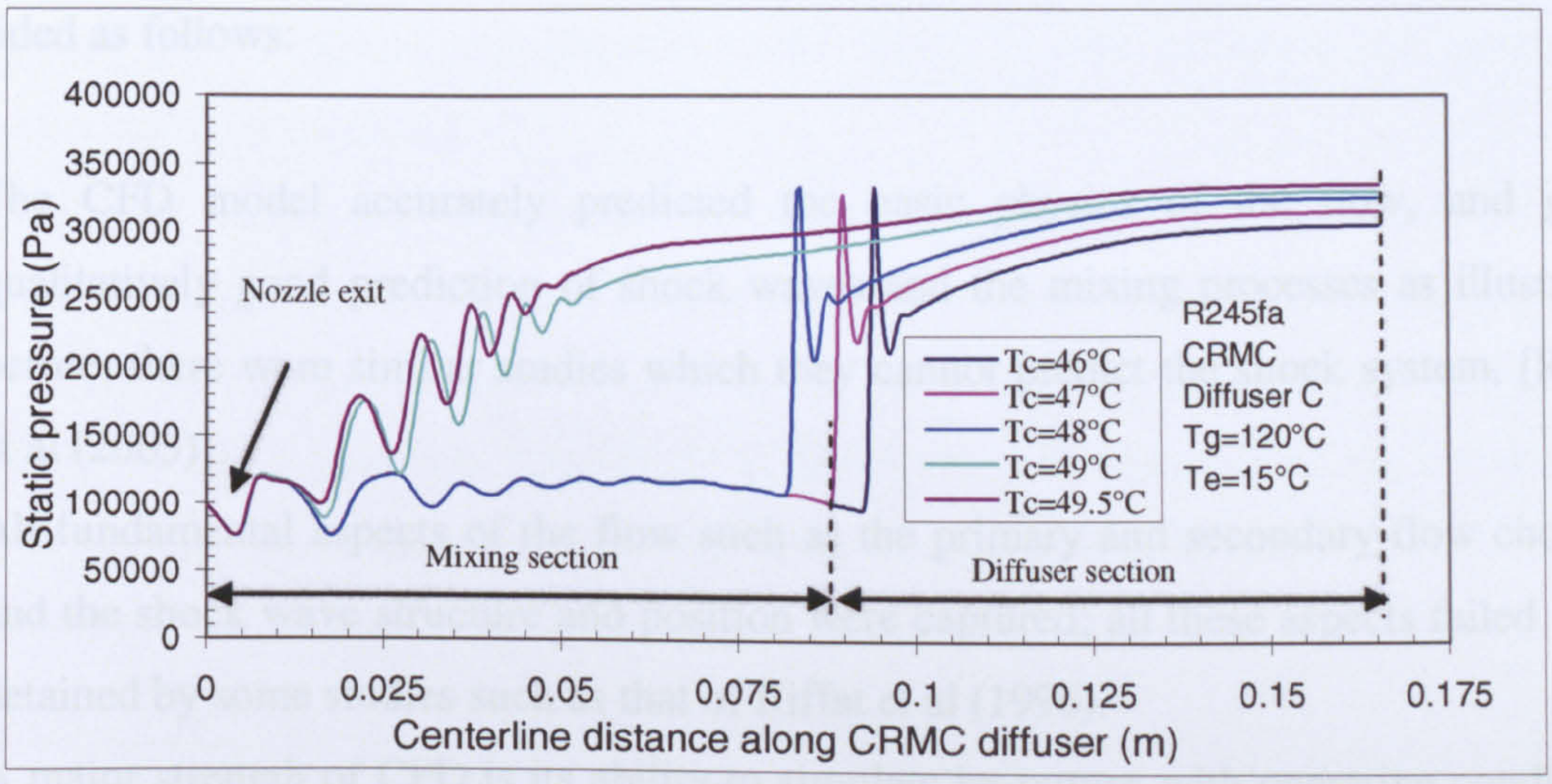

Figure 4. 30 Static pressure profile along the centreline of optimized R245fa-CRMC diffuser (C)

4.3.3.2 CFD Optimized R245fa CRMC Jet-pump Diffuser C "off-design operating condition"

Figure 4.31 shows the design map of optimised R245fa CRMC-diffuser C, with the same previous off-design operating conditions.

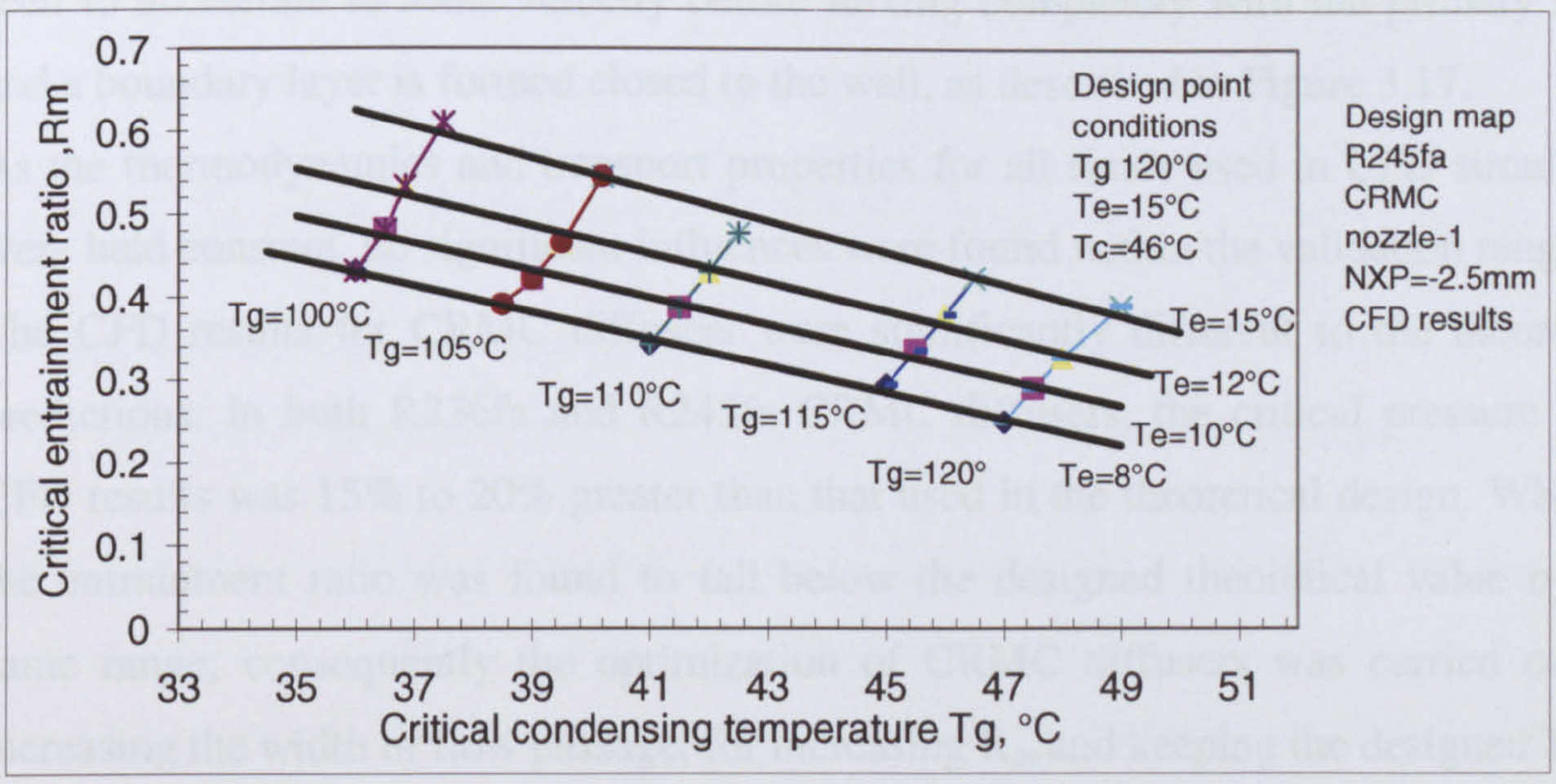

Figure 4. 31 Optimized R245fa CRMC-jet-pump "diffuser C" design map

From the above design map it is possible to get R_m about 0.4 at T_e=8°C, and with T_c^*=38°C when T_g reduced from 120°C to 105°C, or up to 0.44 if T_g reduced to 100°C, and may be much more if the nozzle is moved downstream a little at lower T_g.

4.4 Discussion on CFD Optimisation

From CFD simulation results presented in this Chapter, it clear that CFD does have the potential for predicting correctly the flow behaviour within the jet-pumps. The most significant finding from CFD simulation for all CRMC and conventional jet-pumps are provided as follows:

1. The CFD model accurately predicted the basic physics of the flow, and gives qualitatively good prediction of shock waves and the mixing processes as illustrated before; there were similar studies which they cannot predict the shock system, [Rusly et al (2005)].
2. All fundamental aspects of the flow such as the primary and secondary flow choking and the shock wave structure and position were captured; all these aspects failed to be detained by some studies such as that of Riffat et al (1996).
3. A major strength of CFD is its ability to simulate jet-pumps with operating conditions departing away from the proposed design operating conditions.
4. All simulated jet-pumps presented in this Chapter were observed to produce the well known constant capacity characteristic postulated by Munday and Bagster (1977). The primary flow was shown to initially fan out without mixing. The secondary flow was seen to accelerate to sonic velocity before mixing completely with the primary flow, and a boundary layer is formed closed to the wall, as described in Figure 3.17.
5. As the thermodynamics and transport properties for all fluids used in CFD simulation were held constant, no significant influences were found within the validation ranges.
6. The CFD results for CRMC diffusers were significantly different to the theoretical predictions. In both R236fa and R245fa CRMC diffusers, the critical pressure from CFD results was 15% to 20% greater than that used in the theoretical design. Whereas the entrainment ratio was found to fall below the designed theoretical value by the same range; consequently the optimization of CRMC diffusers was carried out by increasing the width of flow passage, for increasing R_m and keeping the designed T_c*.
7. The CFD results showed that the entrainment process was initiated as the secondary flow enters the mixing region and continued along the entire length of convergent channel, formed between the primary jet and the mixing section wall. Because of differences in velocity between primary jet and secondary flow, a shear mixing layer was formed along the constant surface between both streams. This shear mixing layer

was influenced by operating conditions and NXP. Any increase in primary pressure was shown to increase the width of the expansion jet, which decreased the width and the length of convergent channel formed for secondary flow. Because the velocity of the primary jet was increased the amount of secondary flow induced was almost unaffected. On the other hand any increase in secondary inlet pressure caused the primary jet to expand at a decreased rate which in turn increased the amount of secondary flow entrained.

8. From the supersonic regions as shown in Figure 4.32 for optimized R245fa conventional jet-pump, and also from static pressure plots for each jet-pump presented in this Chapter, it is clear that the primary exit jet is ended by the normal shock system, where the mixing process is believed to finish. Also the location of the shock wave within the diffuser was shown to vary with the change in generating and condensing temperatures.

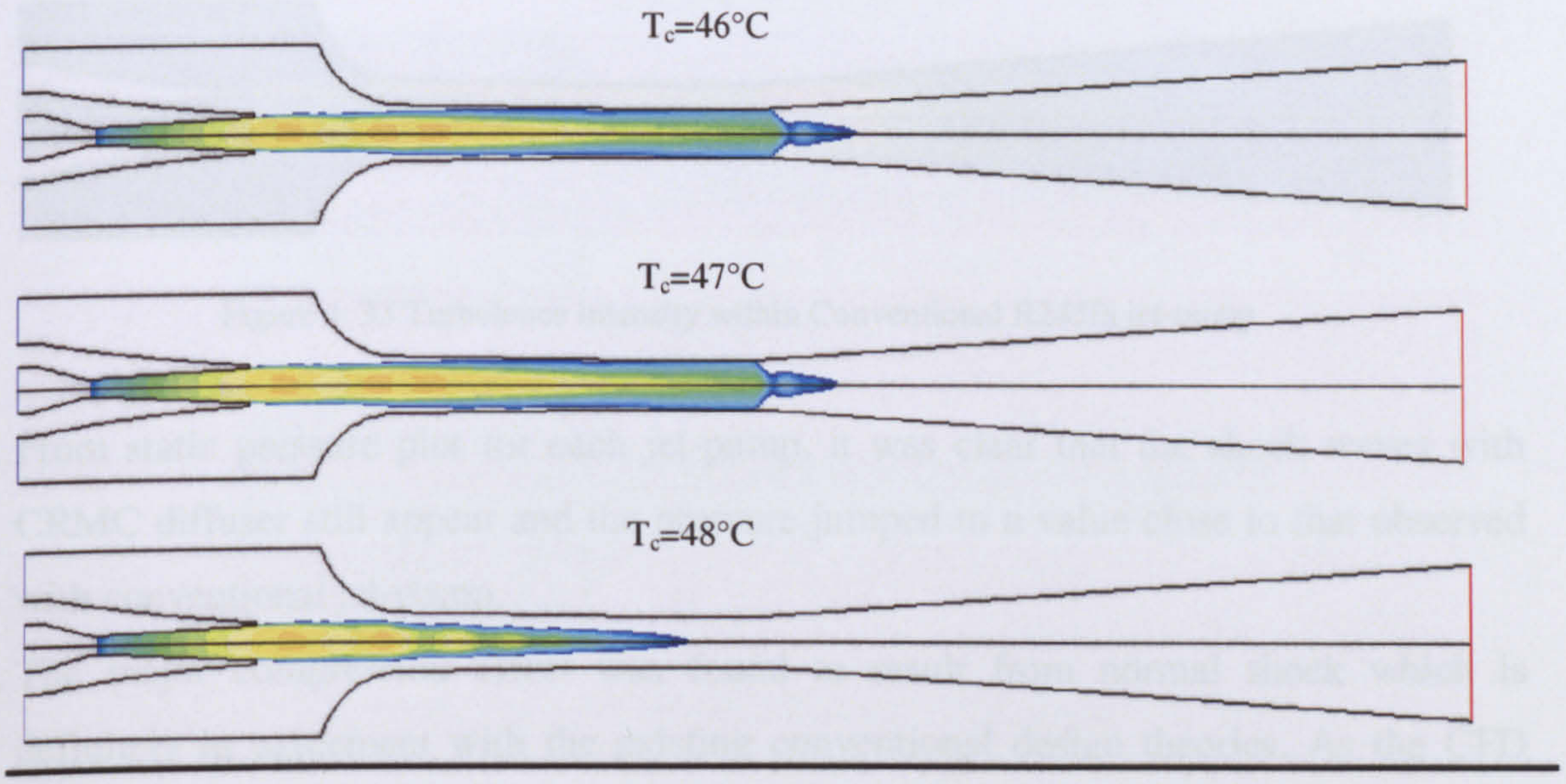

Figure 4. 32 Supersonic region of optimized R245fa conventional jet-pump (β=1.34)

9. For confirmation with each of points 7 and 8, it is possible to visualise the turbulence intensity within the mixing region. Turbulence intensity gives a clear indication for the mixing regions and the shock system position. Figure 4.33 shows turbulence intensity within the optimized conventional R245fa jet-pump at different operating conditions. It is clear from Figure 4.33 that the highest turbulence intensity values exist along the mixing shear layer, where the gradient of velocity between primary and secondary streams is exists, and at the shock system position. Peak values occur at the end of the constant area section, where the shock system occurs. Increasing generator temperature

decrease slightly the intensity of turbulence along the shear mixing layer and increase it at the chock position.

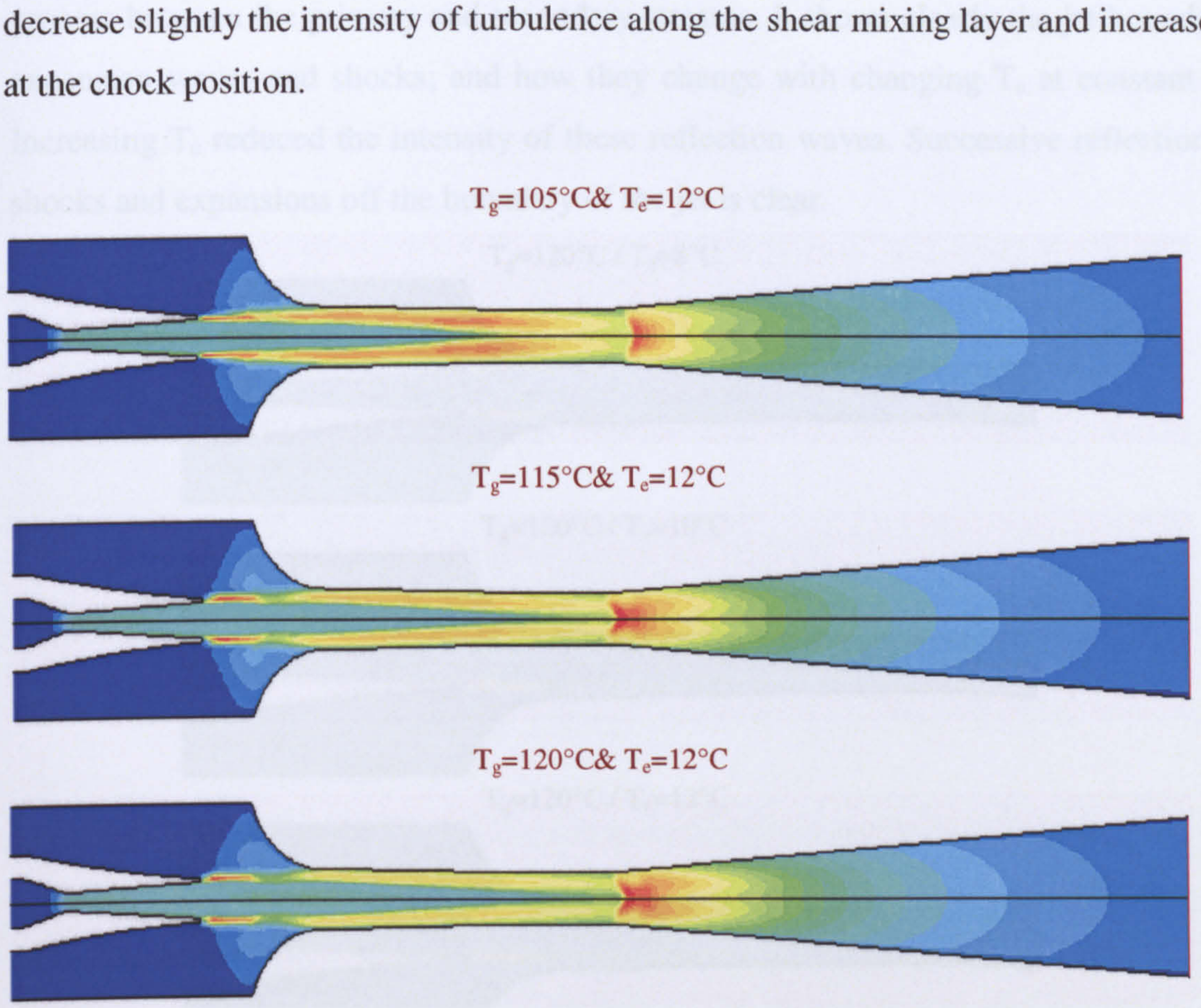

Figure 4. 33 Turbulence intensity within Conventional R245fa jet-pump

10. From static pressure plot for each jet-pump, it was clear that the shock waves with CRMC diffuser still appear and the pressure jumped to a value close to that observed with conventional jet-pump.
11. The major compression effect was found to result from normal shock which is definitely in agreement with the existing conventional design theories. As the CFD results confirmed the theoretical one, the conventional theoretical design method used in this research was thought it is reliable and correct.
12. CFD results was also shown that, at the nozzle exit a high speed flow leaves into a mixing section with expansion waves that form a diamond pattern as stated by Anderson (2002) and Ablwaifa (2005). This was clear with all jet-pumps simulated. The occurrence of a diamond wave within the jet core indicated that the jet core maintained their identity without mixing with the surrounded fluid and the pressure across the boundary is preserved by the effect of these oblique and expansion waves. The pattern of these series of oblique shock and expansion waves was found to change with changing any parameter; Figure 4.34 shows the interpretation of the mixing

process between the primary and secondary streams. It shows clearly the jet boundary, expansion waves and shocks; and how they change with changing T_e at constant T_g. Increasing T_e reduced the intensity of these reflection waves. Successive reflection of shocks and expansions off the boundary of the jet is clear.

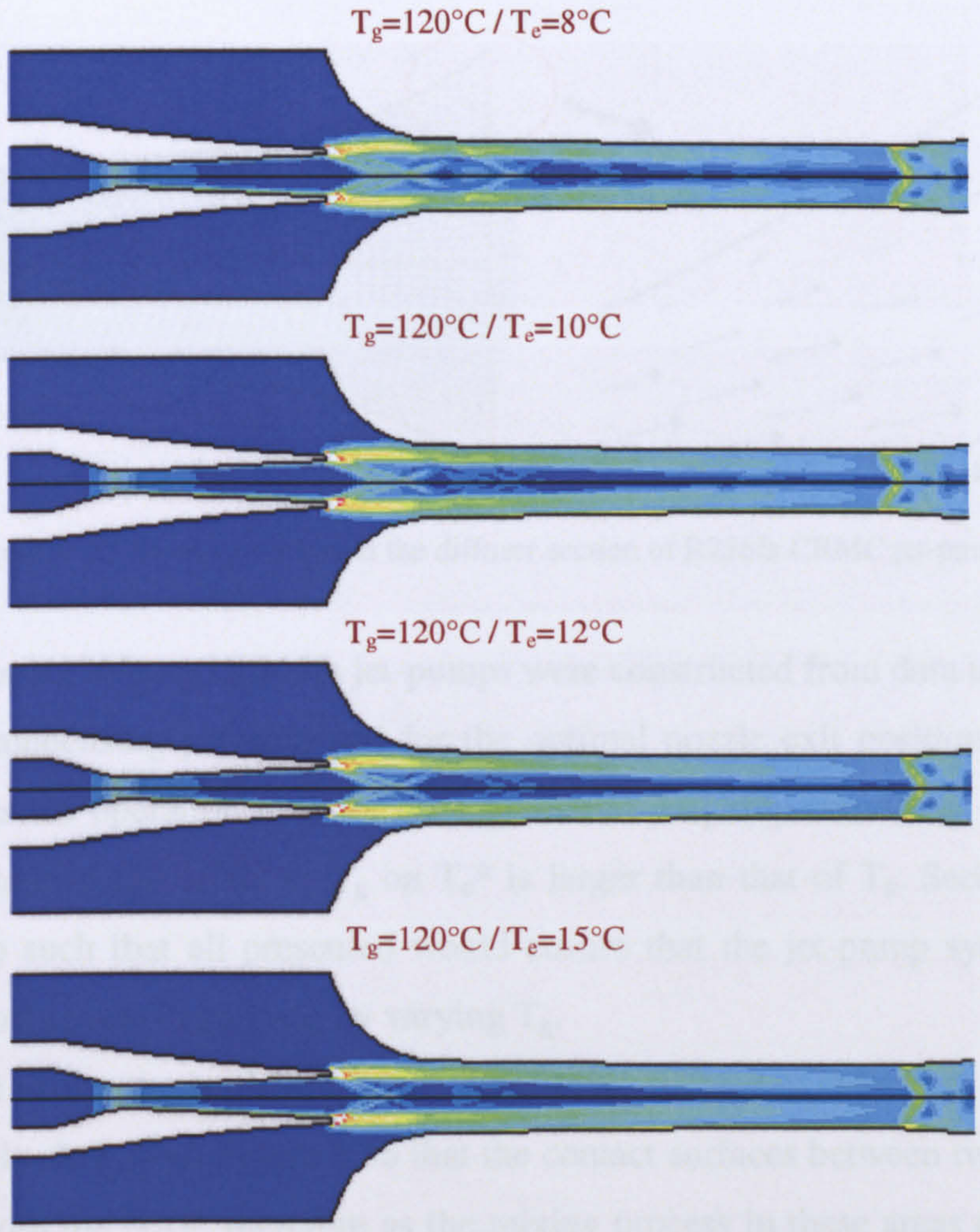

Figure 4. 34 Strain rate contours within Conventional R245fa jet-pump (NXP=0mm)

13. Optimum jet-pump operation occurred at the critical conditions; operating at pressure below the critical points has negligible effect on the jet-pump entrainment ratio.
14. Increasing T_g, would push the oblique shock wave more downstream, increasing the shock intensity and consequently increasing the T_c*.
15. In all cases of the CFD modelling for R236fa CRMC jet-pump, it was observed that there was a reversed flow for the flow layer closest to the wall at the end of the diffuser as shown in Figure 4.35. This is because the end part of CRMC diffusers is wide which makes a boundary layer with little momentum that cannot overcome the pressure at the end of the diffuser. This reverse flow was though to cause large pressure energy losses in the flow, and it must be considered in further optimization of CRMC diffusers; it is

believed that increasing the angle of this part increases the probability of boundary layer separation. However, with R245fa CRMC jet-pump optimization, this problem was avoided with proper profiling of the end part of the CRMC diffuser.

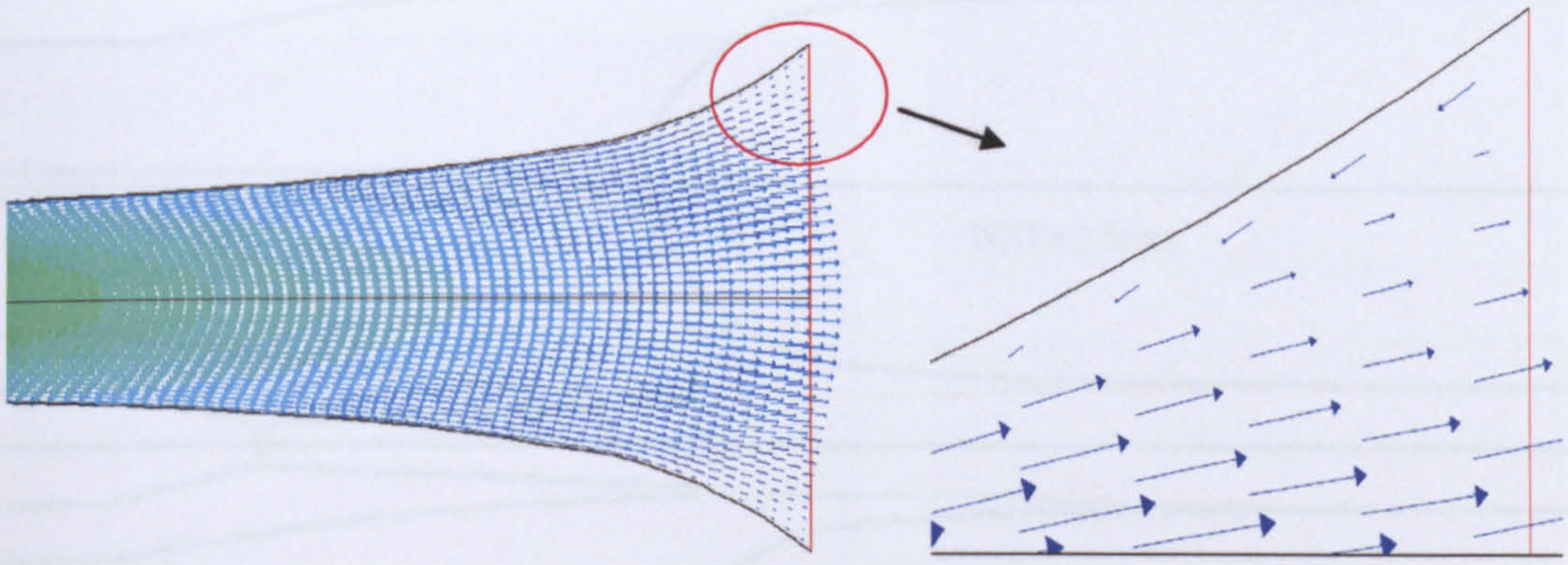

Figure 4. 35 Velocity vectors at the diffuser section of R236fa CRMC jet-pump

16. All maps for R236fa and R245fa jet-pumps were constructed from data taken at critical operating condensing pressure and for the optimal nozzle exit position. They can be inspected as the operation map for each particular jet-pump simulated; first it is clear that the extent of the effect of T_g on T_c* is larger than that of T_e. Second the use of design map such that all presented would ensure that the jet-pump system can cope with the most severe conditions by varying T_g.
17. Figure 4.36 shows the iso Mach, M=1, for CRMC diffuser examined at different value of NXP. It is clear from Figure 4.36 that the contact surfaces between two streams was changing with the NXP; therefore as the mixing process in these areas depends on the shear stress, accordingly the R_m changes. The shear stress layer was formed because of the large velocity difference between the primary and secondary streams both of which were controlled by operating condition. For the cases of NXP downstream of optimum NXP, the supersonic jet at the nozzle exit became under-expanded as the streamlines tend to diverge slightly. However, it is clear that the jet-pump has better performance when the nozzle was positioned at 2.5mm in front of the entry plane of mixing section.

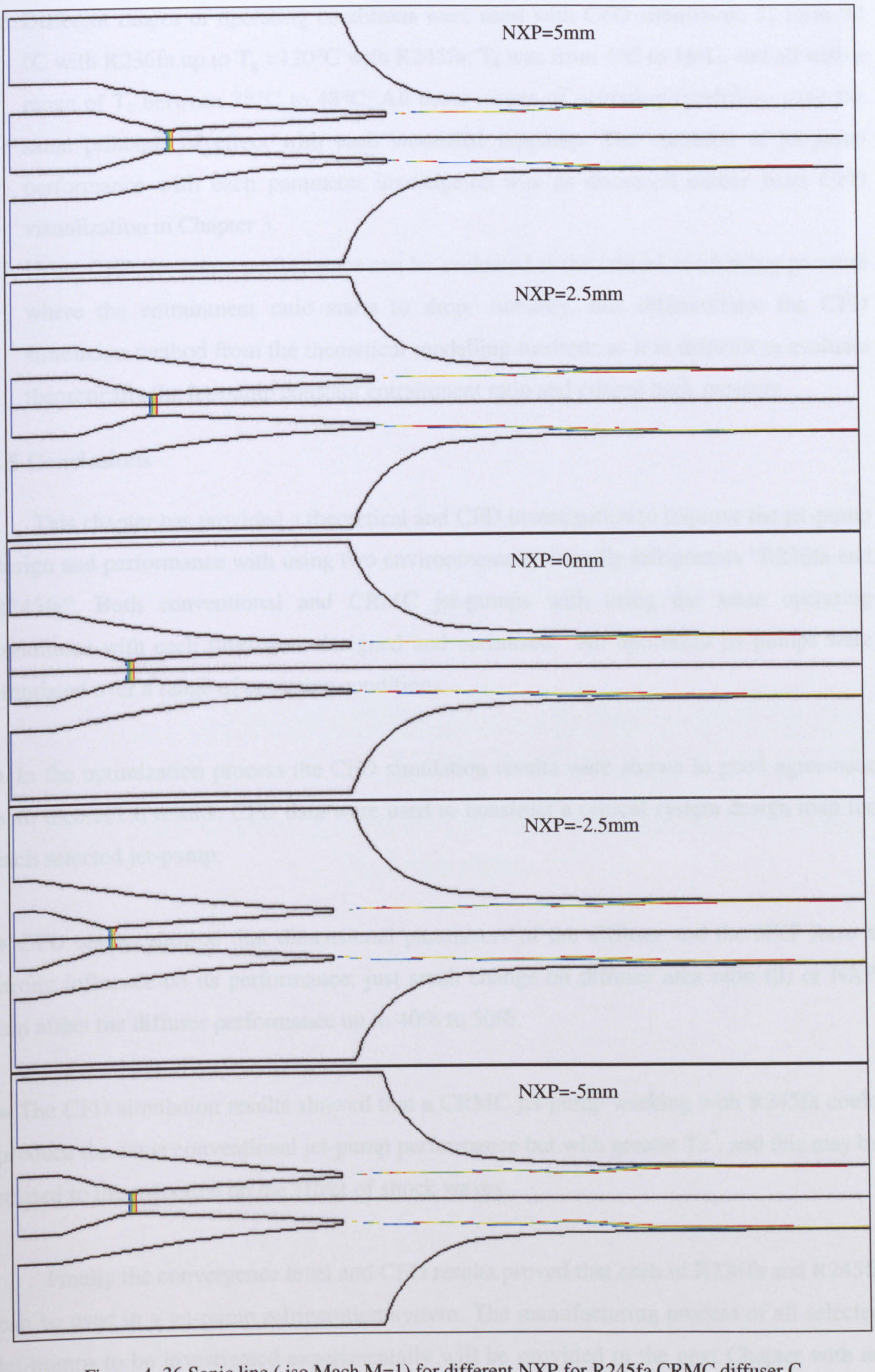

Figure 4. 36 Sonic line (iso Mach M=1) for different NXP for R245fa CRMC diffuser C

18. Different ranges of operating conditions were used with CFD simulation. T_g from 82 °C with R236fa up to T_g =120°C with R245fa; T_e was from 4°C to 15°C, and all with a range of T_c between 28°C to 48°C. All these ranges of operating conditions gave the same principle of effect with each simulated jet-pump. The variation of jet-pump performance with each parameter investigated was as discussed earlier from CFD visualization in Chapter 3.
19. Using CFD, jet-pump performance can be evaluated at the critical condensing pressure where the entrainment ratio starts to drop. Actually, this differentiates the CFD simulation method from the theoretical modelling methods as it is difficult to evaluate theoretically the jet-pump constant entrainment ratio and critical back pressure.

4.5 Conclusions

This chapter has provided a theoretical and CFD investigation to improve the jet-pump design and performance with using two environmentally friendly refrigerants "R236fa and R245fa". Both conventional and CRMC jet-pumps with using the same operating conditions with each fluid were designed and optimized. All optimized jet-pumps were simulated over a range of operating conditions.

- In the optimization process the CFD simulation results were shown in good agreement with theoretical results. CFD data were used to construct a critical system design map for each selected jet-pump.

- CFD results showed that dimensional parameters of the diffuser and the NXP have a strong influence on its performance; just small change on diffuser area ratio (β) or NXP can affect the diffuser performance up to 40% to 50%.

- The CFD simulation results showed that a CRMC jet-pump working with R245fa could produce the same conventional jet-pump performance but with greater Tc^*, and this may be related to the reduction on the effect of shock waves.

Finally the convergence level and CFD results proved that each of R236fa and R245fa can be used in a jet-pump refrigeration system. The manufacturing process of all selected jet-pumps to be investigated experimentally will be provided in the next Chapter with an experimental rig setup.

Chapter 5

Design and Manufacture of the Experimental Jet-pump Refrigerator

5. Design and Manufacture of the Experimental Jet-pump Refrigerator

5.1 Introduction

In this chapter the experimental system is described, and details of all its components including the steam boiler, vapour generator, evaporator, condenser, jet-pump, separator and feed pump are given. The instrumentation and their calibration are explained. Drawings of the cutting tools for all jet-pumps, which were manufactured and tested, are also provided.

5.2 Experimental Apparatus: Design and Construction

The experimental refrigerator was based on a novel cycle and consisted of the following components: boiler, vapour generator, separator, jet-pump, evaporator, condenser, feed pump, pre-heater, pre-cooler and sub-cooler. Figures 5.1 and 5.2 show a schematic diagram and photograph of the experimental refrigerator.

The experimental system was designed to be simple to operate and control. A mobile frame was used to mount all components, and thus it was easy to gain access to all the parts of the rig with a facility for changing the diffuser and the nozzle positions.

The experimental system operated in the following way. Steam was generated in the boiler with temperature close to the design generator temperature. It was then passed to the generator where high pressure refrigerant vapour was generated and passed to the jet-pump nozzle, where it is accelerated to supersonic velocity as it exits into the jet-pump mixing chamber. This vapour jet entrains the suction refrigerant (secondary) stream, they mix together in the mixing section and through transformation of kinetic energy this mixture is brought up to a higher pressure level in the diffuser to equal the condenser pressure at the diffuser exit. The mixed stream then discharges into the condenser, where the heat is removed by cold water (cooling medium solution) circulating through the condenser. The condensed fluid is then passed through sub-cooling heat exchanger to increase its density for better pumping. After cooling the liquid refrigerant is stored in the

receiver, from which a part of the condensed fluid is pumped back to the generator and the remainder is passed to the evaporator through the expansion valve to complete the cycle.

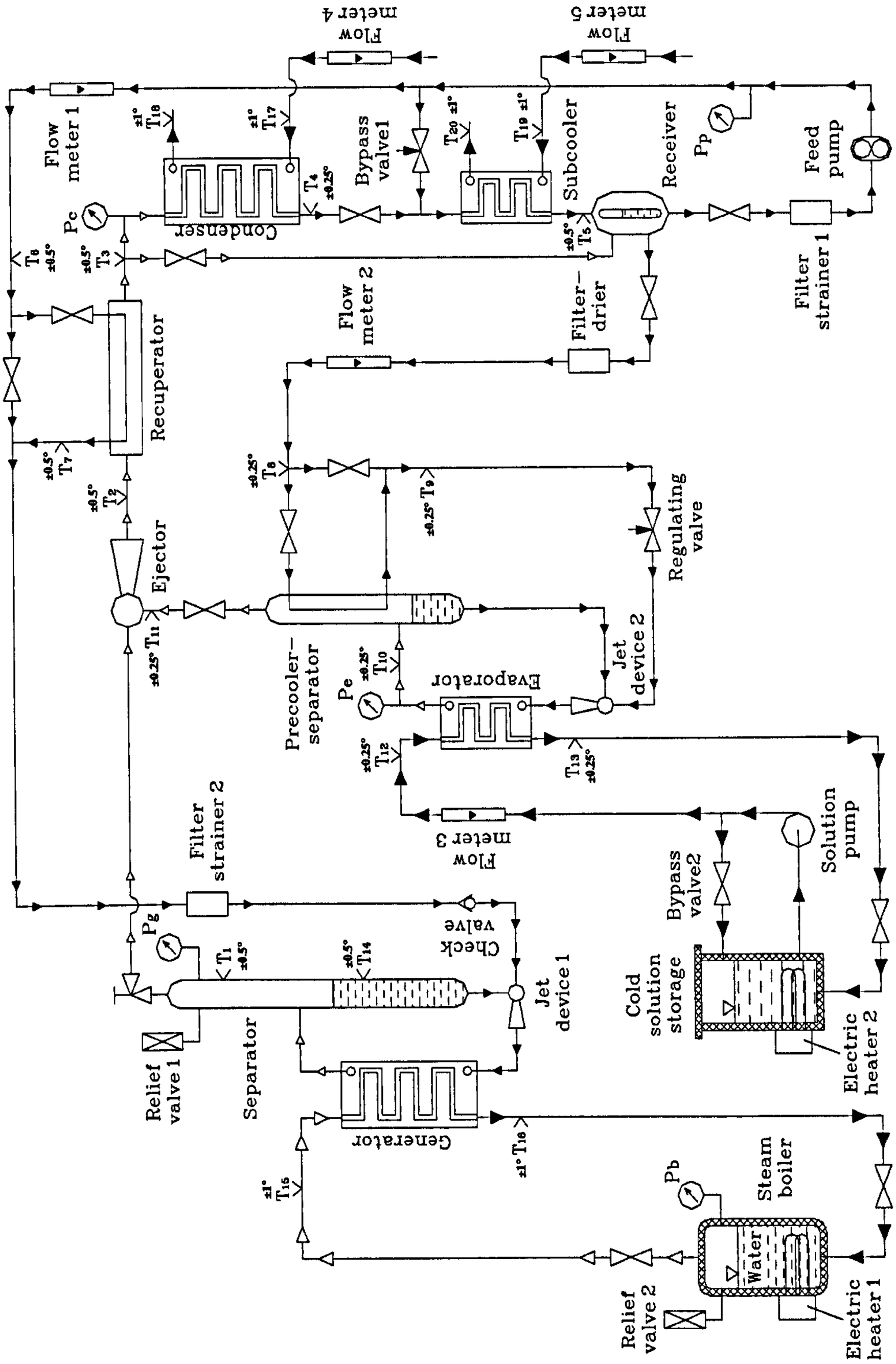

Figure 5.1 Schematic Diagram OF Experimental Rig

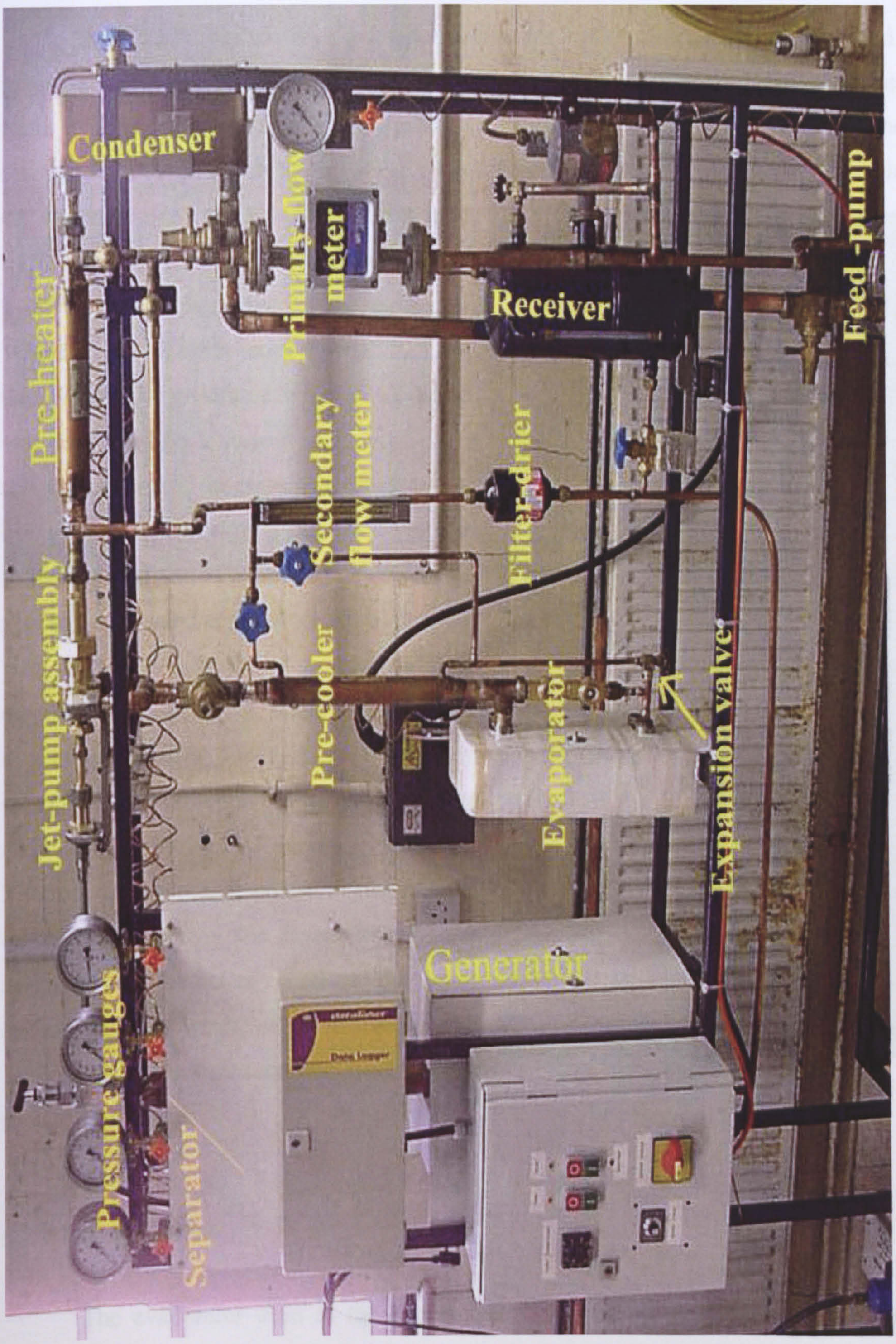

Figure 5. 2 photograph of experimental rig without insulation

5.2.1 The Steam Boiler

A 10.5 kW, electrically powered steam boiler was designed and manufactured. The pressure vessel was made of stainless steel and rated at 3 bar operating pressure. The heat input to the boiler was achieved by means of three 3.5 kW electrical heaters, immersed through the bottom of the boiler. These were controlled by a thermostat. Due to the change of experimental operating condition from 115°C to 85°C for the R236fa jet-pump, only 7 kW were in fact used in the generator. Whereas with R245fa jet-pumps all 10.5 kW were used. The generated steam in the boiler was circulated by a thermo-syphon effect to the generator and re-circulated back to the boiler. A calibrated sight glass was connected to the boiler by an external tube, as shown in Figure 5.3, located at the level at which water was to be monitored and controlled. This ensured that sufficient water was always available inside the boiler. A safety pressure relief valve was fitted to the tube at the boiler exit to prevent excess pressure. Thermocouples and a pressure gauge were installed to measure the steam temperature and pressure. The boiler vessel and the pipes, (steam and hot water) were insulated with 13mm thick Eurobatex rubber insulation to reduce heat losses.

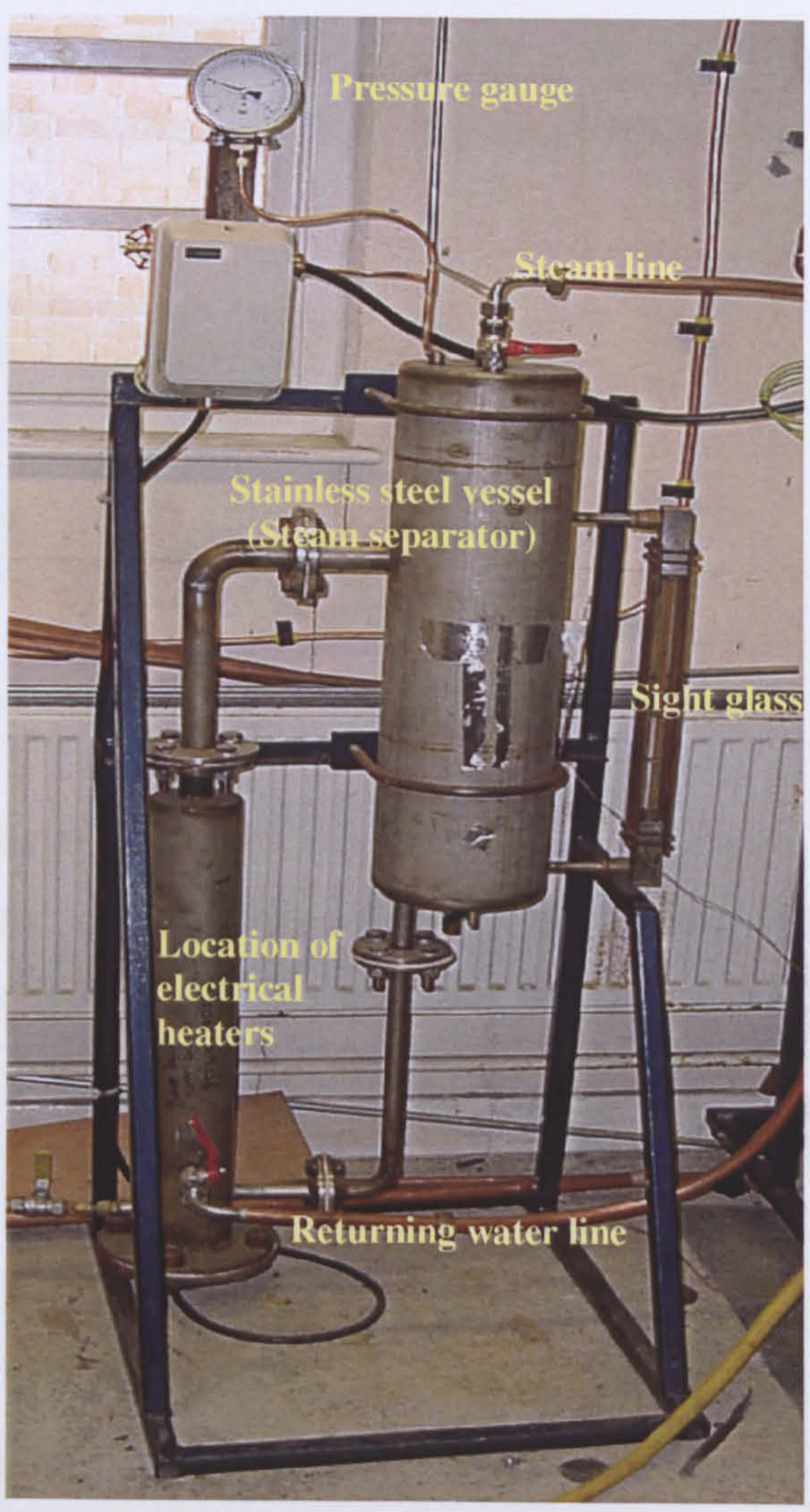

Figure 5. 3 The Steam Boiler

5.2.2 The Evaporator

The evaporator used in the experimental rig was a brazed plate heat exchanger supplied by ALFA LAVAL shown in Figure 5.4. The heating surfaces consisted of thin corrugated metal plates stacked on top of each other, to form channels through which heat

transfer fluid can pass. The corner ports are arranged to make alternate channels counter-current flow arrangement. The channel plates were corrugated to increase heat exchange area and to ensure a high degree of turbulence to improve heat transfer efficiency. Covers, connections and plates are all made of stainless steel ANSI 316, copper was used for brazing. This type was chosen because it has several advantages over traditional evaporators. They are compact and easy to install and they have high heat transfer efficiency. They are also suitable for applications for high temperatures and pressure because there are no gaskets used with them. The catalogue data for the evaporator used is listed in Table 5.1.

Figure 5. 4 The Evaporator

The working fluid is evaporated in the plate evaporator using circulated warm water, supplied from the laboratory main water supply. This water was first heated by recovering heat from the water stream that was used to cool the condenser and then heated by an electrical heater, which was fitted into the pipe line supplying warm water to the evaporator, to further increase its temperature when required.

A small jet device was connected into the refrigerant supply line to the evaporator; as shown in Figure 5.1, to encourage the circulation of working fluid through the evaporator, thus increasing the intensity of the heat exchange process. Figure 5.5 shows the layout of the evaporator with the jet-device.

Sight glasses were used near the evaporator to indicate whether the refrigerant is boiling inside the evaporator to avoid overfilling of evaporator that will affect the entrainment ratio.

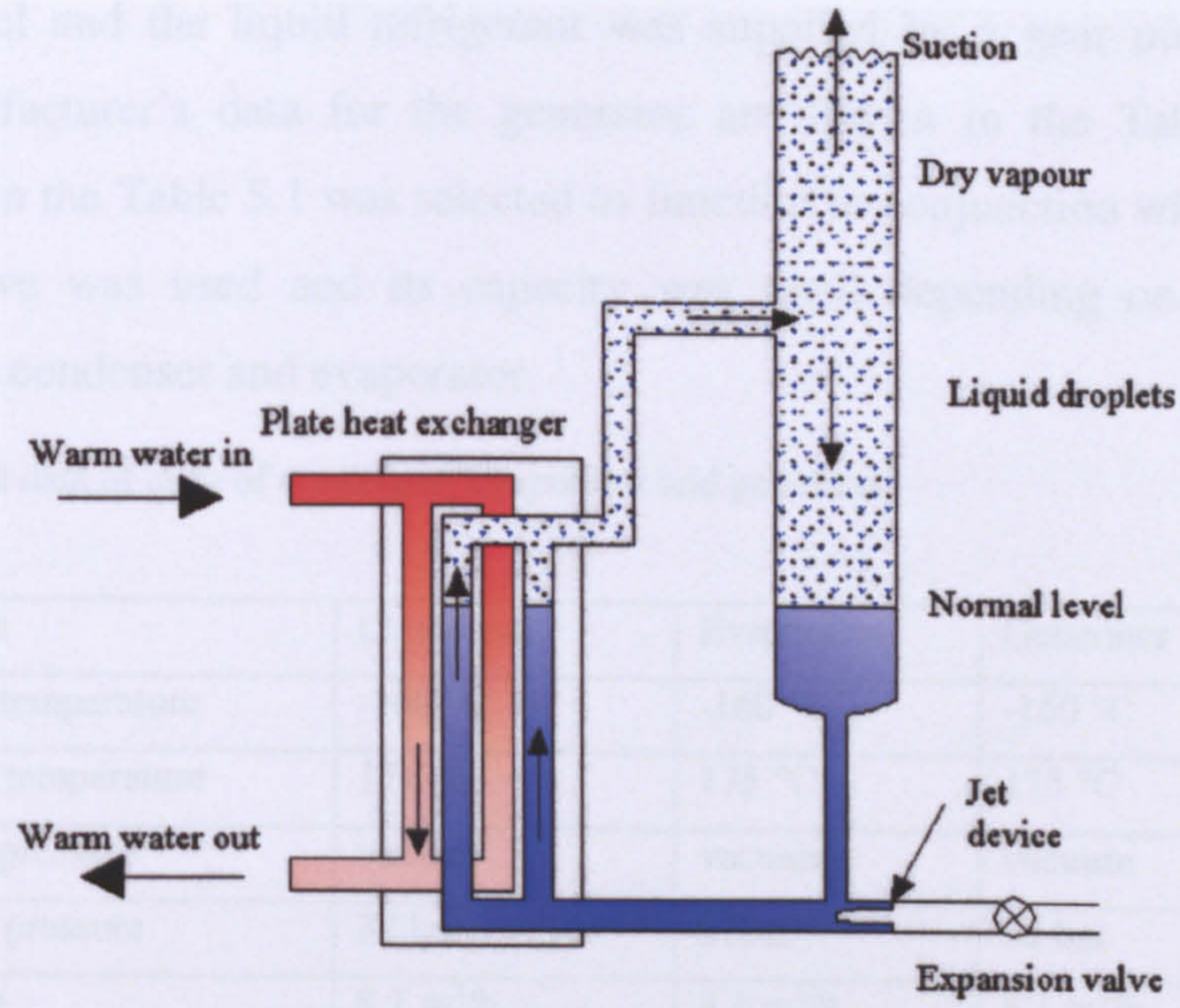

Figure 5. 5 Schematic layout of the evaporator with the jet-device

5.2.3 The Condenser

A brazed plate heat exchanger, supplied by ALFA LAVAL, was used as the condenser. The condenser used, shown in Figure 5.6, has the same characteristics that were mentioned with respect to the evaporator. The counter-current flow was used in the condenser to increase the degree of cooling to the working fluid and thus increase its efficiency; the internal plate pattern is specifically designed for optimal condensation, with asymmetric plate gap to optimise heat transfer and minimize pressure drop. Also this type can provide higher design pressure capabilities. The design data for the condenser are shown in the Table 5.1. The condenser was cooled by water taken from the laboratory chillers; both condenser temperature and pressure were controlled and adjusted by varying the cooling water flow through it.

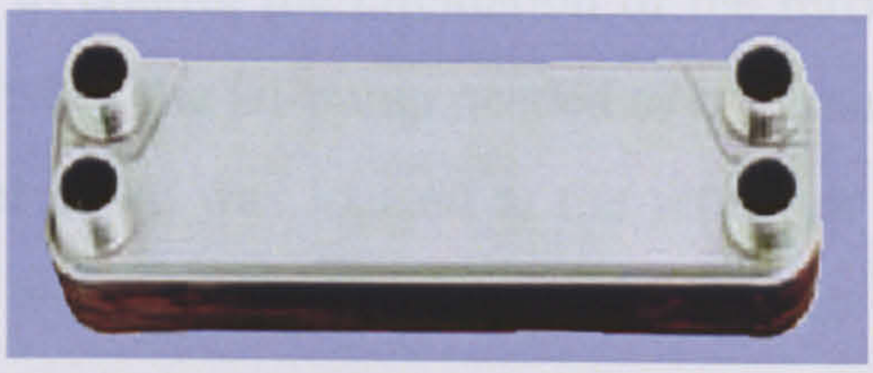

Figure 5. 6 The condenser

5.2.4 The Generator

The maximum working pressure for the generator used was 32 bars. The pressure used in the experiment with R236fa at 85°C is 15 bars and with R245fa at 120°C was approximately 20 bar and therefore considered safe. The generator outlet was connected to

the separator vessel and the liquid refrigerant was supplied by a gear pump and a jet device. The manufacturer's data for the generator are shown in the Table 5.1. Each component, listed in the Table 5.1 was selected to function in conjunction with each other. An expansion valve was used and its capacity was rated depending on the pressure difference between condenser and evaporator.

Table 5. 1 The standard data of each of condenser, evaporator and generator

Standard Data	Condenser	Evaporator	Generator
Min working temperature	-160 °C	-160 °C	-160 °C
Max working temperature	175 °C	175 °C	175 °C
Min working pressure	vacuum	vacuum	vacuum
Max working pressure	32 bar	32bar	32 bar
Max flow rate	8.1 m^3/h	8.1 m^3/h	8.1 m^3/h
Number of plates	400	140	300
Number of channels	38	12	28
Total volume	1.9 L	0.6 L	1.4 L
capacity	13.2 KW	3.8kW	8.7KW

5.2.5 The Separator

The separator was constructed from copper tube with an internal diameter of 15cm and length of 100cm; it was located vertically, downstream of the generator as shown in Figure 5.1. It was designed so that the refrigerant leaving the generator entered at the middle of the separator. Liquid droplets, associated with the vapour, accumulated at the bottom of the separator, whilst the dry vapour continued to the primary nozzle. A control valve was located at the top of the separator to control the circulation of the refrigerant, especially at the starting of each test-run, and when the jet-pump needed to be removed, in order to avoid leakage. Also, a pressure relief valve was located at the separator exit to prevent overpressure within it. Any liquid which accumulated, in the bottom of the separator, was drawn by the jet device and returned to generator.

5.2.6 The Generator Feed Pump

Finding a suitable feed pump that would work with low boiling refrigerant was a difficult task. Two types of pumps were tested. Both were hydraulic gear pump, driven by an electric motor. The first was tested with different ranges of generator temperature. It

was found to work for 5 to 10 seconds. Then it cavitated and stopped feeding liquid. Attempts to modify this pump by enlarging the inlet were carried out, but the problem continued.

The second pump, shown in Figure 5.7, was fitted following the recommendation of the supplying company, who claimed that it would work with this type of refrigerants, as it had a small clearance between the gear teeth. The specifications of this pump type are as follow: the standard pump casing is of Epsilion Iron Nitride, because the refrigerants are low lubricate fluids. The pump rotor is in carbon steel, the bearing are of aluminium bronze alloy with nitrite lip seals for shaft sealing. The power consumption by the driver electric motor at maximum speed is 0.55kW.

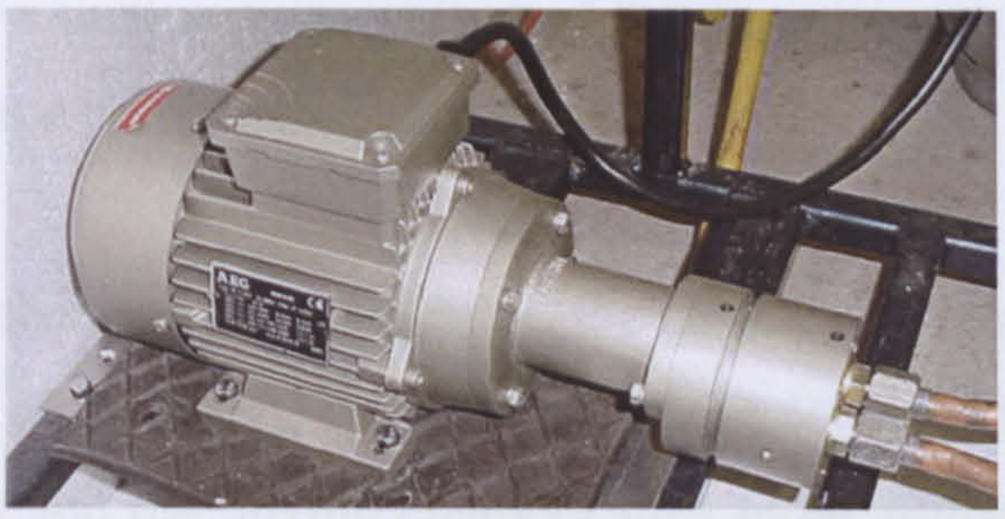

Figure 5. 7 The generator feed pump

The second pump was fitted to the experimental rig and tested over a range of generator temperatures, (pressures). It was found to work better than the first up to generator saturation temperatures of 95°C (for R236fa). At temperatures greater than 95°C, it was found difficult for the pump to work. Because of this it was decided to lower the design generator temperature from 115°C to 85°C, for R236fa. This pump was then used throughout all the experimental tests with R236fa without any particular problem. It was found beneficial to sub-cool the refrigerant at the exit of the condenser and before it entered the pump. This ensured that the liquid refrigerant was below its saturated condition, thus preventing cavitations from occurring. A bypass line (by pass valve) was installed at the exit to the pump to return part of the liquid to the receiver in order to match the capacity of the pump to the demand of the generator. As pump flow is proportional to its speed, an automatic speed controller was also installed and used to control the pump within preferred range. Filter-strainers were located upstream of the suction line of the pump to trap small quantities of dirt and scale before they could enter the pump. A sight glass was also fitted to the receiver, as shown in Figure 5.1, to show the liquid level, and also to indicate whether vapour was present in the suction pipe and receiver. In this case the sub-cooling intensity was increased to condense any vapour present.

5.2.7 The Jet-Pump

Jet-pumps with five different diffuser geometries were manufactured for test. The CRMC diffusers and conventional diffusers were designed and optimized as described in Chapter 4. One primary nozzle was used with three types of diffusers designed to operate with R236fa, and another primary nozzle was used with two diffusers that use R245fa as the working fluid. Details of the design of these jet-pumps with their dimensions are shown in the Figures 4.2, 4.3, 4.7, 4.18, and 4.21a; also in Tables 4.4 and 4.10 in the previous Chapter. The jet-pump assembly was located horizontally; the suction head of the jet-pump was mounted at the top of the experimental rig i.e. higher than the boiler and evaporator as shown in Figure 5.1; two suction ports were used for the suction section, and it is believed that these will improve the performance of the system.

The special mechanism for assembling the primary nozzle with the diffuser was designed with a view to changing the nozzle exit position (NXP). This allowed the distance between the nozzle exit and the mixing chamber inlet to be adjusted in order to study its influence on jet-pump performance. The design made available a relative movement of 30mm between the exit plane of the nozzle and the entrance of the mixing section. With this mechanism there was no need to stop the test runs when changing nozzle position and it only took about 30-60 seconds to change the nozzle position. Figures 5.8 and 5.9 show the general assembly and a photograph of the jet-pump. Further detailed drawings of the components are provided in appendix D.

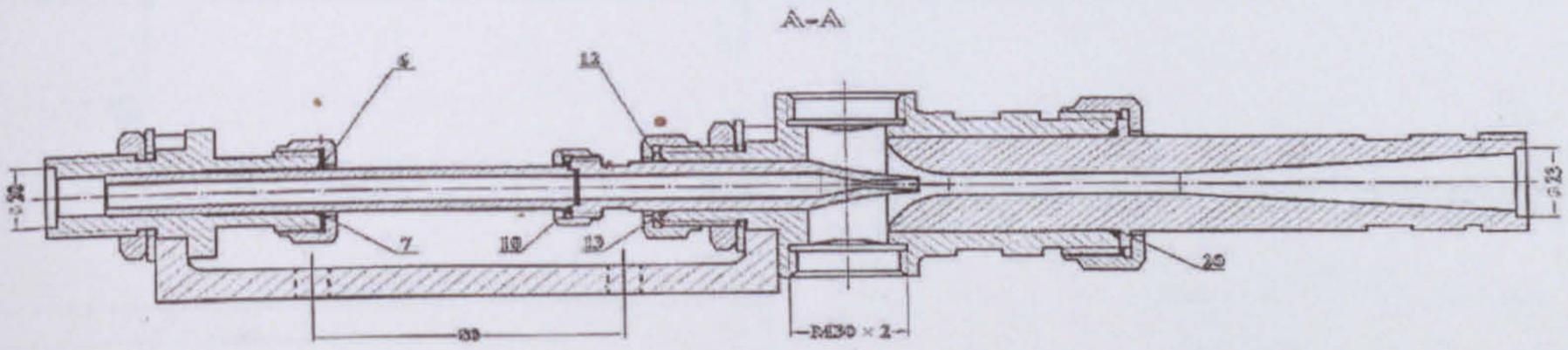

Figure 5. 8 Schematic diagram of jet-pump Assembly

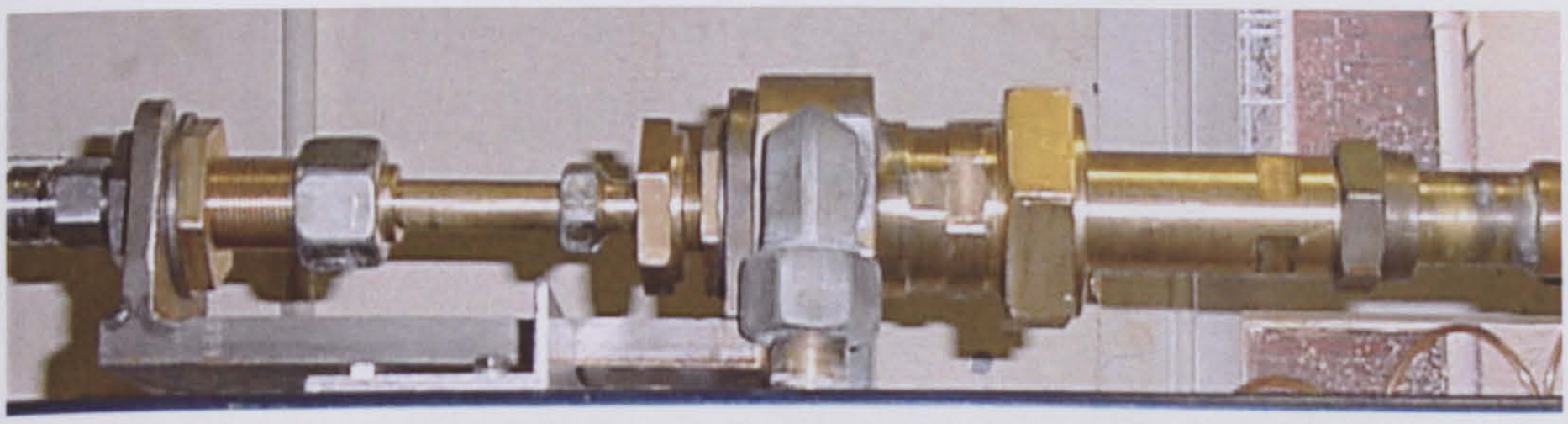

Figure 5. 9 Photograph of Jet-pump Assembly

5.2.7.1 Cutting Tools for R236fa Conventional Jet-pump

All diffusers were manufactured in one piece that could be fitted directly into the suction chamber by using screw and nut. Profiled cutting drilling tools were manufactured for each primary nozzle and diffusers. These were made from suitable carbon steel hardened and tempered. Figure 5.10 shows the details of the profiled cutting tools for the conventional R236fa jet-pump.

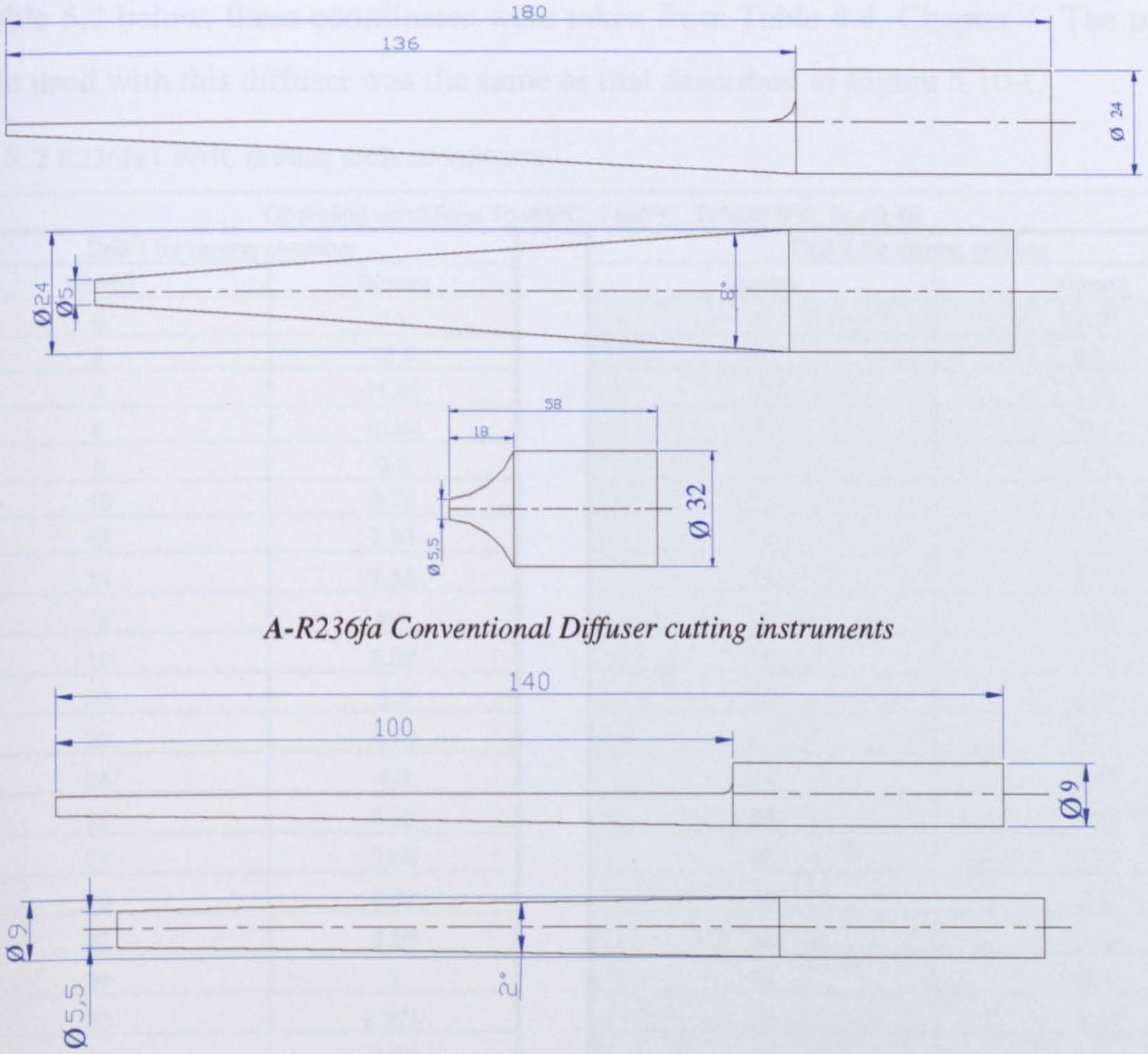

A-R236fa Conventional Diffuser cutting instruments

B-R236fa optimized Conventional Diffuser cutting instruments

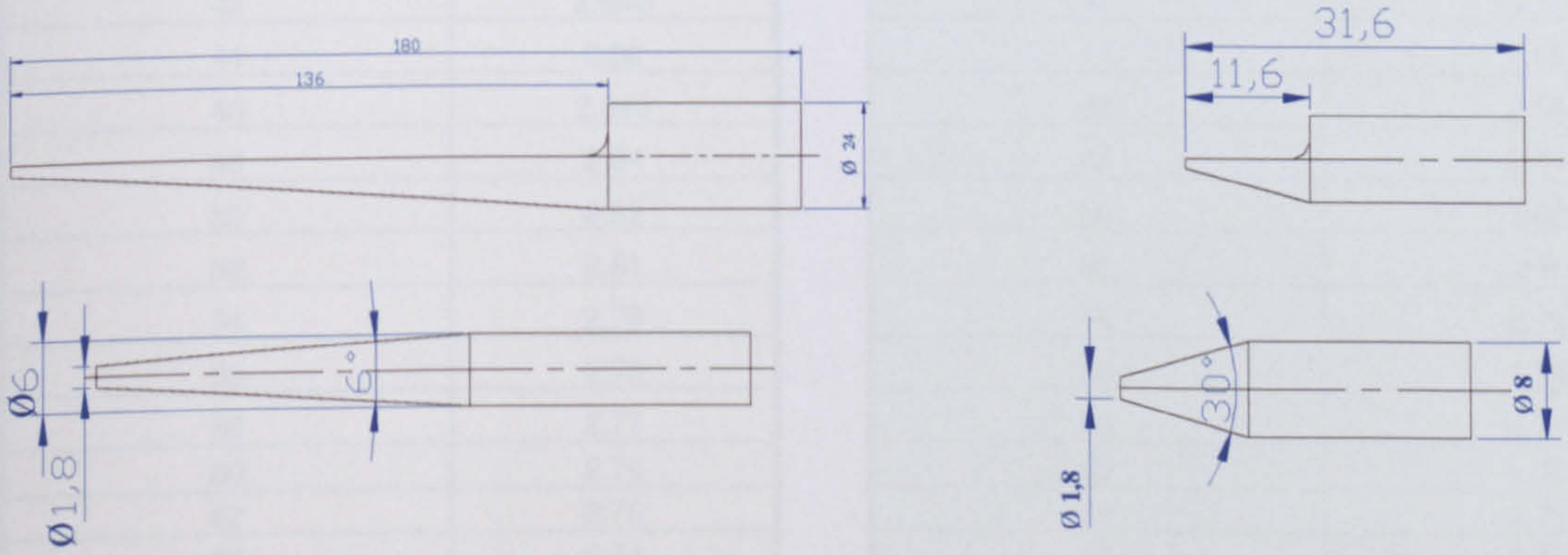

C-R236fa Primary nozzle cutting tool

Figure 5. 10 R236fa conventional jet-pump cutting tools

5.2.7.2 Cutting Tools for Optimized R236fa CRMC Jet-pump

Table 4.4 lists the co-ordinates for the CRMC diffuser. Two profile cutting tools were manufactured. One designed for drilling the mixing section of the diffuser and the second for the subsonic section. The end dimensions of both tools were designed for drilling the throat of the diffuser. Figure 5.11 shows CRMC drilling tools. The coordinates of R236fa CRMC, i.e. the CRMC cutting tools (CRMC drill1& CRMC drill 2), are listed in Table 5.2 below, these coordinates were taken from Table 4.4, Chapter 4. The primary nozzle used with this diffuser was the same as that described in Figure 5.10-C.

Table 5. 2 R236fa CRMC drilling tools coordinates

Operating conditions Tg=85°C, Te=8°C, Tc*=29.5°C, R_m=0.46			
Drill 1 for mixing chamber		Drill 2 for mixing diffuser	
X(mm)	R(mm)	X(mm)	R(mm)
0	14	0	8.1
2	12.8	2	6.75
4	11.65	4	5.95
6	10.64	6	5.3
8	9.6	8	4.9
10	8.75	10	4.65
12	7.93	12	4.4
14	7.15	14	4.18
16	6.4	16	3.95
18	5.82	18	3.82
20	5.3	20	3.68
22	4.75	22	3.57
24	4.3	24	3.45
26	3.92	26	3.37
28	3.58	28	3.28
30	3.32	30	3.2
32	3.08	32	3.15
34	3	34	3.1
36	2.975	36	3.04
38	2.95	38	2.99
40	2.92	40	2.95
42	2.895	42	2.9
44	2.88	44	2.88
46	2.845	46	2.86
48	2.84	48	2.84
50	2.82	50	2.82
52	2.81	52	2.8
54	2.79	54	2.79
56	2.78	56	2.78
58	2.77	58	2.77
60	2.76	60	2.76
62	2.75	62	2.75
64	2.74	64	2.74
66	2.72	66	2.72
68	2.7	68	2.7

I-R236fa CRMC drill 1

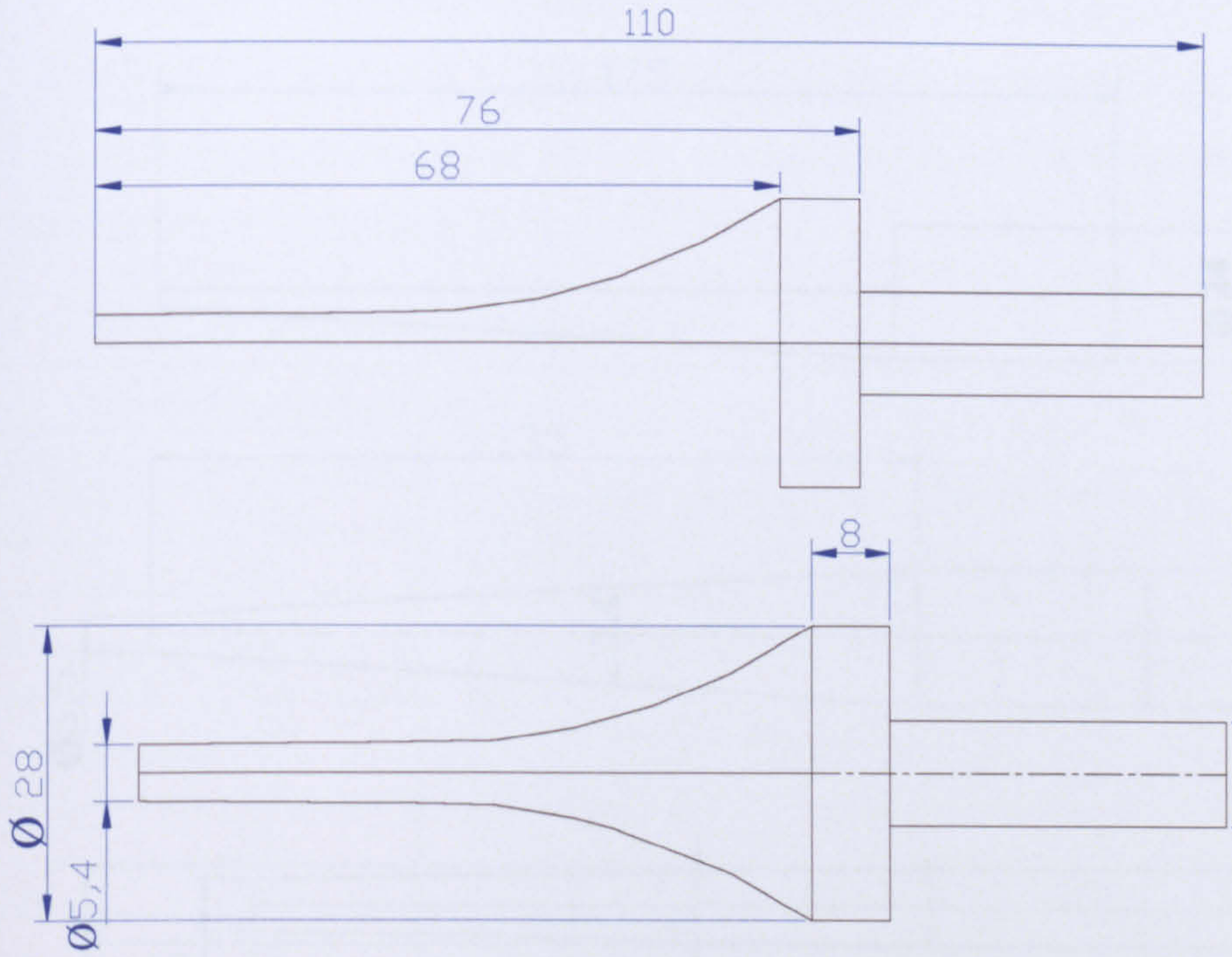

II-R236fa CRMC drill 2

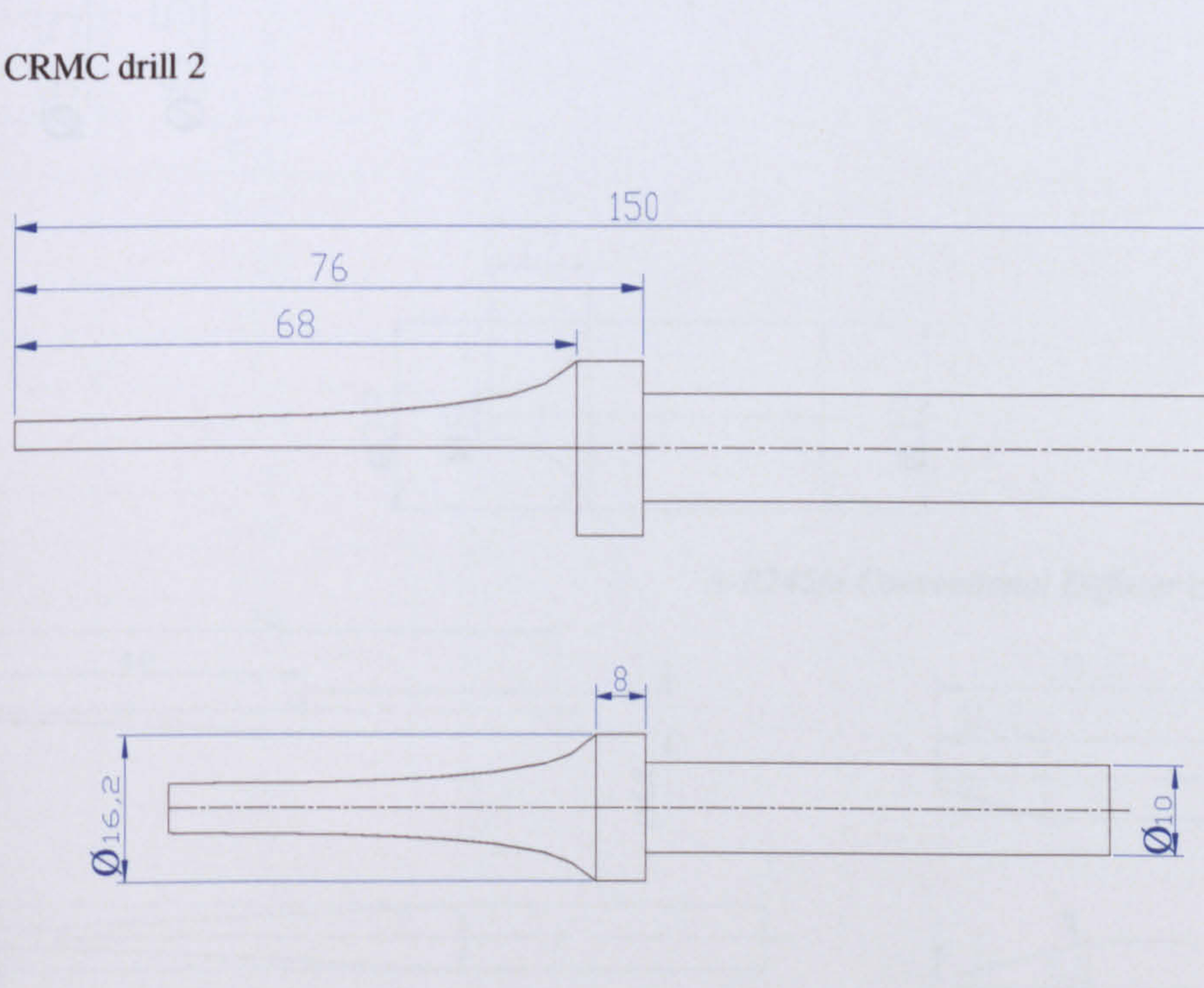

All dimensions in mm drawing scale 1:1

Figure 5. 11 CRMC drilling tools (I for the mixing chamber & II for the diffuser)

5.2.7.3 Cutting Tools for Optimized R245fa Conventional Jet-pump (Diffuser and primary nozzle)

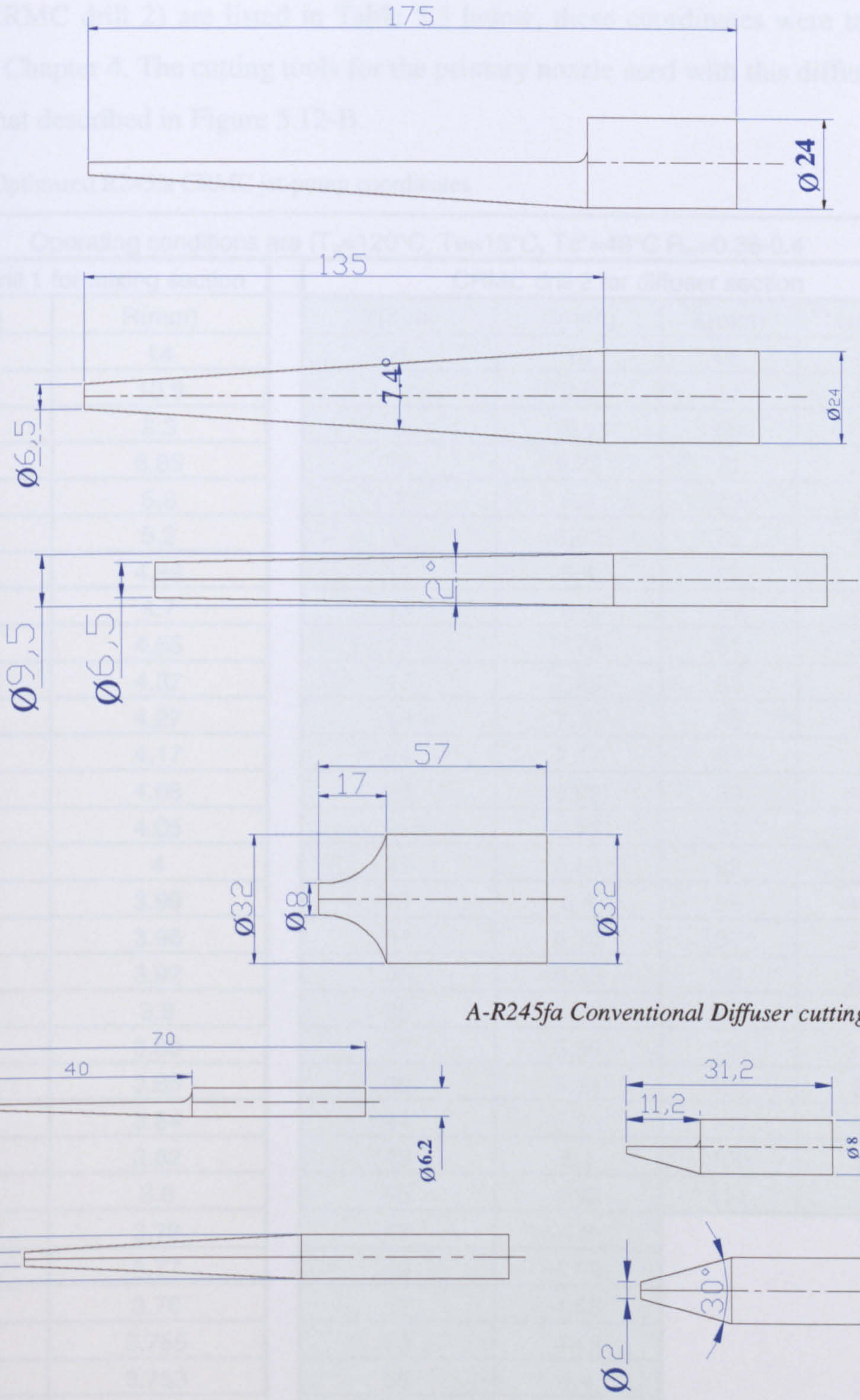

A-R245fa Conventional Diffuser cutting instrument

B-R245fa Primary nozzle cutting tool

Figure 5. 12 R245fa Conventional Experimental nozzle and diffuser cutting instruments

5.2.7.4 Cutting Tools for the Optimized CRMC R245fa Jet-pump

The coordinates of CRMC R245fa diffuser, i.e. the CRMC cutting tools (CRMC drill1& CRMC drill 2) are listed in Table 5.3 below, these coordinates were taken from Table 4.7 Chapter 4. The cutting tools for the primary nozzle used with this diffuser are the same as that described in Figure 5.12-B.

Table 5. 3 Optimized R245fa CRMC jet-pump coordinates

Operating conditions are (T_g=120°C, Te=15°C, Tc*=48°C R_m=0.36-0.4				
CRMC drill 1 for mixing section		CRMC drill 2 for diffuser section		
X(mm)	R(mm)	X(mm)	R(mm)	X(mm)	R(mm)
0	14	0	10	65	4.13
2	10.6	1	9.8	67	4.08
4	8.3	3	9.5	69	4.03
6	6.85	5	9.22	71	3.98
8	5.8	7	8.9	73	3.95
10	5.2	9	8.65	75	3.92
12	4.89	11	8.4	77	3.9
14	4.7	13	8.1	79	3.88
16	4.55	15	7.78	81	3.86
18	4.37	17	7.55	83	3.84
20	4.27	19	7.36	85	3.81
22	4.17	21	7.17	87	3.8
24	4.08	23	6.92	89	3.782
26	4.05	25	6.73	91	3.776
28	4	27	6.58	93	3.77
30	3.99	29	6.4	95	3.765
32	3.96	31	6.16	97	3.758
34	3.92	33	5.95	99	3.755
36	3.9	35	5.73	101	3.752
38	3.88	37	5.59	103	3.751
40	3.85	39	5.34	105	3.75
42	3.84	41	5.22	107	3.74
44	3.82	43	5.1	109	3.72
46	3.8	45	4.92	111	3.7
48	3.78	47	4.8		
50	3.77	49	4.69		
52	3.76	51	4.58		
54	3.755	53	4.48		
56	3.753	55	4.4		
58	3.75	57	4.34		
60	3.74	59	4.28		
62	3.72	61	4.23		
64	3.7	63	4.18		

I-R245fa CRMC Drill 1

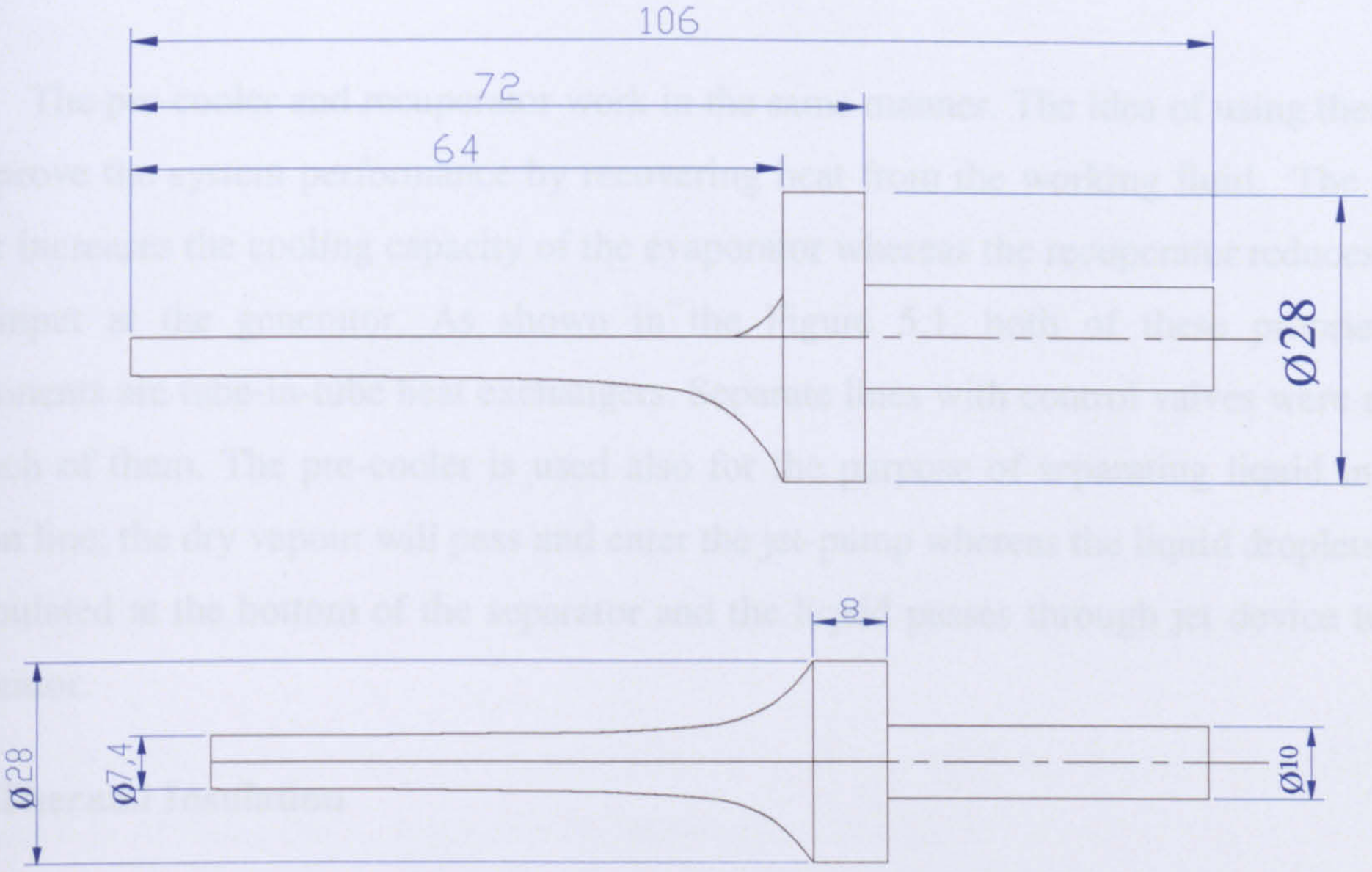

II-R245fa CRMC drill 2

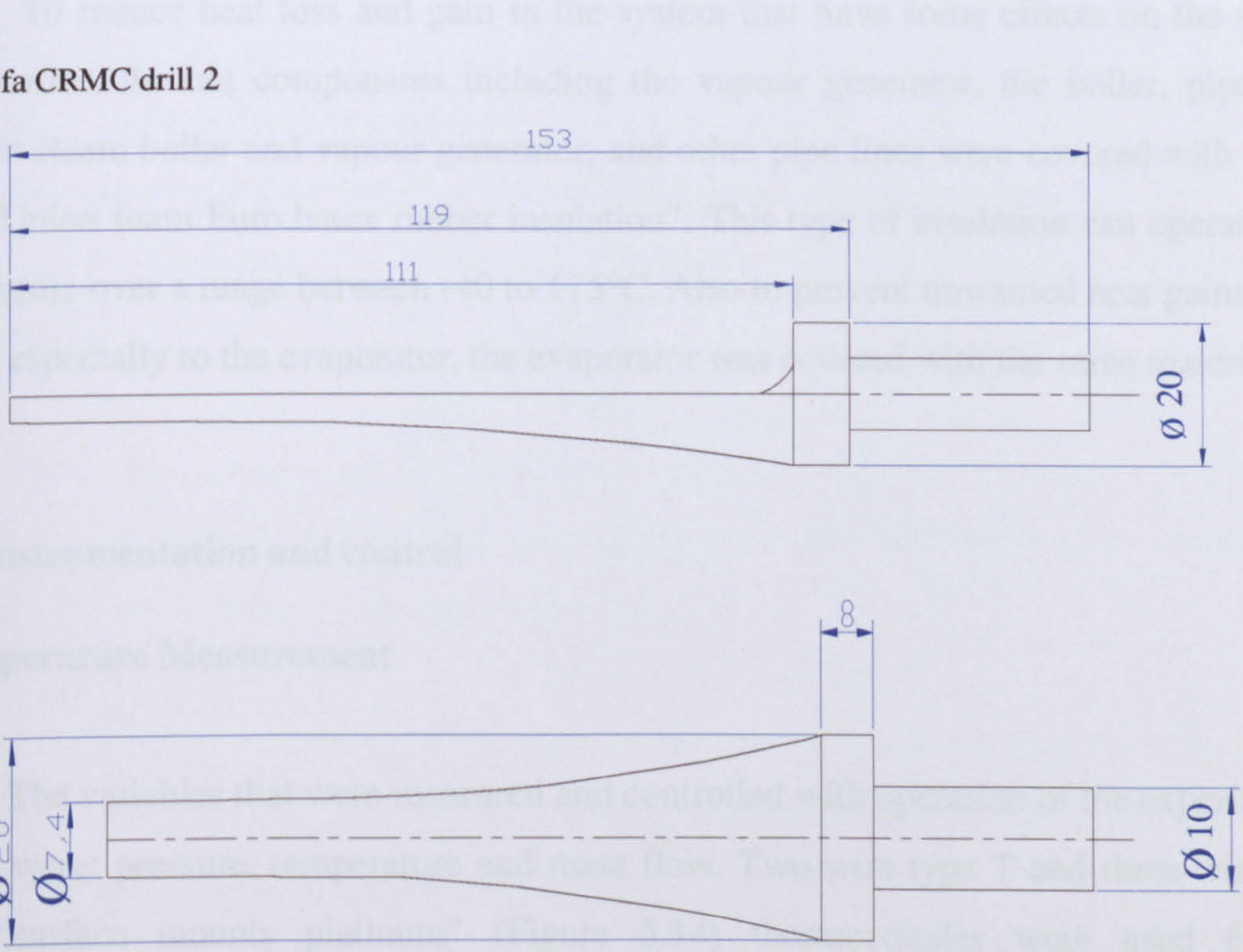

All dimensions in mm drawing scale 1:1

Figure 5. 13 R245fa CRMC diffuser cutting tools

(I for the mixing chamber & II for the diffuser)

5.3 Other Components

5.3.1 The Pre-Cooler and the Recuperator

The pre-cooler and recuperator work in the same manner. The idea of using them is to improve the system performance by recovering heat from the working fluid. The pre-cooler increases the cooling capacity of the evaporator whereas the recuperator reduces the heat input at the generator. As shown in the Figure 5.1, both of these proprietary components are tube-in-tube heat exchangers. Separate lines with control valves were used for each of them. The pre-cooler is used also for the purpose of separating liquid in the suction line; the dry vapour will pass and enter the jet-pump whereas the liquid droplets are accumulated at the bottom of the separator and the liquid passes through jet device to an evaporator.

5.3.2 Thermal Insulation

To reduce heat loss and gain in the system that have some effects on the system performance, the hot components including the vapour generator, the boiler, pipe lines between steam boiler and vapour generator, and other pipe lines were covered with 13mm thick "Union foam Euro batex rubber insulation". This type of insulation can operate with temperature over a range between -40 to 175°C. Also to prevent unwanted heat gains to the system especially to the evaporator, the evaporator was covered with the same material.

5.3.3 Instrumentation and control

- **Temperature Measurement**

The variables that were measured and controlled with operation of the experimental system were: pressure, temperature and mass flow. Two-wire type T and three-wire type RTD "surface mounts platinum" (Figure 5.14) thermocouples were used for the temperature measurement. The T type was used for measuring the water flow temperature at condenser, evaporator and sub-cooler. Also this type was used for measuring steam generator temperature at inlet and outlet. Two types of RTD thermocouple were used "SRTD-1 & SRTD-2" to measuring the refrigerant's temperature at locations shown in the Figure 5.1, (these types are ideal for surface temperature measurements and can provide

precise data with less error (SRTD-1 ±0.5& SRTD-2 ±0.25°C). All thermocouples were connected to a DT-800 data logger from which the collected data was displayed on a computer screen so that the temperature reading could be constantly monitored.

Figure 5. 14 RTD thermocouples

- **Pressure Measurement**

Different scale ranges of direct-reading pressure gauges with an accuracy of, ± 0.2 kPa were used to measure the pressure at the following locations:

1- Within the boiler exit tube.(max 20 bar-gauge)
2- At the top of the separator, as the entrance for jet-pump primary nozzle.
3- At the evaporator outlet.(scale from -1 to 1 bar- gauge)
4- At the entrance of the condenser from diffuser.(maximum 6 bar-gauge)
5- Within the discharge pipe of the feed pump (the generator feed pump (maximum 40 bar-gauge).

However, the primary pressure of motive stream, the evaporator (entrained stream) and the condenser (diffuser discharge pressure) pressure was monitored and controlled by adjusting the boiler temperature and water flow.

The pressure in these gauges was monitored directly at all times of the test, and the measured values were related to the recorded temperatures to avoid errors in reading especially when superheating, was anticipated.

- **Flow Measurement**

A Model MT 3809 flow meter (Figure 5.15) with flange connection was used for measuring primary mass flow and a Model MT 1355 (Figure 5.16) was used to measure secondary mass flow.

Figure 5.15 Primary stream flow meters

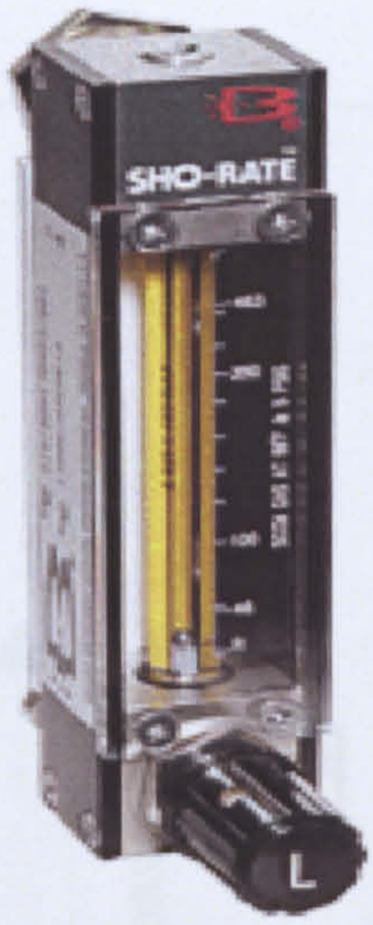

Figure 5. 16 Secondary stream flow meters

In order to calibrate both the primary and secondary flow meters, the experimental rig was modified by connecting another test receiver for calibration purpose. Figure 5.17 a & b show a photo and schematic diagram of the calibration loop.

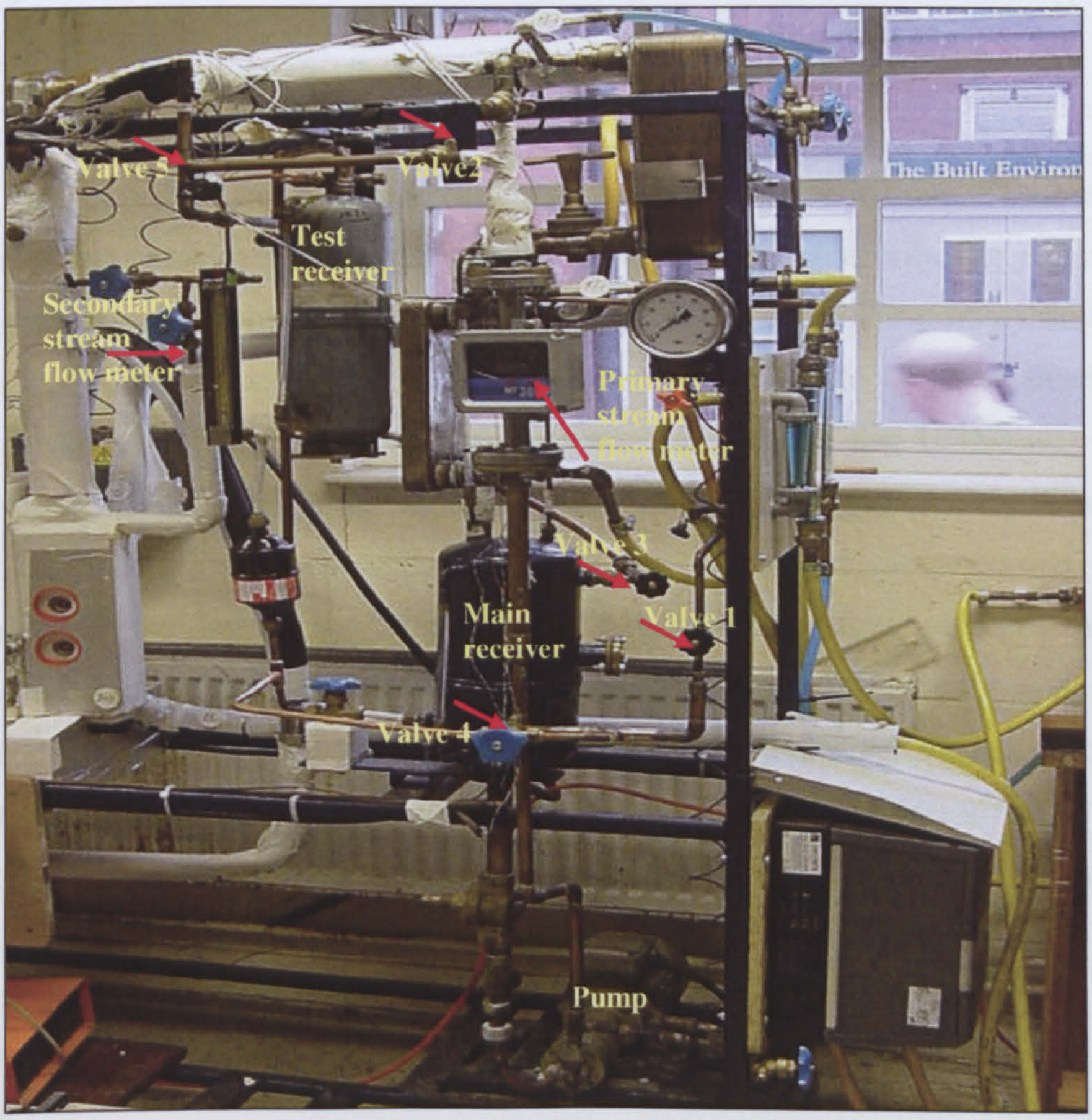

Figure 5. 17a Photograph of Experimental calibration rig

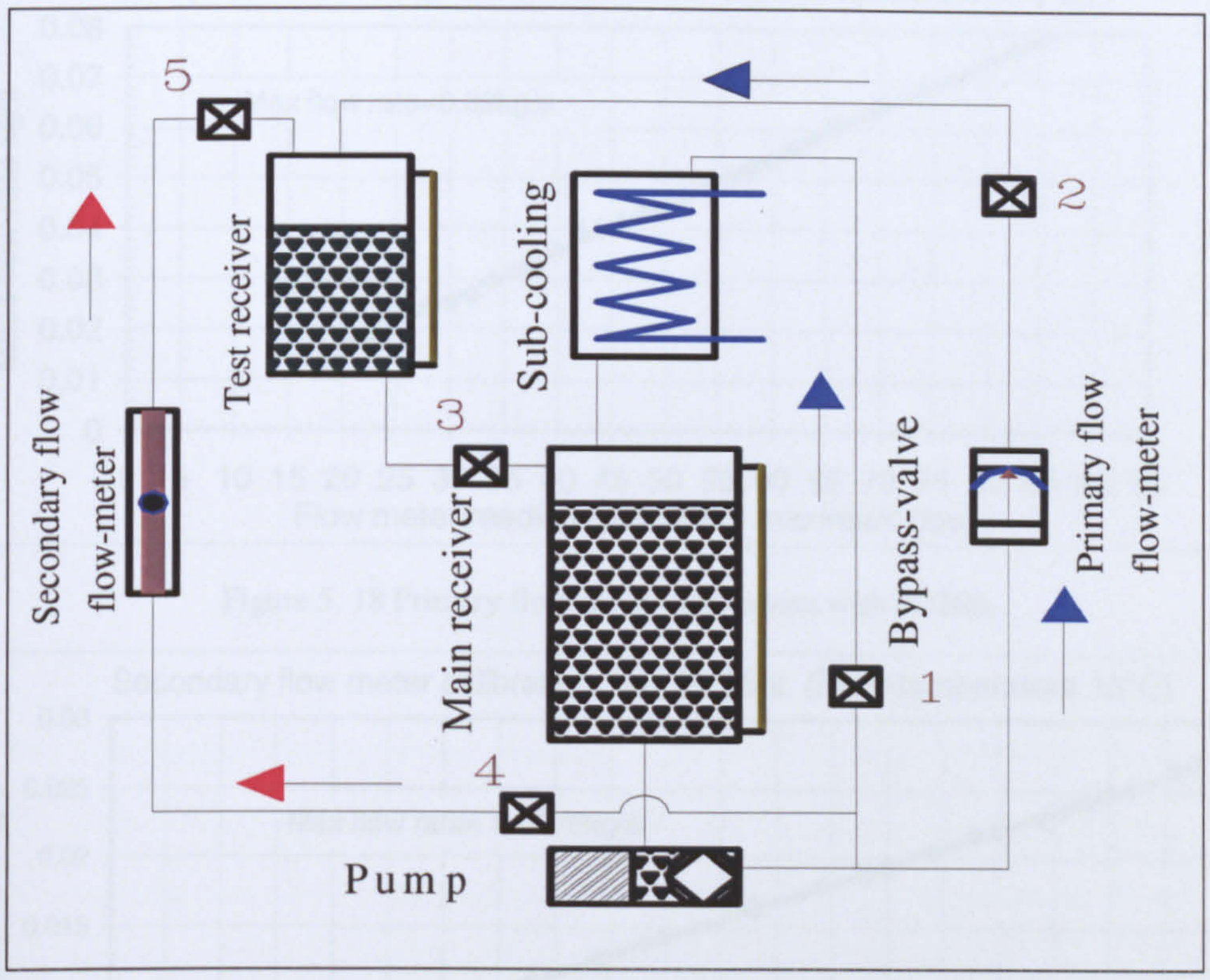

Figure 5. 17b Schematic diagram of the Calibration loop

Referring to Figure 5.17b the calibration process was carried out as follows: each flow meter was connected by a separate loop between the pump and the test receiver and by using the control valves the flow in each loop can be adjusted. For primary flow meter calibration, valves 4 and 5 were closed whereas 2 and 3 were open; at steady state condition valve 3 was closed and the flow rate was adjusted by valve 1. This was used as bypass valve between the pump and the main receiver. For the secondary flow meter calibration, valve 2 was closed, whilst 3, 4 and 5 were opened. For measurements, valve 3 was closed and the flow rate adjusted by valve 1. In both cases flow measurements were taken by measuring the height of the accumulated liquid in the test receiver over specific intervals of time. By knowing the internal diameter of the test receiver, its volume capacity was calculated. The calibration test was repeated many times over different ranges of flow meter reading. The obtained results with using R236fa and R245fa are shown below in Figures 5.18 to 5.21, for both flow meters. The temperature of the liquid was fixed at 15°C with R236fa test and 14 °C with R245fa test.

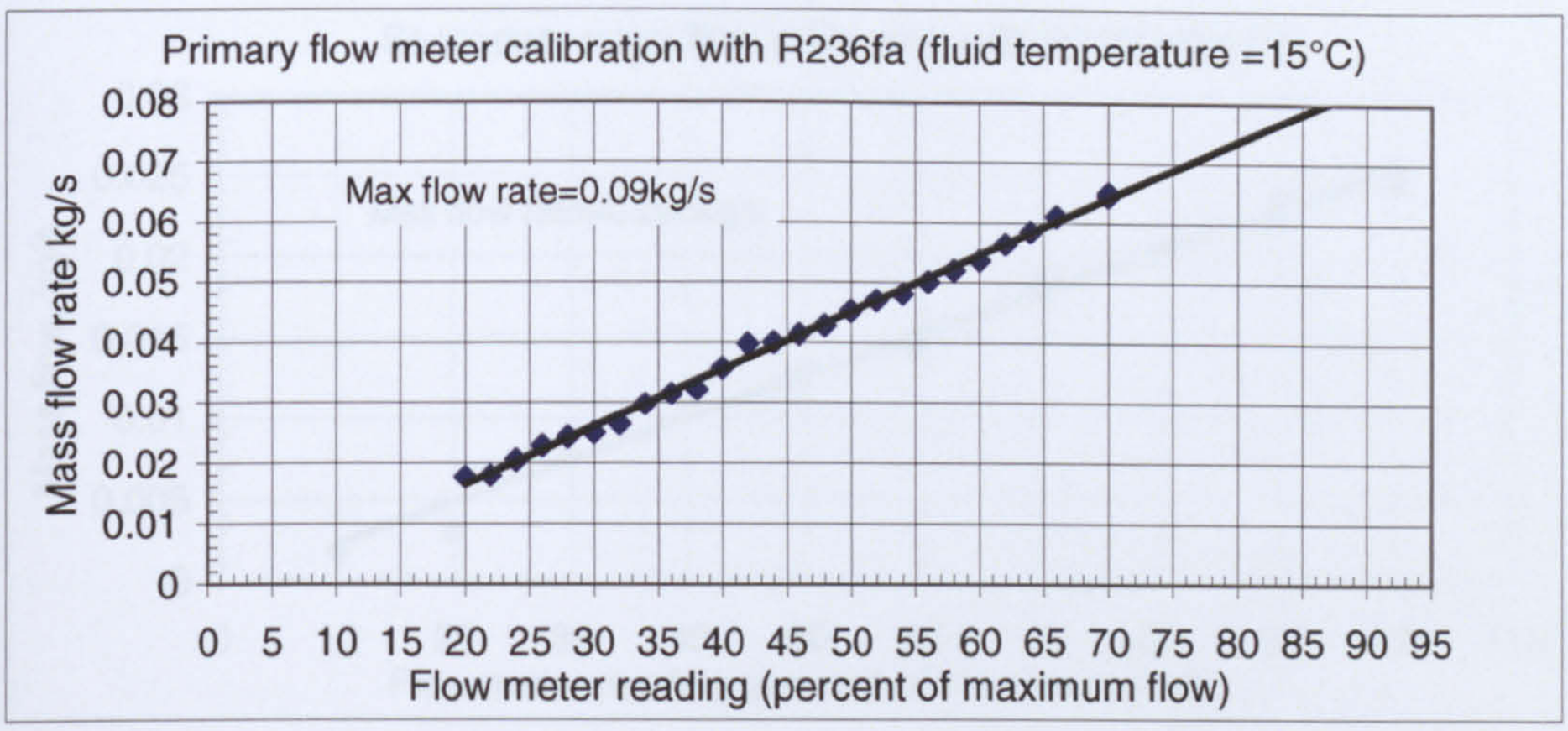

Figure 5. 18 Primary flow meter calibrations with R236fa

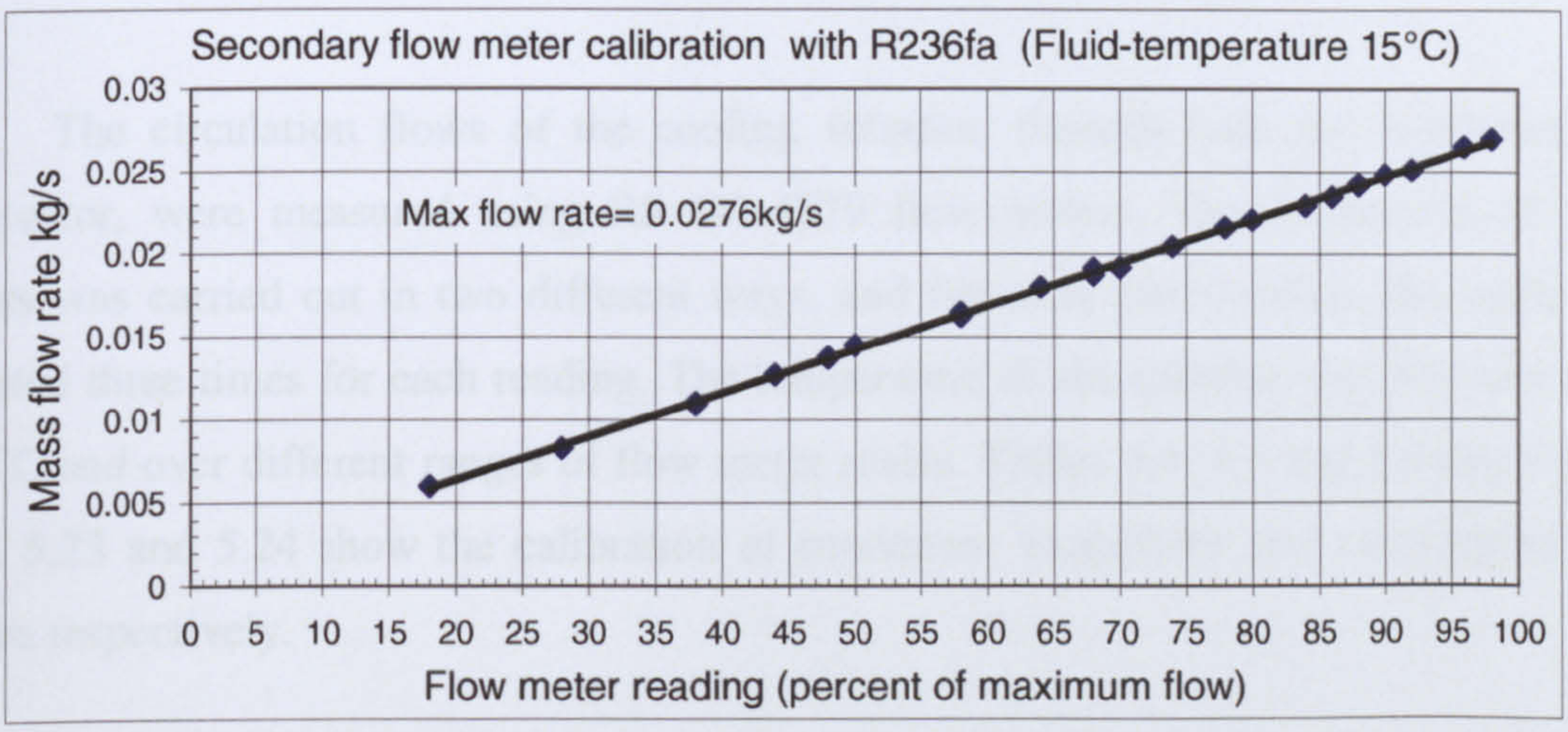

Figure 5. 19 Secondary flow meter calibration with R236fa

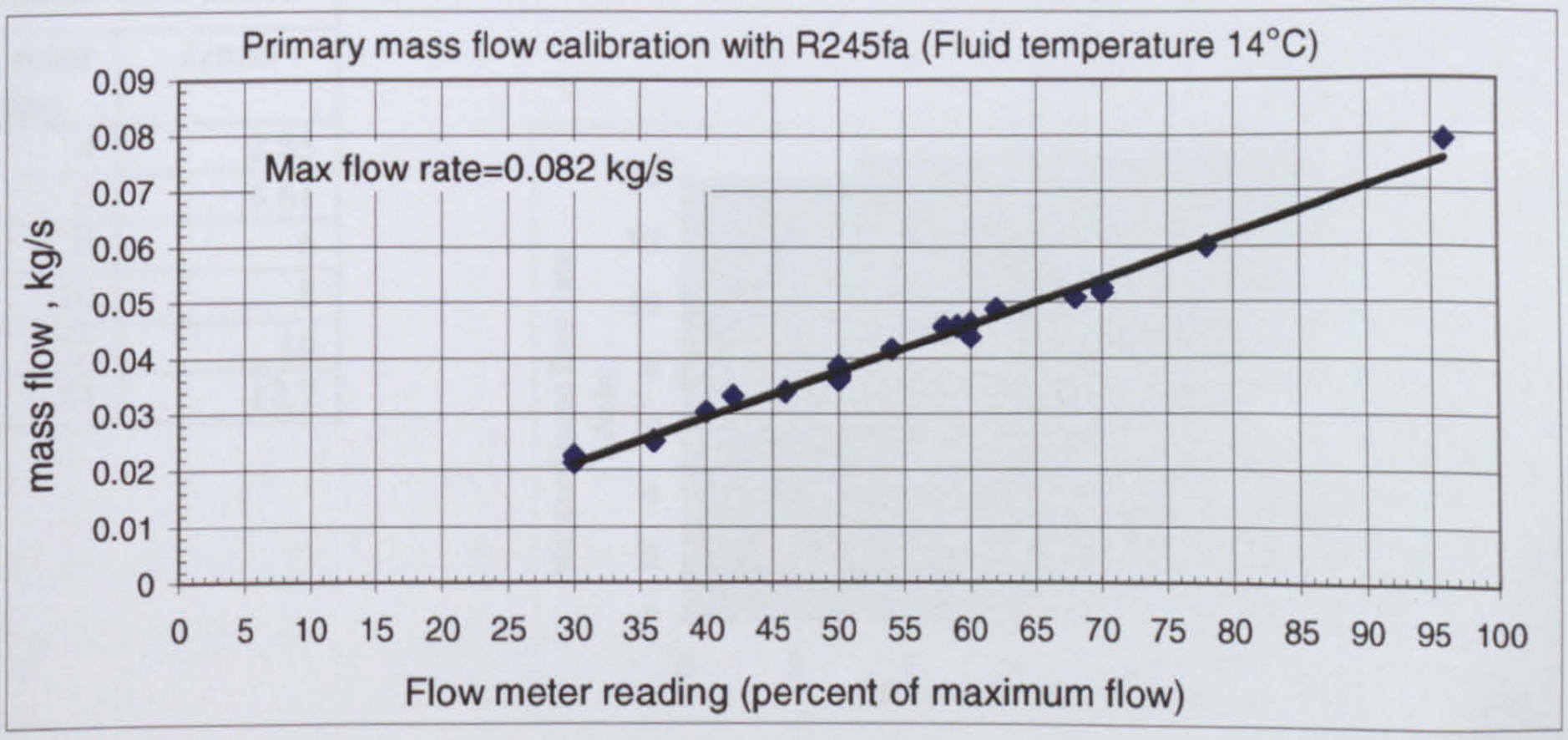

Figure 5.20 Primary flow meter calibration with R245fa

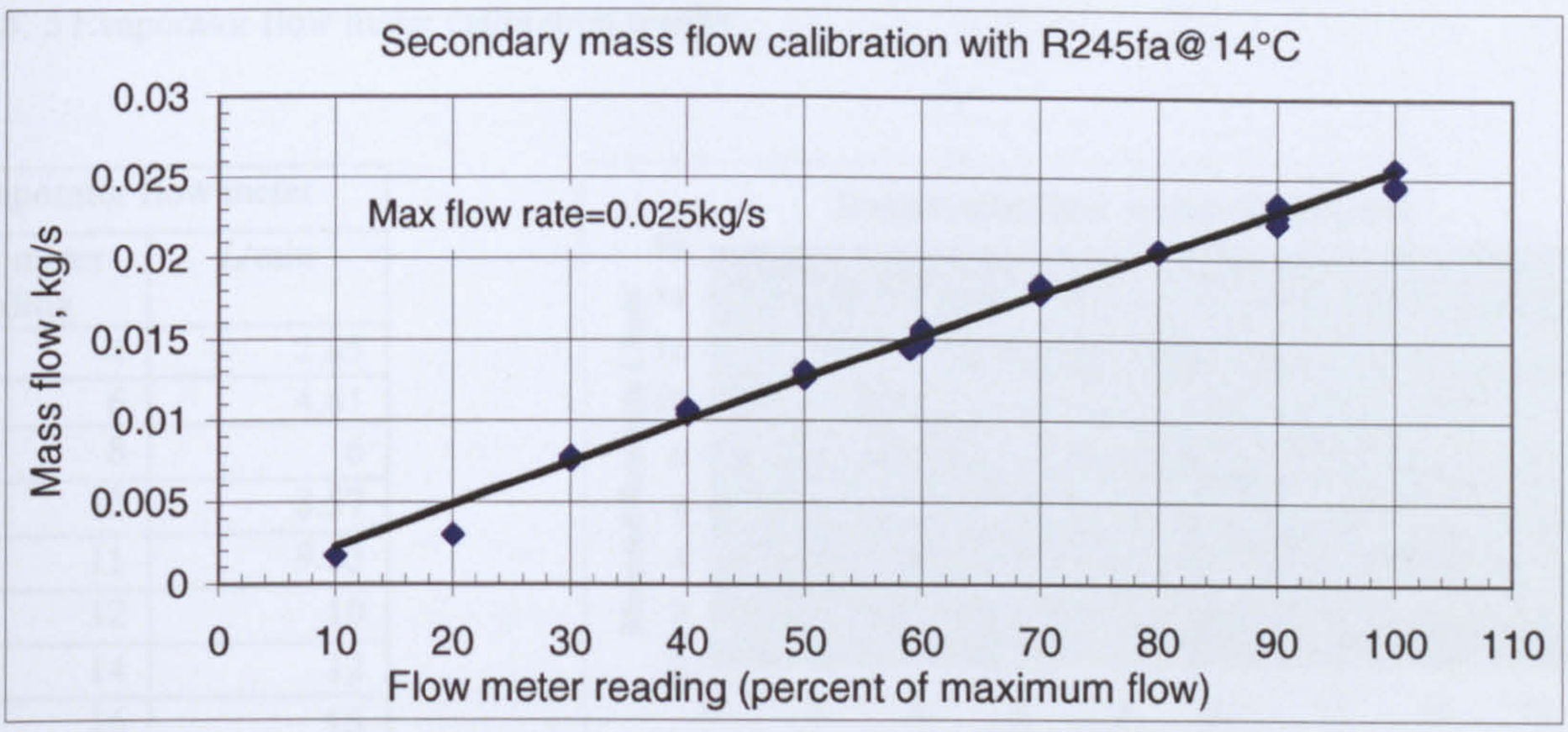

Figure 5. 21 Secondary flow meter calibration with R245fa

The circulation flows of the cooling solution, through both the condenser and evaporator, were measured using RS-441-4879 flow meters. The calibration of these meters was carried out in two different ways, and for more precise data, the calibration repeated three times for each reading. The temperature of the solution was between 13.5-14.5°C and over different ranges of flow meter scales. Tables 5.4, 5.5 and 5.6 and Figures 5.22, 5.23 and 5.24 show the calibration of condenser, evaporator and sub-cooling flow meters respectively.

Table 5. 4 Condenser flow meter calibration results

Condenser flow meter	
Flow meter reading	*L*/min
4	2.85
6	4.61
8	6
10	8
12	10
14	12.7

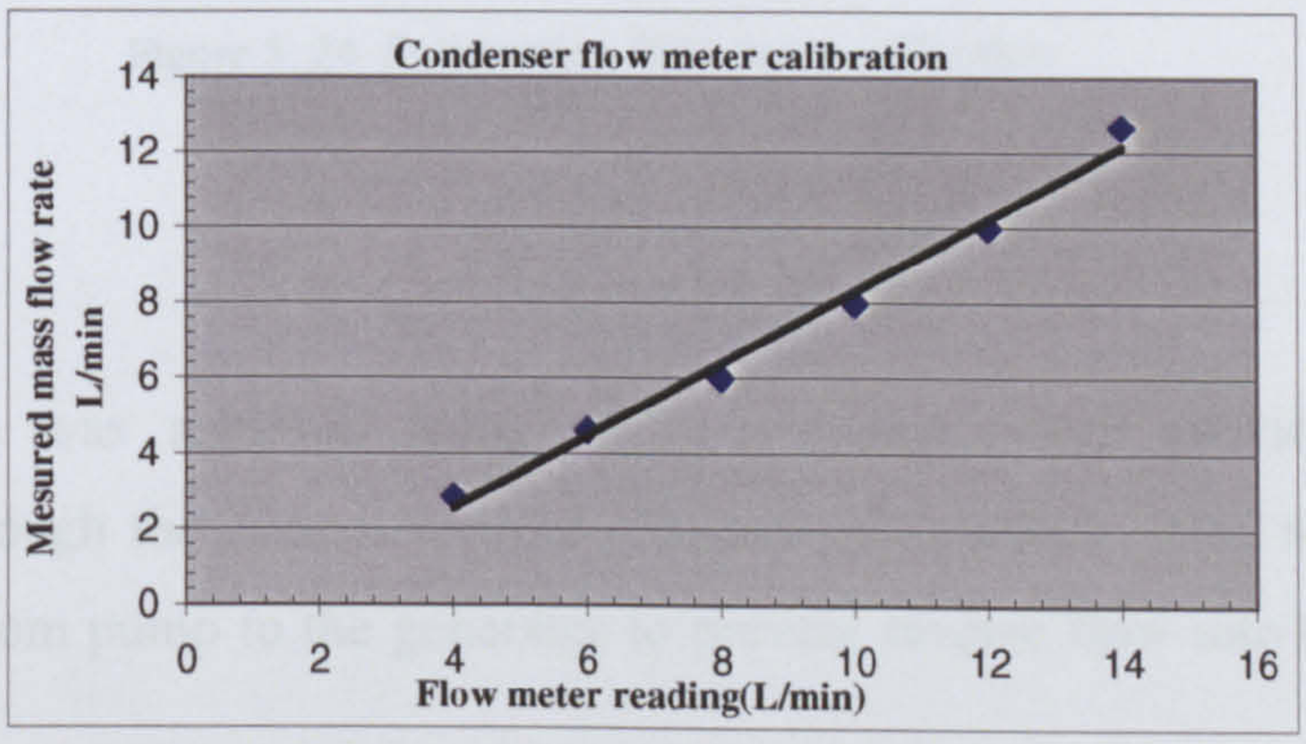

Figure 5. 22 Condenser flow meter calibration

Table 5. 5 Evaporator flow meter calibration results

Evaporator flow meter	
Flow meter reading	*L*/min
4	2.85
6	4.61
8	6
10	8.57
11	9.23
12	10
14	12
16	15

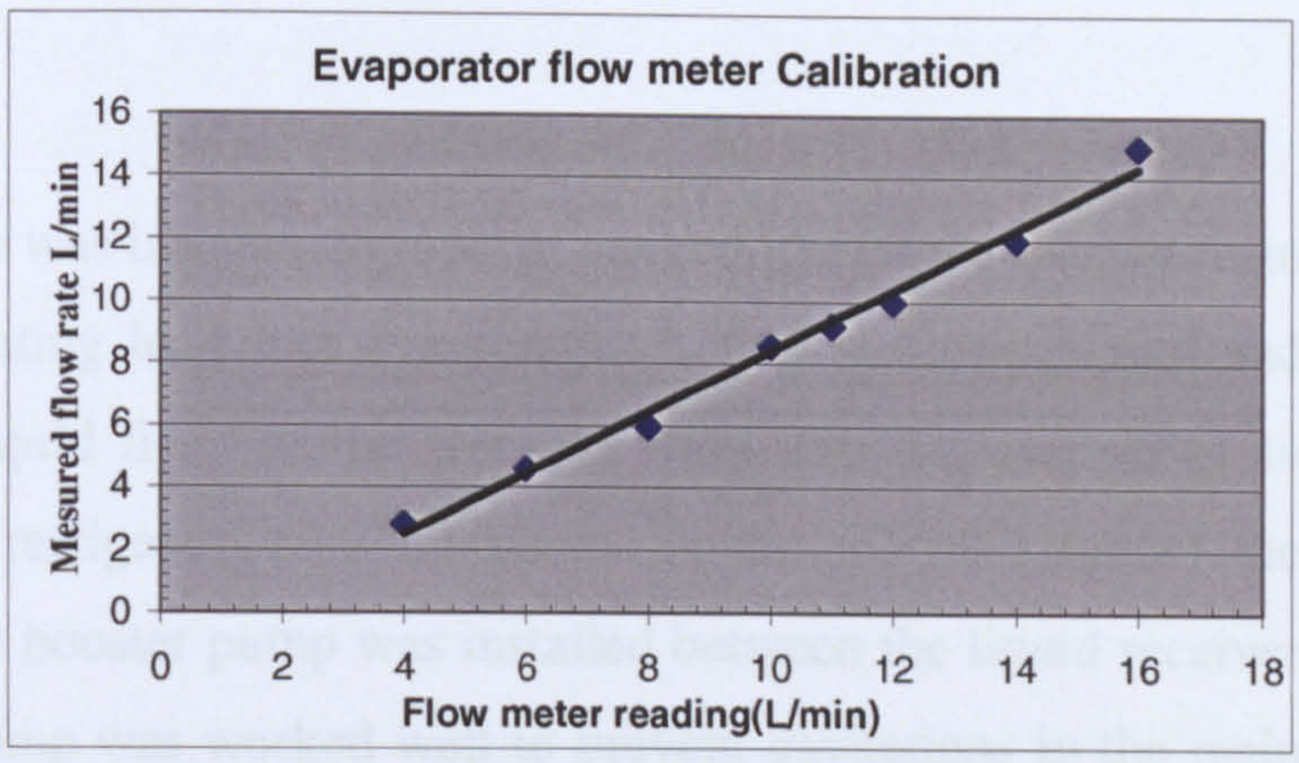

Figure 5. 23 Evaporator flow meter calibrations

Table 5. 6 Sub-cooling flow meter calibration

Sub-cooling flow meter	
Flow meter reading	*L*/min
0.4	1.728
0.6	3
0.8	4.17
0.9	4.65
1	5.61

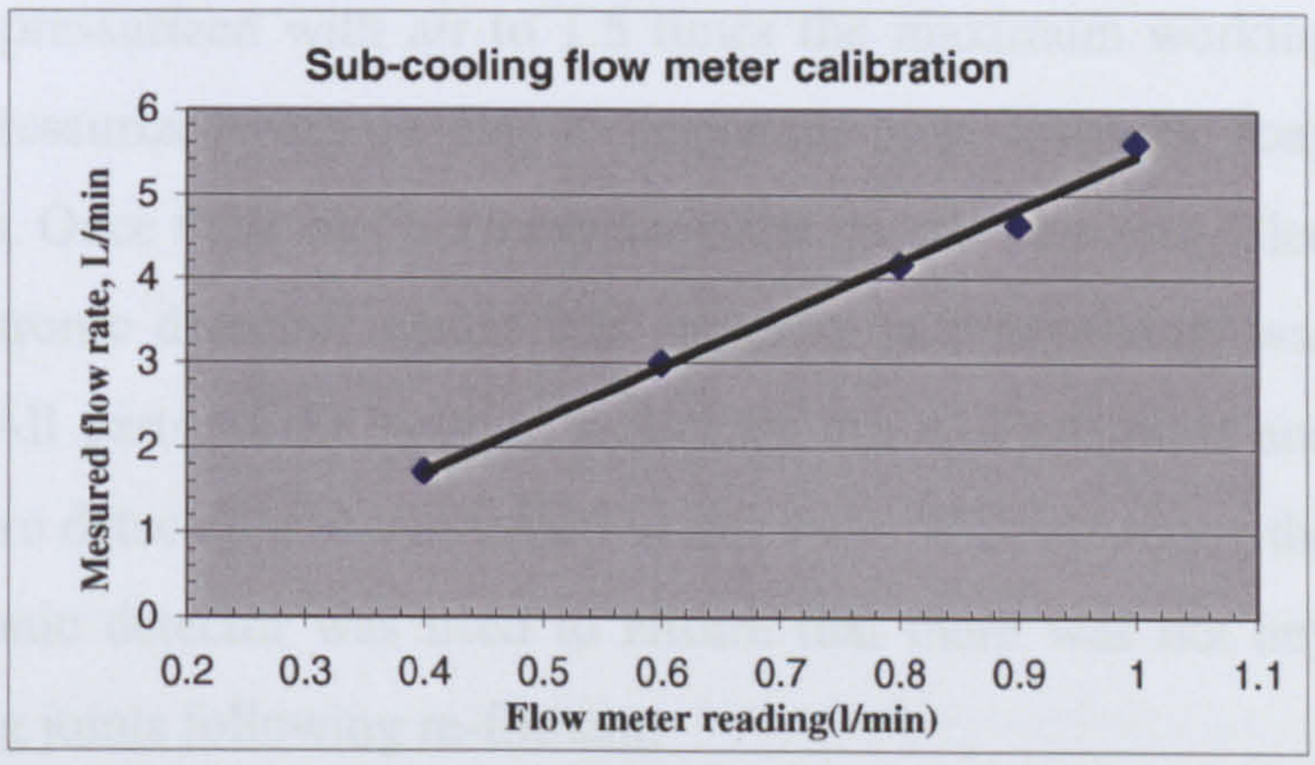

Figure 5. 24 Sub-cooling flow meter calibration

- **System Control**

Control of the system was achieved using shut-off valves, which provided sufficient control of flows, through the system sections. An automatic check valve was used in the feed line coming from pump to the generator to prevent reverse flow into the pump.

Automatic control of the boiler temperature was used so that the desired temperature in the vapour generator could be obtained. The cooling water to the condenser, evaporator and pre-cooler was supplied from the laboratory's water chillers. Condenser

pressure, evaporator pressure and pre cooler were controlled by adjusting control valves in their respective cooling water circuits.

- **Other Instruments**

An external heat exchanger was installed to recover some of the heat absorbed from the condenser to increase the heating load into evaporator. A filter-drier was used and located in the expansion line "liquid line" of the working fluid into the evaporator to reduce the water content of the refrigerant to a minimum. In the second stage of the experimental work with R245fa, a booster pump was installed between the liquid receiver and the feed pump. This small pump was worked well to prevent cavitations in the main feed pump.

5.4 Pressure Test and Leak Detection

For safety reasons after initial assembly of the system, all pressure vessels were first filled with water and then pressurized with air to 1.5 times the maximum working pressure. Then the system was pressurized with air only to determine large leakages, soap suds were used to detect leakages. Once these had been repaired, the system then was filled with R134a vapour and an electronic detector, which was sensitive to refrigerants, was used to detect minor leakages. All parts of the system, especially the welded joints and seals were checked. All leaks were detected and eliminated in this way. With changing the jet-pump by another, the electronic detector was used to ensure that there was not any leakage in all the jet-pump sealing joints following re-fitment.

5.5 Commissioning of the Experimental Rig

The system was charged with R134a for commissioning purposes. Before doing so, the system was evacuated totally by using a vacuum pump and then charged with the refrigerants R134a. Leak detection was repeated. R134a used also to satisfy the maximum working pressure that the generator pump could provide. The steam boiler was evacuated, to be ready for preliminary test, filled to a level with water and then it was switched on. The condenser cooling water was turned on and the circulation pump was activated, controlling its speed to the optimal range. When the pressure inside the generator reached a specific operating value and it was filled with refrigerant, the control valve downstream of the generator was opened and the rig was run continuously for two hours in a stable

condition. When steady state was observed: the level of refrigerant inside the receiver remained constant according to the flow meter reading. Initially, in order to test primary flow circuit and condenser operation, the secondary flow line was closed. Then the secondary flow line was opened to observe the entrainment process. Sight glasses upstream of the evaporator were used to observe the evaporation of the refrigerant, which shown clearly the evaporating process. At the same time both primary and secondary stream flow meters were checked, readings were taken without any fluctuation. All refrigerant pressure gauges reading were evaluated by comparing them to the relevant saturation temperature measurements at different operating conditions. When the rig was running in steady state for long periods all measurement instruments were checked for errors, which was reduced. The rig was then discharged of R134a and recharged with R236fa.

5.6 Heat Balance Test

In order to verify the consistency of the experimental results and that the data collected from the experimental rig were correct, independent evaluation of system heat balance was carried out with each R236fa jet-pump. Heat transfer rates were measured for both refrigerant and cooling medium. The heat transmitted and absorbed by the coolant fluids was determined by knowing the inlet and outlet flow temperatures and mass flows. Then the balance deviations were obtained for each component from which the global energy balance was determined, to make sure that total energy input to the system is equal to the total energy output. Table 5.7a, b, and c list sample data for heat balance tests carried out with the optimized conventional R236fa jet-pump.

Table 5. 7a Heat input and output (condenser and evaporator)

Conventional β=1.36, Tg=85°C		Condenser			Evaporator		
	19.07.04	R236fa	water	difference	R236fa	water	difference
Te	Time	Qc1 KW	Qc2 KW	Qc1-Qc2	Qe1 KW	Qe2 KW	Qe1-Qe2
8	14:12	5.777	6.087	-0.3103	1.875	1.633	0.241
8	14:14	5.828	5.908	-0.0796	1.915	2.064	-0.148
8	14:16	5.828	5.882	-0.05376	1.922	2.135	-0.213
8	14:19	5.911	5.695	0.21589	1.883	2.086	-0.202
8	14:20	6.010	5.232	0.77802	1.939	1.909	0.0299
8	14:22	5.991	5.472	0.51847	1.947	3.002	-1.054
8	14:24	5.831	5.432	0.39915	1.936	1.979	-0.043

Table 5. 7b Heat input and output (sub cooling and generator)

Conventional β=1.36, Tg=85°C		sub-cooler			Generator		
	19.07.04	R236fa	water	difference	R236fa	steam	difference
Te	Time	Qsc1 KW	Qsc2 KW	Qsc1-Qsc2	Qg1 KW	Qg2 KW	Qge-Qg1
8	14:12	0.605	0.762	-0.157	4.430	4.8	0.369
8	14:14	0.599	0.370	0.229	4.402	4.8	0.397
8	14:16	0.592	0.358	0.233	4.384	4.8	0.415
8	14:19	0.609	0.471	0.137	4.525	4.8	0.274
8	14:20	0.598	0.850	-0.252	4.544	4.8	0.255
8	14:22	0.598	0.711	-0.112	4.517	4.8	0.282
8	14:24	0.561	0.728	-0.167	4.350	4.8	0.449

Table 5. 7c Total heat input and output (refrigeration side)

The global heat input and output for the refrigerant " R236fa" side Optimized R236fa conventional Jet-pump Tg=85°C								
	19.07.04	R236fa	R236fa	R236fa	R236fa	heat input	heat output	
Te	Time	Qg1 KW	Qe1 KW	Qc1 KW	Qsc1 KW	Qg1+Qe1 kW	Qc1 +Qsc kW	% difference
8	14:12	4.430	1.875	5.777	0.605	6.305	6.382	0.0764
8	14:14	4.402	1.915	5.828	0.599	6.318	6.428	0.1104
8	14:16	4.384	1.922	5.828	0.592	6.307	6.420	0.1137
8	14:19	4.525	1.883	5.911	0.609	6.409	6.521	0.1118
8	14:20	4.544	1.939	6.010	0.598	6.483	6.609	0.1259
8	14:22	4.517	1.947	5.991	0.598	6.465	6.589	0.1241
8	14:24	4.350	1.936	5.831	0.561	6.287	6.393	0.1059

From the above table it was concluded that the overall accuracy of the experimental results was within ± 8%. Small differences which occur may be due to the uncertainty of measurements and heat losses/gain within the system.

5.7 Experimental Rig Troubleshooting

1. The most severe conditions that faced the test with the experimental rig were finding the feed pump that can work between condenser and generator pressures. However, after examining different types of pumps, the type that was selected and used in the experimental rig had worked adequately in working conditions but with using pre-cooling to avoid cavitations. The first pump worked well in the first stage of experimental work with R236fa. In the second stage of the experimental work with R245fa, the first pump couldn't work properly, and had to be changed. With investigation of the cause of the problem, it was found that, there was blockage in the cleaning filter as it is explained in the next point. It is believed that the first pump could work properly if there is no blockage in the system. The surface of the first pump gears were examined and evaluated by using new high-resolution, silicone-based replicating polymers; the technique gives an exact

copy of the surface which can be removed and examined microscopically in the laboratory [Rollins (2001)]. Figure 5.25 shows 100um scale of a replica taken from one channel in each gear, the replica shows clearly that there is no clear fracture of the surface caused by the fluid.

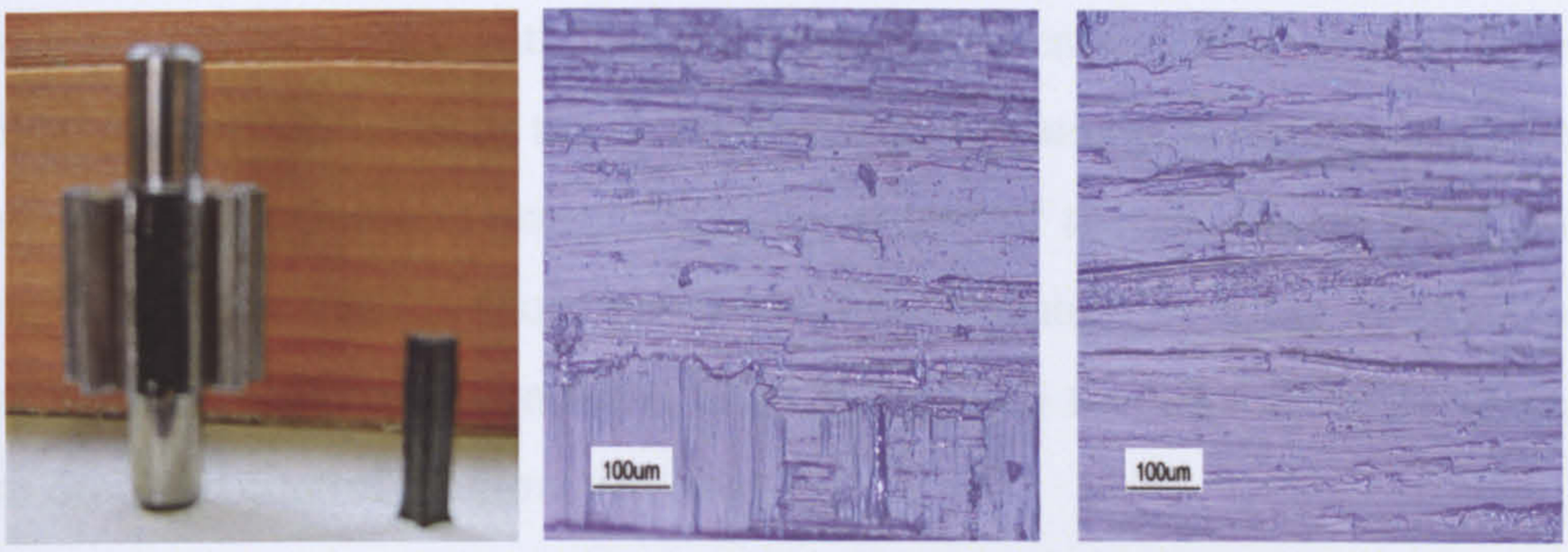

Figure 5. 25 Microscopic replica features of the pump gears surface

2. The second problem that faced the experimental rig was the blockage of the cleanup filter; this made the pump work at very high pressure, approximately double of that of the generator side. At the same time there was not enough fluid reaching the generator. The dust collected from the filter was tested with magnetic bar and it was from magnetic materials as shown in Figure 5.26.

Figure 5. 26 Dust collected from the experimental rig cleanup filter

As some modification of the experimental rig was carried out many times during the test period, some part of this collected dust is believed to be created from the welding of joints, not from the effect of the working fluid. However, cleaning filter and filter drier must be included to permit proper system cleanup and moisture removal.

3. A serious problem that is also considered is that the mixed stream velocity at diffuser exit and entering the condenser may be high which may cause fatigue on the pipe material. However, this velocity was calculated from CFD for all cases and it was in the range of 8 to 10 m/s, and because the pressure and the temperature data obtained from CFD was in good agreement with that obtained experimentally, this range of flow velocity is believed correct, i.e. it seems not to cause effects or damage at the condenser inlet. The back pressure of jet-pump is nearly the same as that of the condenser, provided that the pipe length between them is short; geometrical modification by using different pipe sizes between diffuser outlet and condenser inlet is required to make it easier to match line pressure drop and control the flow velocity.

IV. The pressure losses in suction line may have a direct effect on the amount of secondary flow entrained; it is recommended to route the suction line from the evaporator to the diffuser suction inlet by the shortest path to match the requirements of refrigerant conditions at suction-line with fewer losses.

V. Manual expansion valves were used in the experimental rig between the liquid receiver and the evaporator, and the pressure drop in liquid line was maintained according to the operating conditions without observation of any unusual behaviour; however, in order to provide proper operation throughout the range of operating conditions, an automatic expansion valve should be used to maintain the preferable pressure drop in liquid line.

5.8 Conclusions

- The method of design and construction of the experimental refrigerator have been explained.
- The experimental refrigerator was designed to be simple in operation and control, easy to get access to all parts and easy to change the diffuser without difficulty.
- All jet-pumps were designed to be able to be interchanged and equipped with the test rig easily.
- All main parts used were described and evaluated.
- The specifications of cutting tools used for manufacturing all tested jet-pumps were provided.

- The calibration of the working fluid flow meters based on R236fa and R245fa were shown.
- Details of pressure and leakage tests and Commissioning of the experimental rig were presented.
- The reliability of the experimental results was proved through the provided results of the heat balances tests.
- Experimental rig troubleshooting was evaluated.

Experimental studies based on this presented experimental rig refrigerator are described in the following Chapter.

Chapter 6

Experimental Studies of R236fa and R245fa Jet-pumps

6. Experimental Studies of R236fa and R245fa Jet-pumps

6.1 Introduction

In this chapter, the experimental study of the jet-pump refrigerator system is presented. Three jet-pumps were tested experimentally with R236fa, conventional R236fa (β=1), optimized conventional R236fa (β=1.36) and optimized CRMC R236fa diffusers. The same primary nozzle was used with all of them. Whereas, with R245fa only two diffusers were tested: optimized conventional R245fa (β=1.34), and optimized CRMC R245fa diffusers. Details of geometries of the tested primary nozzles and diffusers were given in Chapter 4. The off-design characteristics of jet-pump are important and difficult to obtain theoretically, so a comprehensive set of tests were carried out to investigate the theoretically designed Conventional R236fa jet-pump configuration and also the two configurations of the R245fa jet-pump. This allowed comparisons of the effect of operating parameters on the performance of the jet-pump system, for fixed jet-pump geometries. The other two R236fa jet-pumps were tested at design operating conditions for generator side and with evaporator temperatures, ranging from 4°C to 12°C. This was to compare the performance of different jet-pump configurations (CRMC geometry with conventional geometry); and also to compare a wide range of experimental results with CFD predictions to determine the general applicability of CFD to simulate jet-pumps and to support using CFD in the future for jet-pump design and for further cycle improvements. Comparisons were made between the critical entrainment ratio, critical condensing temperature and NXP. With each jet-pump the effect of the nozzle position within the mixing section on the jet-pump performance and operating stability was explored and the optimal NXP was determined.

6.2 Experimental Method

After commissioning and physical checks of instruments of the experimental rig within the initial test-run as described in the previous Chapter, the system was charged with R236fa for conducting the first part of experimental study. However, the experimental method, with all tests, was conducted in the following manner:

1- Before each test, an evacuation pump was used to evacuate the air from the steam boiler, because it was found that there was some air leakage into the boiler which was not possible to eliminate.
2- Levels of fluids with testing the circulation pump were assessed to achieve equilibrium between charge and discharge ports of the pump.
3- For each test run, the steam boiler heater was switched on and set to the desired heat input.
4- The chillers which provide the cooling water into condenser and sub-cooling was turned on and adjusted to the specific flow temperature depending on the weather and the operating conditions. The flow of cooling water through the condenser and sub-cooler was adjusted by shut-off valves to an arbitrary flow and during the tests the flow was varied depending on the operating conditions.
5- The hot water flow to the evaporator was adjusted to maintain a steady-state temperature in the evaporator.
6- When the desired temperature in the boiler was reached, the control valve downstream of the separator was opened, and in the same time the vapour generator feed pump switched on.
7- The pressure within the condenser was adjusted by controlling the cooling water flow rate, and the pressure at the generator was adjusted by controlling the steam temperature within the steam boiler.
8- The first task with using R236fa or R245fa was to calibrate the primary flow with the designed nozzles under different primary pressures. In this test, the rig was running without using the suction line. Steady state was obtained easily; calibration test was repeated three times to ensure there is no variation on the data taken and to adjust the generator pump to work in optimal speed to provide the related primary flow rate.
9- When the primary nozzle was calibrated over a range of generator temperatures, the refrigerator machine was ready to conduct the full test for different designed jet-pumps over a range of design and off-design operating conditions.
10- For each jet-pump an independent nozzle exit position "NXP" test was carried out using the related design operation conditions. The optimal nozzle position which provides the optimal jet-pump performance was used to test each jet-pump under design and off-design operating conditions (for each series of tests with design and off-design operating conditions, only one property of the system was varied whilst

keeping the others constant in order to determine its influence on the system performance.

11- All the required data was recorded, and the matching between pressure and temperatures for saturation conditions was achieved. Also in each test the critical condenser temperature was established and determined precisely. The secondary flow reading was measured from the related flow meter and it was recorded when there was superheating in the suction flow to avoid overfilling in the evaporator, and this was verified from the differences in the temperature readings between evaporator exit and jet-pump suction inlet "point 10 and point 11" respectively, in Figure 5.1, In all tests the range of superheating was between 3°C to 8°C, and by knowing the primary mass flow rate, the entrainment ratio was then calculated.

12- The effect of the Pre-cooler and recuperator in the system performance were also investigated with each jet-pump at design operating conditions and with optimal nozzle positions.

13- In order to evaluate the system performance, the entrainment ratio, the evaporator cooling capacity and the power consumption within the steam boiler were determined and the system heat balance was checked.

14- The evaporator cooling capacity was determined from the rate at which the refrigerant was vaporized, by knowing the secondary mass flow rate over a time interval and knowing the temperatures at inlet and outlet.

15- The power consumption within the steam boiler was taken from recorded value in the domestic electric power gauge over the same time interval in order to calculate the heat balance test for the whole system.

In the first stage of experimental investigation, the R236fa conventional jet-pump with its designed primary nozzle that matches the diffuser under design conditions was tested followed by R236fa optimized conventional jet-pump and then R236faCRMC jet-pump. In second stage, the R245fa optimized conventional jet-pump was first tested and followed by R245fa optimized CRMC jet-pump. After all tests on each jet-pump were completed, the installed diffuser was replaced by another. The method of changing the diffuser in the experimental rig was simple, closing the control valve to avoid leakage, and then opening the related nuts. When the new diffuser was placed, the vacuum pump was used to remove any introduced air from the system, and then the rig was run in the same manner described in the previous paragraph. After this, steady state conditions were

obtained within 10 to15 min from start up. It was possible to run the rig continuously for many hours with stable conditions.

The results of all experiments are presented in this Chapter with a full comparison with CFD predicted results.

6.3 Experimental Results

Experimental results for both tested fluids are presented and discussed in the following sections. Example of calculation for derived data, such as, R_m, Q_g, Q_e, COP, ete, based on Conventional R236fa jet-pump are given in Appendix E.

6.3.1 Calibration of Primary Nozzles

Figures 6.1 and 6.2 show comparison between experimental, CFD and theoretical critical mass flow of the tested R236fa and R245fa primary nozzles respectively. It is observed that within the range of the experiment, the primary mass flow varies approximately linearly with T_g. The same trend was observed for all results, and all values agree closely.

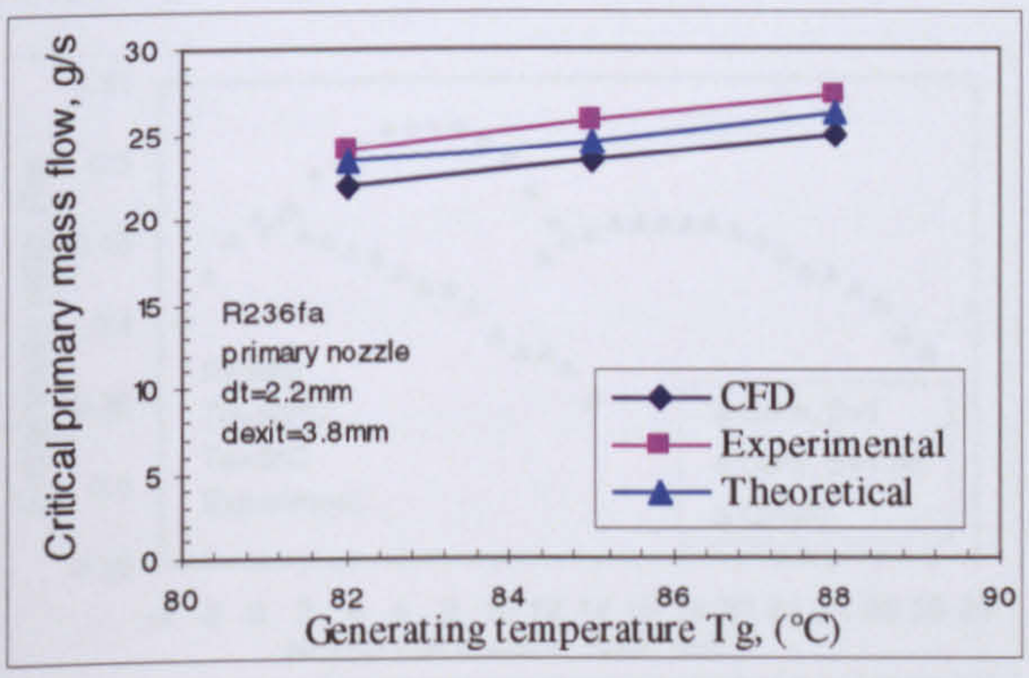

Figure 6. 1 Calibration of R236fa primary nozzle

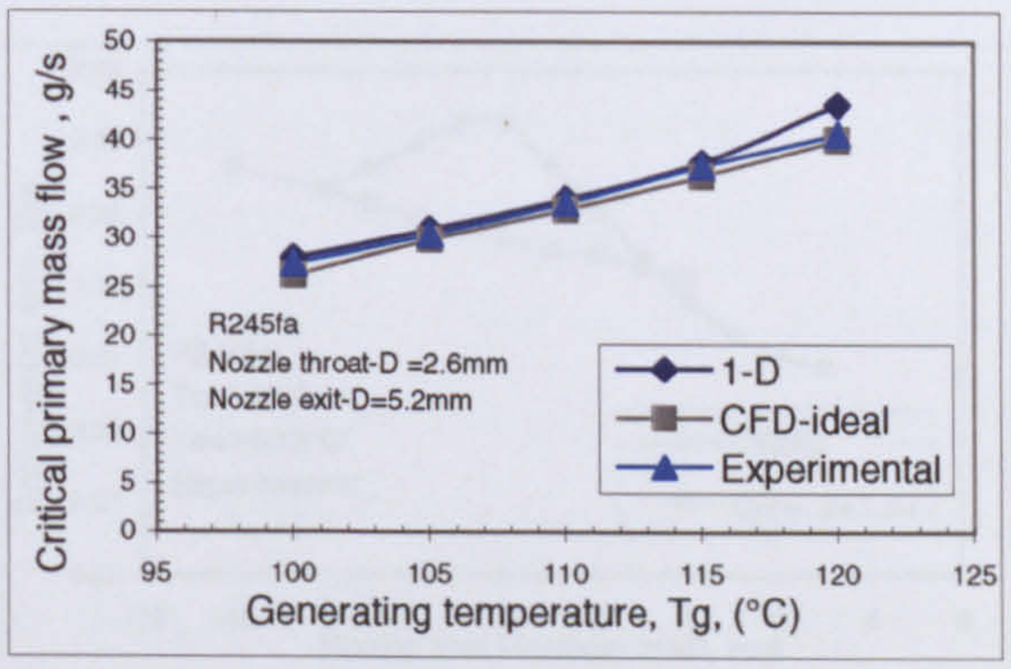

Figure 6. 2 Calibration of R245fa primary nozzle

Also from Figure 6.1 it can be seen that the experimental value was slightly higher than others, the CFD and theoretical prediction. The most likely reasons for this are the geometry of the primary nozzle used. Because it was dimensionally so small it was difficult to manufacture to a tolerance better than ± 0.025mm. Also, another possible reason is that of the measurement of the primary mass flow. Because flow was measured using a direct reading meter with small scale; small errors in reading were possible. The results presented in Figures 6.1 and 6.2 were for the maximum value recorded in each case.

6.3.2 Optimal Nozzle Exit Position "NXP"

NXP was measured from the primary nozzle exit plane to the entry plane of the first conical part of the jet-pump as shown in Figure 3.1. The system was run with the design operating conditions for each jet-pump whilst the condenser temperature was varied between 26°C to 32°C in the case of using R236fa and between 40°C to 49°C in the case of using R245fa. With using R236fa the nozzle exit was first placed at the main entrance of the diffuser (i.e. NXP=0mm) and it gradually moved downstream in steps of 2mm up to the constant area section entrance. Whereas, with using R245fa the nozzle was gradually moved upstream in steps of 2.5mm from the main entrance of the diffuser up to 10mm in front of entry of the mixing section. It was not possible to move the nozzle back upstream of the mixing section entrance more than 10mm, because of the restriction of the nozzle assembly mechanism. At each position steady state operation was established and the critical condensing temperature was recorded. The test was then repeated, with each jet-pump, by moving the nozzle in the same manner in opposite direction to verify precisely the optimal nozzle position. Figures 6.3 and 6.4 show the experimental results in terms of critical entrainment ratio at different NXP for all R236fa jet-pumps and for the two R245fa jet-pumps respectively.

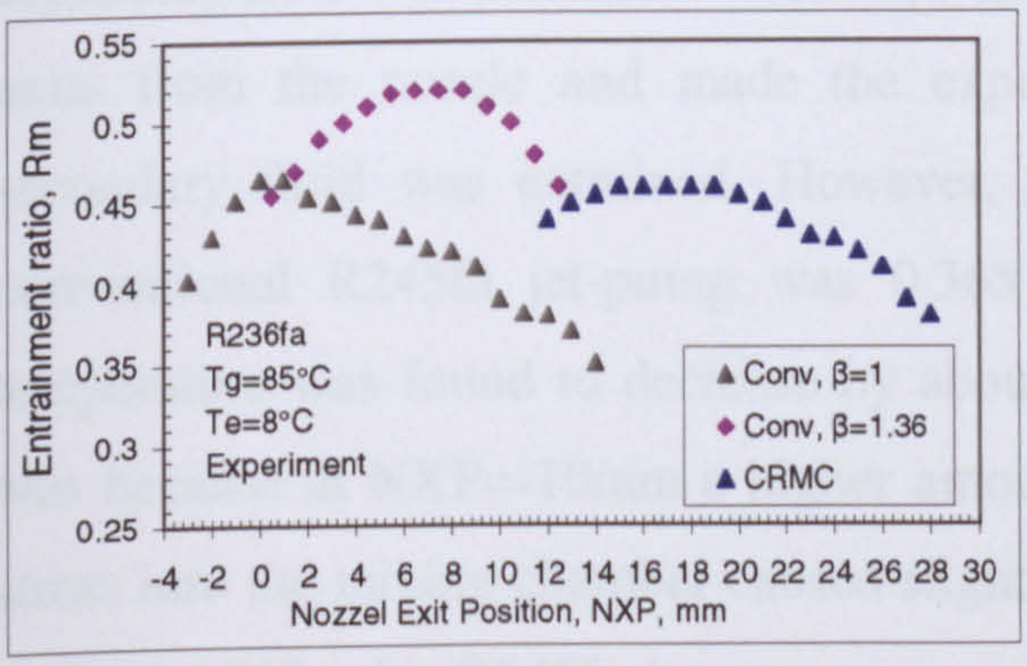

Figure 6. 3 Measured variations in the entrainment ratio (R_m) with NXP R236fa Jet-pumps (Experimental)

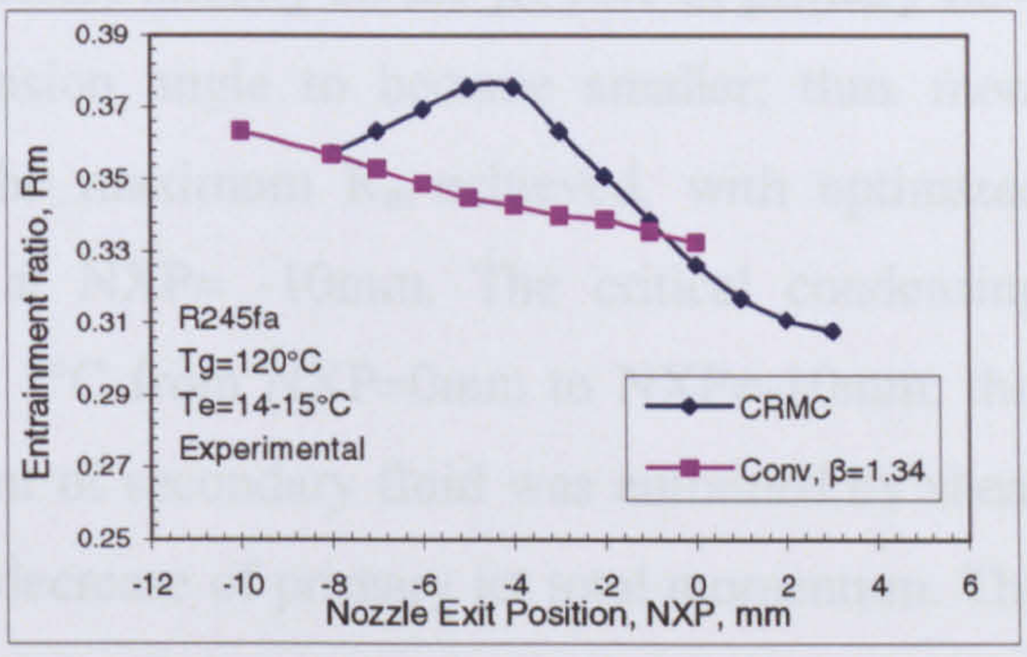

Figure 6. 4 Measured variations in the entrainment ratio (R_m) with NXP R245fa Jet-pumps (Experimental)

From Figure 6.3 it is clear that NXP=1mm was the optimal nozzle position at which maximum entrainment ratio was achieved with critical condenser temperature of 30°C for conventional R236fa jet-pump. Whereas, NXP=7.5mm was the optimal nozzle position for optimized conventional R236fa jet-pump and NXP=17mm for optimized CRMC R236fa jet-pump. From Figure 6.3 also it can be observed that when the nozzle was moved downstream from NXP=-4mm to NXP=26mm, the entrainment ratio increased at first, until a limiting value was reached. This occurred at the optimal NXP for each jet-pump. After this, R_m decreased as the nozzle was moved further into the mixing chamber.

The R_m value of each jet-pump could vary by as much as 25 to 30 % depending on the nozzle position within the mixing section. The optimal position could enable the larger converging duct and larger effective area for the secondary flow to be entrained as explained before in Chapter 4. The NXP at which the peak value was reached was changed from 1mm in the original conventional R236fa jet-pump to 7.5mm with optimized conventional R236fa jet-pump. The reason for that is that the increases in diameter of the conical entrance lead to move the nozzle downstream to maintain the designed critical condensing pressure with the maximum effective area for secondary flow. When the nozzle was moved upstream from the optimal position, the primary flow at the nozzle exit changed in structure which pushed away the secondary flow; thus a lower amount of secondary flow entered which itself affected the total momentum of the combined flow: and hence less T_c^* was achieved.

From Figure 6.4 it can be seen that the optimal NXP was changed from -10mm with conventional R245fa jet-pump to -4mm with CRMC jet-pump. Also it can be seen that moving the nozzle out of the mixing chamber caused an increase of entrainment ratio. When the nozzle was moved out of the mixing chamber, the compression effect of secondary flow was increased, which has an effect directly on the jet core of primary flow exits from the nozzle and made the expansion angle to became smaller; thus more secondary fluid was entrained. However, the maximum R_m achieved, with optimized conventional R245fa jet-pump was 0.365 at NXP= -10mm. The critical condensing temperature was found to decrease by about 1°C from NXP=0mm to NXP=-10mm; this was because at NXP=-10mm a higher amount of secondary fluid was entrained by shear stress into the mixing chamber caused slight decrease of primary jet total momentum. The optimal NXP with R245fa jet-pumps were in the front of the entry plane of the mixing section not like that of R236fa jet pumps which took place downstream of the main entry, the reason for that, is the difference in nozzle area ratio and the higher vapour generator pressure used in the case of R245fa jet-pumps. Also, it can be seen from optimized CRMC NXP profiles in both aforementioned Figures that varying the NXP by small range did not affect the entrainment ratio significantly, and there is a range between NXP=15mm to NXP=19mm that could provide best performance for R236fa, this because of shape of the CRMC mixing section profile. Even though the same nozzle and the same operating conditions were used for finding the optimal NXP with each fluid used; the optimal NXP was found to vary significantly. This was because the expansion jet angle controlled with

the internal wall of mixing section the size of the effective area that allowed the primary fluid to entrain a highest rate of secondary fluid into the mixing section, which provided the higher entrainment ratio. The first part of the mixing section for the CRMC diffuser is wider than that with conventional jet-pump. For example the internal diameter for the inlet of mixing section in conventional R245fa diffuser is 8.8mm, whereas with CRMC R245fa diffuser is 9.78mm; thus small difference has significant effect on the optimal NXP. It is obvious that varying the NXP has a significant effect on the performance of the jet-pump. When the nozzle is moved away in any direction from the optimal position it caused deterioration in the performance.

6.3.3 R236fa and R245fa Jet-pumps (with Design and Off-design Operating Conditions)

The effects of generator and evaporator temperatures on system performance were investigated. In each test T_e and T_g were fixed at predetermined values and the condenser temperature was varied depending on each couple of operating conditions used. T_c* was determined by the same manner described in the experimental method section. To precisely determine the T_c*, the condenser temperature was incrementally raised from lower value "less from critical value" until the jet-pump failed to function. For these tests the nozzle was located at its optimum design position, as defined before for each jet-pump. R_m, COP and cooling capacity were calculated at each step.

- **Effect of Condensing Temperature**

For the conventional R236fa jet-pump R_m, COP and Q_e were plotted against condenser temperature in Figures, 6.5, 6.6, and 6.7 to show how they change with respect to changes in T_c.

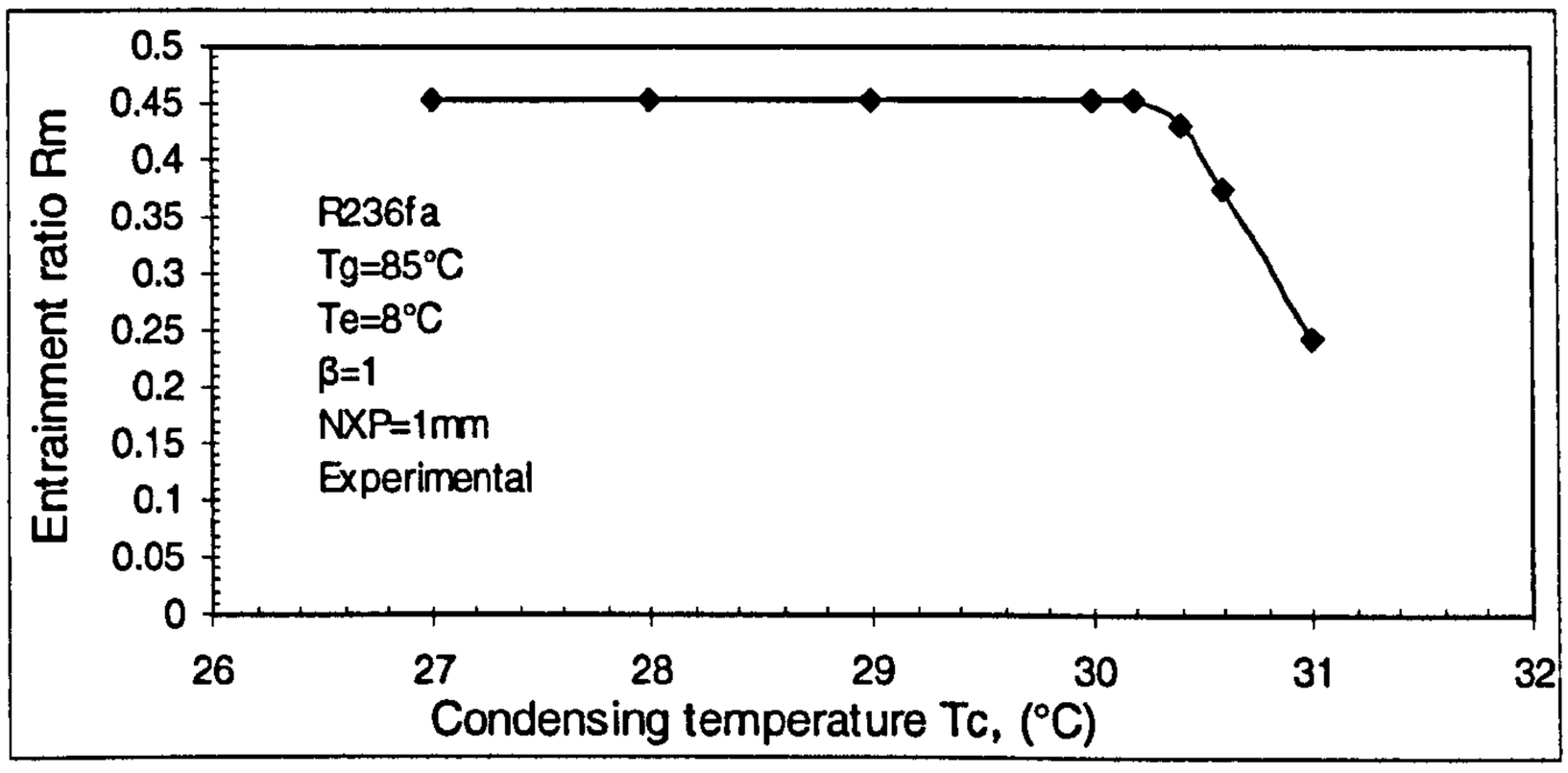

Figure 6. 5 Effect of T_c on the R_m, conventional R236fa jet-pump (experimental)

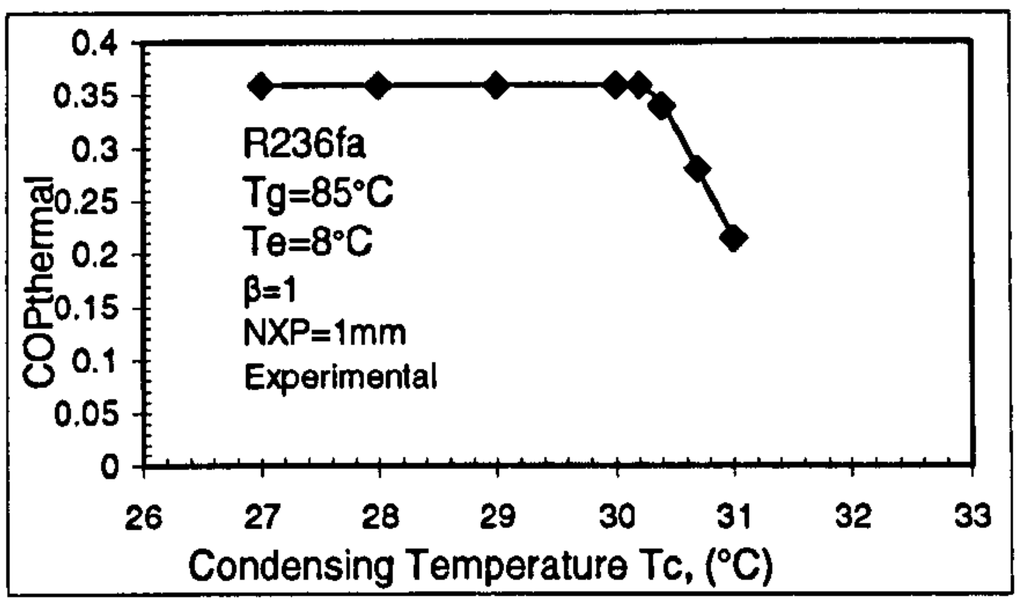

Figure 6. 6 Effect of T_c on the COP, conventional R236fa jet-pump (experimental)

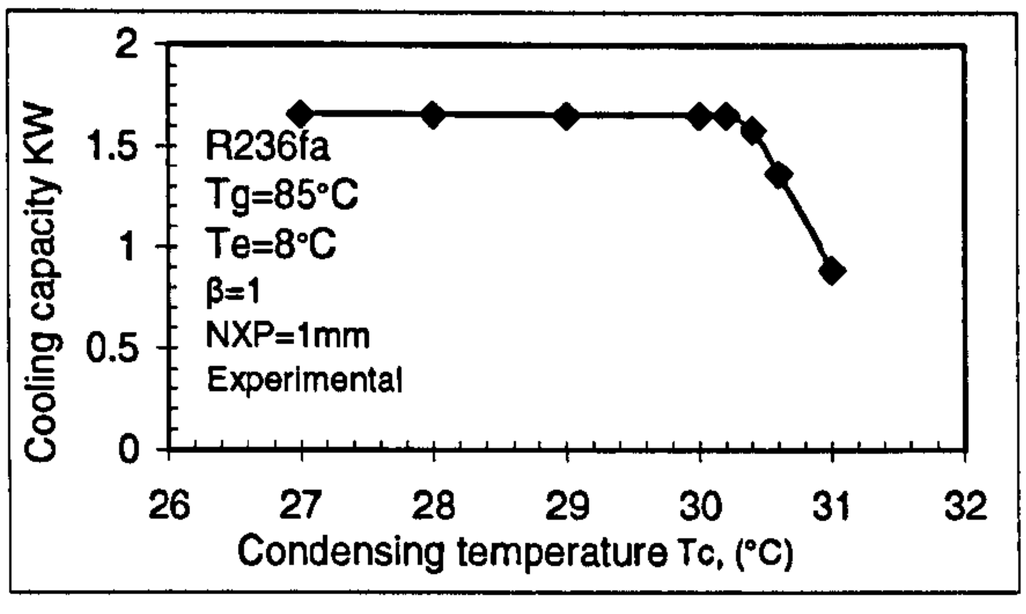

Figure 6. 7 Effect of T_c on the Q_e, conventional R236fa jet-pump (experimental)

The experimental results presented in Figures 6.5, 6.6 and 6.7 provide an understanding of the characteristics of the jet-pump at different T_c. It can be observed that, as T_c increased R_m, COP and Q_e remain essentially constant until a certain point was reached, at which they all started to decrease rapidly as T_c was further increased. The condenser temperature at which change was first observed is the critical condenser temperature for which the jet-pump was designed. Thus the effect of T_c on jet-pump performance is noticed as has also been explained in Chapter 3. However, when the condenser temperature was increased beyond the critical point, it caused the COP and cooling capacity of the system to decrease significantly with unstable operating conditions; a rapid rise in evaporator temperature and pressure was observed by only increasing the condensing temperature by 3 to 4 degrees further from the critical temperature. Condensing pressure is directly controlled by the cooling medium temperature which should be less than the saturation temperature of refrigerant vapour entering the condenser by a range of 5°C to 8°C. Thus the designed value of critical condenser temperature which is restricted by the availability of cooling medium must be considered.

- **Effect of Evaporator Temperature**

Figures 6.8 to 6.12 show the variation in entrainment ratio with condenser temperature for different evaporator temperatures at given generator temperature (design value of T_g) for all jet-pumps tested. It can be seen that with fixed generator temperature, as T_e was increased the entrainment ratio also increased. Also the critical condenser temperature increased because with higher secondary pressure the more momentum was potentially possessed. The amount of secondary flow entrained was increased with increasing T_e, and this was under the pressurization effect which caused a reduction of

primary flow expansion angle and widen the secondary flow effective area; more secondary flow was entrained, higher momentum mixed flow was achieved; higher T_c* was obtained.

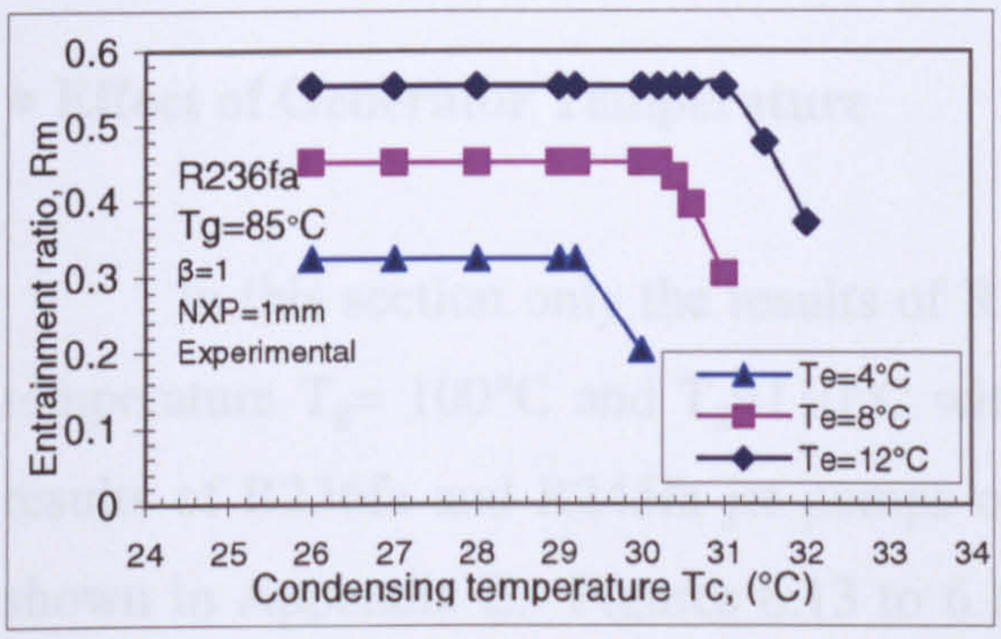

Figure 6. 8 Conventional R236fa jet-pump performance T_g=85°C (experimental)

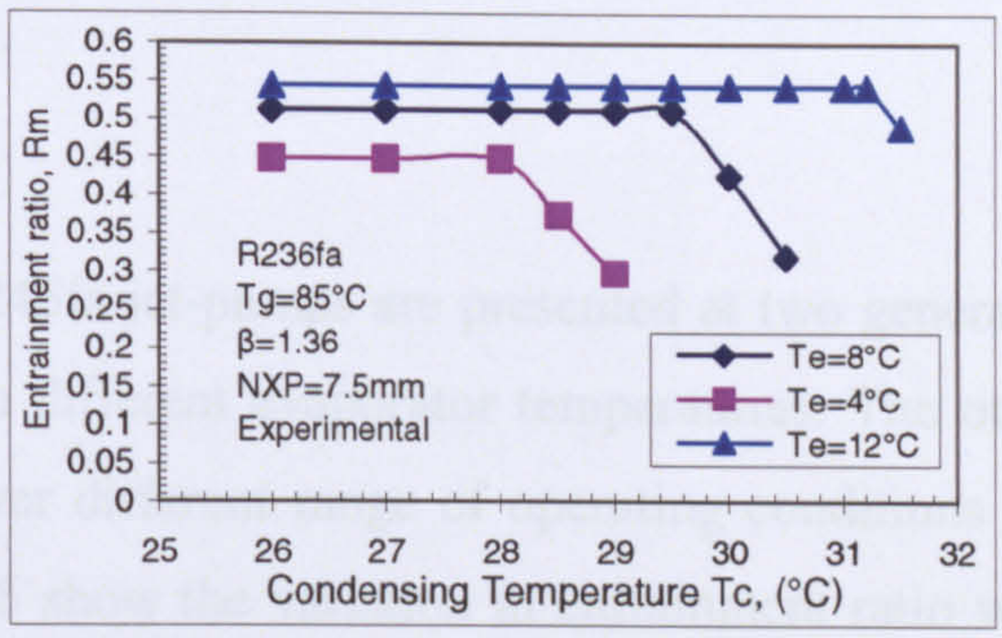

Figure 6. 9 Optimized conventional R236fa jet-pump performance T_g=85°C (experimental)

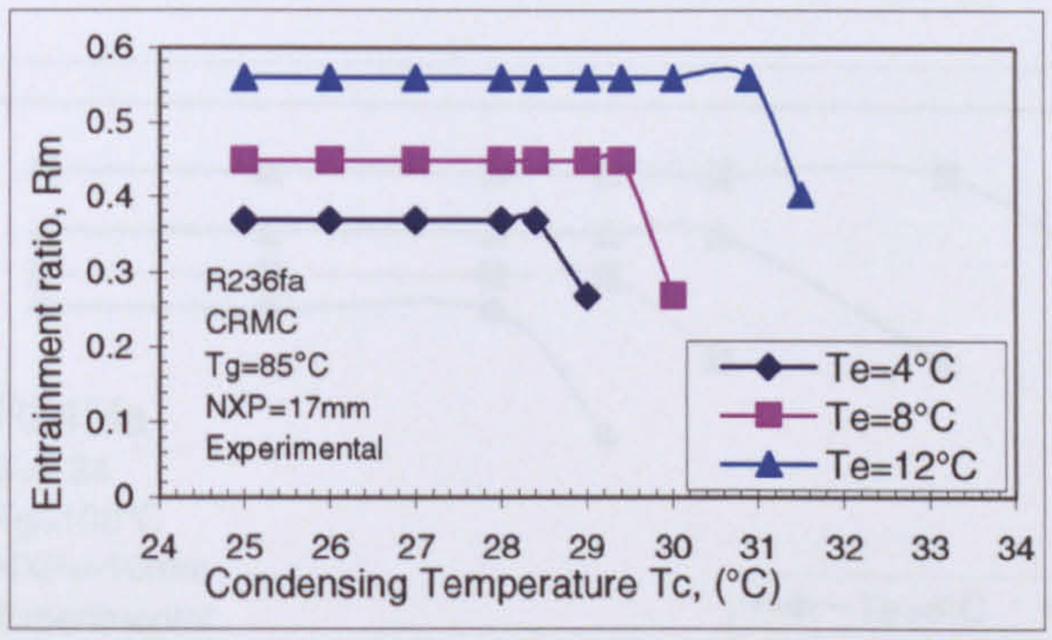

Figure 6. 10 Optimized CRMC-R236fa jet-pump performances T_g=85°C (experimental)

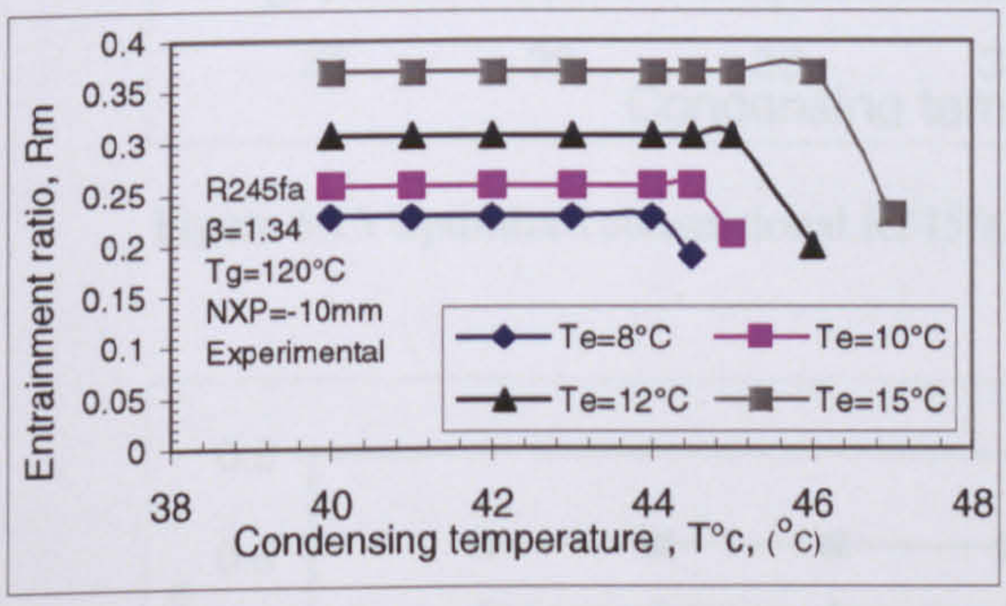

Figure 6. 11 Optimized conventional R245fa jet-pump performance T_g=120°C (experimental)

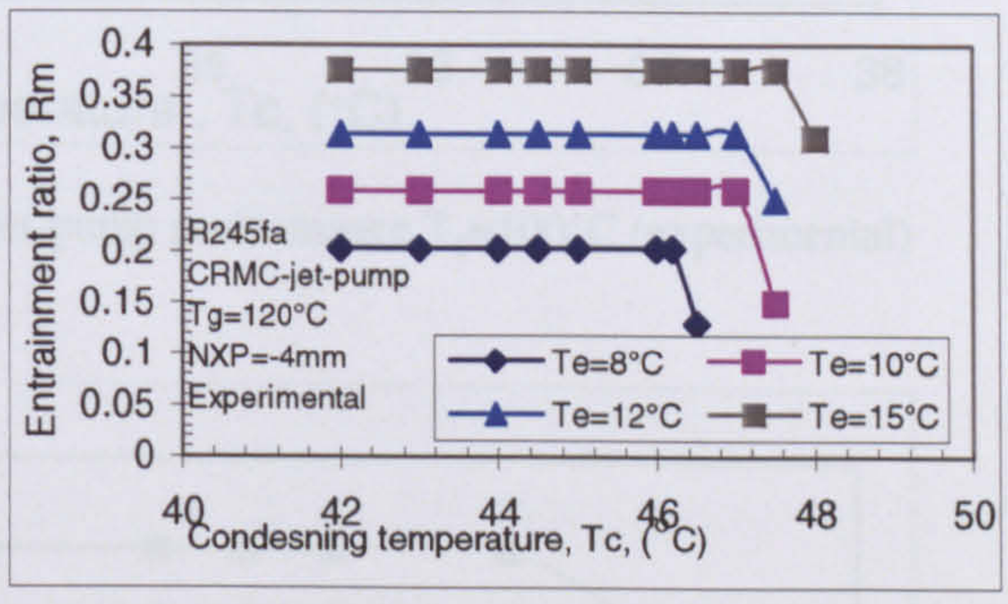

Figure 6. 12 Optimized CRMC R245fa jet-pump performance T_g=120°C (experimental)

From Figures 6.8 and 6.9 for conventional R236fa jet-pumps, it can be seen that the difference in R_m between trend lines of T_e=4°C and T_e=8°C is larger than the difference between trend lines of T_e=8°C and T_e=12°C. This difference can be explained by saying that at T_e=4°C, the flow at the exit of nozzle was over-expanded and thus the jet-angle restricted the amount of secondary flow to be entered; however, to increase the jet-pump

performance at T_e=4°C, the nozzle must be readjusted. Figures 6.11 and 6.12 for R245fa jet-pumps it is clear that both jet-pumps provide nearly the same entrainment ratio at the same operating conditions.

- **Effect of Generator Temperature**

In this section only the results of R245fa jet-pumps are presented at two generator temperature T_g= 100°C and T_g=110°C with different evaporator temperatures. The other results of R236fa and R245fa jet-pumps over different range of operating conditions are shown in Appendix E. Figures 6.13 to 6.16 show the variation in entrainment ratio with condenser temperature for different generator and evaporator temperatures for the tested R245fa jet-pumps.

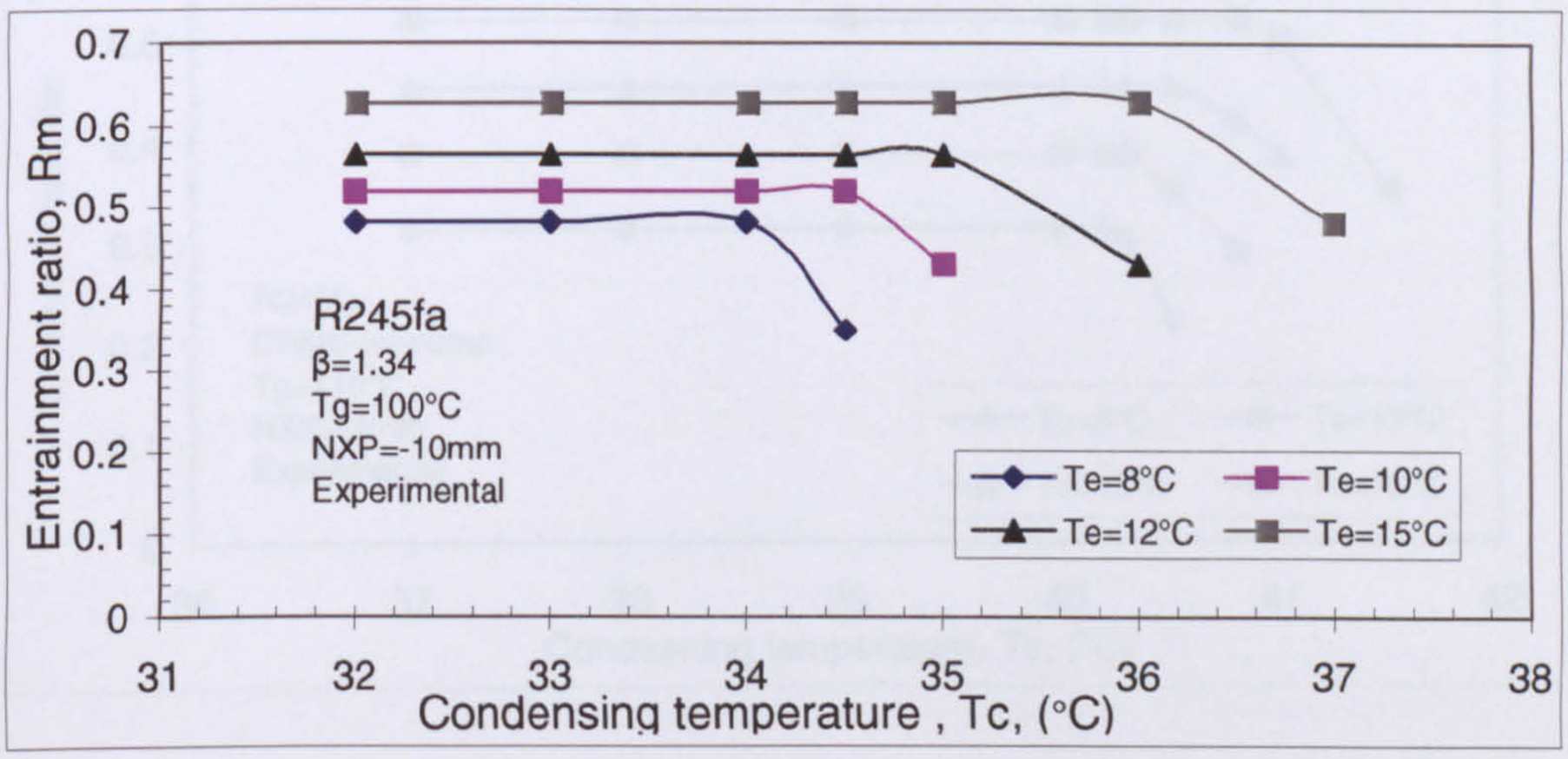

Figure 6.13 Optimized conventional R245fa jet-pump performance T_g=100°C (experimental)

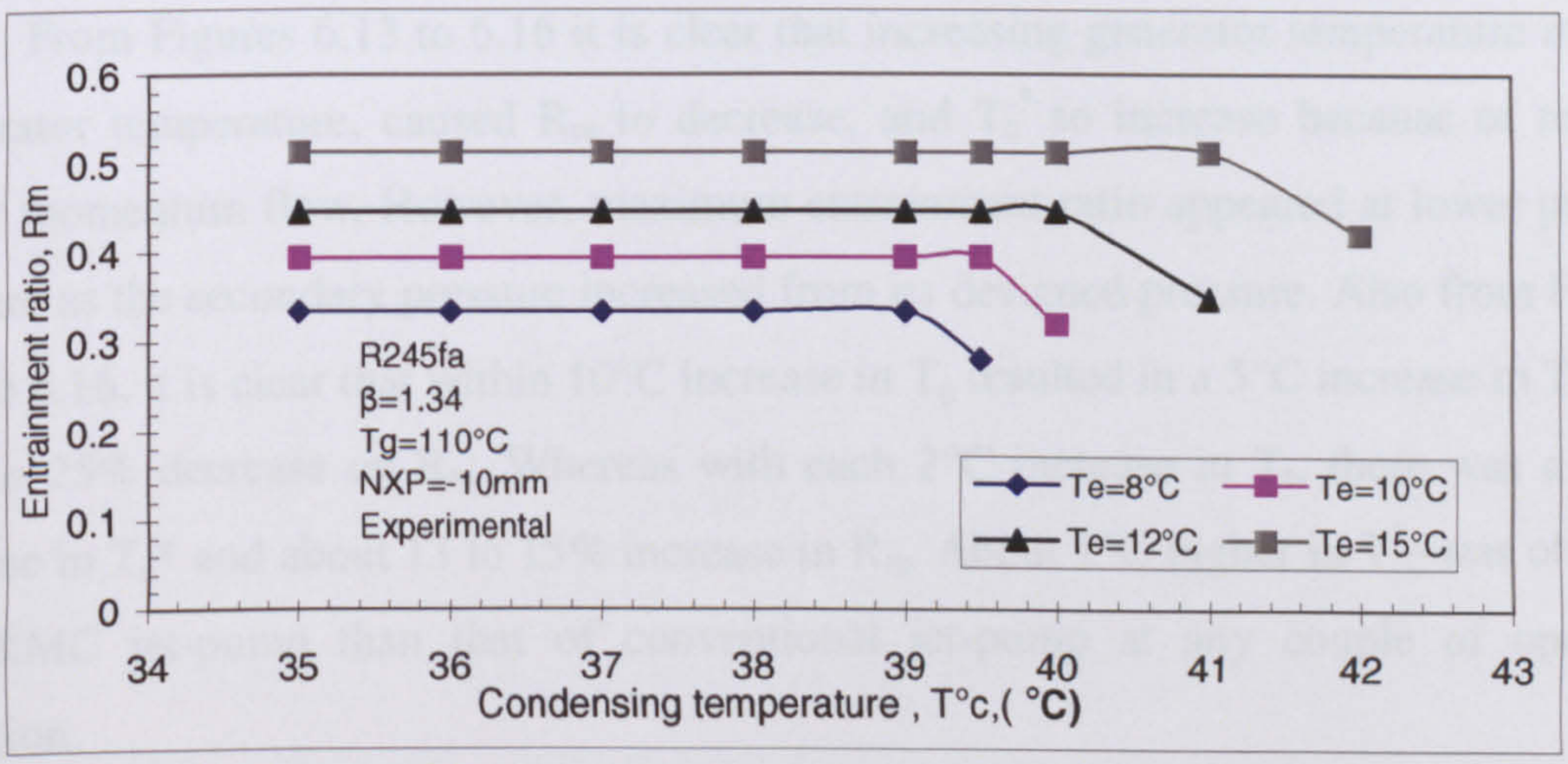

Figure 6. 14 Optimized conventional R245fa jet-pump performance T_g=110°C (experimental)

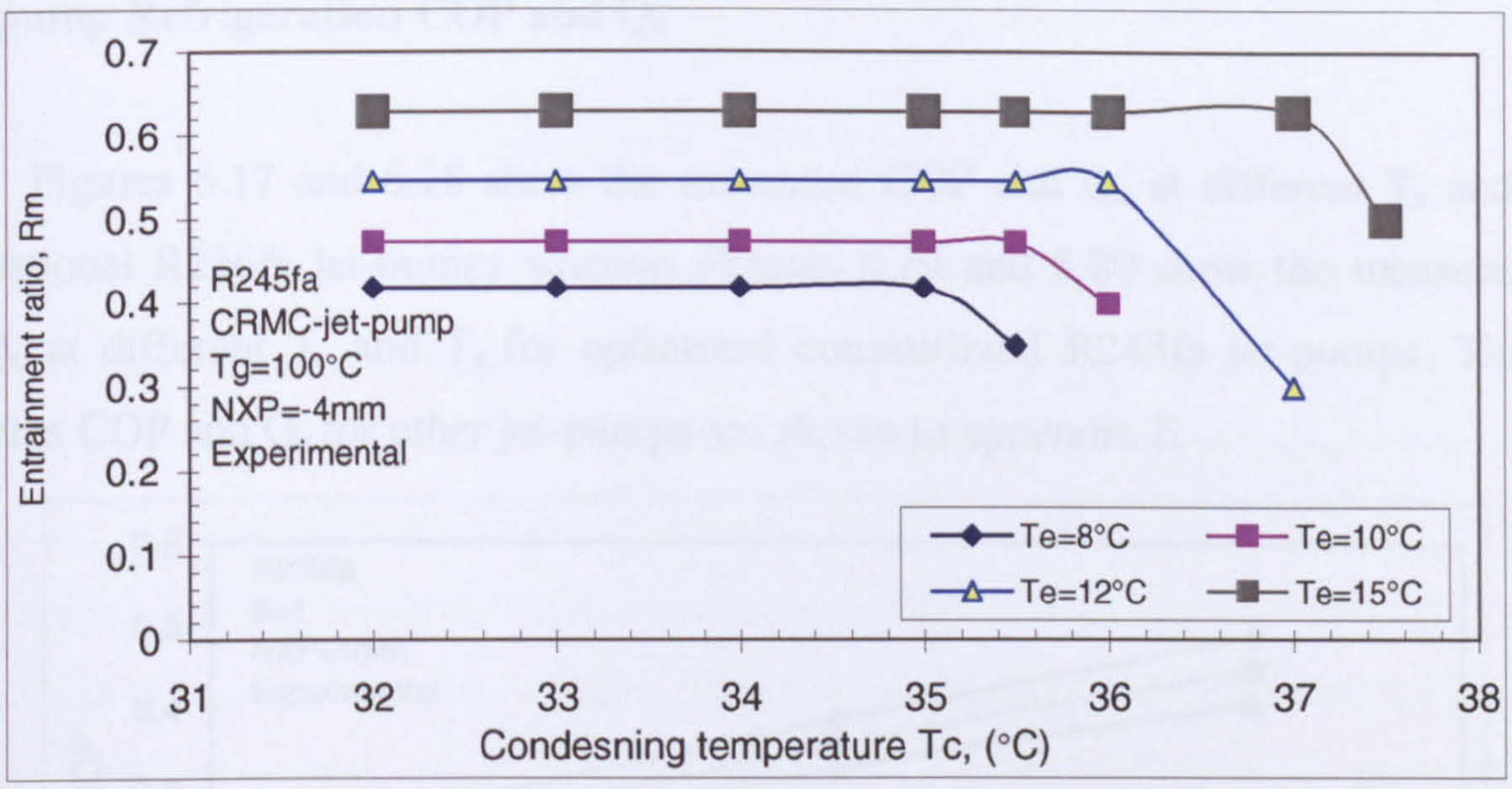

Figure 6. 15 Optimized CRMC R245fa jet-pump performance T_g=100°C (experimental)

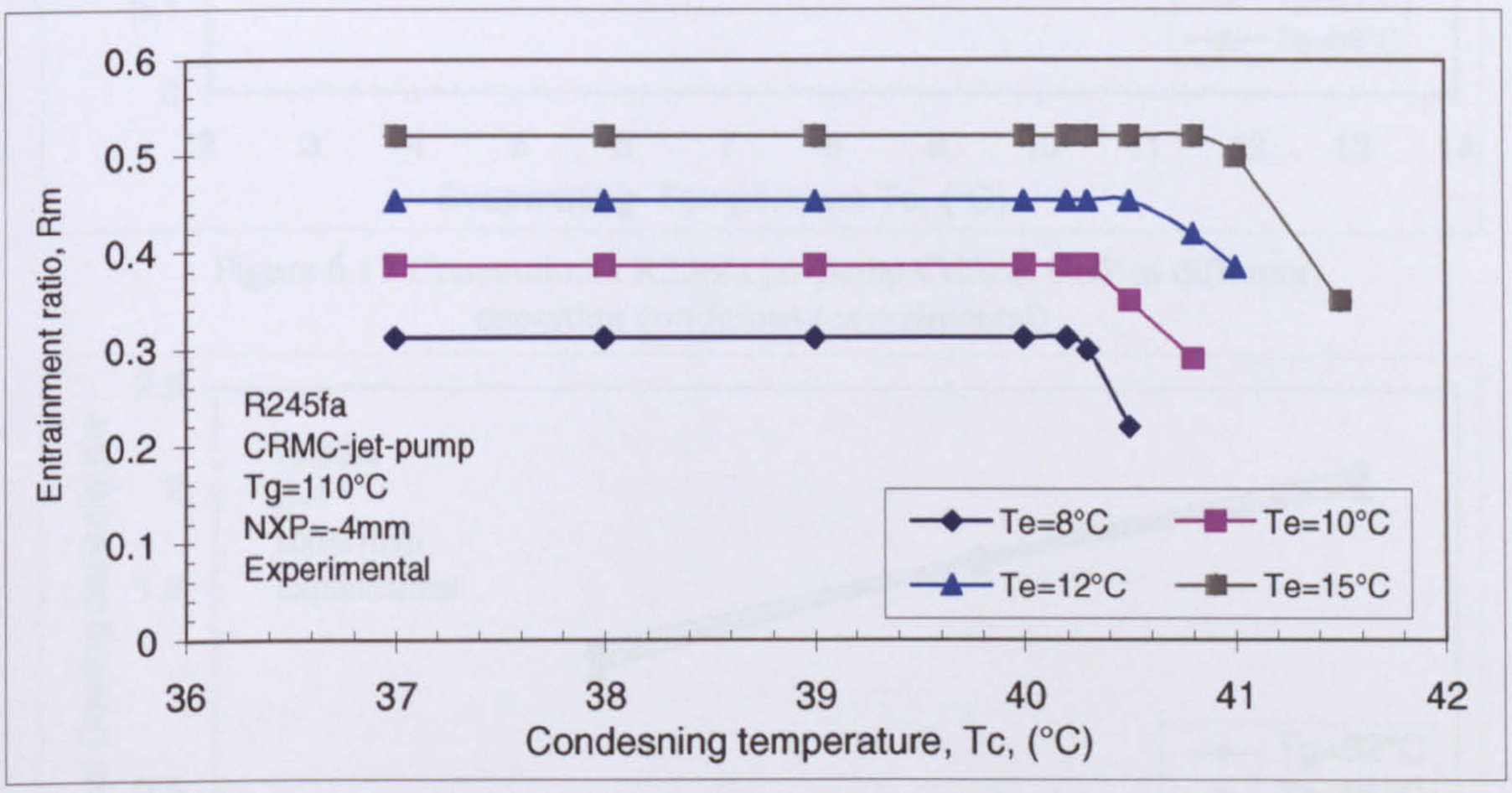

Figure 6. 16 Optimized CRMC R245fa jet-pump performance T_g=110°C (experimental)

From Figures 6.13 to 6.16 it is clear that increasing generator temperature at fixed evaporator temperature, caused R_m to decrease, and T_c^* to increase because of resulted higher momentum flow. However, maximum entrainment ratio appeared at lower primary pressure as the secondary pressure increased from its designed pressure. Also from Figures 6.13 to 6.16, it is clear that within 10°C increase in T_g resulted in a 5°C increase in T_c* and 15% to 25% decrease on R_m. Whereas with each 2°C increase in T_e, there was a 0.5°C increase in T_c* and about 13 to 15% increase in R_m. About 1°C higher in T^*_C was obtained by CRMC jet-pump than that of conventional jet-pump at any couple of operating condition.

•Jet-pump Refrigeration COP and Q_e

Figures 6.17 and 6.18 show the measured COP and Q_e at different T_e and T_g for conventional R236fa jet-pumps whereas Figures 6.19 and 6.20 show the measured COP and Q_e at different T_e and T_g for optimized conventional R245fa jet-pumps. The other measures COP and Q_e for other jet-pumps are shown in appendix E.

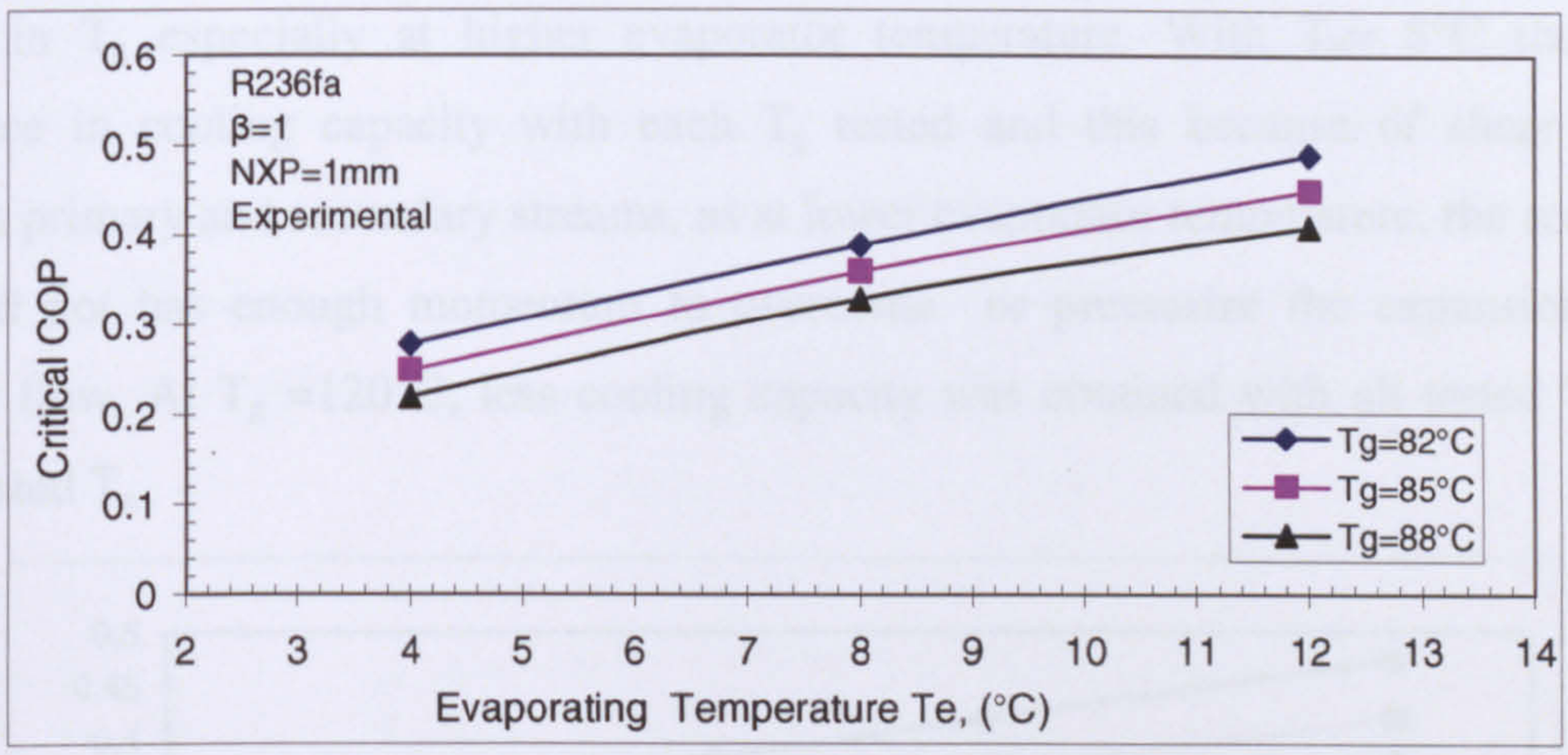

Figure 6.17 Conventional R236fa jet-pump Critical COP at different operating conditions (experimental)

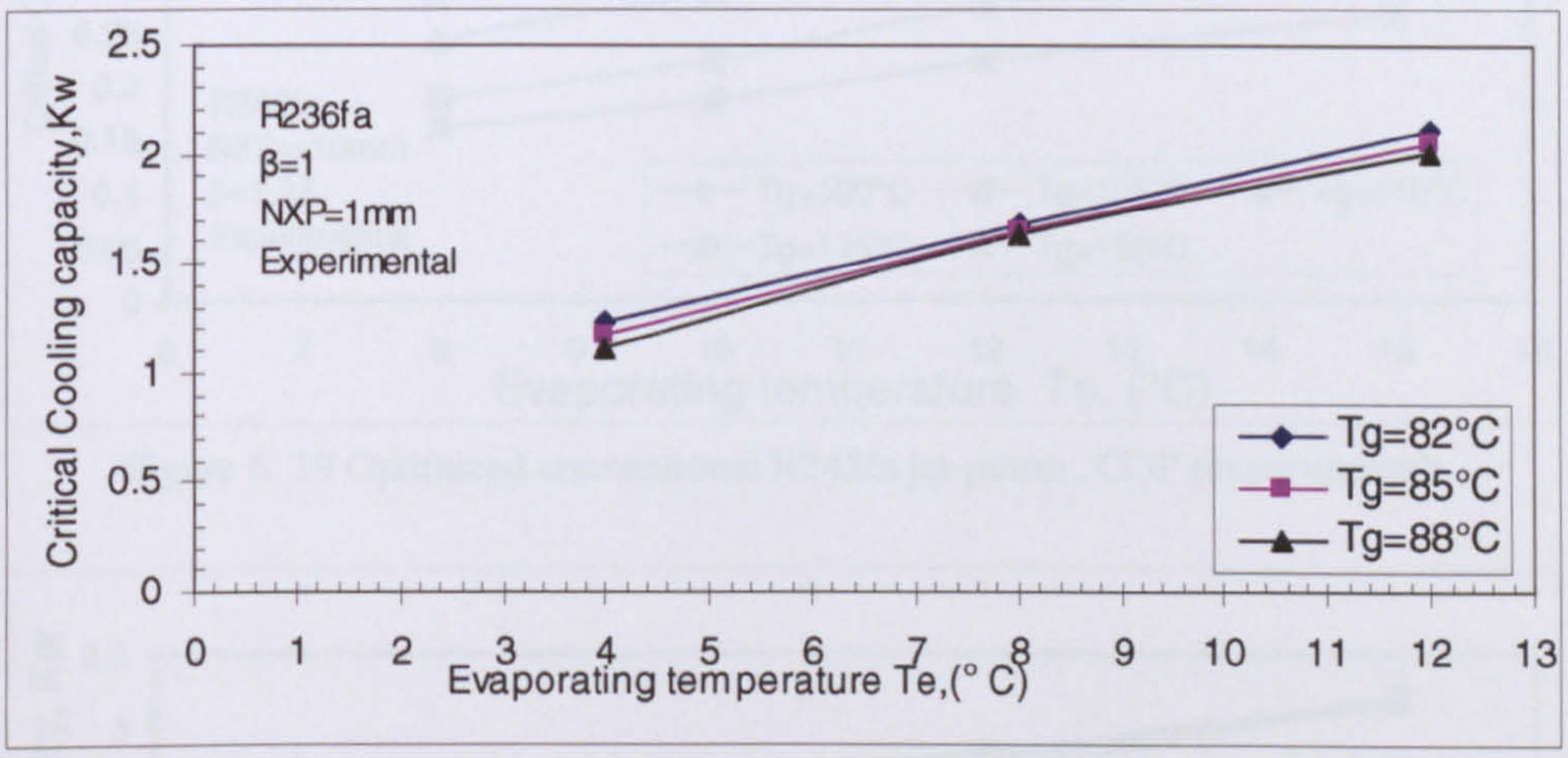

Figure 6. 18 Conventional R236fa jet-pump-Critical cooling capacity at different operating conditions (experimental)

From Figure 6.17 it is clear that the variation in COP was of the same manner as those for R_m described in the preceding section. However, increasing evaporator temperature (and pressure) at constant generator temperature caused the COP to increase, whereas increasing generator temperature (and pressure) at constant evaporator temperature caused the COP to decrease. But the increased COP values with lowering T_g were at the expense of T_c^*. In the case of the design point T_c^*, the optimal COP was at the design operating conditions. Figure 6.18 show clearly that the cooling capacity (Q_e)

increase significantly as T_e increased. Whereas it remains nearly constant or decrease slightly with increasing T_g .

From Figures 6.19 and 6.20, it is clear that the percentage of increase in COP was the same with decreasing T_g gradually from T_g=120°C to T_g =100°C; also it increased linearly with increasing T_e and P_e. Whereas the change in cooling capacity was small with change in T_g especially at higher evaporator temperature. With T_e= 8°C there was difference in cooling capacity with each T_g tested and this because of shear mixing between primary and secondary streams, as at lower evaporator temperature, the secondary flow did not has enough momentum to overcome or pressurize the expansion jet of primary flow. At T_g =120°C, less cooling capacity was obtained with all tested T_e, than other tested T_g.

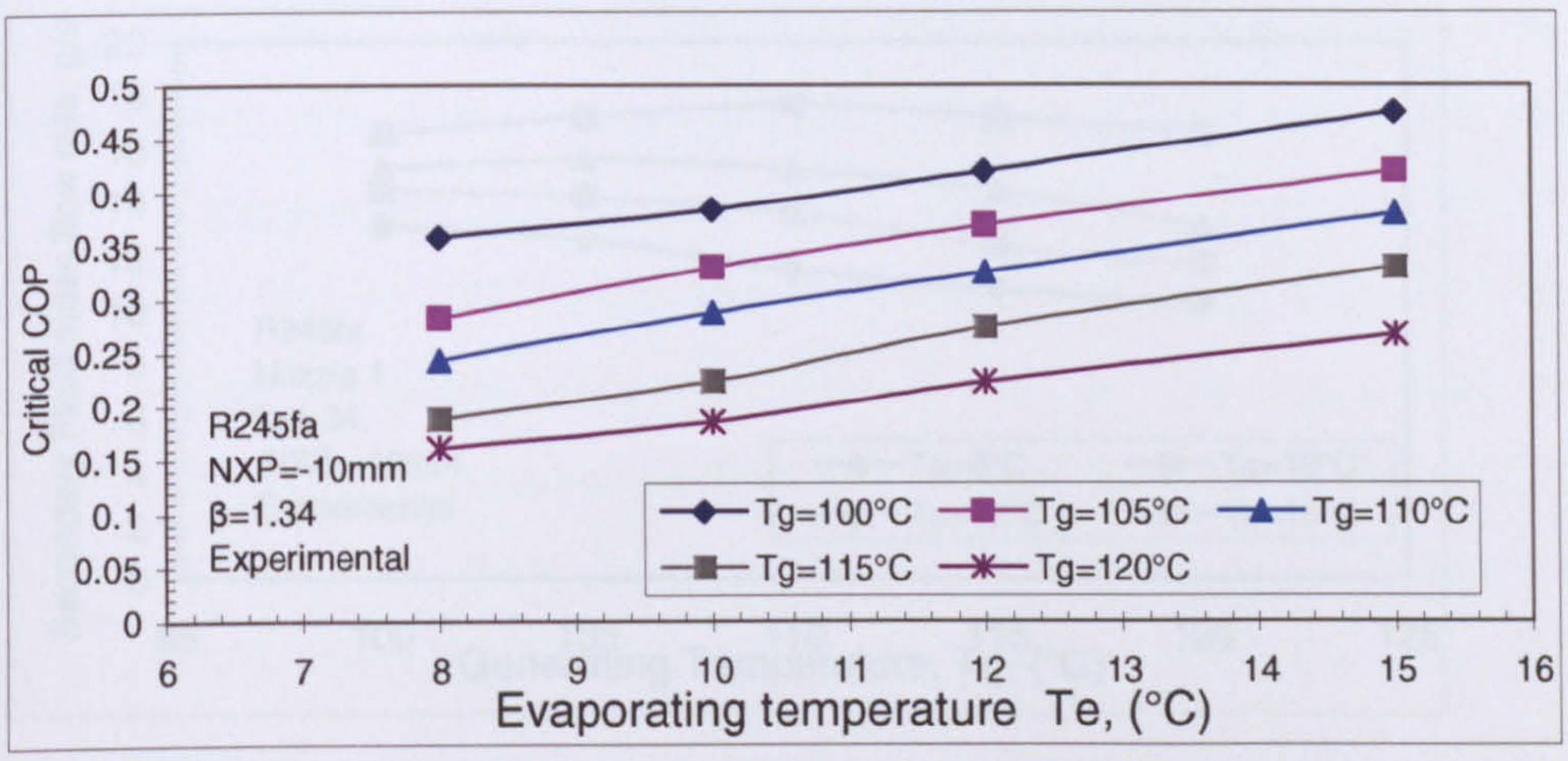

Figure 6. 19 Optimized conventional R245fa jet-pump , COP (experimental)

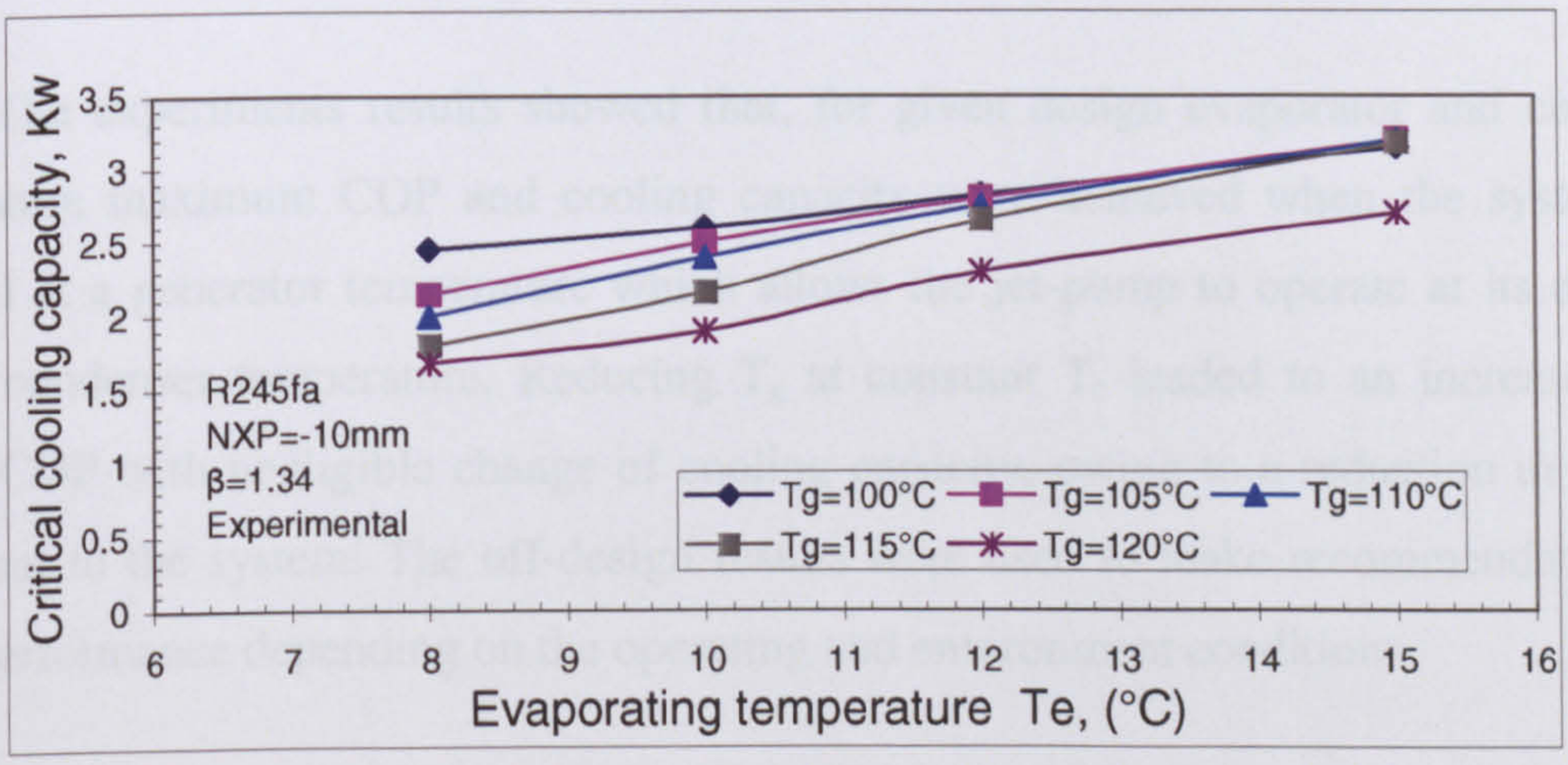

Figure 6. 20 Optimized conventional R245fa jet-pump, cooling capacity (experimental)

An increase in generator temperature has a slight influence upon the entrained secondary flow; this was observed experimentally and by CFD with each jet-pump. Figure 6.21 shows the change of secondary mass flow with changing generator temperature at different evaporator temperatures for optimized conventional R245fa jet-pump. From Figure 6.21 it can be seen that, at evaporator temperatures of 12°C and 15°C the amount of secondary flow were slightly increased with increasing generator temperature up to T_g=110°C; then the secondary mass flow rate began to fall as T_g was raised. At evaporator temperatures of 8°C and 10°C, an increase in generator temperature has no beneficial influence upon the level of induced flow. However, referring to Figures 6.20 and 6.21 it seems that for a fixed evaporator temperature, there were no potential benefits of increasing generator temperature upon cooling capacity; only higher critical condensing temperature could be obtained.

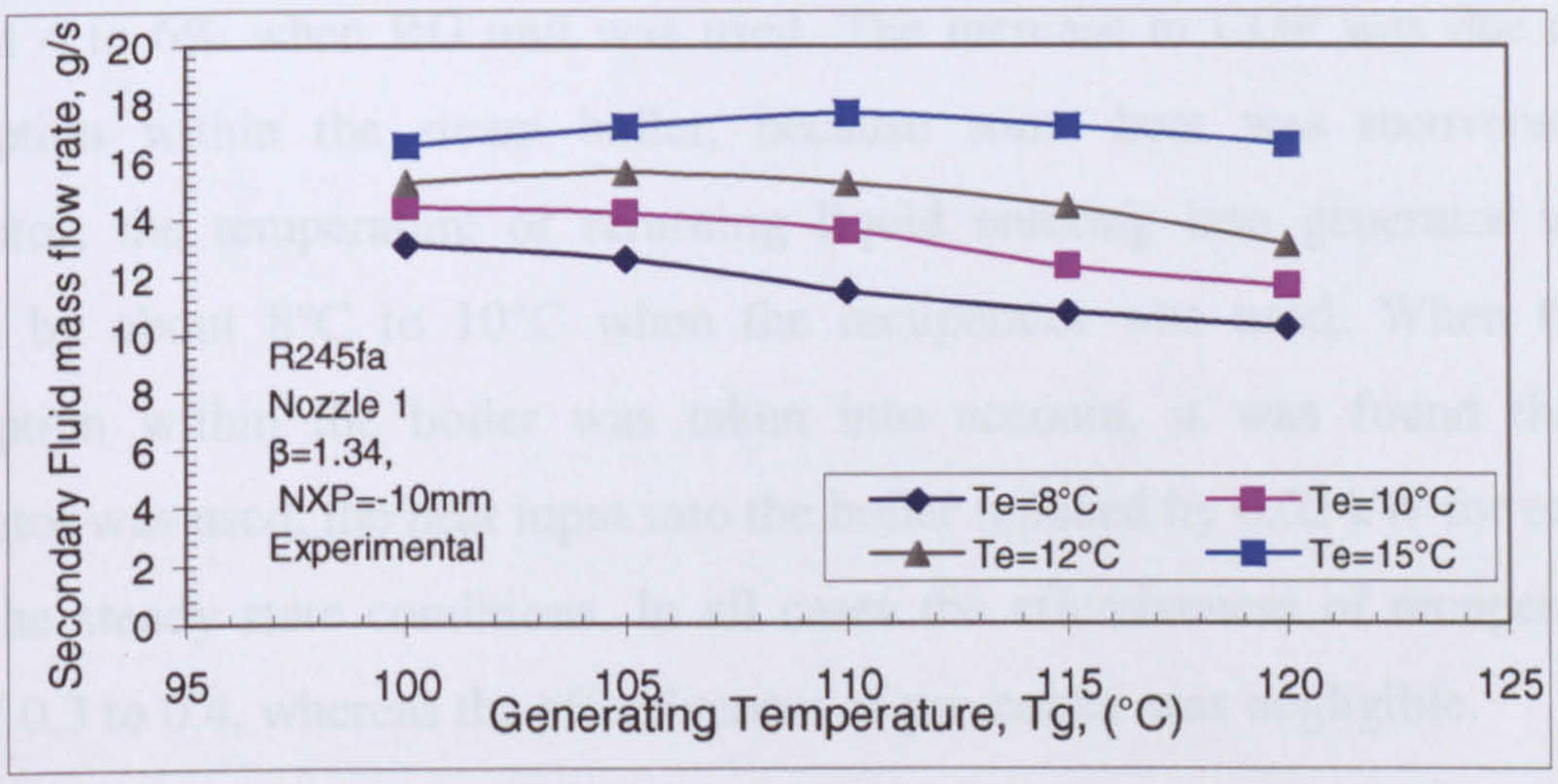

Figure 6. 21 Optimized conventional R245fa jet-pump 'secondary mass flow rates' (experimental)

The experiments results showed that, for given design evaporator and condenser temperature maximum COP and cooling capacity were achieved when the system was operated at a generator temperature which allows the jet-pump to operate at its designed critical condenser temperature. Reducing T_g at constant T_e leaded to an increase in the system COP with negligible change of cooling capacity, owing to a reduction in primary heat input to the system. The off-design results were used to make recommendations for better performance depending on the operating and environment conditions.

6.3.4 The Effect of Using Regeneration Unit (RG) (pre-cooler and recuperator)

The proposed idea of using RG unit (especially the pre-cooler) is based on the fact that the jet-pump performance is highly dependent on the secondary flow pressure, as

was observed that increasing secondary flow pressure increases R_m and T_c* of the jet-pump. However, the effect of using the pre-cooler and recuperator was investigated with each jet-pump at design operating conditions, with the conventional R236fa jet-pump two more T_e were tested, T_e=4°C, and T_e=12°C. Also, with R245fa jet-pumps T_e of 8°C, 10°C, 12°C and 15°C at T_g=120°C were investigated. With each test the related lines for both pre-cooler and recuperator were linked to the main circulation circuit of the working fluid and the rig was run with the design operating condition and with the optimum nozzle position. From the measured results there was no obvious effect of these components on the jet-pump performance, both measured R_m and T_c^* were the same as in the normal circuit without these components; the only variation was in COP as is shown in Table 6.1 , and Figure 6.22 for R236fa jet-pumps, and in Figures 6.23 and 6.24 for R245fa jet-pumps. It is seen from Table 6.1 and aforementioned Figures that the COP of the system increased by about 4 to 6% when RG unit was used. The increase in COP was due to the energy consumption within the steam boiler, because some heat was recovered within the recuperator; the temperature of returning liquid entering into generator was found to increase by about 8°C to 10°C when the recuperator was used. When the electricity consumption within the boiler was taken into account, it was found that, when the recuperator was used, the heat input into the boiler reduced by 0.02 kW for each 5 minutes within the steady state conditions. In all cases the effectiveness of recuperator is in the range of 0.3 to 0.4, whereas the effectiveness of pre-cooler was negligible.

Table 6. 1 The effect of using pre-cooler and recuperator in the R236fa jet-pump system

Jet-pump	T_g °C	T_e °C	RG unit	R_m	T_c* °C	Q_e kW	COP
Conventional R236fa Jet-pump	85	4	yes	0.325	29.2	1.20	0.266
	85	8	yes	0.452	30.2	1.62	0.367
	85	12	yes	0.554	31	2.02	0.456
	85	4	no	0.325	29.2	1.17	0.247
	85	8	no	0.452	30.2	1.659	0.357
	85	12	no	0.554	31	2.05	0.437
optimized conv R236fa jet-pump	85	8	yes	0.51	29.5	1.89	0.425
	85	8	no	0.511	29.5	1.87	0.398
Optimized CRMC-R236fa Jet-pump	85	8	yes	0.457	29.5	1.69	0.350
	85	8	no	0.455	29.2	1.63	0.351

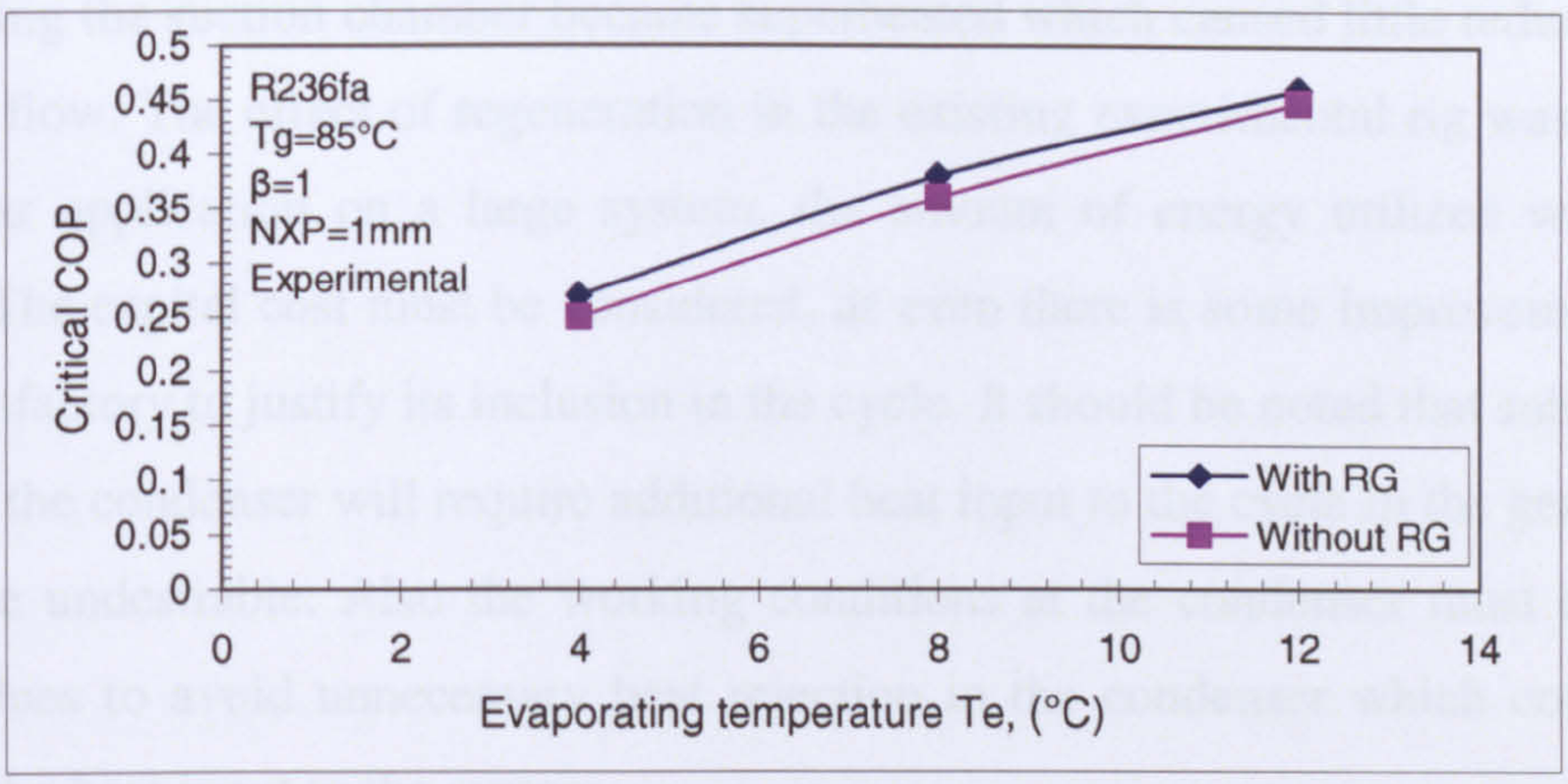

Figure 6. 22 The effect of using RG unit (conventional R236fa jet-pump)(experimental)

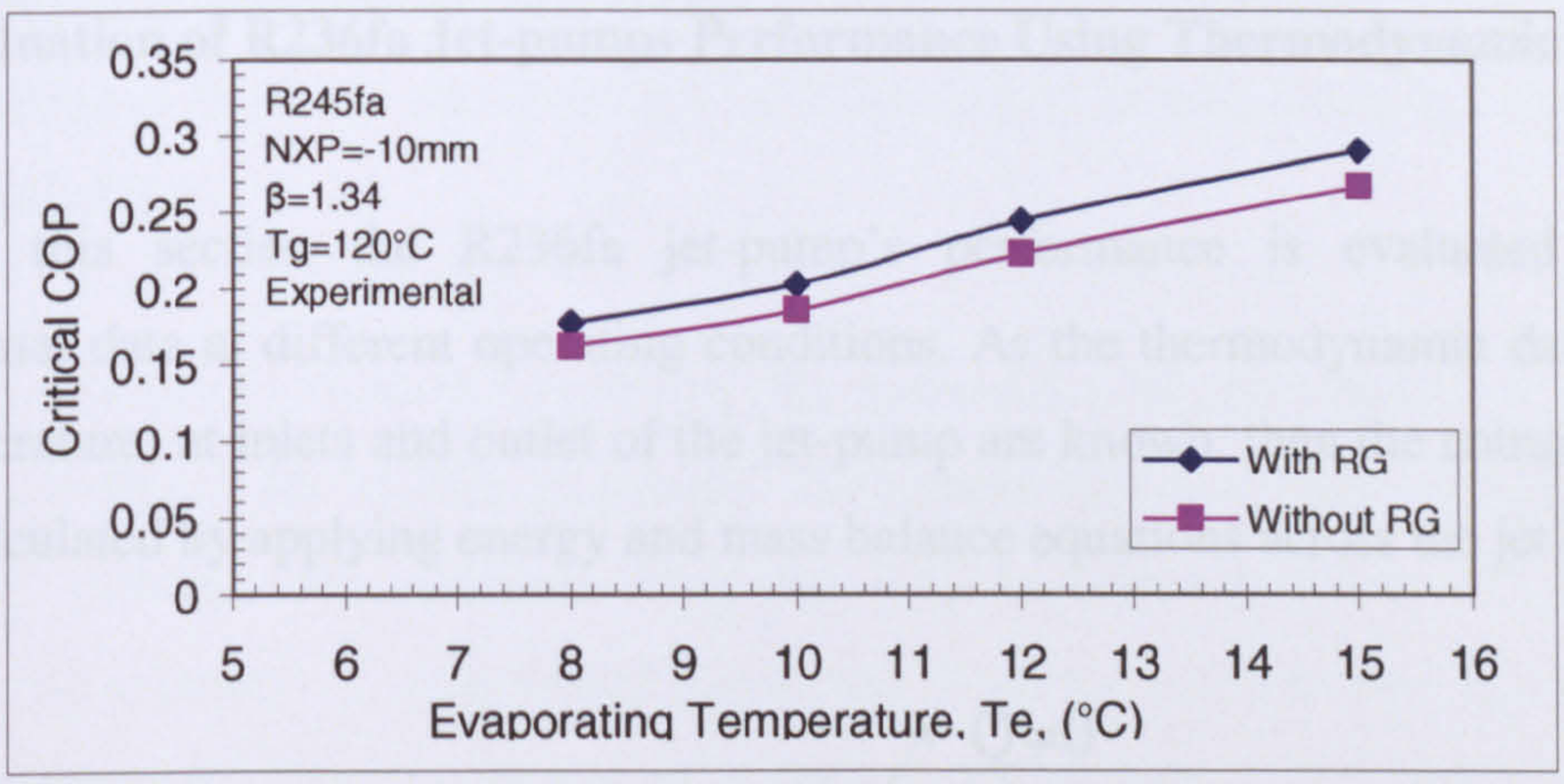

Figure 6. 23 The effect of using RG (conventional R245fa jet-pump) (experimental)

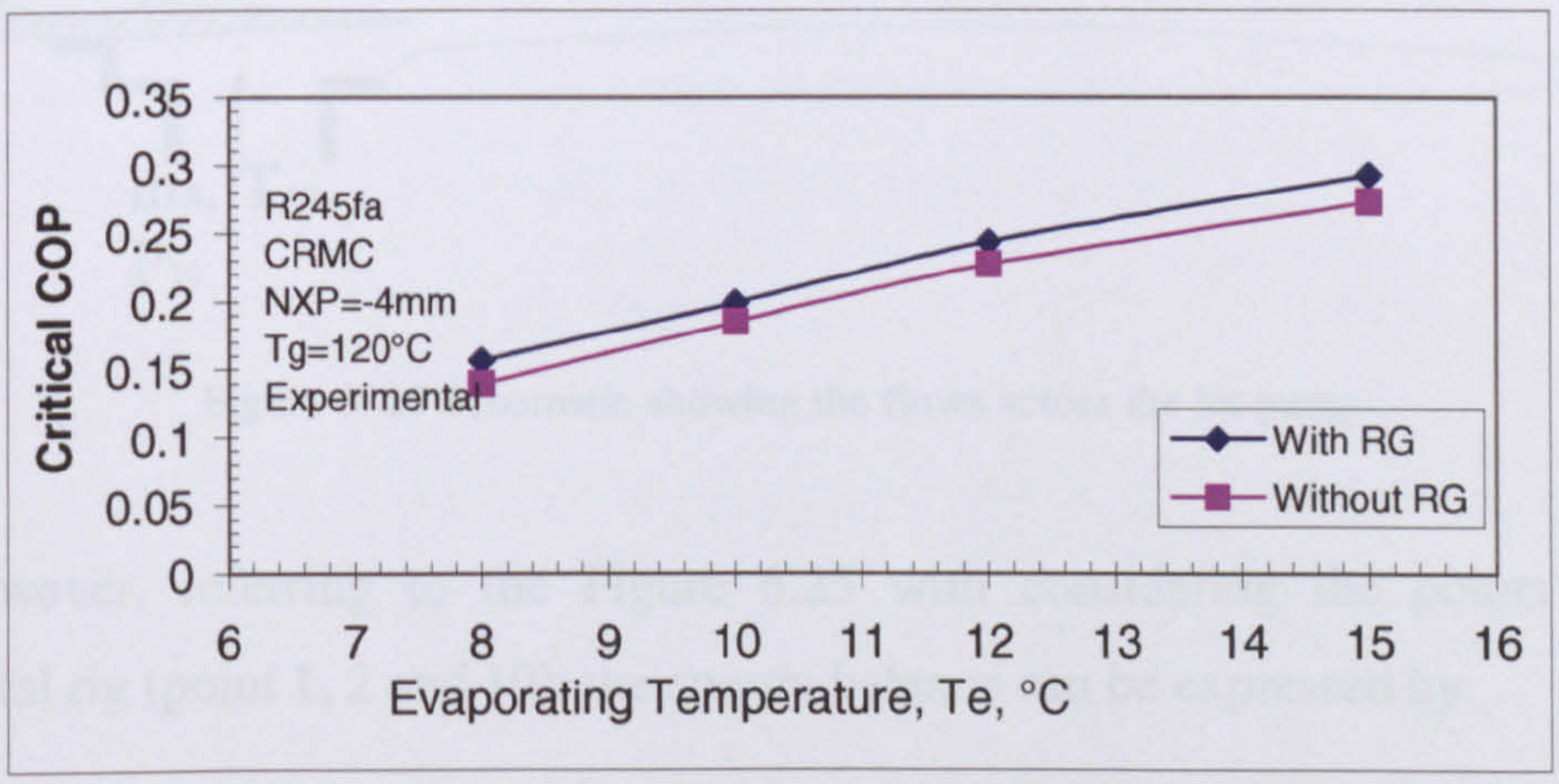

Figure 6. 24 The effect of using RG (CRMC R245fa jet-pump) (experimental)

Negligible variation in cooling capacity was observed when the pre-cooler was used; in some cases it was found that the cooling capacity decreases. The reasons for that are: first, the liquid refrigerant was sub-cooled at the condenser exit with lowering its temperature, thus there was not enough heat to be transported within the pre-cooler; second, in the cases when some heat was exchanged within the pre-cooler, the secondary

fluid entering the suction chamber became superheated which caused little reduction in the secondary flow. The effect of regeneration in the existing experimental rig was small, but in a similar application on a large system, the amount of energy utilized will be very effective. The capital cost must be considered, as even there is some improvement; it may not be satisfactory to justify its inclusion in the cycle. It should be noted that sub-cooling at the exit of the condenser will require additional heat input to the cycle in the generator and is therefore undesirable. Also the working conditions at the condenser must be close to critical values to avoid unnecessary heat rejection in the condenser which could lead to minimize the heat input to the system.

6.3.5 Evaluation of R236fa Jet-pumps Performance Using Thermodynamic Data

In this section the R236fa jet-pump's performance is evaluated using the experimental data at different operating conditions. As the thermodynamic data (pressure and temperature) at inlets and outlet of the jet-pump are known, then the entrainment ratio can be calculated by applying energy and mass balance equations across the jet-pump.

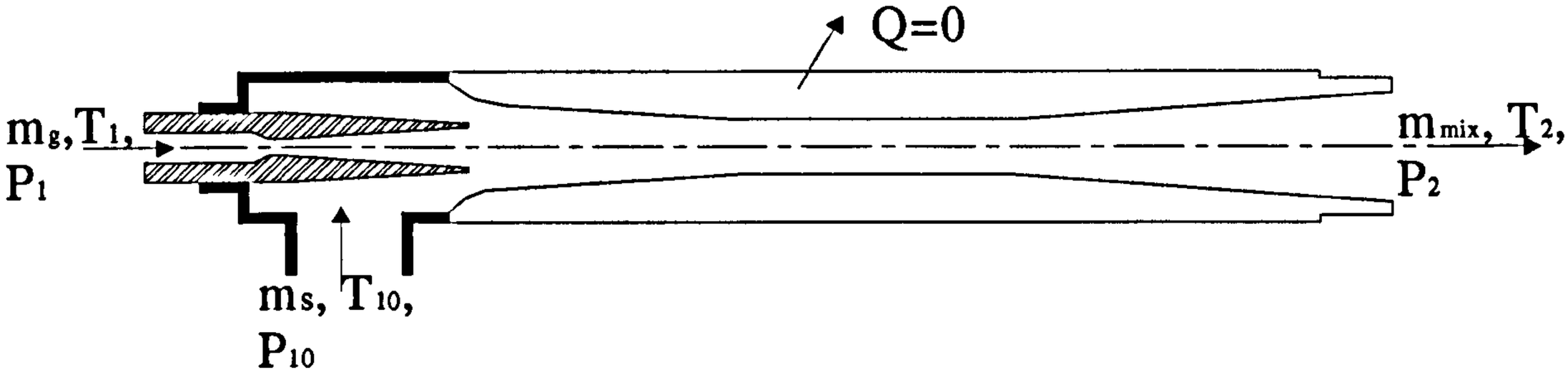

Figure 6. 25 Schematic showing the flows across the jet-pump

However, referring to the Figure 6.25 with considering the points as in the experimental rig (point 1, 2 and 10), the energy balance can be expressed by:

$$m_{mix}\, h_2 = m_g\, h_1 + m_s\, h_{10} \qquad [6.1]$$

Whereas mass balance can be expressed by:

$$m_{mix} = m_g + m_s \qquad [6.2]$$

Referring to entrainment ratio equation, [3.5] then:

$$R_m = \frac{h_1 - h_2}{h_2 - h_{10}} \qquad [6.3]$$

The jet-pump body was treated as adiabatic as there is no heat loss or gain to the jet-pump. The thermodynamic conditions for the suction flow were taken at point 10 instead of point 11 (as indicated by T_{10} and T_{11} in Figure 5.1) because all experimental data was taken when there was a difference of 5 to 8°C between points 10 and 11 to avoid overfilling of evaporator as this may lead to incorrect measurement of secondary flow rate. This difference of temperature was generated by internal heat transfer from primary flow through the jet-pump body and therefore, this amount of heat has already been accounted for in equation 6.1.

To determine entrainment ratio by this method for all experimental data at critical operating conditions for R236fa jet-pumps. The temperature was taken at these points and the related enthalpy was obtained from the R236fa thermodynamic properties tables depending on saturated or superheated conditions. Equation 6.3 was used and the obtained results for the three jet-pumps are shown in Table 6.2a, b and c.

Table 6. 2a Energy balance calculated R_m (conventional R236fa jet-pump)

Conventional R236fa jet-pump, β=1							
T_g °C	T_e°C	h_1 kJkg^{-1}	h_2 kJkg^{-1}	h_{10} kJkg^{-1}	Calculated R_m	Experimental R_m	Discrepancy
82	4	411.6	397.3	362.4	0.409	0.355	13.31
82	8	411.6	396.3	365.1	0.490	0.488	0.40
82	12	411.6	396	367.9	0.555	0.594	-7.01
85	4	413	399	362.4	0.382	0.324	15.06
85	8	413	399.5	365.1	0.392	0.452	-15.19
85	12	413	397.2	367.9	0.539	0.553	-2.71
88	4	414.3	401.6	362.4	0.323	0.286	11.65
88	8	414.3	399.9	365.1	0.413	0.412	0.303
88	12	414.3	399.6	367.9	0.463	0.506	-9.23

Table 6. 2b Energy balance calculated R_m (optimized conventional R236fa jet-pump)

Optimized R236fa conventional jet-pump, β=1.36							
T_g°C	T_e°C	h_1 kJkg^{-1}	h_2 kJkg^{-1}	h_{10} kJkg^{-1}	Calculated R_m	Experimental R_m	Discrepancy
85	4	413.5	396.5	362.7	0.502	0.447	10.95
85	8	413	395.7	365.1	0.565	0.512	9.42
85	12	413.4	394.5	368	0.713	0.543	23.74

Table 6. 2c Energy balance calculated R_m (optimized CRMC R236fa jet-pump)

Optimized CRMC R236fa jet-pump							
T_g°C	T_e°C	h_1 kJkg^{-1}	h_2 kJkg^{-1}	h_{10} kJkg^{-1}	Calculated R_m	Experimental R_m	Discrepancy
85	4	429.56	411.7	362.4	0.362	0.369	-1.961
85	8	413	397.6	365.1	0.473	0.448	5.39
85	12	434.12	406.38	367.9	0.720	0.560	22.27

It is clear from these Tables that there is variation of difference in most cases. Sometimes the difference is quite small, and the results seem to be in good agreement; sometimes the difference is large. The range of discrepancy is from 2% to 23%. This range of experimental error can be related to many effects such as potential error in temperatures measurements, and potential error in flow measurements, moreover to some heat losses within the jet-pump body.

6.4 Comparison of CFD and Experimental Results

- **Comparison of NXP**

As one most important aim of this study is to be assured that the CFD has the ability to predict the jet-pump performance correctly, a comparison between experimental and CFD results was carried out. The first parameter of comparison is the NXP. Table 6.3 shows the optimum NXP obtained experimentally and by CFD for each jet-pump.

Table 6. 3 Comparison of NXP results

Fluid	Jet-pump	NXP - CFD	NXP - experimentally
R236fa	Conventional "β=1"	4mm	1mm
R236fa	Optimized Conv "β=1.36"	9mm	7.5mm
R236fa	Optimized CRMC	15mm	17mm
R245fa	Optimized Conv "β=1.34"	-12.5mm	-10mm
R245fa	Optimized CRMC	-2.5mm	-4mm

Qualitatively the experimental NXP results matched well with that obtained from CFD simulation. The NXP obtained experimentally is in good agreement with that predicted by CFD with ±3mm. The optimal range of NXP obtained experimentally with each jet-pump was also found to provide the maximum R_m with CFD, but with little difference on T_c* by about ±0.5K. In the case of optimized conventional R245fa jet-pump

the optimum nozzle position was found by CFD = -12.5 mm, experimentally this nozzle position could not be tested because of the restriction of nozzle assembly mechanism; but the increase in R_m was observed experimentally as the nozzle was moved upstream to the NXP=-10mm.

However, with all jet-pumps that were used, the NXP was found in good agreement with CFD, thus this is proof of the validity of using CFD to predict correctly the optimal NXP that is difficult to determine by theoretical analysis and expensive to determine experimentally. The considerable variation of NXP with each jet-pump makes it clear that NXP was highly dependent on the construction shape of the mixing section that restricted the space of secondary flow entry with the nozzle lips; even though the recommendations of ESDU (ESDU 1986), that suggested placing the nozzle exit between 0.5 and 1.0 length of the mixing section throat diameter upstream of the mixing chamber, the experimentally jet-pump performance was found to vary remarkably within this range.

- **Comparison of Critical Condensing Temperature (T^*_C)**

Comparing predicted and measured critical condensing temperature values (T_c^*) for all jet-pumps show valuable finding. Figures 6.26 and 6.27 show the comparison of T_c* at different T_e with design value of T_g for optimized R236fa jet-pumps, whereas Figures 6.28 and 6.29 show the comparison of T_c* at different T_g with design value of T_e for optimized R245fa jet-pumps. The comparisons of T_c^* results at other operating conditions tested are presented in Appendix E.

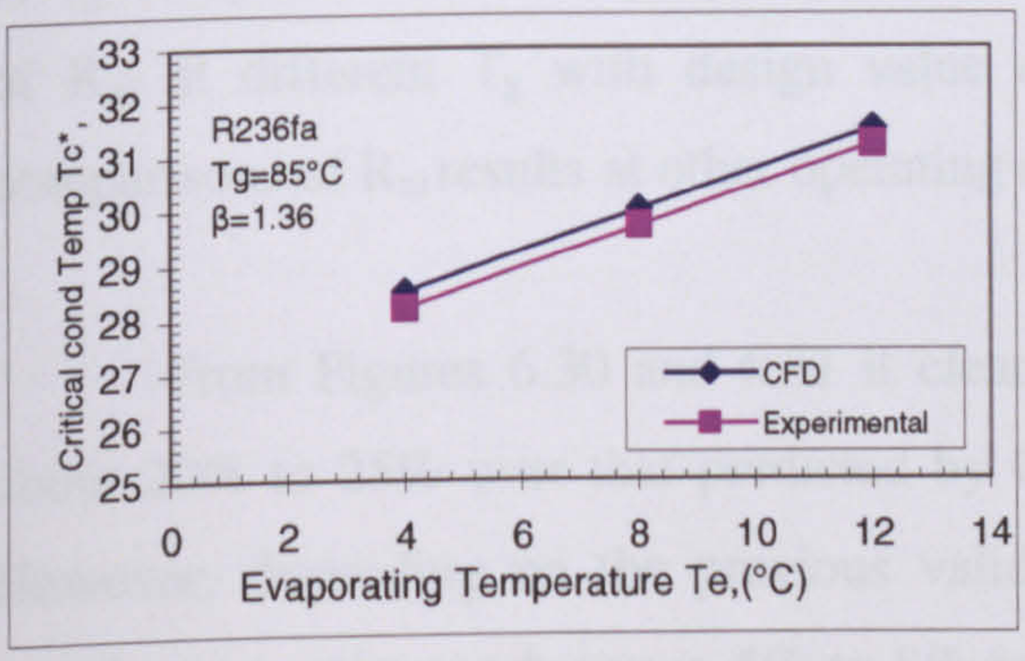

Figure 6. 26 Comparison of T_c^* at different T_e (T_g=85°C)
Optimized conventional R236fa jet-pump

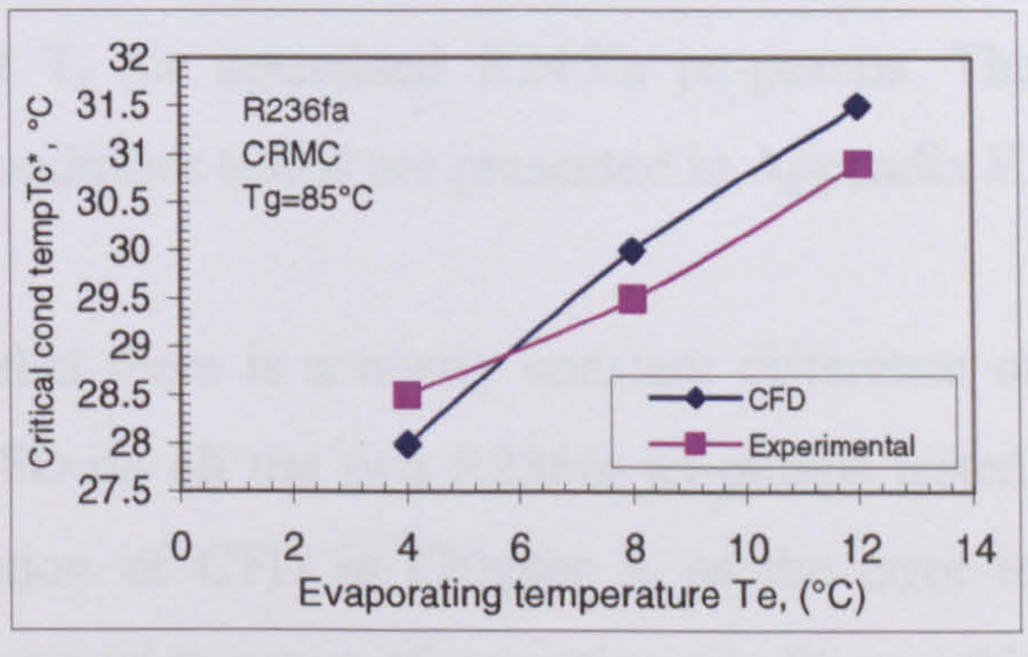

Figure 6. 27 Comparison of T_c^* at different T_e (T_g=85°C)
Optimized CRMC R236fa jet-pump

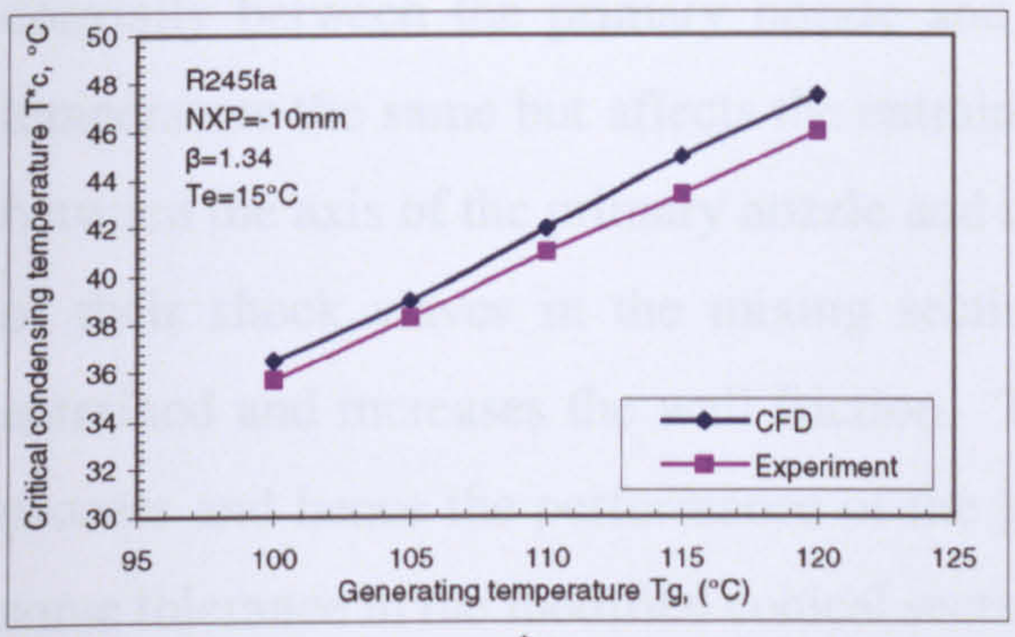

Figure 6. 28 Comparison of T_c^* at different Tg (T_e=15°C) Optimized conventional R245fa jet-pump

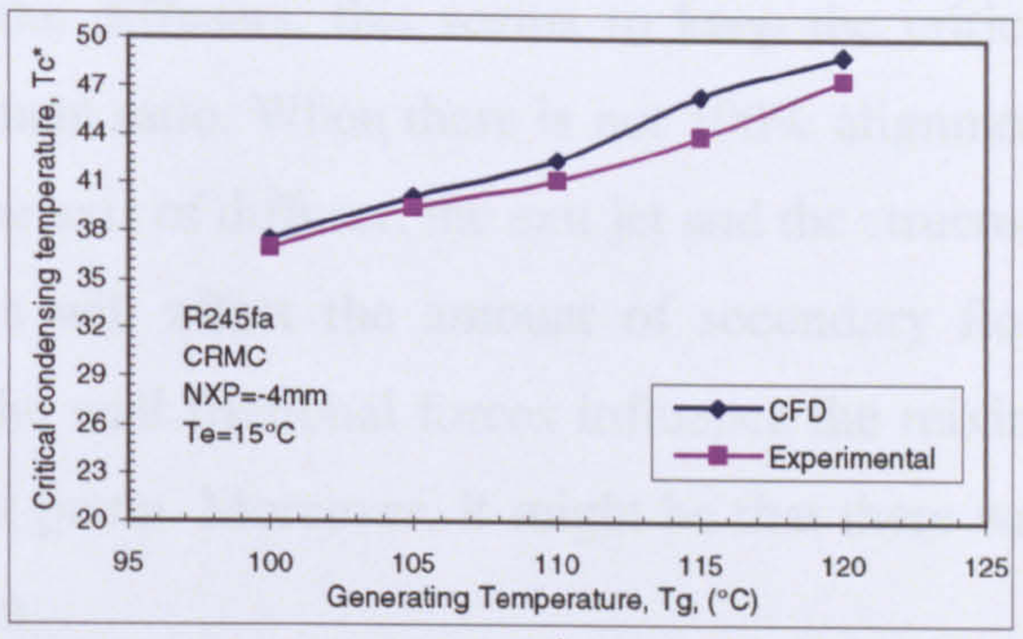

Figure 6. 29 Comparison of T_c^* at different T_g (T_e=15°C) Optimized CRMC R245fa jet-pump

From above Figures it can be seen that the CFD results have good agreement with the experimental results at all T_g and T_e values tested. In most cases with R236fa jet-pumps the error in T_c^* is nearly constant and does not exceed 0.5°C. In both R236fa jet-pumps with T_e=8°C, (designed evaporator temperature) the difference was only from 0.2°C to 0.4°C, which is believed to be acceptable. In the case of the optimized CRMC R236fa jet-pump, the overall discrepancies at all T_e tested are within ±2% of the CFD values. The fluctuation in the difference of T_c^* at different T_e, may be related to the shape of mixing section wall where the primary jet meet, that control the mixing rate between the primary and secondary streams. While with R245fa jet-pumps the T_c* was found to be about 4% different, i.e. 1°C less than predicted CFD values for all cases. This agreement of both obtained results is thought to demonstrate that there can be confidence in the CFD results.

- **Comparison of Critical Entrainment Ratio (R_m)**

Figures 6.30 and 6.31 show the comparison of R_m at different T_e with design value of T_g for optimized R236fa jet-pumps, whereas Figures 6.32 and 6.33 show the comparison of R_m at different T_g with design value of T_e for optimized R245fa jet-pumps. The comparisons of R_m results at other operating conditions tested are presented in Appendix E.

From Figures 6.30 and 6.31 it clear that there is a nearly constant difference of about 20% to 25% over that predicted by CFD on all the two R236fa jet-pumps tested. However, depending on the previous validation of CFD in Chapter 3, as the error in entrainment ratio was between 5% to 8% over a wide range of operating conditions: this error between CFD and experimental results for these jet-pumps may be related to the manufacturing of the jet-pump itself. It was found that there was small error in the

coaxially between the primary nozzle and the diffusers, this seems to keep the critical temperature the same but affects the entrainment ratio. When there is not 100% alignment between the axis of the primary nozzle and the axis of diffuser, the exit jet and the structure of their shock waves in the mixing section will affect the amount of secondary flow entrained and increases the wall friction. The wall frictional forces influence the mixing process and hence the performance of the jet-pump. Moreover, it might be that there was some tolerance in the modified conical section.

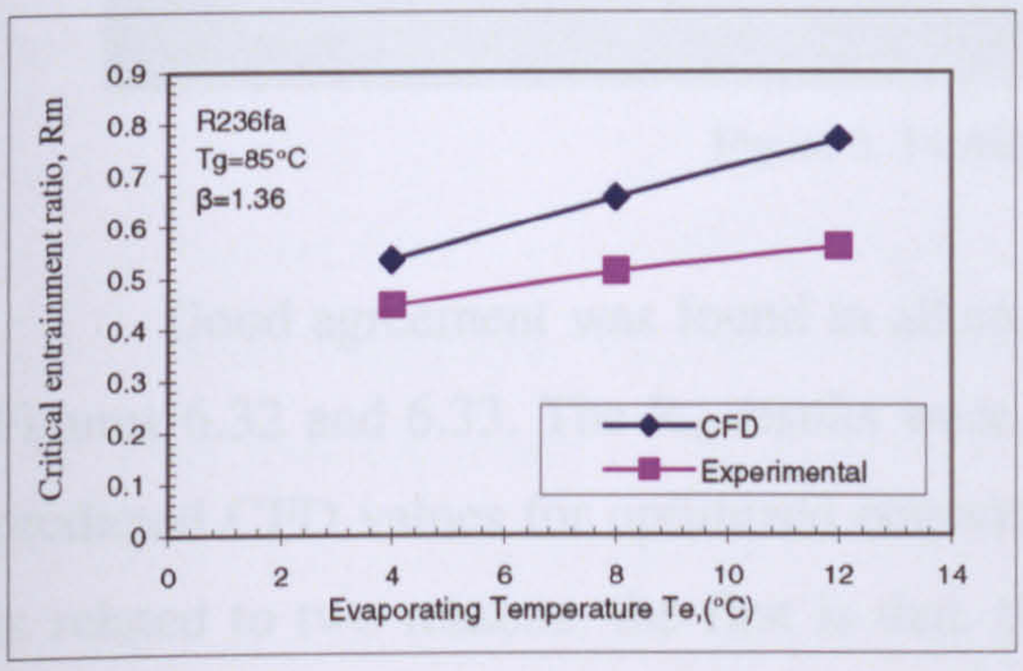

Figure 6. 30 Comparison of R_m at different T_e (T_g=85°C)
Optimized conventional R236fa jet-pump

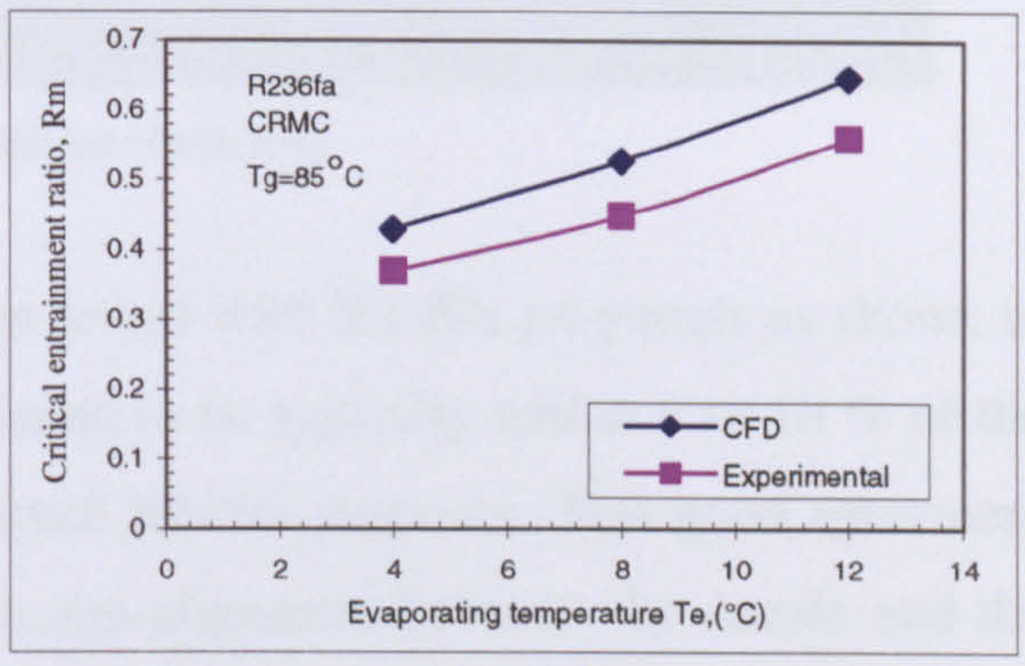

Figure 6. 31 Comparison of R_m at different T_e (T_g=85°C)
Optimized CRMC R236fa jet-pump

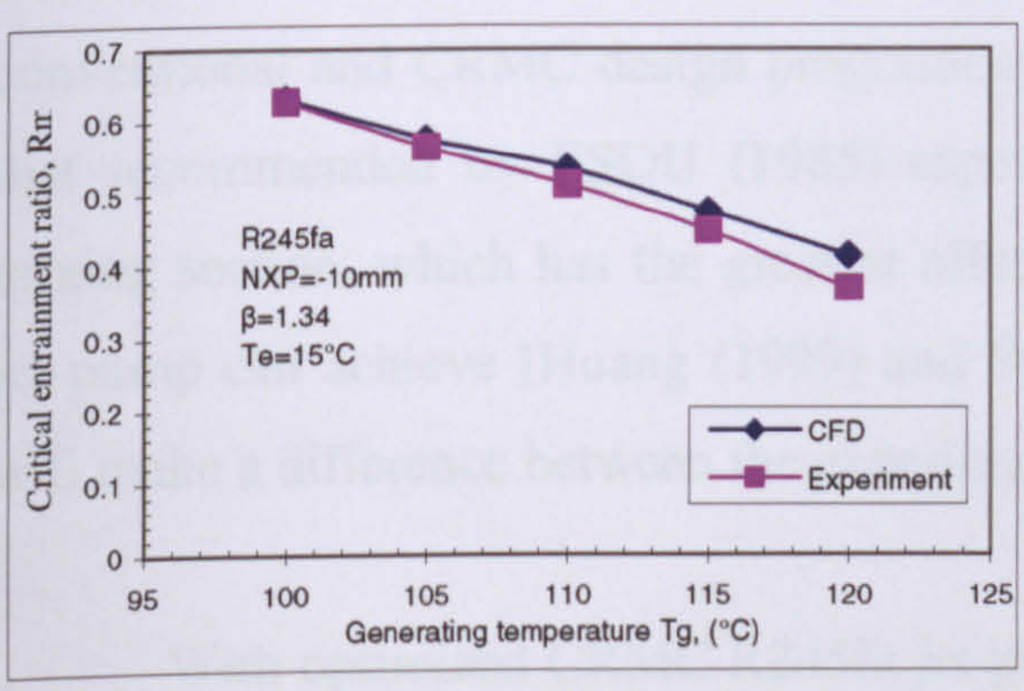

Figure 6. 32 Comparison of R_m at different T_g (T_e=15°C)
Optimized conventional R254fa jet-pump

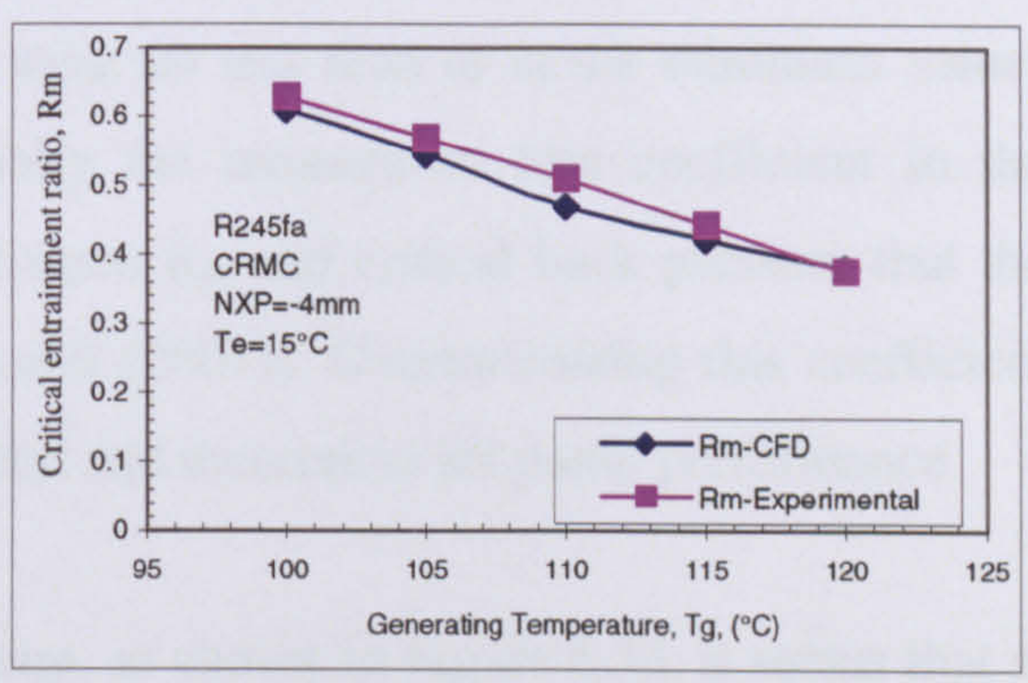

Figure 6. 33 Comparison of R_m at different T_g (T_e=15°C)
Optimized CRMC R245fa jet-pump

There was a special tool (Figure 6.34) designed to make sure of alignment of both axes. By using this tool, it was found that there was small misalignment between the primary nozzle and the diffuser. Thus the small percentage difference in R_m between CFD and experimental results for R236fa jet-pumps is thought to be due to this non-alignment effect. Also, pressure losses in the secondary flow in the suction line could have direct effect on change of R_m, but a small effect on change of T_c^*.

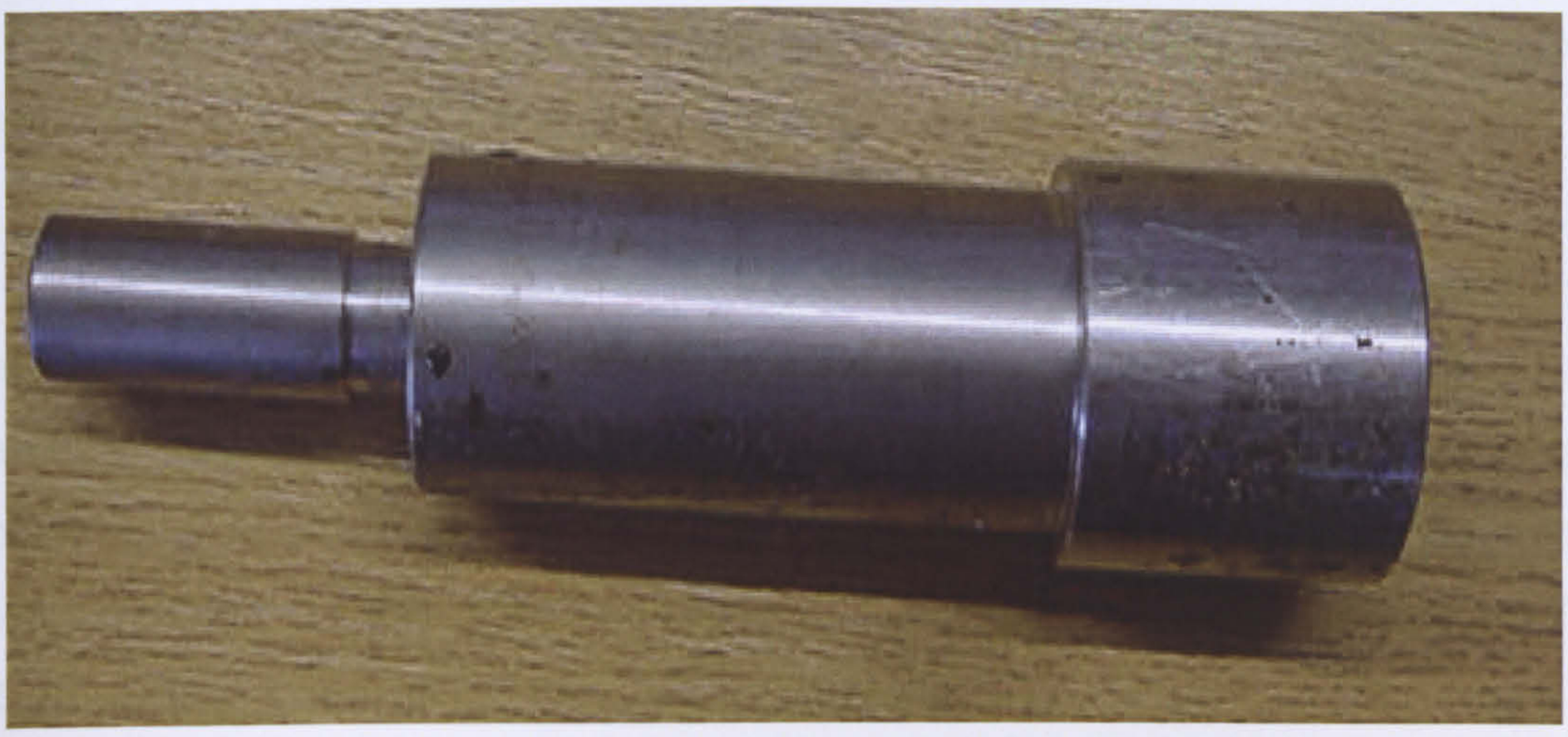

Figure 6. 34 Alignment check tool

Good agreement was found in all cases tested with R245fa jet-pumps as shown in Figures 6.32 and 6.33. The R_m results were found to be typically within 8 to 10 % of the predicted CFD values for optimized conevntional R245fa jet-pump. This good agreement is related to two reasons, the first is that, the non-alignment between the nozzle and the diffuser was avoided with R245fa jet-pumps. The second is that in the theoretical design, as mentioned in Chapter 4, the values of loss coefficients that were used in the conventional and CRMC design programme were set less than or at the minimum values that recommended by ESDU (1985) especially the momentum loss coefficient in the mixing section, which has the greatest effect upon R_m and critical back pressure that the jet-pump can achieve [Huang (1999) and Worall (2001)]. Overestimating this coefficient will make a difference between the experimental and theoretical jet-pump performance.

With optimized CRMC R245fa jet-pump, as shown in Figure 6.33, it seems that at higher T_e, the experimental R_m is higher than that of predicted by CFD; One reason for that is that as it is well known that secondary flow is very sensitive to inlet geometry, any surface roughness or sharp bend causes significant losses due to fluid friction at the wall, whereas surface smoothness and large annular area at the secondary flow entrance will reduce any losses. The entrance of optimized CRMC R245fa diffuser is seems more smoothly than the conventional diffuser. Also, because at the NXP=-4mm the distance between the primary jet and the wall of the entry cone is larger than that was used in CFD simulation, this enhances the amount of secondary flow entrained with rapid acceleration to sonic velocity. Referring to the static pressure profiles along the jet-pump centre line in Chapter 4, the pressure at the secondary flow entrance is lower than that at the nozzle exit,

this would allow greater expansion of secondary flow, and thus higher mass flow is entrained with a consequent increase in entrainment ratio.

A percentage of this range of errors in entrainment ratio also is caused by the secondary flow measurements, during the experimental test it was observed that the entrainment ratio can be enhanced by approximately 10% to 15 % by reducing the temperature of the water supply into the evaporator; all experimental results shown in this section were taken at a difference between load temperature and operating condition T_e , of 10 °C to 12 °C.

Further significant differences between CFD predictions and experiment results for all jet-pumps tested were thought to result from pressure losses within the suction line and also some pressure losses within primary nozzle. It is worth mentioning that the degree of superheating of entrained flow may affect the jet-pump performance and make the results of experiment vary. However, the CFD approach appears strongly viable for predicting the flow fields associated with jet-pump operation in refrigeration system.

6.5 Effect of Primary Nozzle Geometry

In order to study the influences of the primary nozzle geometry on jet-pump performance, the primary nozzle that was used with R236fa diffusers was tested with the optimized CRMC R245fa jet-pump. Details of this nozzle construction were provided in Chapter 4. The same experimental procedure of calibration and finding the optimal NXP for this nozzle were conducted. Then at the optimal NXP the jet-pump was tested at T_g of 110°C, 115°C and 120°C, with an evaporator temperature of 10°C ,12°C and 15°C and condenser temperature ranges from 32°C to 40°C. The system working stability was achieved with this nozzle without facing any problem.

Figure 6.35 represents the performance characteristic of the optimized CRMC R245fa jet-pump with 2.2mm throat diameter nozzle. Figures 6.36 and 6.37 show the COP and the cooling capacity respectively at all operating conditions tested with this nozzle.

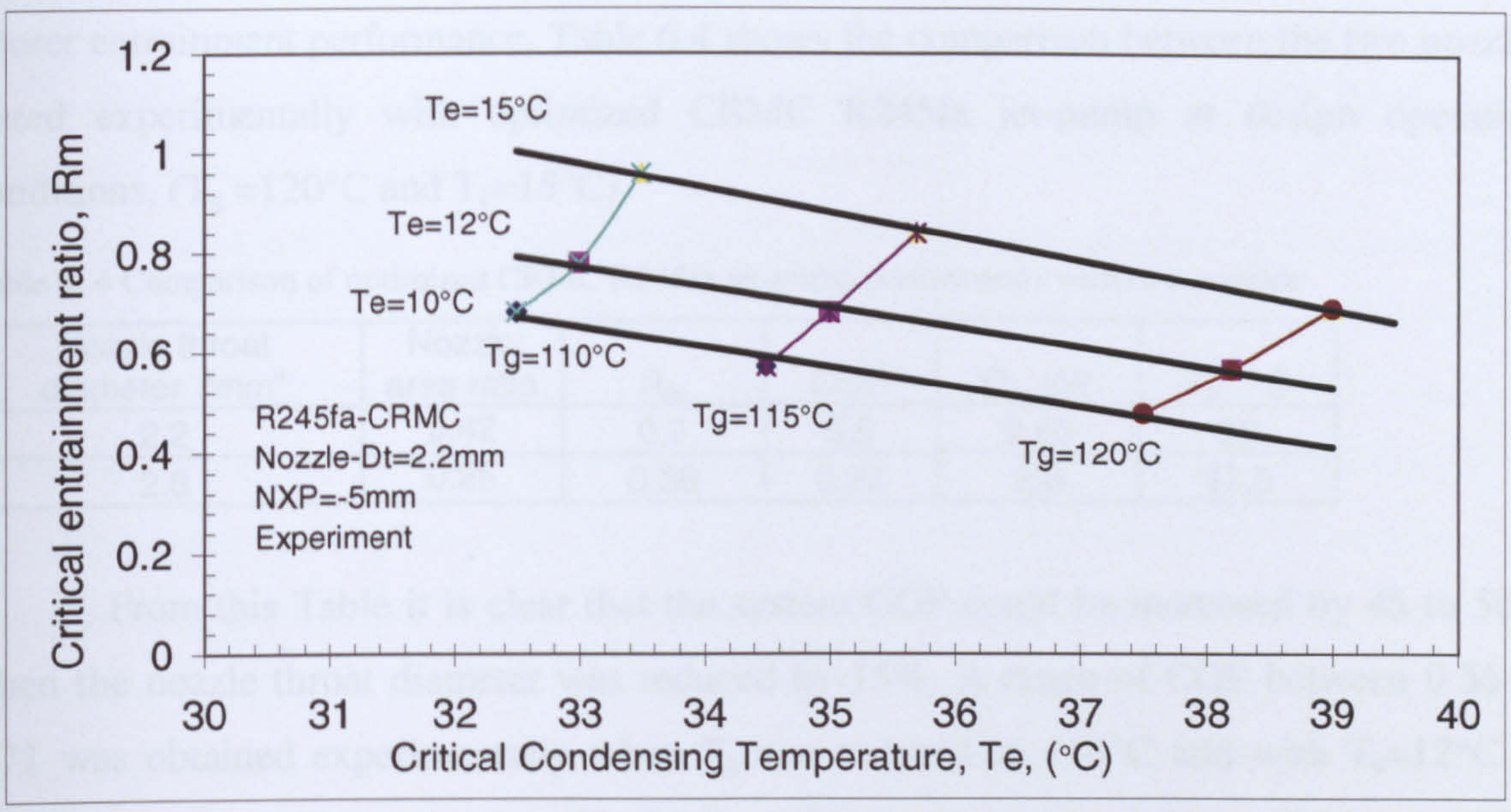

Figure 6. 35 Optimized CRMC R245fa jet-pump characteristics with 2.2mm nozzle (experimental)

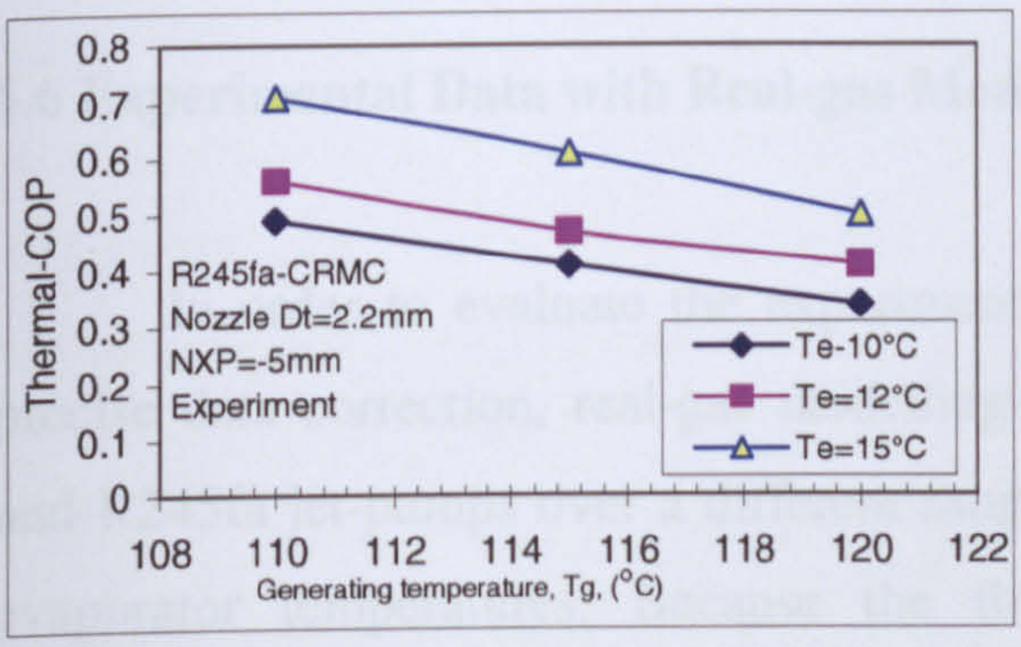

Figure 6. 36 Optimized CRMC R245fa jet-pump COP with 2.2mm nozzle (experimental)

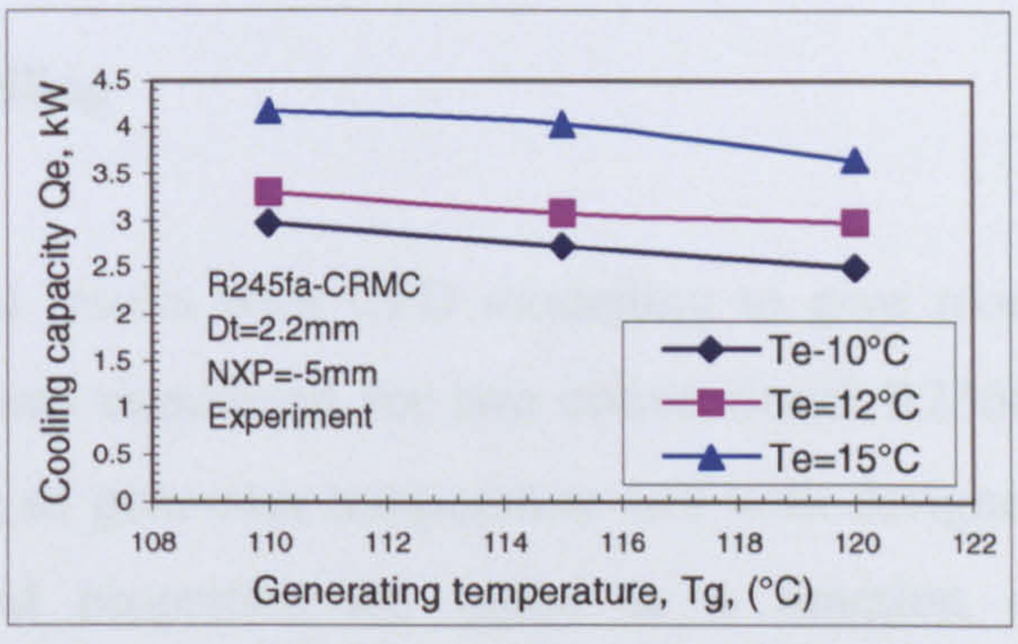

Figure 6. 37 Optimized CRMC R245fa jet-pump Q_e with 2.2mm nozzle (experimental)

It is clear from these three Figures that there is a significant effect of primary nozzle geometry on the jet-pump performance, when the jet-pump was equipped with a smaller primary nozzle. The entrainment ratios, COP and cooling capacity were increased dramatically. However, only the critical condensing temperature was decreased, and this is because of the effect of motive jet-core; at fixed operating conditions, a smaller primary nozzle produced smaller jet-core and thus less momentum was produced, and a larger amount of secondary fluid was allowed to be entrained. As the two nozzles have the same slope angle for the diverging section, the isentropic efficiency for the two nozzles may be the same, but the effect only due changing the size which reduces the amount of primary flow and also the jet angle in the mixing section. Comparing the jet-pump performance with that used in CFD simulation, section 4.3.2.3, as that nozzle has large exit area and thus longer divergent expansion piece. That nozzle has less isentropic efficiency and

poorer entrainment performance. Table 6.4 shows the comparison between the two nozzles tested experimentally with optimized CRMC R245fa jet-pump at design operating conditions, (T_g =120°C and T_e=15°C).

Table 6. 4 Comparison of optimized CRMC R245fa jet-pump performance with two nozzles

Nozzle throat diameter "mm"	Nozzle area ratio	R_m	COP	Q_e kW	T_c* °C
2.2	0.42	0.7	0.5	3.65	39
2.6	0.25	0.38	0.27	2.8	47.5

From this Table it is clear that the system COP could be increased by 45 to 50% when the nozzle throat diameter was reduced by 15%. A range of COP between 0.56 to 0.71 was obtained experimentally when T_g was reduced to 110°C and with T_e=12°C to 15°C respectively. However, there is a high confidence to say that it is possible to get COP of 0.6 to 0.8 with T_c* around 38°C.

6.6 Experimental Data with Real-gas Modelling

In order to evaluate the experimental results with CFD modelling to give more precise data correction, real-gas modelling was conducted for two conventional R236fa and R245fa jet-pumps over a different range of generator temperature and with designed evaporator temperatures. Because the fluid properties are taken as a function of temperature in real-gas modelling which is time consuming, no further simulation was conducted.

Figure 6.38 shows the CFD real-gas simulation results for R236fa conventional jet-pump compared with previous ideal-gas and experimental results.

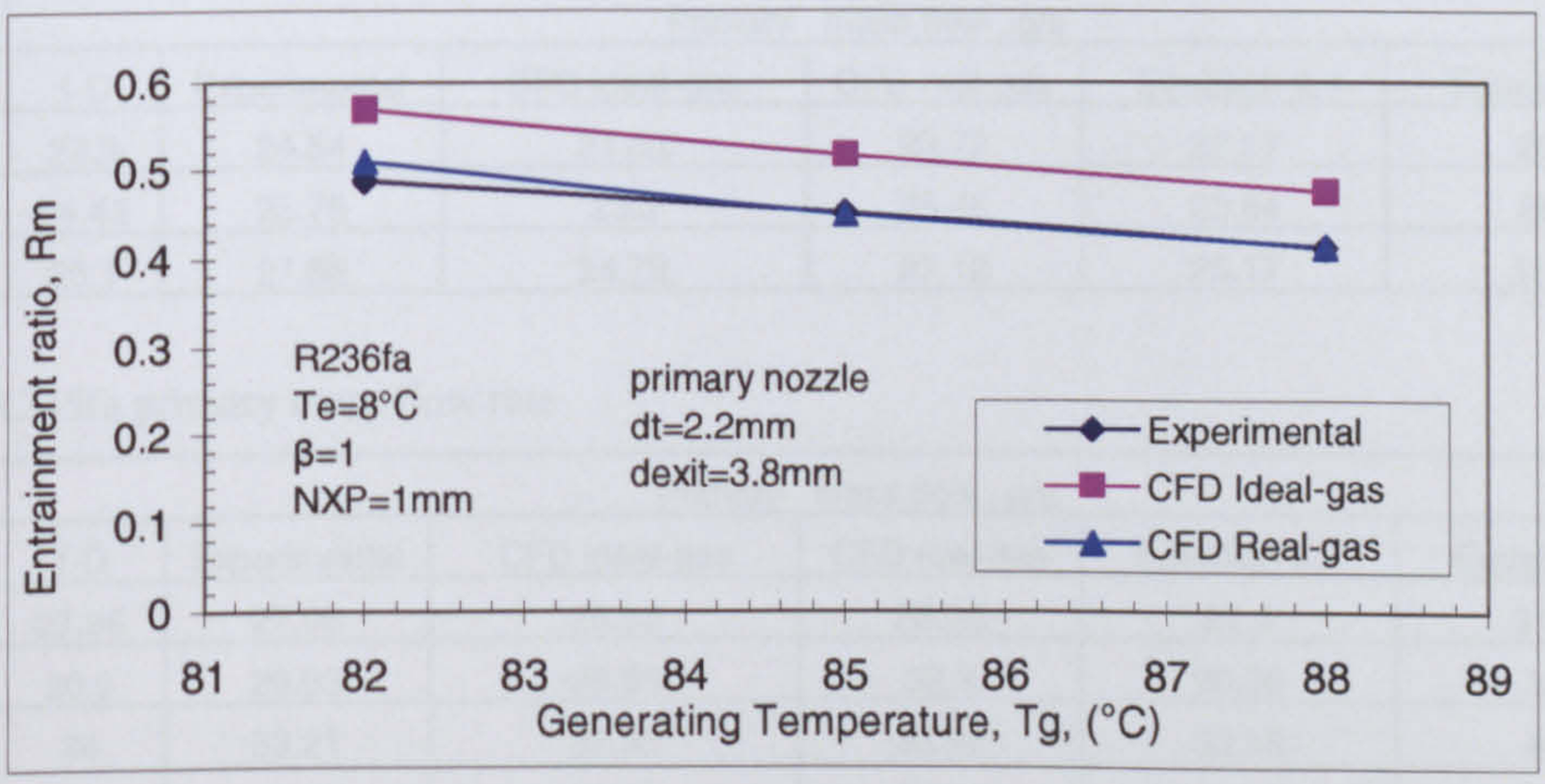

Figure 6. 38 Conventional R236fa jet-pump performances with real gas modelling

From the Figure 6.38 it can be seen that the CFD real-gas results are in good agreement with experimental ones; but with deviations of 8 to 10% with that obtained from CFD ideal-gas modelling. This difference in entrainment ratio between ideal-gas and real-gas modelling results was found to be based on a difference in primary mass flow only as shown on the Table 6.5a and 6.5b below. The secondary mass flow was found nearly the same with 1 to 2% deviation between experimental and CFD ideal or real gas simulations. The other parameters which are NXP, and T_c^* were almost constant between ideal-gas and real-gas modelling. Tables 6.5a and 6.5b show a comparison between all results of primary flow rates obtained for both R236fa and R245fa primary nozzles respectively at different generating temperatures, including results obtained from Equations 6.4 and 6.5 which are shown below. Equation 6.4 was defined by Rogers and Mayhew (1988) to calculate the primary mass flow within the primary nozzle by setting M=1 as the flow is sonic at the throat. Whereas, Equation 6.5 was presented by Robinson (1927), and it shows that the primary mass flow is independent of the throat pressure and temperature and if the real-gas data of primary flow is taken from tables, then it automatically provides some allowance for real-gas effect such as compressibility.

$$A_t = \frac{1}{M}\frac{\dot{m}}{P_g}\left[\frac{RT_g}{\gamma}\left(1+\frac{\gamma-1}{2}M^2\right)^{\frac{\gamma+1}{\gamma-1}}\right]^{\frac{1}{2}} \qquad [6.4]$$

$$\frac{\dot{m}}{A_t} = \sqrt{\gamma\left(\frac{2}{\gamma+1}\right)^{\frac{\gamma+1}{\gamma-1}}\left(\frac{p_g}{V_g}\right)} \qquad [6.5]$$

Table 6. 5a R236fa primary mass flow rate

R236fa	Primary mass flow , g/s					
T_g °C	1-D	Experimental	CFD ideal-gas	CFD real-gas	Equation 6.4	Equation 6.5
82	23.3	24.54	21.83	23.72	22.17	26.7
85	24.43	25.78	23.3	25.46	23.64	28.7
88	26.1	27.86	24.78	27.12	25.17	31.03

Table 6. 5b R245fa primary mass flow rate

R245fa	Primary mass flow , g/s					
T_g °C	1-D	Experimental	CFD ideal-gas	CFD real-gas	Equation 6.4	Equation 6.5
100	27.96	27.06	26.93	28.95	27.4	31.87
105	30.9	29.93	29.86	32.3	30.36	35.8
110	34	33.21	32.98	35.92	33.55	40.1
115	37.7	36.9	36.35	39.89	36.98	46.1
120	43.6	40.18	40	44.23	40.66	50

From these two Tables it can be seen that the primary mass flow is under-predicted by the ideal-gas simulation, and that is why the entrainment ratio is slightly over-predicted by ideal gas modelling. Equation No 6.4 gives results in good agreement with ideal gas modelling both with R236fa and R245fa. Whereas, equation No 6.5 gives results that seem quite far from accurate results, thus this equation is not recommended to be used in primary nozzle design. The experimental results lie between 1-D and real-gas results.

Since the flow is supersonic and the operating conditions were below the critical points, the compressibility factor for this type of flow tended to be closed to one, making this approach of using ideal gas relationship justifiable. However, the 1-D method that is based on the conservation of mass equation and was used in this thesis is seems to be more accurately in predicting the primary mass flow within the primary nozzle.

6.7 Conventional and CRMC Jet-pumps Performance

From conventional R236fa jet-pumps, it is obviously clear that the performance of optimized R236fa jet-pump "β=1.36" was increased by about 15% over that of the conventional one "β=1", with keeping nearly the same design critical condensing temperature. However, this is proof that the constant pressure mixing jet-pump has a better performance over the constant-area mixing jet-pump "conventional jet-pump, β=1". So it is clear that the secondary flow is very sensitive to inlet geometry; a 1mm increase at entrance bends could cause significant increase in R_m. Referring to CFD simulation in the previous Chapter, and Eames (2004a), the increase in diffuser area ratio (β) from 1 to 1.36 increases R_m significantly: thus (β) must be carefully chosen, to provide smooth flow and provide optimal space for entraining secondary flow with keeping designed critical condensing pressure. If it is too large, frictional effects increase and thus reduce the total momentum of the flow.

Figure 6.39 shows a performance comparison between the three jet-pumps that have been tested with R236fa at design operating conditions. It is clear that the obtained results for optimized CRMC R236fa jet-pump were in good agreement with those obtained from the conventional jet-pump "β=1". Only 0.5°C less in critical condensing temperature with optimized CRMC jet-pump. This is because of boundary reverse flow losses at the

CRMC diffuser, as shown in Chapter 4, and poor profiling of the mixing section. No improvement was proved with CRMC R236fa jet-pump.

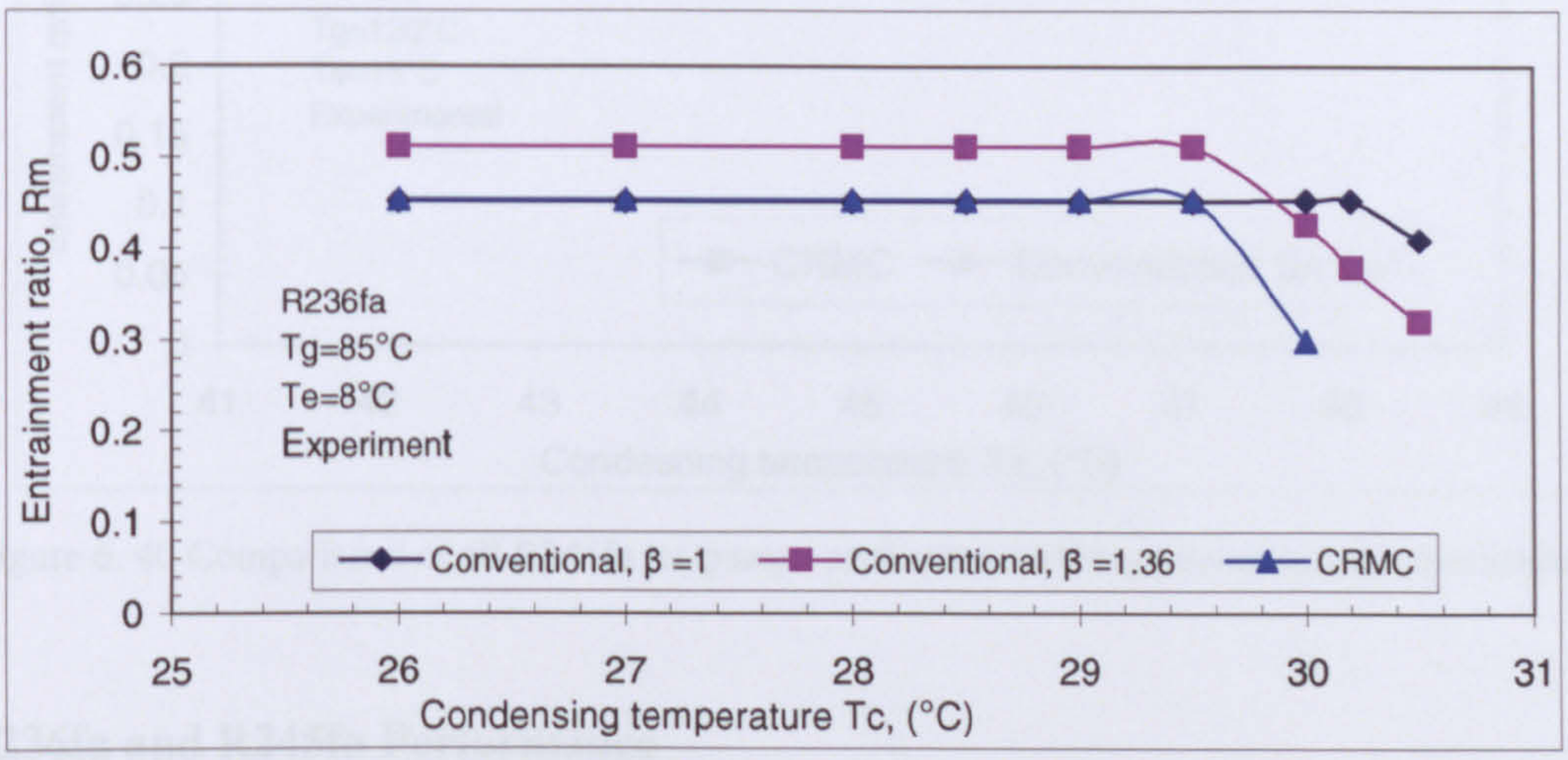

Figure 6. 39 Comparisons of all R236fa jet-pumps performance (design conditions) (experimental)

Figure 6.40 compares the Conventional and CRMC R245fa jet-pumps at the same design operating conditions. It is clear that both jet-pumps have provided the same entrainment ratio. 1°C greater in critical condensing pressure was achieved by the CRMC R245fa jet-pump. However, in all cases the critical condensing temperature obtained by optimized CRMC R245fa jet-pump with any couple of operating conditions was higher by 1 to 1.5°C than that of conventional jet-pump for the same operating conditions. One reason for that is the effect of chock system was decreased within CRMC jet-pump or the losses in the mixing section were minimized, because the entrance profile of the mixing section is seems smoother than the conventional R245fa jet-pump.

This was not achieved with R236fa CRMC jet-pump, because the length of mixing section was of particular importance and it was reduced and optimized with R245fa CRMC diffuser. However, if the same thing was done with R236fa CRMC diffuser the same percentage of increase could be obtained. On the other hand, for evolution both jet-pump performances the same working principle of the two jet-pumps was achieved theoretically by CFD and experimentally and this in contrast with results obtained by Worall (2001) who stated that the assumption with CRMC is not justified. The general trend of all curves in the CRMC Figures is the same as that obtained with other jet-pumps, showing that the optional mode under different T_c at fixed T_g and T_e is the same for any jet-pump.

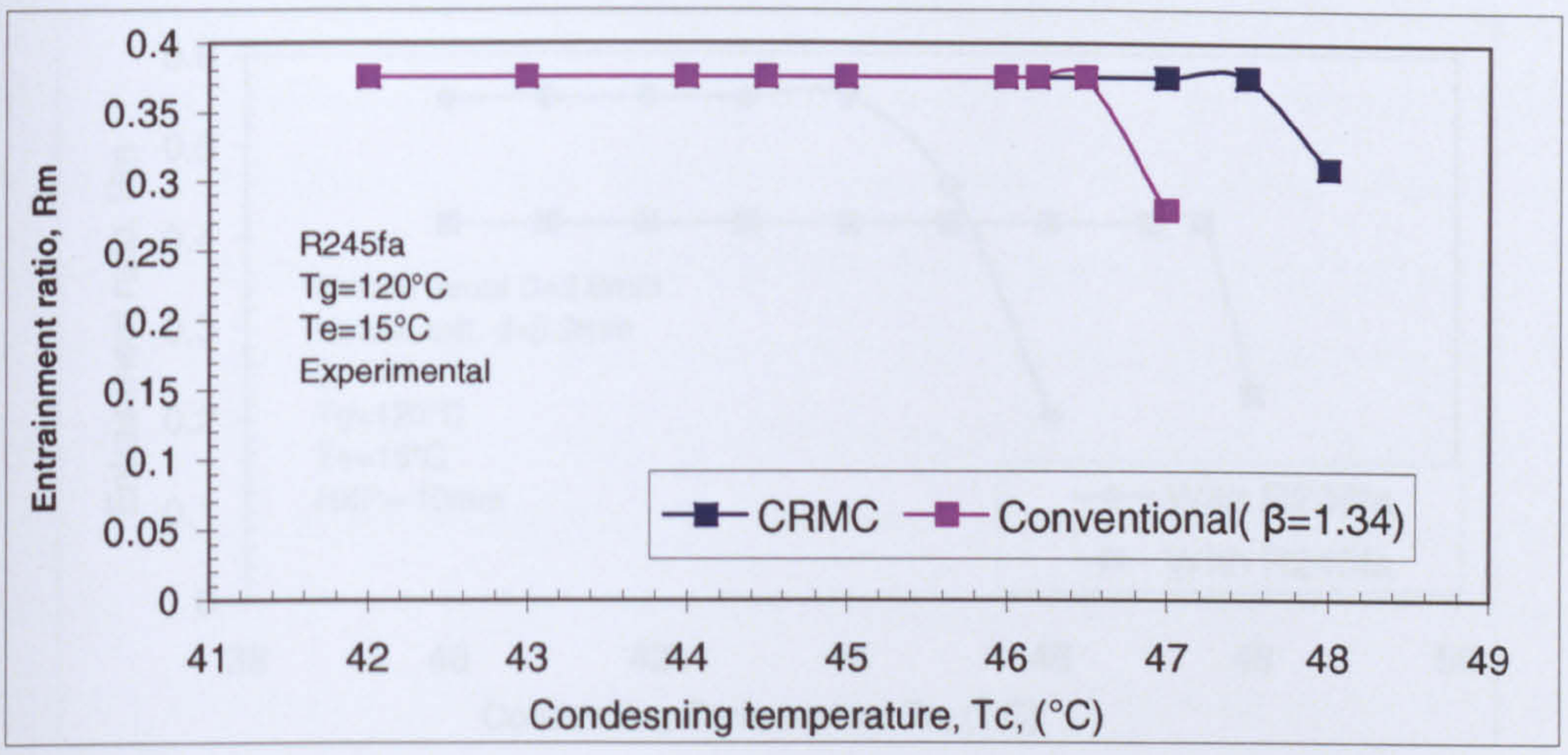

Figure 6. 40 Comparisons of all R245fa jet-pumps performance (design conditions) (experimental)

6.8 R236fa and R245fa Performance

The comparison between R236fa and R245fa as the working fluid in this research is based on their performance with jet-pump refrigeration system. Both of the fluids were tested successfully and they seem to be practical and appropriate choice of working fluid for jet-pump refrigeration systems; they could provide higher performance with using low source of heat; thus the system can be run by low grade energy especially when ample condenser cooling facilities are available.

Unfortunately these two fluids were not tested experimentally under the same operating conditions or the same jet-pump geometry. This was because of feed pump cavitations problem with R236fa at higher generator pressure. But as there was good validation for both of them from CFD modelling, it is possible to evaluate their performance at fixed jet-pump geometry and specific operating condition. Figure 6.41 shows the predicted CFD results for optimized Conventional R245fa jet-pump with both R236fa and R245fa, at T_g=120°C, and T_e=15°C, while Figure 6.42 show the CFD results at T_g=110°C, T_e=15°C.

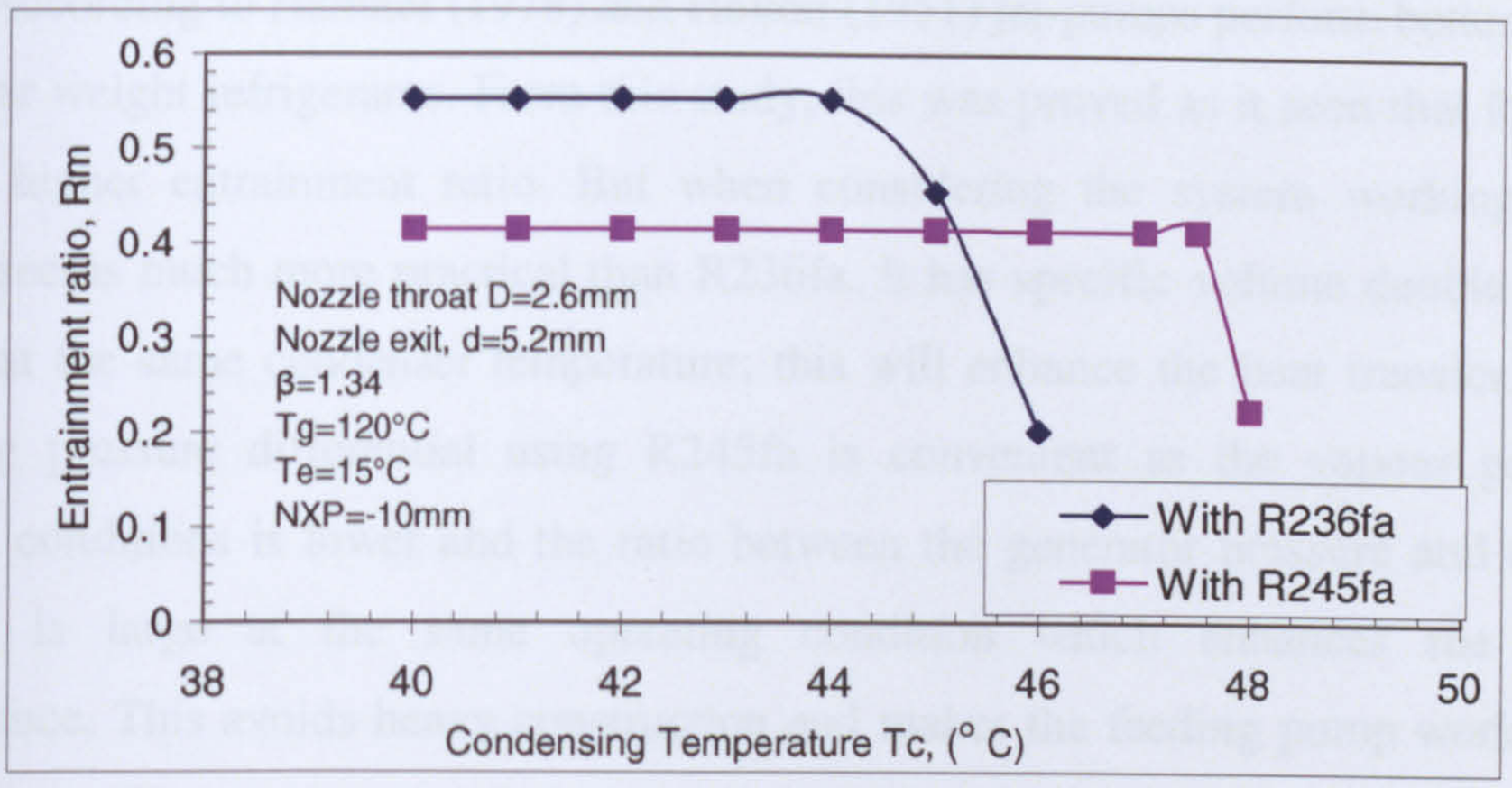

Figure 6. 41 Optimized conventional R245fa Jet-pump with R236fa, T_g=120°C (CFD results)

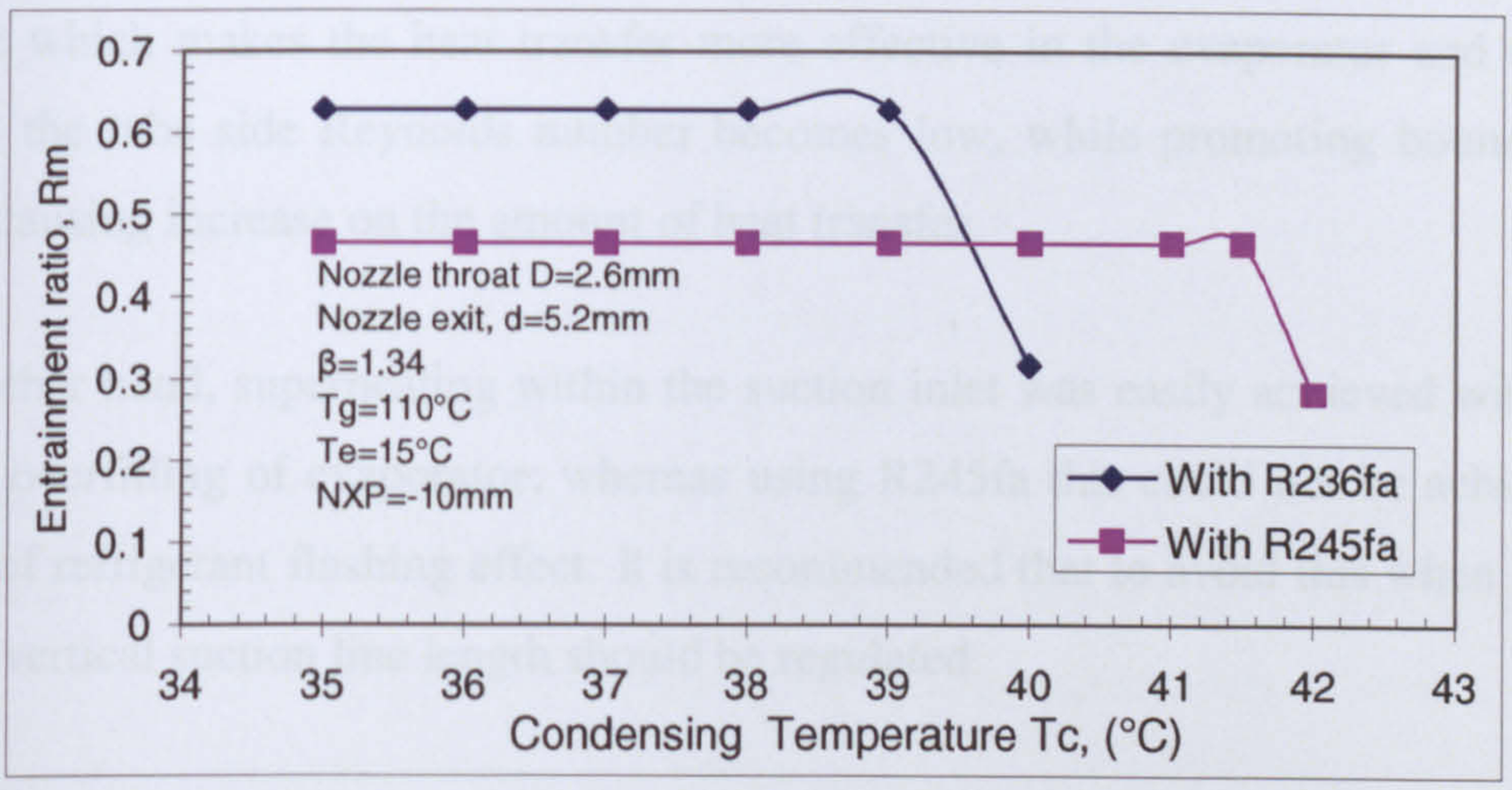

Figure 6. 42 Optimized conventional R245fa Jet-pump with R236fa, T_g=110°C (CFD results)

From these two Figures, it is clear that, entrainment ratio and critical condensing temperature changed when R236fa was used instead of R245fa under the same jet-pump geometry, operating conditions, and nozzle exit position. In both cases with T_g=120°C, and T_g=110°C, the entrainment ratio of this jet-pump was increased by about 25% when R236fa was used. But the critical condenser temperature was reduced by 2.5°C. This increase in entrainment ratio and decrease in critical condensing temperature give indication of that both of R236fa and R245fa can give the same performance at the same operating condition but with slightly difference in jet-pump dimensions. This finding of that most of refrigerant can give the same performance was stated before by Cizungu et al (2001) and Selvaraju (2004). Different NXP were also simulated with this jet-pump when R236fa was used, the same trend like that with R245fa was obtained, indicating that the type of fluid does not affect the optimal NXP.

According to Hamner (1978) and Holton (1951) jet-pumps perform better with high molecular weight refrigerants. From this study, this was proved as it seen that R236fa can provide higher entrainment ratio. But when considering the system working stability, R245fa seems much more practical than R236fa. It has specific volume double of that of R236fa at the same condenser temperature; this will enhance the heat transfer. Also the operating pressure differential using R245fa is convenient as the vapour pressure at working conditions is lower and the ratio between the generator pressure and condenser pressure is large at the same operating condition which enhances the jet-pump performance. This avoids heavy construction and makes the feeding pump work in stable conditions. Thus enhances the operation stability and the jet-pump performance. Moreover, the critical temperature of R245fa is much higher than R236fa and it has higher viscosity which makes the heat transfer more effective in the evaporator and condenser sides, as the tube side Reynolds number becomes low, while promoting boundary layer growth, causing increase on the amount of heat transfer.

On the other hand, superheating within the suction inlet was easily achieved with R236fa to avoid overfilling of evaporator; whereas using R245fa this could not be achieved, this because of refrigerant flashing effect. It is recommended that to avoid this when R245fa is used the vertical suction line length should be regulated.

Finally, both of these refrigerants can substitute other harmful refrigerants that have similar boiling points and molecular mass in chillers and air conditioning systems.

6.9 Conclusion

In this Chapter, the experimental jet-pump test rig was calibrated and used to test a different range of jet-pump configurations using two environmentally friendly refrigerants, R236fa and R245fa, and to compare the conventional with CRMC jet-pump performance. The experimental tests were carried out to find the operational characteristics of the system with each jet-pump over different range of operating conditions at the optimal NXP which was defined experimentally. The results were used to analyse the system performance at design and off-design operating conditions in order to make recommendations for best working performance depending on ambient conditions. Comparisons with CFD obtained results for each jet-pump were described, and the effect of using the RG unit with each jet-pump was evaluated.

- The results for the calibration of all nozzles used in the experimental tests showed that a simple one-dimensional compressible flow theoretical model and real-gas modelling by CFD can predict the flow to within 4% to 6% of the actual value, whereas the ideal-gas modelling can predict the flow to within 8% all of which give good estimation of primary flow within the primary nozzle.
- Experimental studies showed that all the tested jet-pumps with both refrigerants provided reasonably good performance compared to that obtained theoretically and by CFD. Also they showed that the jet-pump refrigerator could be operated with a waste heat source with a temperature range between 80°C to 120°C.
- The COP was found to be very sensitive to the operating conditions, whereas the cooling capacity was found to be nearly the same for fixed evaporator conditions; but both were very sensitive to the condenser temperature close to critical.
- Experimental results for each jet-pump showed that the hypothetical area for secondary flow was not constant but it was varied with jet-pump operating condition. The critical condensing pressure is dependent on momentum and pressure of the mixed flow within the mixing section, which is, mostly dependent on T_g and P_g.
- Concerning the comparison between experimental and CFD results for all parameters used in this Chapter, a very good comparison with experimental measurements was achieved, the simulation correctly predicted each of the primary mass flow rate, the NXP and the critical condensing temperature. Good agreement for optimal NXP with deviation of 2% which may be related to little difference in geometry or some losses. The R_m results relay between 0% to 20% lower than the CFD. The critical condensing temperature has reasonable correlation with CFD predicted results with deviations of 2% to 5%. This small range of error has given confidence that the CFD simulation were realistic.
- The effect of using RG unit was evaluated with each jet-pump at design operating conditions. Negligible variations in entrainment ratio and cooling capacity were observed when the pre-cooler and recuporator were used; only 4% to 6% increase in COP was achieved.
- A higher COP with acceptable T_c* was achieved when the jet-pump was equipped with a smaller nozzle.
- R236fa and R245fa were shown to give the same operational characteristics of the jet-pump.

Finally the most significant and important conclusion are presented in the next Chapter.

Chapter 7

Conclusions and Recommendations

7. Discussion, Conclusions and Recommendations

7.1 Discussion

This Chapter draws together the most significant and novel contributions made during the research programme and provides most significant conclusions from the work.

This thesis focused on potential performance improvements to jet-pump refrigeration systems. Four methods were studied;

(1) Improve jet-pump design by combination of novel design theories.
(2) The application of computational fluid dynamics to the design of jet-pumps.
(3) The use of new environmentally fluids, R236fa and R245fa, in jet-pump refrigeration system.
(4) Innovative cycle modifications by incorporating a pre-cooler and recuperator into jet-pump refrigerators.

Two jet-pump design theories were investigated and compared. These were the conventional design theory and CRMC theory. The premise behind the evaluation of these design theories was that CRMC jet-pump could outperform existing 1-D conventional jet-pump, as the losses associated with normal shock system in conventional jet-pump could be minimized. A CFD code for simulation of supersonic jet-pump flow was realized, the implementation of CFD to the compressible flow within the jet-pump was intended to explore the flow characteristics and the mixing behaviour within the jet-pump in order to understand and improve its performance. The potential of using different low-boiling working fluid is the target for those systems to be enhanced and to be used widely; whereas testing of incorporation the pre-cooler and recuperator with the jet-pump refrigeration system is to improve experimentally their extent of usefulness in such system.

The literature survey showed that previously there were no experimental comparative studies on the evaluation of CRMC jet-pump design theory against conventional theory. Also, the literature survey showed that the use of the pre-cooler and recuperator and using the aforementioned fluids had not been studied experimentally.

Moreover, it was also shown that there have been very few studies of flow characteristics and mixing processes with the jet-pumps.

The characteristics of axisymmetric jet-pumps were successfully evaluated by means of computational fluid dynamics and an adaptable experimental test-rig both of which give high quality and reliable results. The first part of this research concentrated on the validation of a CFD code which could simulate compressible flow within supersonic jet-pumps for a variety of geometries, working fluids and operating conditions (Chapter 3 and Appendix B). As is often the case for supersonic compressible flows involving shock, mixing layer interaction and compression shock systems, the choice of mesh and turbulence model are crucial decisions. However, to ensure a model's validity and to confirm that the results are grid independent, mesh and turbulent model studies were carried out incorporating steam and R141b as the working fluid as there were experimental data on them to be used for the code's validation. Mesh studies showed that the mesh size plays an important role for correct representation of the flow mixing process and related phenomena and it should be kept in range that could combine the qualitative results with a saving of the computational time. Mesh refinement using adaptive mesh techniques was used in some cases and it was particularly useful to resolve shock structure properly.

Turbulent model studies showed that two types were better at predicting flow behaviour in the case of jet-pumps. Both the standard and realisable k-ϵ models gave results that were in good agreement with experimental data with deviation of ±3.

The use of standard wall functions for producing the required fineness of the computational grid worked very well with all types of fluids used in this study. It reduced computer time requirements by several orders of magnitude over using any fine grid close to the wall. However, the realized CFD yielded promising predicted results and appeared to simulate correctly the basic physics of the flow.

Following its validation, the CFD code was used to study the effects of a wide range of operating parameters and geometry on the performance of steam and R141b jet-pumps in order to establish the theory that describes the flow characteristics and the mixing process inside the wetted area of the jet-pumps. The effects of these different parameters could be satisfactory explained using the results from the CFD simulations. This study aided the understanding of the operating principle of jet-pumps, particularly choking of

primary and secondary streams and the constant pressure mixing process. Furthermore, it is possible to approximate the starting and ending points of the mixing process and it gave qualitatively predictions of shock wave position and strength.

As strength of CFD is its flow visualisation aspect, this was used in the interpretation of data, including plots of supersonic flow, strain rate, static temperature contours, and so on. Both the numerical data and visualisation aspects of the flow field were used to interpret the effects of each jet-pump performance parameter. The flow field data obtained were studied extensively to provide insights into the jet-pump operating conditions-performance relationship. The operational modes of the simulated jet-pumps showed the flow structure with each performance parameter. Supersonic flow regions clearly showed chocking within the nozzle and diffuser throats. Static pressure plots confirmed the constant pressure mixing process assumption and the position of shock waves at the end of constant area section.

The second part of this research project was devoted to the use of the validated CFD code to assess and optimize different jet-pumps configurations with two new fluids. Chapter 4 described theoretical and CFD results for R236fa and R245fa over a range of operating conditions and different ranges of conventional and CRMC jet-pump geometries. In order to compare the theoretical (CFD) designed and optimized jet-pumps (both conventional and CRMC design), several jet-pumps were manufactured and tested in a purpose built, calibrated rig, as described in chapter 5.

This research has shown that CFD has the ability to model jet-pumps at both design and off-design operating conditions and was used to measure the shock system structure with conventional and CRMC jet-pumps. However, from CFD results the working theory for any jet-pump can be illustrated as follow:

- Primary fluids always choke and leave the primary nozzle with larger jet-core and supersonic speed.
- This jet-core creates with the mixing section wall a converging duct for the secondary stream. The converging duct size depends on the primary and secondary flow pressures; a larger secondary pressure means a large duct and more secondary flow entrained.
- The mixing process starts and completes with supersonic speed of the primary jet which is ended by shock waves at the end of constant area section.

• The mixing fluid pressure jumps within the shock waves to the pressure nearly equal to that at the diffuser back pressure.

The shock waves were observed clearly within all jet-pumps tested, and this was consistent with the assumption of the presence of a chock in the one-dimensional model for conventional jet-pumps. Shock-less CRMC jet-pump could not be approved by this study, only little reduction in shock system was observed which did not improve the jet-pump performance significantly.

The third part of this research was the experimental investigation of the performances of all selected jet-pumps using the aforementioned fluids; and also for testing the benefits of incorporating the RG unit with the jet-pump refrigeration system. The experimental studies were presented in Chapter 6, which also included the comparisons between experimental results and CFD simulation results.

In order to provide a meaningful comparison between CFD (Theory) and experiments, the same range of operating conditions were used in both cases. Results of this comparison were favourable. These are summarised in Table 7.1.

Table 7. 1 Summary of CFD and experimental results for all jet-pump tested

Design method	Working Fluid	Design operating conditions			CFD predicted results			Experimental obtained results		
		Tg °C	Te °C	Tc* °C	NXP mm	Rm	Tc* °C	NXP mm	Rm	Tc* °C
Conventional	R236fa	85	8	30	4	0.53	30	1	0.45	30
Optimized conventional	R236fa	85	8	30	9	0.655	30	7.5	0.52	29.5
Optimized CRMC	R236fa	85	8	30	15	0.53	30	17	0.46	29.5
Optimized conventional	R245fa	120	15	46	-12	0.44	47	-10	0.37	46
Optimized CRMC	R245fa	120	15	46	-2.5	0.39	49	-4	0.38	47.5

The various experimental plots obtained were consistent with those predicted by CFD, indicting that the R_m is strongly dependent on the nature of the flow within the mixing sections. It was found that the best performance "R_m" at designed T_c* for each particular fluid used was obtained at the design operating conditions. In other words, the confirmation of CFD simulation results and experimental results with theoretical design proved the validity of the theoretical design. All the CFD and experimental plots of the entrainment ratio as a function of generator temperature T_g, or evaporator temperature T_e consisted of curves which illustrated that the R_m decreased as the T_g increased for fixed

evaporator temperature and fixed jet-pump geometry, whereas for fixed T_g the entrainment ratio increases with increasing T_e. The thermal COP which was calculated from the experimental data was found to change proportionally to the change in R_m with any parameter studied, whereas the cooling capacity for a fixed evaporator temperature was found to remain nearly constant as generator temperature increased, it increases with increasing T_e. With each jet-pump the NXP was found to have significant influence on the performance of the jet-pump when it is altered from its optimal position.

7.2 Conclusions

The scopes of all objectives targeted by this study have been practically fulfilled, and the conclusions which are most significant are summarized as follows:

- The theoretical design procedures for the jet-pump used in this thesis, which is related to publish work in this field and was used in the determination of all the dimensional parameters for primary nozzle and diffusers, are acceptable.
- The assumptions that were made in the theoretical analysis, including that the flow is one-dimensional and axisymmteric and also the behaviour of the fluid at higher speed is like that of an ideal gas, were shown to be valid.
- The validated CFD code was very useful for the testing potential improvements of jet-pump designs.
- The CFD model provided a basis for quantifying the effects of changes in operating conditions and geometry on the jet-pump performance.
- CFD analysis offered more complete flow field information for jet-pump simulation and could produce a better correlation coefficient to experimental results than the one-dimensional model.
- Due to the nature of the flow in the mixing section, it is difficult to identify the optimal NXP using a 1-D theoretical analysis. However, CFD was found to be practical and inexpensive tool for determining the optimal NXP.
- In the optimization process for conventional jet-pumps, increasing (β) leads to increase m_s. This increases entrainment ratio (R_m) and in turn the total momentum to overcome backpressure. However, under such conditions of increasing (β) to get higher R_m, the exit critical pressure must decrease, or alternatively, the same critical back pressure can be maintained by increasing primary pressure.

- Jet-pump efficiency can be improved significantly by using an iterative design procedure based on an accurate CFD simulation of the flow. It is felt that more optimization for CRMC jet-pumps can be obtained in this way.
- The CFD would allow different jet-pump geometries, and different types of working fluids to be examined accurately.
- The study showed that the most important part affecting the jet-pump performance, for fixed operating conditions and geometry, was the mixing section profile. Jet-pump performance was found to be sensitive to small changes in mixing section wall profile and NXP. The length and width of the convergent zone of the mixing section plays an important role in the equilibrium between the amount of secondary flow entrained and the critical back pressure that can be achieved, as it seen in the optimization of CRMC jet-pumps.
- It seems that with the optimized CRMC R245fa jet-pump a little reduction in the shock contribution was obtained. As a result of this the maximum isentropic compression was achieved along with some increase in critical back pressure.
- The CFD code with a properties real gas model was found to predict more accurately the behaviour of jet-pumps, but it is expensive in time. Because of this it was concluded that assuming the fluid to be an ideal gas provides sufficiently accurate results for most design cases.
- The CFD obtained results were in good agreement with theoretically designed conventional jet-pumps especially with R245fa fluid. It is worth mentioning that the nozzle and momentum efficiencies have a significant influence on the jet-pump performance especially on the exit pressure of the jet-pump as was stated by Selvaraju et al (2004). However, as in conventional theoretical designs an effort was made to use efficiency values less than those used with R236fa and recommended by ESDU, the CFD and experimental results with conventional R245fa were more realistic than those with R236fa. Therefore, care is needed when selecting efficiency data, particularly for small sizes of nozzle or diffuser, and efficiencies should be taken to vary with jet-pump scale.
- Experimental results are in good agreement with the CFD model performance. Overall discrepancies at off-design are within 8% to 15% of the CFD values while Tc* and R_m were obtained to within 3% and 10% respectively. All experimental results for optimal NXP in each jet-pump were in reasonable agreement with those obtained by CFD; but the range of NXP was varied from -10 to +10mm. All NXP results were found to vary with values recommended by ESDU.

- The closed agreement of CFD and experimental results, over the range of jet-pumps, fluids and operating conditions that were tested, indicates that CFD may be a useful aid in the design and performance optimization (optimum entrainment ratio with designed critical condensing temperature) of jet-pumps with a high degree of confidence using any particular refrigerant. Prior simulation of all parameters affecting the jet-pump performance can reduce the time and the cost of development work.
- The R_m and COP can be varied by as much as 100% by changing the nozzle exit position (NXP), as this controls the distance over which mixing between primary and secondary streams takes place.
- Optimum NXP was found to depend on the shape of the mixing section. However, the NXP was shown not to significantly effect T_c^*.
- The coefficients of performance were about 0.5 to 0.8 at practical operating conditions for air conditioning; COP of 0.7 with T_c* of 38°C could be achieved with evaporator temperature of 12°C. The COP of the jet-pump system was found to improve further by properly selecting T_g, and related primary nozzle geometry. Higher COP can be obtained with T_g ranges between 100°C to 120°C, by considering that higher driving pressure means higher initial and running costs for jet-pump systems operation. Experiments showed that if the geometry of the jet-pump is fixed it is impossible to raise the system COP by increasing T_g. What doing so was shown to waste heating energy at the generator.
- The jet-pump performance maps presented in Chapter 4 and Chapter 6 are a useful aid to the practical design of a jet-pump refrigeration. However, they can be inspected as the controlling operation maps for the refrigeration system with the jet-pumps tested in this research. From these maps, it can be concluded that, under the restriction of the critical temperature of the primary flow, it is desirable to design a refrigerator that will work at considerably reduced primary pressure for the thermal energy used by the generator to be fully utilised. Only for the relatively rare circumstance when condenser pressure is high, will a use of higher primary flow pressure be then required.
- Depending on previous point, it is possible to recommend that a system which is sensitive to the operating conditions should use a variable geometry jet-pump that can maintain the optimum performance of the jet-pump refrigeration system when operating conditions change; especially to cope with changes in condenser temperature, and make more efficient use of primary energy. This variation in

geometry should first take place at the primary nozzle throat or at the mixing section throat as stated by Sun (1996).

- To obtain better performance, the heat input to the system should be adjusted automatically, especially in the case of a less demanding cooling load.
- Any reduction in condenser temperature with a simultaneous decrease in T_g will always yield benefits for operation of the jet-pump and the whole system.
- The system COP and critical condensing pressure can increase together only when the evaporator temperature is increased.
- Analysis has shown that raising the T_c* with optimising jet-pump geometry, means that a small condenser can be used i.e. low initial cost.
- At constant geometry and T_e, there is an optimum T_g that can provide greater R_m and higher COP.
- The greater the design primary pressure leads to higher capital and running costs for jet-pump refrigerator operation. This is because higher heat input into generator and heavy construction are required.
- The constant capacity characteristic requires that the jet-pump refrigeration cycle should operate under the critical conditions; beyond these conditions, some input energy at the generator will be wasted and the COP will be reduced.
- Sub-cooling downstream of the condenser requires additional heat input in the generator and is therefore undesirable. The system performance can be improved by avoiding rejection of unnecessary heat from the condenser.
- There was no obvious change in COP when the system was operating at condenser temperatures close to the jet-pump critical temperature or at any less than that; but in real applications, energy would be wasted if the system was operating at a lower condenser temperature. Thus for the economical purposes, at low environment temperatures, it shown be possible to reduce the primary flow pressure. Therefore, controls must be used to obtain the highest performance at lowest anticipated condenser pressure. Moreover, for greater reliability, the jet-pump refrigerator should be designed for the most commonly encountered conditions at both the condenser and evaporator.
- The design of the primary nozzle was found to have a strong effect on COP for fixed operating conditions and geometry. COP could be increased by as much as 50% with smaller primary nozzle. Also, when the nozzle size was altered the related optimum NXP also changed, because the jet-angle and the total momentum of the primary flow altered.

- The performance of jet-pumps is thought to be affected by the quality of the surface finish, suction bend-wall configuration and the alignment between the primary nozzle and diffuser. In the case of poor surface finish, the amount of turbulence and pressure energy loss increased and this was affected the total jet-pump performance.
- Both R236fa and R245fa fluids seem to be a practical working fluid for jet-pump refrigeration system. Both are environmentally friendly; but as the saturation pressure at the vapour generator should not to be too high, in order to avoid heavy construction, and to minimize the mechanical power required by the pump, R245fa is considered the more suitable. One disadvantage of using R245fa is that the vacuum pressure in the evaporator can be expected below 15°C, which can results in air leakage, and a fall in COP.
- The effect of each of pre-cooler and recouporator within the system was examined, and no obvious effect was obtained only an increase by 4% to 6% of system COP was achieved. The effect of the pre-cooler was negligible in this system and that is because of using sub-cooling downstream of the condenser.
- This research has shown that the jet-pump refrigerator is attractive for applications where sources of low-grade heat are available. Improvement described in this thesis make the jet-pump refrigerator competitive with all other types- particularly heat powered cycles.

7.3 Recommendations

The recommendations for future work under such conditions are:

- For the theoretical computer programme, different ranges of γ value must be used in the programme; this will probably give more realistic results and reduce errors in the presented design method.
- In the 1-D theoretical design, empirical models for momentum loss, (including two-phase effects) and turbulent viscosity in the mixing region are required.
- The use of real gas model should be investigated with different turbulence models; the codes capability should be extended to handle all flow phenomena.
- More CFD simulation for fixed operating conditions and fluid, but with different scaled-dawn jet-pumps to ensure that the size of the jet-pump will not affect the

results obtained from the original scale, and this could be implemented for experimental work as well.

- Improvement to the presented CFD code should be explored particularly regarding the geometric investigation of the mixing section revealed that the CRMC diffuser could be enhanced through smoothness of bends wall. Future researchers may conduct investigation in the nozzle external profile shape, and optimal length of CRMC mixing section.
- Due to good agreement between CFD and experimental results for NXP values, it is possible for further work to investigate the effect of working fluid on NXP as viscosity of the fluid would have an effect on the mixing process, by using fixed operating conditions and fixed geometry to observe the effect of fluid in this position.
- Also to the reasonably agreement obtained, it is recommended for future work to use high manufacturing technique for each of primary nozzle and diffuser to avoid the errors with the jet-pump specification; thus more precise experimental results can be obtained which can be used to evaluate precisely the CFD code.
- Automatic control of the system, particularly the control of flows and liquid levels should be investigated.
- The possibility of a device for controlling the position of the primary nozzle and its flow passage geometry should be investigated.

References

References

Abdel-Aal H.K., Al-Zakri A.S., El-Sarha M.E., EL-Swify M.E. and Assassa G.M.;(1990), Other options of mass and energy input for steam jet refrigeration systems, Chem Engng J;45:pp. 99-110.

Ablwaifa E.A. Eames I, W. and Petrenko V.; (2005), Use of CFD in prediction of jet-pump performance with R141b as refrigerant, XIX National Congress of Thermodynamicists, Poland 5-8 September.

Alexis G.K. and Rogdakis E. D.;(2002a), Performance of solar driven methanol-water combined ejector-absorption cycle in the Athens area, Renewable Energy;25:pp.249-266.

Alexis G.K. and Rogdakis E.D.;(2002b), Performance characteristics of two combined ejector-Absorption cycles, Applied thermal engineering Vol 22:pp.97-106.

Alexis G.K. and Rogdakis E.D.;(2003), A verification study of steam-ejector refrigeration model, Applied thermal Engineering 23:pp.29-36.

Alexis G.K. and Katsanis J.S.;(2004), Performance characteristics of a methanol ejector refrigeration unit. Energy conversion and management 45:pp.2729-2744.

Al-khalidy N. and Zayonia.A.;(1995), Design and experimental investigation of an ejector in an air–conditioning and refrigeration system, ASHRAE transactions 101(2):pp. 383-391.

Al-Khalidy N.;(1997), Performance of solar refrigerant ejector refrigeration machine ASHRAE transaction, 103 (1):pp.55-65.

Al-Khalidy N.;(1998), An experimental study of an ejector cycle refrigeration machine operating on R113, Int J. Refrig. Vol 21(No.80: pp.617-625.

Anderson J.D.;(2002), Modern compressible flow, with historical prospective, Third Edition, McGraw Hill.

Aphornratana S.;(1994), Theoretical and experimental investigation of a combine ejector-absorption refrigerator, PhD thesis, University of Sheffield, Uk.

Aphornratana S. and Eames I.W.;(1997), A small capacity steam-ejector refrigerator: experimental investigation of a system using ejector with movable primary nozzle, Int J. Refrig. Vol.20, (No.5):pp.352-358.

Arbel A., Shklyar A., Hershgal D., Barak M. and Sokolov M.;(2003), Ejector Irreversibility Characteristics. Fluids Engineering J Vol.125, (No.1): pp.121-129.

Arbel a. and Sokolov M.;(2004), Revisiting solar powered ejector air conditioner-the greener the better, Solar energy 77:pp.57-66.

ASHRAE;(1979), ASHRAE handbook-equipment, Atlanta: American Society of Heating, Refrigerating and Air Conditioning Engineers. Inc:PP.13.1-13.6.

ASHRAE.;(1983), Steam-jet refrigeration equipment, ch.13.In: ASHRAE equipment handbook:pp.13.1-13.6.

ASHRAE.;(1984), ASHRAE thermodynamic properties of Refrigerants. ASHRAE, Atlantes, GA, USA.

Chang Y.J. and Chen Y.M.;(2000), Enhancement of a steam-jet refrigerator using a novel application of the petal nozzle, Experimental Thermal and fluid Science vol 22:pp. 203-211.

Chen F.C. and Hus C.T.;(1987), Performance of ejector heat pump, energy Res vol 11 :pp.289-300.

Chen L.T.;(1998), A new ejector-absorber cycle to improve the COP of an absorption system, Applied energy, Vol 30:pp.37-41.

Chen S.L., Yen J.Y. and Hunag, M.C.;(1998), An experimental investigation of ejector performance based upon different refrigerants, ASHRAE Trans; 104 (part2):pp.153-160.

Chen Y.M., and Sun C.Y.;(1997), Experimental study of the performance characteristics of a steam-ejector refrigeration system, Experimental Thermal and fluid Science,15:pp.384-394.

Chin S.B, Eames I. W and Popov A.;(1997), Computational fluid dynamics study of a compressible steam ejector pump design, International heat powered cycles conference 1997 , Nottingham, UK, pp.302-310.

Chung H., Huor M.H. Provost, M. and Bugarel R.;(1984), Domestic heating application of and absorption heat pump, directly fired heat pump, Intentional proceedings international conference University of Bristol. 19-20 September.

Chunnanond K. and Aphornratana S.;(2004a), An experimental investigation of a steam ejector refrigerator : the analysis of the pressure profile along the ejector" Applied thermal engineering Vol 24:pp.311-322.

Chunnanond K. and Aphornratana S.;(2004b), Ejectors applications in refrigeration technology, Renewable & sustainable energy reviews. pp. 129-155.

Chunnanond K.;(2005), A study of steam ejector refrigeration cycle, parameters affecting performance of the ejector, PhD thesis, Thammasat University Thailand.

Cizungu K., Mani A. and Groll M.;(2001), Performance comparison of vapour jet refrigeration system with environment friendly working fluids, Applied Thermal Engineering Vol 21:pp.585-598.

Croft D.R. and Lilley D.G.;(1976), Finite-Difference Analysis of Jet Pumps, AIAA Jn., 14:pp.1347-1348.

Defrate L.A. And Hoerl A.E.;(1959), Optimum design of ejector using digital computers. Chem. Eng progr .Symp.ser.55.(No.21):.pp.43-51.

Desevaux P.A.;(2001), Method for visualizing the maxing zone between two co-axial flows in an ejector, Optics lasers Engan ;35:pp.317-23.

Dorantes R., Estrada C.A. and Pilatowsky. I.;(1996), Mathematical simulation of a solar ejector-compression refrigeration system, Applied thermal engineering Vol 16:pp.669 675.

Dupont Fluoroproducts"; (2004), from:
:http://www.dupont.com/suva/na/usa/literature/pdf/h77974.pdf

Eames I.W. and Aphornratana S.;(1995a), A novel ejector/Ansorption cycle Refrigerator for Building Air Conditioning, proc. CIBSE national Conference, Eastbourne.

Eames I.W., Aphornratana S. and Haider H.;(1995b), A theoretical and experimental study of a small-scale steam jet refrigerator, Int, J. Refrig. Vol. 18, (No.6): pp.378-386.

Eames I.W., Wu S. and Worall M.; (1999a), The design and performance of steam ejector for application in jet-Pump refrigerators, Recent Res. Devel. Heat, Mass & Momentum Transfer, Vol 2:pp.199-215.

Eames I.W., WU S. and Aphornratana S.;(1999b), An experimental investigation of steam ejector for application in jet-pump refrigerators powered by low-grade heat, Proc Instn Mech Engrs Vol. 213 part A.

Eames I.W. and Wu. S.;(2000), A theoretical study of an innovative ejector powered absorption-recompression cycle refrigerator, International Journal of refrigerator, 23:pp.475-484.

Eames I.W. and WU S.;(2001), A theoretical study of new ejection –absorption heat transformer, Applied energy; 68:pp.161-171.

Eames I.W.;(2002), A new prescription for the design of supersonic jet-pumps: the constant rate of momentum change method, APPL Therm Engng; Vol.22:pp.121-31.

Eames I. W., Petrenko V. and Ablwaifa E. A.;(2004a), Design and experimental investigation of a jet-pump refrigerator, 3rd International Conference on heat Powered Cycles, Larnaca, Cyprus, ISBN 01874418353.

Eames I.W and Ablwaifa A. E.;(2004b), Use of CFD in the prediction of jet-pump perfroamce, 3rd International Conference on heat Powered Cycles, Larnaca, Cyprus, ISBN 01874418353.

Eames I.W., Knowles S. and Ablwaifa A.E.;(2005), Manufacture and testing of a jet-pump refrigerator for solar -powered air conditioning, XIX National Congress of Thermodynamicists, Poland 5-8 September.

El-Dessouky H. Ettouney H., Alatigi I. and Al-Nuwaibit G.;(2002), Evaluation of steam jet ejectors, Chemical engineering and processing Vol 41 issue 6:pp 551-561.

ESDU.;(1985), Ejector and Jet Pumps, Data Item 86030, ESDU International Ltd.

Fluent INC, Fluent 6.1.18 user's guide;(2003), Vols. 1-5, Fluent Inc, Lebanon NH USA.

Gosney W.B.; (1982), Cambridge University Press, ISBN 0 521 23671 1.

Hart J.H.;(2002), Supersonic Ejector Simulation and Optimisation, PhD thesis Sheffield University.

Hedges K.R. and Hill P.G.;(1974), Compressible flow Ejector. Part 1- development of a Finite Difference Model., IN. fluids Engineering, Trans. ASME.,96:pp.272-281.

Hodge B.K. and Koenig K.;(1995), Chap.2.3, pp 54-62, pub. Prentice-hall Inc., ISBN 013 308552X.

Holton W.C.;(1951), Effect of molecular weight of entrained fluid on the performance of steam-jet ejector, ASME Trans :pp. 905 -910.

Huang B.J., Jiang C.B and Hu F.L.;(1985), Ejector performance characteristics and design-analysis of jet refrigeration system, Journal of Eng for gas turbines and Power, Vol 107:pp.792-802.

Huang B.J, Chang J.M., Petrenko V.A. and Zhuk K.B.;(1998), A solar ejector cooling system using refrigerant R141b, Solar energy Vol.64(No.4-6):pp.223-226.

Huang B.J, Chang J.M, Wang C.P. and Petrenko;(1999a), V.A., A 1-D analysis of ejector performance , Int refrigeration 22:pp.354-364.

Hunag B.J and Chang J.M.;(1999b), Empirical Correlation for ejector design, International Journal of refrigeration 22:pp.379-388.

Huang B.J., Chang J.M., Petrenko V.A. and Samofatove I.Y.;(2001), A joint research on ejector cooling technology, 2nd international workshop on Non-compression Refrigeration & cooling Odessa, Ukraine.

Issa R.I. and Lockwood F.C.;(1986), Two- Dimensional Supersonic Viscous Interactions, AIAA Jn. Comp. Phys., 62:pp. 40-65.

Jiang L., Gu Z., Feng, X. and Li Y.;(2002), Thermo-economical analysis between new absorption-ejector hybrid refrigeration system and small double-effect absorption system, Applied thermal engineering Vol 22:pp.1027-1036.

Keenan J.H. and Neumann E.P.;(1942), A simple air ejector. ASME J Appl Mech trans ;64:pp.A75-A81.

Keenan J.H., Neumann E.P. and Lustwerk F.;(1950), An investigation of ejector design by analysis and experimenment, ASME J Appl Mech Trans 72:pp. 299-309.

Khattab N.M. and Barakat M.H.;(2002), Modelling the design and performance characteristics of solar steam- jet cooling for comfort air conditioning. Solar energy Vol.73 (No4): pp.257-267.

Kim S.E., Choudhury D. and Patel. B.;(1997), Computations of Complex Turbulent-Flows Using the Commercial Code FLUENT. In Proceedings of the ICASE/LaRC/AFOSR Symposium on Modeling Complex Turbulent Flows, Hampton, Virginia.

Mehta U.B.;(1991) Some Aspects of Uncertainty in Computational Fluid Dynamics results, Jn. Of Fluids Eng., 113:pp.538-543.

Munday J.T. and Bagster D.F.;(1977), New ejector theory applied to steam jet refrigeration, Ind .Eng. Chem. Process.Res. Vol. 16 (No.4):pp. 442-449.

Narmine H.A., Aly K. and Shamloul M.M.;(1999), Modelling and simulation of steam jet ejectors. Desalination 123:pp.1-8.

Nguyen V.M., Riffat S.B. and Doherty P.s.;(2001), Development of a solar-powered Passive ejector cooling system, Applied Thermal Engineering 21:pp.157-168.

Niavalagen S., Ravindran M. and Radhakrishna H.C.;(1988), Analysis of mixing Characteristics of flow in a jet pump using a Finite-Difference method, the Chem. Eng.In, 39:pp.97-109.

Ouzzane M. and Aidoun Z.;(2003), Model development and numerical procedure for detailed ejector analysis and design, Applied Thermal engineering 23:pp.2337-2351.

Riffat S.B., Gan. and Smith S.;(1996), Computational Fluid Dynamics Applied to Ejector heat pumps, Appl. Thermal Eng., 16,4: pp.291-297.

Redshaw S., Wolpert J.L. and Wonghorsub C.;(2004), Design and construction of solar powered supersonic ejector air–conditioning system, International Conference on sustainable Energy technologies Nottingham, Uk, 28-30 June.

Robinson, W.;(1927), Applied Thermodynamics, Pitman.

Rogdakis E.D. and Alexis G.K.;(2000), Investigation of ejector design at optimum operation conditions, Energy Conver Mangmnt ; 41:pp.1841-9.

Rogers G.F.C. and Meyhew Y.R.;(1988), Thermodynamic and transport properties of fluids, 4th Edition, Blackwell publishers, Oxford.

Rollins V.;(2001), Surface Defect Inspection- At The Double" Featured in Materials World,Volume 9.

Rusly E., Aye Lu., Charters W.W.S. and Ooi A.;(2005), CFD analysis of ejector in a combined ejector cooling system, International Journal of Refrigeration.

Selvaraju A. and Mani A.;(2004), Analysis of a vapour ejector refrigeration system with environment friendly refrigerants, International Journal of Thermal Sciences 43:pp.915-921.

Shih T.H., Liou W.W., Shabbir A. and Zhu. J.;(1995), A New k-Є Eddy-Viscosity Model for High Reynolds Number Turbulent Flows - Model Development and Validation, Computers Fluids, 24(3):pp.227-238.

Smith S.J. and Riffat S.B.;(1997), low pressure ejectors: prediction of performance by Computational Fluid Dynamics, pro.CIBSE A: Building Serv. Eng. Res. Technol., 18,3:pp.179-182.

Sokolov M. and Hershgal D.;(1990a), Enhanced ejector refrigeration cycles powered by low grade heat, Part 1 system characterization, Int J Refrig, vol 13:pp.351-356.

Sokolov M. and Hershgal D.;(1990b), Enhanced ejector refrigeration cycles powered by low grade heat. Part 2 design procedures, Int J Refrig, vol 13:pp.357-363.

Sokolov M. and Hershgal D.;(1990c), Enhanced ejector refrigeration cycles powered by low grade heat. Part 3, Experimental results, Int J Refrig vol 14:pp.24-31.

Sokolov M. and Hershgal D.;(1993), Solar powered compression enhanced ejector air conditioner, Solar energy 51:pp.183-194.

Sozen A., Arcaklioglu, E. and Ozalp M.;(2003), A new approach to thermodynamic analysis of ejector-absorbtion cycle : Artificial neural networks, Applied Thermal Engineering Vol 23:pp.937-952.

Stoecker W.F.;(1958), Steam-jet refrigeration. Boston, MA: McGraw-Hill.

Sun D.W., Eames I.W. and Aphornratana S.;(1996), Evaluation of a novel combined ejector-Absorption refrigeration Cycle-I: computer simulation, Int, J, refrigeration; 19(No.3):pp.172 -180.

Sun D.W.;(1996), Variable geometry ejectors and their applications in ejector refrigeration systems, energy Vol, 21.10:pp. 919-929.

Sun D.W. and Eames I.W.;(1996), performance characteristics of HCFC-123 Ejector refrigeration Cycles, Inter J of Energy Research Vol 20:pp.871-885.

Sun. D.W.;(1999), Comparative study of the performance of an ejector refrigeration cycle operating with various refrigerants, Energy Conversion & Management vol 40:pp. 873-884.

Trott A.R. and Welch T.C.;(2000), Refrigeration & Air Conditioning, Reed educational and professional Publishing Ltd.

Versteeg H.K. and Malasekera W.;(1995), An introduction to Computational Fluid Dynamics-The Finite Volume method, 1st Edition, Longman.

Worall M.;(2001), An investigation of a jet-pump thermal (ice) storage system powered by low-grade heat, PhD thesis University of Nottingham.

Work L.T. and Haedrich V.W.;(1939), Performance of ejector as a function of the molecular weight of vapours, ind, and Eng, Chemistry .Vol.31(NO.4):P.464-477.

Wu S. and Eames I.W.;(1998), A novel absorption –recompression refrigeration cycle, Appl Thermal Energy; 19:pp.1149-57.

Appendix A

Working Fluid Thermodynamics Properties

1- Steam

Temp	pressure	Volume	Enthalpy			Entropy			Specific heat	Specific heat	C_p/C_V
°C	MPa	Vapour M^3/kg	Liquid KJ/kg	Latent kJ/kg	Vapour kJ/kg	Liquid kJ/kgK	Latent kJ/kgK	Vapour kJ/kgk	C_p liquid kJ/kg k	C_p Vapour kJ/kg Cp	γ
0	0.006112	206.1	0	2500.8	2500.8	0	9.155	9.155	4.229	1.868	1.3
2	0.007505	179.9	8.4	2495.9	2504.3	0.031	9.071	9.102	4.22	1.869	1.3
4	0.008129	157.3	16.8	2491.3	2508.1	0.061	8.989	9.05	4.2	1.87	1.3
6	0.009346	137.8	25.2	2486.6	2511.8	0.091	8.908	8.999	4.195	1.871	1.3
8	0.01072	121	33.6	2481.9	2515.5	0.121	8.828	8.949	1.19	1.872	1.3
10	0.01227	106.4	42	2477.2	2519.2	0.151	8.749	8.9	1.188	1.874	1.3
12	0.01401	93.83	50.4	2472.5	2522.9	0.18	8.671	8.851	4.186	1.875	1.3
14	0.01597	82.89	58.8	2467.8	2526.6	0.21	8.594	8.804	4.184	1.877	1.3
16	0.01817	73.38	67.1	2463.1	2530.2	0.239	8.518	8.757	4.184	1.878	1.3
18	0.02063	65.08	75.5	2458.4	2533.9	0.268	8.444	8.712	4.184	1.88	1.3
20	0.02337	57.84	83.9	2453.7	2537.6	0.296	8.37	8.666	4.183	1.882	1.3
22	0.02642	51.49	92.2	2449	2541.2	0.325	8.297	8.622	4.183	1.884	1.3
24	0.02982	45.92	100.6	2444.2	2544.8	0.353	8.226	8.579	4.183	1.886	1.3
26	0.0336	41.03	108.9	2439.5	2548.4	0.381	8.155	8.536	4.183	1.889	1.3
28	0.03778	36.73	117.3	2434.8	2552.1	0.409	8.085	8.494	4.183	1.89	1.3
30	0.04242	32.93	125.7	2430	2555.7	0.436	8.016	8.452	4.183	1.892	1.3
32	0.04754	29.57	134	2425.3	2559.3	0.464	7.948	8.412	4.183	1.894	1.3
34	0.05318	26.6	742.4	2420.5	2562.9	0.491	7.881	8.372	4.183	1.896	1.3
36	0.0594	23.97	150.7	2415.8	2566.5	0.518	7.814	8.332	4.182	1.98	1.3
38	0.06624	21.63	159.1	2411	2570.1	0.545	7.749	8.294	4.182	1.9	1.3
40	0.07375	19.55	167.5	2406.2	2573.7	0.572	7.684	8.256	4.182	1.905	1.3
42	0.08198	17.69	175.8	2401.4	2577.2	0.599	7.62	8.219	4.182	1.909	1.3
44	0.091	16.3	184.2	2396.6	2580.8	0.625	7.557	8.182	4.182	1.911	1.3
46	0.1009	14.56	192.5	2391.8	2584.3	0.651	7.494	8.145	4.182	1.913	1.3
48	0.1116	13.23	200.9	2387	2587.9	0.678	7.433	8.111	4.182	1.916	1.3
50	0.1233	12.04	209.3	2382.1	2591.4	0.704	7.371	8.075	4.182	1.919	1.3
55	0.1574	9.578	230.2	2370.1	2600.3	0.768	7.223	7.991	4.182	1.928	1.3
60	0.0992	7.678	251.1	2357.9	2609	0.831	7.078	7.909	4.183	1.937	1.3
65	0.2501	6.201	272	2345.7	2617.7	0.893	6.937	7.83	4.184	1.947	1.3
70	0.3116	5.045	293	2333.3	2626.3	0.955	6.8	7.755	4.187	1.958	1.3
75	0.3855	4.133	313.9	2320.8	2634.7	1.015	6.666	7.681	4.19	1.97	1.3
80	0.4736	3.408	334.9	2308.3	2643.2	1.075	6.536	7.611	4.194	1.983	1.3
85	0.578	2.828	355.9	2295.6	2651.5	1.134	6.41	7.544	4.199	1.996	1.3
90	0.7011	2.361	376.9	2282.8	2659.7	1.192	6.286	7.478	4.204	2.011	1.3
95	0.8453	1.982	398	2269.8	2667.8	1.25	6.166	7.416	4.21	2.027	1.3
100	1.01325	1.673	419.1	2256.7	2675.8	1.307	6.048	7.355	4.217	2.044	1.3
105	1.2079	1.42	440.2	2243.4	2683.6	1.363	5.9326	7.2956	4.224	2.062	1.3
110	1.4324	1.2106	461.3	2230	2691.3	1.4186	5.82	7.2386	4.232	2.082	1.3
115	1.6902	1.037	482.5	2216.3	2698.8	1.4735	5.7098	7.1833	4.24	2.103	1.3
120	1.9848	0.8922	503.8	2202.4	2706.2	1.5278	5.6019	7.1297	4.249	2.126	1.3
125	2.3201	0.7709	525.1	2188.3	2713.4	1.5815	5.4962	7.0777	4.258	2.15	1.4
130	2.7002	0.6687	546.4	2174	2720.4	1.6346	5.3926	7.0272	4.268	2.176	1.4
135	3.1293	0.5823	567.8	2159.4	2727.2	1.6873	5.2907	6.978	4.278	2.203	1.4
140	3.6119	0.509	589.2	2144.6	2733.8	1.7394	5.1908	6.9302	4.288	2.233	1.4

2- R141b

Temp	Pressure	Density	Volume	Enthalpy		Entropy		Specific heat	C_p/C_V
°C	MPa	Liquid Kg/m^3	Vapour M^3/kg	Liquid kJ/kg	Vapour kJ/kg	Liquid kJ/kg k	Vapour kJ/kg k	Vapour C_P kJ/kg K	γ
0	0.02811	1275.8	0.68033	200	437.8	1	1.8706	0.726	1.119
4	0.03362	1268.4	0.57579	204.6	440.51	1.0167	1.8679	0.733	1.119
8	0.03998	1261	0.49008	209.21	443.22	1.0332	1.8655	0.741	1.119
12	0.04726	1253.5	0.41936	213.82	445.94	1.0494	1.8635	0.749	1.119
16	0.05557	1246	0.36067	218.42	448.67	1.0655	1.8618	0.757	1.12
20	0.065	1238.4	0.31167	223.02	451.4	1.0812	1.8603	0.765	1.12
22	0.07016	1234.6	0.29022	225.32	452.76	1.089	1.8596	0.769	1.121
24	0.07565	1230.8	0.27055	227.61	454.12	1.0968	1.859	0.773	1.121
26	0.08147	1226.9	0.25248	229.91	455.49	1.1045	1.8585	0.777	1.121
28	0.08764	1223.1	0.23586	232.21	456.85	1.1121	1.858	0.782	1.122
30	0.09417	1219.2	0.22055	234.51	458.22	1.1197	1.8576	0.786	1.122
32	0.10108	1215.3	0.20644	236.82	459.58	1.1273	1.8573	0.79	1.123
34	0.10838	1211.5	0.19342	239.13	460.94	1.1348	1.857	0.795	1.124
36	0.11608	1207.5	0.18139	241.44	462.31	1.1423	1.8567	0.799	1.124
38	0.12421	1203.6	0.17026	243.76	463.67	1.1497	1.8565	0.803	1.125
40	0.13277	1199.7	0.15996	246.09	465.03	1.1572	1.8562	0.808	1.126
42	0.14179	1195.7	0.15041	248.42	466.39	1.1646	1.8561	0.812	1.126
44	0.15127	1191.7	0.14155	250.76	467.75	1.1719	1.8561	0.817	1.127
46	0.16124	1187.7	0.13332	253.11	469.1	1.1793	1.8561	0.822	1.128
48	0.17171	1183.7	0.12567	255.47	470.46	1.1866	1.8561	0.826	1.129
50	0.1827	1179.6	0.11855	257.83	471.81	1.194	1.8561	0.831	1.13
52	0.19422	1175.6	0.11192	260.21	473.17	1.2012	1.8562	0.836	1.131
54	0.2063	1171.5	0.10573	262.59	474.52	1.2085	1.8563	0.841	1.132
56	0.21893	1167.4	0.06663	264.99	475.87	1.2158	1.8565	0.846	1.133
58	0.23216	1163.2	0.09458	267.39	477.21	1.223	1.8566	0.851	1.134
60	0.24598	1159.1	0.08954	269.8	478.56	1.2303	1.8569	0.856	1.135
62	0.26043	1154.9	0.08483	272.23	479.9	1.2375	1.8571	0.861	1.136
64	0.27551	1150.7	0.08042	274.66	481.24	1.2447	1.8574	0.866	1.138
66	0.29124	1146.5	0.07629	277.1	482.58	1.2518	1.8577	0.872	1.139
68	0.30765	1142.2	0.07241	279.55	483.91	1.259	1.858	0.877	1.14
70	0.32475	1137.9	0.06877	282.01	485.24	1.2662	1.8584	0.883	1.142
72	0.34255	1133.6	0.06536	284.48	486.57	1.2733	1.8588	0.888	1.143
74	0.36108	1129.2	0.06215	286.95	487.9	1.2804	1.8592	0.894	1.145
76	0.38035	1124.8	0.05912	289.44	489.22	1.2875	1.8597	0.9	1.147
78	0.40038	1120.4	0.05628	291.93	490.54	1.2946	1.8601	0.906	1.148
80	0.4212	1116	0.0536	294.43	491.86	1.3016	1.8606	0.911	1.15
82	0.44282	1111.5	0.05108	296.94	493.17	1.3086	1.8611	0.918	1.152
84	0.46525	1107	0.04869	299.46	494.48	1.3156	1.8617	0.924	1.154
86	0.48853	1102.5	0.04644	301.98	495.78	1.3226	1.8622	0.93	1.156
88	0.51266	1097.9	0.04432	304.51	497.08	1.3296	1.8628	0.936	1.158
90	0.43767	1093.2	0.04231	307.05	498.38	1.3365	1.8634	0.943	1.16
94	0.59041	1083.9	0.03861	312.15	500.95	1.3504	1.8646	0.956	1.165
98	0.6469	1074.3	0.03528	317.28	503.51	1.3641	1.8659	0.97	1.17
100	0.67661	1069.5	0.03375	319.86	504.94	1.371	1.8666	0.978	1.172
105	0.75532	1057.2	0.03024	326.35	507.94	1.3881	1.8682	0.997	1.18
110	0.84065	1044.5	0.02715	332.91	511.04	1.4051	1.87	1.017	1.188
115	0.93295	1031.5	0.02441	339.56	514.1	1.4221	1.8718	1.038	1.197
120	1.0326	1018.2	0.02198	346.31	517.1	1.4391	1.8736	1.062	1.208

3-R2336fa

Temp	Pressure	Density		Volume		Enthalpy			Entropy	
C°	kPa	Liquid Kg/m^3	Vapour Kg/m^3	Liquid m^3/kg	Vapour m^3/kg	Liquid kJ/kg	Latent kJ/kg	Vapour kJ/kg	Liquid kJ/kg-k	Vapour kJ/kg-k
0	107.6	1440	7.56	0.0007	0.132	200	159.6	359.6	1	1.584
4	126.5	1428	8.816	0.0007	0.113	204.9	157.5	362.4	1.018	1.586
8	148	1415	10.23	0.0007	0.098	209.7	155.4	365.1	1.035	1.588
12	172.2	1402	11.82	0.0007	0.085	214.7	153.2	367.9	1.052	1.59
16	199.3	1390	13.6	0.0007	0.074	219.6	151.1	370.7	1.07	1.592
20	229.6	1376	15.58	0.0007	0.064	224.6	148.8	373.4	1.087	1.594
22	246.1	1370	16.66	0.0007	0.06	227.1	147.7	374.8	1.095	1.595
24	263.4	1363	17.79	0.0007	0.056	229.7	146.5	376.2	1.104	1.597
26	281.6	1356	18.99	0.0007	0.053	232.2	145.3	377.5	1.112	1.598
28	300.8	1350	20.25	0.0007	0.049	234.7	144.2	378.9	1.121	1.599
30	321	1343	21.57	0.0007	0.46	237.3	142.9	380.2	1.129	1.6
32	342.2	1336	22.97	0.0008	0.044	239.8	141.8	381.6	1.137	1.602
34	364.4	1329	24.43	0.0008	0.041	242.4	140.5	382.9	1.146	1.603
36	387.8	1322	25.98	0.0008	0.039	245	139.3	384.3	1.154	1.604
38	412.2	1315	27.6	0.0008	0.036	247.6	138	385.6	1.162	1.606
40	437.8	1308	29.3	0.0008	0.34	250.2	136.7	386.9	1.171	1.607
42	464.5	1300	31.09	0.0008	0.032	252.8	135.4	388.2	1.179	1.608
44	492.5	1293	32.97	0.0008	0.03	255.5	134	389.5	1.187	1.61
46	521.8	1285	34.95	0.0008	0.029	258.1	132.7	390.8	1.195	1.611
48	552.3	1278	37.03	0.0008	0.027	260.8	131.3	392.1	1.204	1.613
50	584.2	1270	39.21	0.0008	0.026	263.4	130	393.4	1.212	1.614
52	617.4	1263	41.5	0.0008	0.024	266.1	128.5	394.6	1.22	1.615
54	652	1255	43.9	0.0008	0.023	268.8	127.1	395.9	1.228	1.617
56	688.1	1247	46.43	0.0008	0.022	271.5	125.6	397.1	1.236	1.618
58	725.7	1238	49.08	0.0008	0.02	274.2	124.2	398.4	1.244	1.619
60	764.7	1230	51.87	0.0008	0.019	277	122.6	399.6	1.253	1.621
62	805.4	1222	54.81	0.0008	0.018	279.7	121.1	400.8	1.261	1.622
64	847.7	1213	57.89	0.0008	0.017	282.5	119.5	402	1.269	1.623
66	891.6	1205	61.14	0.0008	0.016	285.3	117.8	403.1	1.277	1.625
68	937.2	1196	64.55	0.0008	0.015	288.1	116.2	404.3	1.285	1.626
70	984.5	1187	68.15	0.0008	0.015	290.9	114.5	405.4	1.293	1.627
72	1034	1177	71.94	0.0009	0.014	293.8	112.7	406.5	1.301	1.628
74	1085	1168	75.94	0.0009	0.013	296.6	111	407.6	1.31	1.629
76	1138	1158	80.16	0.0009	0.012	299.5	109.1	408.6	1.318	1.63
78	1192	1148	84.62	0.0009	0.012	302.4	107.3	409.7	1.26	1.631
80	1249	1138	89.33	0.0009	0.011	305.4	105.3	410.7	1.334	1.632
82	130.8	1127	94.33	0.0009	0.011	308.3	103.3	411.6	1.342	1.633
84	1369	1116	99.62	0.0009	0.01	311.3	101.3	412.6	1.351	1.634
86	1432	1105	105.2	0.0009	0.01	314.4	99.1	413.5	1.359	1.635
88	1497	1093	111.2	0.0009	0.009	317.4	96.9	414.3	1.367	1.636
90	1565	1081	117.6	0.0009	0.009	320.5	94.6	415.1	1.376	1.637
92	1635	1069	124.4	0.0009	0.008	323.6	92.2	415.8	1.384	1.637
94	1707	1056	131.7	0.001	0.008	326.8	89.7	416.5	1.392	1.637
96	1782	1042	139.6	0.001	0.007	330	87.2	417.2	1.401	1.637
98	1860	1028	148	0.001	0.007	333.2	84.5	417.7	1.409	1.637
100	1940	1013	157.1	0.001	0.006	336.5	81.7	418.2	1.418	1.637
102	2022	997.8	167.1	0.001	0.006	339.8	78.8	418.6	1.427	1.637
104	2108	981.3	177.9	0.001	0.006	343.3	75.5	418.8	1.436	1.636
108	2288	944.9	202.9	0.0011	0.005	350.3	68.7	419	1.454	1.634
112	2481	902.6	233.9	0.0011	0.004	357.8	60.7	418.5	1.473	1.63
116	2687	851.1	274.5	0.0012	0.004	365.8	51.2	714	1.493	1.624
120	2907	782.4	332.7	0.0013	0.003	375	38.7	413.7	1.516	1.614

4-R245fa

Temp	Pressure	Volume	Density	Enthalpy		Entropy		Specific heat		Specific heat	
°C	kPa	Vapour m^3/kg	Liquid Kg/m^3	Liquid kJ/kg	Vapour kJ/kg	Liquid kJ/kg k	Vapour kJ/kg	C_p liquid	C_p vapour	C_v liquid	C_v vapour
0	54	0.3076	1404	200	404.93	1	1.7502	1.29	0.84	0.91	0.77
4	64	0.2599	194	205.2	407.96	1.0189	1.7504	1.3	0.86	0.92	0.78
8	76	0.2208	1384	210.45	411	1.0376	1.751	1.32	0.87	0.93	0.79
10	83	0.204	1378	213.08	412.53	1.047	1.7513	1.32	0.88	0.93	0.8
12	90	0.1886	1373	215.73	414.06	1.0563	1.7518	1.33	0.88	0.94	0.81
14	98	0.1747	1368	218.39	415.59	1.0655	1.7523	1.33	0.89	0.94	0.81
16	106	0.162	1363	22210	417.13	1.0748	1.7529	1.34	0.9	0.95	0.82
20	124	0.1397	1352	226.43	420.21	1.0932	1.7542	1.35	0.91	0.96	0.83
24	144	0.1211	1341	231.85	423.3	1.1115	1.7558	1.36	0.93	0.96	0.84
28	167	0.1054	1331	237.31	426.4	1.1297	1.7576	1.37	0.94	0.97	0.85
30	179	0.0984	1325	240.06	427.95	1.1388	1.7586	1.37	0.95	0.98	0.86
32	192	0.0921	1320	242.82	429.5	1.1478	1.7596	1.38	0.96	0.98	0.87
34	206	0.0862	1314	245.59	431.05	1.1568	1.7606	1.39	0.96	0.98	0.87
36	220	0.0807	1308	248.37	432.6	1.1658	1.7617	1.39	0.97	0.99	0.88
38	236	0.0757	1303	251.16	434.16	1.1748	1.7629	1.4	0.98	0.99	0.88
40	252	0.071	1297	253.97	435.71	1.1837	1.7641	1.4	0.99	1	0.89
42	269	0.0667	1291	256.79	437.26	1.1926	1.7653	1.41	0.99	1	0.9
44	287	0.0627	1285	259.62	438.81	1.2016	1.7666	1.42	1	1	0.9
46	305	0.059	1280	262.46	440.36	1.2104	1.7579	1.42	1.01	1.01	0.91
48	325	0.0555	1274	265.31	441.9	1.2193	1.7692	1.43	1.02	1.01	0.91
50	345	0.0523	1268	268.18	443.45	1.2282	1.7705	1.43	1.03	1.02	0.92
54	390	0.0465	1256	273.95	446.53	1.2458	1.7733	1.45	1.04	1.02	0.93
58	438	0.0415	1243	279.77	449.6	1.2634	1.7762	1.46	1.06	1.03	0.94
62	490	0.0371	1231	285.65	452.65	1.2809	1.7792	1.47	1.08	1.04	0.96
66	548	0.0332	1218	291.58	455.69	1.2983	1.7822	1.49	1.1	1.05	0.97
68	578	0.0315	1211	294.57	457.2	1.307	1.7837	1.5	1.11	1.05	0.97
70	610	0.0298	1205	297.57	458.7	1.3157	1.7853	1.5	1.12	1.05	0.98
72	643	0.0283	1198	300.58	460.19	1.3244	1.7869	1.51	1.13	1.06	0.98
74	677	0.0268	1191	303.61	461.68	1.3331	1.7884	1.52	1.14	1.06	0.99
76	713	0.0255	1184	306.66	463.16	1.3417	1.79	1.53	1.15	1.07	1
78	750	0.0242	1177	309.72	464.63	1.3504	1.7916	1.54	1.16	1.07	1
80	789	0.023	1170	312.8	466.09	1.359	1.7931	1.54	1.17	1.07	1.01
82	829	0.0218	1163	315.89	467.54	1.3677	1.7947	1.55	1.18	1.08	1.01
84	870	0.0207	1156	319	468.99	1.3763	1.7963	1.56	1.19	1.08	1.02
86	913	0.0197	1148	322.13	470.41	1.3849	1.7978	1.57	1.2	1.08	1.03
88	958	0.0187	1141	325.27	471.83	1.3936	1.7994	1.58	1.21	1.09	1.03
90	1004	0.0178	1133	327.44	473.23	1.4022	1.8009	1.59	1.23	1.09	1.04
92	1052	0.017	1126	331.62	474.62	1.4108	1.8024	1.6	1.24	1.1	1.04
96	1153	0.0154	1110	338.04	477.35	1.4281	1.8054	1.63	1.27	1.1	1.06
100	1261	0.0139	1093	344.54	480	1.4453	1.8083	1.65	1.3	1.11	1.07
104	1377	0.0126	1076	351.14	482.57	1.4626	1.8111	1.68	1.34	1.12	1.08
108	1500	0.0114	1058	357.83	485.04	1.4799	1.8137	1.71	1.38	1.13	1.09
110	1565	0.0109	1049	361.12	486.24	1.4886	1.815	1.73	1.4	1.13	1.1
112	1632	0.0104	1039	364.62	487.4	1.4974	1.8161	1.75	1.42	1.13	1.11
114	1700	0.0099	1029	368.07	488.53	1.5061	1.8173	1.77	1.45	1.14	1.11
116	1772	0.0094	1019	371.54	489.62	1.5149	1.8183	1.79	1.48	1.14	1.12
120	1921	0.0085	998	378.59	491.68	1.5325	1.8202	1.84	1.54	1.15	1.13

Appendix B

Realized CFD Code Setup

Appendix B-Realized CFD Code Setup

This appendix illustrates the setup of the realized code which was used to simulate and optimize all the jet-pumps that have been investigated in this thesis. The realized code was based on the simulation of axisymmetric two-dimensional compressible turbulent fluid flow.

Problem description

The problem consists of a converging / diverging nozzle with different shapes of diffusers; each nozzle and diffuser constructs the jet-pump configuration as it is shown schematically in Figure B.1.

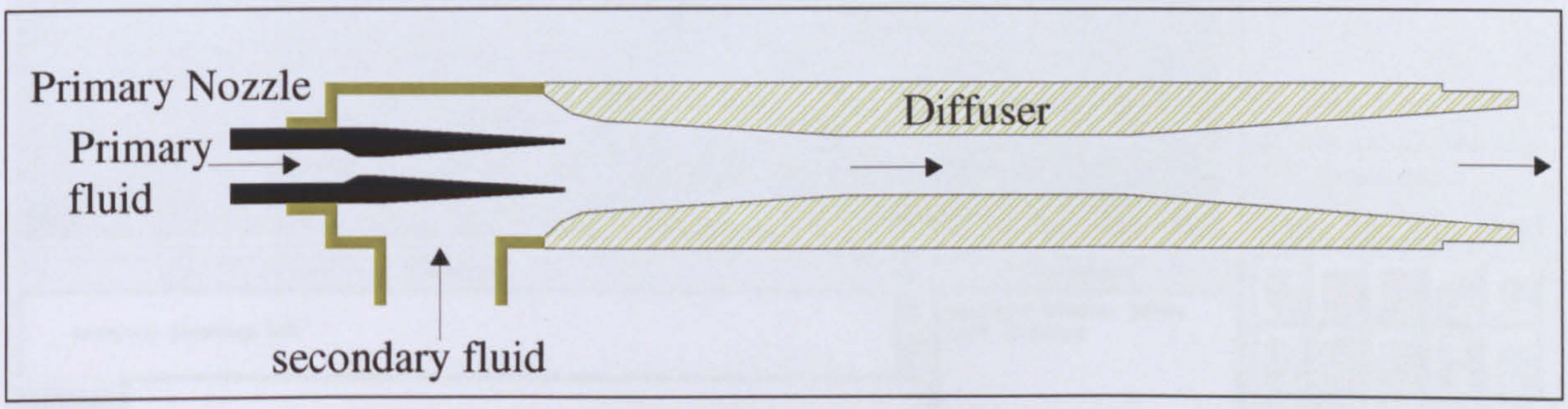

Figure B.1 Problem configuration (jet-pump)

The operating mode of this jet-pump was introduced within the thesis body with different working fluids. From the CFD simulation, the internal flow through the jet-pump, including the primary mass flow, secondary mass flow, temperature and pressure distribution and all other relevant parameters were computed.

In this appendix, the R236fa Conventional jet-pump (chapter 4) will be used for explanations of the CFD code setup.

Part1 Create Geometry in Gambit

Since the jet-pump has a circular cross-section, it was assumed that the flow is axisymmetric. Thus the geometry was created two-dimensionally. The steps used in Gambit are:

- *Building the jet-pump* geometry using down-top approach, thus creating vertexes, edges, and then faces.
- Mesh the geometry by adjusting the distribution of nodes on individual edges of the geometry; allowing control of the mesh density in specific areas.
- Specifying the boundary conditions

- Export the case to the Fluent software.

The Gambit graphical user interface is shown below.

Figure B.2 The Gambit graphical user interface *(GUI)*

Step 1: creating the geometry

* Depending on the dimensions of each nozzle and diffuser, vertices are located using real vertex and move-copy vertex forms, as shown above.

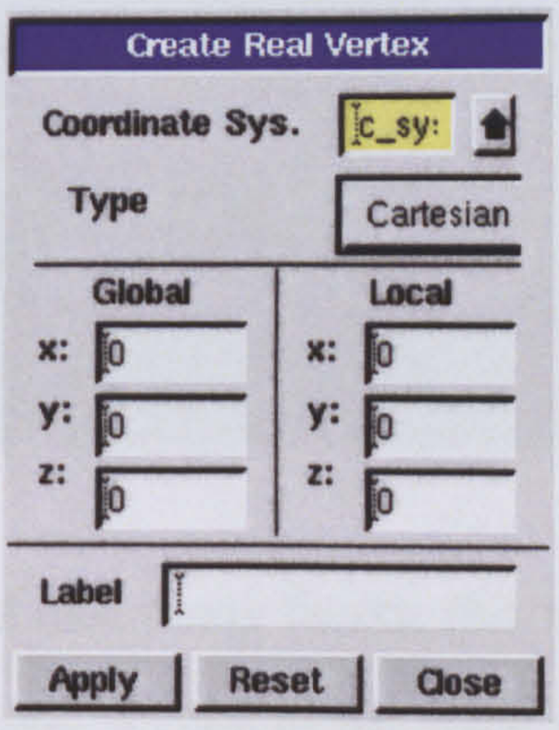

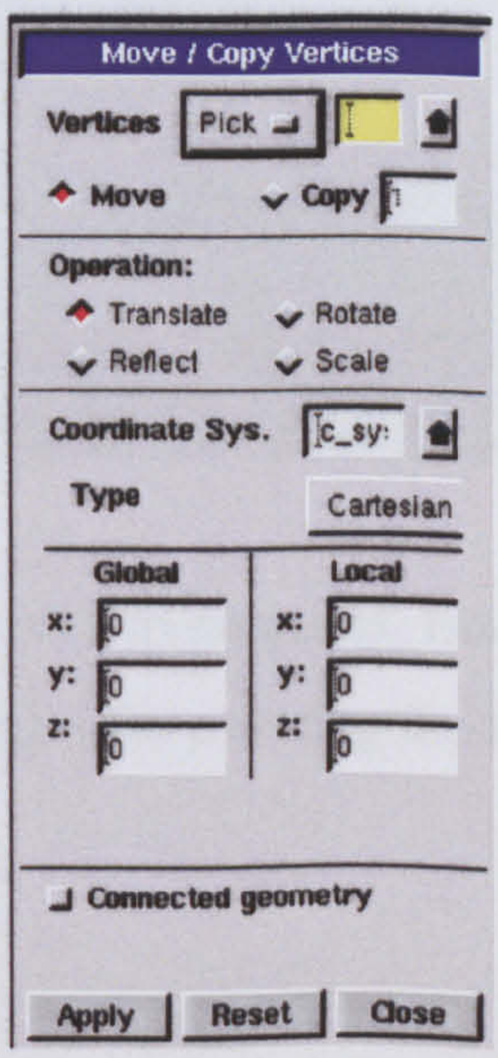

* Creating the edges using "Create straight edge" dialog

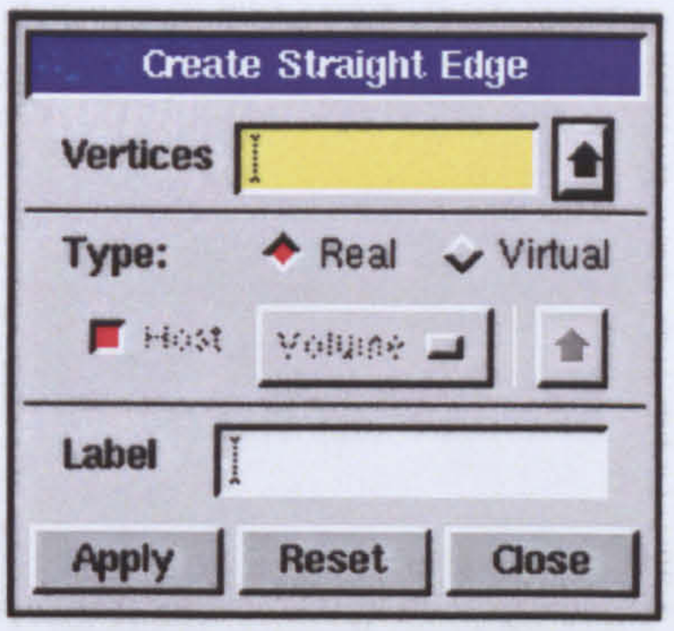

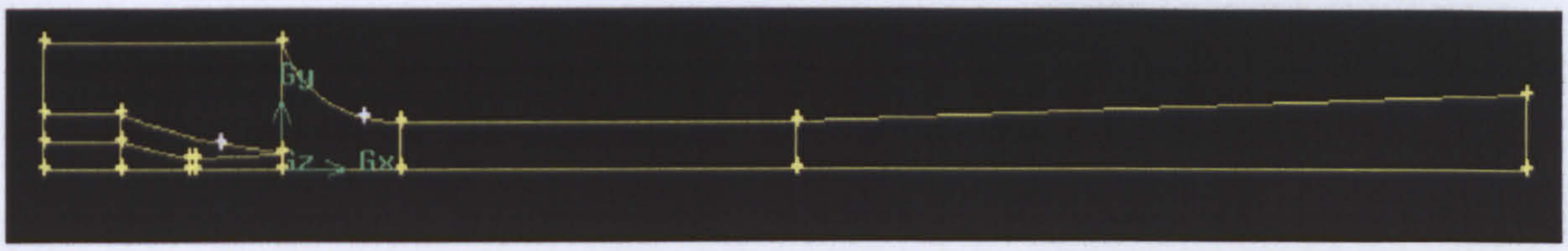

* Creating the faces using the "Create face dialog"

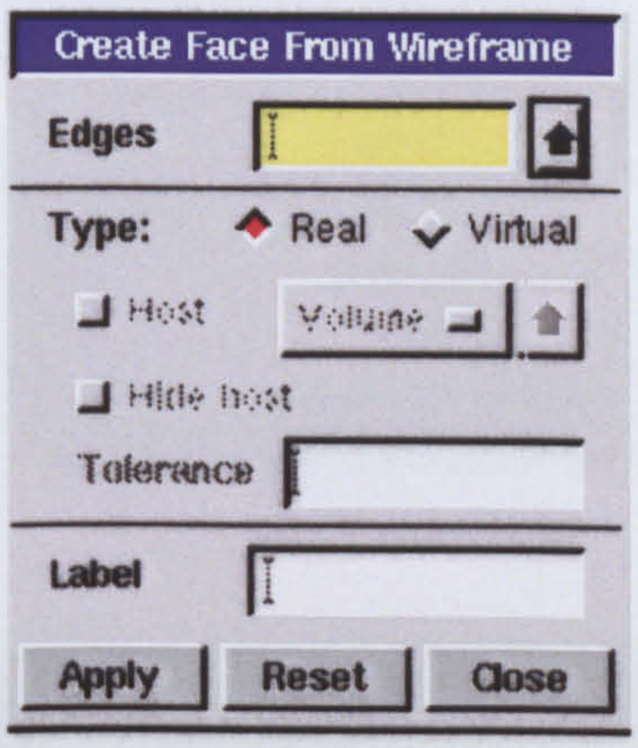

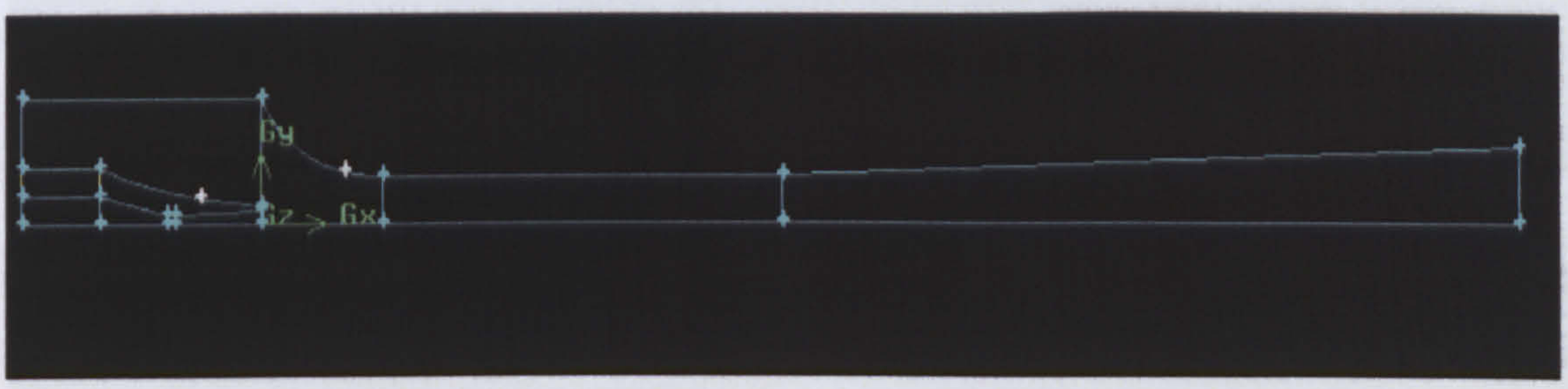

Each of the nozzle and diffuser are divided into many facets, this is for two purposes, first, to control the mesh density within each face, and second to use these facets for patching the flow over different scales.

Step2 Meshing the geometry

* Meshing the edges

Each edge is meshed depending on the required number of intervals in each edge, with the requirement that each two parallel edges must have the same number of intervals. "Mesh edges"dialog is used to create the edge mesh.

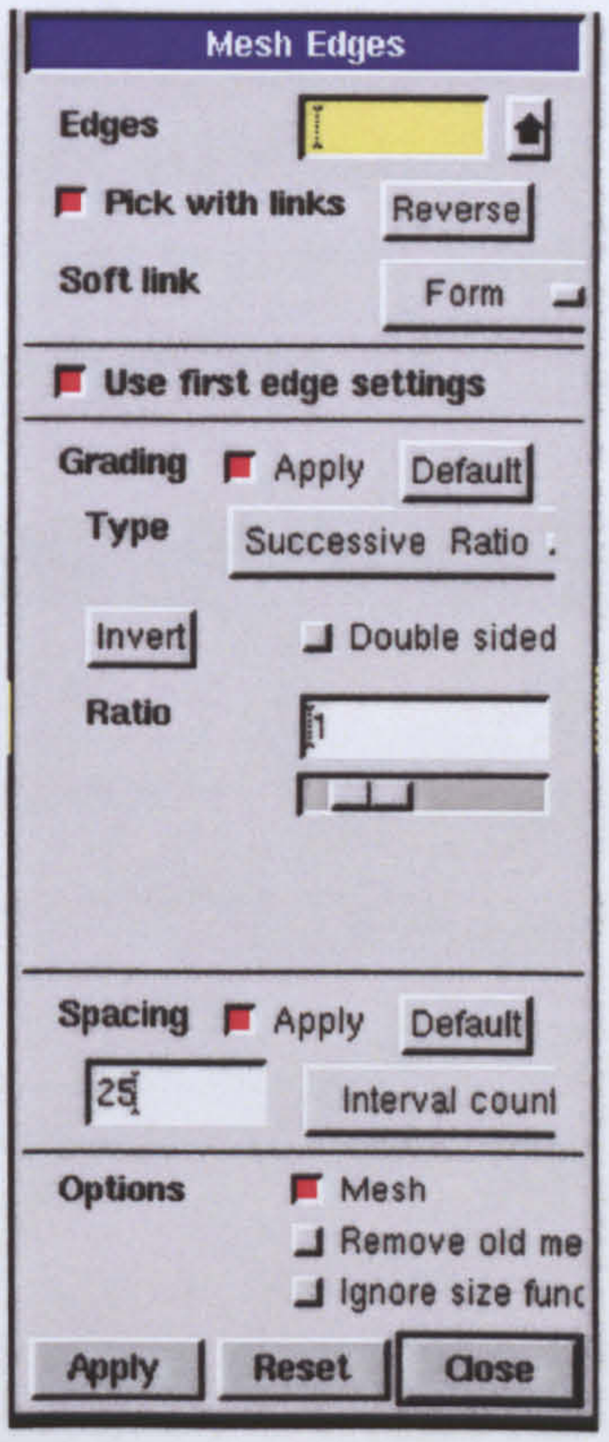

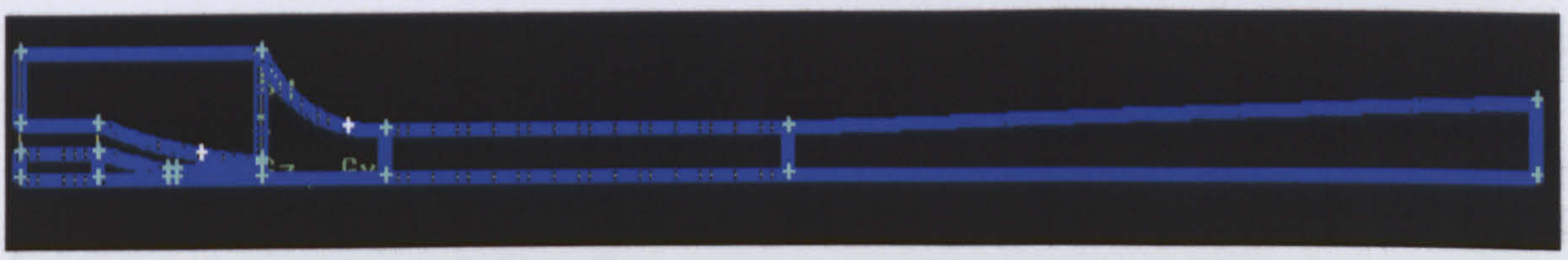

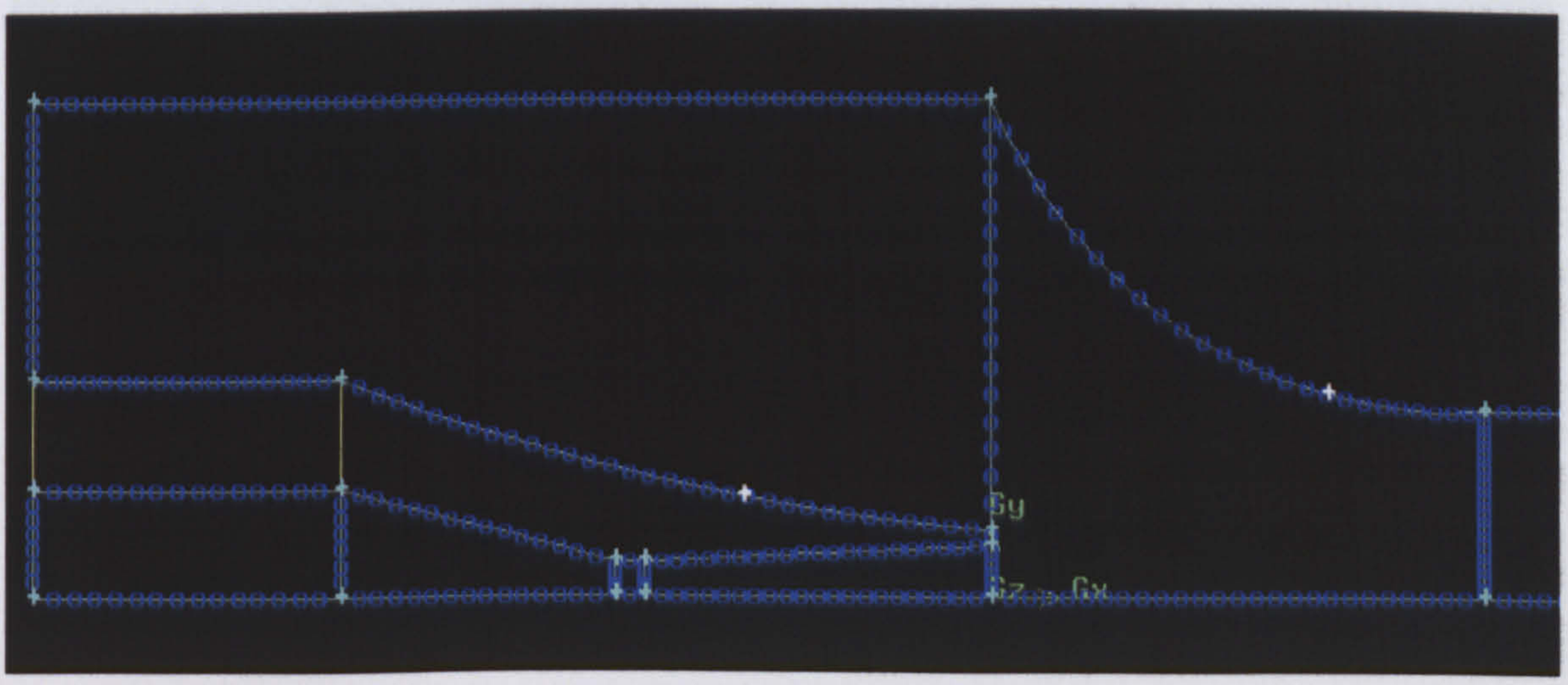

*** Meshing the faces**

As mentioned in chapter 3, the quadrilateral mesh was used in all cases since the flow has one predominant direction along the nozzle and the diffuser. In order to resolve the turbulent boundary layers, the grid is packed near all nozzle and diffuser walls. Also within the mixing region "near the nozzle exit" denser grid is used to capture the expansion jet. "Mesh faces" dialog is used to create the mesh for all faces.

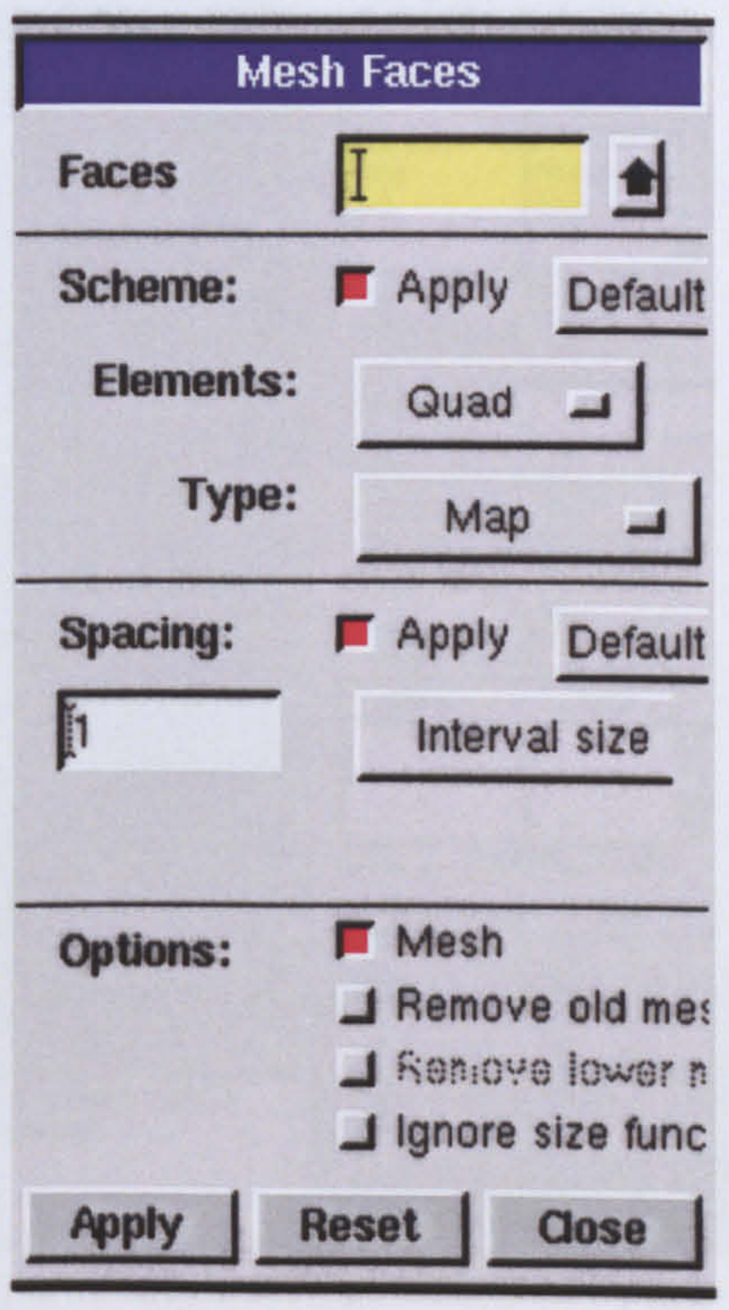

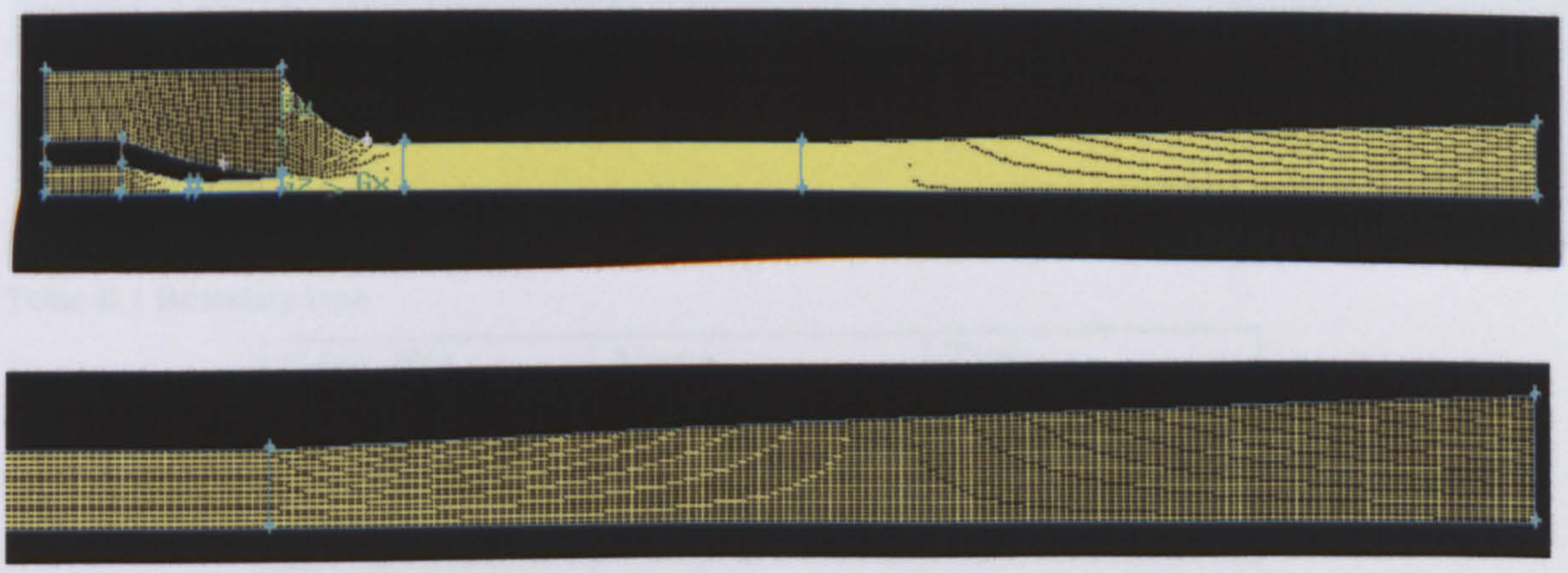

Quadrilateral mesh

Step3 specifying the boundary type in GAMBIT

Fluent 5/6 is selected from solver menu in the Gambit graphical user interface, and the boundary types are created for each of the edges as specified in table B.1 below.

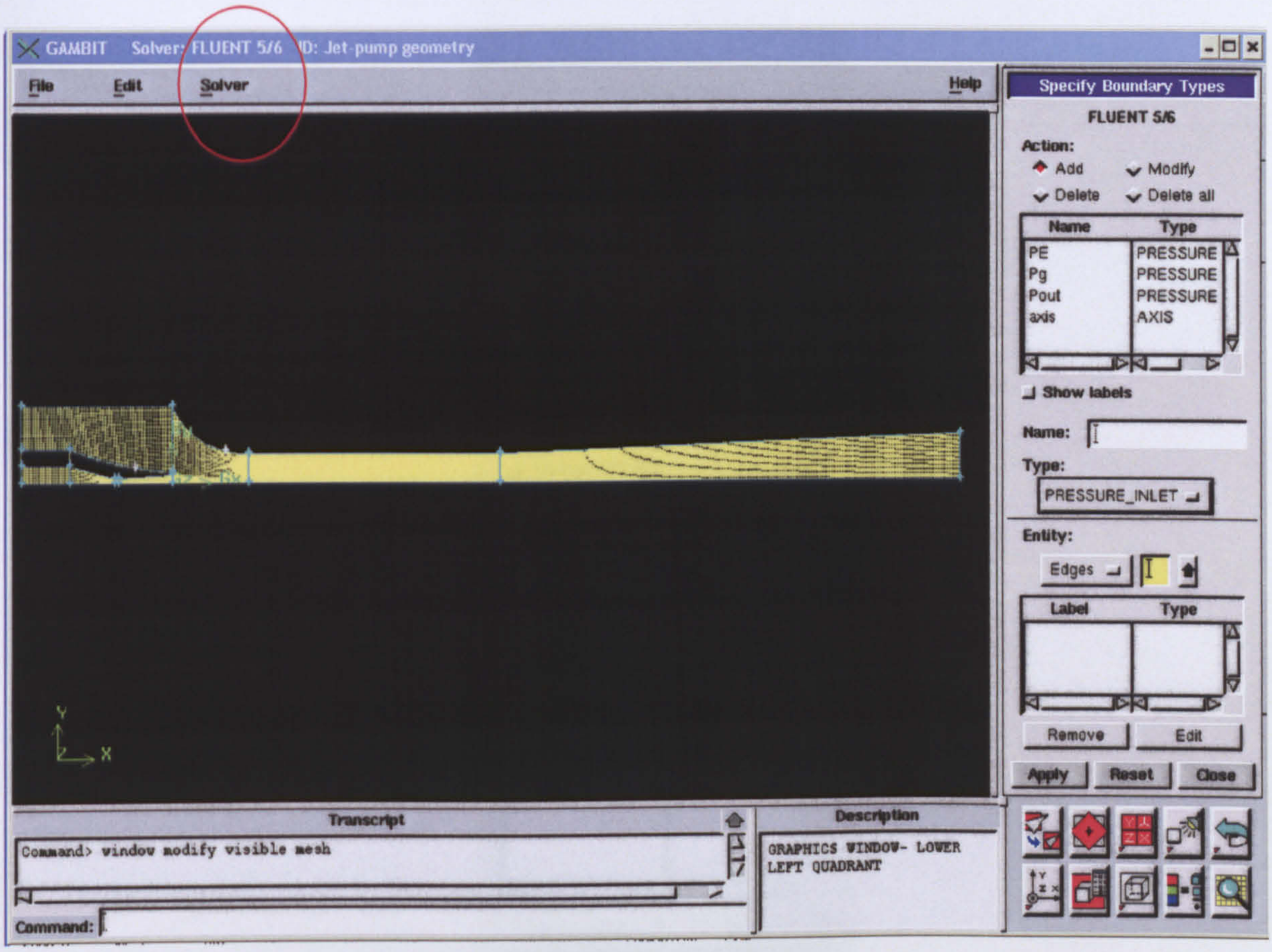

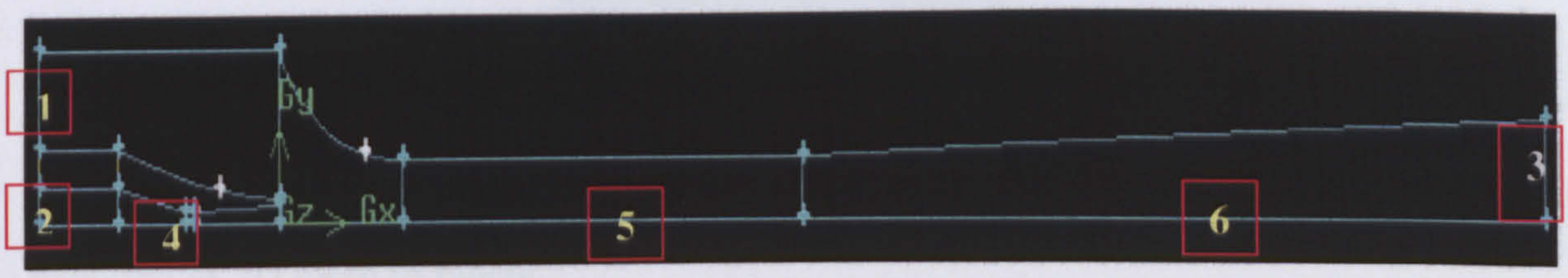

Table B.1 Boundary type

Edge NO	Name	Type
1	Evaporator inlet	Pressure-inlet
2	Generator inlet	Pressure-inlet
3	Outlet	Pressure-outlet
4,5,6	Centreline	Axis
All other external edges	Wall	WALL

As the primary and secondary fluids are of the same fluid, all faces can be treated as one fluid in Gambit, but for the ease of using patching technique in Fluent, three different zones are defined under different fluid names. This is done by using the "Specify Continuum Type" dialog, as shown below.

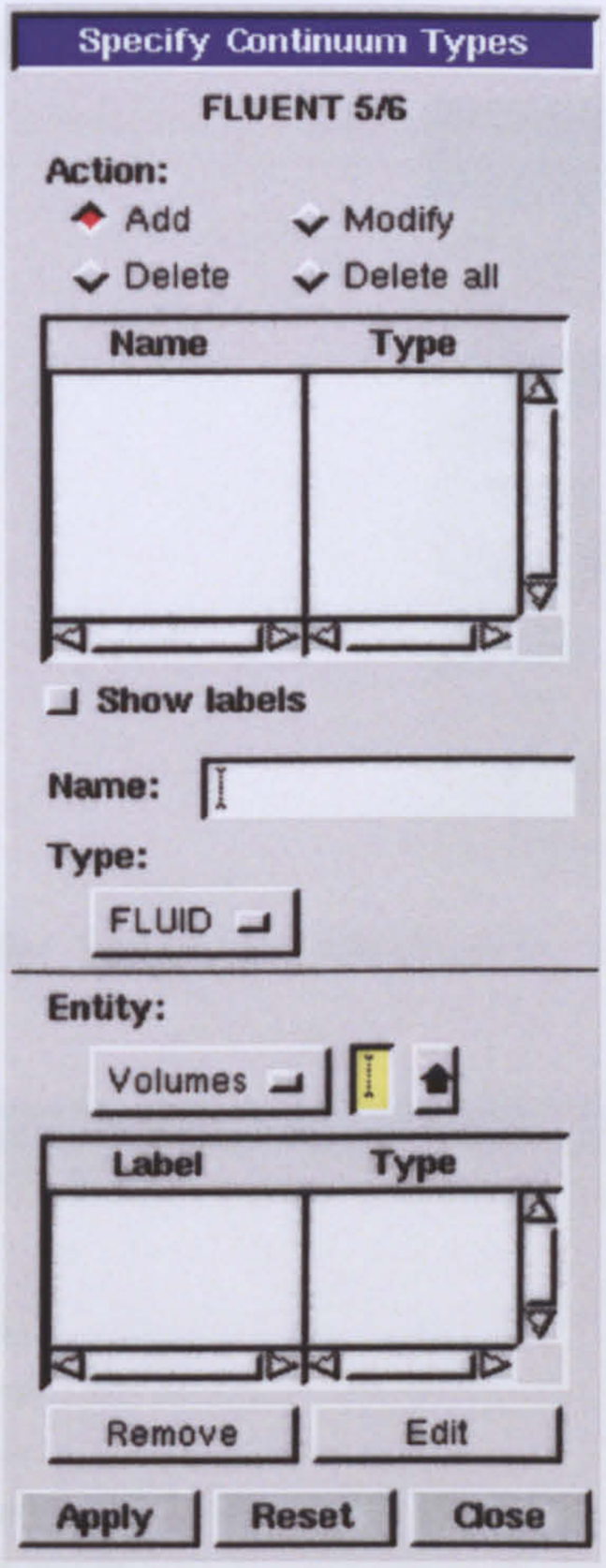

Step 4 Save and Export

When all setting is finished, the example is saved under a distinctive name, and then is exported as 2D mesh to Fluent.

Part 2 Set up problem in FLUENT

Step 1 Exporting the case into FLUENT

FLUENT 6.1 is used. After launching the Fluent, 2ddp is selected from the list of options, and then the GAMBIT saved case is imported.

When the case file is imported the following information should appear in the FLUENT window.

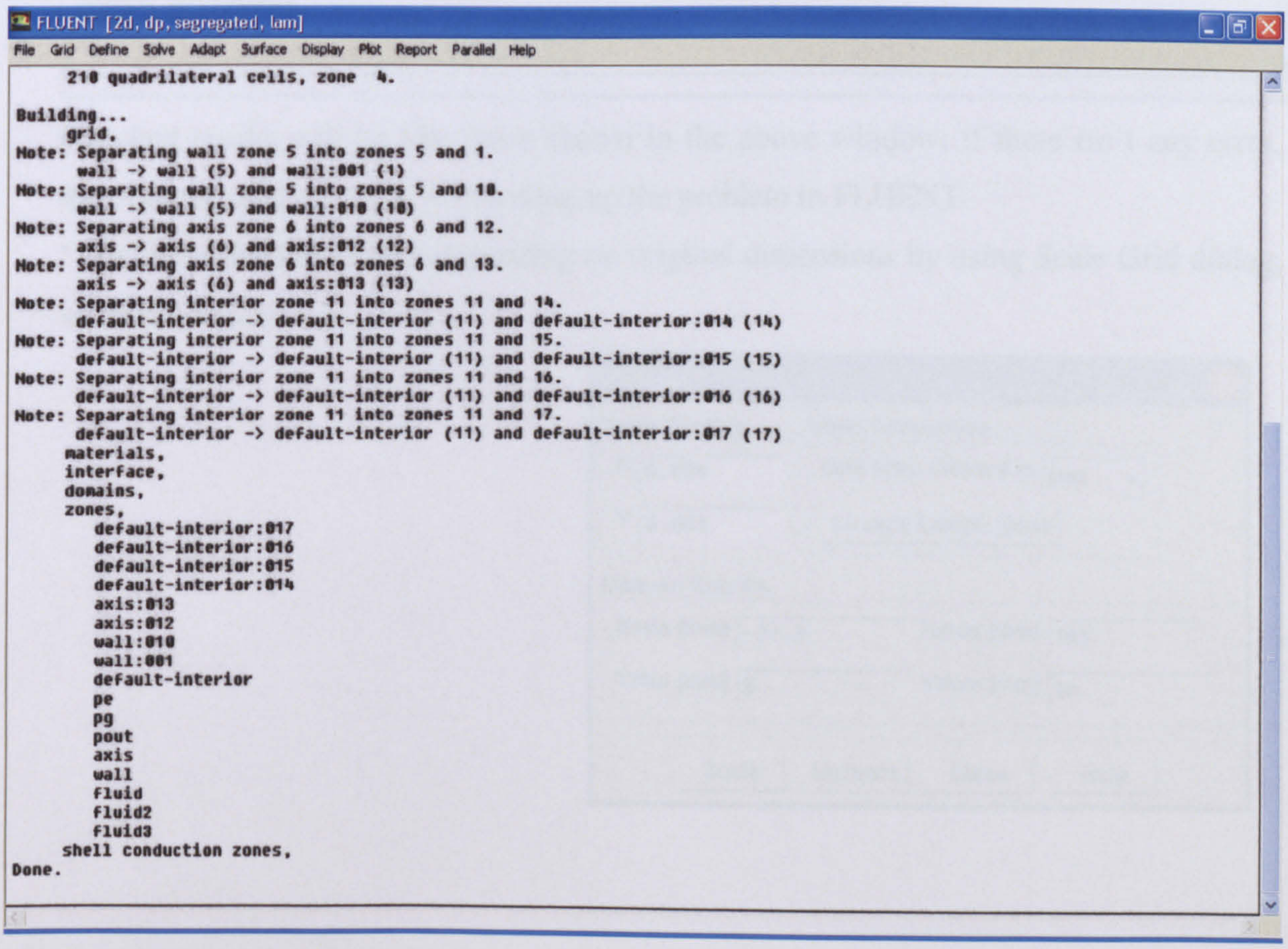

The consistently of the displayed information with the grid case that is exported from GAMBIT is checked in this window.

Also it is possible to check that if there are any errors with the grid, by using the grid check menu in FLUENT.

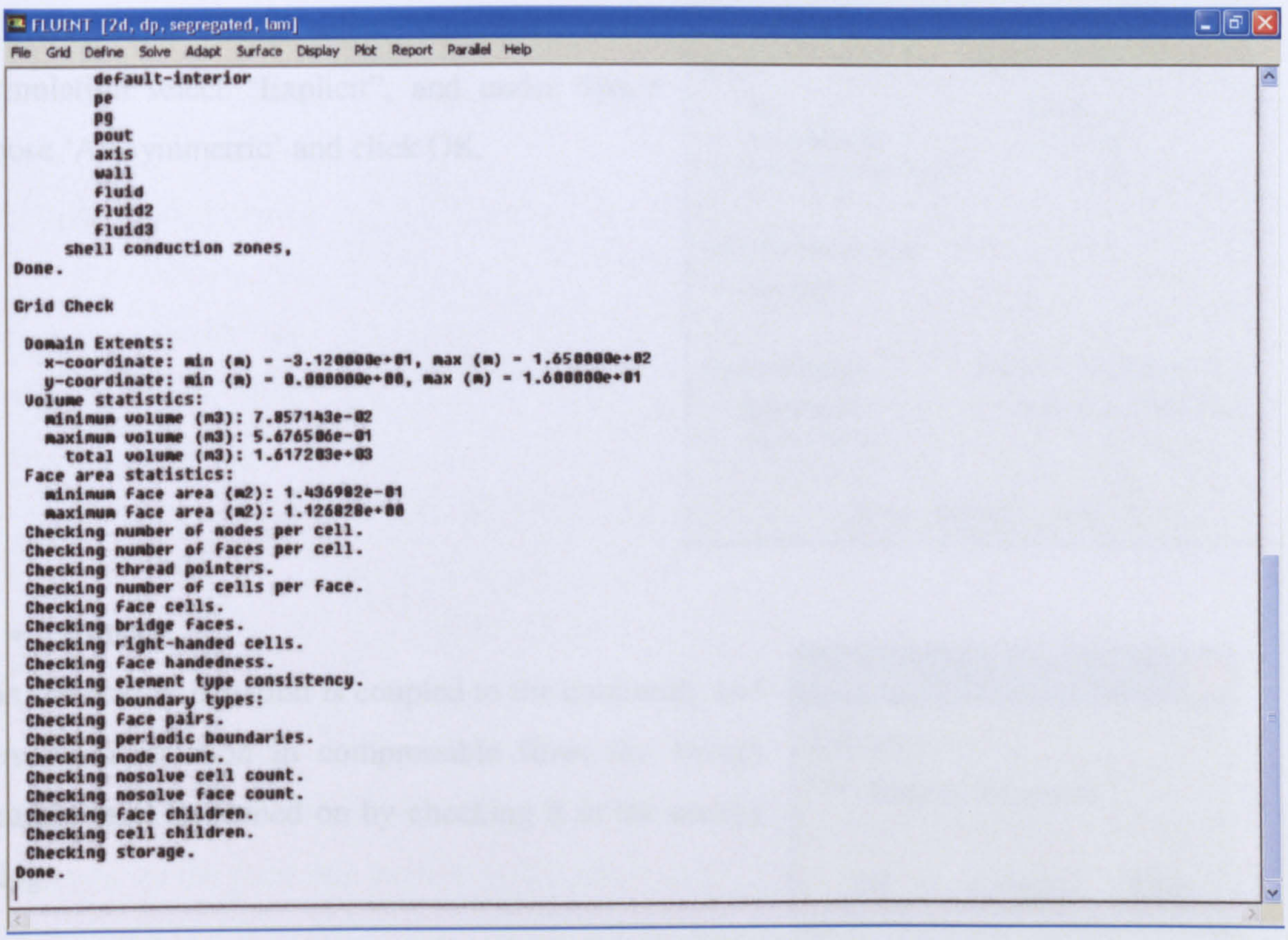

Checked results will be like these shown in the above window; if there isn't any error, then execute and continue with setting up the problem in FLUENT.

* The Grid must be scaled depending on original dimensions by using Scale Grid dialog, as shown below.

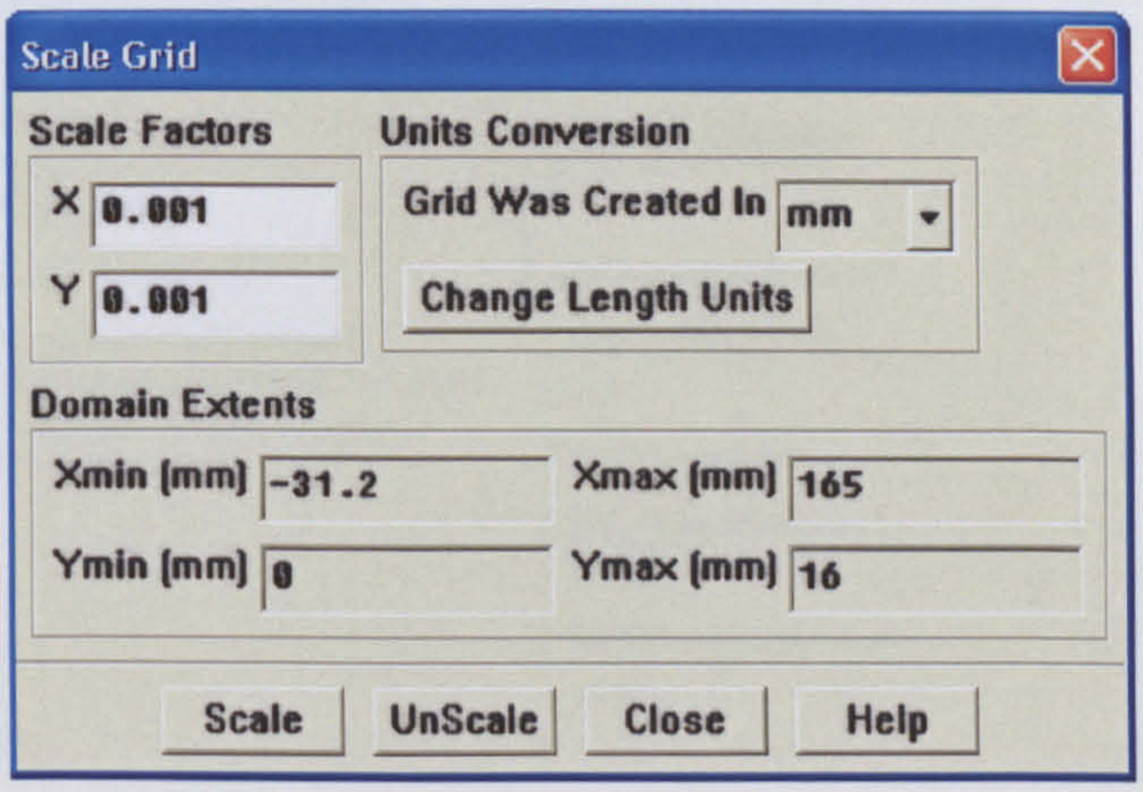

Step 2 Define solve properties

- **Solver**

* Under solver dialog, select "Coupled", under Formulation select "Explicit", and under Space choose 'Axisymmetric' and click OK.

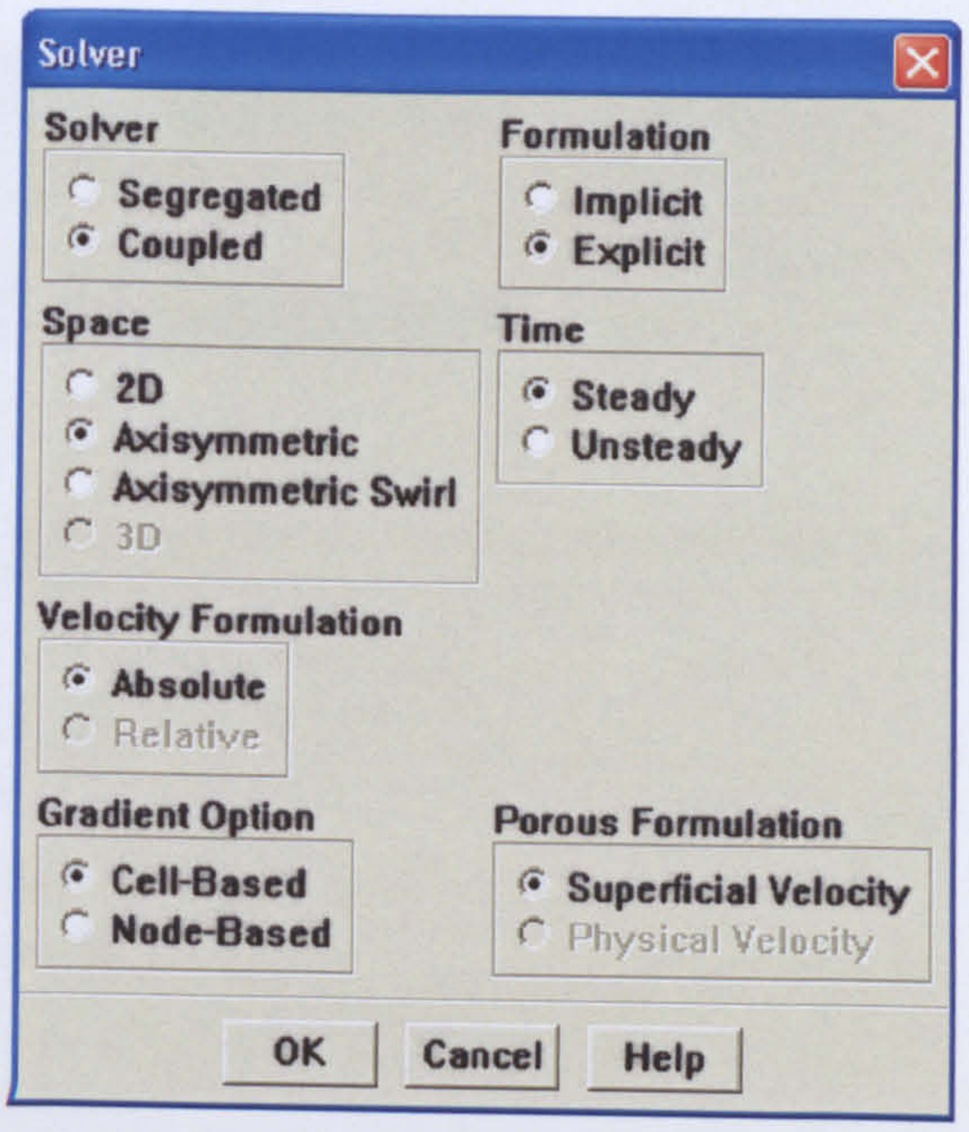

- **Energy**

* *As the energy equation is coupled to the continuity* and momentum equation in compressible flow, the energy equation must be turned on by checking it in the energy dialog.

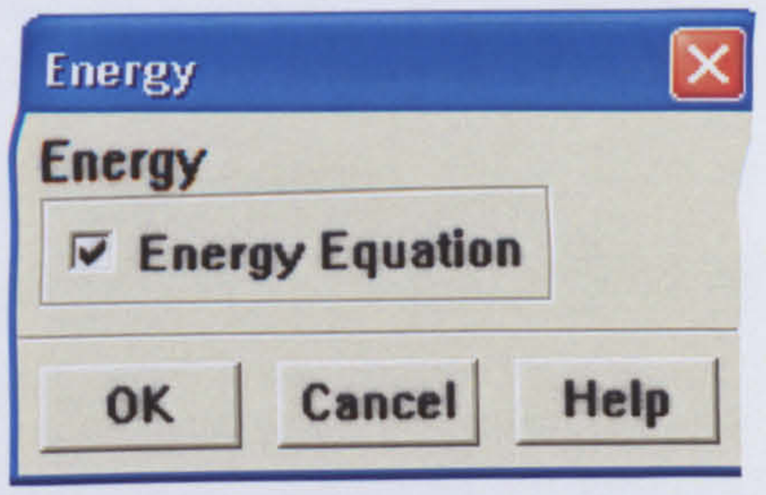

- **Viscous**

* Standard or RNG, K- epsilon (2 equation), is selected with standard wall functions for Near-wall Treatment.

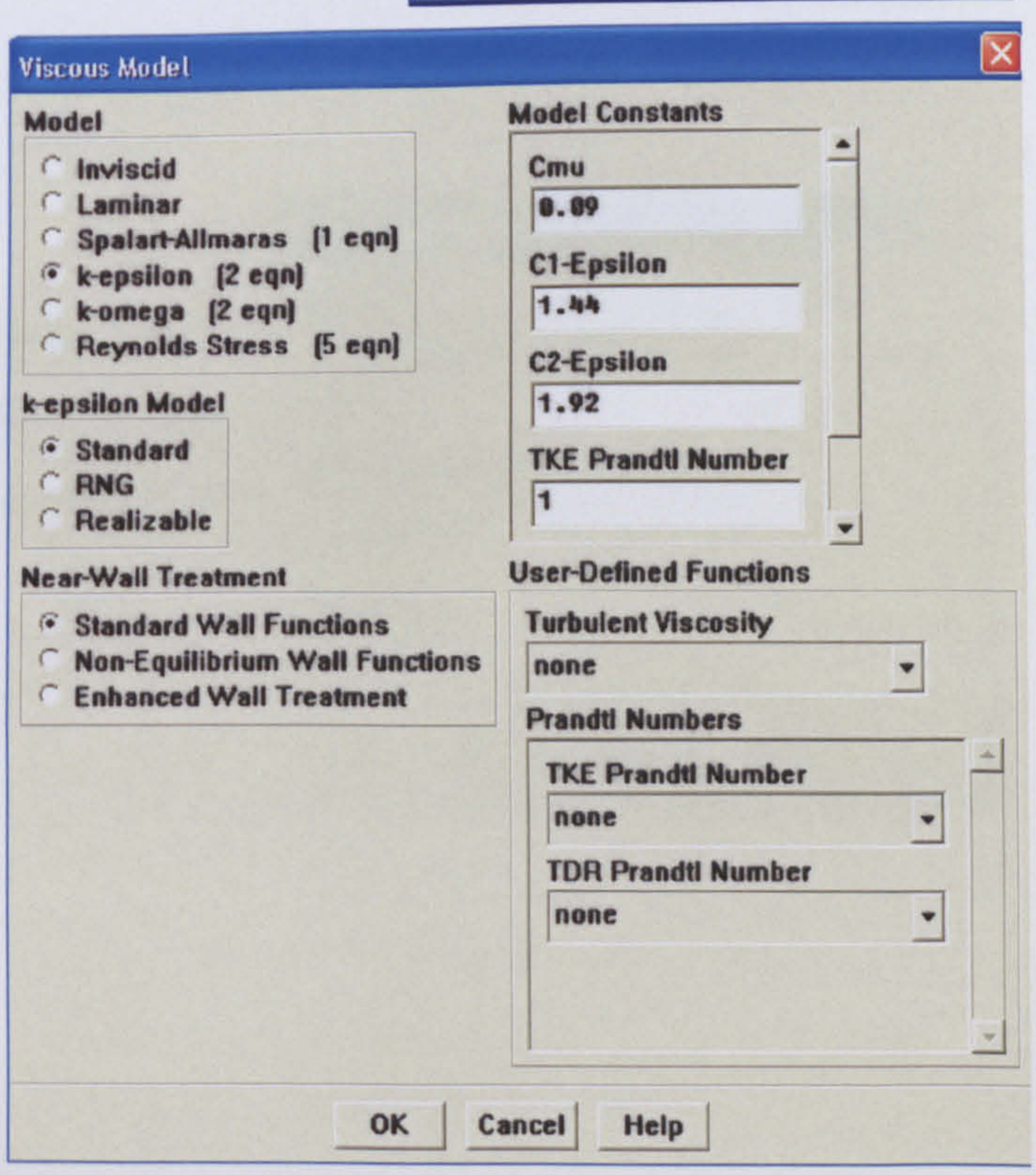

- **Materials**

* In the case of ideal gas modelling, the material form is used to enter the thermo physical properties of the working fluid. For Density, the ideal-gas is selected, , and the Cp, K, υ and M are entered as constant.

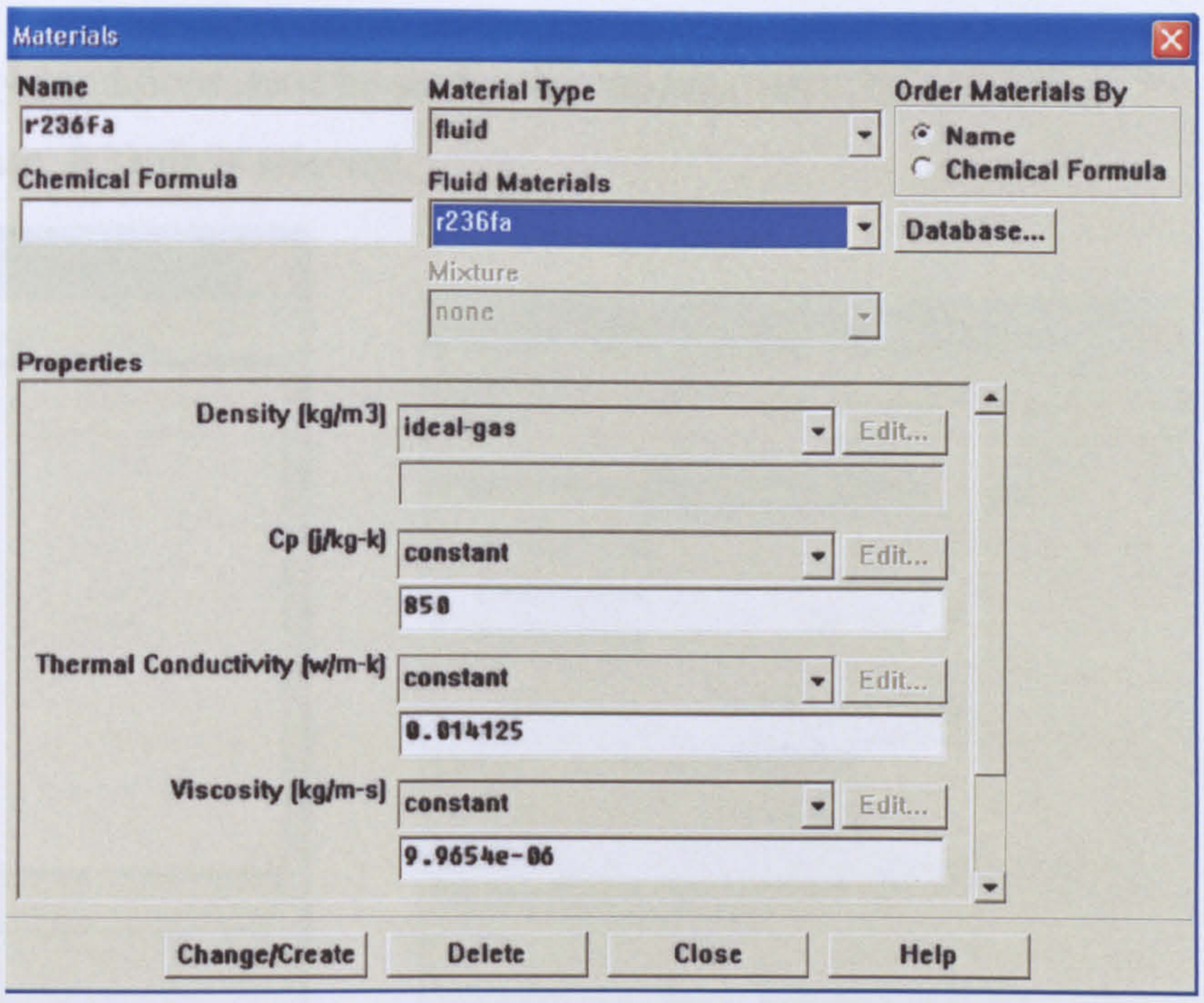

* In the case of real gas, the material dialog does not used and instead the real gas model is activated using the user-defined/real-gas and selecting the pure-working fluid from the REFPROP database list. Once the real gas model is activated, the Fluent's solver ignores any information for the fluid that is displayed in the material dialog.

- **Operating Conditions**

* As with the coupled solver it is preferred to use absolute pressure rather than gauge pressures, thus the operating pressure is set to zero, as shown in the dialog.

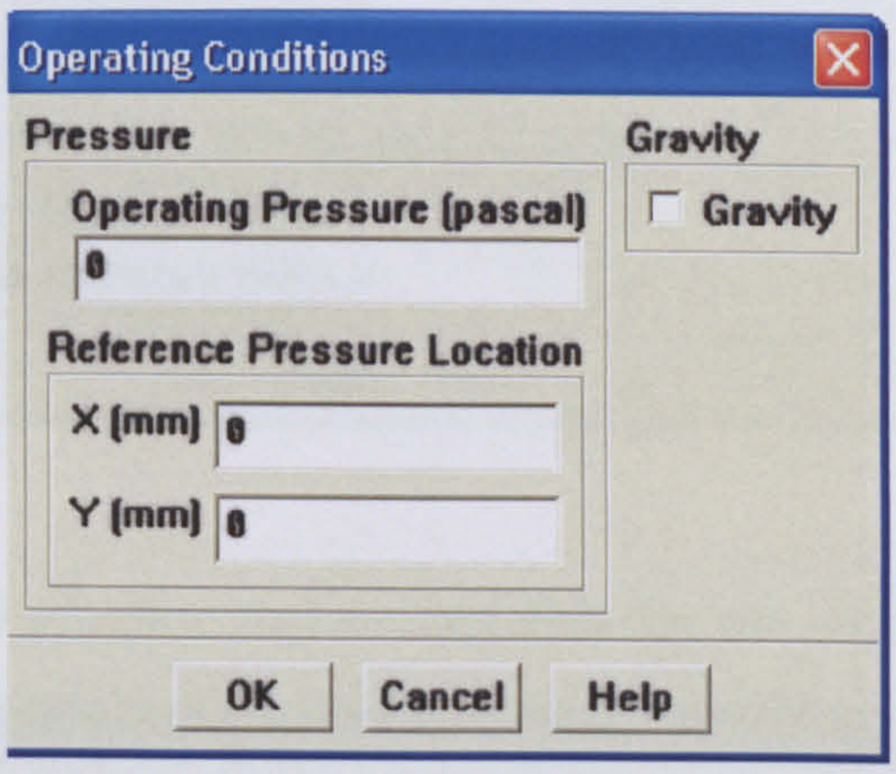

- **Boundary conditions**

* Each fluid in boundary conditions must be set for the working fluid defined in the material form; in this case, R236fa is selected.

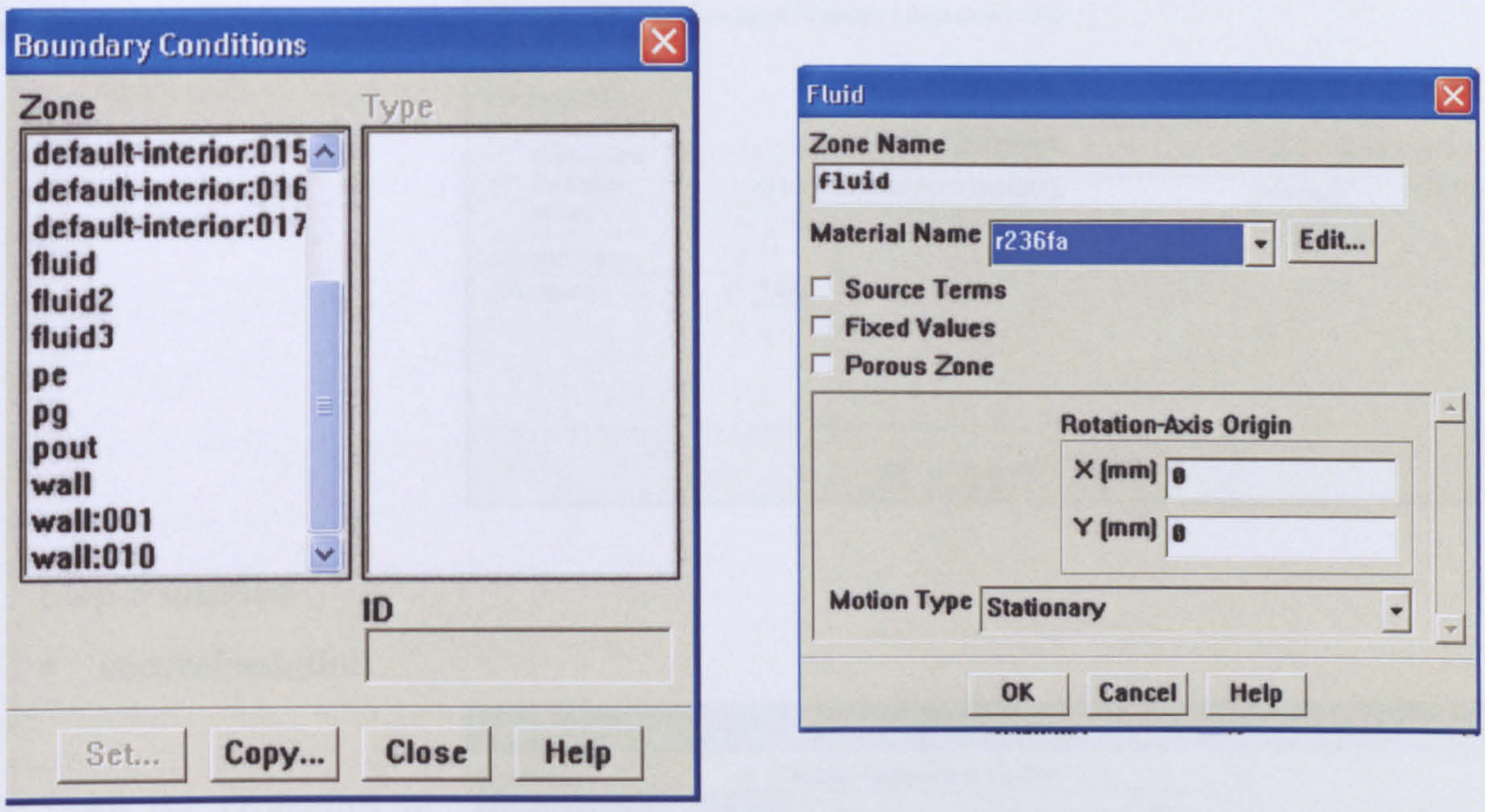

* The pressure at inlet from the generator and evaporator are set using the pressure inlet form. In this form, the total pressure and temperature are entered. In the supersonic /initial gauge pressure, if the static pressure is entered this will account to the speed for the fluid at each inlet.

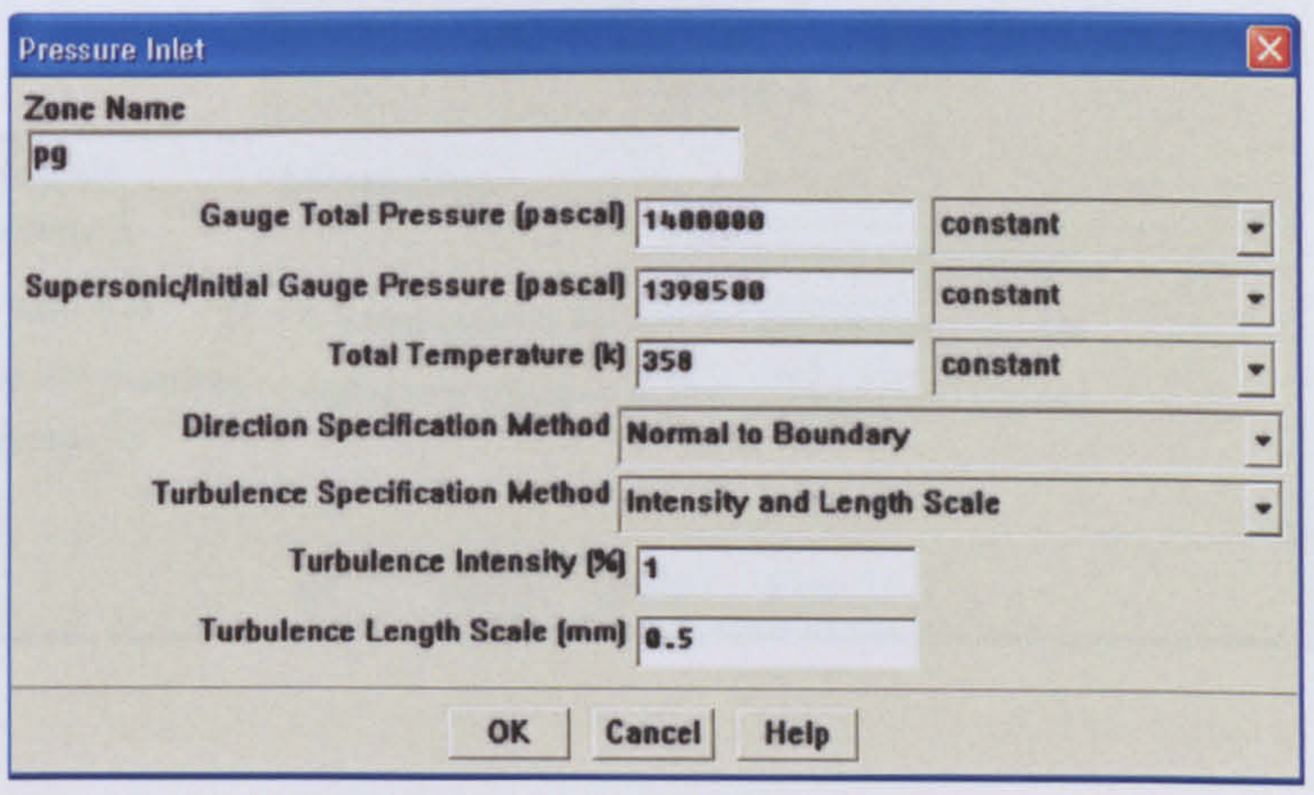

* For the diffuser outlet pressure, only the total pressure and temperature for the studied case are entered in the pressure outlet dialog, noting that in each form of pressure inlet and pressure outlet, the turbulence intensity and length scale are specified.

*All walls are treated as adiabatic walls, thus heat flux is set equal to zero in the Wall dialog.

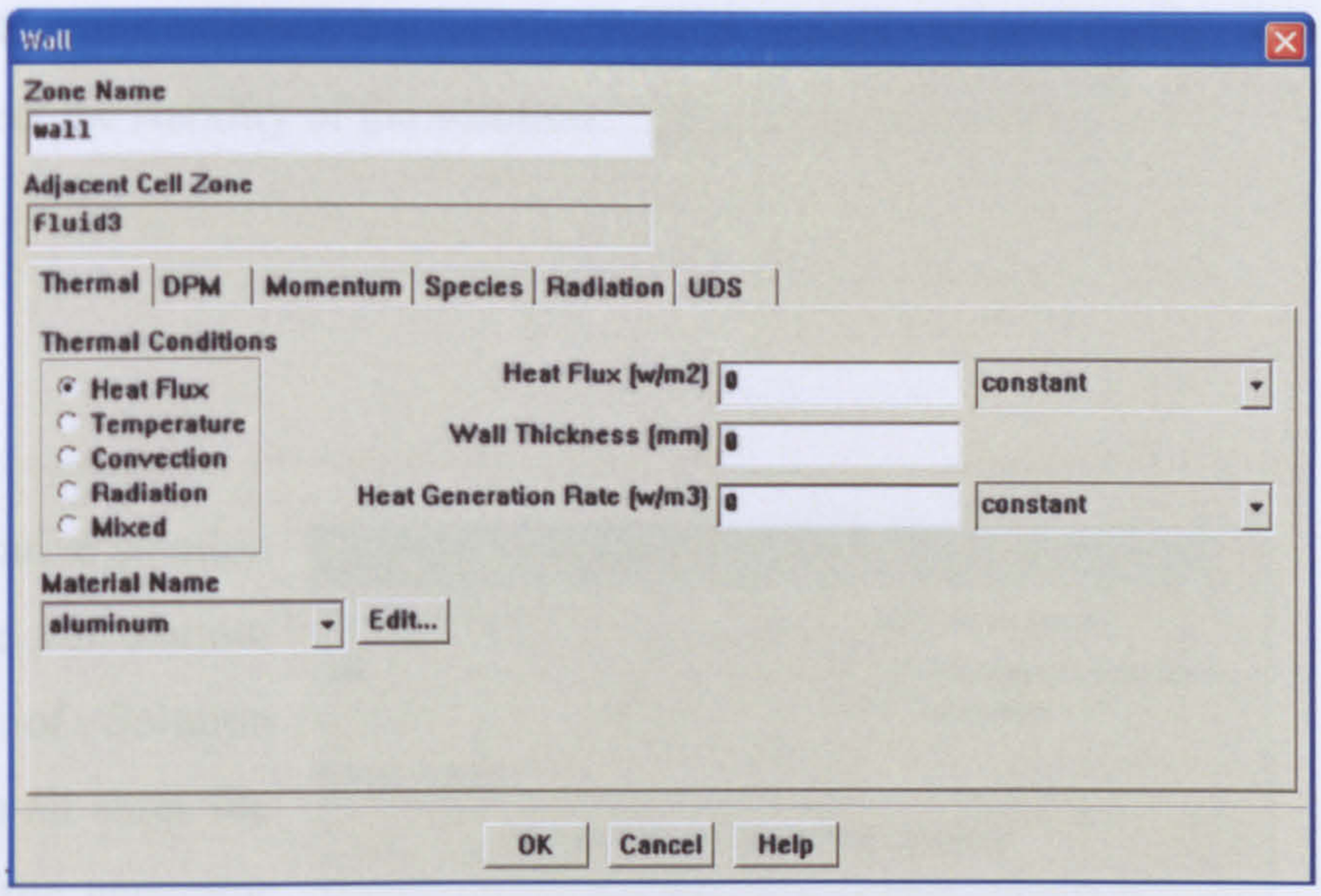

Step 3 solution

- **control solution**

* All the properties of the problem have been defined in the previous stages, now the solve setting will be set through use the Solution Controls dialog shown above.

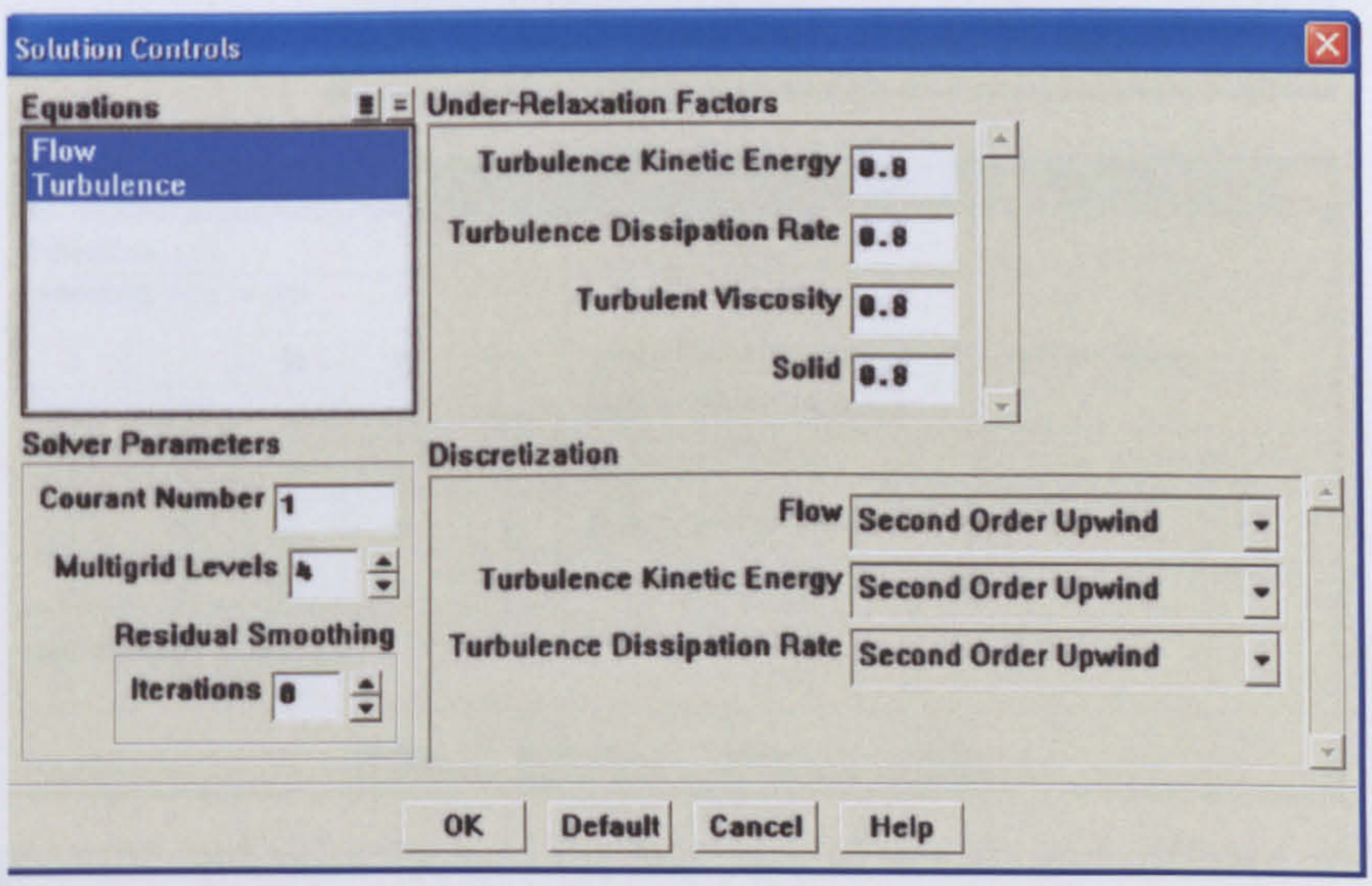

* The discretization scheme for each of the flow, turbulence kinetic energy and turbulence dissipation rate are changed and set to second order upwind which resolve the boundary layer and shock more accurately than the first-order scheme.

* Under-relaxation factor for all variables are set to 0.8, this can provide stability at the initial stage of the solution, and then can be reset to 1 for prompting the convergence. If the solution diverges or large oscillations in residual are observed, the under-relaxation must be reduced.

&-The Courant number can be set to 1 or slightly less, actually the solution generally converges faster for a large Courant number, but as the coupled explicit solver is used, the high Courant number can affect the stability of the solution.

* Multigrid level is set to 4.

- **Initialize solution**

* An initial guess for the iterative solution must be defined to start the calculation; this is done by the use of Solution initialization dialog above. In all cases the initial guess is set equal to the generator inlet pressure, by selecting the (P_g) inlet generator pressure, under Compute from and then by clicking Init.

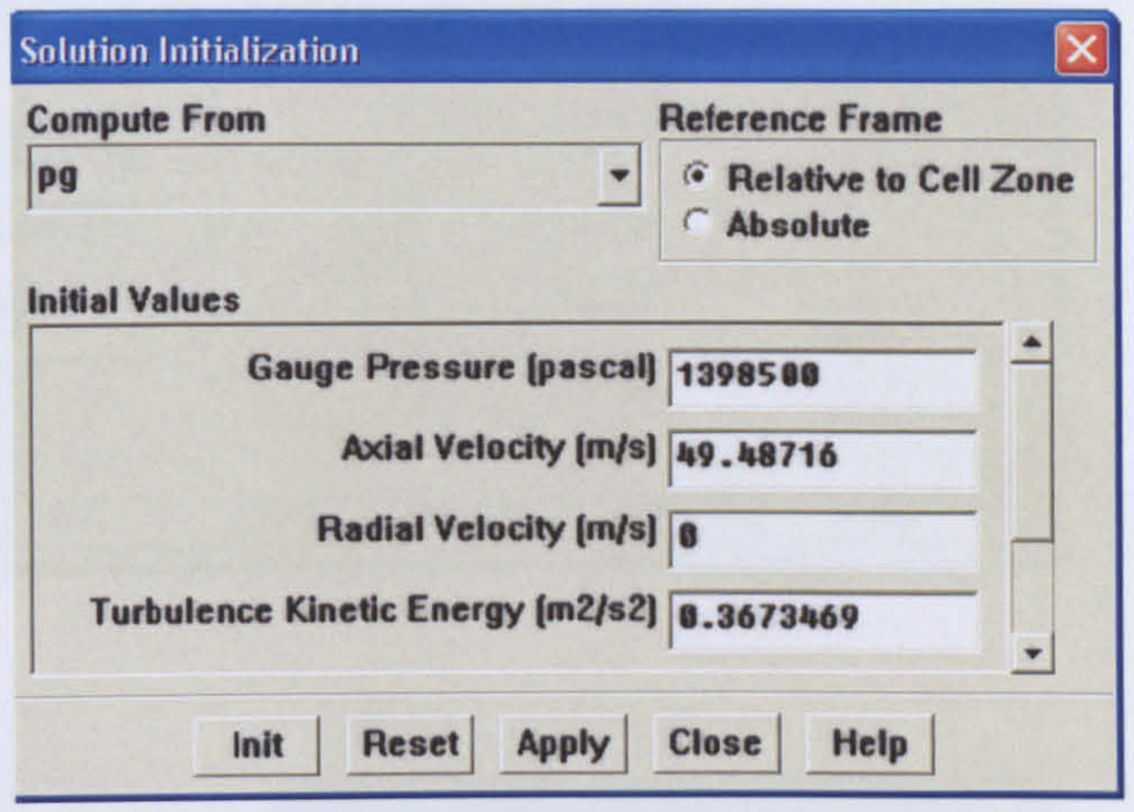

* Also for a better starting solution, a custom field function was used to provide a patching technique that was used to patch through the jet-pump an appropriate flow field variation in the pressure, temperature and velocity, and for that each of nozzle and diffuser are divided into zones. Two zones are used through the nozzle, and the diffuser is considered as one zone. Custom field function is defined for each zone separately using the Custom field function calculator dialog shown above.

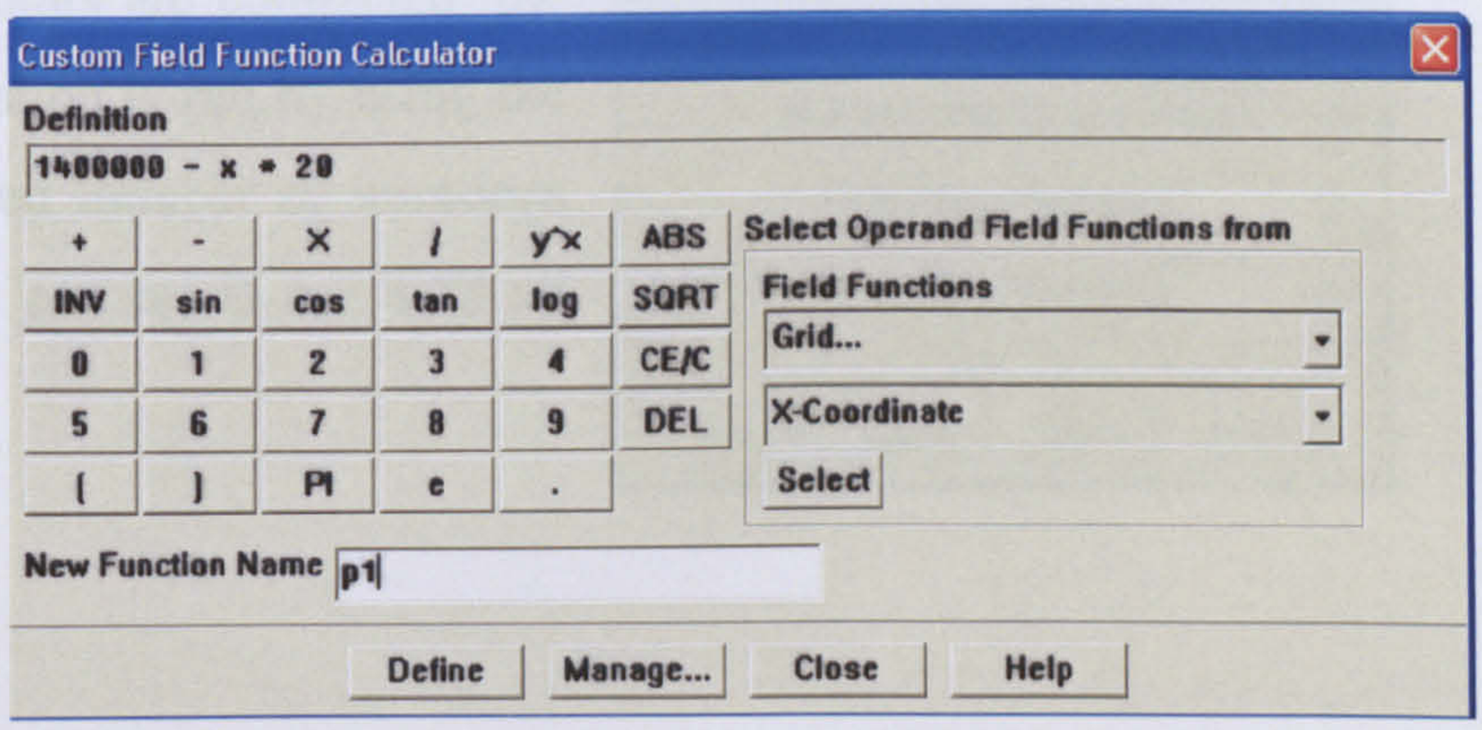

Then from the patch dialog shown above, each zone is patched in each of pressure, axial velocity and temperature.

***Solution monitoring**

* The residuals and their Convergence level are set using the Residual Monitors dialog, shown below.

For all Residuals the convergence level value were set to 1e-06, this level of convergence is good enough for the solution. From this form also, the residual can be plotted by selecting Plot under options.

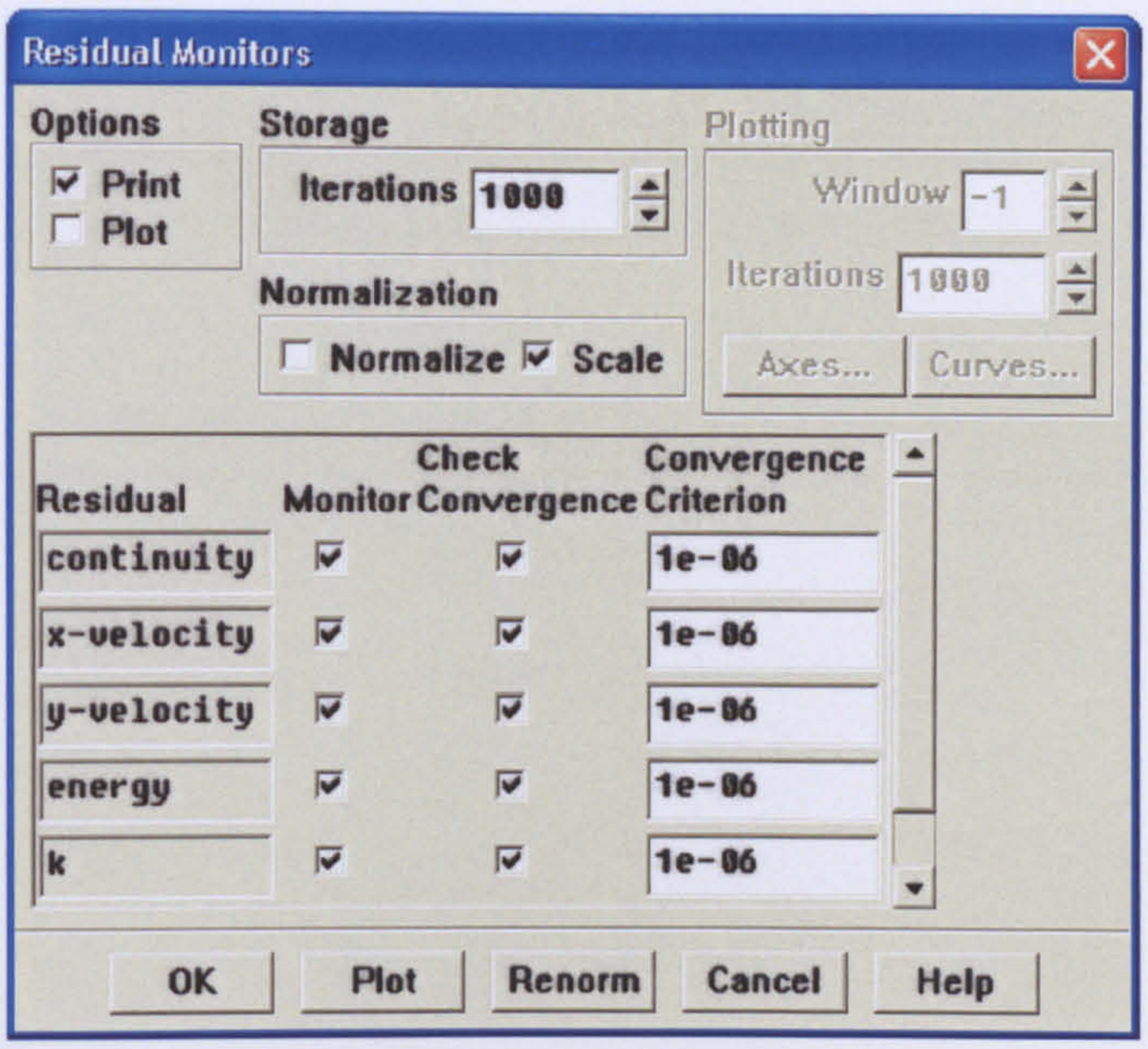

- **Iteration**

* Once all the mentioned points are completed, the case is saved then the calculation is run by using the Iterate dialog, set the required number of iterations and click Iterate. The iterate process is run until all the Residuals are converged.

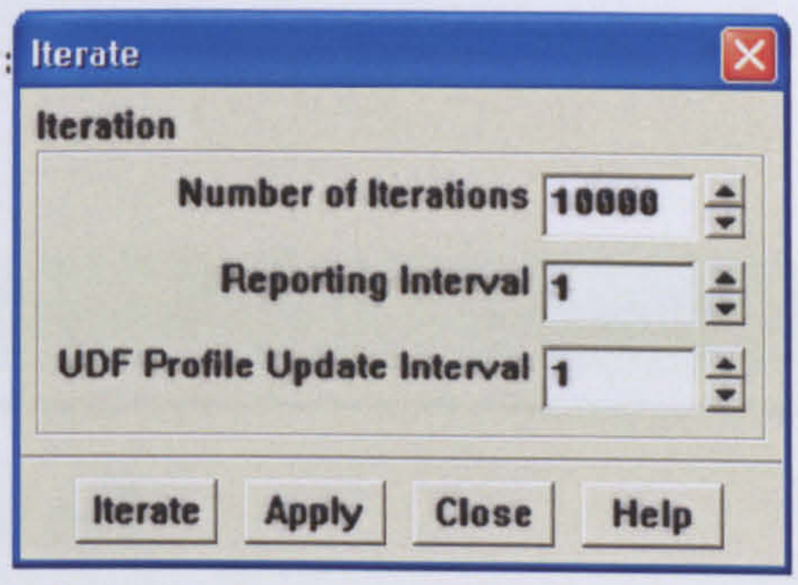

Appendix C

Computational Mesh

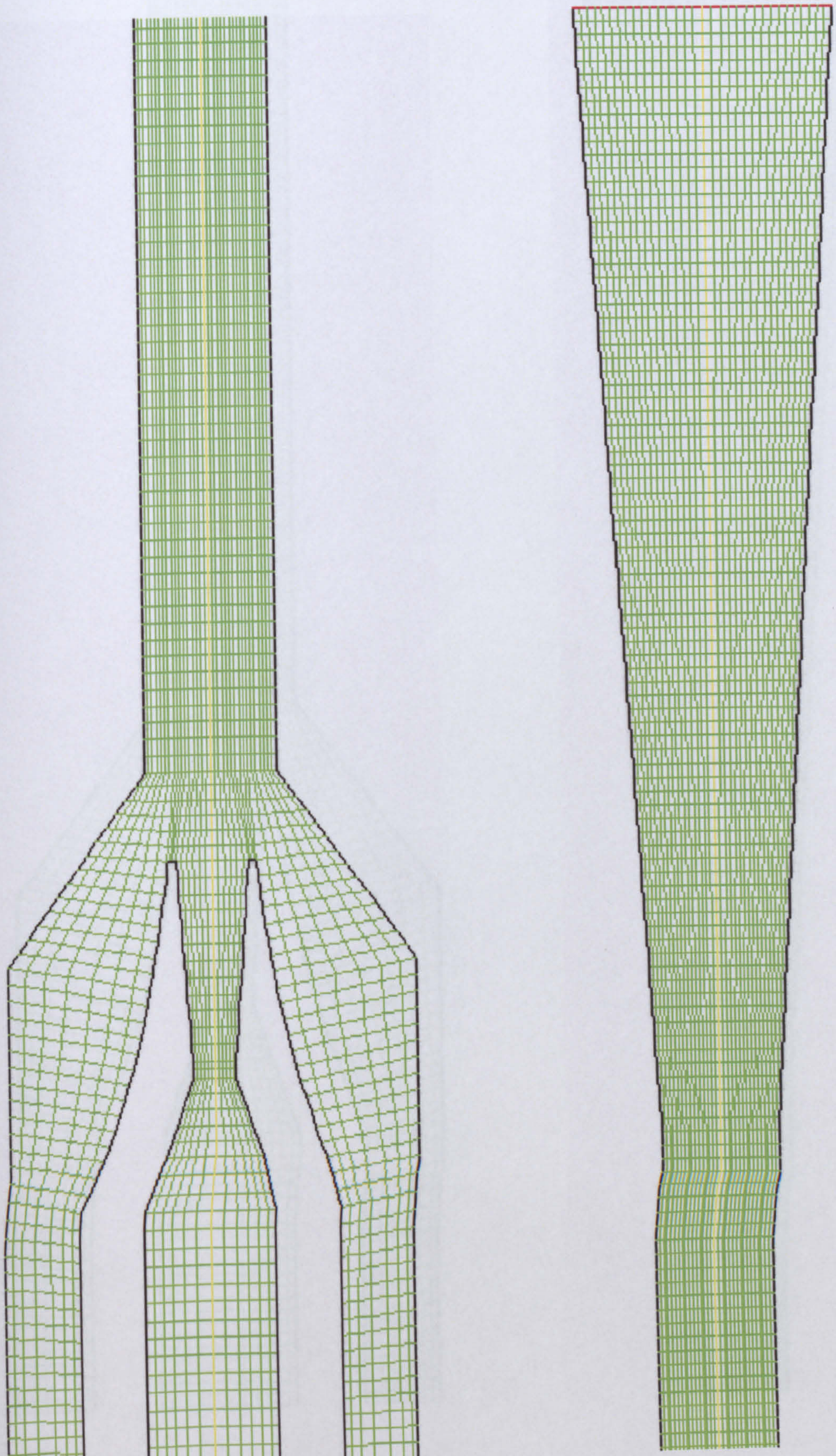

Figure C.1 R141b jet-pump computional mesh: Mesh R-1

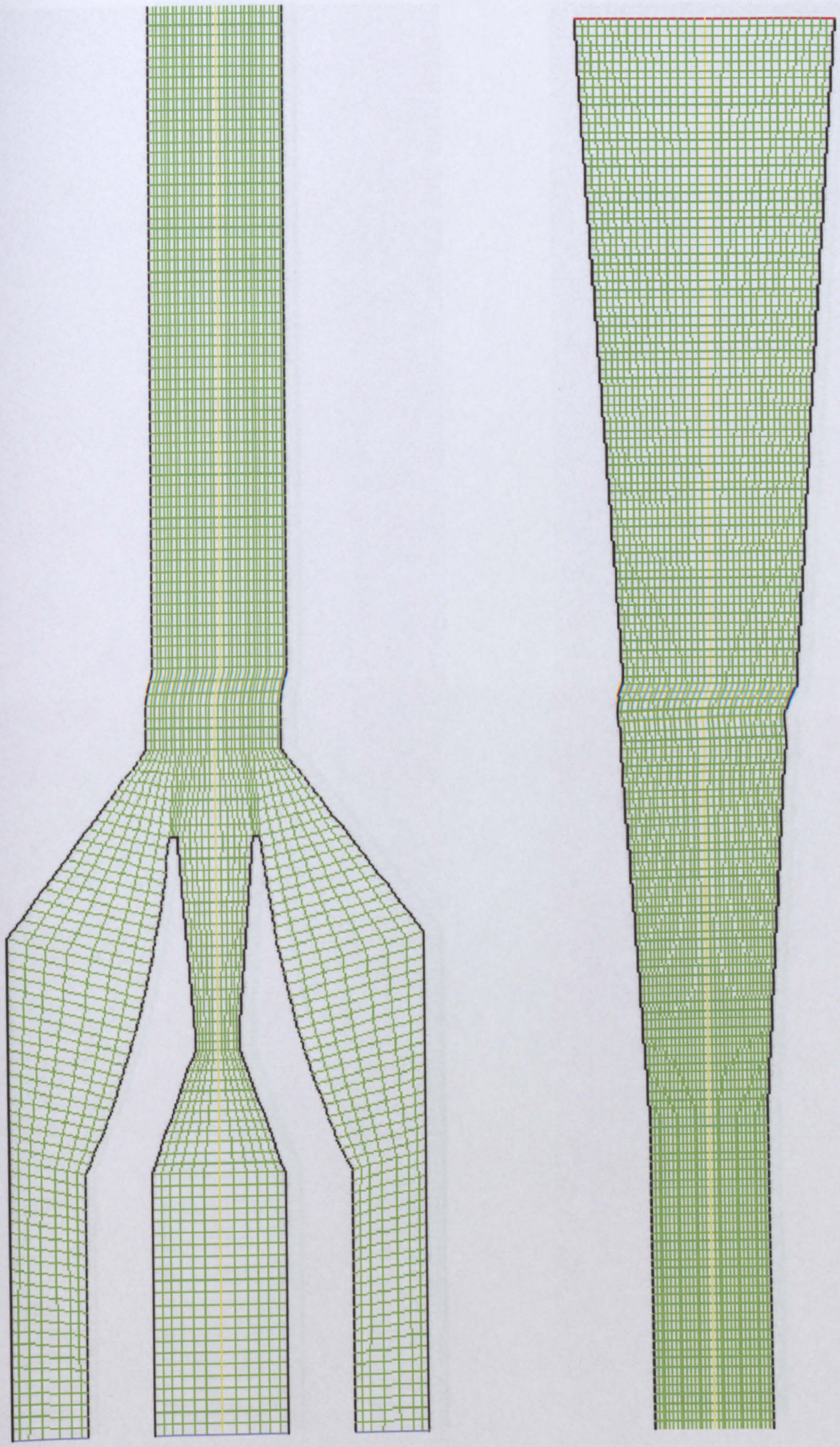

Figure C.2 R141b jet-pump computional mesh: Mesh R-2

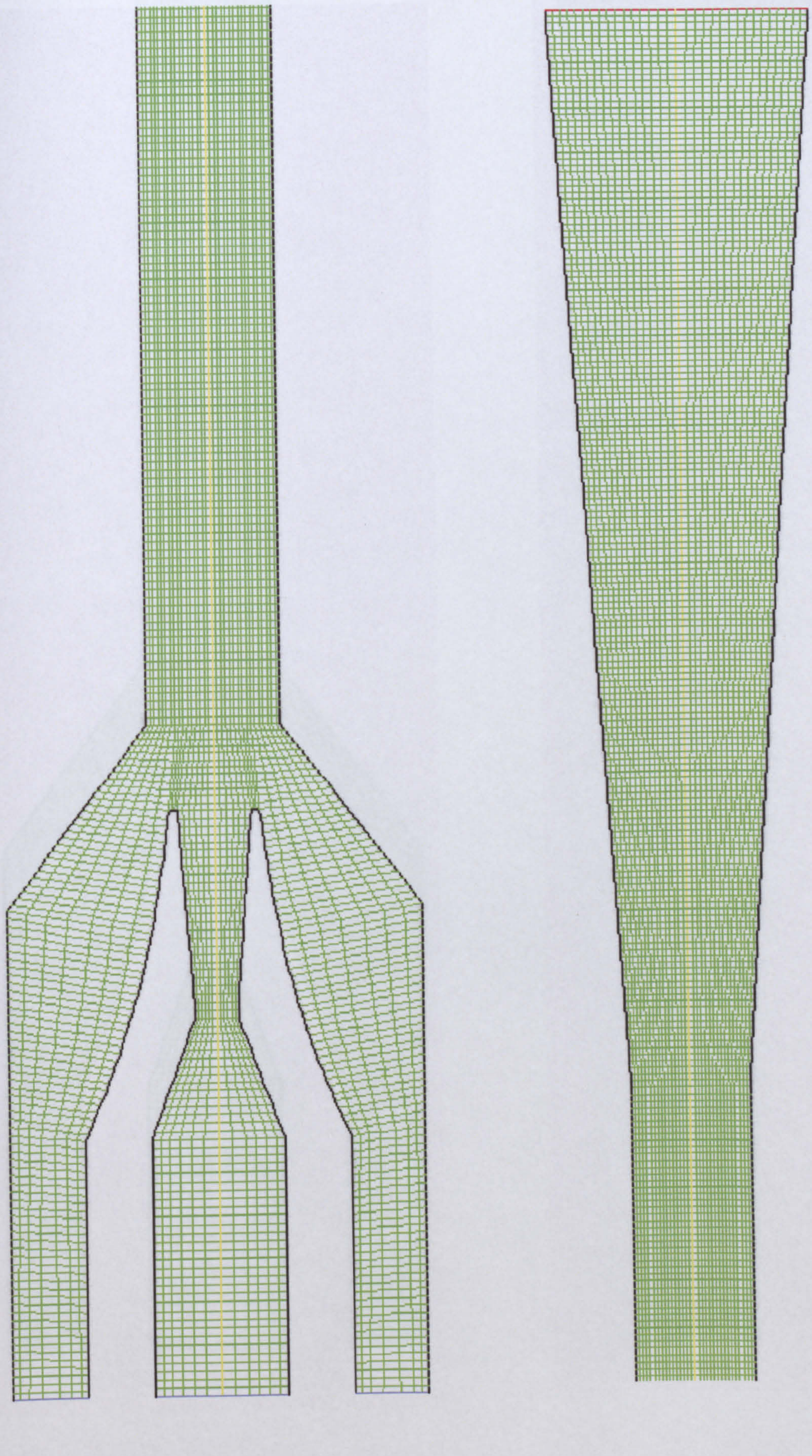

Figure C.3 R141b jet-pump computional mesh: Mesh R-3

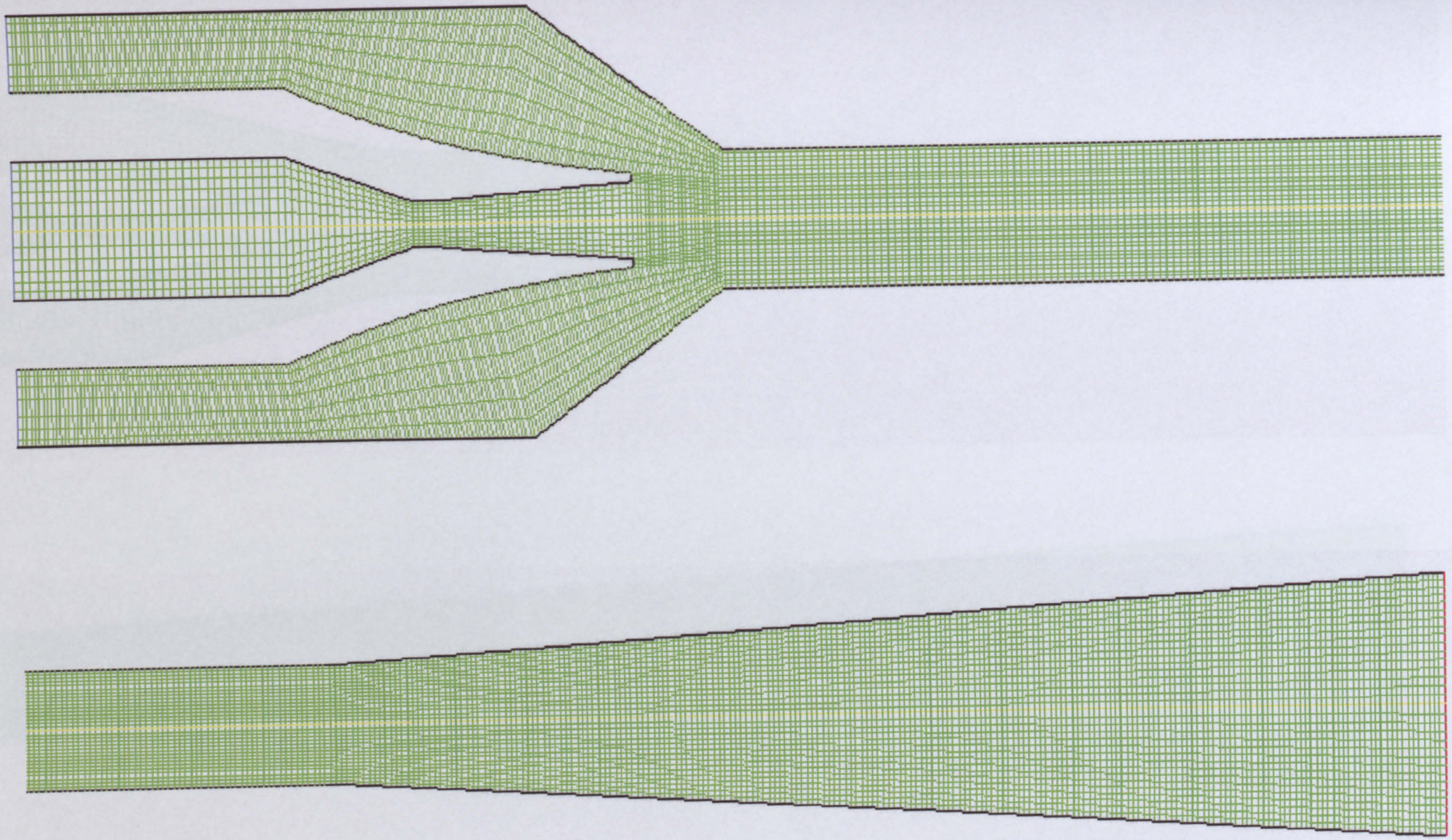

Figure C.4 R141b jet-pump computional mesh: Mesh R-4

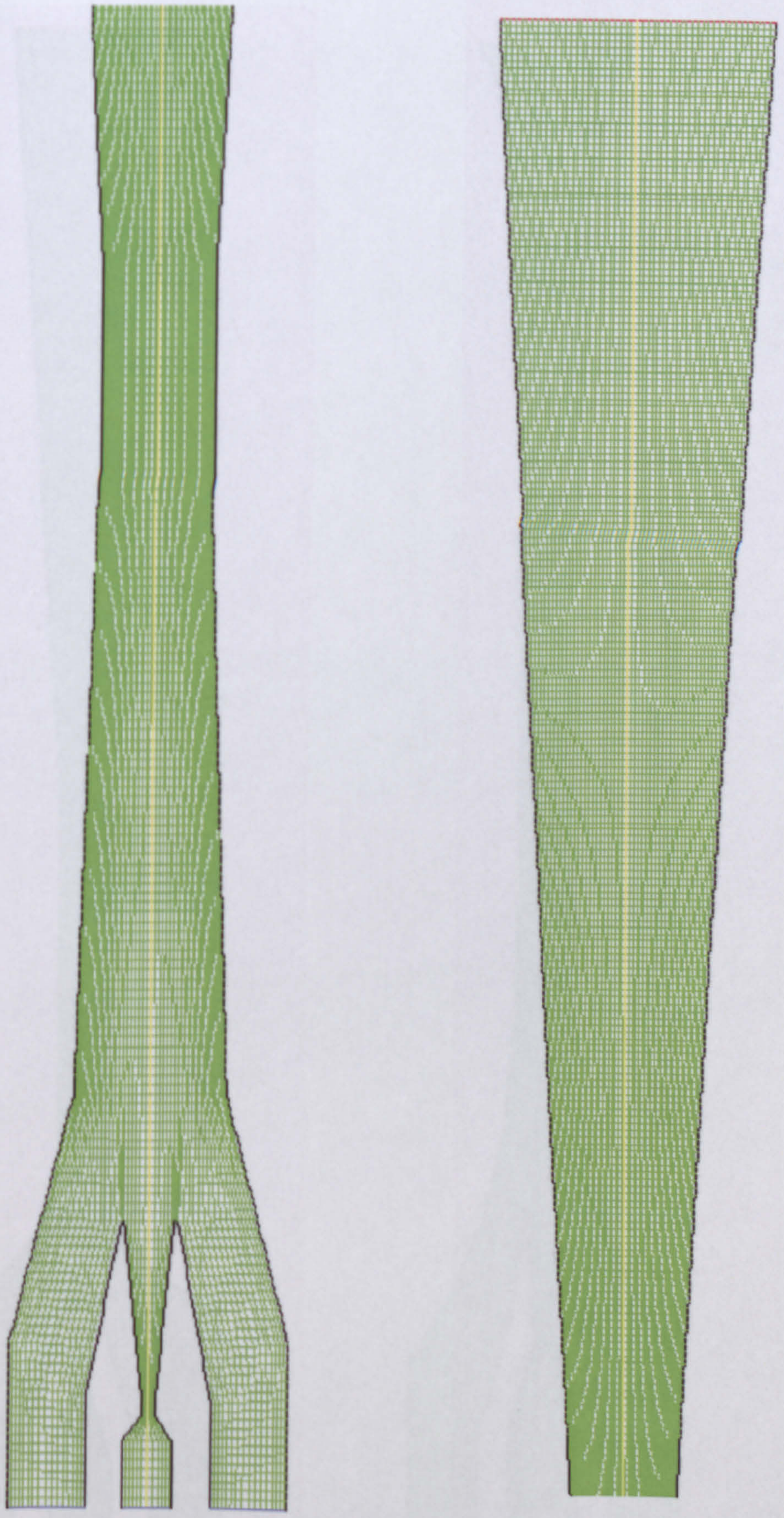

Figure C.5 Steam jet-pump computional mesh: Mesh S-3

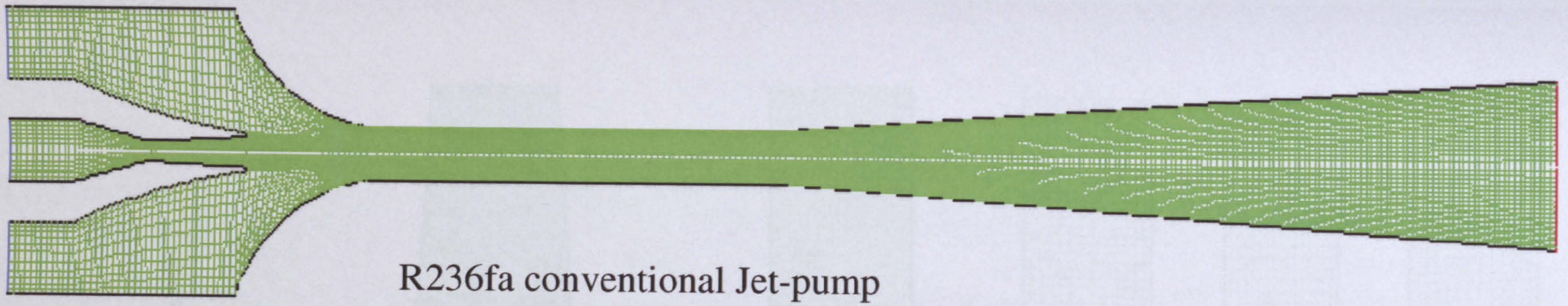

R236fa conventional Jet-pump

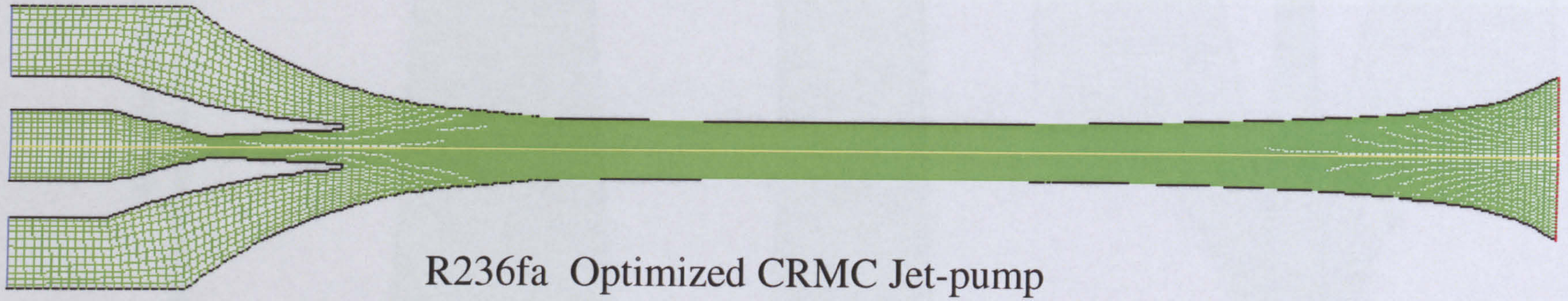

R236fa Optimized CRMC Jet-pump

Figure C.6 R236fa jet-pump computio

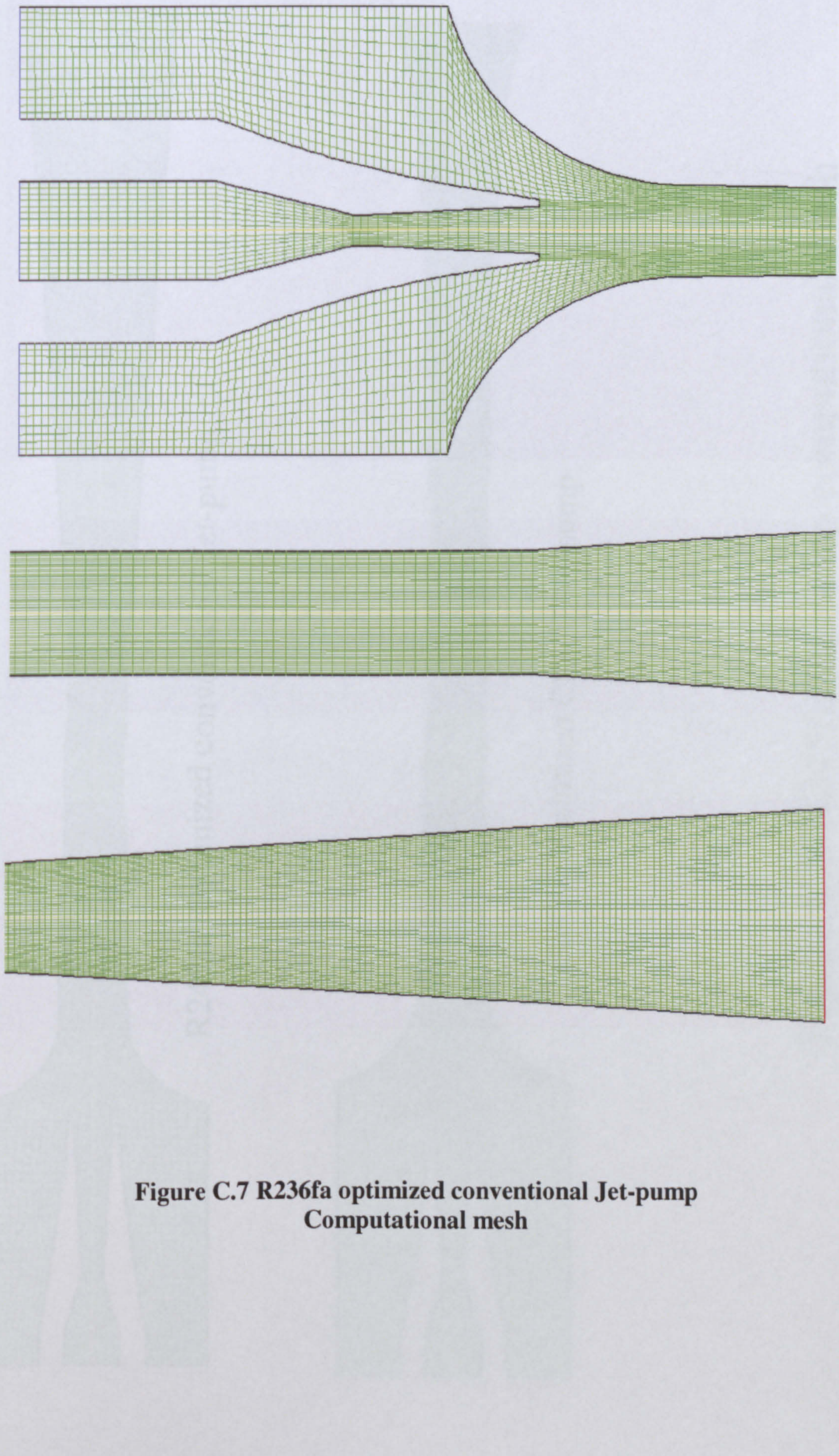

Figure C.7 R236fa optimized conventional Jet-pump Computational mesh

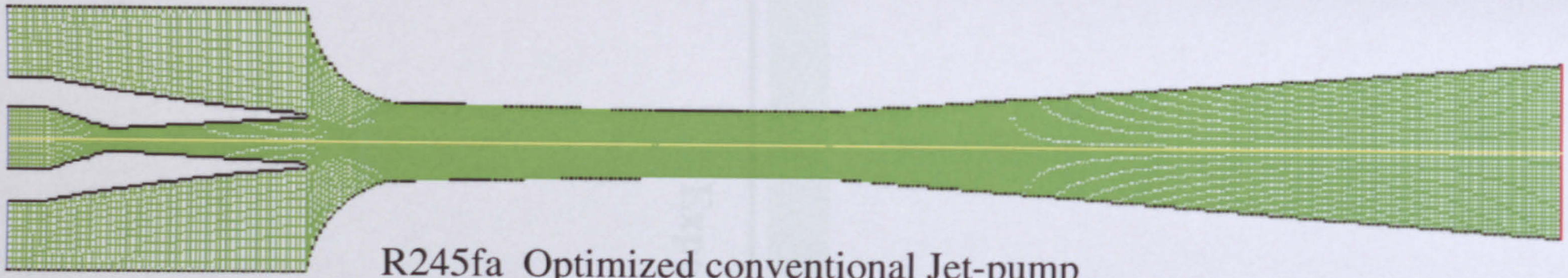

R245fa Optimized conventional Jet-pump

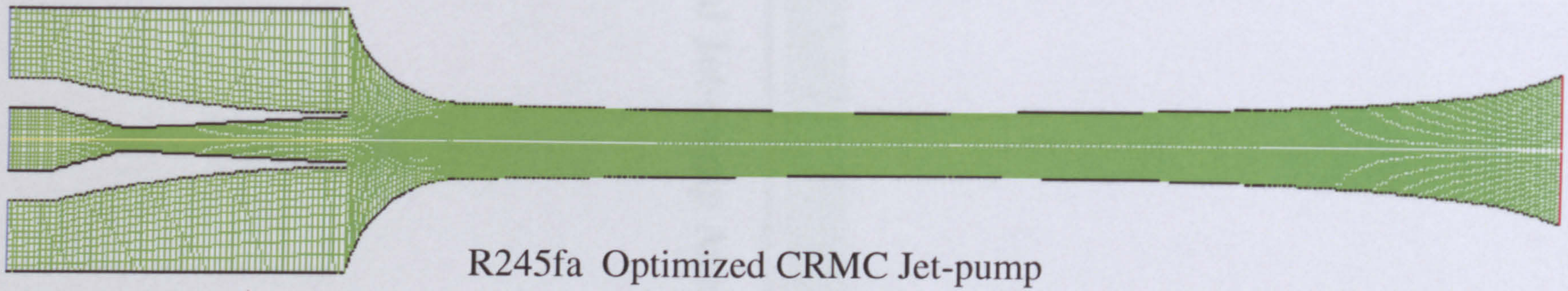

R245fa Optimized CRMC Jet-pump

Figure C.8 R245fa jet-pump computional mesh

Appendix D

Experimental Jet-pump Assembly

Appendix D: Experimental jet-pump assembly

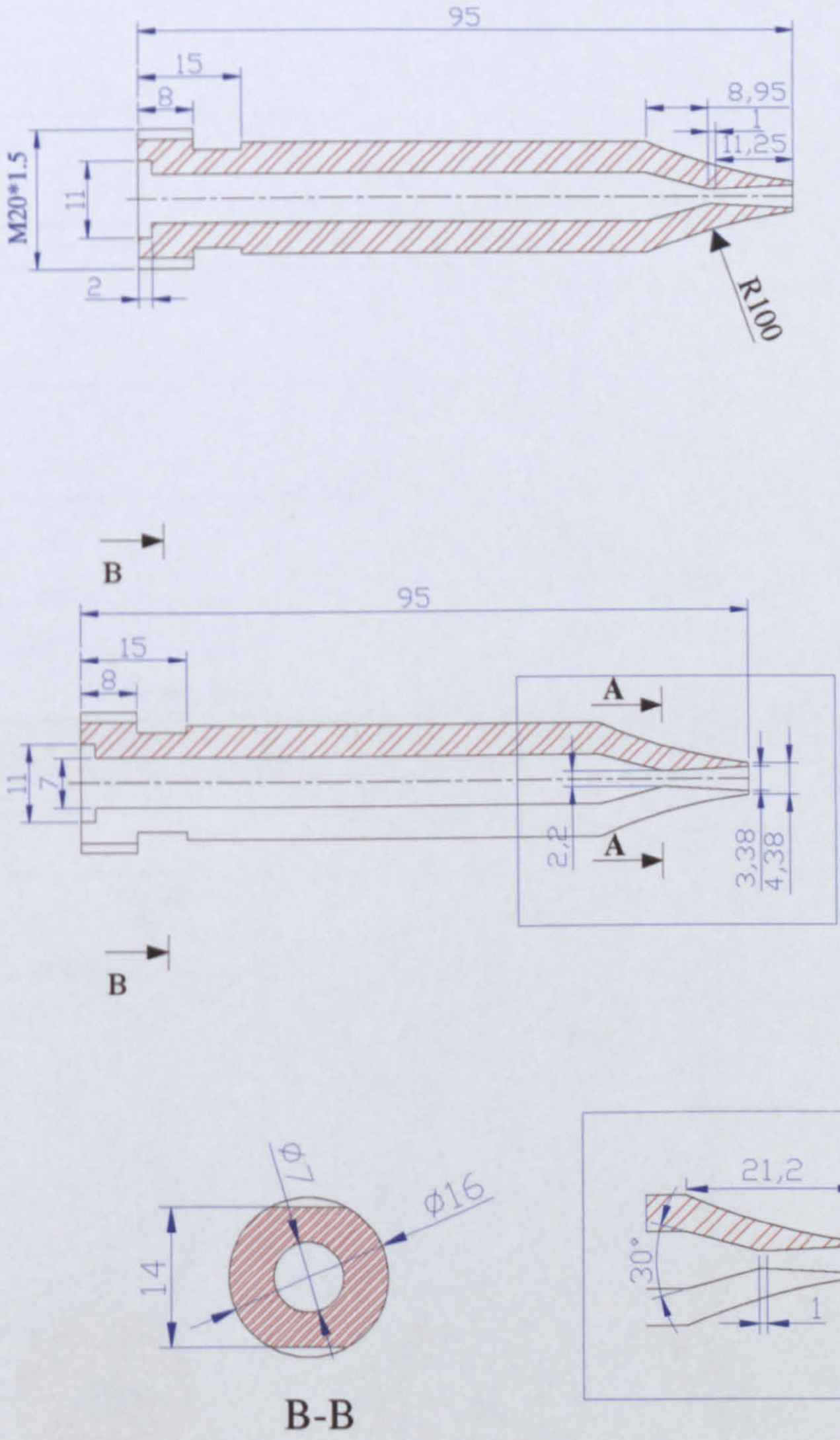

All dimensions in mm

R236fa Experimental nozzle specifications

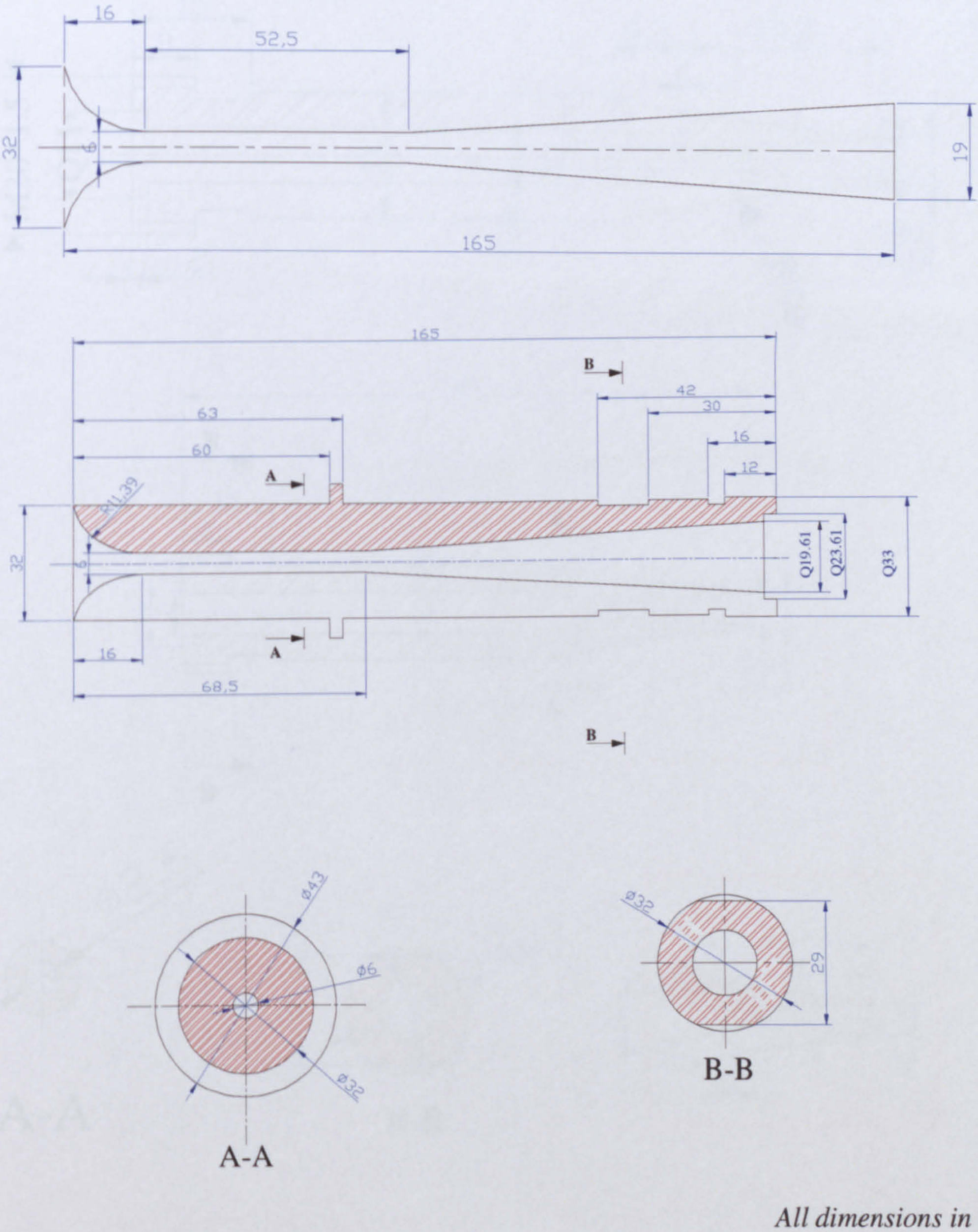

All dimensions in mm

Conventional R236fa Experimental diffuser specifications

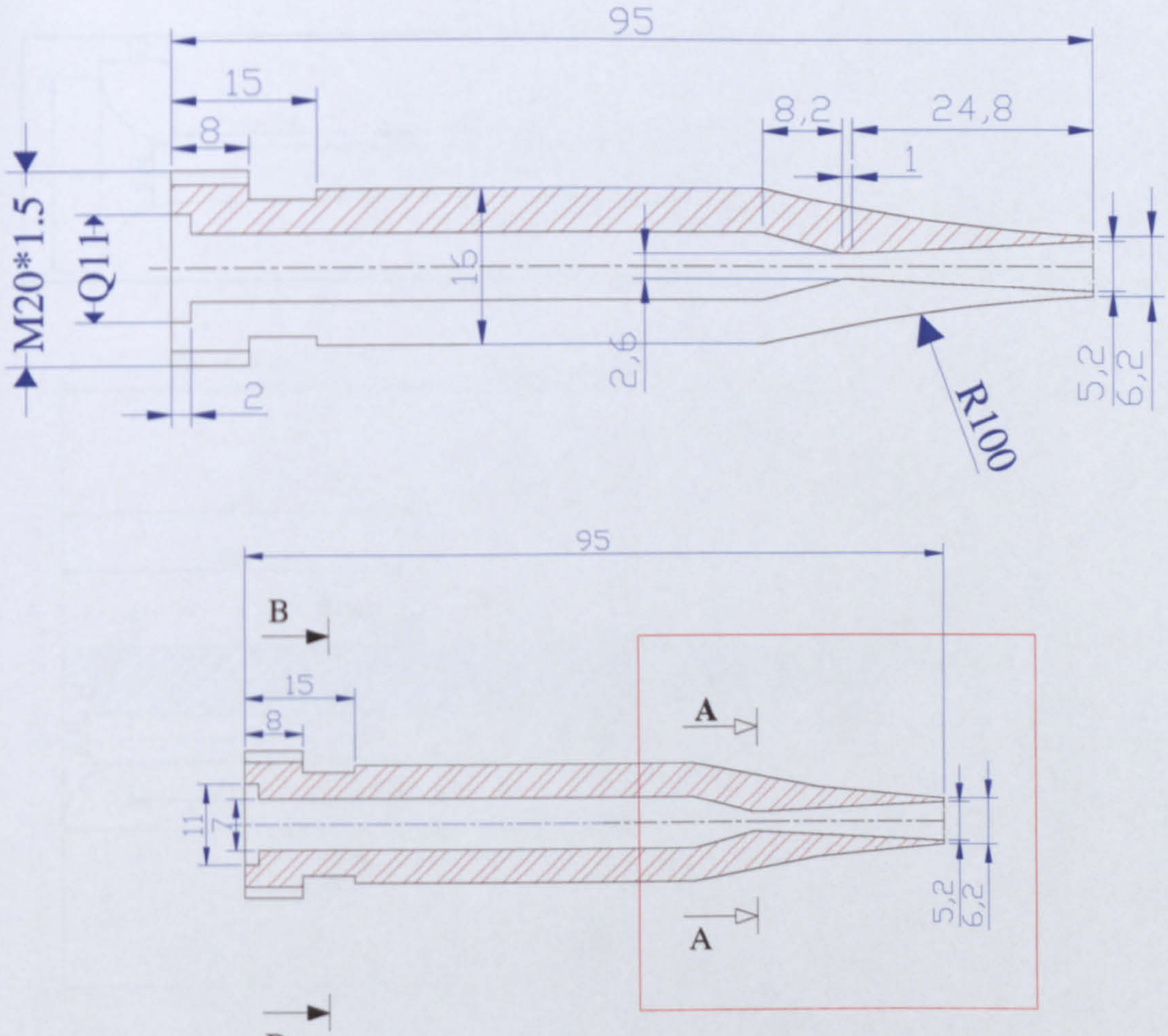

All dimensions in mm

R245fa Experimental nozzle specifications "nozzle A"

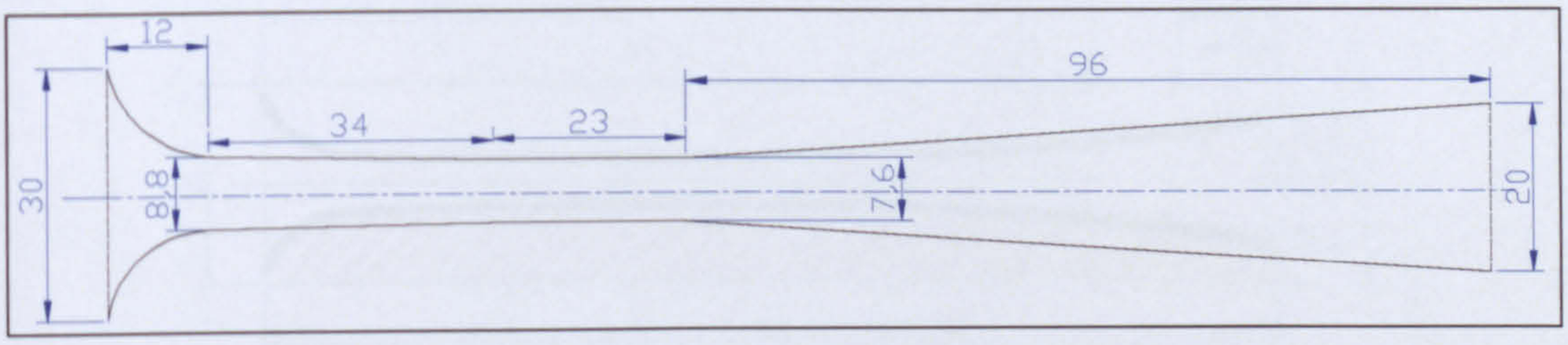

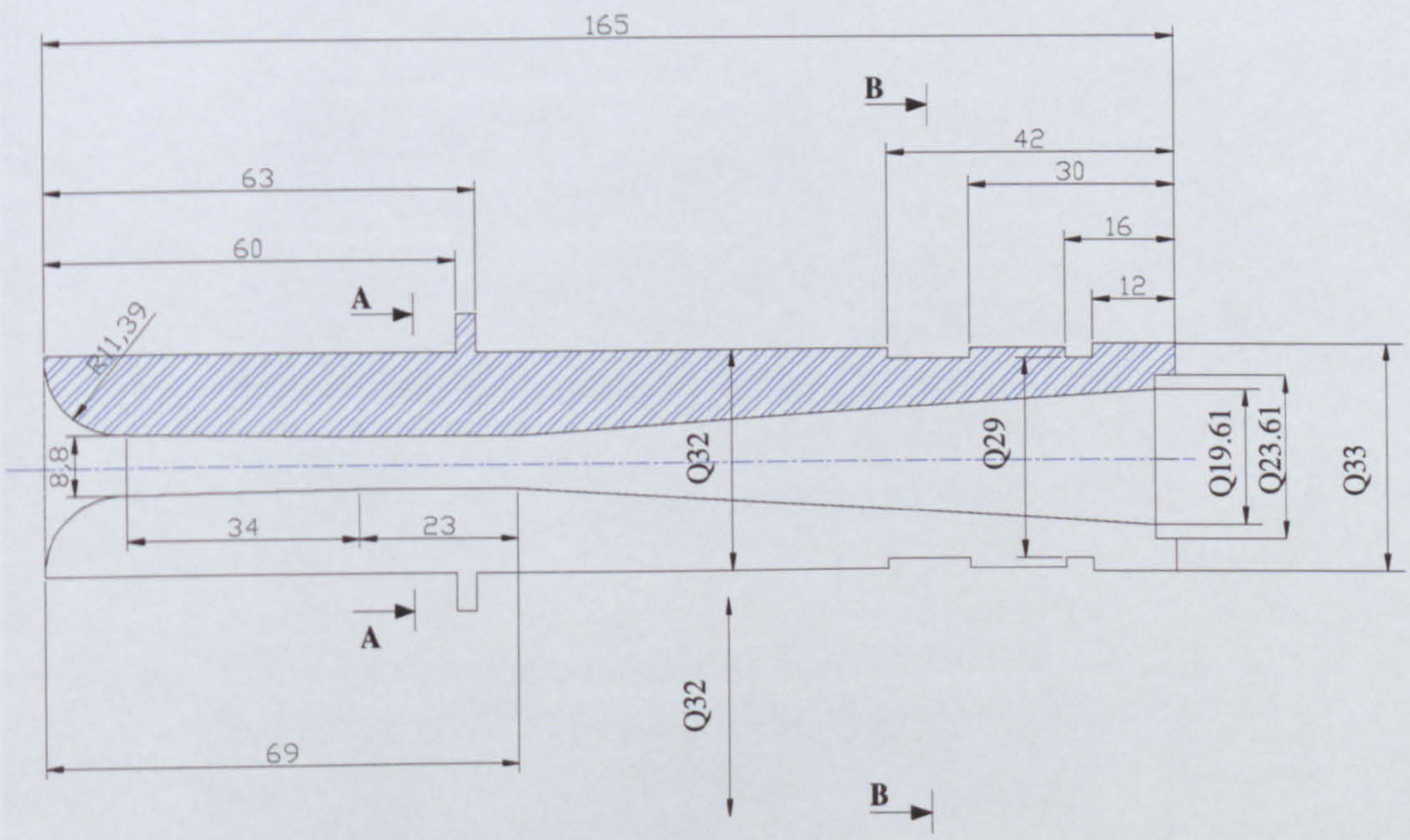

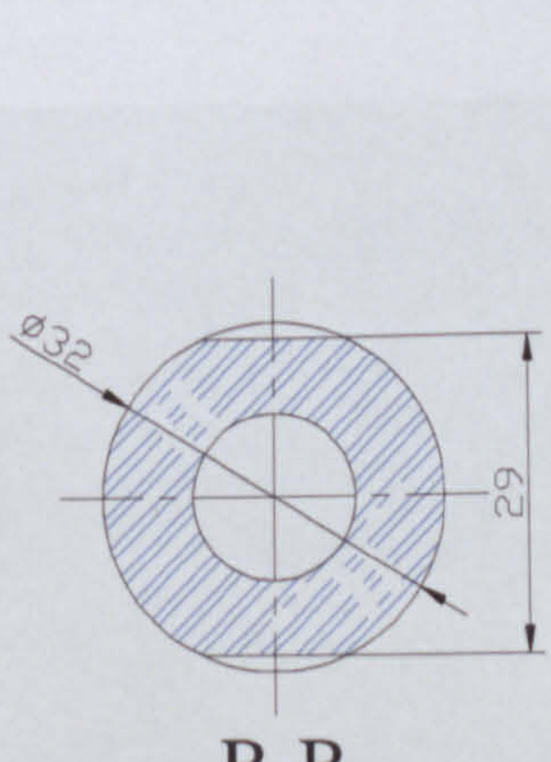

B-B

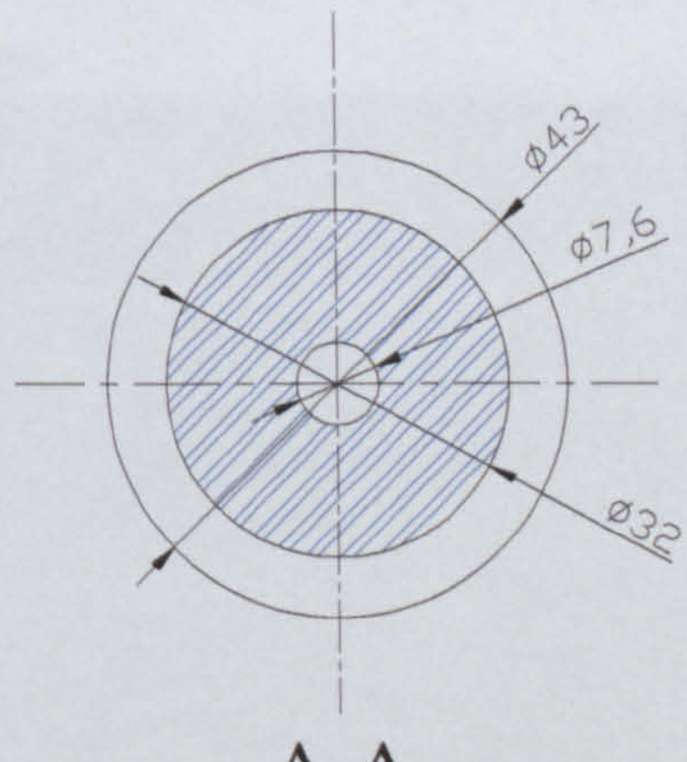

A-A

All dimensions in mm

R245fa-Experimental diffuser specifications "diffuser of A_r=1.34"

R245fa CRMC experimental diffuser

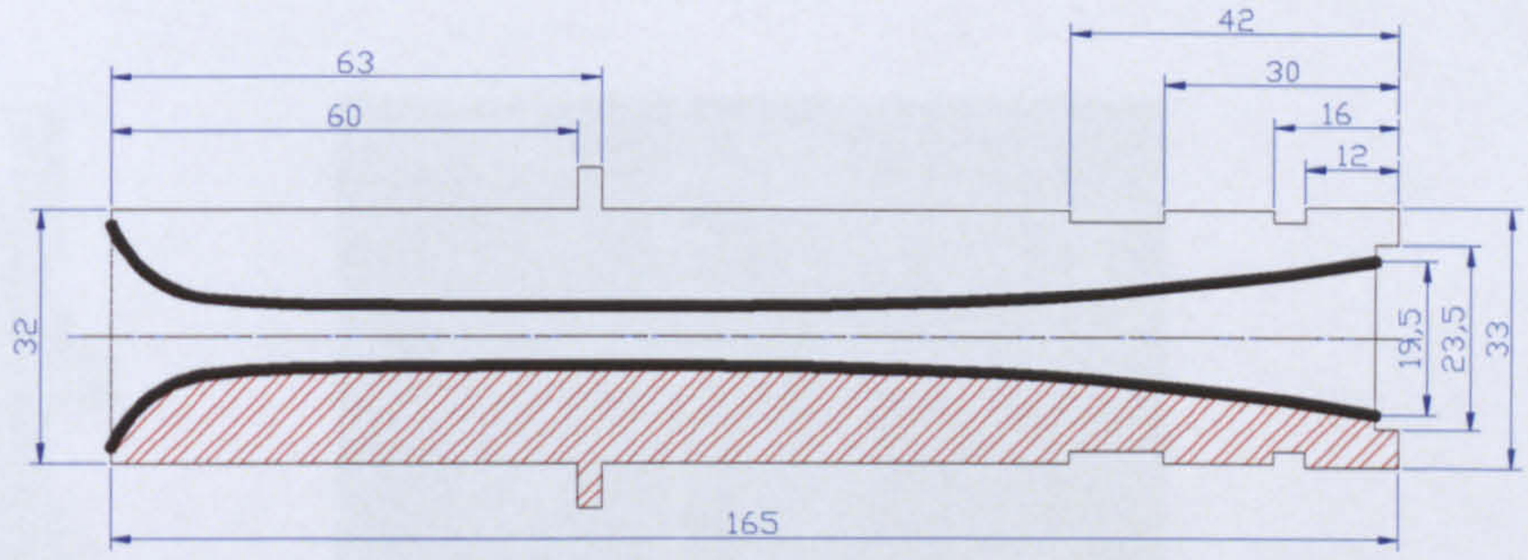

Primary nozzles

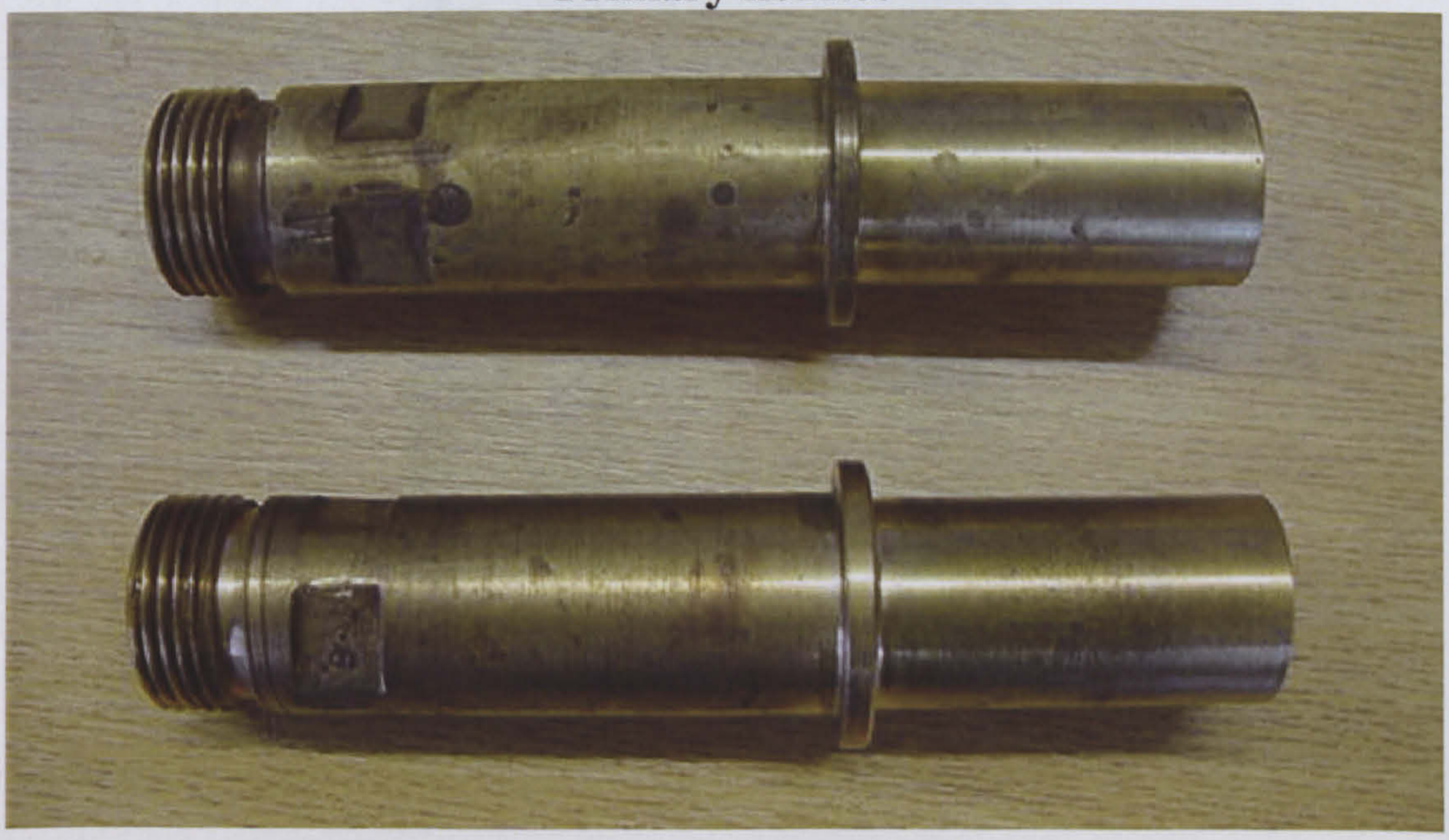

Diffusers

Jet-pump assembly

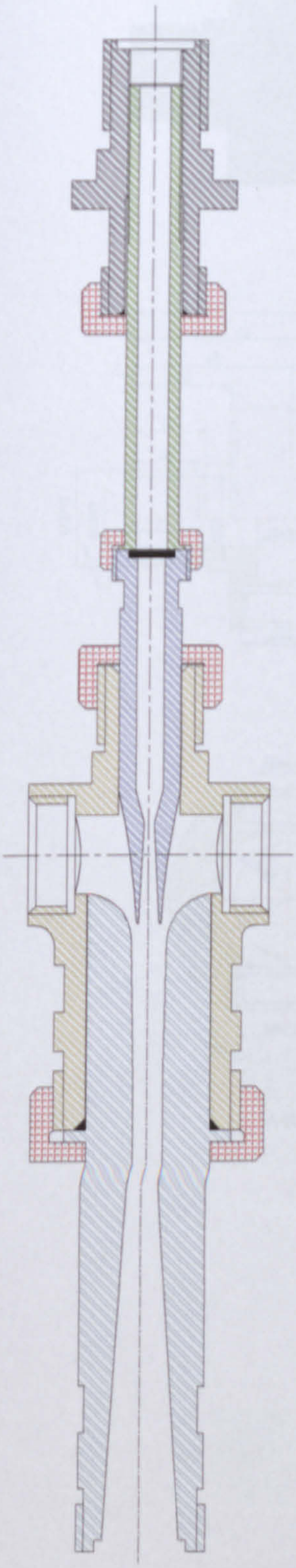

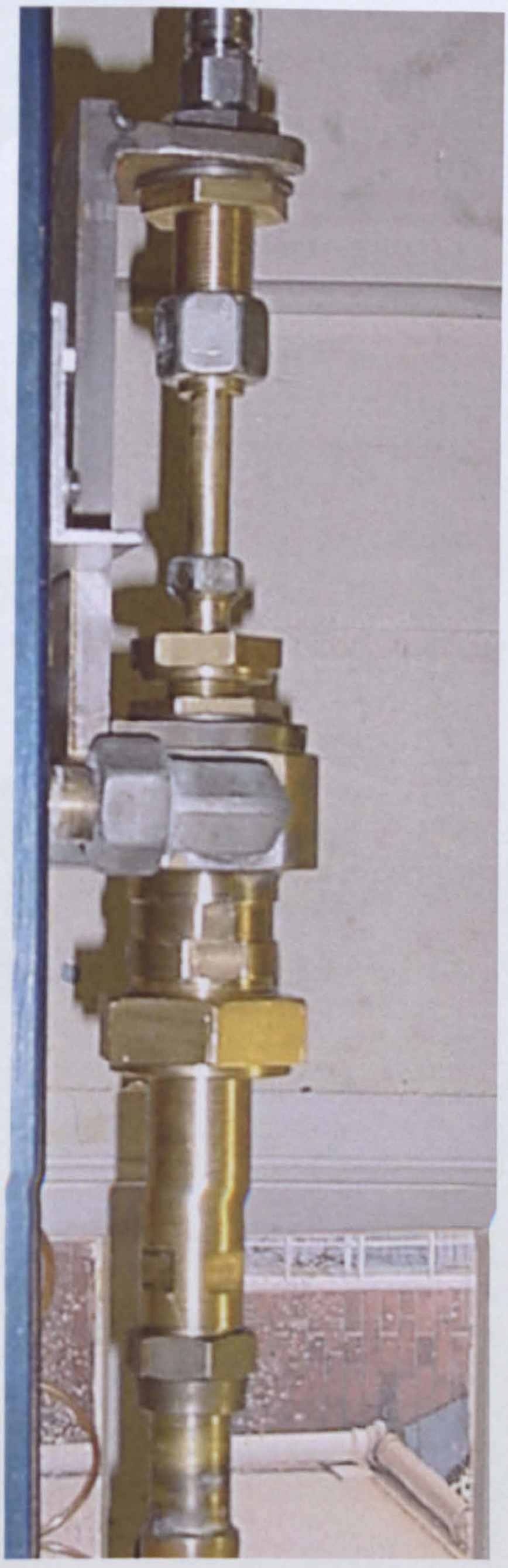

Jet-pump assembly mechanism

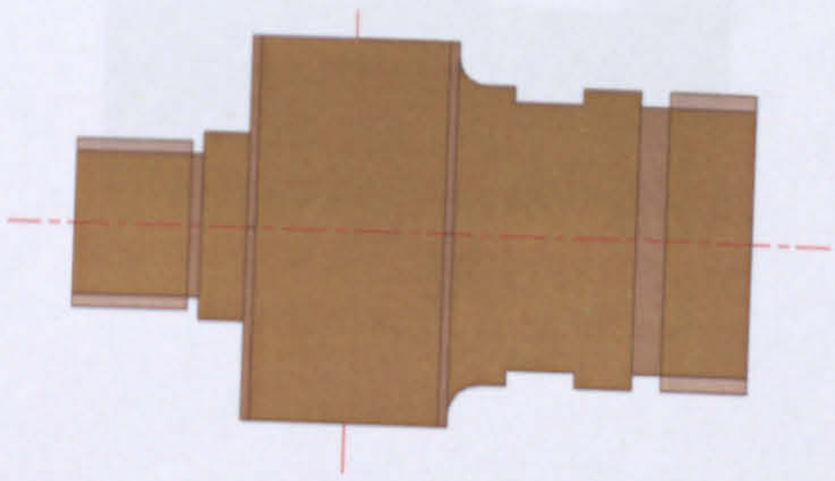

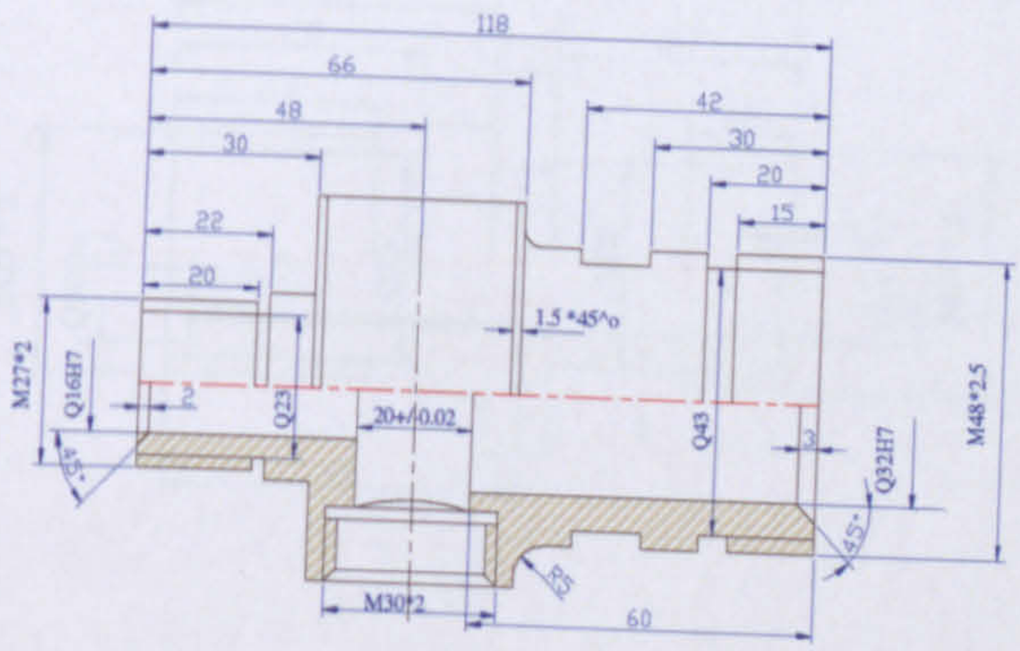

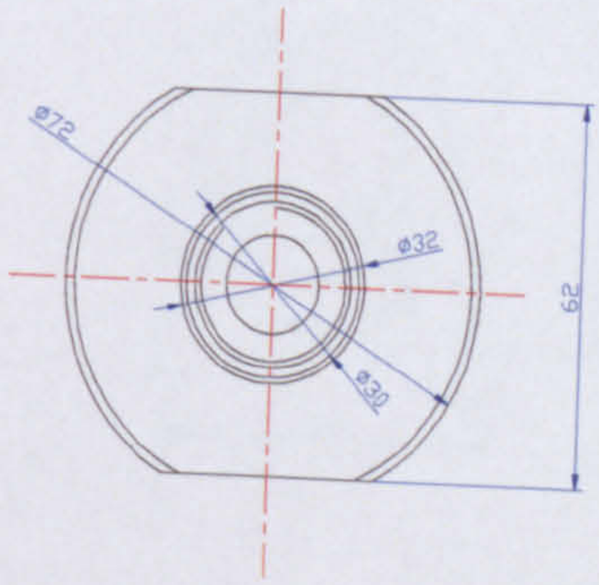

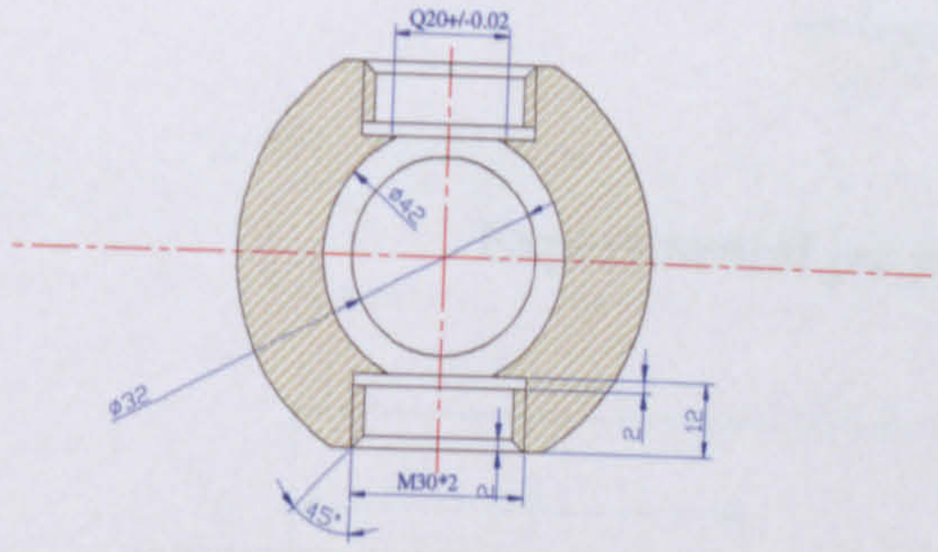

A-A

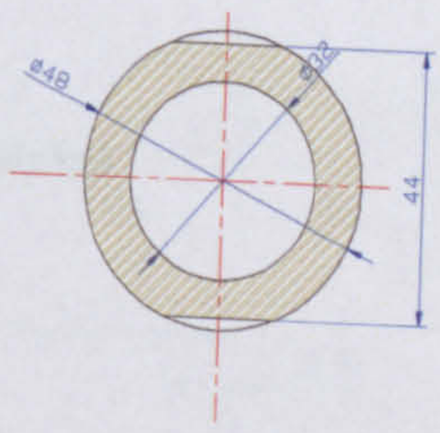

B-B

Experimental Jet-pump body

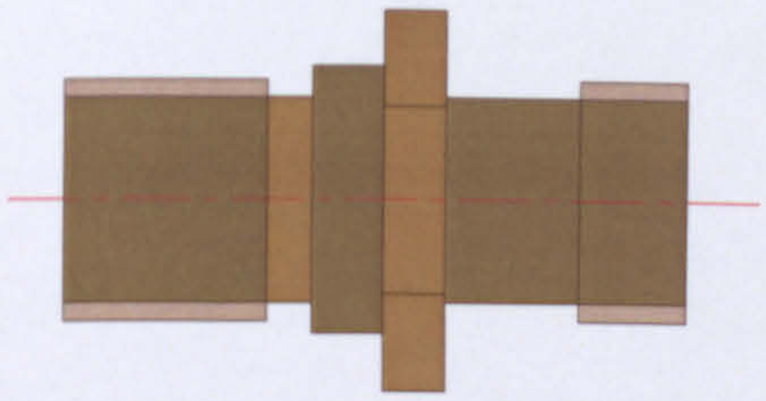

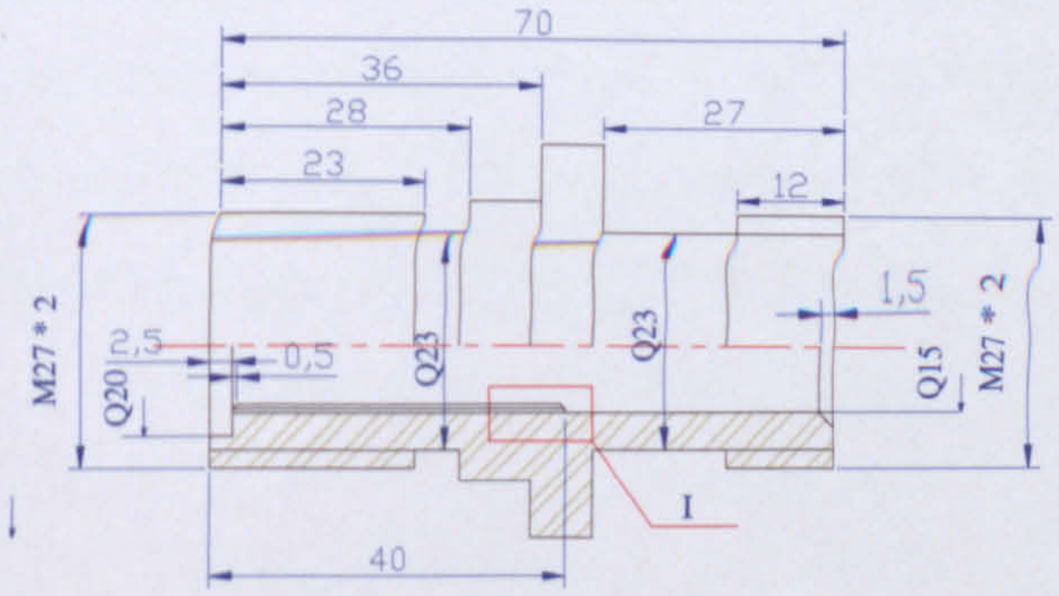

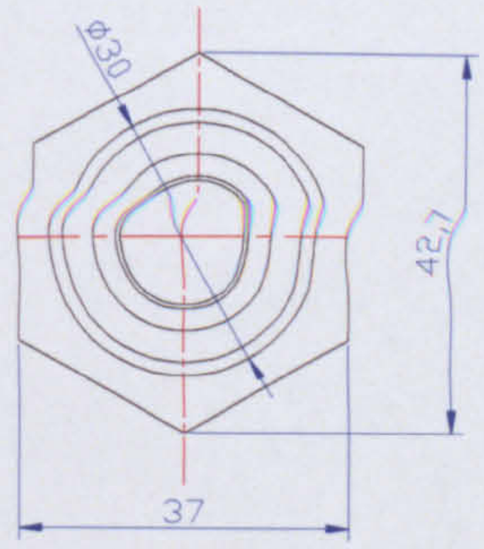

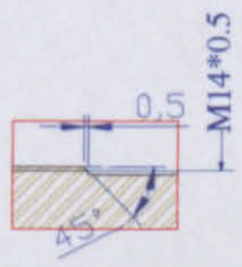

Experimental jet-pump adjusting connector

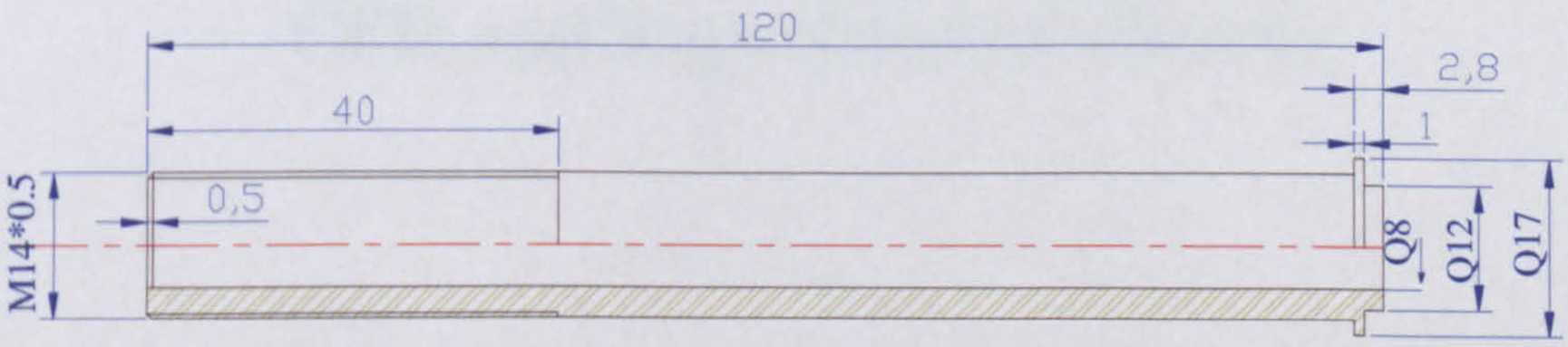

Experimental jet-pump connecting tube

Appendix E

CFD and Experimental Results

Sample of calculation

Sample of calculation for the jet-pump cooling cycle performance characteristics is presented in this section for the *Conventional R236fa jet-pump* at design operating conditions. This sample of calculation was carried out for all jet-pumps tested at varying operating conditions. All the measurements of temperature at inlet and outlet of each component were taken for points of interest as shown in the Figure 5.1. Also the primary and secondary mass flow rate besides the cooling solution flow rate for the condenser and evaporator were taken. The heat input or output is calculated from following equation:

Note, *all points are related to Figure 5.1, chapter 5*

$$R_m = \frac{m_s}{m_g} \qquad [6.1]$$

$$Q_g = m_g * (h_1 - h_6) \qquad [6.2]$$

$$Q_e = m_s * (h_{10} - h_9) \qquad [6.3]$$

$$Q_c = (m_g + m_s) * (h_2 - h_4) \qquad [6.4]$$

$$Q_{sub} = (m_g + m_s) * (h_4 - h_8) \qquad [6.5]$$

$$W_{pump} = m_g (h_6 - h_8) \qquad [6.6]$$

$$COP_{therm} = Q_e / Q_g \qquad [6.7]$$

$$COP_{mech} = Q_e / W_{pump} \qquad [6.8]$$

Table E1 Sample of Cycle performance characteristics calculation

R236fa , T_g=85°C, T_e=8°C, T_c*=30.0°C, system without Pre-cooler and recuperator			
Primary nozzle 1 of , d_t=2.2mm and d_{exit}=3.38mm, diffuser D_t=6mm and β=1, NXP=1mm			
State *" referring Fig 5.1"*	T(°C)	P (kPa)	Enthalpy, h (KJ/Kg)
1	85	1400.0	415.7
2	51.3	321.0	400.1
4	30.0	321.0	237.3
5	21.1	321.0	225.8
6	26.5	1400.0	232.1
8	20.0	321.0	224.1
9	18.5	321.0	222.2
10	8	148.0	365.8
11	14.8	148.0	371.5

Heating and cooling mediums conditions

State	12	13	15	16	17	18	19	20
T (°C)	18	13.8	87.7	32.9	15.1	25.8	15.4	22.6

Measured mass flow rates

Primary mass flow rate , m_g	25.788 g/s
Secondary mass flow rate m_s	11.658 g/s
Evaporator solution flow rate , m_{we}	0.086 g/s
Condenser solution flow rate, m_{wc}	0.123 g/s

Jet-pump performance "Heat input and output within the system + COP of the system"

R_m	Q_e	Q_g	Q_C	Q_{sub}	W_{pump}	COP_{therm}	COP_{mec}
0.452	1.674 kW	4.73kW	6.09kW	0.49kW	0.206kW	0.354	8.126

Experimental Results

A- R236fa as working fluid

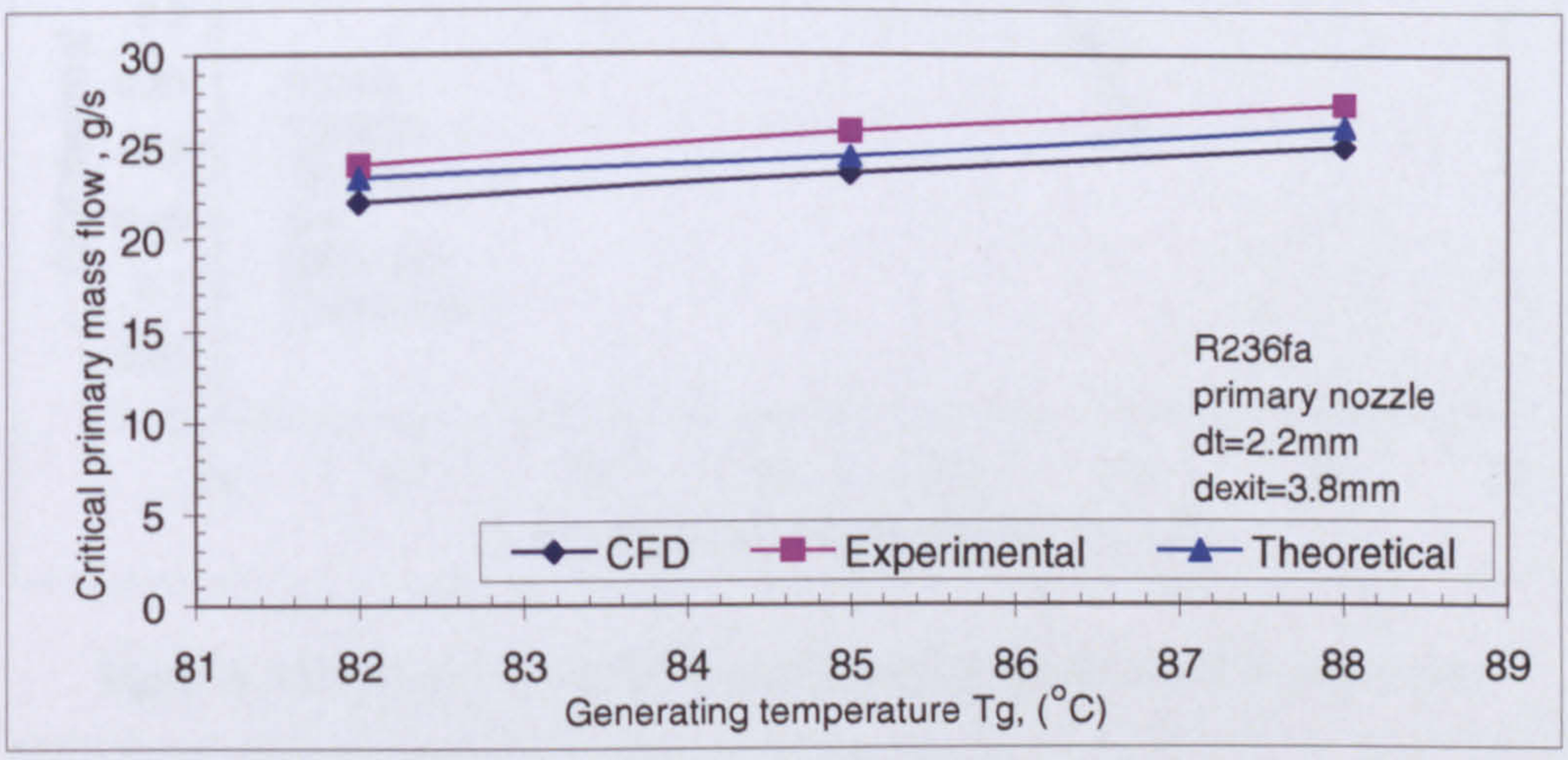

Figure A.1 Calibration of R236fa primary nozzle

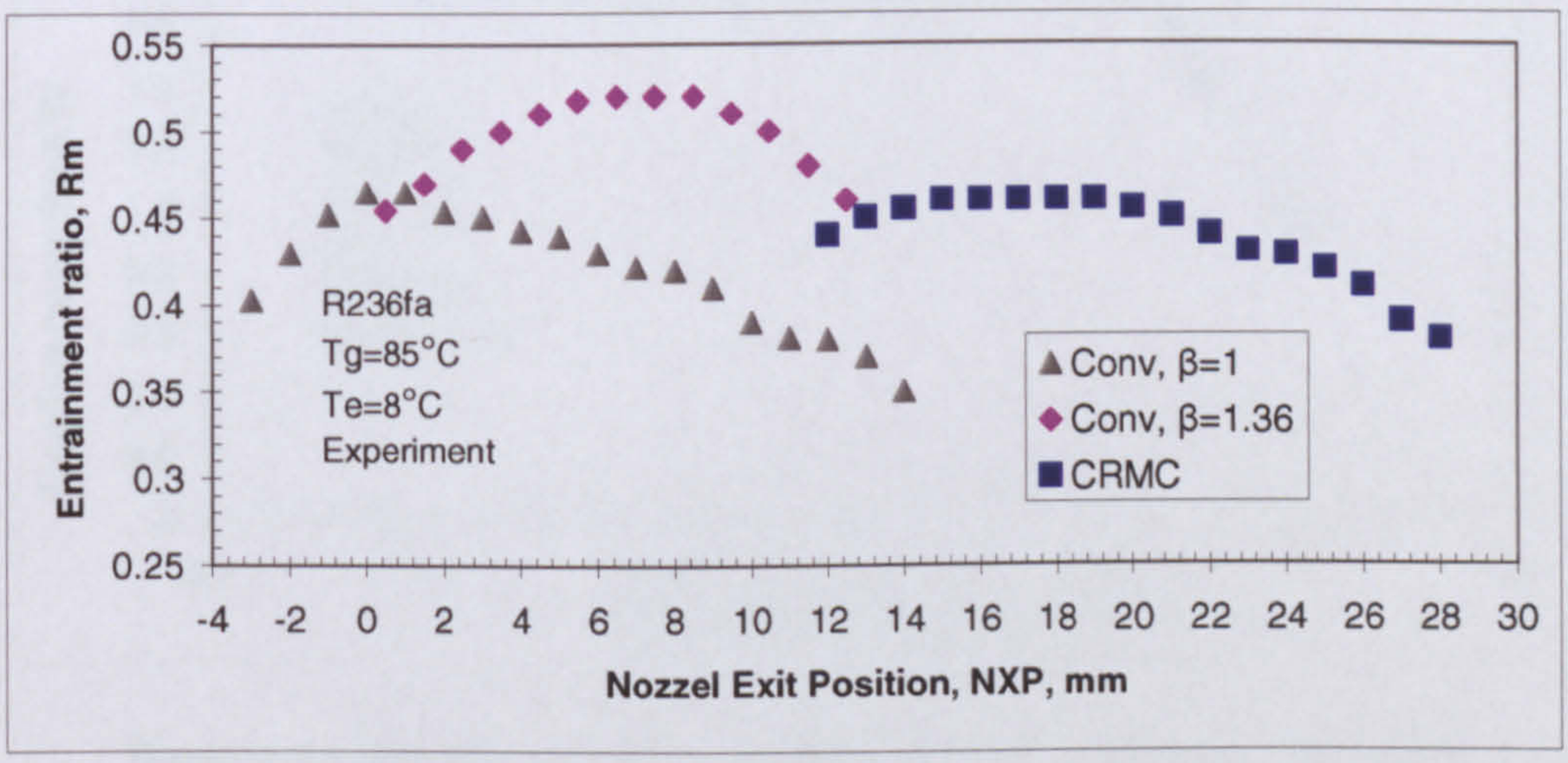

Figure A. 2 Measured variations in the entrainment ratio (R_m) with NXP

R236fa Jet-pumps (Experimental)

• Conventional R236fa Jet-pump

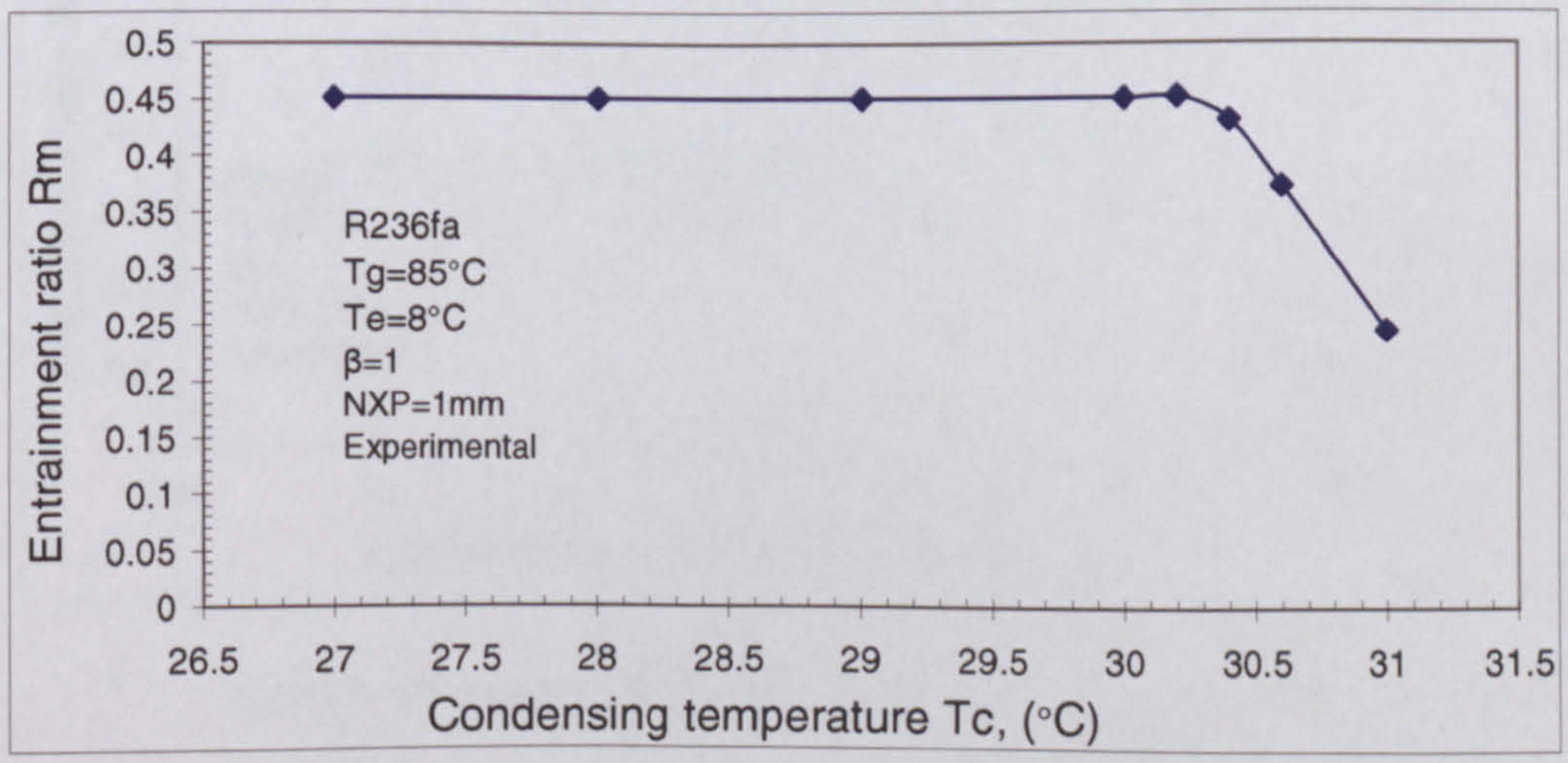

Figure A. 3 Effect of T_c on the R_m, conventional R236fa jet-pump (experimental)

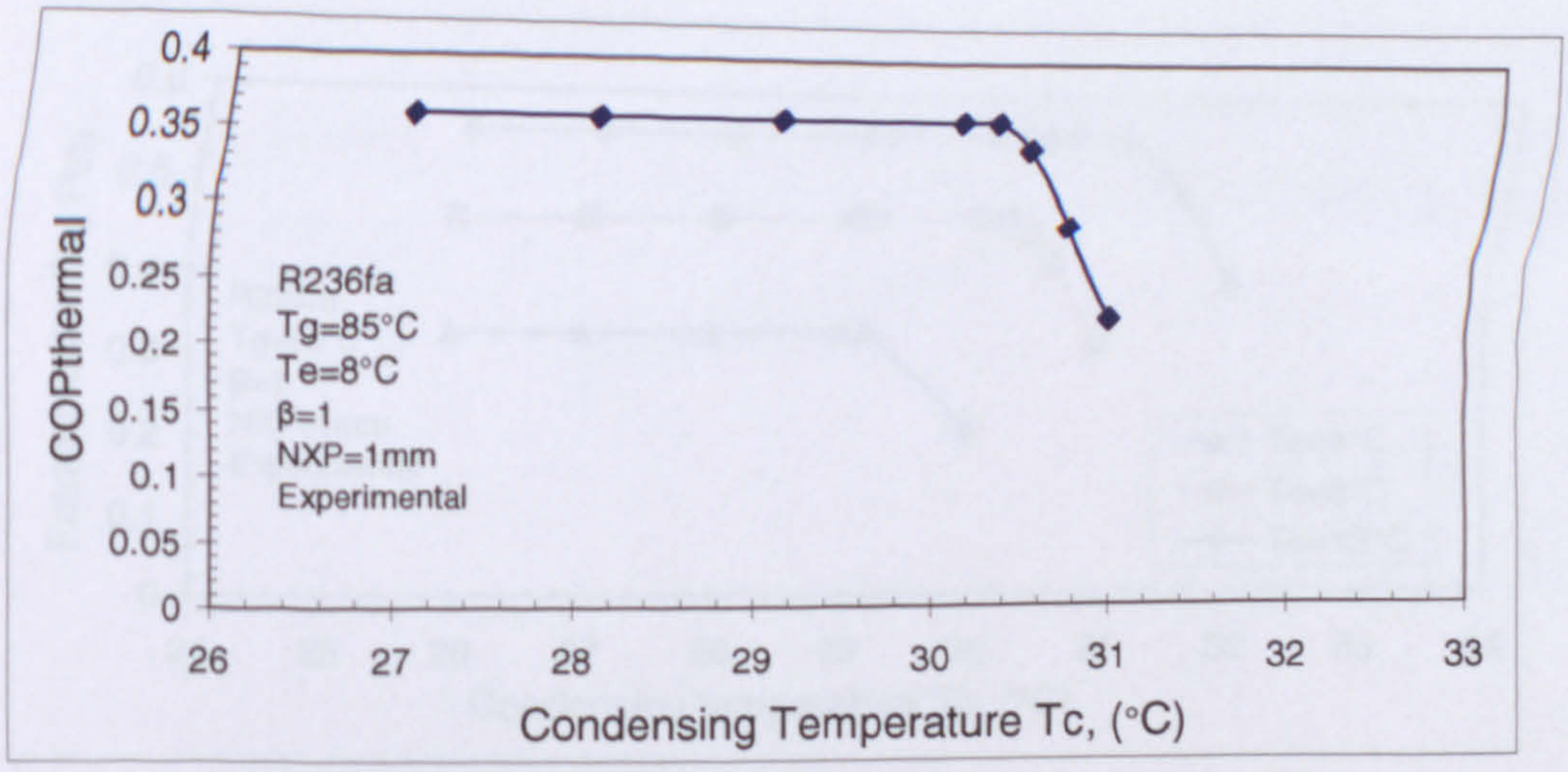

Figure A. 4 Effect of T_c on the COP, conventional R236fa jet-pump (experimental)

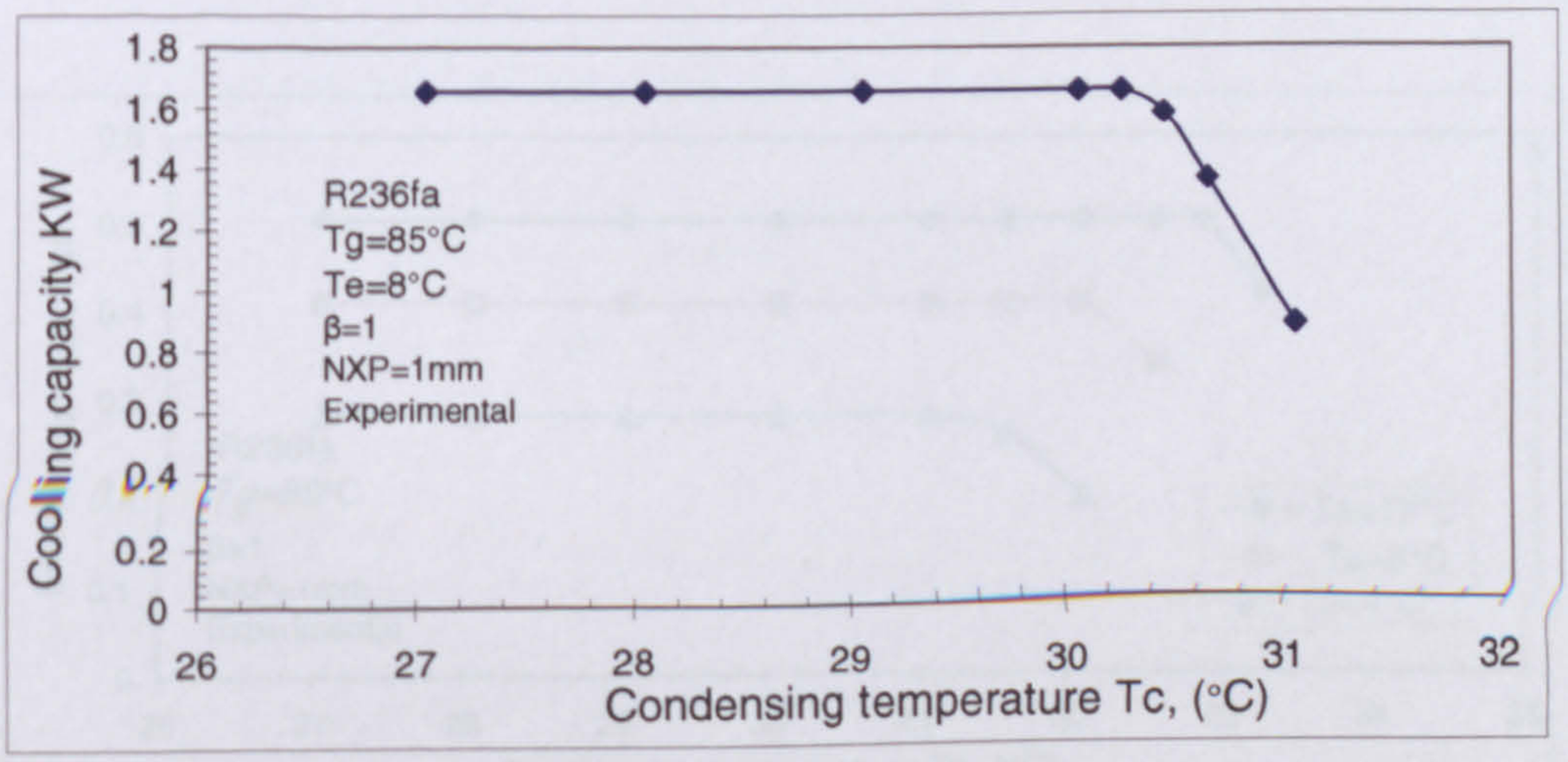

Figure A. 5 Effect of T_c on the Q_e, conventional R236fa jet-pump (experimental)

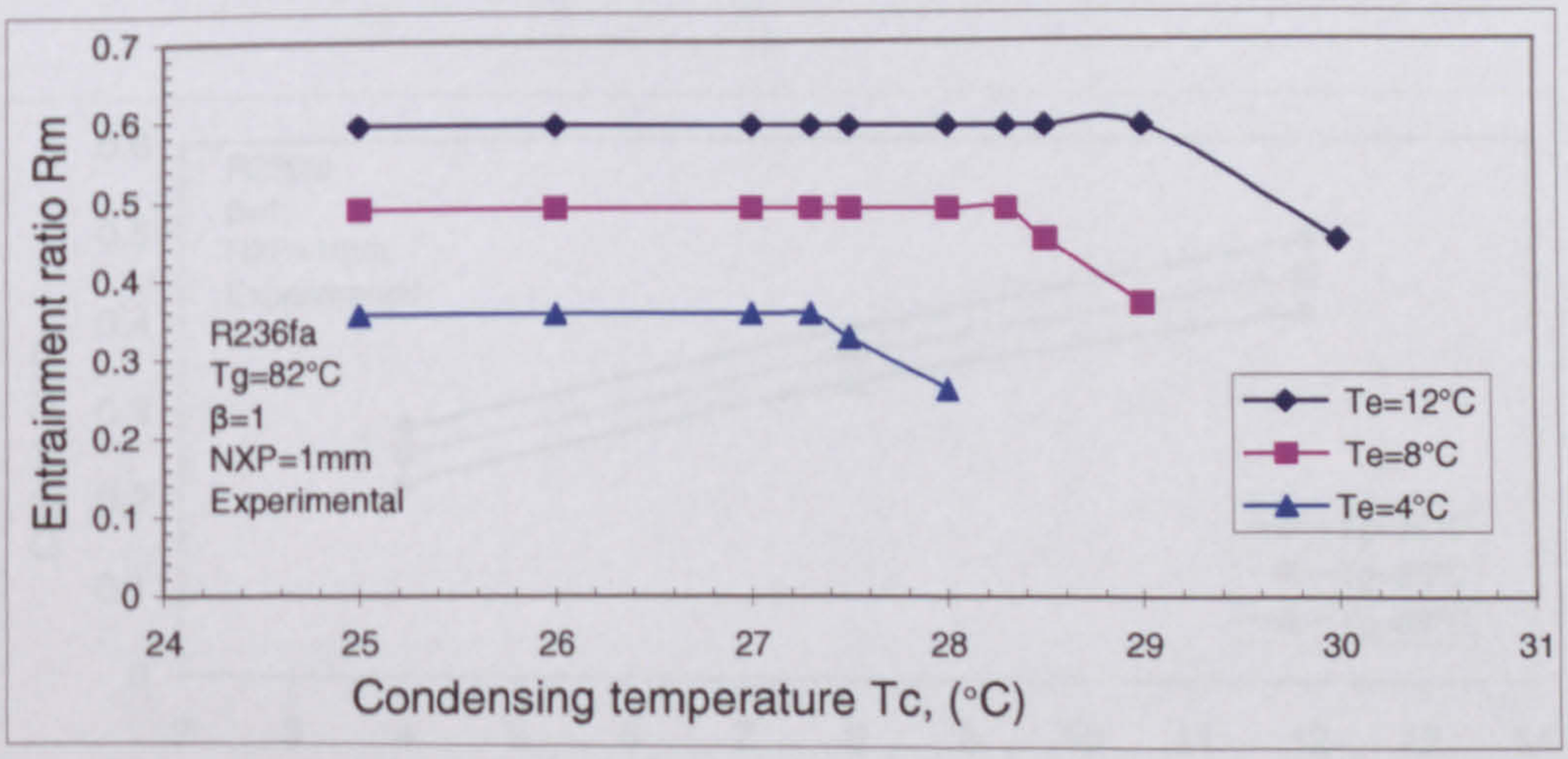

Figure A. 6 Conventional R236fa jet-pump T_g=82°C (experimental)

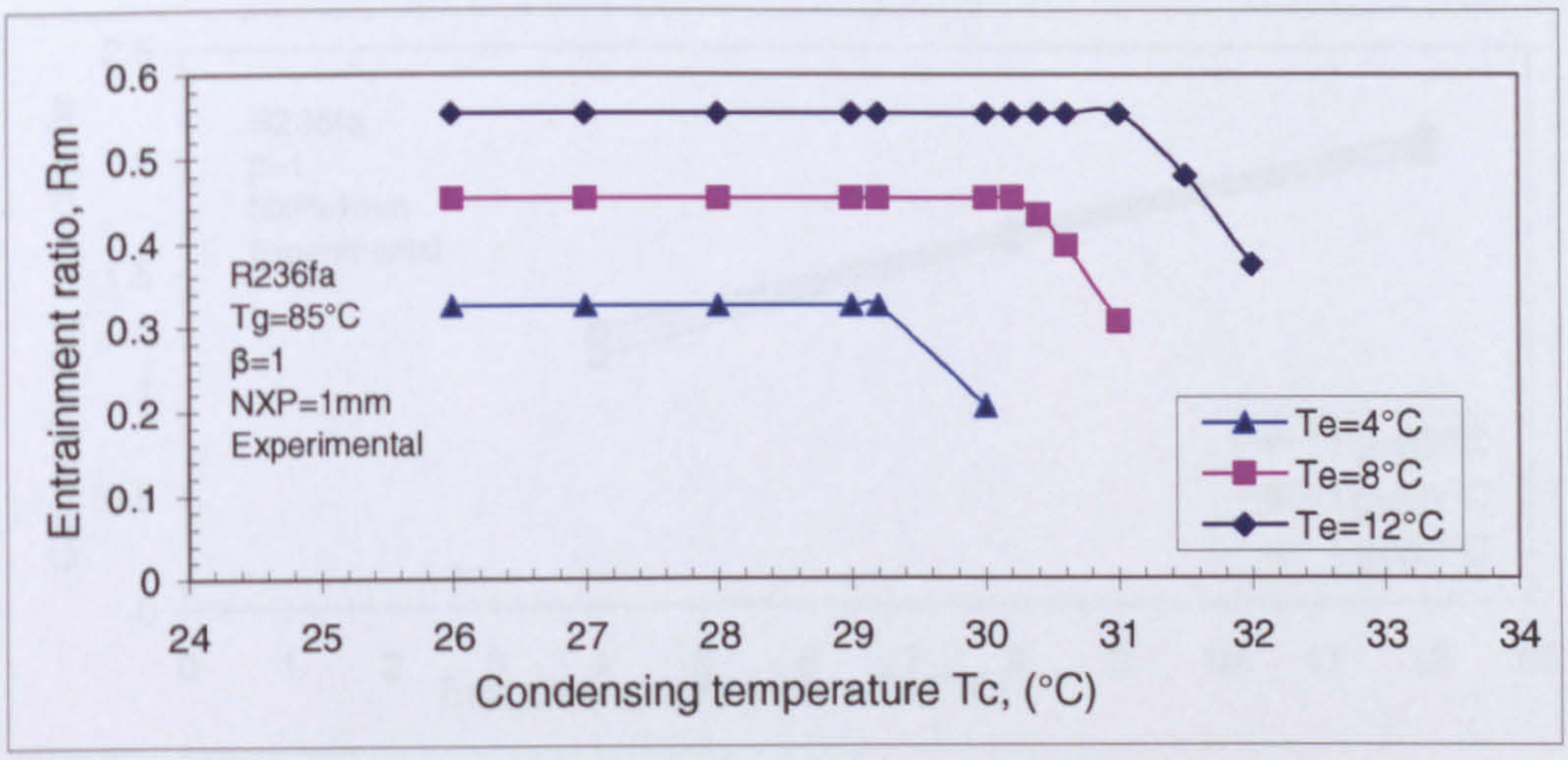

Figure A. 7 Conventional R236fa jet-pump T_g=85°C (experimental)

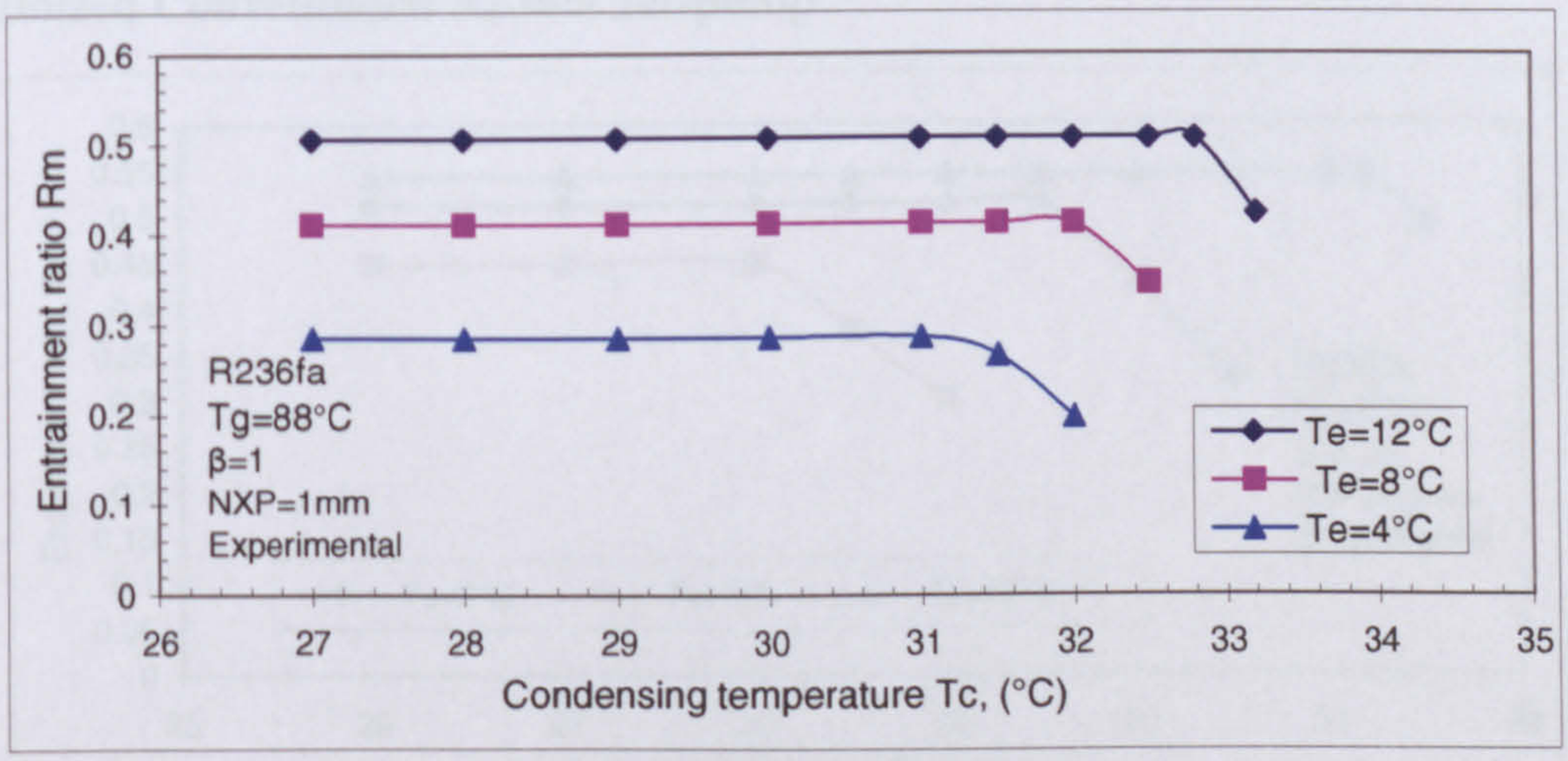

Figure A. 8 Conventional R236fa jet-pump T_g=88°C (experimental)

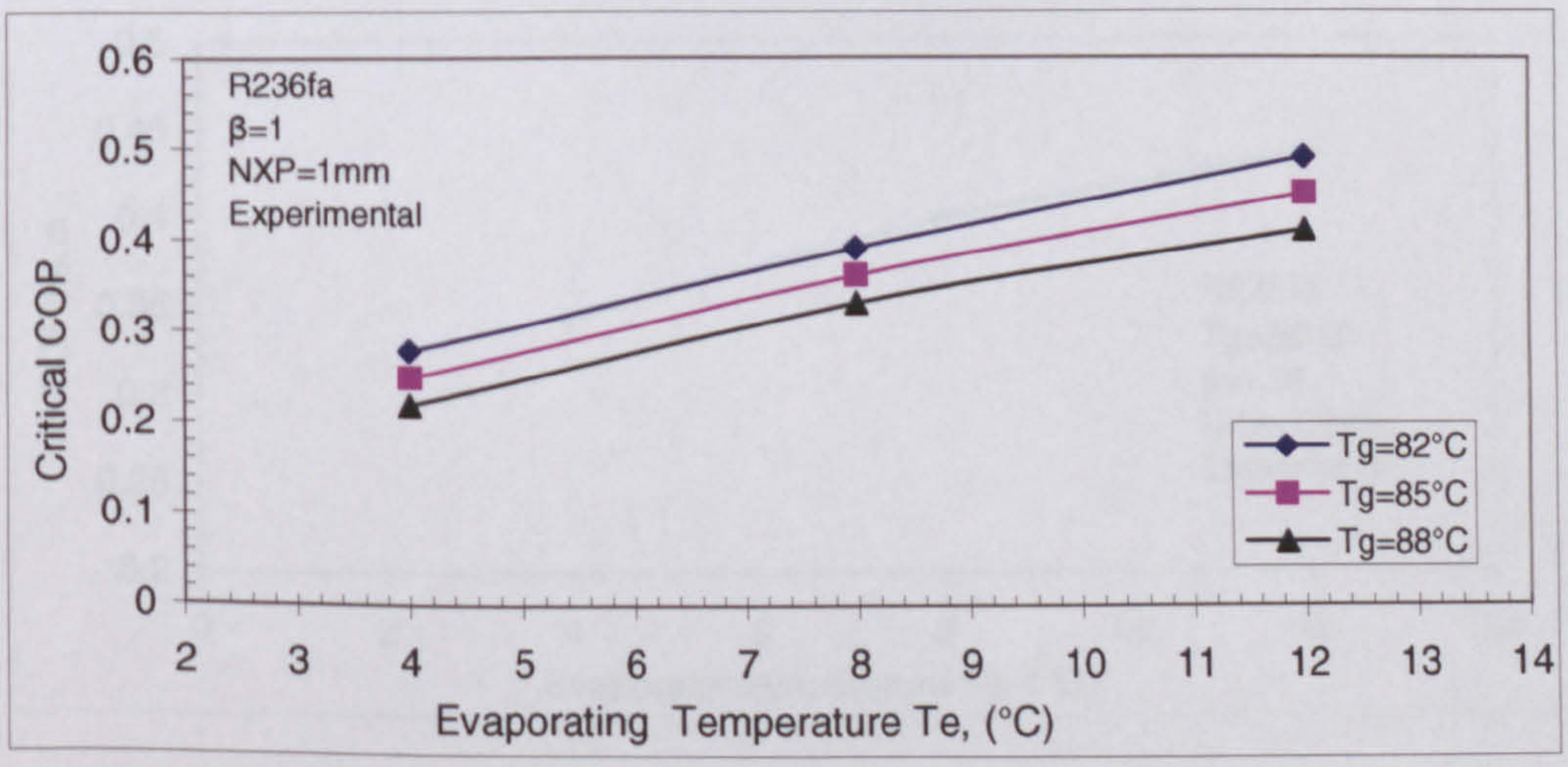

Figure A. 9 Conventional R236fa jet-pump Critical COP at different operating conditions (experimental)

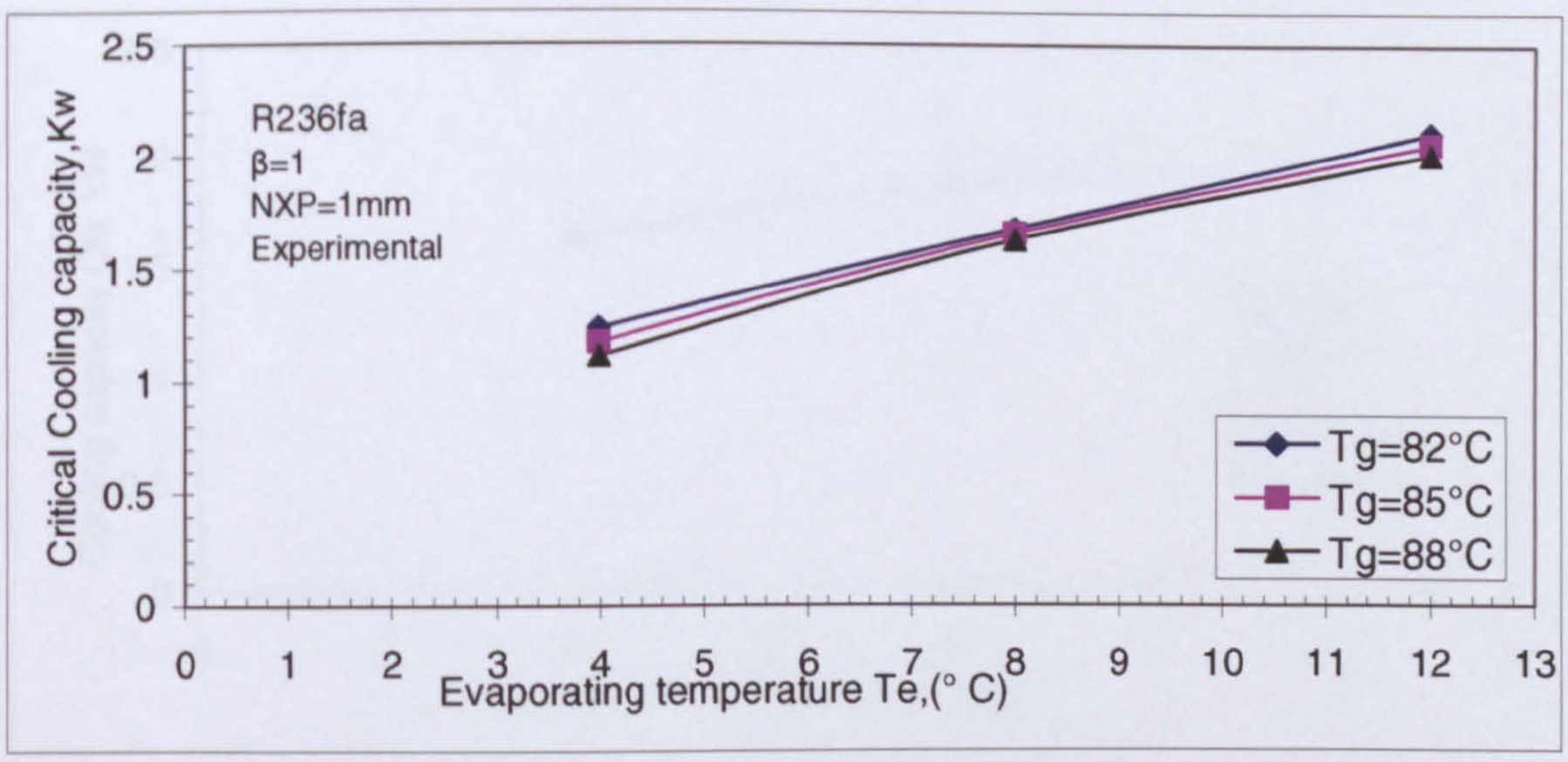

Figure A. 10 Conventional R236fa jet-pump-Critical cooling capacity at different operating conditions (experimental)

- **Optimized Conventional R236fa Jet-pump**

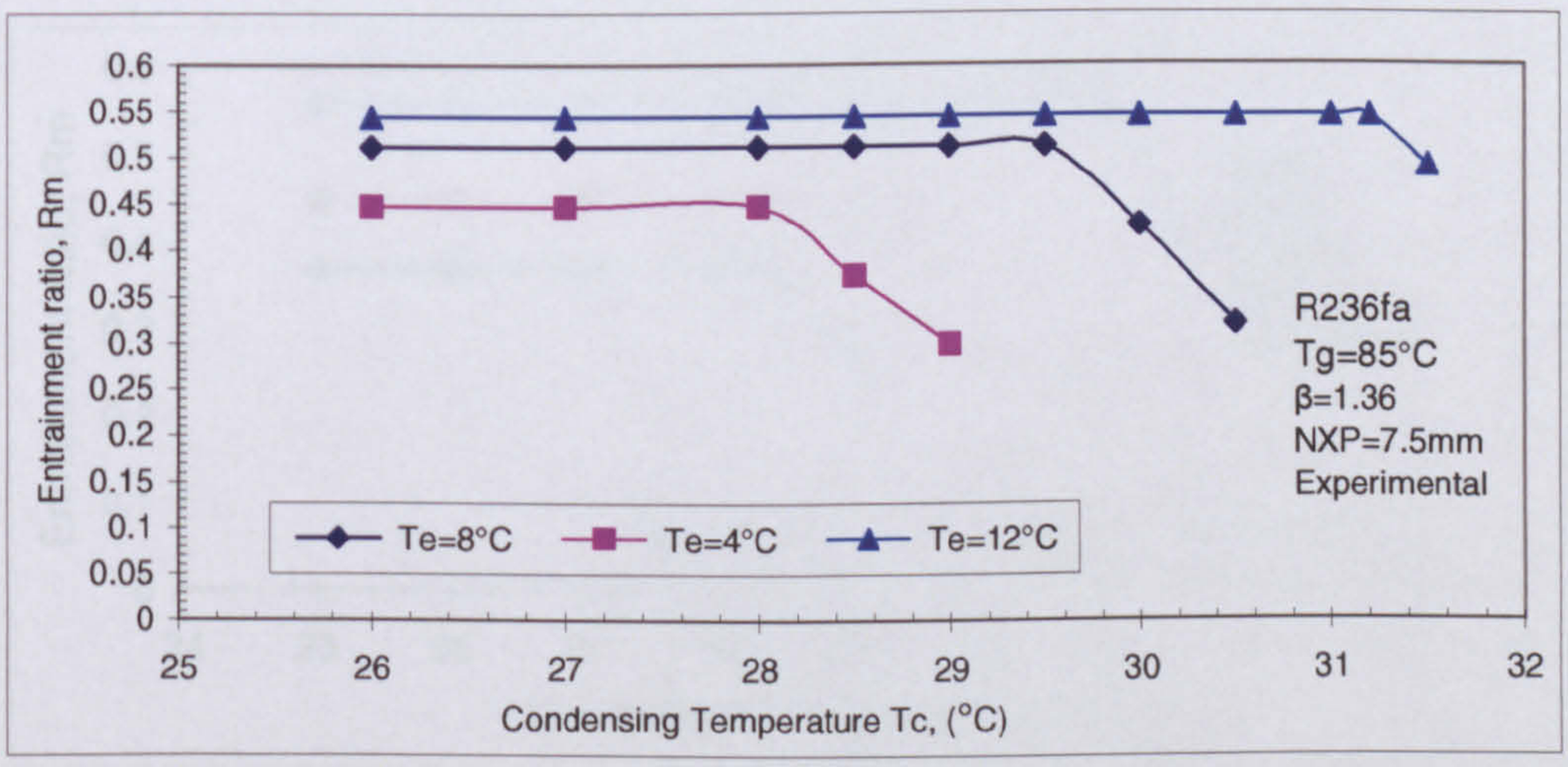

Figure A. 11 Optimized R236fa conventional jet-pump performances (off-design) (experimental)

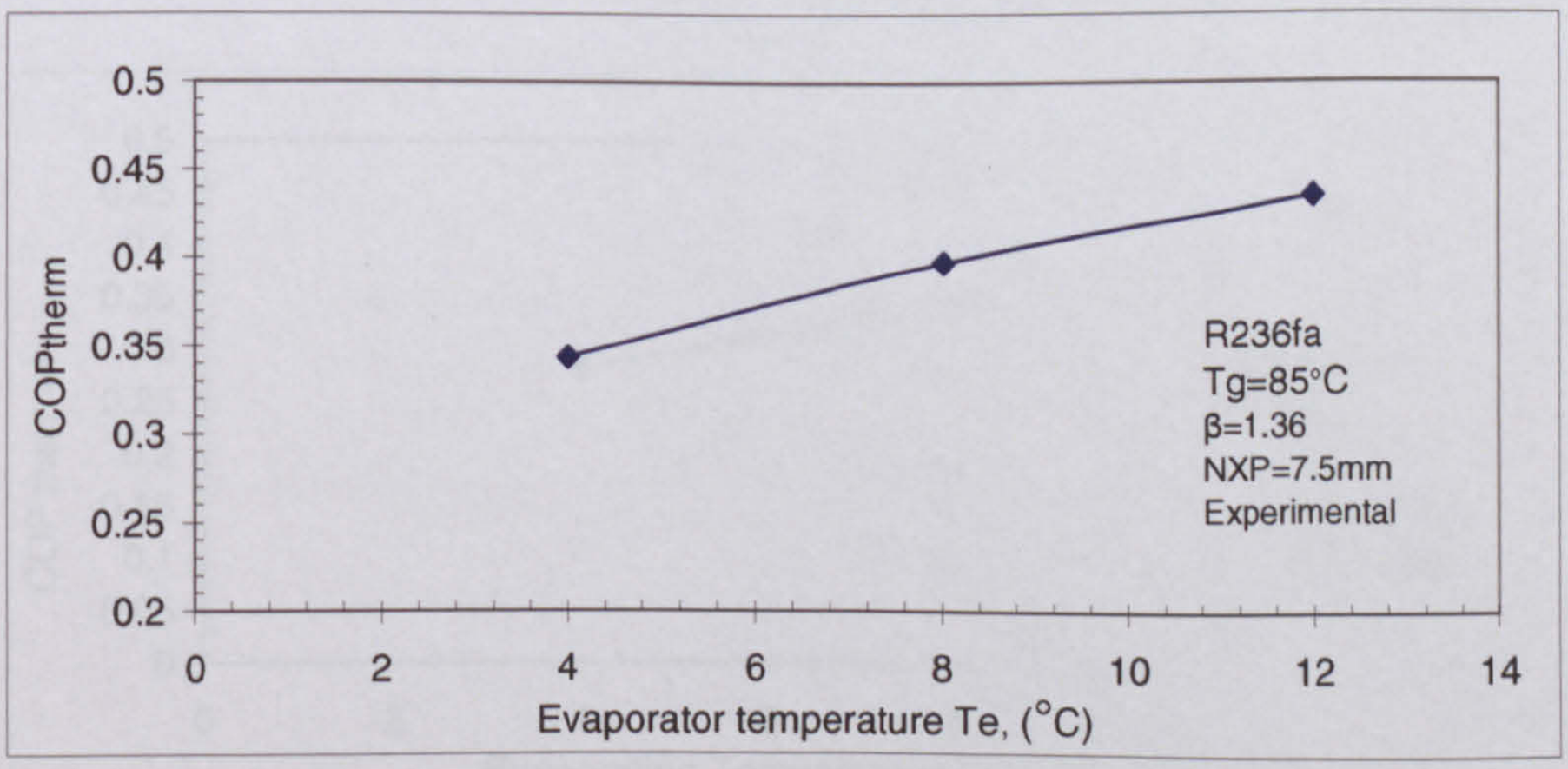

Figure A. 12 Optimized R236fa conventional jet-pump (COP at off-design) (experimental)

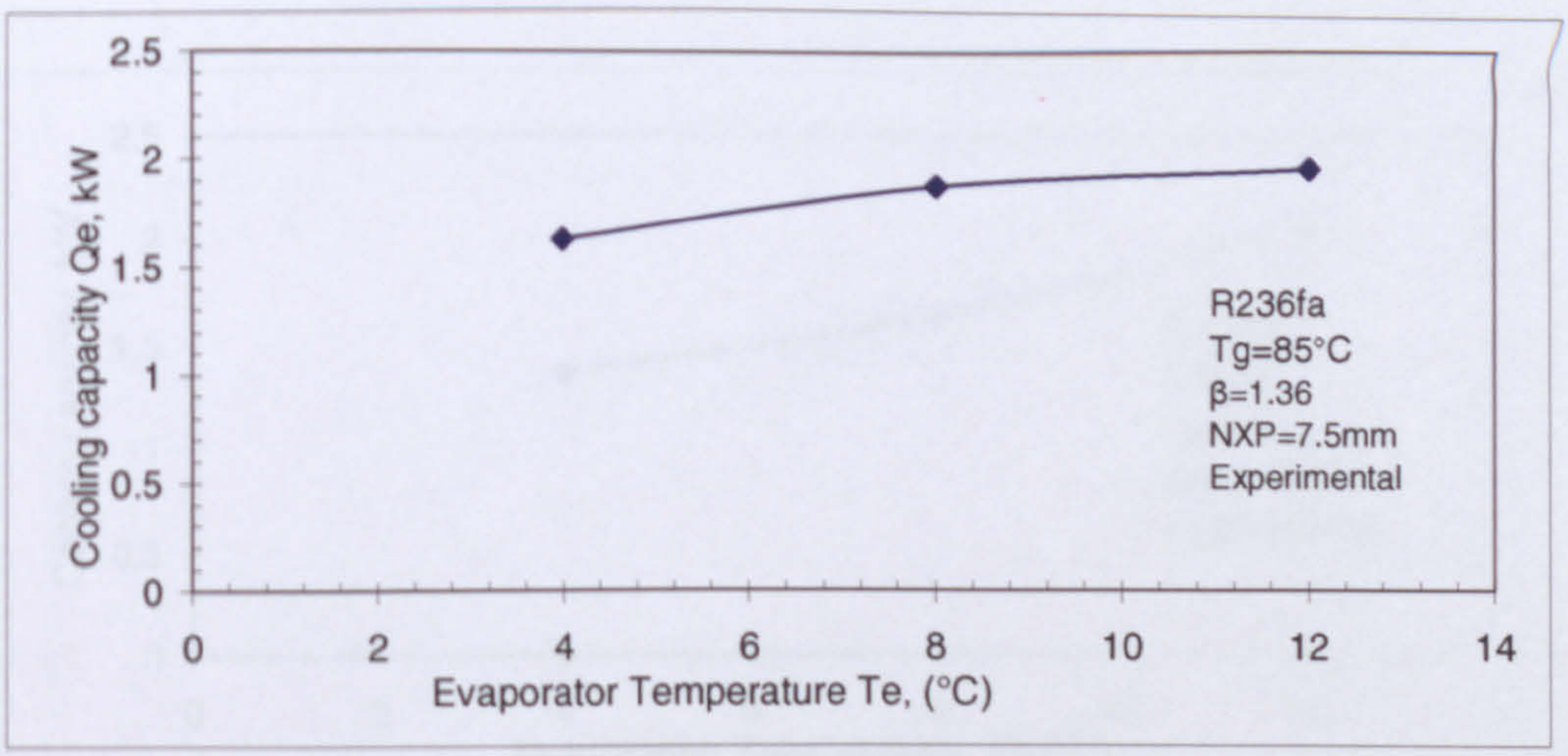

Figure A. 13 Optimized R236fa conventional jet-pump (Q_e at off-design) (experimental)

- **Optimized CRMC R236fa Jet-pump**

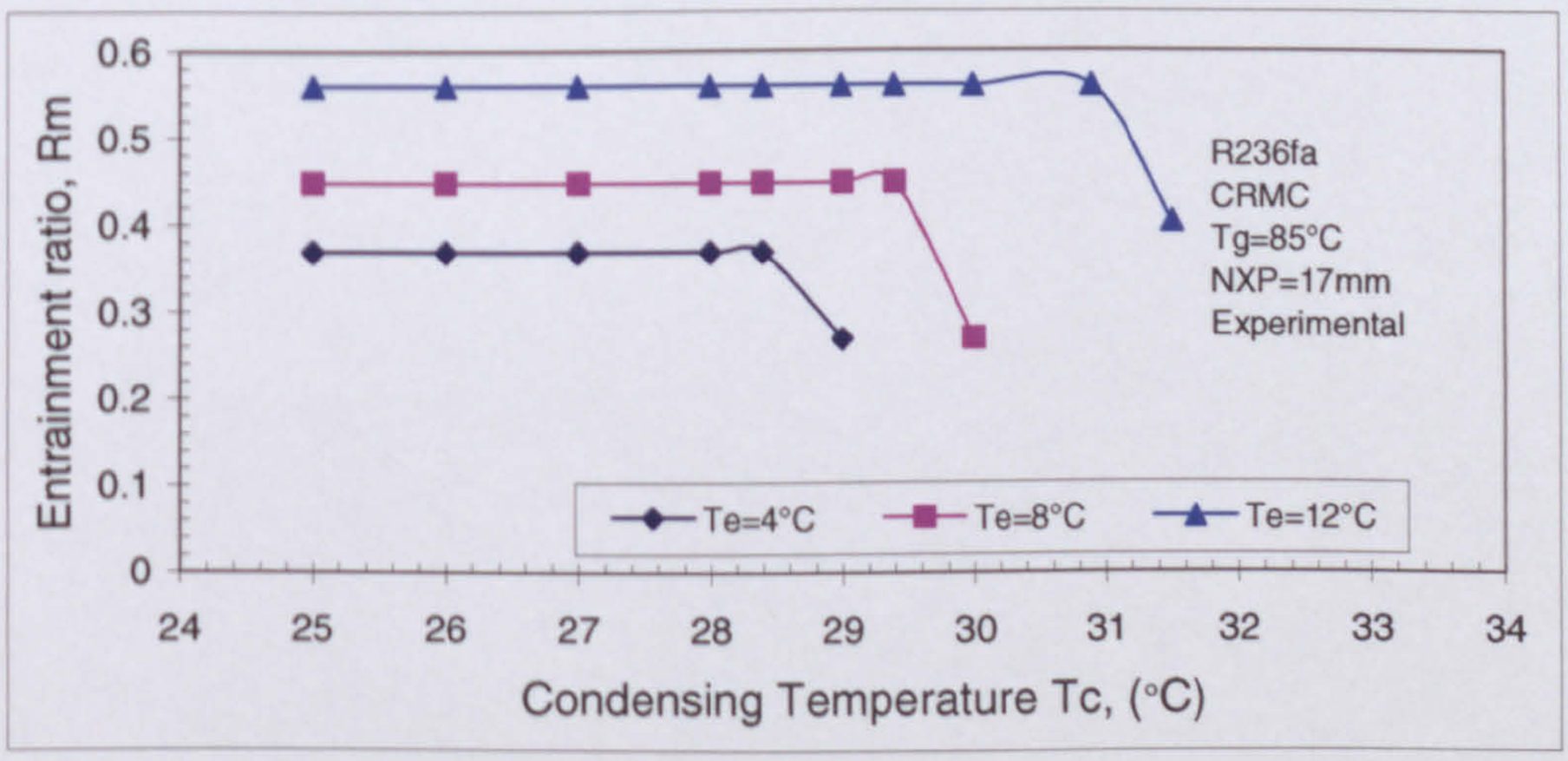

Figure A. 14 Optimized CRMC-R236fa jet-pump performances (Off-design R_m) (experimental)

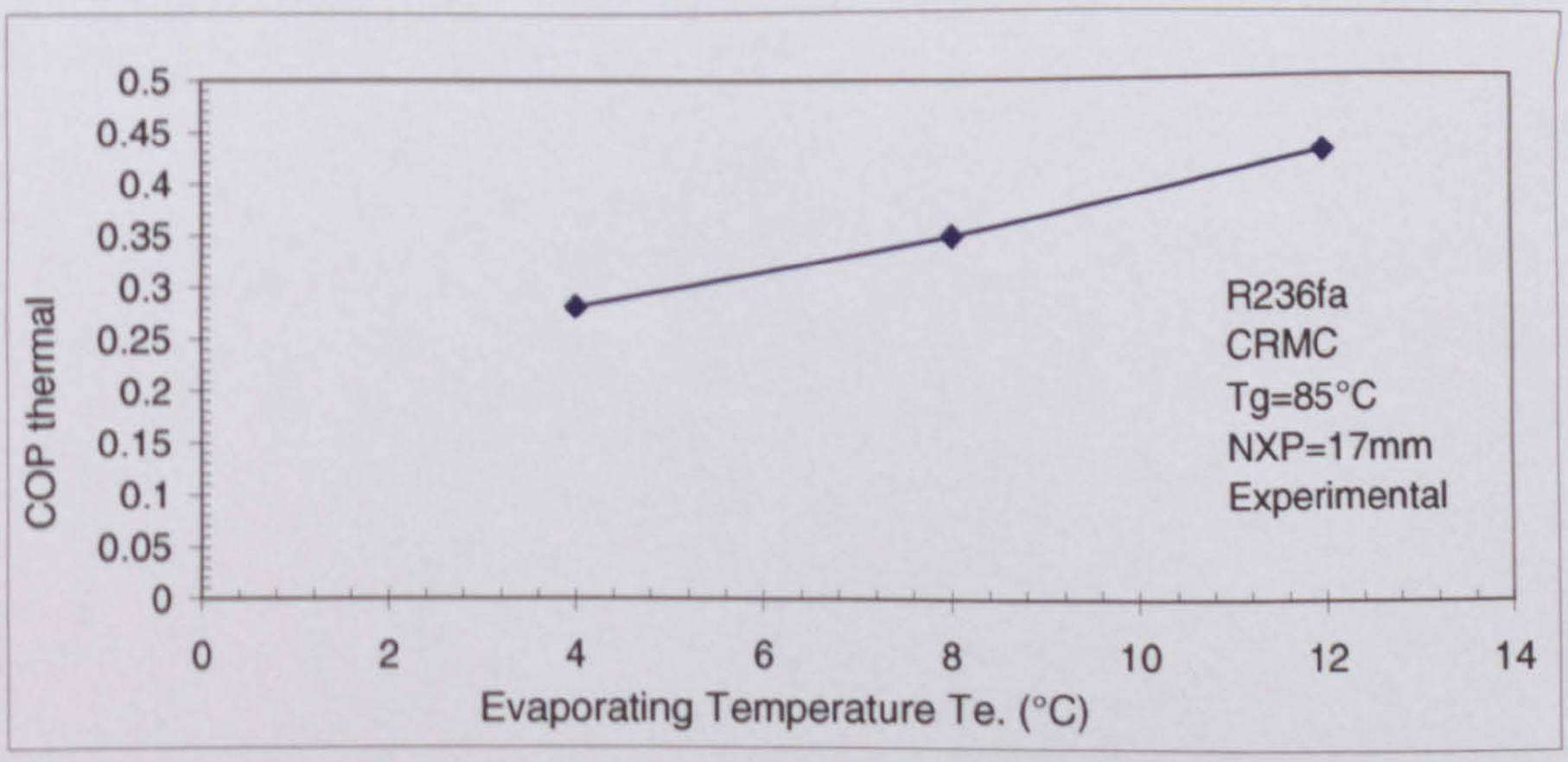

Figure A. 15 Optimized CRMC R236fa jet-pump performances (off-design COP)(experimental)

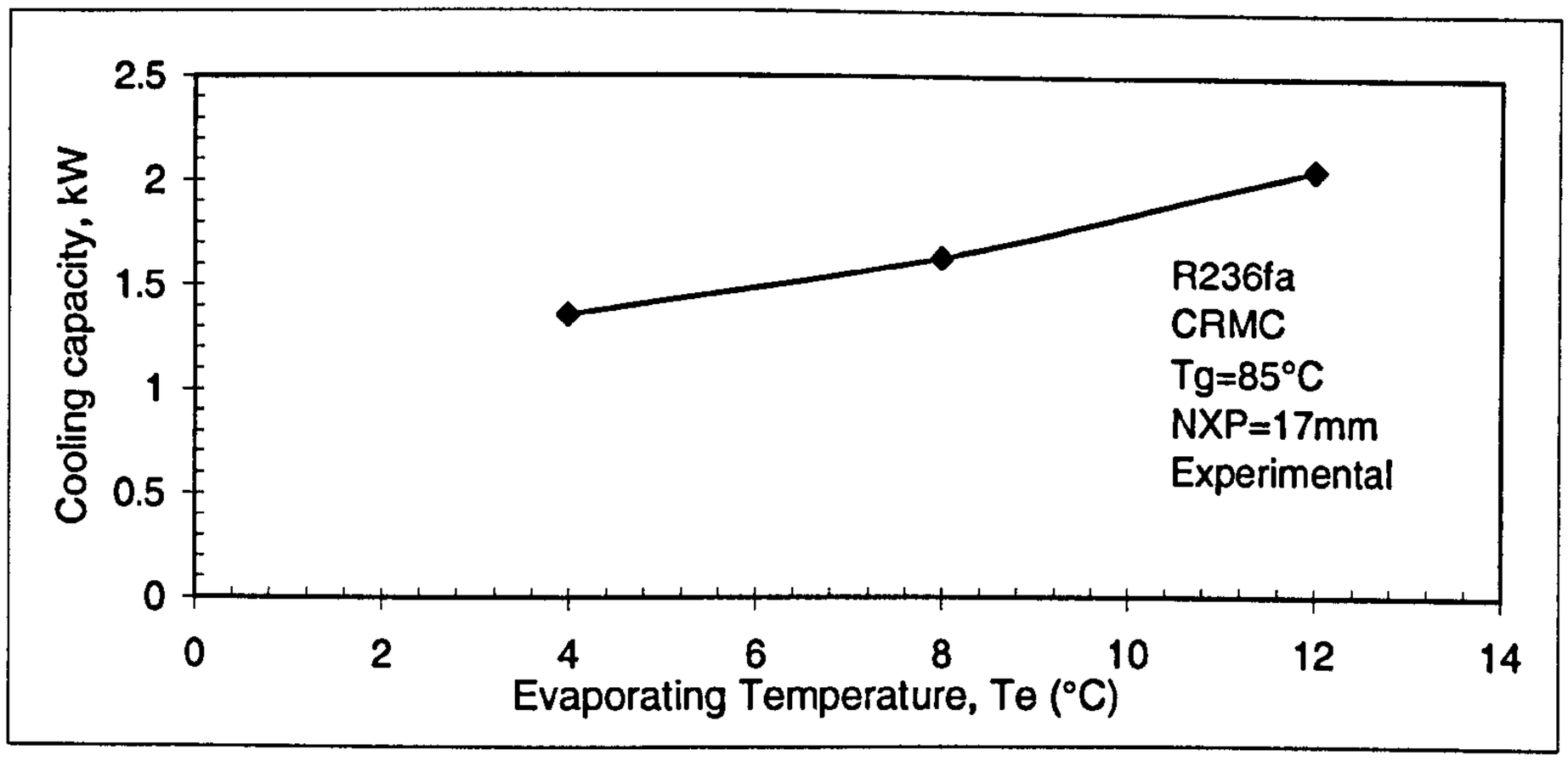

Figure A. 16 Optimized CRMC-R236fa jet-pump performances (off-design Q_e)(experimental)

B- R245fa as working fluid

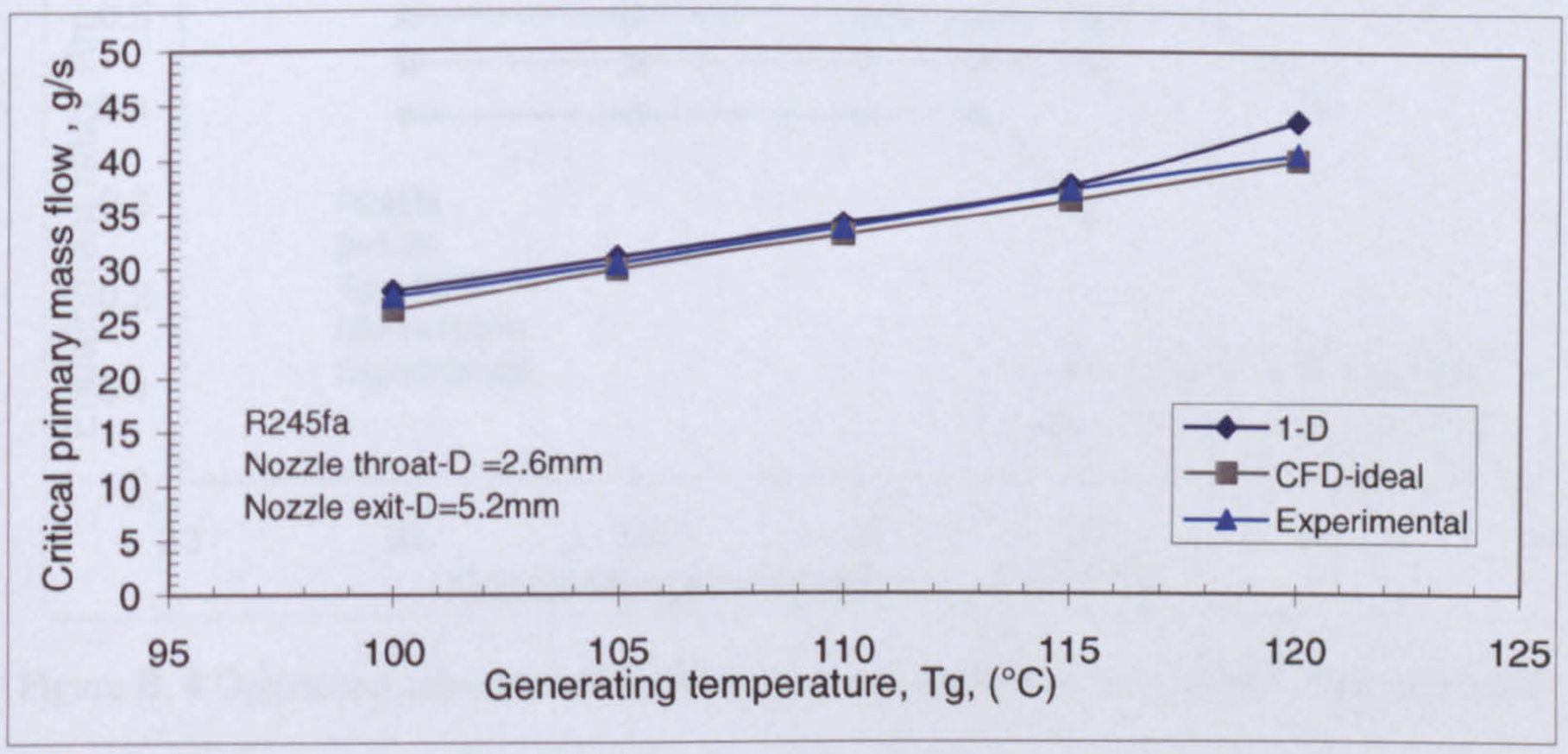

Figure B. 1Calibration of R245fa primary nozzle

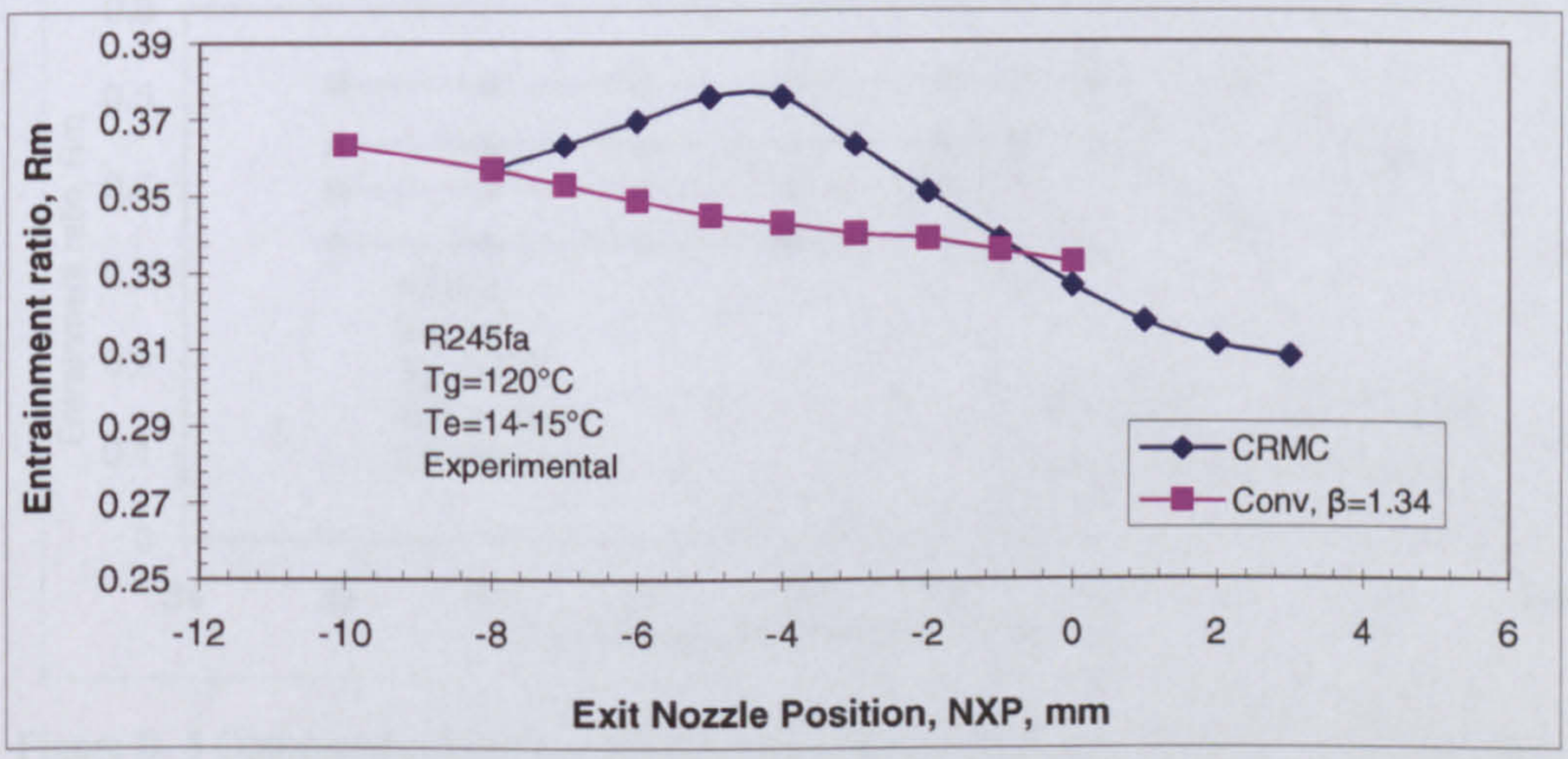

Figure B. 2 Measured variations in the entrainment ratio "R_m" with NXP

R245fa Jet-pumps (Experimental)

• Optimized Conventional R245fa Jet-pump

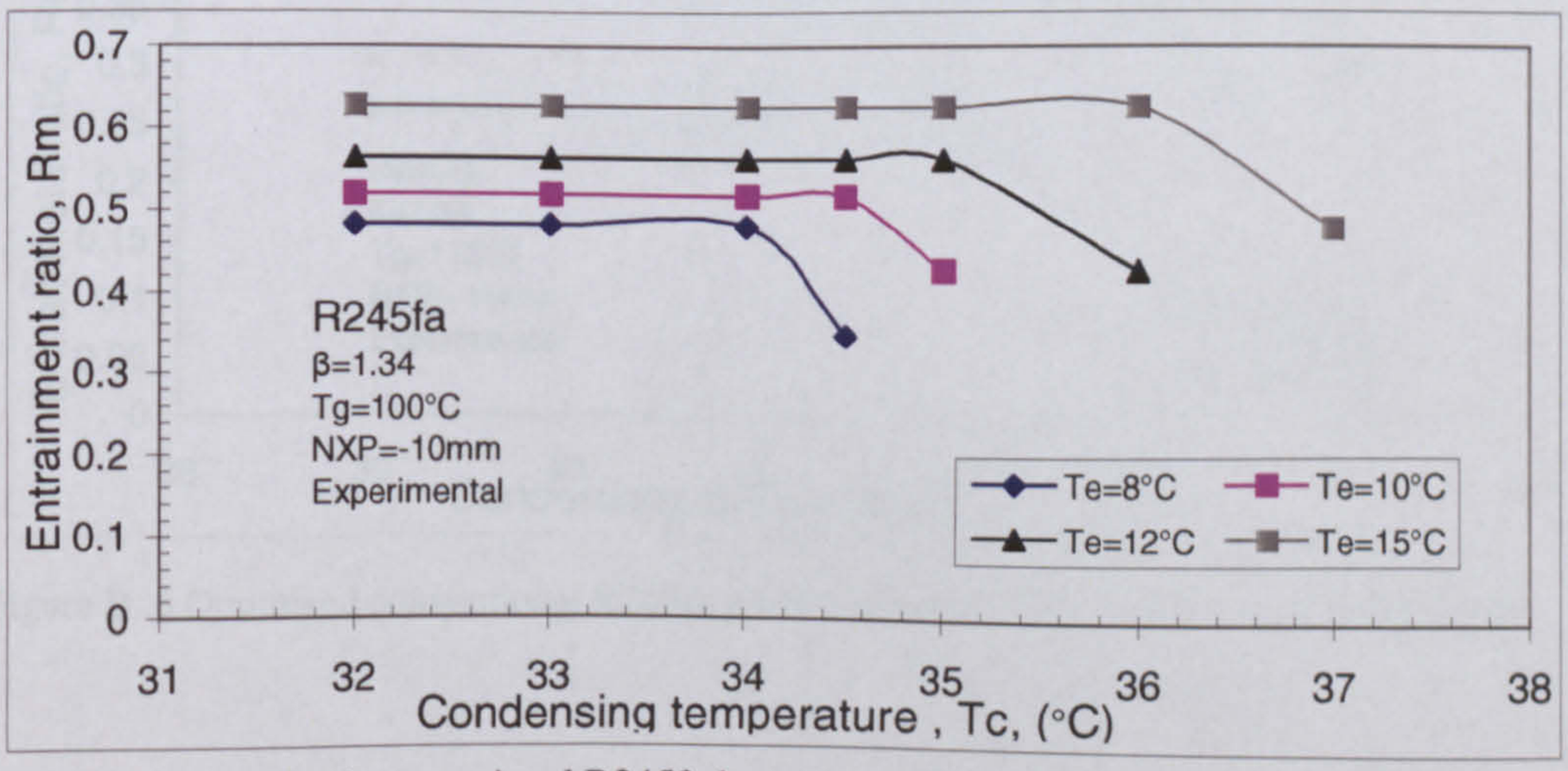

Figure B. 3 Optimized conventional R245fa jet-pump performance T_g=100°C (experimental)

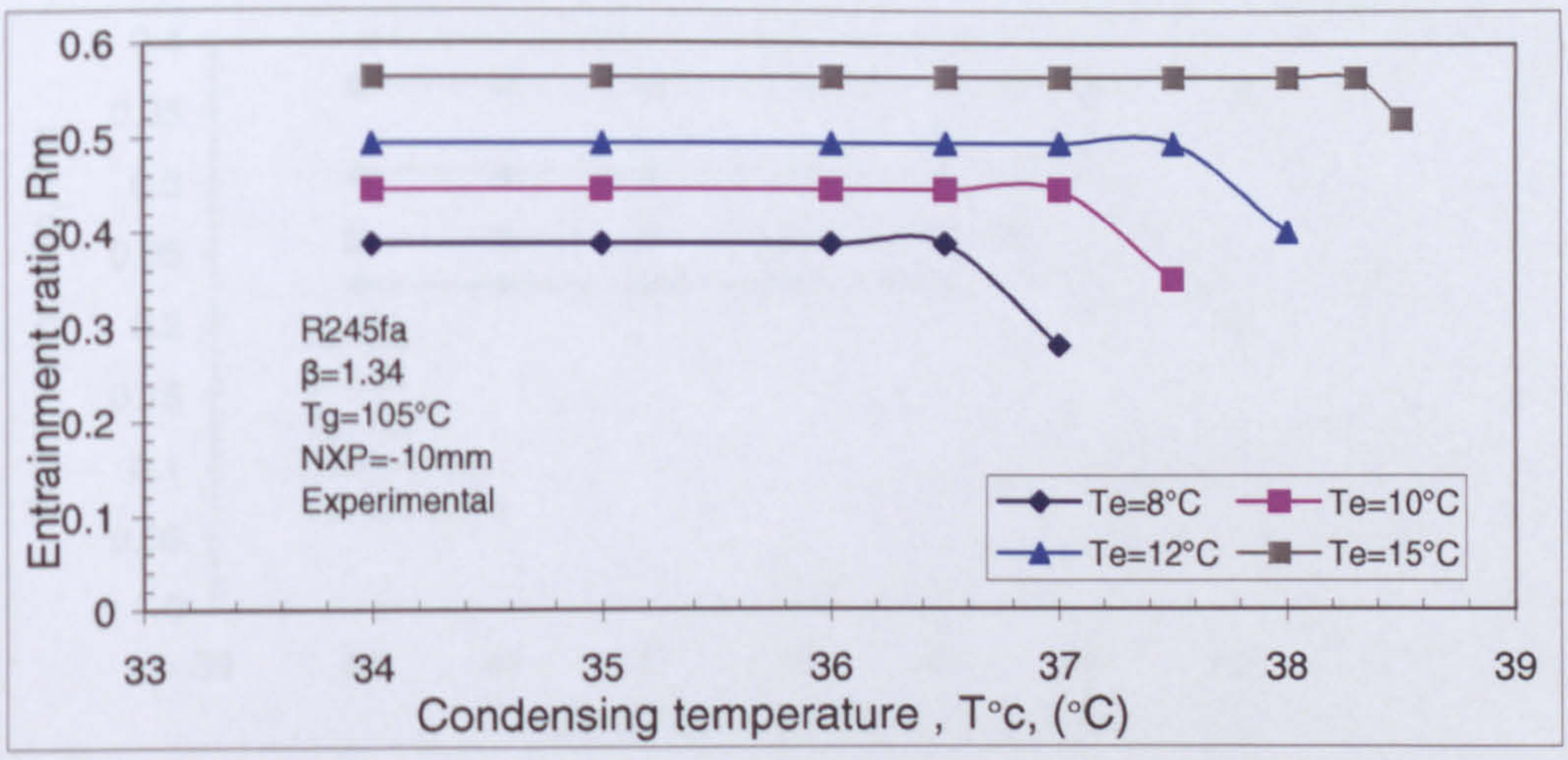

Figure B. 4 Optimized conventional R245fa jet-pump performance T_g=105°C (experimental)

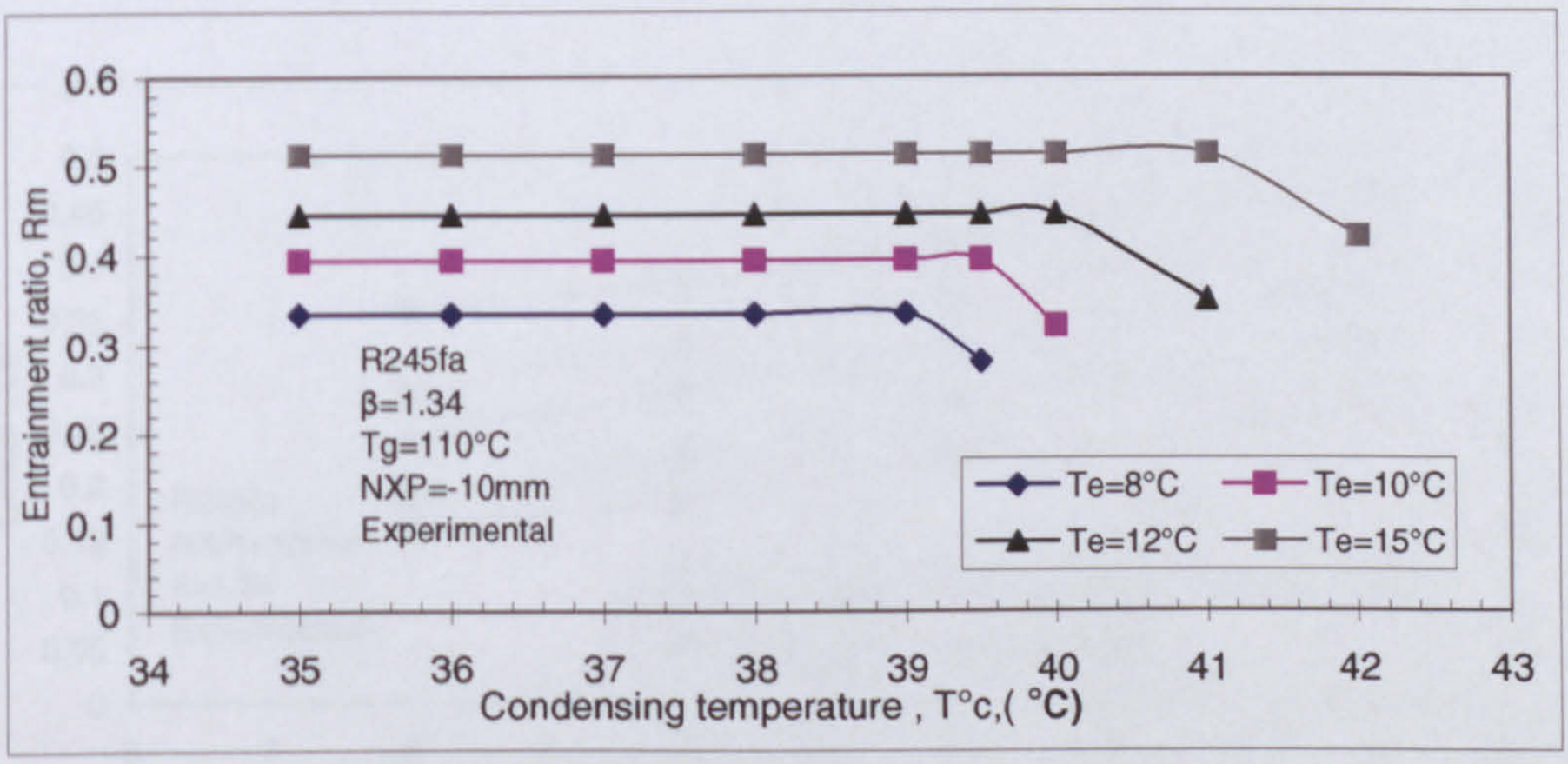

Figure B. 5 Optimized conventional R245fa jet-pump performance T_g=110°C (experimental)

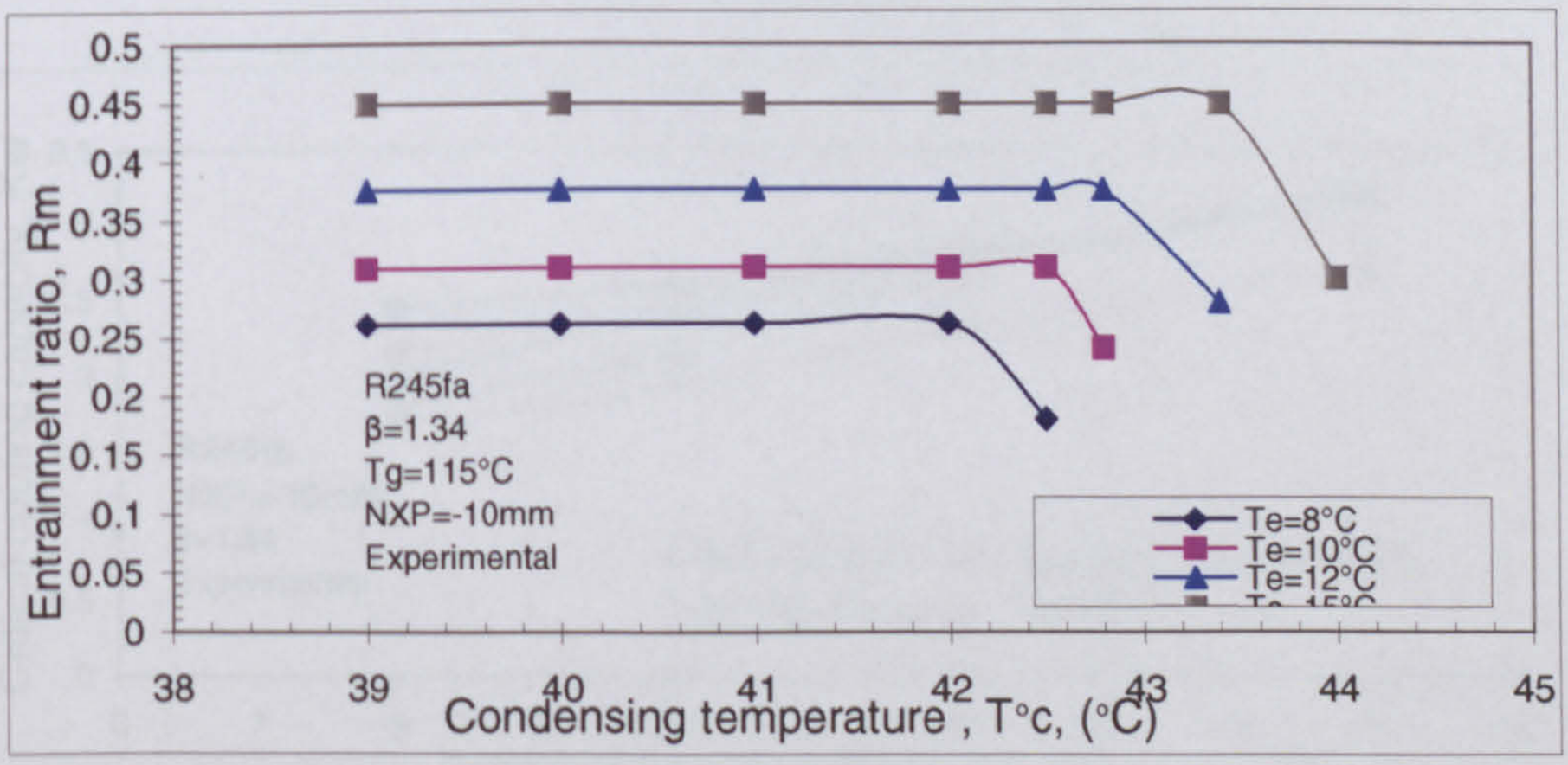

Figure B. 6 Optimized conventional R245fa jet-pump performance T_g=115°C (experimental)

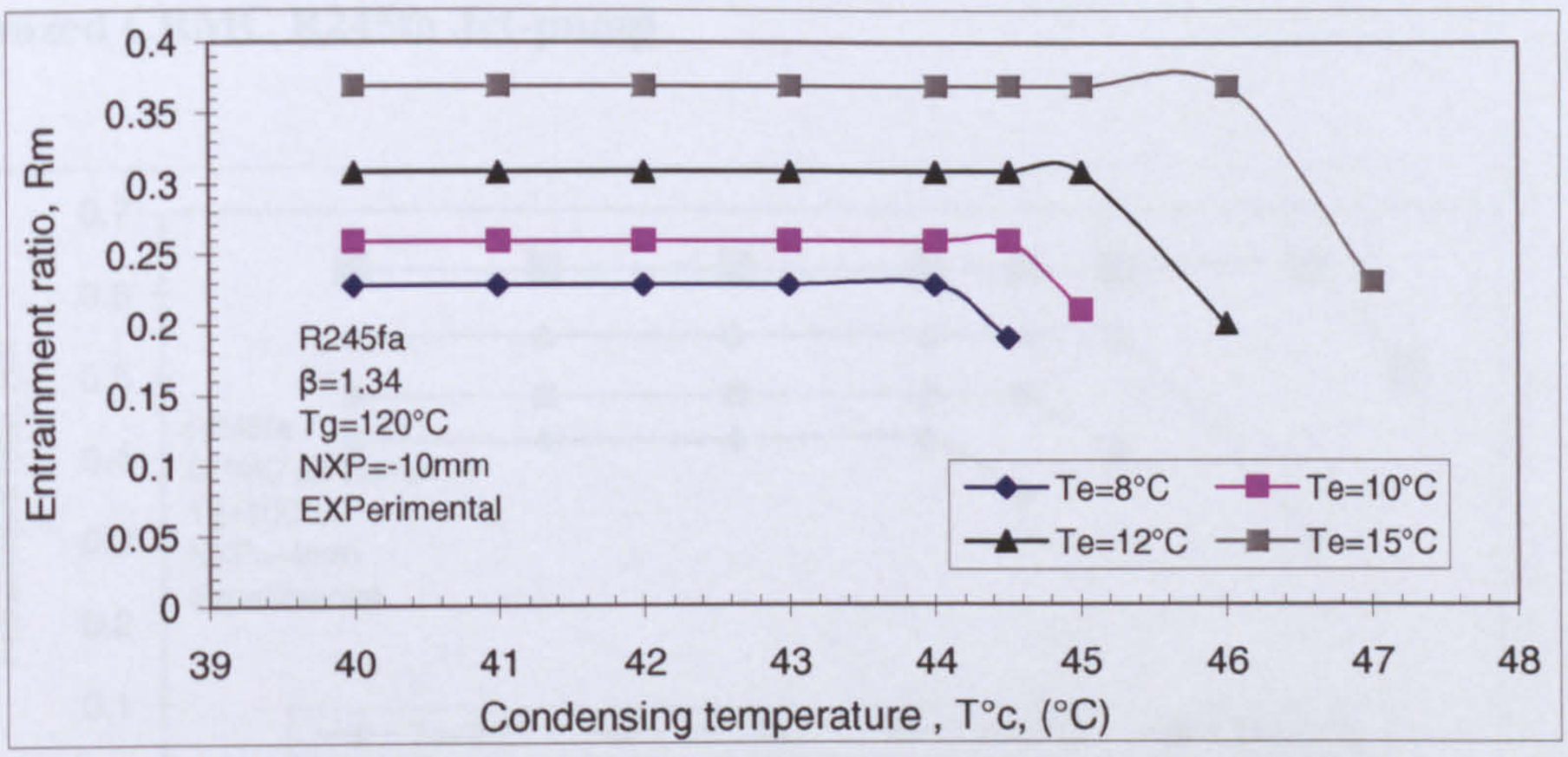

Figure B. 7 Optimized conventional R245fa jet-pump performance T_g=120°C (experimental)

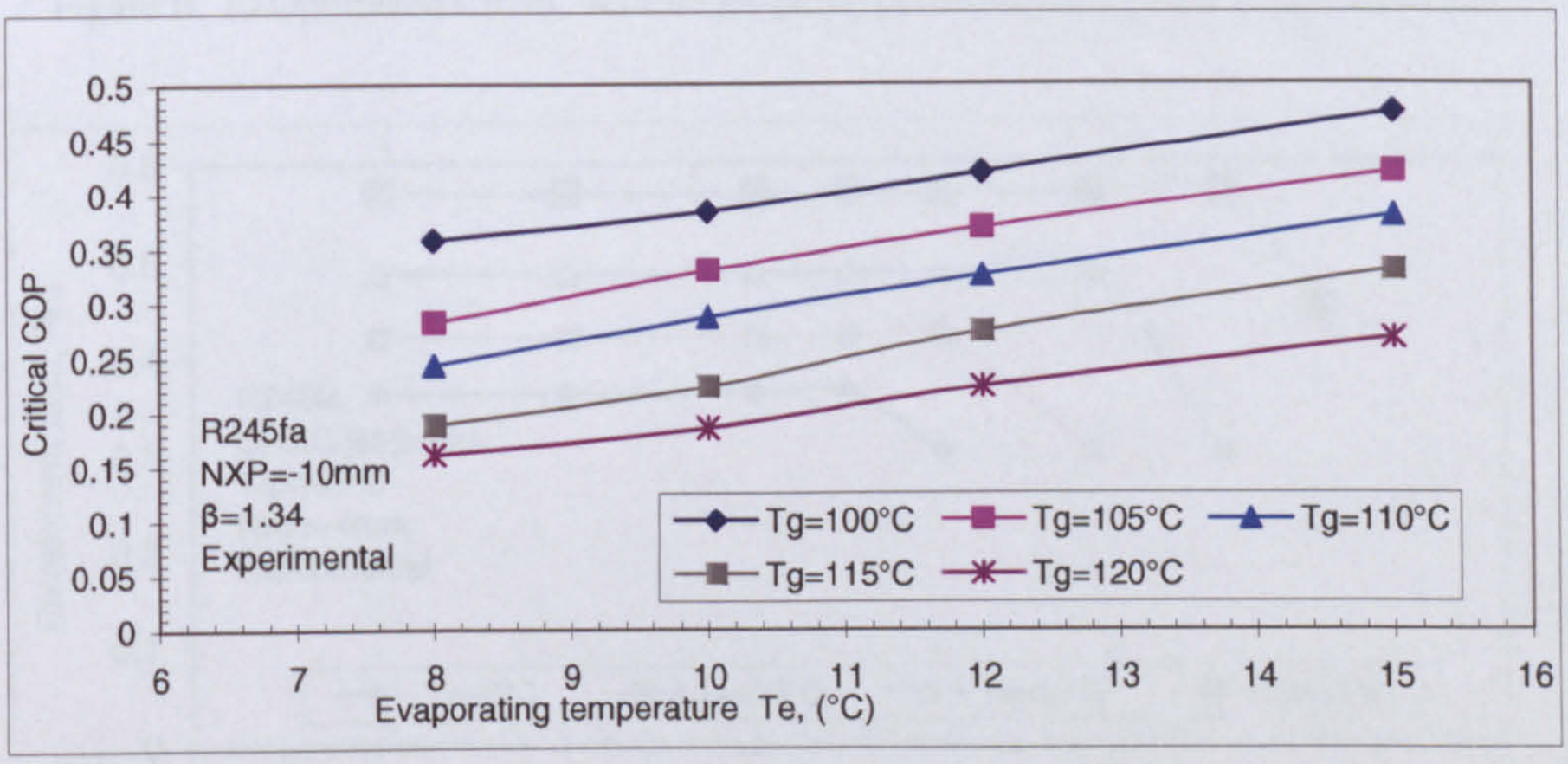

Figure B. 8 Optimized conventional R245fa jet-pump , COP (experimental)

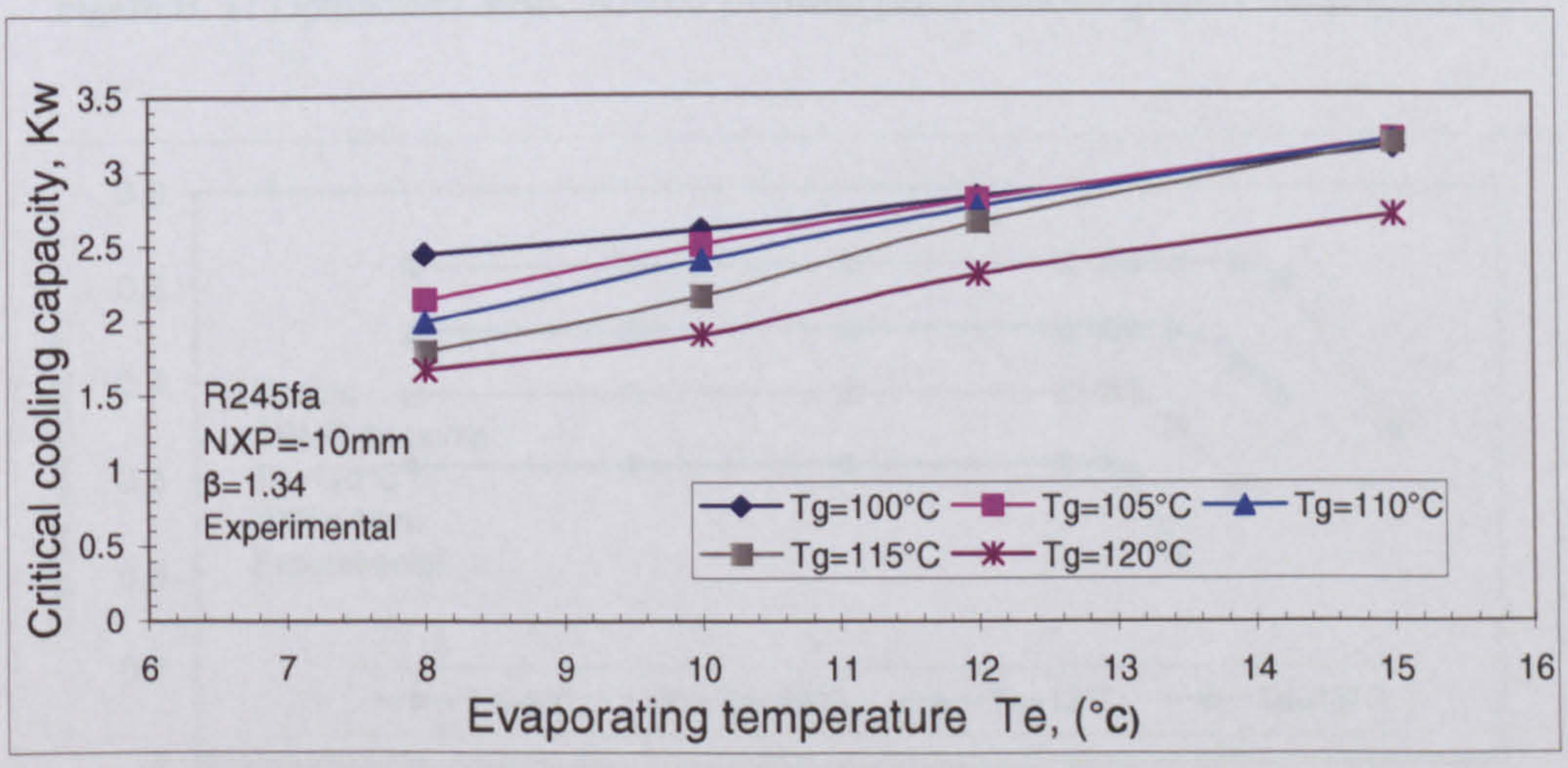

Figure B. 9 Optimized conventional R245fa jet-pump, cooling capacity (experimental)

• Optimized CRMC R245fa Jet-pump

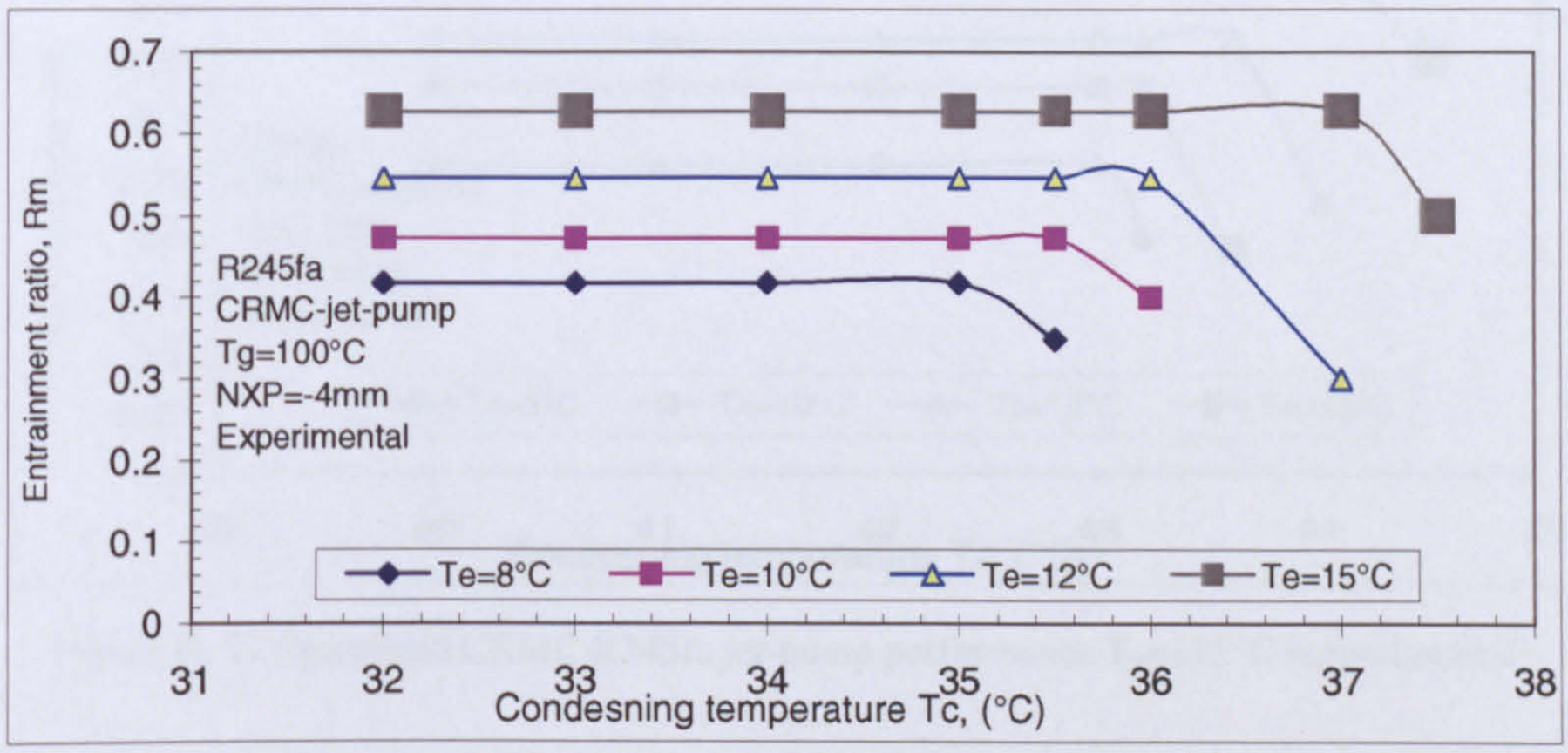

Figure B. 10 Optimized CRMC R245fa jet-pump performance T_g=100°C (experimental)

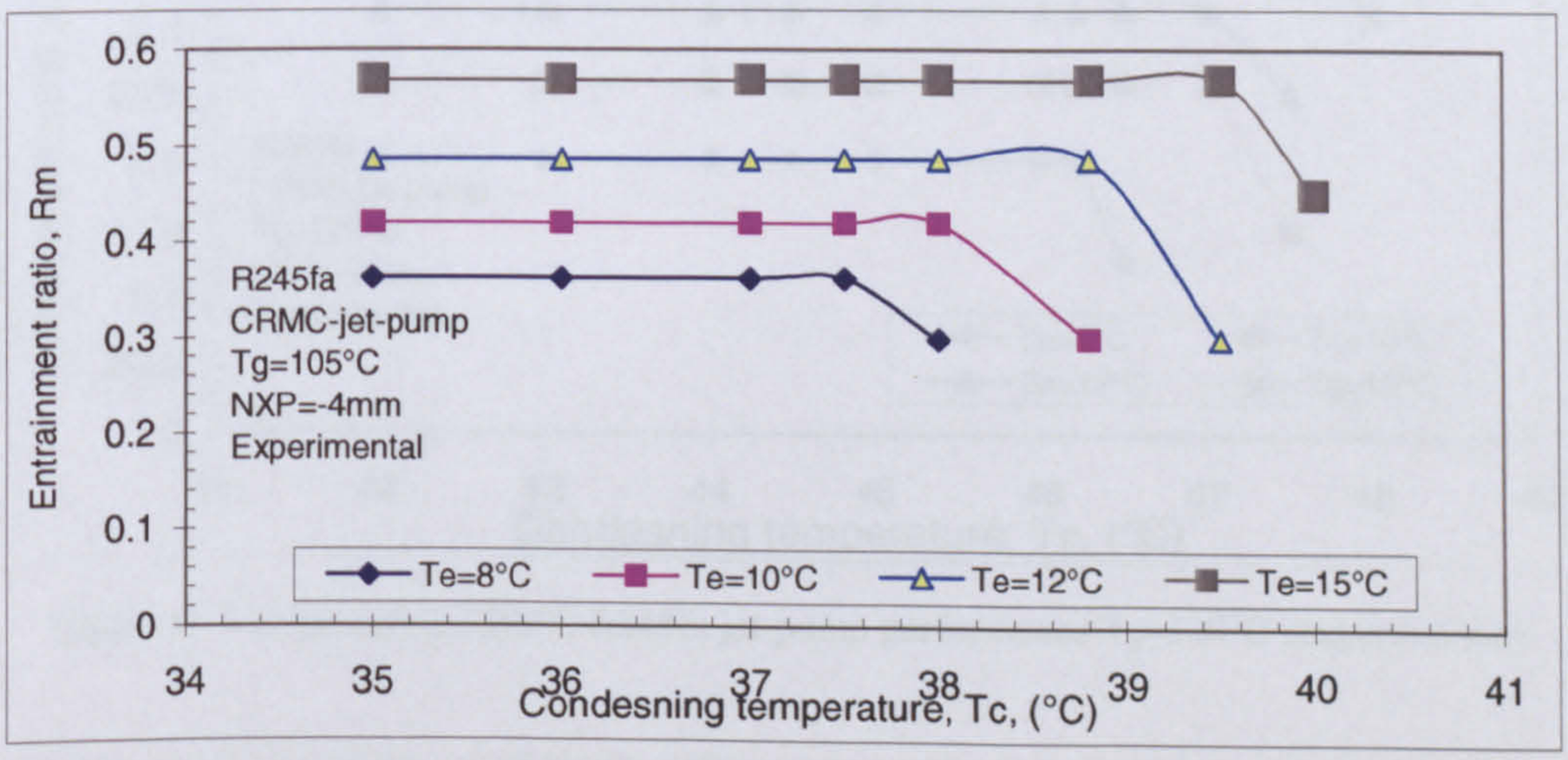

Figure B. 11 Optimized CRMC R245fa jet-pump performance T_g=105°C (experimental)

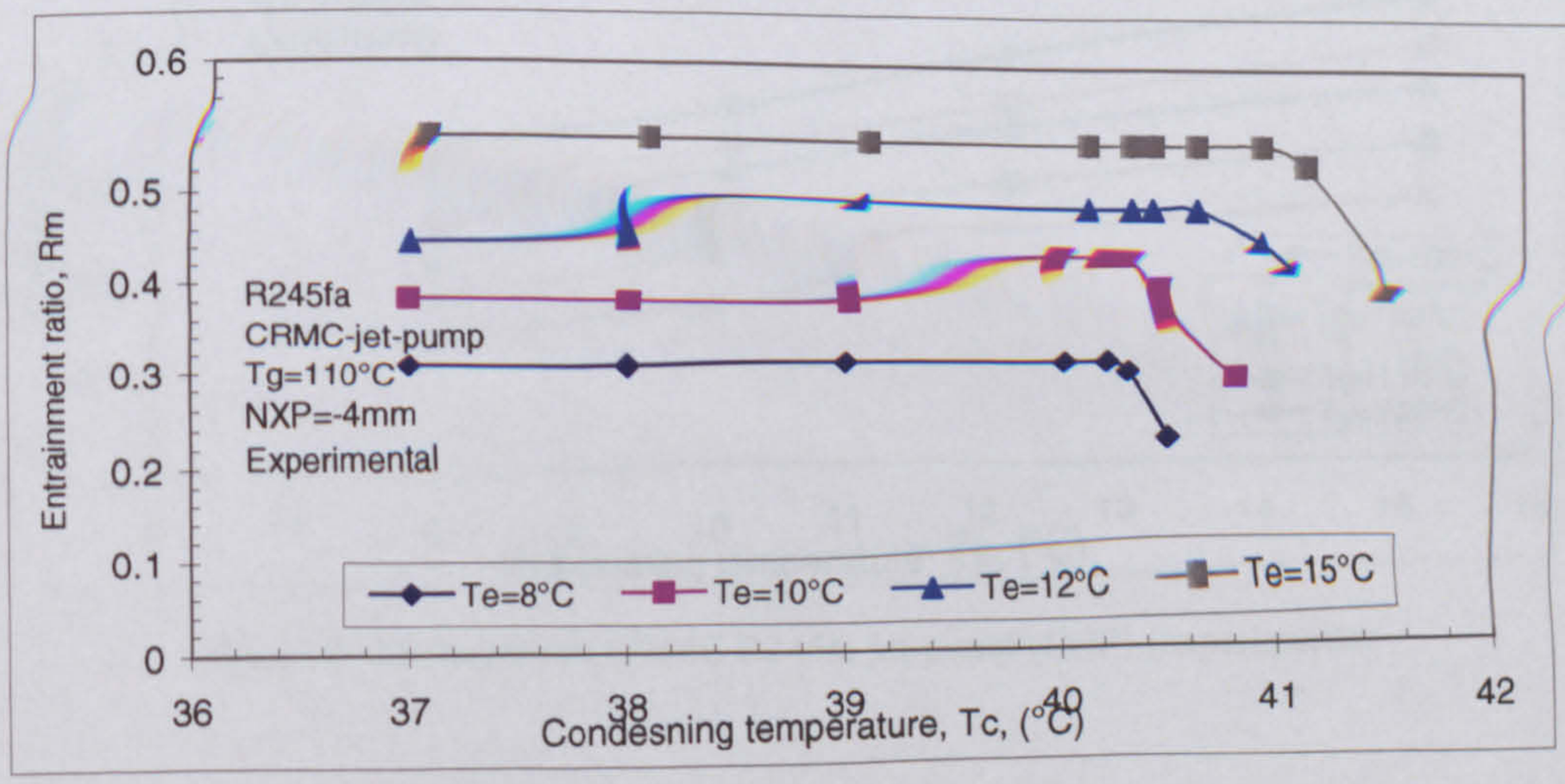

Figure B. 12 Optimized CRMC R245fa jet-pump performance T_g=110°C (experimental)

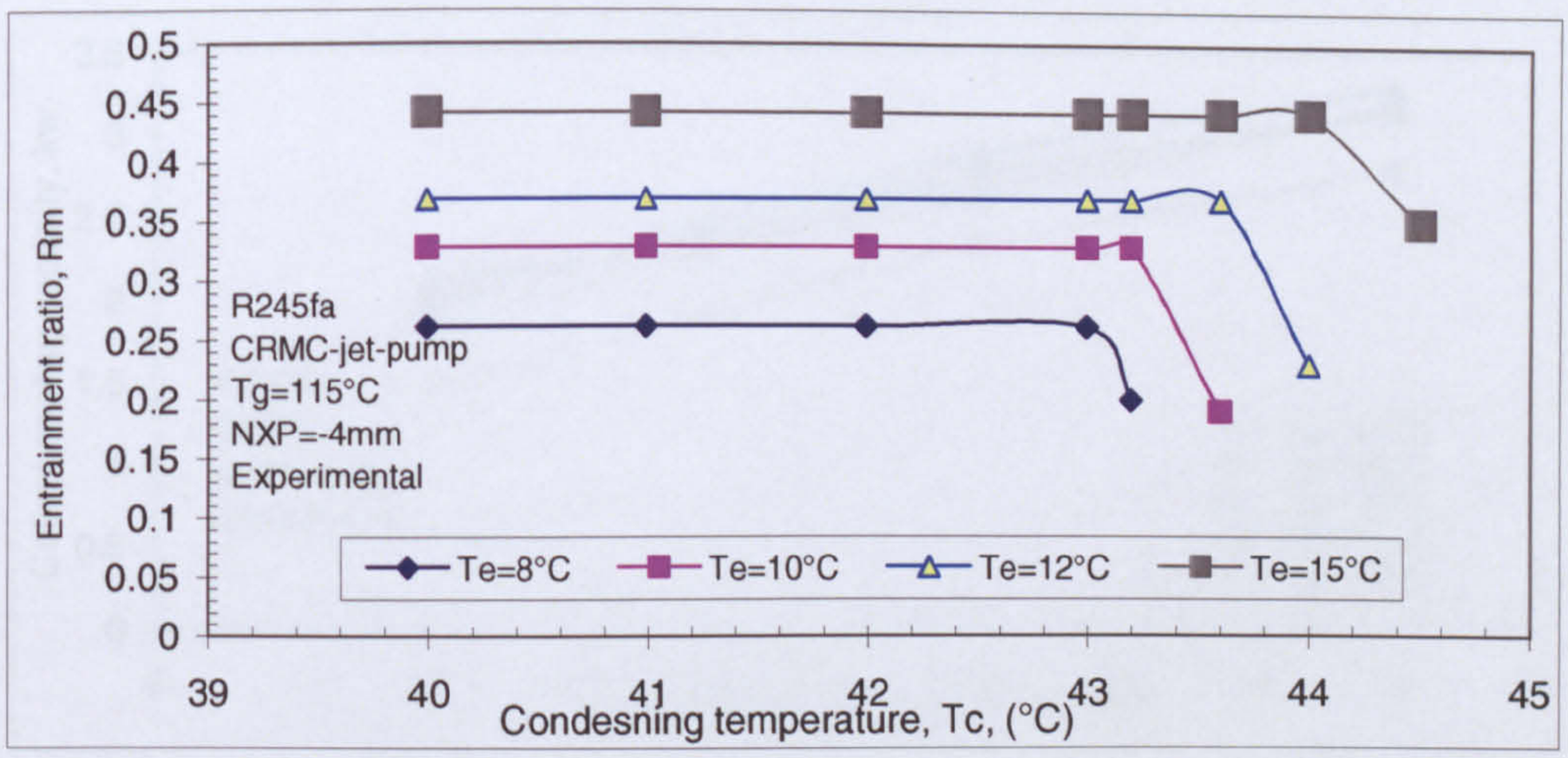

Figure B. 13 Optimized CRMC R245fa jet-pump performance T_g=115°C (experimental)

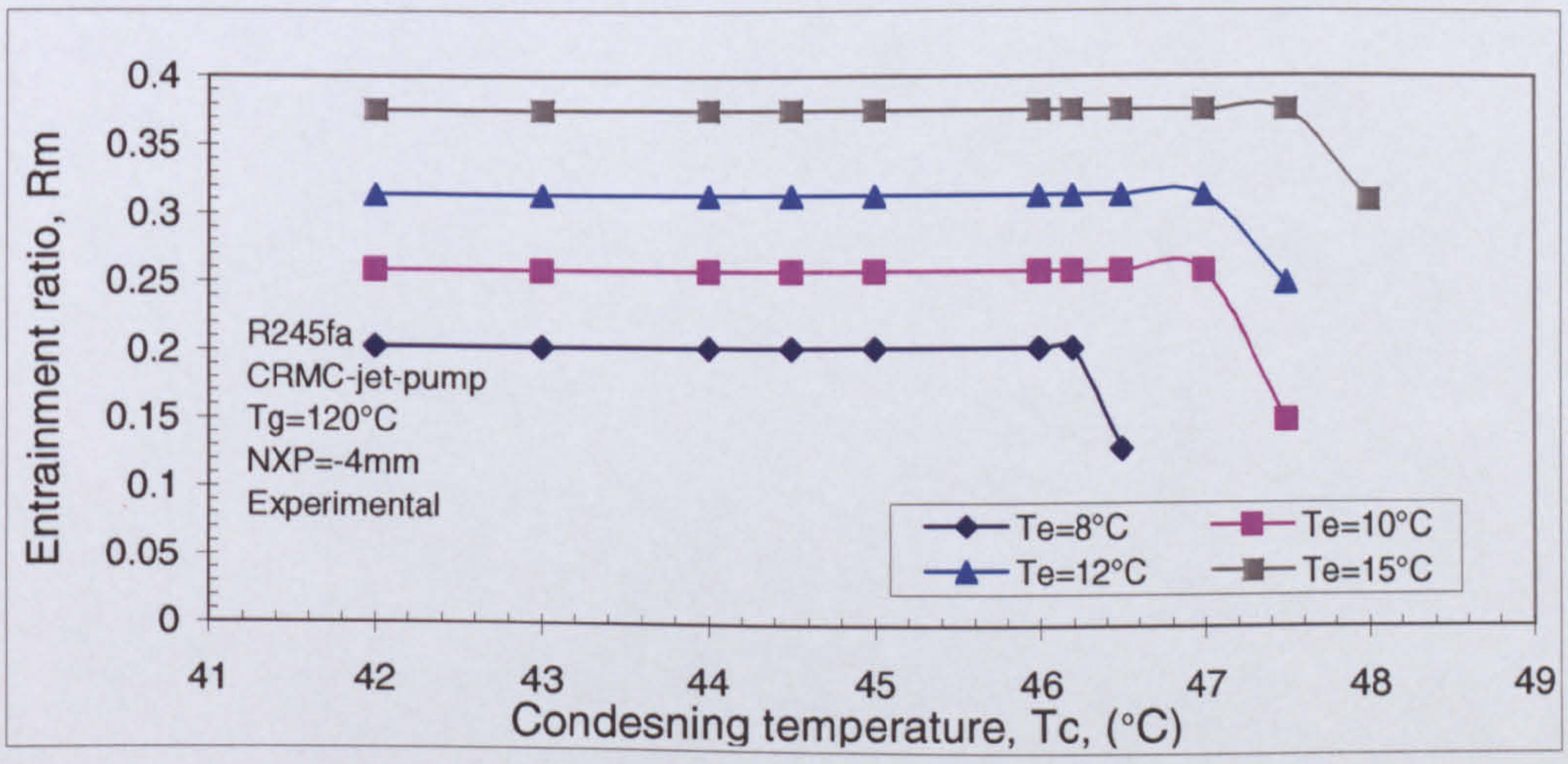

Figure B. 14 Optimized CRMC R245fa jet-pump performance T_g=120°C (experimental)

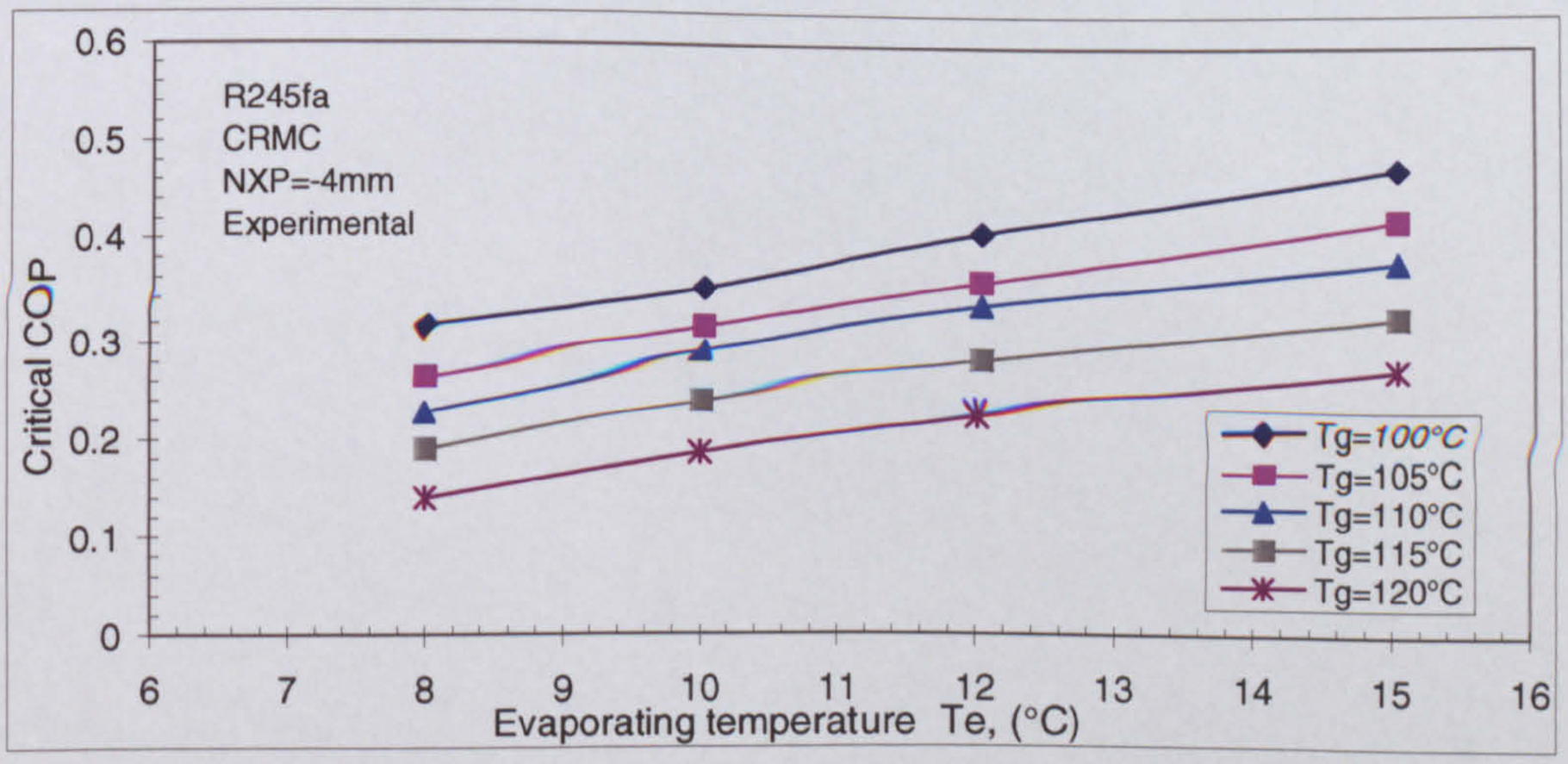

Figure B. 15 Optimized CRMC R245fa jet-pump (COP) (experimental

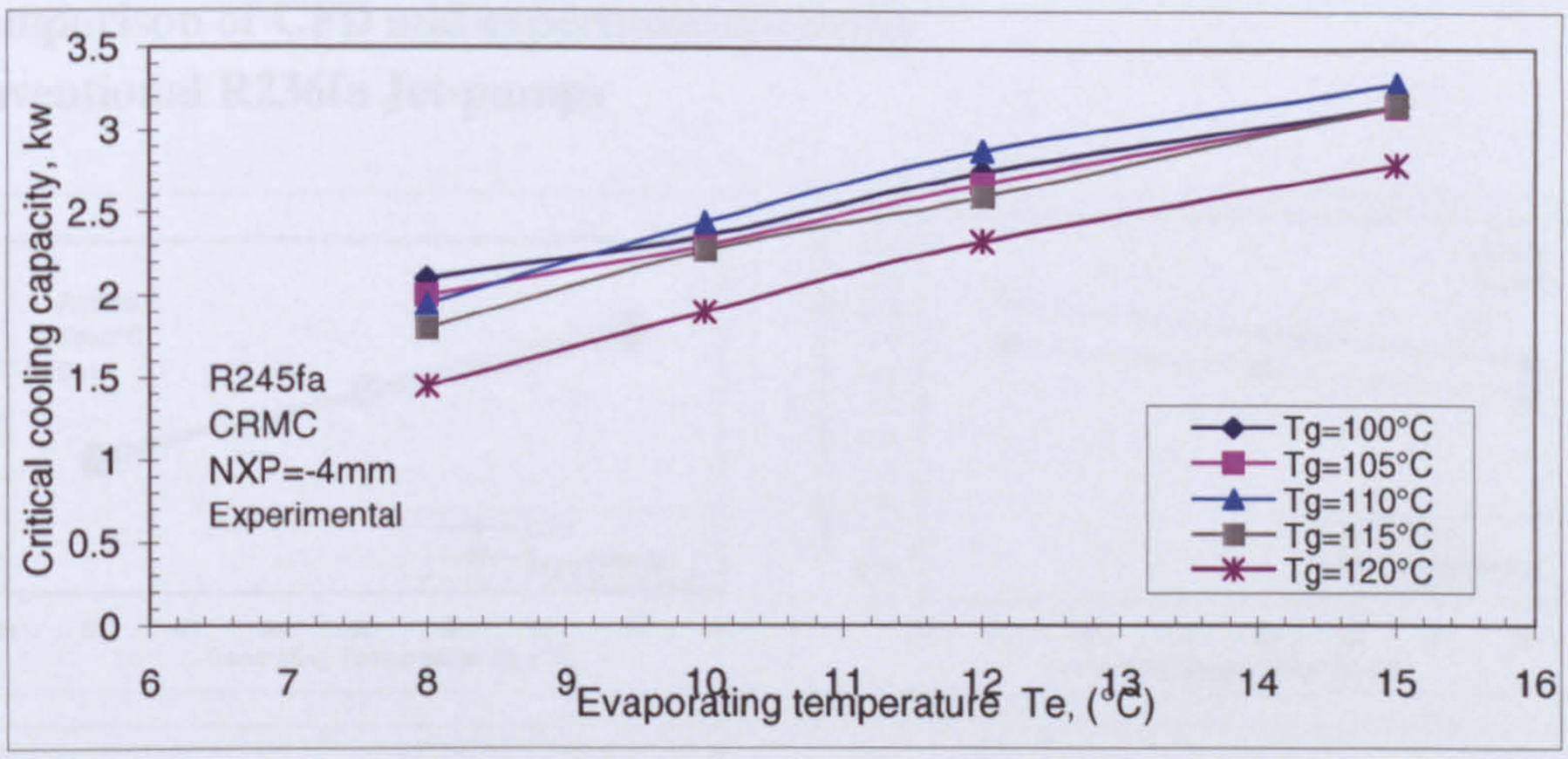

Figure B. 16 Optimized CRMC R245fa jet-pump, cooling capacity (experimental)

C- Comparison of CFD and experimental results

• Conventional R236fa Jet-pumps

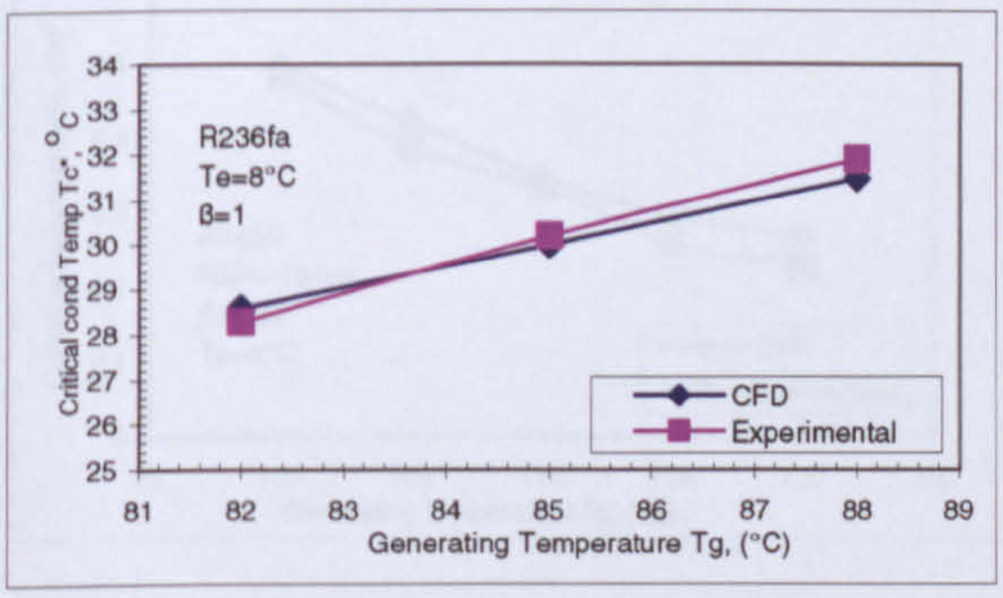

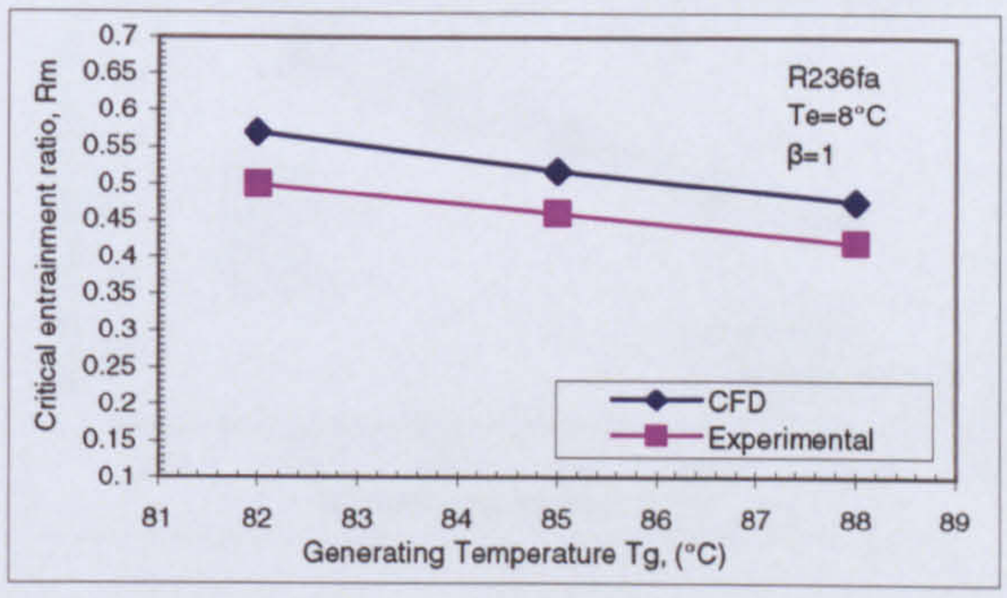

Figure C. 1 Comparison of T_c^* at different T_g and T_e
Conventional R236fa jet-pump

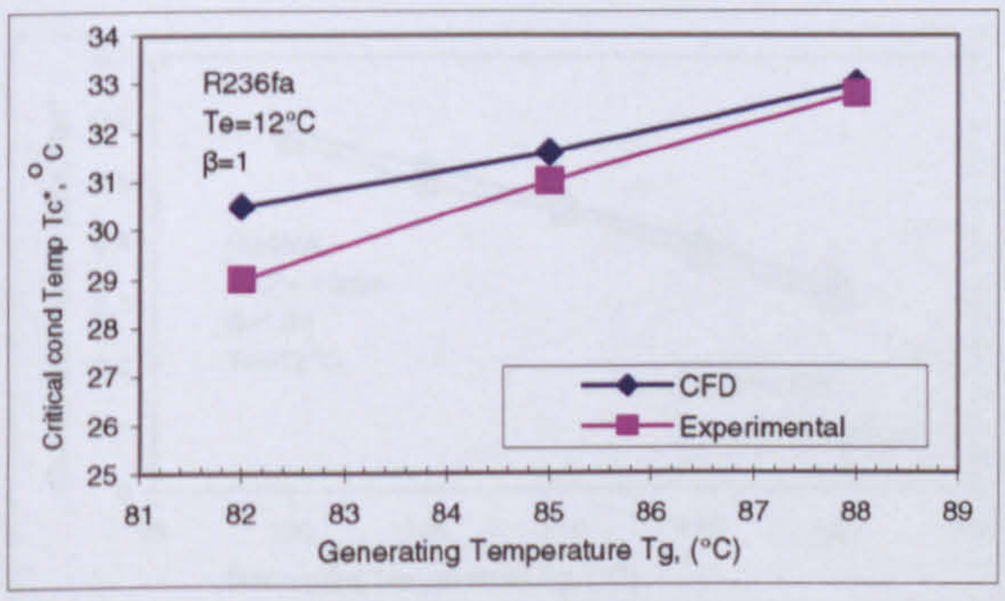

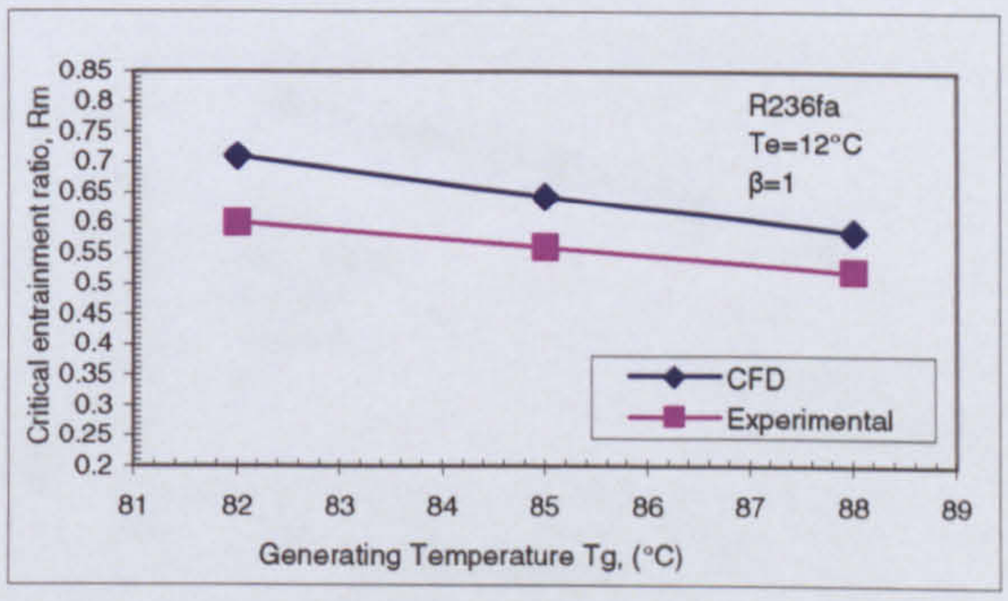

Figure C. 2 Comparison of R_m at different T_g and T_e
Conventional R236fa jet-pump

• Optimized Conventional R236fa Jet-pump

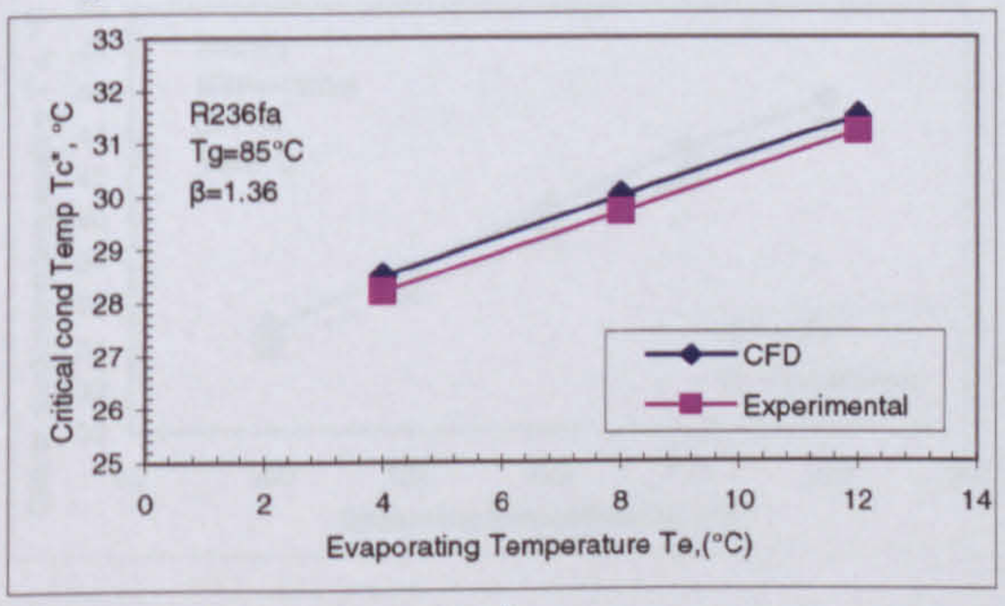

Figure C. 3 Comparison of T_c^* at different T_e (T_g=85°C)
Optimized conventional R236fa jet-pump

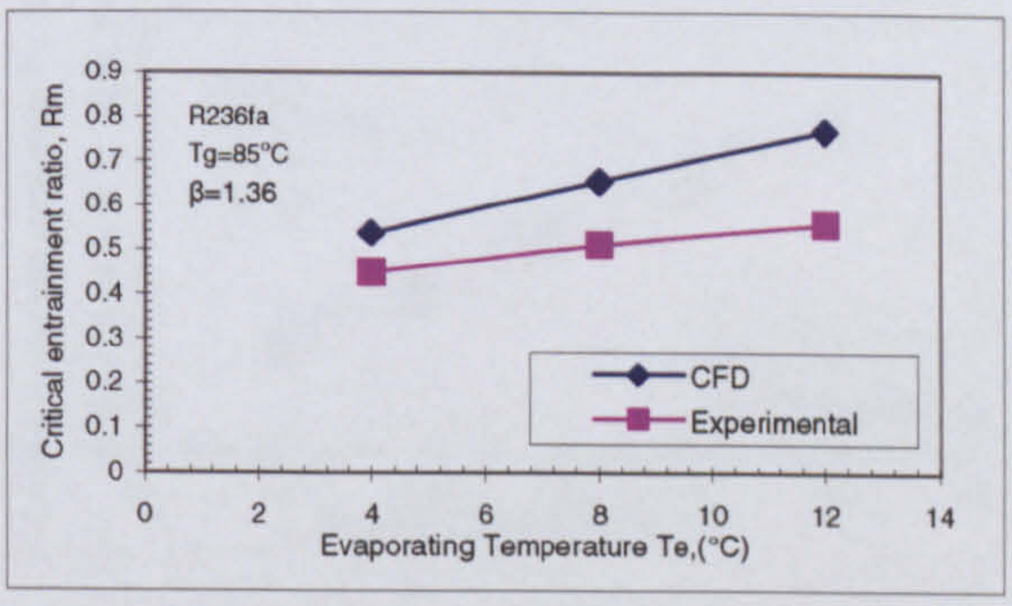

Figure C. 4 Comparison of R_m at different T_e (T_g=85°C)
Optimized conventional R236fa jet-pump

• Optimized CRMC R236fa Jet-pump

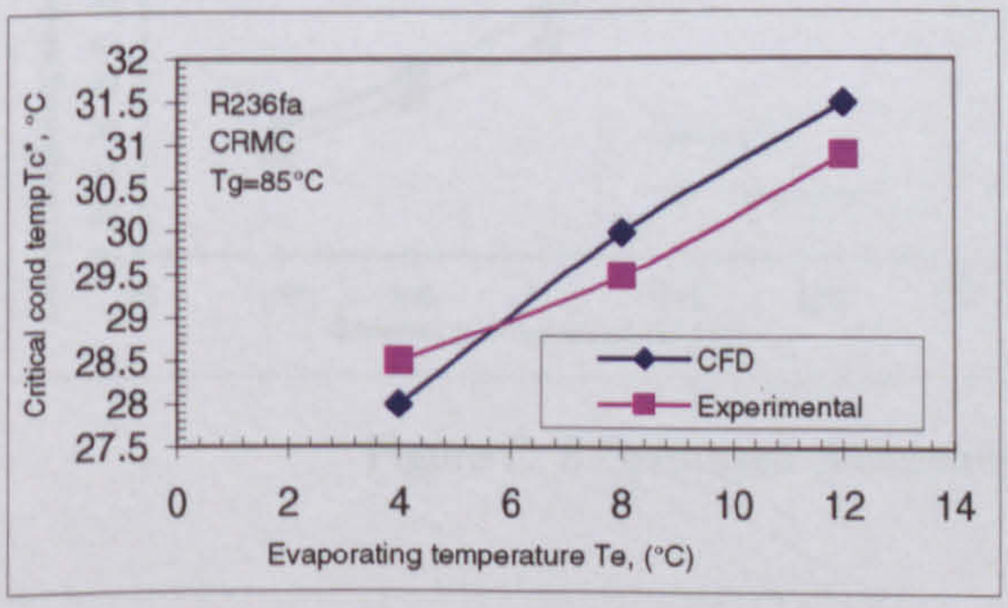

Figure C. 5 Comparison of T_c^* at different T_e (T_g=85°C)
Optimized CRMC R236fa jet-pump

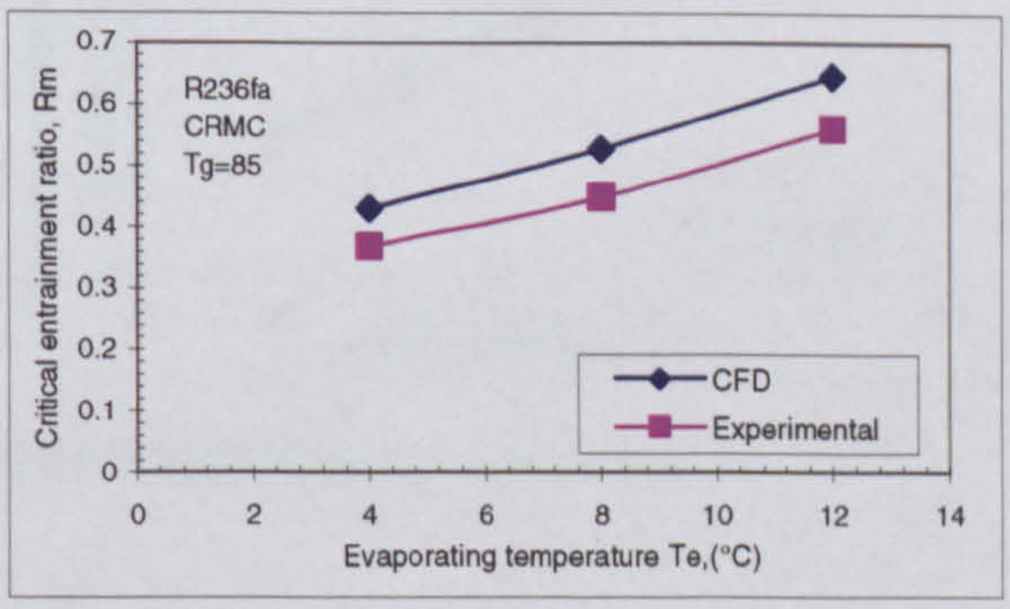

Figure C. 6 Comparison of R_m at different T_e (T_g=85°C)
Optimized CRMC R236fa jet-pump

• Optimized Conventional R245fa Jet-pump

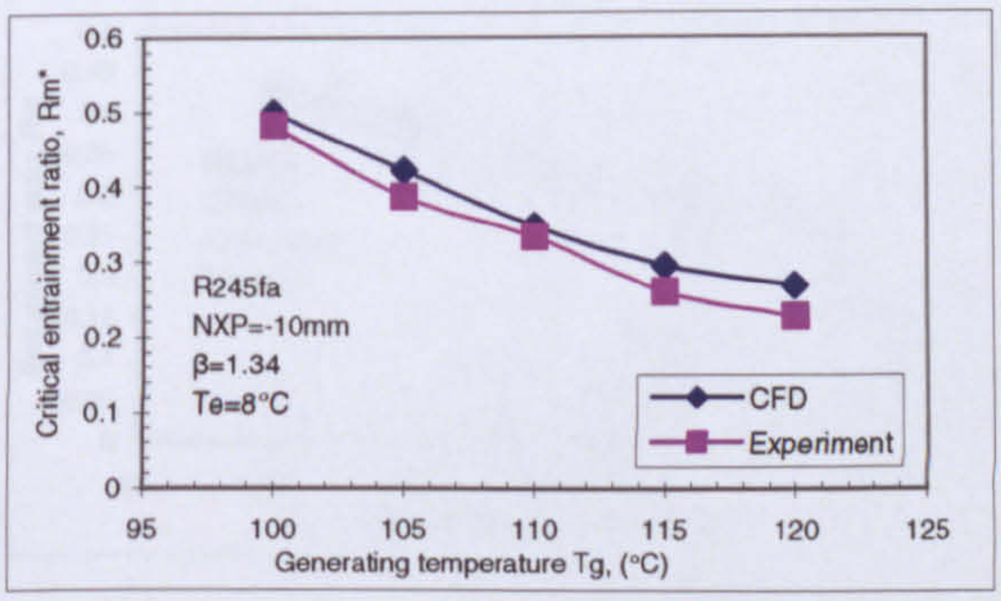

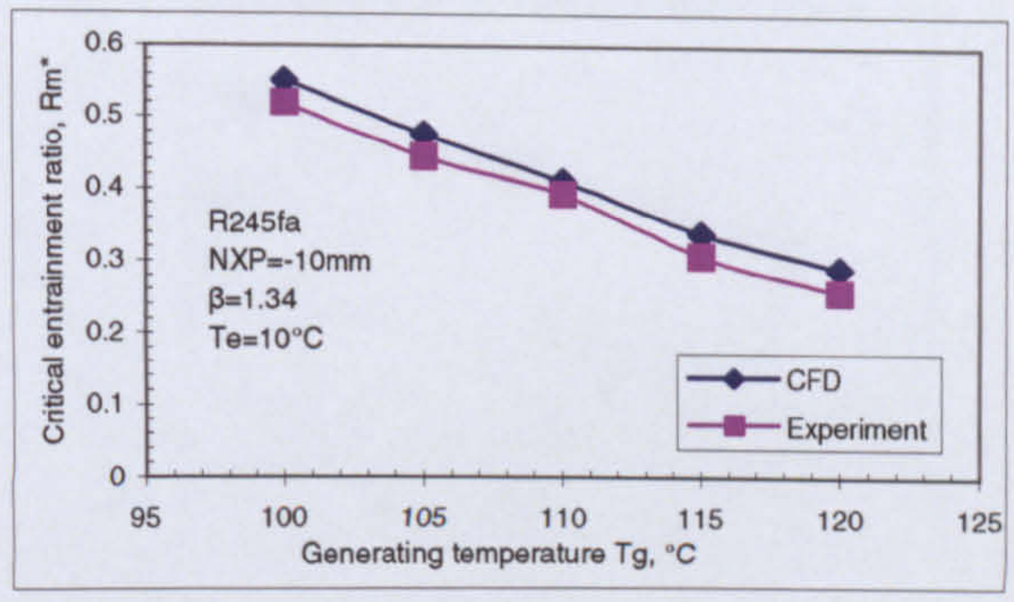

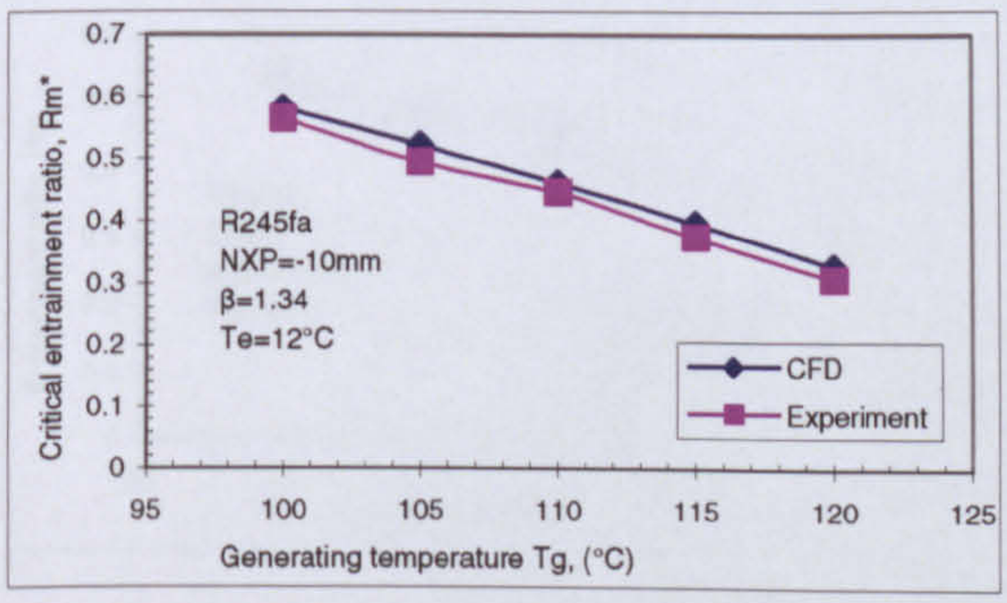

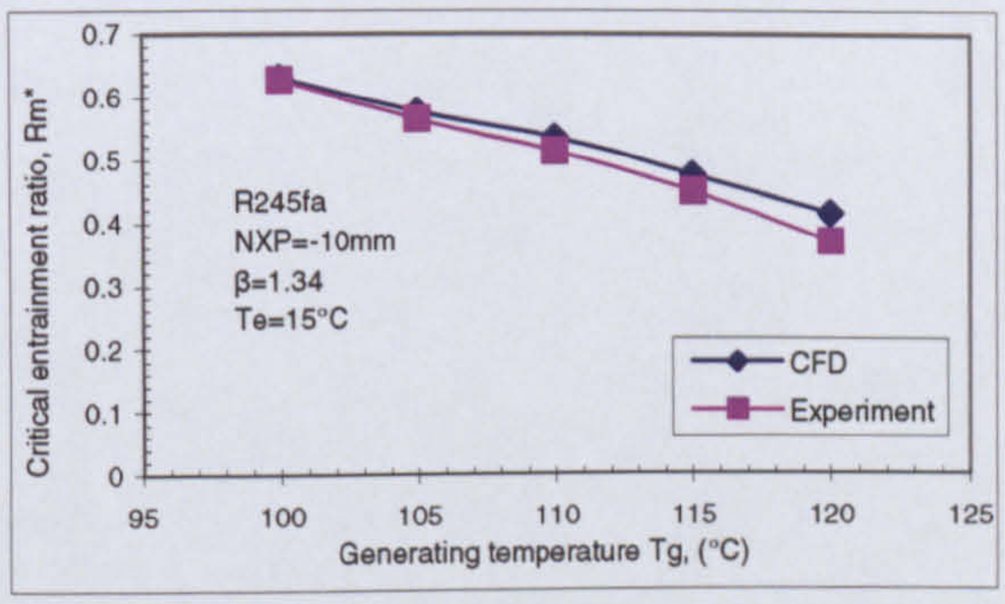

Figure C. 7 Optimized conventional R245fa jet-pump, R_m comparison

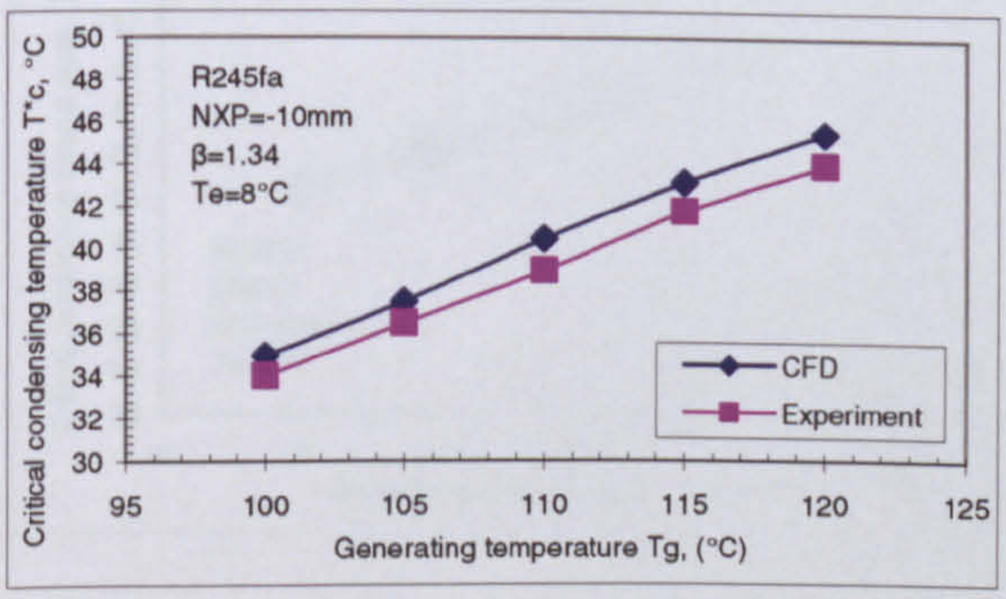

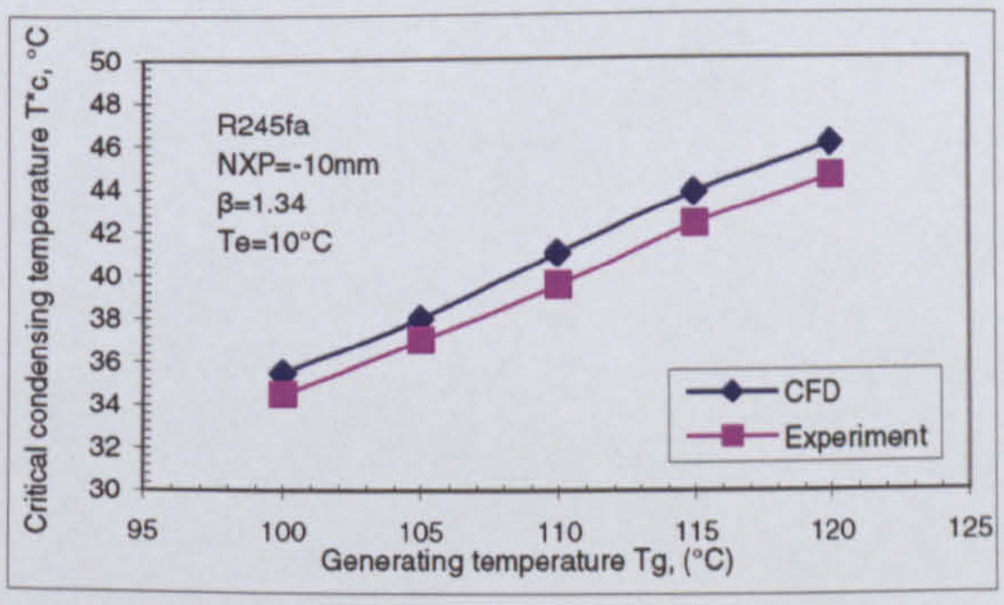

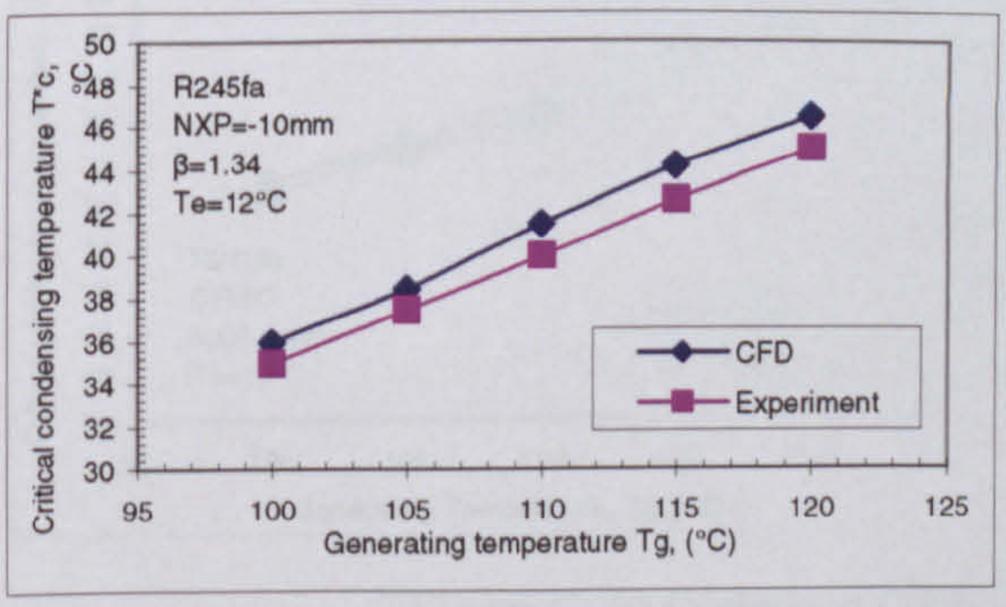

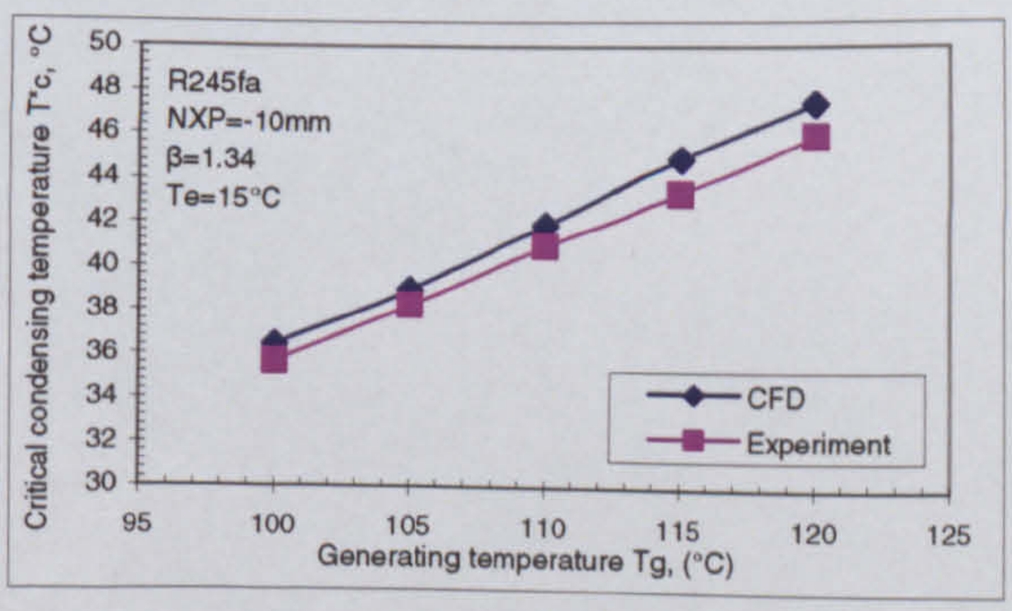

Figure C. 8 Optimized conventional R245fa jet-pump, T_c* comparison

• Optimized CRMC R245fa Jet-pump

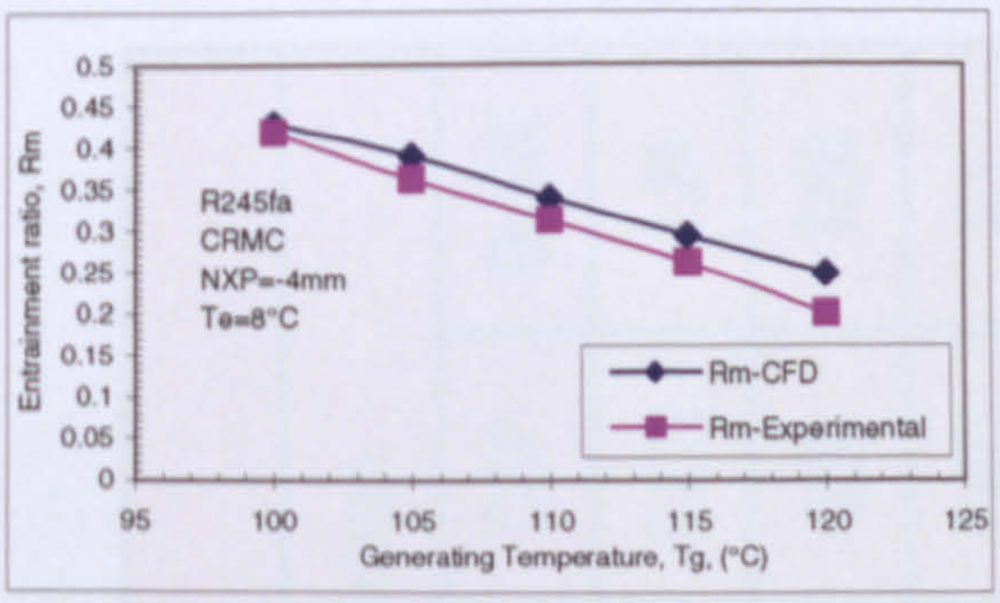

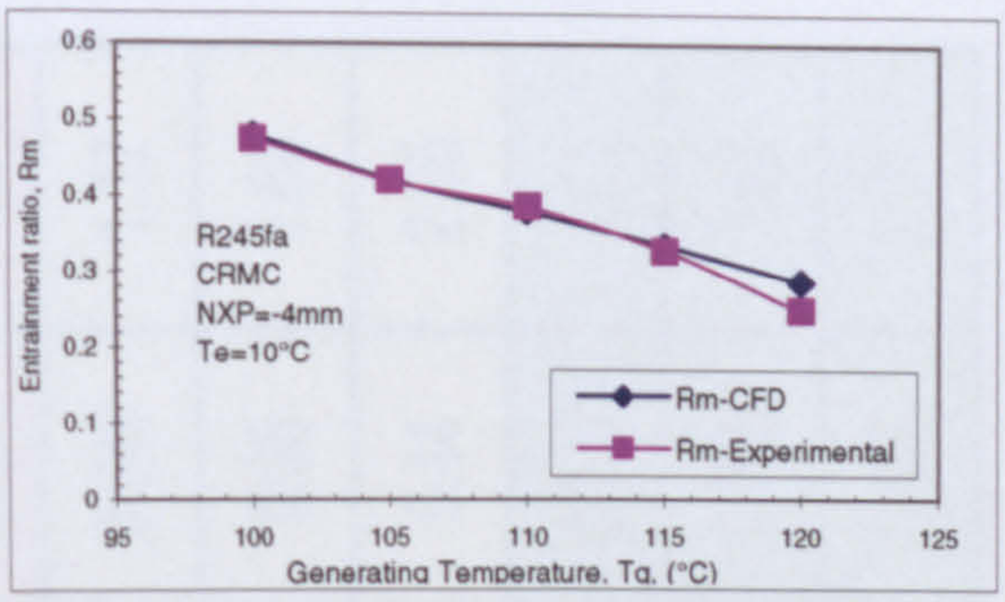

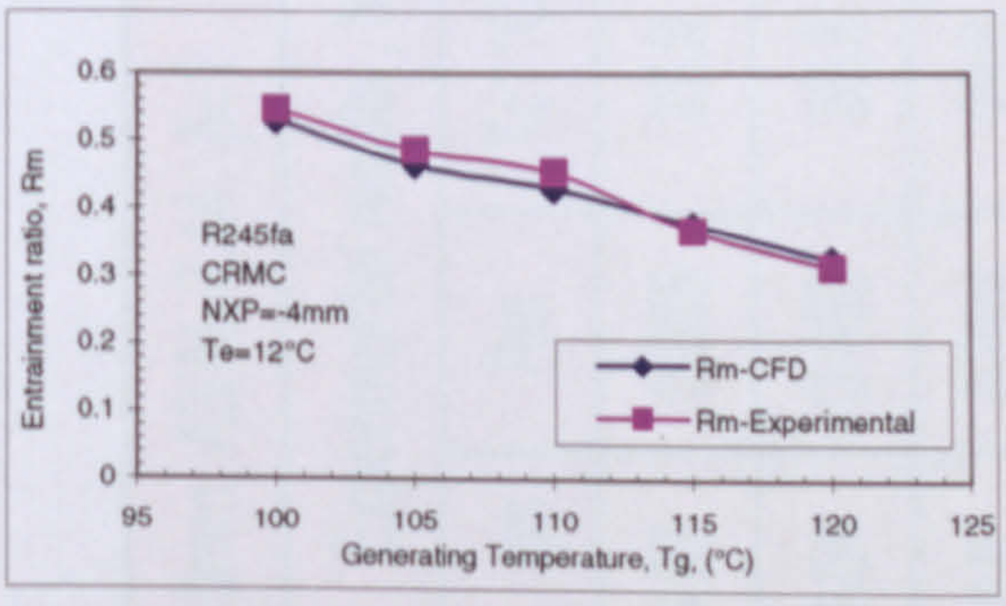

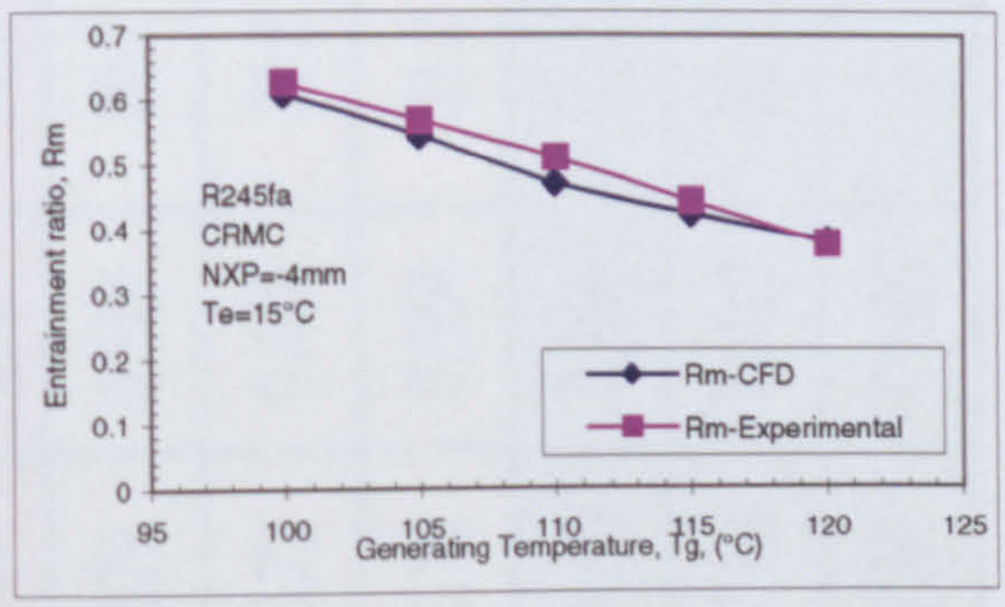

Figure C. 9 Optimized CRMC R245fa jet-pump, R_m comparison

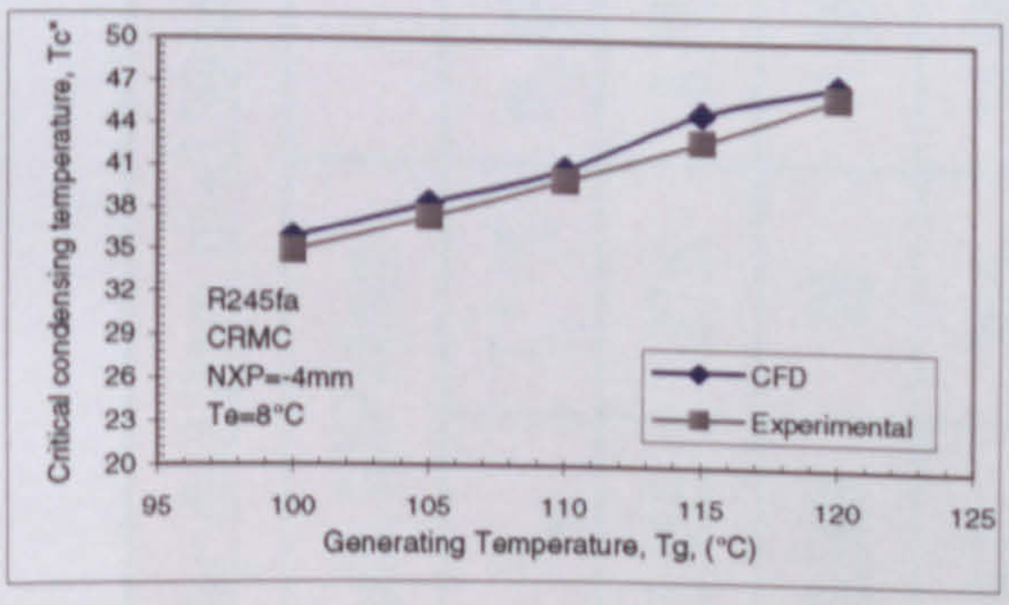

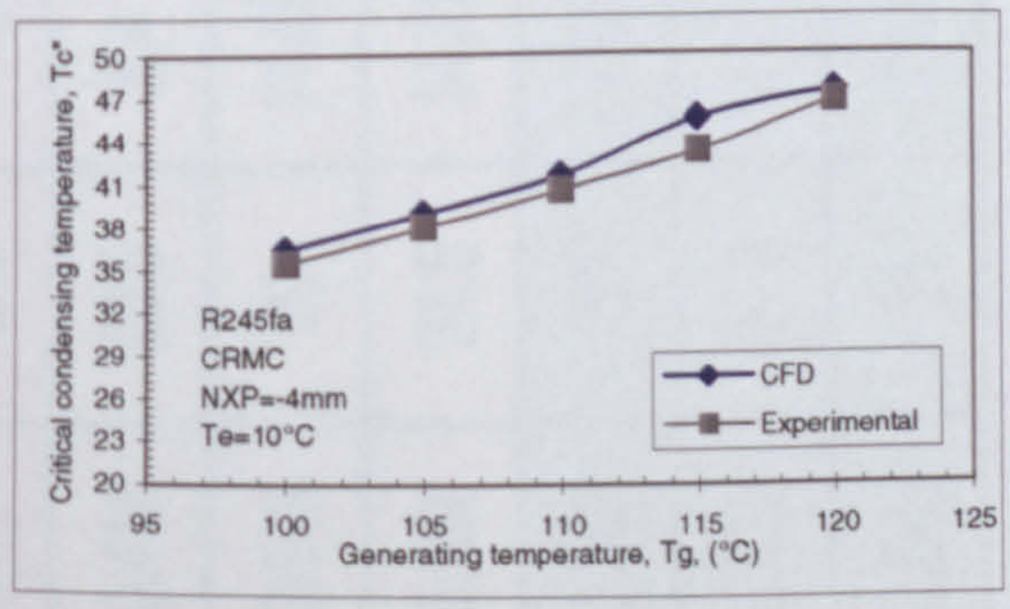

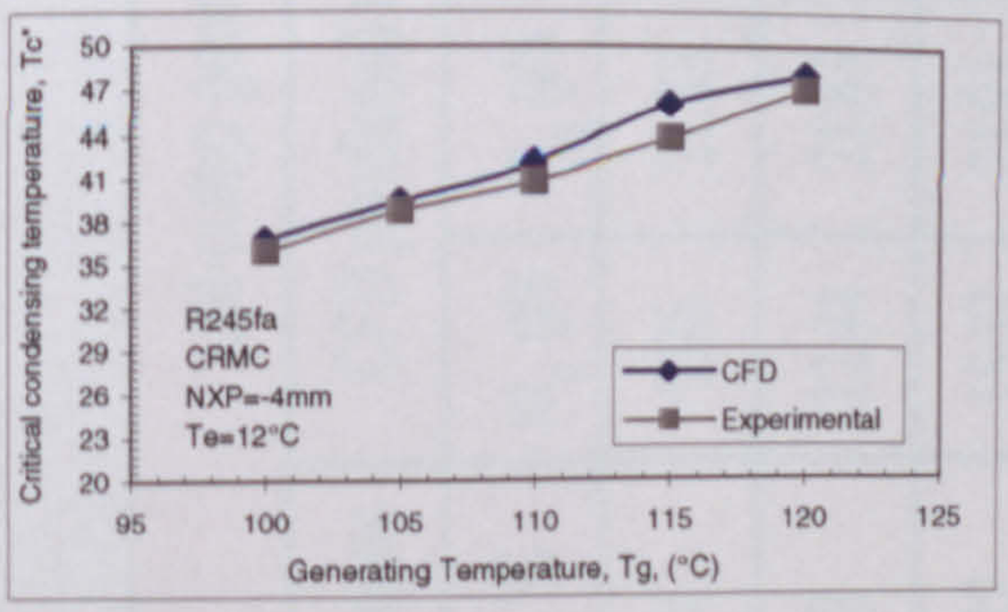

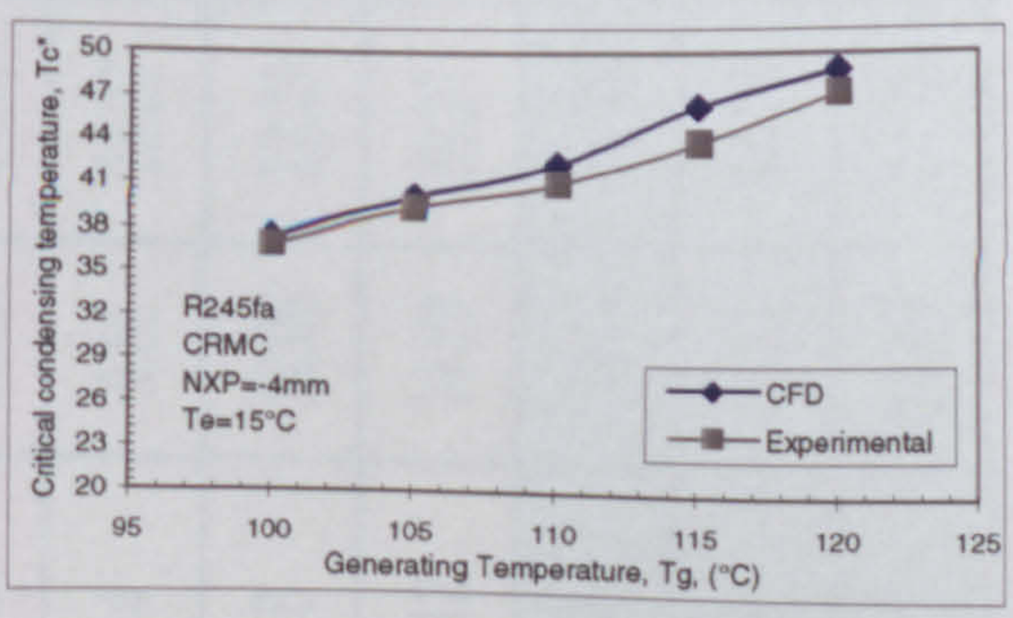

Figure C. 10 Optimized CRMC R245fa jet-pump, T_c* comparison

Jet-pump geometry: dt=2.2mm, d1=3.38mm, d3=6.0mm, A3/At=7.44, β=1											
Operating conditions		CFD predicted results, NXP=4mm				Experimental results , NXP=1mm					
T_g °C	T_e °C	m_s g/s	m_g g/s	R_m	T_c^* °C	m_s g/s	m_g g/s	Rm	Tc* °C	COP	Qe kW
82	4	9.96	21.83	0.456	27.5	8.72	24.57	0.355	27.3	0.276	1.24
82	8	12.44	21.83	0.569	29	11.99	24.54	0.488	28.3	0.38	1.66
82	12	15.52	21.83	0.71	30.5	14.56	24.5	0.594	29.5	0.477	2.1
85	4	9.65	23.27	0.414	28.5	8.4	2579	0.325	29.2	0.247	1.17
85	8	12.08	23.27	0.519	30	11.66	25.79	0.452	30.2	0.36	1.66
85	12	14.99	23.27	0.644	31.5	14.28	25.79	0.554	31.2	0.44	2.05
88	4	9	24.78	0.363	30	7.98	27.86	0.286	31.5	0.217	1.11
88	8	11.81	24.78	0.476	31.5	11.5	27.86	0.412	32.2	0.319	1.63
88	12	14.49	24.78	0.585	33	14.1	27.86	0.506	33	0.397	2.01

Jet-pump geometry: dt=2.2mm, d1=3.38mm, d3=6.0mm, A3/At=7.44, β=1											
Operating conditions		CFD predicted results, NXP=4mm				Experimental results , NXP=1mm					
T_g °C	T_e °C	m_s g/s	m_g g/s	R_m	T_c^* °C	m_s g/s	m_g g/s	Rm	Tc* °C	COP	Qe kW
82	4	9.96	21.83	0.456	27.5	8.72	24.57	0.355	27.3	0.276	1.24
82	8	12.44	21.83	0.569	29	11.99	24.54	0.488	28.3	0.38	1.66
82	12	15.52	21.83	0.71	30.5	14.56	24.5	0.594	29.5	0.477	2.1
85	4	9.65	23.27	0.414	28.5	8.4	2579	0.325	29.2	0.247	1.17
85	8	12.08	23.27	0.519	30	11.66	25.79	0.452	30.2	0.36	1.66
85	12	14.99	23.27	0.644	31.5	14.28	25.79	0.554	31.2	0.44	2.05
88	4	9	24.78	0.363	30	7.98	27.86	0.286	31.5	0.217	1.11
88	8	11.81	24.78	0.476	31.5	11.5	27.86	0.412	32.2	0.319	1.63
88	12	14.49	24.78	0.585	33	14.1	27.86	0.506	33	0.397	2.01

Jet-pump geometry: dt=2.2mm, d1=3.38mm, d3=6.0mm, A3/At=7.44 β=1.36											
Operating conditions		CFD predicted results, NXP=10mm				Experimental results , NXP=7.5mm					
T_g °C	T_e °C	m_s g/s	m_g g/s	R_m	T_c^* °C	m_s g/s	m_g g/s	Rm	Tc* °C	COP	Qe kW
82	4	12.72	21.81	0.58	27.5	/	/	/	/	/	/
82	8	15.23	21.81	0.6983	29	11.55	24.54	0.47	28.8	0.37	1.64
82	12	18.2	21.81	0.835	30.5	/	/	/	/	/	/
85	4	12.49	23.25	0.537	28.5	11.56	25.75	0.45	28.5	0.34	1.62
85	8	15.26	23.25	0.657	30	13.18	25.75	0.512	29.5	0.398	1.87
85	12	17.94	23.25	0.772	31.5	13.97	25.75	0.543	31.2	0.42	2
88	4	11.96	24.75	0.483	30	/	/	/	/	/	/
88	8	14.88	24.75	0.6	31.5	11.55	27.79	0.415	31.5	0.32	1.63
88	12	17.66	24.75	0.713	33	/	/	/	/	/	/

Jet-pump geometry dt=2.6mm, d1=5.2mm, d3 =7.6mm, β=1.34											
Operating conditions		CFD results , NXP=-10mm				Experimental results, NXP=-10mm					
T_g °C	T_e °C	m_s g/s	m_g g/s	R_m	T_c^* °C	m_s g/s	m_g g/s	Rm	Tc* °C	COP	Qe kW
100	8	13.115	26.204	0.5	35	13.25	27.47	0.482	34	0.358	2.45
100	10	14.436	26.204	0.55	35.5	14.25	27.47	0.518	34.5	0.384	2.6
100	12	15.265	26.204	0.58	36	15.5	27.47	0.564	35	0.42	2.82
100	15	16.554	26.204	0.63	36.5	17.25	27.47	0.628	35.7	0.475	3.15
105	8	12.611	29.825	0.42	37.5	11.75	30.34	0.387	36.5	0.283	2.14
105	10	14.202	29.825	0.47	38	13.5	30.34	0.445	37	0.33	2.5
105	12	15.586	29.825	0.52	38.5	15	30.34	0.494	37.5	0.369	2.8
105	15	17.202	29.825	0.57	39	17.125	30.34	0.564	38.3	0.42	3.2
110	8	11.499	32.946	0.35	40.5	11.25	33.62	0.334	39	0.244	2
110	10	13.577	32.946	0.41	41	13.25	33.62	0.394	39.5	0.288	2.4
110	12	15.223	32.946	0.46	41.5	15	33.62	0.446	40	0.325	2.75
110	15	17.665	32.946	0.53	42	17.25	33.62	0.513	41	0.38	3.2
115	8	10.757	36.311	0.29	43.5	9.75	37.31	0.261	42	0.189	1.8
115	10	12.349	36.311	0.34	44	11.5	37.31	0.308	42.5	0.224	2.16
115	12	14.425	36.311	0.39	44.5	14	37.31	0.375	42.8	0.274	2.65
115	15	17.272	36.311	0.47	45	16.75	37.31	0.449	43.4	0.33	3.18
120	8	10.758	39.926	0.27	45.5	9.25	40.59	0.228	44	0.162	1.68
120	10	11.667	39.926	0.29	46	10.5	40.59	0.258	44.5	0.186	1.9
120	12	13.115	39.926	0.328	46.5	12.5	40.59	0.308	45	0.223	2.3
120	15	16.572	39.926	0.415	47.5	15	40.59	0.369	46	0.267	2.7

Jet-pump geometry dt=2.6mm, d1=5.2mm, d3 =7.6mm, β=1.34											
Operating conditions		CFD results , NXP=-10mm				Experimental results, NXP=-10mm					
T_g °C	T_e °C	m_s g/s	m_g g/s	R_m	T_c* °C	m_s g/s	m_g g/s	Rm	Tc* °C	COP	Qe kW
100	8	13.115	26.204	0.5	35	13.25	27.47	0.482	34	0.358	2.45
100	10	14.436	26.204	0.55	35.5	14.25	27.47	0.518	34.5	0.384	2.6
100	12	15.265	26.204	0.58	36	15.5	27.47	0.564	35	0.42	2.82
100	15	16.554	26.204	0.63	36.5	17.25	27.47	0.628	35.7	0.475	3.15
105	8	12.611	29.825	0.42	37.5	11.75	30.34	0.387	36.5	0.283	2.14
105	10	14.202	29.825	0.47	38	13.5	30.34	0.445	37	0.33	2.5
105	12	15.586	29.825	0.52	38.5	15	30.34	0.494	37.5	0.369	2.8
105	15	17.202	29.825	0.57	39	17.125	30.34	0.564	38.3	0.42	3.2
110	8	11.499	32.946	0.35	40.5	11.25	33.62	0.334	39	0.244	2
110	10	13.577	32.946	0.41	41	13.25	33.62	0.394	39.5	0.288	2.4
110	12	15.223	32.946	0.46	41.5	15	33.62	0.446	40	0.325	2.75
110	15	17.665	32.946	0.53	42	17.25	33.62	0.513	41	0.38	3.2
115	8	10.757	36.311	0.29	43.5	9.75	37.31	0.261	42	0.189	1.8
115	10	12.349	36.311	0.34	44	11.5	37.31	0.308	42.5	0.224	2.16
115	12	14.425	36.311	0.39	44.5	14	37.31	0.375	42.8	0.274	2.65
115	15	17.272	36.311	0.47	45	16.75	37.31	0.449	43.4	0.33	3.18
120	8	10.758	39.926	0.27	45.5	9.25	40.59	0.228	44	0.162	1.68
120	10	11.667	39.926	0.29	46	10.5	40.59	0.258	44.5	0.186	1.9
120	12	13.115	39.926	0.328	46.5	12.5	40.59	0.308	45	0.223	2.3
120	15	16.572	39.926	0.415	47.5	15	40.59	0.369	46	0.267	2.7